AD-A240 915

PROCEEDINGS OF THE SECOND
INTERNATIONAL SYMPOSIUM ON

# DIAMOND MATERIALS

Edited by

A J Purdes
Texas Instruments Inc
Dallas, Texas

B M Meyerson
IBM T J Watson Research Center
Yorktown Heights, New York

J C Angus
Case Western Reserve University
Cleveland, Ohio

K E Spear
Pennsylvania State University
University Park, Pennsylvania

R F Davis
North Carolina State University
Raleigh, North Carolina

M Yoder
Office of Naval Research
Arlington, Virginia

DISTRIBUTION STATEMENT A
Approved for public release;
Distribution Unlimited

DTIC
ELECTE
SEP 17 1991
S D
C

*DIELECTRIC SCIENCE AND TECHNOLOGY ELECTRONICS AND HIGH TEMPERATURE MATERIALS DIVISIONS*

Proceedings Volume 91-8

THE ELECTROCHEMICAL SOCIETY INC 10 South Main St Pennington, NJ 08534-2896

SECURITY CLASSIFICATION OF THIS PAGE

# REPORT DOCUMENTATION PAGE

Form Approved
OMB No 0704-0188

| | |
|---|---|
| 1a REPORT SECURITY CLASSIFICATION: (U) | 1b RESTRICTIVE MARKINGS: NA |
| 2a SECURITY CLASSIFICATION AUTHORITY: NA | 3 DISTRIBUTION/AVAILABILITY OF REPORT: Distribution Unlimited |
| 2b DECLASSIFICATION/DOWNGRADING SCHEDULE: NA | |
| 4 PERFORMING ORGANIZATION REPORT NUMBER(S): The Electrochemical Society, Inc. | 5 MONITORING ORGANIZATION REPORT NUMBER(S): NA |
| 6a NAME OF PERFORMING ORGANIZATION: The Electrochemical Society, Inc. / 6b OFFICE SYMBOL (If applicable): NA | 7a NAME OF MONITORING ORGANIZATION: Office of Naval Research |
| 6c ADDRESS (City, State, and ZIP Code): Pennington, New Jersey 08534-2896 | 7b ADDRESS (City, State, and ZIP Code): 33 Third Avenue, New York, NY 10003-9998 |
| 8a NAME OF FUNDING/SPONSORING ORGANIZATION: Office of Naval Research / 8b OFFICE SYMBOL (If applicable): 1114SS | 9 PROCUREMENT INSTRUMENT IDENTIFICATION NUMBER: N0014-91-J-1419 |
| 8c ADDRESS (City, State, and ZIP Code): 800 North Quincy St., Arlington, VA. 22217-5000 | 10 SOURCE OF FUNDING NUMBERS: PROGRAM ELEMENT NO: / PROJECT NO: 414s010---01 / TASK NO: / WORK UNIT ACCESSION NO: |

11 TITLE (Include Security Classification)

Second International Symposium on Dimond Materials

12 PERSONAL AUTHOR(S)

A. J. Purdes

| 13a TYPE OF REPORT | 13b TIME COVERED | 14 DATE OF REPORT (Year, Month, Day) | 15 PAGE COUNT |
|---|---|---|---|
| Annual | FROM 5/91 TO 4/92 | 91/9/5 | |

16 SUPPLEMENTARY NOTATION

| 17 COSATI CODES | | | 18 SUBJECT TERMS (Continue on reverse if necessary and identify by block number) |
|---|---|---|---|
| FIELD | GROUP | SUB-GROUP | Diamond Materials |
| | | | |
| | | | |

19 ABSTRACT (Continue on reverse if necessary and identify by block number)

This symposium will address all aspects of diamond materials science and technology from growth fundamentals to applications. Both invited and contributed papers will be included. Contributed papers are solicited on the following topics: (1) synthesis techniques; (2) vapor phase diagnostics; (3) nucleation and crystal growth; (4) microstructural characterization and local atomic order; (5) mechancial behavior; (6) optical properties; (7) electronic properties; and (8) manufacturing issues. Papers on appropriate related topics are also welcome.

91-10696



| 20 DISTRIBUTION/AVAILABILITY OF ABSTRACT | 21 ABSTRACT SECURITY CLASSIFICATION |
|---|---|
| ☒ UNCLASSIFIED/UNLIMITED ☐ SAME AS RPT ☐ DTIC USERS | Unclassified |
| 22a NAME OF RESPONSIBLE INDIVIDUAL: Max Yoder | 22b TELEPHONE (Include Area Code): 703 696-4218 / 22c OFFICE SYMBOL: 1114SS |

DD Form 1473, JUN 86 — Previous editions are obsolete — SECURITY CLASSIFICATION OF THIS PAGE

PROCEEDINGS OF THE SECOND
INTERNATIONAL SYMPOSIUM ON

# ••• DIAMOND MATERIALS •••

Edited by


A. J. Purdes
Texas Instruments Inc.
Dallas, Texas

B. M. Meyerson
IBM T. J. Watson Research Center
Yorktown Heights, New York

J. C. Angus
Case Western Reserve University
Cleveland, Ohio

K. E. Spear
Pennsylvania State University
University Park, Pennsylvania

R. F. Davis
North Carolina State University
Raleigh, North Carolina

M. Yoder
Office of Naval Research
Arlington, Virginia



Accession For
NTIS GRA&I ☑
DTIC Tab ☐
Unannounced ☐
Justification
By
Distribution/
Availability Codes
Dist | Avail and/or Special
A-1






*DIELECTRIC SCIENCE AND TECHNOLOGY, ELECTRONICS, AND HIGH TEMPERATURE MATERIALS DIVISIONS*

Proceedings Volume 91-8

THE ELECTROCHEMICAL SOCIETY, INC., 10 South Main St., Pennington, NJ 08534-2896

Copyright 1991
by
The Electrochemical Society, Incorporated

***Papers contained herein may not be reprinted and may not be digested by publications other than those of The Electrochemical Society in excess of 1/6 of the material presented.***

This work relates to Department of Navy Grant N00014-91-J-1419 issued by the Office of Naval Research. The United States Government has a royalty-free license throughout the world in all copyrightable material contained herein.

Library of Congress Catalog Number: 91-174037
Printed in the United States of America

# PREFACE

The **Second International Symposium on Diamond Materials** was held as part of the 179th Meeting of The Electrochemical Society in Washington, DC, May 5-10, 1991.

In recognition of the growing worldwide interest in CVD diamond science and technology, the objective of The Electrochemical Society was to provide an international forum for the presentation and discussion of recent research and development in this field. The following Symposium Organizers from the U.S.A., Europe, and Japan were responsible for inviting internationally recognized diamond workers, soliciting contributed papers, planning, and chairing Symposium sessions.

**U.S.A.**

| | |
|---|---|
| A. J. Purdes | Texas Instruments Inc., MS 147, P.O. Box 655936, Dallas, TX 75265 |
| J. C. Angus | Chemical Engineering Department, Case Western Reserve University, Cleveland, OH 44106 |
| R. F. Davis | Department of Materials Science and Engineering, North Carolina State University, Raleigh, NC 27695 |
| B. M. Meyerson | IBM T. J. Watson Research Center, P. O. Box 218, Yorktown Heights, NY 10598 |
| T. D. Moustakas | College of Engineering, Boston University, 44 Cummington St, Boston, MA 02215 |
| K. V. Ravi | Lockheed Missles and Space Co., Res. and Dev. Division Org. 93/10 B204, 3251 Hanover St., Palo Alto, CA 94304 |
| K. E. Spear | Department of Materials Science and Engineering, The Pennsylvania State University, University Park, PA 16802 |
| M. Yoder | ONR Code 1114, Office of Naval Research, Arlington, VA 22217 |

**Europe**

| | |
|---|---|
| P. Koidl | Fraunhofer-Institut fur angewandte Festkorperphysik, Eckerstrasse 4, D-7800, Freiburg, Germany |
| B. Lux | Technical University of Austria, Getreidemarkt 9, A-1060 Wein, Austria |

**Japan**

| | |
|---|---|
| N. Setaka | National Institute for Research in Inorganic Materials, 1-1 Namiki, Tsukuba, Ibaraki 305, Japan |
| S. Yazu | Itami Research Laboratories, Sumitomo Electric Industries Ltd., 1-1-1, Koyakita, Itami, Hyogo 664, Japan |

This **Proceedings Volume** contains 76 of the 92 papers which were presented at the Washington, D.C. meeting in May 1991. Due to an anticipated strong continuing interest in CVD diamond, the Dielectric Science and Technology, Electronics, and High Temperature Materials Divisions of The Electrochemical Society have planned future diamond symposia on a 2-year schedule.

The **Third International Symposium on Diamond Materials** will be held in Honolulu, Hawaii, May 16-21, 1993. This symposium will be part of the 183rd Electrochemical Society Meeting, to be held in cooperation with the Japanese Society of Applied Physics and The Japanese Electrochemical Society. The **Call for Papers** for this symposium is shown on the following page.

ANNOUNCEMENT AND CALL FOR PAPERS

# Third International Symposium on Diamond Materials

May 16-21, 1993
Honolulu, Hawaii

The Third International Symposium on Diamond Materials will be held in Honolulu, Hawaii during May 16-21, 1993 as part of the 183rd Meeting of The Electrochemical Society, Inc. The Symposium is co-sponsored by The Electrochemical Society of Japan with cooperation of the Japanese Society of Applied Physics. The three organizing divisions of The Electrochemical Society are: Dielectric Science and Technology, Electronics, and High Temperature Materials.

The Symposium objective is to provide an international forum for the presentation and discussion of recent developments in the science, process technology, and applications of diamond and related materials. The following is a partial list of topics to be addressed:

Fundamental Principles Related to Diamond Synthesis:
- Theoretical modeling and measurements of gas and surface chemistry, thermochemistry, kinetics, mass and energy transport, and fluid dynamics.
- Mechanisms of nucleation and renucleation, growth, and partial equilibrium.
- Influence of gaseous species or transport processes on mechanisms, rates, and deposit quality.

Experimental Approaches and Control:
- Single crystal growth, homo- and hetero-epitaxy.
- Polycrystalline microstructure control.
- Advanced in situ characterization for diagnostics and control.
- Unique growth and activation methods.

Properties and Applications:
- Physical, chemical, and mechanical behavior
- Electrical and electronic devices, thermal characteristics, optical, optoelectronics, and tribology.

Manufacturing:
- Scaleup, product uniformity, reliability, and yield.

Continued on reverse.

Call for Papers continued.

As in preceding symposia in this series, a Symposium Proceedings volume will be published and will include invited and contributed papers. Contributed papers will include both oral and poster presentations. All authors must strictly meet the following deadlines:

Oct. 31, 1992: 75-word abstract and extended abstract due to:
(i) The Electrochemical Society Headquarters, with copies sent to:
(ii) K.E. Spear (addresses for both given below).

Feb. 1, 1993: Authors meeting above abstract deadline will be sent instructions for proceedings volume manuscripts.

April 1, 1993: Camera-ready manuscripts completed according to instructions due to K.E Spear.

Symposium inquiries and suggestions for invited speakers and special session topics should be sent to any of the following three ECS conference organizers:

K.E. Spear
201 Steidle Bldg
Penn State University,
University Park, PA 16802
Tel: (814) 865-4992 FAX: (814) 865-2917

J. P. Dismukes
Exxon Research and Engineering Co.
Annandale, NJ 08801
Tel: (908) 730-2997 FAX: (908) 730-3042

K.V. Ravi
Lockheed Missiles and Space Co.
R&D Org.
93/10 - B204
Palo Alto, CA 94304
Tel: (415) 424-2588 FAX: (415) 354-5795

Address for sending abstracts and for information on program and accommodations: The Electrochemical Society, Inc., 10 South Main Street, Pennington, NJ 08534-2896 U.S.A.

## CONTENTS


| | | PAGE |
|---|---|---|
| | PREFACE | iii |
| | **PART I: SYNTHESIS** | |
| * | DIAMOND GROWTH WITH THERMAL ACTIVATION OF CARBON-HYDROGEN-HALOGEN SYSTEMS AND GROWTH ENHANCEMENT WITH THE ADDITION OF OXYGEN<br>D. Patterson, C.J. Chu, B.J. Bai, Z.L. Xiao, N.J. Komplin, R.H. Hauge, & J. L. Margrave | 3 |
| | $F_2$-$CH_4$ AND $H_2$-$CF_4$ GAS INTERACTIONS ACROSS A HEATED GRAPHITE ELEMENT<br>R. A. Rudder, R.E. Thomas, G.C. Hudson, M.J. Mantini & R.J. Markunas | 12 |
| * | DIAMOND SYNTHESIZED BY THE MICROWAVE PLASMA CVD METHOD<br>M. Kamo & Y. Sato | 20 |
| | ALTERNATING CHEMISTRY SYNTHESIS OF DIAMOND<br>K.V. Ravi | 31 |
| | SYNTHESIS OF DIAMOND FILMS WITH PULSED PLASMAS<br>M. Aklufi & D. Brock | 39 |
| | MINIMIZATION OF INFRARED ABSORPTION OF FLAME DEPOSITED DIAMOND FILMS BY SEQUENTIAL DEPOSITION AND ETCHING PROCESSES<br>Y. Tzeng & R. Phillips | 49 |
| | PARAMETRIC STUDY OF DIAMOND FILM DEPOSITION IN A RADIO-FREQUENCY THERMAL PLASMA<br>C. Li, Y.C. Lau, & S.L. Girshick | 57 |
| | LASER PLASMA DEPOSITION OF DIAMONDLIKE CARBON FILMS IN VACUUM AND HYDROGEN AMBIENTS<br>A. Rengan, J.L. Park, J. Narayan, & J. Hunn | 65 |
| | HFCVD OF DIAMOND ON COPPER SUBSTRATE<br>X.K. Chen, G. Matera, S. Pramanick, & J. Narayan | 73 |
| | HIGH RATE HOMOEPITAXIAL SYNTHESIS OF DIAMOND IN A FLAME<br>K.A. Snail, J.A. Freitas, C.L. Vold, & L.M. Hanssen | 81 |


*Invited Paper

GROWTH OF HIGH QUALITY DIAMOND FILMS IN A TURBULENT FLAME 91
K.A. Snail, C.J Craigie, R.G. Vardiman, C.M. Marks, & J.A. Freitas, Jr.

HIGH RATE HOMOEPITAXIAL GROWTH OF DIAMOND IN THERMAL PLASMA 99
Z.P. Lu, K. Snail, C. Marks, J. Heberlein, & E. Pfender

EFFECTS OF PROCESS PARAMETERS ON CHEMICAL VAPOR DEPOSITION OF DIAMOND IN THERMAL PLASMAS 107
Z.P. Lu, L. Stachowicz, J. Heberlein, & E. Pfender

HIGH RATE DEPOSITION OF DIAMOND USING LIQUID ORGANIC PRECURSORS IN ATMOSPHERIC PLASMAS 115
Q.Y. Han, T.W. Or, Z.P. Lu, J. Heberlein, & E. Pfender

## PART II: GROWTH MECHANISMS

* NUCLEATION AND GROWTH PROCESSES IN CHEMICAL VAPOR DEPOSITION OF DIAMOND 125
J.C. Angus, Z. Li, M. Sunkara, R. Gat, A.B. Anderson, S.P. Mehandru, & M.W. Geis

* MOLECULAR PROCESSES IN DIAMOND FORMATION 142
M. Frenklach

* MOLECULAR BEAM EPITAXY OF DIAMOND WITH CARBON ATOMS $^{1}D$: A THEORETICAL EXPERIMENT BASED ON QUANTUM CHEMISTRY 154
M. Tsuda, S. Oikawa, C. Sekine, & S. Furukawa

GROWTH FROM ACETYLENE ON THE DIAMOND (110) SURFACE 170
D.N. Belton & S. J. Harris

NEGATIVE ION MASS SPECTROMETRY IN A FILAMENT ASSISTED CVD DIAMOND GROWTH APARATUS 181
P.A. Sullivan, F.P. Doty, J.W. Boring, W.A. Jesser, & R.A. Baragiola

THERMAL DESORPTION FROM HYDROGENATED DIAMOND (100) SURFACES 186
R.E. Thomas, R.A. Rudder, & R.J. Markunas

*Invited Paper

GAS PHASE CHEMISTRY IN DIAMOND-DEPOSITING dc-ARC-JET 194
G.P. Smith & J.B. Jeffries

OBSERVATION OF OH RADICALS IN A FILAMENT-ASSISTED DIAMOND GROWTH ENVIRONMENT 202
U.E. Meier, L.E. Hunziker, D.R. Crosley, & J.B. Jeffries

ACETYLENE PRODUCTION IN A DIAMOND-PRODUCING LOW PRESSURE rf-PLASMA ASSISTED CHEMICAL VAPOR DEPOSITION ENVIRONMENT 209
R.A. Rudder, G.C. Hudson, J. B. Posthill, R.E. Thomas, R. J. Markunas, R.J. Nemanich, Y.M. LeGrice & T.P. Humphreys

QUANTITITVE ANALYSIS OF THE GASEOUS COMPOSITION DURING FILAMENT-ASSISTED DIAMOND GROWTH 217
W.L. Hsu

* TEXTURED GROWTH AND TWINNING IN POLYCRYSTALLINE CVD DIAMOND FILMS 224
C. Wild, P. Koidl, N. Herres, W. Muller-Sebert, & T. Eckermann

AGGREGATE PROCESS MODEL OF DIAMOND FILM GROWTH 240
A.K. Miller & K.V. Ravi

THE EFFECT OF GAS-PHASE RESIDENCE TIME ON MICROWAVE PLASMA DIAMOND CVD 249
F. G. Celii, D. White, Jr., & A.J. Purdes

INVESTIGATIONS OF NUCLEATION AND CRYSTAL GROWTH OF CVD DIAMOND USING THE SENTAXY TECHNIQUE 258
H. Yagyu, J. S. Ma, H. Kawarada, T. Yonehara, & A. Hiraki

DIAMOND ON SILICON: A HOT FILAMENT CVD STUDY OF NUCLEATION 266
P. Ascarelli, S. Fontana, E. Molinari, R. Polini, M.L. Terranova, & E. Cappelli

SUBSTRATE EFFECTS AND THE GROWTH OF HOMOEPITAXIAL DIAMOND (100) LAYERS USING LOW PRESSURE rf PLASMA-ENHANCED CHEMICAL VAPOR DEPOSITION 274
J.B. Posthill, R. A. Rudder, G.C. Hudson, D.P. Malta, G.G Fountain, R.E. Thomas, R.J. Markunas, T.P. Humphreys, R.J. Nemanich & D.R. Black

*Invited Paper

INVESTIGATION OF LOW PRESSURE DIAMOND GROWTH BY ELASTIC SCATTERING OF LIGHT AND REFLECTANCE SPECTROSCOPY 282
A.M. Bonnot, T. Lopez-Rios, B. Mathis & J. Leroy

CHARACTERIZATION OF DC PLASMAS FOR THE CONTROL OF DIAMOND DEPOSITION 290
L.S. Plano, D.A. Stevenson, & J.R. Carruthers

## PART III: DIAMOND FILM PROPERTIES

* STRUCTURE-PROPERTY RELATIONSHIPS AND APPLICATIONS OF DIAMOND FILMS 301
K.V. Ravi

* NUCLEATION AND GROWTH OF WEAR-RESISTANT DIAMOND COATINGS 314
B. Lux & R. Haubner

THE MECHANICAL PROPERTIES OF CVD DIAMOND 326
M.D. Drory, C.F. Gardinier, J.M. Pinneo, & J.S. Speck

ULTIMATE TENSILE STRENGTH OF POLYCRYSTALLINE DIAMOND FILMS 333
J.L. Davidson & X. Cao

INDENTATION BEHAVIOR OF DIAMOND FILMS ON CEMENTED CARBIDE 340
M.D. Drory & M.G. Peters

ADHESION BETWEEN CVD DIAMOND FILMS AND TUNGSTEN 348
M. Alam, D.E. Peebles, & D.R. Tallant

EXCIMER LASER ETCHING AND POLISHING OF DIAMOND FILMS 357
A. Blatter, U. Bogli, L.L. Bouilov, N.I. Chapliev, V.I. Konov, S.M. Pimenov, A.A.Smolin, & I.V. Spitsyn

SEM TRIBOMETRY OF FLUORINATED CVD DIAMOND COATINGS 365
M.N. Gardos, B.L. Soriano, D.E. Patterson, R.H. Hauge, & J.L. Margrave

*Invited Paper

* TEMPERATURE AND BIAS EFFECTS ON THE PHYSCIAL AND TRIBOLOGICAL PROPERTIES OF DIAMOND-LIKE CARBON 374
A. Grill, V. Patel, & B.S. Meyerson

ATOMIC COORDINATION AND MACROSCOPIC PROPERTIES OF HYDROGENATED DIAMOND-LIKE CARBON 385
M.A. Tamor & K.R. Carduner

DIAMOND-LIKE NANOCOMPOSITES A NEW CLASS OF ELECTRONIC MATERIALS 393
V.F. Dorfmann, T.A. Skotheim, B.N. Pypkin

PHYSICAL DEPOSITION OF DIAMOND - TECHNOLOGY, PROPERTIES, AND APPLICATIONS 400
S. Aisenberg, A. Altshuler, & J.L. Sprague

* VISIBLE LIGHT EMISSION FROM DIAMOND 408
A.T. Collins

FREE EXCITON AND BOUND EXCITON RECOMBINATION RADIATION IN UNDOPED AND BORON-DOPED CVD DIAMONDS 420
H. Kawarada, Y. Yokota, H. Matsuyama T. Sogi, & A. Hiraki

SPATIALLY AND SPECTRALLY RESOLVED CATHODOLUMINESCENCE MEASUREMENTS OF CVD-GROWN DIAMOND PARTICLES AND FILMS 427
L.H. Robins, E.N. Farabaugh, & A. Feldman

LATTICE VIBRATIONAL MODES AND DEFECT-ACTIVATED IR ABSORPTIONS IN CVD DIAMOND 435
C. Klein, T. Hartnett, R. Miller, C. Robinson

THERMAL CONDUCTIVITY OF NATURAL TYPE IIA DIAMOND BETWEEN 500K AND 1250K 443
J.W. Vandersande, C.B. Vining, A. Zoltan

THE ROLE OF ELASTIC INTERACTION OF PHONONS IN DIAMOND 451
V.I. Nepsha, V.R. Grinberg, Yu. A. Klyuev, N.A. Kolchemanov, & A.M. Naletov

HIGH TEMPERATURE GRAPHITIZATION OF DIAMOND 455
J.K. Lewis, H. Chen, S. Nafis, M. Nielsen, S. Bonafede, R.O. Dillion, & T. Furtak

OXIDATION OF CVD DIAMOND FILMS 463
Q. Sun & M. Alam

*Invited Paper

ELECTRICAL CONDUCTIVITY OF DIAMOND FILMS FROM ROOM TEMPERATURE ON 1200 °C 471
S.F. Adams, J.W. Vandersande, D. Zoltan, B.R. Stoner, & J.A. von Windheim

THE EFFECT OF HYDROGEN ON THE ELECTRICAL RESISTIVITY OF POLYCRYSTALLINE DIAMOND FILMS 479
M.L. Lake, D.C. Ingram, J.W. Vandersande, & D. Zoltan

CHANGE OF RESISTANCE OF DIAMOND SURFACE BY REACTION WITH HYDROGEN AND OXYGEN 487
H. Nakahata, T. Imai, & N. Fujimori

HALOGENATION OF DIAMOND (100) USING ATOMIC BEAMS 494
A. Freedman & C.D. Stinespring

CHARACTERIZATION OF CVD DIAMOND FILMS WITH ATOMIC FORCE AND SCANNING TUNNELING MICROSCOPY 502
A.W. Phelps & T. Owens

## PART IV: APPLICATIONS

* DIAMOND: WHAT, WHEN, AND WHERE 513
M.N. Yoder

IGFET FABRICATION ON HOMOEPITAXIAL DIAMOND USING INSITU BORON AND LITHIUM DOPING 523
G.G. Fountain, R.A. Rudder, D.P. Malta, S.V. Hattangady, R.G. Alley, G.C. Hudson, J.B. Posthill, R.J. Markunas, T.P. Humphreys, R.J. Nemanich, V. Venkatesan, & K. Das

SIMULATION OF DIAMOND POWER DIODES 530
K. Grahn, S. Eranen, & P. Kuivalainen

DIAMOND COLD CATHODES 539
M.W. Geis, N.N. Efremow, J.D. Woodhouse & N.D. McAleese

METAL-INSULATOR-SEMICONDUCTOR DIODES USING POLYCRYSTALLINE DIAMOND THIN FILMS 543
K. Miyata, D.L. Dreifus, K. Das, J.T. Glass, & K. Kobashi

RELIABILITY OF OHMIC CONTACTS TO DIAMOND 551
M. Roser, C.A. Hewett, K.L. Moazed, & J.R. Zeidler

*Invited Paper

EFFECT OF THIN INTERFACIAL $SiO_2$ FILMS ON METAL CONTACTS TO BORON DOPED DIAMOND FILMS 558
V. Venkatesan, K. Das, D.L. Dreifus, G.G. Fountain, R.A. Rudder, J.B. Posthill, & R.J. Markunas

FORMATION OF SINGLE-CRYSTAL SEMICONDUCTORS-α-C:H FILM HETEROJUNCTIONS 566
V.M. Elinson, V.V. Sleptsov, S.S. Gerasimovich, G.F. Ivanovsky, V.I. Polyakov, O.N. Ermakova, M.G. Ermakov, P.I. Perov

IMPLANTATION AND DIFFUSION OF ELECTRICALLY ACTIVE DOPANTS IN POLYCRYSTALLINE DIAMOND 574
M.I. Landstrass, M.A. Plano, D. Moyer, S.P. Smith & R.G. Wilson

ELECTRICAL CHARACTERIZATION OF BORON-IMPLANTED DIAMOND 581
C.A. Hewett, P.R. de la Houssaye, M. Roser, R.G. Wilson, & J.R. Zeidler

THIN, BORON-DOPED DIAMOND FILMS 589
M.I. Landstrass, M.A. Plano, & D. Moyer

THE GROWTH AND SOME PROPERTIES OF DIAMOND FILMS OF P- AND N-TYPE CONDUCTIVITY OBTAINED BY CRYSTALLIZATION FROM THE GAS PHASE 597
B.V. Spitsyn & A. E. Alexenko

PRODUCTION OF LARGE-AREA MOSAIC DIAMOND FILMS APPROACHING SINGLE CRYSTAL QUALITY 605
M.W. Geis & H. I. Smith

CONSTRUCTION AND CHARACTERIZATION OF A DIAMOND THIN FILM ANEMOMETER 608
D.A. Jaworske, C.D. Ellis, R. Ramesham, & T. Roppel

FABRICATION OF MICROCHANNELS IN SYNTHETIC POLYCRYSTALLINE DIAMOND THIN FILMS FOR HEAT SINKING APPLICATIONS 615
R. Ramesham, T. Roppel, C. Ellis, & M.F. Rose

NEW MATERIAL FOR ELECTRONIC PACKAGING: DIAMOND THIN FILMS BY CHEMICAL VAPOR DEPOSITION 625
M. Buck, T.J. Chuang, H. Seki, & M. Anschel

*Invited Paper

PROGRESS IN THE DIAMOND FILM RESEARCH AT UT DALLAS 633
F. Davanloo, D.R. Jander, T.J. Lee, H. Park, J.H. You, & C.B. Collins

WIDE-BANDGAP DIAMOND-LIKE CARBON FILMS FORMED BY RF-DEPOSITION USING MAGNETRON DISCHARGE 640
V.V. Sleptsov, V.M. Elinson, N.V. Simakina, & A.M. Baranov

DIAMOND-LIKE CARBON FILMS: DEPOSITION PROCESSES, PROPERTIES AND APPLICATIONS 645
G.F. Ivanovsky, V.V Sleptsov, V.M. Elinson, A.M. Baranov, A.A. Kuzin, S.S. Gerasimovich

Author Index 653

Keyword Index 659

*Invited Paper

## FACTS ABOUT THE ELECTROCHEMICAL SOCIETY, INC.

The Electrochemical Society, Inc., is a nonprofit, scientific, educational, international, individual membership organization founded for the advancement of the theory and practice of electrochemistry, electrothermics, electronics, and allied subjects. The Society was founded in Philadelphia in 1902 and incorporated in 1930. There are currently over 5000 scientists and engineers from more than 40 countries who hold individual membership; the Society is also supported by more than 100 corporations through Benefactor, Patron, and Sustaining Memberships.

The technical activities of the Society are carried on by Divisions and Groups. Local Sections of the Society have been organized in a number of cities and regions.

Major international meetings of the Society are held in the Spring and Fall of each year. At these meetings, the Divisions and Groups hold general sessions and sponsor symposia on specialized subjects.

The Society has an active publications program which includes the following.

JOURNAL OF THE ELECTROCHEMICAL SOCIETY - The JOURNAL is a monthly publication containing technical papers covering basic research and technology of interest in the areas of concern to the Society. Papers submitted for publication are subjected to careful evaluation and review by authorities in the field before acceptance, and high standards are maintained for the technical content of the JOURNAL.

EXTENDED ABSTRACTS - Extended abstracts of the technical papers presented at the Spring and Fall Meetings of the Society are published in serialized softbound volumes.

PROCEEDINGS VOLUMES - Papers presented in symposia at Society and Topical Meetings are published from time to time as serialized softbound Proceedings Volumes. These provide up-to-date views of specialized topics and frequently offer comprehensive treatment of rapidly developing areas.

MONOGRAPH VOLUMES - The Society has, for a number of years, sponsored the publication of hardbound Monograph Volumes, which provide authoritative accounts of specific topics in electrochemistry, solid state science and related disciplines.

# PART I: SYNTHESIS

# DIAMOND GROWTH WITH THERMAL ACTIVATION OF CARBON-HYDROGEN-HALOGEN SYSTEMS AND GROWTH ENHANCEMENT WITH THE ADDITION OF OXYGEN

D. E. Patterson, C. J. Chu, B. J. Bai, Z. L. Xiao, N. J. Komplin, R. H. Hauge, and J. L. Margrave

Rice University, Department of Chemistry, P. O. Box 1892, Houston, TX 77251 and The Houston Advanced Research Center, 4800 Research Forest Drive, The Woodlands, TX 77381

## ABSTRACT

Diamond deposition has been primarily carried out with hydrocarbon-hydrogen-oxygen based systems. In these systems, the hydrogen atom as well as other free radicals, e. g., $CH_3$, are formed with hot filaments, plasmas, flames, etc. In most cases, diamond is thought to form with the evolution of $H_2$ as the final step in the carbon bond formation process. In halogen containing systems, the evolution of HX (where X is a halogen atom) has been suggested as being in part responsible for the lower diamond growth temperatures in these systems. The importance of oxygen as an additive which enhances the halogen-assisted process is discussed.

## INTRODUCTION

At present, there are a variety of techniques for producing chemical vapor deposited (CVD) diamond films and particles. Common to all of these processes are reactive species containing carbon and hydrogen in some form. Most of these techniques further employ some high energy method for dissociating hydrogen molecules into atoms in order to make the process viable. All have their relative merits and problems. It has been hypothesized by a number of researchers that with a halogen-based system CVD diamond growth could be accomplished with results exceeding those presently achieved. These systems incorporate either elemental halogen in conjunction with a hydrocarbon or some halogen-containing carbon species. These suggestions are based on a thermodynamic argument that a halogen-based reaction will produce as a major by-product HX molecules (where X is a halogen atom) instead of the less stable hydrogen molecules which are produced in standard CVD diamond systems. While diamond has been produced with some success in reaction systems where a halogen has been added to the reactant mixture, most of this work still employs high energy activation of the reactant species (1, 2, 3).

There have also been a few citations in the literature of CVD diamond deposition methods employing halogens that work without some high energy preactivation. B. V. Spitsyn and B. V. Derjagin were the first to report a simple pyrolytic halogen-based process for growing CVD diamond on diamond substrates employing either $CBr_4$ or $CI_4$ as the principle reactive species (4). R. A. Rudder, et al., also reported the use of elemental fluorine in conjunction with $CF_4$ to grow diamond on diamond (5). This process,

however, appears not to be thermodynamically sound, and the diamond growths were most likely due to impurities in the reactor such as residual hydrogen. A recent Japanese patent reports a simple chlorine-based pyrolytic technique which claimed the production of CVD diamond on a variety of substrates using elemental chlorine in combination with methane or using $CCl_4$ and hydrogen (6). Most recently, the authors have reported a method for producing CVD diamond films and particles employing a simple thermally activated halogen-assisted technique operating at ambient pressures. This method uses a variety of halogen-based reactant gases with deposition temperatures between ca. 750 and 250 °C (7). We report here on further developments with low temperature halogen-assisted CVD diamond deposition.

## EXPERIMENTAL

All of the reactions were carried out in a simple flow tube system that allows the reactant gases (whose structures are comprised of carbon, hydrogen, oxygen, and halogen atoms) to be passed dynamically through a resistively heated reaction chamber into which a suitable growth substrate has been placed. The spent gases flow out of the chamber, can be trapped for further analysis, and finally flow into various cleaning traps before exiting into a vent hood. The entire system works at ambient pressure although studies are underway to determine the effects of other pressures in the system. The reactant gases are comprised of either elemental fluorine (Air Products, 98%) and a simple hydrocarbon such as methane or ethane (various sources) or of hydrogen (AirCo, 99%) and a simple halocarbon (various sources). It has been found that the addition of oxygen to the reactants in the form of pure $O_2$, air, $H_2O$, $CO_2$, or bound to the carbon in the reactant molecule, e. g., as $CH_3OH$, enhances the growth of diamond. The reactant gases are typically diluted with an inert gas such as He. The gases (other than fluorine) can be dried with $CaSO_4$ or used as supplied, the liquid reactants are used as supplied, and the $F_2$ is treated with NaF beforehand in order to remove HF. The carbon containing gas is typically held to less than 5% of the overall gas composition in order to retard the formation of non-diamond carbon. Flow rates are monitored by mass flow meters and are typically on the order of 0 25 to 10 sccm for the carbon containing gas, 0.5 to 20 sccm for fluorine (for reactions using fluorine), 50 to 200 sccm for hydrogen (for reactions using hydrogen), 0.001 to 1 sccm for oxygen, air, $H_2O$, or $CO_2$, and 0 to 250 sccm for any inert gas.

The flow tube reaction chambers are made of Monel 400 and range from 6.35 to 50.8 mm in inside diameter and from 0.3 to 1 meter in length. Some experiments not involving fluorine are performed in quartz or Vycor tubing of the same dimensions as those for the Monel tubing. The reactors are heated resistively from 700 to 950 °C with temperatures being monitored by standard thermocouples. The tube reactors are water-cooled (for the Monel system) or air-cooled (for the quartz/Vycor system) before the fittings that connect them to the rest of the system. This sets up a temperature gradient in the reactors which allows for diamond growth typically in the region of the reactors between ca. 250 °C and 750 °C.

Sample substrates are prepolished with fine diamond grit (<1 μm) and then cleaned of any residual diamond. They are subsequently placed into the reactors before gas flow begins. Diamond deposition times range from several hours to several days depending on

the amount of growth desired.

Verification of diamond growth was provided via Raman spectroscopy (Spex Model #1403 employing a Liconix 5300 Ar+-ion laser operating at 488 nm) and X-ray diffraction (Phillips Model #PW 1840/01/11). Diamond growth rates and morphologies were determined via optical and SEM (Jeol Model #5300) photomicrographs of diamond crystallites.

Off gases from the experiments were analyzed via matrix isolation FT-IR spectroscopy. The details of this apparatus have been previously explained (8). In this analysis, the gases were trapped with Ar in approximately a 1:1000 reactant gas:Ar ratio at ca. 12 K. FT-IR analysis of the trapped gases was performed using an IBM 98 FT-IR interfaced to the matrix isolation unit.

## RESULTS

### Thermodynamics

As has been pointed out earlier, a partial rationale for the low temperature halogen-assisted process for producing diamond films and particles is a simple thermodynamic argument. That is, if a more stable end-product other than elemental hydrogen can be produced in the CVD diamond process, it should be easier to deposit CVD diamond, i. e., the more exothermic that the basic reaction for producing diamond is, the more likely it is that diamond will be produced and the more likely that diamond will be produced at lower temperatures. Table I explicitly illustrates the increased free energies of formation that are achieved by producing solid carbon and a hydrogen halide and/or water as opposed to solid carbon and hydrogen ( 9, 10). It is important to note that these values are for the formation of graphite and not diamond as diamond is metastable under the conditions for these values. The mystery of why diamond forms instead of graphite is not evident. However, recall that the free energy of formation of diamond is only slightly higher than that of graphite ($\Delta G$ = 2.87 kJ/mol) (10). Further, it is important to note that we have achieved our best diamond depositions with non-stoichiometric amounts of reactants. A number of these systems will be discussed in more detail below.

### Hydrocarbon / $F_2$ / He Systems

We have earlier reported that simple hydrocarbons such as methane and ethane could be used in combination with elemental fluorine to produce diamond on a number of substrates (7). In an effort to better understand the halogen-assisted process, the previous reaction systems were modified to be leak tight, i. e., the new systems were pressurized to greater than three atmospheres with no apparent leakage of gas. Upon doing this, however, diamond growth decreased substantially using a standard mixture of methane and fluorine diluted with helium. This mixture, in the past, had always produced diamond. As the best diamond growth in the past had also been achieved with natural gas instead of pure methane, this was employed in the new reactor. Enhanced diamond growth using natural gas was again found to occur using approximately 5% natural gas and 0.5% fluorine diluted in helium. A SEM photomicrograph of this growth is given in Figure 1, and the Raman spectrum of this growth showed a single peak at 1332 $cm^{-1}$ indicating pure diamond growth in the deposition region. Figure 1 indicates that single crystals of diamond (as opposed to a film) were grown. The diamond was deposited in a region of the reactor

ranging in temperature from ca. 750 °C to ca. 300 °C. Diamond deposition in a cooler region of the reactor rather than the hot (ca. 875 °C) central portion of the reactor is the same as reported earlier.

A typical analysis of natural gas is : $CH_4$ 93.63 %, $C_2H_6$ 3.58%, $C_3H_8$ 1.02%, $CO_2$ 0.70%, $N_2$ 0.47%, isobutane 0.21%, n-butane 0.19%, isopentane 0.06%, n-pentane 0.06%, hexane 0.02%, and heptanes and larger hydrocarbons 0.06% (11). T-butyl mercaptan is usually added to natural gas as an odorizer in a few parts per million and trace amounts of oxygen and water may also be present. This points to the likelihood of one of the "impurities" in natural gas as having an important role in diamond deposition. This is most likely due to the presence of oxygen in some form, e. g., $CO_2$, water, etc.

In order to test this hypothesis, trace amounts of oxygen (pure or in compressed air), $CO_2$, and water were added to a mixture of pure methane and fluorine which was again diluted with helium (typically 4% methane, 0.5% fluorine, and the balance helium). In all cases, diamond growth (based on the number of diamond crystallites formed) was enhanced by the incorporation of small amouts of these additives. Typical amounts of these additives are: 0.4 - 1% $CO_2$, 0.01 - 0.1% oxygen, and 0.2 -1% water in the overall gas mixture. Figure 2 gives the SEM of a single diamond grown in an oxygen-addition system again showing that the growth of single particles, as opposed to films, is favored in this system and further showing that rather large single crystals can be grown with this method. Note the growth layers that are quite evident in this particle. Diamond growth again decreased if significantly larger amounts of the additives were included in the reaction mixture. The diamond that is being produced in these systems is usually accompanied by graphite.

**Alcohol / $F_2$ / He Systems**

As oxygen apparently enhances the growth of diamond in the halogen-assisted system, it seemed likely that good diamond depositions might be achieved by incorporating oxygen into the reaction system by using an alcohol, aldehyde, ketone, organic acid, or similar molecule. To date, we have only been successful with $CH_3OH$. The $CH_3OH$ is supplied to the reaction system in place of other hydrocarbons in amounts ranging from 0.5% to 3% of the total gas mixture (again supplying ca 0.5 % fluorine and the balance being helium) and produces pure diamond particles as evidenced by a single Raman peak at 1332 $cm^{-1}$ and no graphite signature (see Figure 3). Growth rates are still rather slow (< 1μm per hour) and particles tend to form rather than continuous films. In this case, the best growths were noted with ca. 1% methanol in the gas mixture. It is also noted in using methanol that the reaction produces much less graphite than found when methane or natural gas is the source of carbon.

In the methane / natural gas reactions, there is a considerable graphitic deposit in the hot central portion of the reactor as well as a graphitic deposit in the cooler diamond growing region in the oxygen addition experiments. In the methanol case, however, there is no noticeable graphite formation anywhere in the reactor. In both cases, diamond formation occurs in that region of the reactor which is held from ca. 750 °C to ca. 300 °C.

### Chlorofluorocarbon (CFC) / $H_2$ / He Systems

In the past, a number of fluorocarbons, chlorofluorocarbons, chlorocarbons, and even bromoform, and iodomethane were found to produce diamond when mixed with an excess of hydrogen and reacted as described previously. Again, as we moved to our new clean, air-tight system, the diamond growths were significantly decreased or ceased altogether. Air was subsequently added to the reactant gases, and diamond growth was enhanced. Typical reaction conditions for this case are: CFC: 0.5 - 1% in He, $H_2$: 50 % in He, and air: 0.5 - 1% in He. The diamond formed by these reactions is often accompanied by more graphite than are the reactions employing elemental fluorine. This is indicated in Figure 4. It should furthermore be noted that this type of CFC / hydrogen reaction produces both HF and HCl, and that high flow rates, e. g., >5 sccm $CCl_2F_2$, of the reactant gases leads to failure of the reaction chambers.

### Hot Chamber Wall Reactions

As previously pointed out, the chamber material reacts with the reactant gases in many if not all of these reactions. This is true for all types of reaction chamber materials tested to date. Some of the reaction by-products that have been detected and identified from the Monel 400 and Vycor chambers include: $NiF_2$, $CuF_2$, $MnF_2$, $CrF_3$, $AlF_3$, $NiCl_2$, $CuCl_2$, CuCl, NiO, $Cu_2O$, CuO, and $SiF_4$. Reaction chamber design modifications are underway in an attempt to solve this problem.

### Matrix Isolation Studies

Infrared matrix isolation analysis of the gases produced in a Monel hot wall reactor indicate that the main carbon - fluorine containing species are $CF_4$ and $C_2F_6$ when fluorine is added to methane in an excess of helium. The addition of $O_2$, $CO_2$, and $H_2O$ produces CO, and, in the case of $CO_2$ and $H_2O$, some methanol is produced.

## CONCLUSIONS

While it is quite evident that diamond growth occurs using the low temperature halogen-assisted technique, the mechanism for this growth is not understood nor is it understood exactly what precursor species are necessary for the best diamond growths. It appears highly unlikely that the methyl radical mechanism which operates in other CVD reactors is responsible for diamond growth at the low temperatures (250 - 750 °C) observed for the above process (12, 13, 14). For example, the methyl radical mechanism is known to work best over the substrate temperature range of 900 - 1000 °C while a clear high temperature limit of ca. 750 °C is known in the halogen-assisted case.

It also appears likely that the reactive species are long lived as they exist in the downstream flow for periods of seconds. The flow velocity through the reactor is of the order of 1 - 5 cm/sec, and the diamond is found to be produced over a 10 cm. long area in the cooler exit region of the tubular reactor.

A requirement for low temperature diamond growth seems to be that the reaction be highly thermodynamically favored as shown in Table I. This is generally accomplished by formation of solid carbon and very stable gaseous fluorides and chlorides such as HF and HCl.

The most important result of the present work has been to establish the importance of having oxygen present in some form in the halogen-assisted CVD diamond process. The addition of $O_2$, $CO_2$, and water enhances the growth of diamond. When water and $CO_2$ are added, gas analysis has shown that methanol is formed in the reactor. It has also been shown that methanol is an effective diamond precursor without the addition of auxiliary oxygen. We have futher shown that CO does not lead to diamond growth.

## ACKNOWLEDGEMENTS

The authors would like to thank the Texas Higher Education Coordination Board through the Texas Advanced Technology Program (#003604-055) and the Office of Naval Research for supporting this project.

## REFERENCES

1. S.R. Ovshinsky and J. Flasck, U. S. Patent #4,663,183 (5 May 1987).
2. M. Frenklach, R. Kematick, D. Huang, W. Howard, K. E. Spear, A. W. Phelps, and R. Koba, J. Appl. Phys. 66, 395 (1989).
3. M. Matsumura and T. Yoshida, U. S. Patent #4,873,115 (10 October 1989).
4. B. V. Spitsyn and B. V. Derjagin, U. S. S. R Patent #339,134 (5 May 1980).
5. R. A. Rudder, J. B. Posthill, G. C. Hudson, M. J. Mantini, and R. J. Markunas, SDIO/IST-ONR, Diamond Technology Initiative Symp. Proc., Crystal City, VA July 11-13, 1989.
6. K. Mukaii, H. Kano, and M. Ikesue, Japanese Kokai Patent #Sho 63(1988)-297299 (5 December 1988).
7. D. E. Patterson, B. J. Bai, C. J. Chu, R. H. Hauge, and J. L. Margrave, New Diamond Science and Technology (Proc. 2nd International Conference on New Diamond Science and Technology), R. Messier and J. T. Glass, eds., MRS International Conference Proceedings Series (Materials Research Society, Pittsburg, PA, 1991), in press.
8. R. H. Hauge, L. Fredin, Z. H. Kafafi, and J. L. Margrave, Appl. Spec. 40 (5), 588 (1986).
9. M. W. Chase, Jr., C. A. Davies, J. R. Downey, Jr., D. J. Frurip, R. A. McDonald, and A. N. Syverud, JANAF Thermochemical Tables, 3rd Ed., New York: American Chemical Society and the Institute of Physics for the National Bureau of Standards (1986).
10. G. N. Lewis and M. Randall, Thermodynamics, 2nd Ed., New York: McGraw-Hill Book Company, 1961.
11. W. Braker and A. L. Mossman, The Matheson Gas Data Book, 5th Ed., East Rutherford, NJ: Matheson Gas Products, 1971.
12. C. J. Chu, M. P. D'Evelyn, R. H. Hauge, and J. L. Margrave, J. Mat. Res. 5 (11), 2405, 1990.
13. S. J. Harris and A. M. Weiner, J. Appl. Phys. 67 (10), 6520 (1990).
14. D. G. Goodwin, "Simulations of High-Rate Diamond Synthesis: Methyl as Growth Species," Appl. Phys. Lett. (submitted).

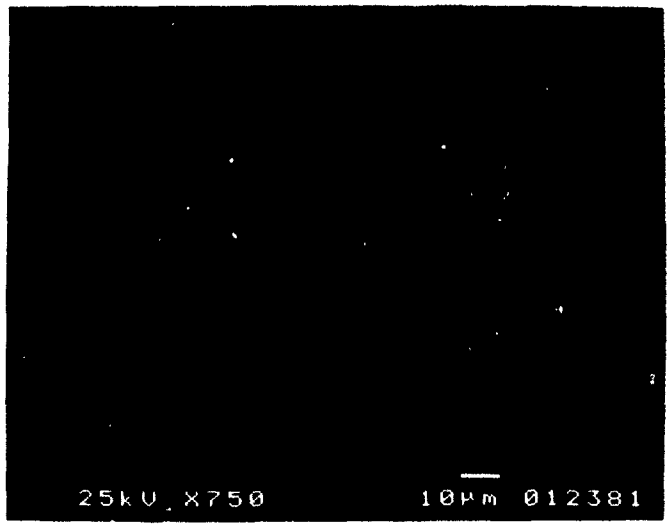



Figure 1. SEM photomicrograph of the diamond particles deposited on a Monel substrate. Natural Gas Flow Rate = 4 sccm, F2 Flow Rate = 0.5 sccm, He Flow Rate = 100 sccm, Central Furnace Temperature = 880 °C, Deposition Time = 137 hr. Note growth along a scratch in the surface.

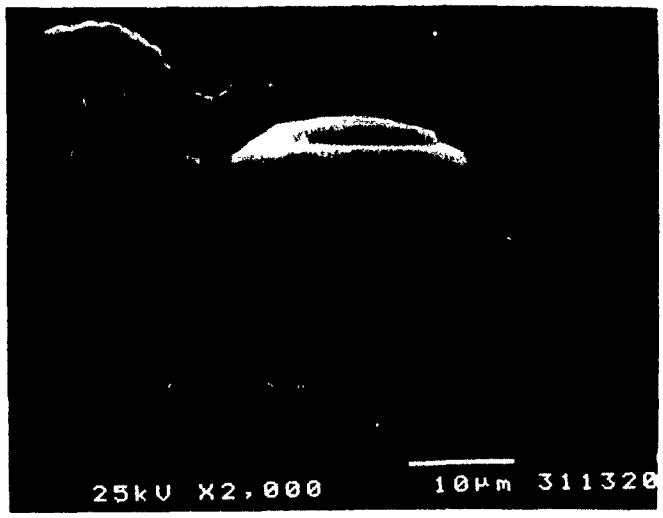



Figure 2. SEM photomicrograph of a diamond particle deposited on a copper substrate. CH4 Flow Rate = 6 sccm, F2 Flow Rate = 0.5 sccm, O2 Flow Rate = 0.05 sccm, He Flow Rate = 100 sccm, Central Furnace Temperature = 880 °C, Deposition Time = 48 hr.

TABLE I. Reaction Free Energies at 1000 K. (9, 10)

| Reaction | $-[\Delta G°-\Delta H°]/T$ (J/K mol) | $\Delta H°$ (kJ/mol) | $\Delta G°$ (kJ/mol) |
|---|---|---|---|
| $CH_4 \rightarrow C + 2H_2$ | 94.3 | 89.8 | -4.5 |
| $CH_4 + 2F_2 \rightarrow C + 4HF$ | 117.9 | -1008.6 | -1126.5 |
| $CH_3F + F_2 \rightarrow C + 3HF$ | 110.5 | -576.1 | -686.6 |
| $CH_2F_2 \rightarrow C + 2HF$ | 114.4 | -88.3 | -202.7 |
| $CHF_3 + H_2 \rightarrow C + 3HF$ | 139.6 | -121.0 | -260.6 |
| $CF_4 + 2H_2 \rightarrow C + 4HF$ | 175.4 | -164.6 | -340.0 |
| $CHClF_2 + H_2 \rightarrow C + HCl + 2HF$ | 128.9 | -158.8 | -287.7 |
| $CHCl_3 + H_2 \rightarrow C + 3HCl$ | 137.7 | -179.2 | -316.9 |
| $CCl_2F_2 + 2H_2 \rightarrow C + 2HCl + 2HF$ | 158.1 | -249.5 | -407.6 |
| $CCl_4 + 2H_2 \rightarrow C + 4HCl$ | 171.7 | -288.0 | -459.7 |
| $CH_3OH + F_2 \rightarrow C + H_2O + 2HF$ | 119.0 | -606.9 | -725.9 |
| $CH_3CH_2OH + 2F_2 \rightarrow 2C + H_2O + 4HF$ | 231.7 | -1127.0 | -1358.7 |
| $HCOOH + F_2 \rightarrow C + O_2 + 2HF$ | 123.2 | -178.3 | -301.5 |

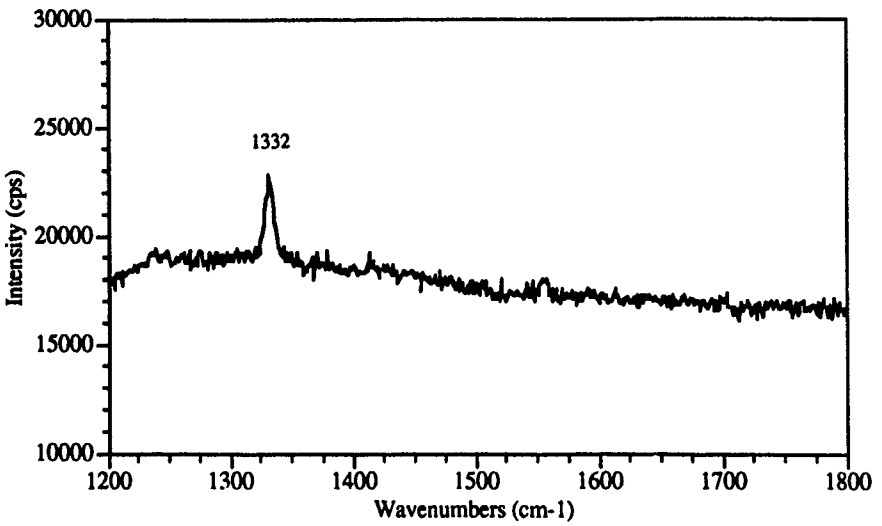



Figure 3. Raman spectrum of diamond deposited on a Monel substrate at ca. 450 °C. MeOH Flow Rate = 1.2 sccm, F2 Flow Rate = 0.5 sccm, He Flow Rate = 100 sccm, Central Furnace Temperature = 890 °C, Deposition Time = 44 hr.

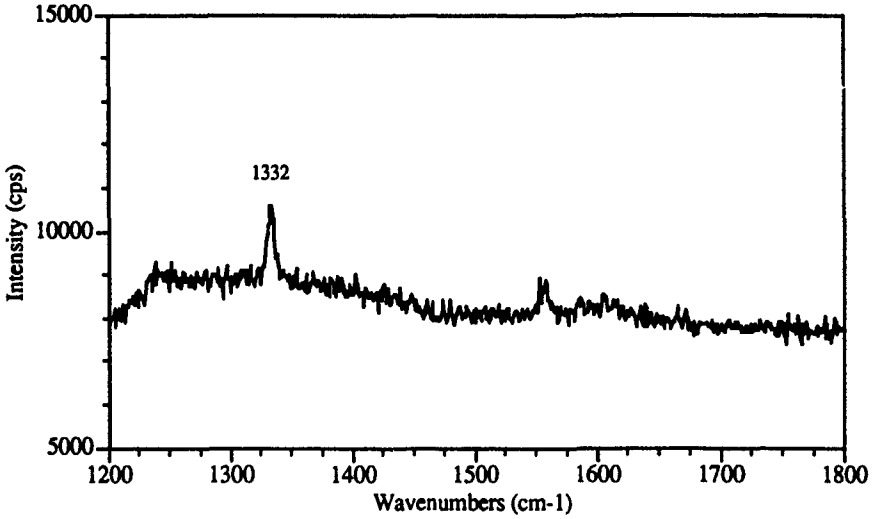



Figure 4. Raman spectrum of diamond deposited on a Monel substrate at ca. 350 °C. CCl2F2 Flow Rate = 0.5 sccm, H2 Flow Rate = 100 sccm, Air Flow Rate = 0.5 sccm, He Flow Rate = 100 sccm, Central Furnace Temperature = 860 °C, Deposition Time = 19 hr.

# $F_2 - CH_4$ AND $H_2 - CF_4$ GAS INTERACTIONS ACROSS A HEATED GRAPHITE ELEMENT

R.A. Rudder, R.E. Thomas, G.C. Hudson, M.J. Mantini, and R.J Markunas
Research Triangle Institute, P.O.Box 12194, Research Triangle Park, NC 27709

## ABSTRACT

We have investigated diamond film formation using mixed hydrogen-halogen chemistries at sub-atmospheric pressures. This work has been implemented in two reduced pressure cells. One cell contained a heated graphite element upon which reactant gasses were passed. Only thermal activation was used in this reduced pressure cell. Quadrupole mass spectroscopy was used to identify reaction products in the cell. The other cell was a low pressure rf-plasma assisted chemical vapor deposition system. Gasses which showed no thermal activation in the thermal cell were admitted to this cell. It was found that $F_2$ is activated in the thermal cell and can participate in reactions both in the gas phase and at the graphite surface. HF and $C_2F_2H_x$ were observed as by-products of $F_2 - CH_4$ gas interactions near the graphite oven. Carbon films that were deposited on nearby substrates proved not to be diamond. Activation of $H_2 - CF_4$ in the thermal cell was not observed even at temperatures as high as 1000 °C. Plasma activation, on the other hand, does show evidence for HF and $C_2H_2$ formation from the $H_2$ - $CF_4$ gas system. With plasma activation of $H_2 - CF_4$ gas system, diamond deposition on as-received Si wafers without any ex situ treatment of the surface to enhance diamond nucleation is possible.

## Introduction

Recent work by Patterson et al.(1) and previous work by Rudder et al.(2) have shown that diamond deposition from a fluorine-based environment is possible. Patterson exploited the use of mixed fluorine-hydrogen chemistries (i.e., $F_2$ and $CH_4$) to form solid carbon through a proposed reaction of:

$$CH_4 + 2F_2 \rightarrow C_{(s)} + 4HF \quad (1)$$

This reaction would be more exothermic than a corresponding hydrogen-based reaction involving $CH_4$ and $H_2$. The hot zone of the Patterson-type reactor operated between 700 and 950 °C, and diamond growth occurred only in

regions of the reactor where the temperature was between 250 and 750 ° C. Mixtures of either $H_2$ and $CF_4$ or $F_2$ and $CH_4$ were reported to deposit diamond.

**Experimental Apparatus and Approach**

To gain insight into the fluorine-based process, we have performed a quadrupole mass spectroscopy of $F_2/CH_4$ and $H_2/CF_4$ gas interactions as a function of temperature of the graphite surface. This work has been implemented in two reduced pressure cells. One cell contained a heated graphite element upon which reactant gasses were passed. Only thermal activation was available in this reduced pressure cell. The other cell was a low pressure rf-plasma assisted chemical vapor deposition system. Gasses which showed no activation in the thermal cell were admitted to this cell.

The thermal work was performed in an UHV compatible chamber that is evacuated by a corrosive series, 1000 l/s turbomolecular pump. Gases are admitted into the chamber using mass flow controllers. The pressure in the chamber is maintained at 0.500 Torr for $F_2 - CH_4$ or $H_2 - CF_4$ gas work described here. A graphite resistive heater is enclosed in the chamber as well as a sample heater stage whereby growth attempts, independent of the graphite resistive heater, can be assessed. The graphite heater is machined from a dense, fine-grain graphite and is not highly oriented pyrolytic graphite. A mass quadrupole operating at low emission (0.25 mA) is used to sample the gases exiting the reactor. Changes in the gas composition as a function of substrate temperature or the graphite heater temperature are monitored.

The plasma activated cell was a low pressure rf-plasma assisted chemical vapor deposition system which has been used for the growth of diamond from $H_2$ - $CH_4$ mixtures(3). The reactor cell consists of a stainless steel, 150 mm conflat flange, 6-way cross to which the reactor tube, pumps, control orifice valve, vacuum gauges, mass spectrometer, and load lock are appended. The vacuum system is evacuated by a Balzers 500 l/s corrosive series turbomolecular pump. The base pressure of the reactor is $1.0 \times 10^{-7}$ Torr. The heater stage is comprised of alumina standoffs separating the graphite susceptor from a graphite serpentine resistive heater. The reaction tube consists of a double-walled 50 mm inside diameter quartz tube sealed to the stainless chamber by compression viton o-ring seals. The reactor tube is water cooled to maintain the water temperature at 15 ° C. An 8 mm water-cooled copper tube formed into a 3-turn helix 100 mm long provides the inductive coupling from the rf generator to the discharge. Wall deposits, for a limited time, can protect the quartz tube from erosion by fluorine based processes.

**Experimental Results in Thermal Cell**

The interactions of F atoms with both solid carbon such as graphite and with gaseous carbon such as $CH_4$, a graphite strip heater were studied in the thermal cell. By adjusting the current through the graphite element, the reactions of $F_2$ and/or F with the densified graphite were monitored as a function of temperature. One advantage in using a graphite heater to study the $F_2/CH_4$ gas interactions is that reactions of fluorine with graphite have been previously studied(4) so there exists comparative information. A second advantage to the graphite heater is that it avoids questions of metal catalysis reactions. Two difficulties with the graphite heater are memory effects from gasses absorbing in the porous graphite and delocalization of the hot zone across the machined graphite. This results in some areas of the heater operating about 100 °C colder than the heater center. To minimize the memory effects, the heater was degassed at high temperatures before setting the temperature for each data point.

Fluorine reactions with the heated graphite were monitored by admitting the $F_2$ without $CH_4$ into the thermal cell. At elevated temperatures, fluorine reacted with the graphite to form $CF_4$. The $CF_4$ formation was monitored in the mass quadrupole through the mass peak at 69 arising from $CF_3$. $CF_3$ is the dominant fragment in the ionizer when $CF_4$ is introduced. Figure 1 shows the observed $CF_3$ mass counts in the reactor as a function of the graphite cell temperature. The $CF_4$ production is maximum at 600 °C and is observed to decrease for temperatures in excess of 950 °C. The decrease in $CF_4$ production below 600 °C is probably a consequence of the formation of solid graphite fluoride. The temperature dependence is complicated by the fact that there is a sub tantial temperature variation ± 100 °C across the graphite heater element.

After observing the $CF_4$ production from the hot cell with only $F_2$ (admitted as 1% $F_2$ in He), $CH_4$ was introduced into the hot cell. Upon introduction of $CH_4$ into the hot fluorine, the $CF_4$ production decreased. Fluorine interactions with the $CH_4$ in the gas phase apparently depleted the gas phase of fluorine, resulting in a lower incident flux of F atoms to the graphite surface and, consequently, a lower production rate of $CF_4$. This is the first evidence for $F_2 - CH_4$ gas phase interactions. Besides the reduction in $CF_4$ production, the introduction of $CH_4$ into the hot fluorine resulted in production of HF and $C_2F_2H_x$ molecules. Figure 2 shows the production of those molecules as a function of the graphite temperature. Both exhibit a maximum in production around 900 °C. The temperature dependence for the HF production is more pronounced than the temperature dependence for the $C_2F_2H_x$ production.

This work suggests that the proposed reaction of Patterson et al. for solid carbon production via equation (1) is basically correct. Our observations of graphite gasification and the formation of HF and $C_2F_2H_x$ suggests that the reaction in equation (1) should be extended.

$$2F_2 + CH_4 \rightarrow C_{solid} + 4HF \qquad (700\,^\circ C)$$

$$4F_2 + 2CH_4 \rightarrow C_2H_2F_2 + 6HF \qquad (700\,^\circ C)$$

$$2F_2 + C_{graphite} \rightarrow CF_4 \qquad (500 - 700\,^\circ C)$$

In a similar manner, the $H_2$ - $CF_4$ system was evaluated in the thermal cell. At the pressure of 0.50 Torr, no evidence of by-product formation was observed for temperatures below 1000 °C. Temperatures higher than 1000 °C and pressures higher than 0.50 Torr were not evaluated. We assumed that temperatures under 1000 °C are not sufficient to produce H atoms from the $H_2$ or F atoms from the $CF_4$. Consequently, the $H_2$ - $CF_4$ gas system in this pressure and temperature range does not react with the graphite to produce gasification products, nor do they react with each other to form HF molecules.

**Experimental Results in Plasma Cell**

As a consequence of the inactivity of the $H_2$ - $CF_4$ in the thermal cell, gas mixtures of $H_2$ and $CF_4$ were admitted into the low pressure rf plasma assisted chemical vapor deposition system. Details of that work are being submitted elsewhere(5). Briefly, dense nucleation of polycrystalline diamond films on Si(100) substrates has been accomplished without the use of any surface pre-treatments such as diamond scratching, oil-coating, or diamond-like carbon predeposition. Films deposited at 5 Torr at 850 °C, using an 8% $CF_4$ in $H_2$ mixture, show dense nucleation, well-defined facets, and crystallite sizes ranging from 500 - 10,000 Å. Figure 3 shows scanning electron micrographs of the diamond surface and a cleaved cross-section. Some roughening of the Si substrate is observed from the cleaved section suggesting that the Si surface underwent some chemical modification prior to or during diamond nucleation. X-ray photoelectron spectroscopy show the films to be diamond with no major chemical impurity and no detectable graphitic bonding. Besides carbon, fluorine is detected in the x-ray photoelectron spectrum. A high resolution spectrum of the C 1s line shows that some carbon is bound to fluorine on the surface as exhibited by a distinct feature at 288 eV, removed from the C-C bonding at 283 eV. A high resolution spectrum of the C 1s region is shown in Figure 4. The graphite $\pi - \pi^*$ plasmon is not present in the spectrum. The 34 eV bulk diamond plasmon is clearly present, but not shown in the high-resolution spectrum. A pronounced 1332 $cm^{-1}$ Raman line was observed from the polycrystalline films along with a broad

band at 1500 $cm^{-1}$.

Quadrupole mass spectroscopy of the gases downstream from the plasma discharge reveals that the $CF_4$ - $H_2$ plasma converts the carbon tetrafluoride into HF and $C_2H_2$. No fluoromethane groups were observed. Given that, after 15 min into the plasma process, no fluorocarbon groups were detectable in the mass spectrum, the generation rate of HF and $C_2H_2$ must have been equal to the gas flow of $CF_4$ into the reactor, 3.2 sccm.

Preliminary data indicates that this process is applicable to substrates other than silicon. This process will have important applications in areas where surface pretreatments, such as diamond polishing, are not viable. In particular, this process may prove invaluable to those workers developing heteroepitaxy. With conventional methane-based processes, nucleation is inhibited on substrates other than diamond and c-BN. This process may allow heteroepitaxial studies to be undertaken on substrates whereby previously there has been little diamond nucleation.

*Acknowledgements* The authors wish to thank the Strategic Defense Initiative Organization/Innovative Science and Technology Office through the Office of Naval Research (N-00014-86-C-0460) for the financial support of this work.

## REFERENCES

(1) Donald E. Paterson, Benjamin J. Bai, C. Judith Chu, Robert H. Hauge, and John L. Margrave, "Halogen-Assisted Chemical Vapor Deposition", presented at the second International Conference on the New Diamond Science and Technology, Washington, DC(USA), September 23-27, 1990.

(2) R.A. Rudder, J.B. Posthill, R.J. Markunas, Electronics Lett. 25, 1220 (1989).

(3) R.A. Rudder, G. C. Hudson, Y. M. LeGrice, M.J. Mantini, J.B. Posthill, R.J. Nemanich, and R.J. Markunas, Mat. Res. Soc. EA-19

(4) D.E. Rosner and J. Strakey, J. Phys. Chem. 77, 690 (1973).

(5) R.A. Rudder, G.C. Hudson, J.B. Posthill, R.E. Thomas, and R.J. Markunas, submitted to Appl. Phys. Lett.

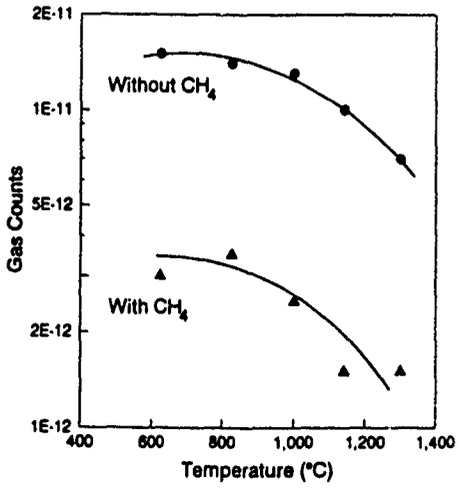



Figure 1. Observed $CF_3$ counts in the mass spectrometer as a function of the graphite heater temperature. Notice that the introduction of $CH_4$ into the graphite hot zone diminishes the $CF_4$ production.

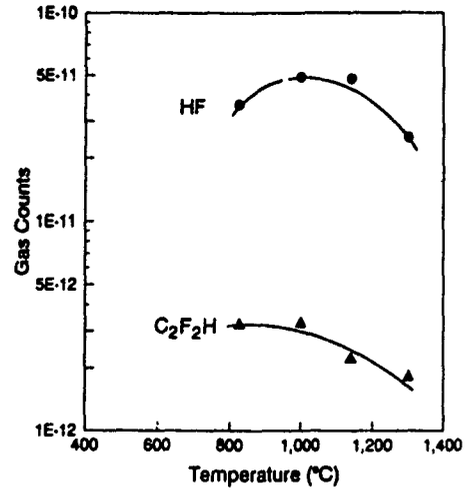



Figure 2. Dependence of by-product production on graphite heater temperature.

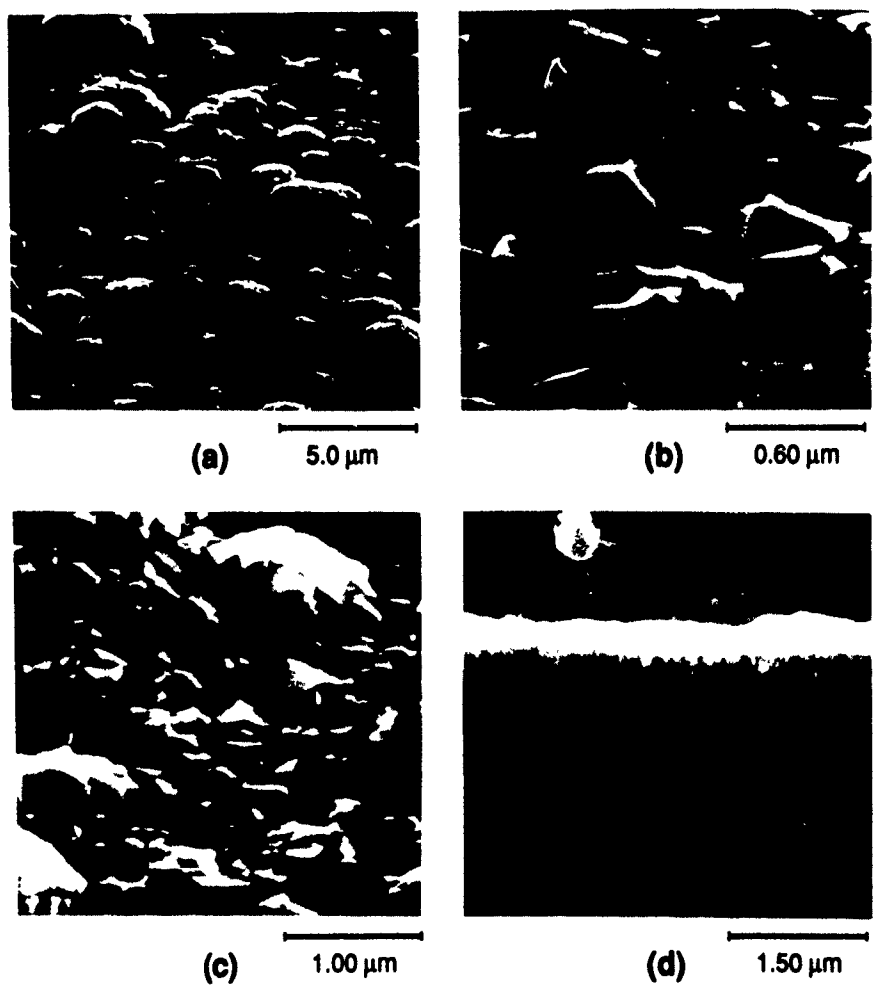



Figure 3. SEM micrographs of a polycrystalline diamond film deposited from the $H_2$ - $CF_4$ process.

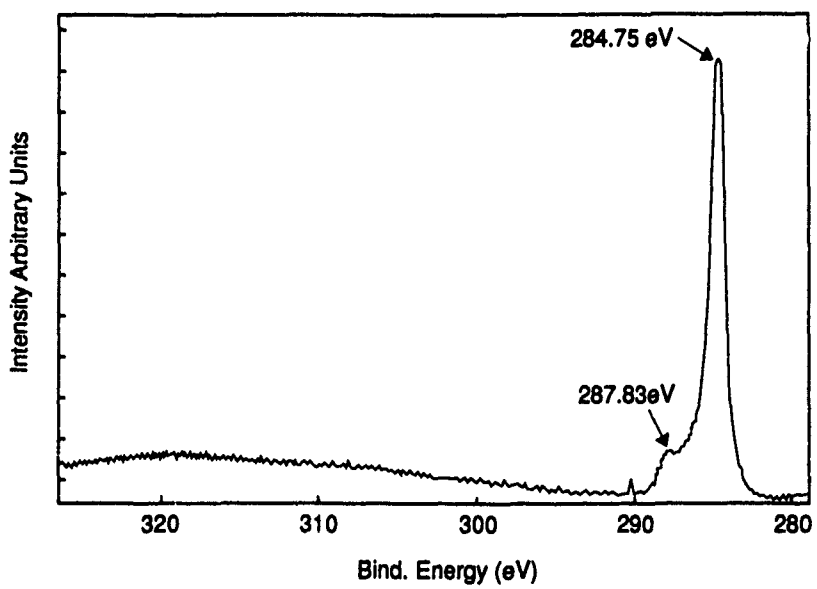



Figure 4. A high resolution x-ray photoelectron spectrum of the C 1s line.

# DIAMOND SYNTHESIZED BY THE MICROWAVE PLASMA CVD METHOD

Mutsukazu KAMO and Yoichiro SATO

National Institute for Research in Inorganic Materials
Namiki 1-1, Tsukuba, Ibaraki 305, Japan

Abstract

This paper reports some properties of diamond prepared by the microwave plasma method which have been studied using Raman, absorption and cathodoluminescence spectroscopies, and secondary ion mass spectroscopy (SIMS) analysis. It has been shown that single crystals have good crystalline quality. In contrast, the polycrystalline films grown under the same conditions have appreciable amounts of double bonds and strain. Contamination by elements contained in the substrate holder was observed in the epitaxially grown diamond. In addition, attempts to grow diamond at substrate temperatures lower than 500°C are reported.

## 1.Introduction

Many methods have been developed for diamond synthesis from the gas phase under thermodynamically metastable conditions. The growth features of diamond obtained by the methods appear to have much in common. One of the most interesting features is that the crystals have well-defined habits and often appear as octahedral, cubo-octahedral or multiply-twinned particles truncated by the substrates. However, the properties of diamond obtained from the gas phase seem to be influenced by the preparation methods. Such a tendency may be especially marked for optical properties sensitive to internal structure such as impurities, defects and strain.

A microwave plasma method for diamond synthesis[1] has high stability of experimental conditions during the deposition, good reproducibility of products and possibility for enlargement of the deposition area[2].

This paper reviews structural features and some properties of diamond prepared by the microwave plasma method which have been studied using Raman, absorption, cathodoluminescence spectroscopies, and secondary ion mass spectroscopy (SIMS).

## 2. Experimental

Figure 1 shows a schematic drawing of the microwave plasma CVD apparatus[1]. A silica glass tube 50mm in diameter was used as the deposition chamber. The substrate, held on a pedestal in the chamber, was heated to deposition temperatures by microwave absorption and heat transfer from the plasma without the need of an additional heat source.

Diamond was deposited on silicon and diamond substrates from gaseous mixtures of methane and hydrogen. The synthesis conditions were; total pressure

of 5.3kPa, substrate temperatures in the range 300 to 900 °C and methane concentrations in hydrogen from 0.3 to 3.0%. Growth of diamond at substrate temperatures lower than 500°C was carried out using seed crystals, obtained at substrate temperatures of 800-850°C in the same apparatus, as substrates. Diamond particles and some films were also synthesized in a mixed gas of methane and hydrogen containing 0.5 to 1% water vapor. Three crystallographic planes (100), (110) and (111) of natural diamond were used as substrates for epitaxial growth. Diamond films for measurement of absorption spectra were polished using a specially designed polishing apparatus.

Raman spectra were measured using the 488.0 or 514.5 nm lines of an argon ion laser for excitation. Cathodoluminescence and absorption spectra were measured with the diamonds at 77K. SIMS analyses were performed using Cameca IMS-3f and IMS-4f ion microanalyzers. For the primary ion beam, $O_2^+$ and $Cs^+$ ions were used. Positive and negative secondary ions were measured for $O_2^+$ and $Cs^+$ primary ions, respectively.

## 3. Characterization of Diamond Synthesized by Microwave Plasma CVD

### 3.1 Raman spectroscopy

Since Raman spectroscopy was used for the evaluation of CVD diamond [3], the technique has been widely used in the field of CVD diamond research. The technique is suitable not only to detect graphitic carbon contained in CVD diamond but also to estimate the quality of diamond.

Figure 2a shows typical change in the Raman spectra of polycrystalline films obtained at 910 °C as a function of methane concentration[4]. Changes in the spectra are clearly observed when the concentrations increase from 2 to 3%. The Raman line of diamond at about 1333$cm^{-1}$ is fairly weak for the 3% film. Broad bands at around at 1360 and 1600$cm^{-1}$, due to highly disordered carbon, gradually appear for concentrations higher than 2%. The concentrations at which the band begins to be detected are dependent on the deposition temperature. The lower the temperature the higher the concentration . Otherwise, the broad band near 1500 $cm^{-1}$ is observable in all of the samples shown in Fig.2. The band is thought to be due to other types of double bonded carbon such as the linearly conjugated double bond.

The Raman spectrum of the individual particles up to 100 μm (Fig. 3)[5] shows that the width of the Raman line is around 2.3 $cm^{-1}$, defined as the full width at half maximum(FWHM). These values may be compared with the values of around 2.0 - 3.0 $cm^{-1}$ observed in natural type Ia and type IIa single crystals used in this study. The line width increased with increasing methane concentrations during preparation. The generation of secondary nucleation on the crystal surface was also more prominent for the higher methane concentrations. The results indicate that defects and impurities are more concentrated in the particles obtained at higher methane concentrations. The peak position was observed to agree within ±0.15 $cm^{-1}$ with those of the high pressure and natural single crystals. The spectrum measured in the wide range has shown that the broad Raman band centered at 1450-1550 $cm^{-1}$ due to double bonds is undetectably weak.

On the other hand, the Raman spectrum of polycrystalline films, obtained

under the same conditions as the particles which exhibited an FWHM of 2.3 $cm^{-1}$, showed the line width broadened to 7.5 $cm^{-1}$, and the peak position shifted to higher Raman energies by around 1.5 $cm^{-1}$, which may be due to strain caused by stress. It is also noted that the 1450-1550 $cm^{-1}$ band is present, though weak.

3.2 Absorption spectroscopy

Figure 4 shows absorption spectra of a single crystal, grown at 1.0% methane and containing water vapor, and a polished polycrystalline film grown at 0.3% methane[6]. Both samples show a continuously increasing absorption from low energies to high energies. The absorption edge at 5.5 eV is clearly observed for both the samples. However, for the polished films grown at methane concentrations higher than 0.5%, the absorption edge was undetectable because of the strong underlying absorption. The absorption in the UV region appears to be due to non-diamond carbon. Since the Raman spectra of such a sample exhibit a broad line centered at 1450-1550$cm^{-1}$, the above observation seems to be consistent with the Raman results.

3.3 Cathodoluminescence spectroscopy

Figure 2b shows the results of cathodoluminescence measurements of diamond films prepared at methane concentrations from 0.3 to 3%[4]. The bright blue emission has been observed in the cathodoluminescence spectrum of the film obtained using 0.3% methane. The emission is attributed to donor-acceptor pair recombination, and is identical to that observed for type IIa natural diamond. The features detected at around 2.33eV, 2.47eV, and 2.57eV (Fig.2b) are characteristic of CVD diamond, and are not observed in natural diamond or diamond prepared by high pressure methods. As Raman lines indicating disordered carbon are observed with increasing methane concentrations(Fig.2a), the weak features observed at low energies in Fig.5a become relatively stronger, and additional lines are observed in the spectra.

Diamond polycrystalline film with (100) preferred orientation[5], obtained at 850 °C and 3% methane, exhibits the emissions associated with the nitrogen atom, interstitial carbon and the vacancy. The 5RL band with a zero-phonon line at 4.582 eV was typically detected for the film obtained at 3% methane. The results indicate that diamond may be contaminated with free carbon atoms at higher methane concentrations.

Figure 5 shows intrinsic edge emission from diamond particles obtained at 0.5-2% methane containing water vapor[7]. The emissions indicate that the diamond particles are pure with few structural defects. The edge emission is strong in particles grown at lower methane concentration than 1%, and becomes relatively weak with increasing concentrations. The emission is only observed in type IIa diamond which is relatively free from defects[8]. No intrinsic edge emission is observed in the polycrystalline diamond films prepared under the same conditions as those for the particles exhibiting the edge emission. The results imply that the growth and aggregation of particles with few structural defects result in films being heavily strained, and that it is hard to get the polycrystalline film free from strain. This tendency is supported by the Raman spectra of particles and film.

3.4 Secondary ion mass spectroscopy

Secondary ion mass spectroscopy(SIMS) has the possibility of detecting all elements from hydrogen to uranium, and is a highly sensitive analytical method.

The depth profile of SIMS analysis of non-doped diamond epitaxially grown on a substrate held on an alumina holder is given in Fig.6[9]. Values 1, 12 and 27 of m/e indicate hydrogen, carbon and aluminum, respectively. Aluminum is considered to come from the substrate holder by impact of the plasma particles. A similar phenomenon has been observed in the results of diamond film grown using a boron nitride holder.These results suggest that contamination by the elements in the substrate holder cannot be neglected for the film obtained using the plasma enhanced method. Hydrogen is abundantly present in the starting gas mixture. However, hydrogen seems to be present in the same concentration as in natural diamond. In fact a growth layer with hydrogen concentration lower than that in natural diamond has been obtained, as shown in Fig.6. Impurities with concentrations higher than that in natural diamond have not been detected.

SIMS analyses of epitaxially grown films doped with boron have shown that the concentrations of boron in the films depend on the concentrations in the starting gas mixtures. The ratios of boron to carbon in the growth layers on (100), (110) and (111) faces are shown in Fig.7. The results indicate that boron may be doped in (111) and (110) at concentrations higher than that in the (100) face.

Growth layers doped with phosphorus were also analyzed using SIMS. In the range of substrate temperature from 820 to 1000°C, impurities in the growth layer increased with increases in substrate temperatures. On the other hand, growth rates increased as substrate temperatures decreased. Typical depth profiles of SIMS analyses of phosphorus-doped diamond films obtained on (110) planes at 0.3% methane and 820°C are shown in Fig.8. The ratios of phosphorus to carbon in the growth layer increase on (110) faces compared with (100) faces. The ratios appear to be related to phosphorus concentrations in the starting gas mixtures. The intensities of m/e=1 and 28 increase with increases of phosphorus in the growth layer. Hydrogen seems to be bonded with phosphorus in diamond, since the contents increase with increasing phosphorus intensities. A SIMS analysis of the epitaxial growth layer with primary ion of $Cs^+$ was performed for the detection of oxygen. However, intensities of m/e=16 were almost the same in the growth layer and the substrate. The result suggests that the content of oxygen in the growth layer may be negligible.

4. Growth of diamond at lower temperatures.

Since typical substrate temperatures in CVD methods for diamond synthesis are in the range 700 to 1000°C, substrates are restricted to heat-resistant materials and the area of application is considerably limited. Growth of diamond at substrate temperatures lower than 500 °C has been attempted using the microwave plasma CVD method[10]. For all the growth-stage studies, individual cubo-octahedral crystals of 2-5μm size grown at temperatures higher than 800°C were employed as nuclei for growth.

Typical changes in morphology of an individual crystal at 500°C are shown in

Fig.9. In the early stage of the growth, the morphology changes from the original cubo-octahedron to octahedron, which indicates that the growth rate of the (100) face, i.e., growth rate perpendicular to (100) plane, is substantially faster than that of the (111) face. Further observation showed that once octahedral morphology is attained, the crystal grows without changing the morphology. The growth rate at 500°C is estimated to be about 150Å/hr. The morphological change at 400°C is similar to that observed at 500°C. The growth rate at 400°C is observed to be 60Å/hr. Growth at 300°C is also shown to be faster on the (100) face than on the (111) face, and gives granular deposits on (100) faces, differing from the crystals grown at higher temperatures. The growth rate at 300°C is approximately 10Å/hr. The growth rates in the range between 300 and 900°C shown in Fig.10 change linearly depending on the substrate temperatures.

Figure 11 shows the Raman spectra of a seed crystal and crystals grown at substrate temperatures ranging from 400 to 700°C. It is noted that the broad band at around 1450-1550cm$^{-1}$, due to a double bond structure, is undetectably weak in the range 500 to 700°C. In the Raman spectrum of the crystal grown at 400°C, the 1450-1550 cm$^{-1}$ band is observed, though weak. The line widths as FWHM are shown in the parenthesis of Fig.11. The data show that the crystals grown at 400-700°C are of reasonably high quality. Deposition at 280°C, the lowest temperature in this study which is restricted by the detectable range of radiation thermometer used here, gave deposits which are identified as diamond by electron diffraction.

## 5. Summary

Diamonds obtained by the microwave plasma CVD method have been characterized using Raman spectroscopy, absorption spectroscopy, cathodoluminescence and secondary ion mass spectroscopy.

It has been shown from the results of measurements of optical properties that single crystals of up to 100 μm in size have good crystalline quality. In contrast, the polycrystalline films grown under the same conditions have appreciable amounts of double bond and strain.

SIMS analyses have indicated that contamination by elements of substrate holder cannot be neglected for the diamond obtained, that contents of hydrogen and oxygen are negligible small, that other impurities with concentration higher than that in natural diamond are not detected, and that boron and phosphorus may be doped in CVD diamond.

Growth of diamond at temperatures lower than 500°C has been attempted. The Raman spectra have indicate that diamonds grown at 400 and 500°C are high quality and similar to natural diamond. The deposition of diamond at 280°C was confirmed.

## References

[1] M.Kamo, Y.Sato, S.Matsumoto and N.Setaka J.Cryst.Growth, **62**, 642(1983).
M.Kamo, Y.Sato and N.Setaka Chem.Soc.Jpn., **1984**, 1642(1984).
[2] M.Kamo, F.Takamura and Y.Sato Proc. 1st Int. Conf. New Diamond

Sci.Tech., (Tokyo), p183,1988
[3] S.Matsumoto, Y.Sato, M.Kamo and N.Setaka Jpn.J.Appl.Phys., **21**,L183 (1982).
[4] M.Kamo, Y.Sato and A.T.Collins Diamond Optics II, p180(1989)
[5] Y.Sato and M.Kamo Surf. Coating Tech., **39/40**, 183(1989).
[6] A.T.Collins, M.Kamo and Y.Sato J. Mater.Res., **5**,2507(1990)
[7] A.T.Collins, M.Kamo and Y.Sato J.Phys.: Condens. Matter, **1**, 4029(1989)
[8] P.J.Dean, E.C.Lightowlers and D.R.Wight Phy.Rev., **140** A352(1965)
[9] M.Kamo,H.Yurimoto and Y.Sato Appl.Surf.Sci., **33/34**,553(1988)
[10] K.Bando, M.Kamo and Y.Sato Proc. 2nd Int. Conf. New Diamond Sci. Tech., (Washington), 1990, in press

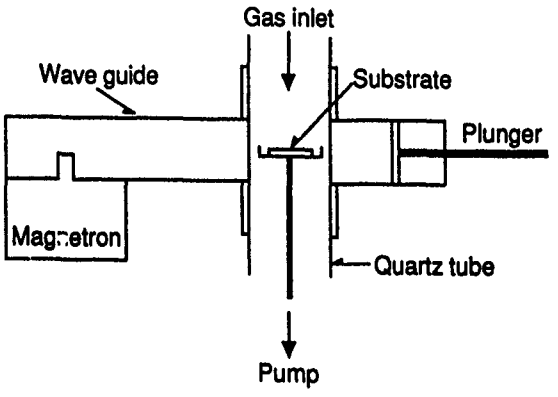



Fig.1 Schematic drawing of the deposition system[1].

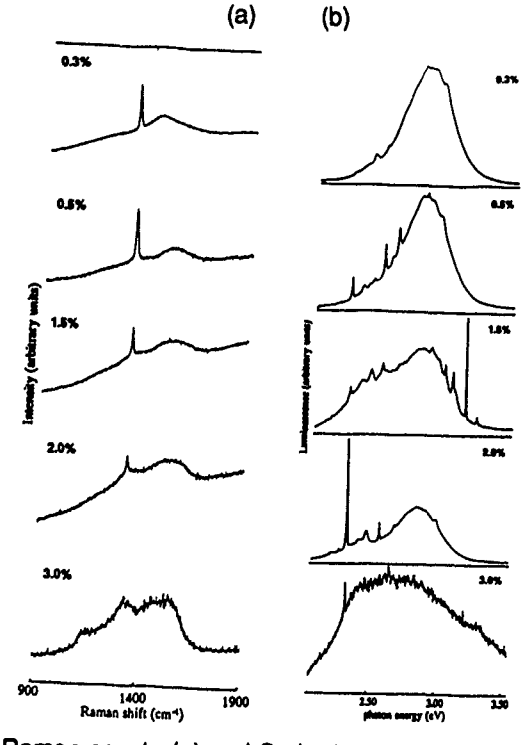



Fig.2 Raman spectra(a) and Cathodoluminescence spectra(b) of diamond films grown at 0.3% and 910°C[4].

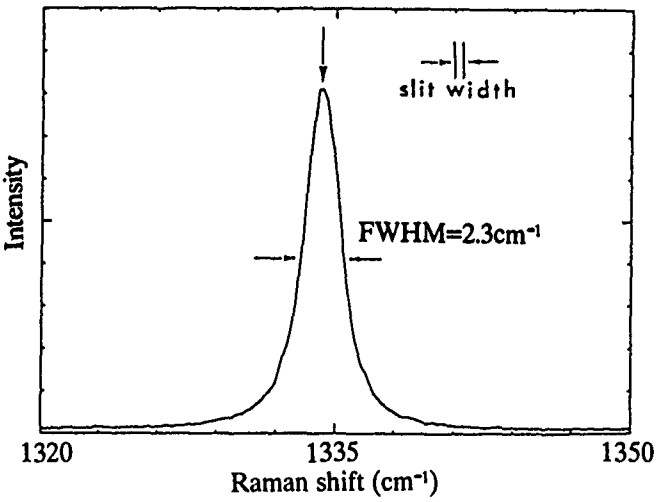



Fig.3 Raman spectrum of individual particles obtained at 0.5% and 850°C[5].

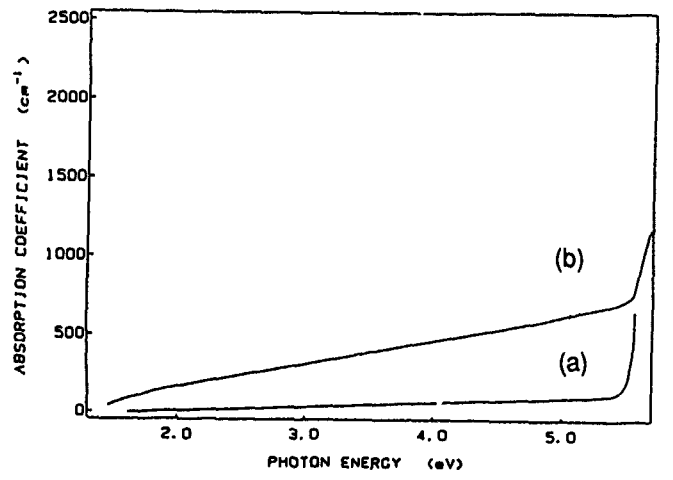



Fig.4. Absorption spectra of a single crystals grown at 1% methane(a) and a polished polycrystalline film grown at 0.3% methane(b)[6].

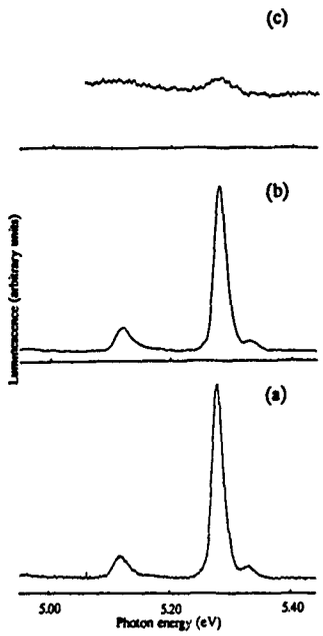



Fig.5 Edge emission from diamond particles grown at 0.5(a), 1.0(b) and 2.0%(c) methane and 850°C[7].

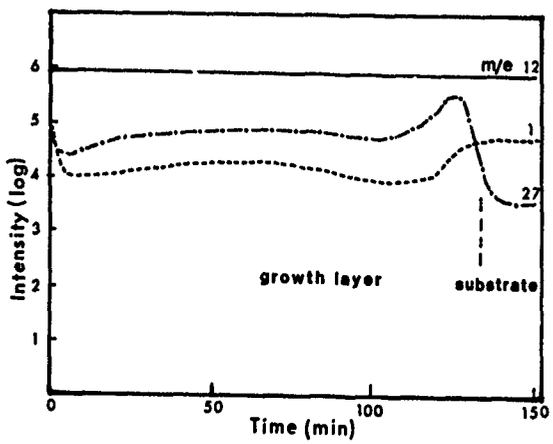



Fig.6 Depth profile of SIMS analysis of an epitaxially grown film[9].

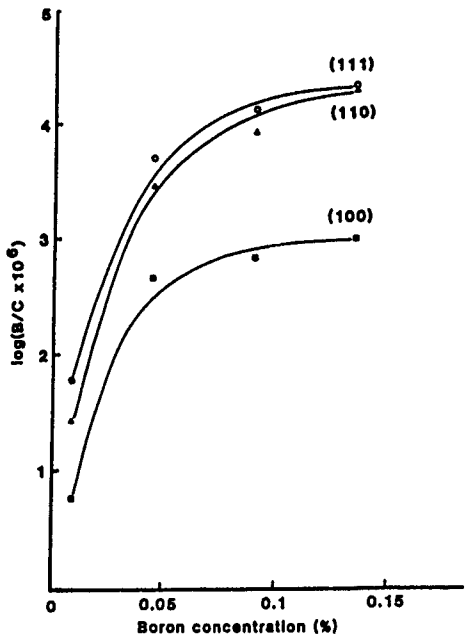



Fig.7 Relations of B/C detected by SIMS with boron concentrations in gas phase.

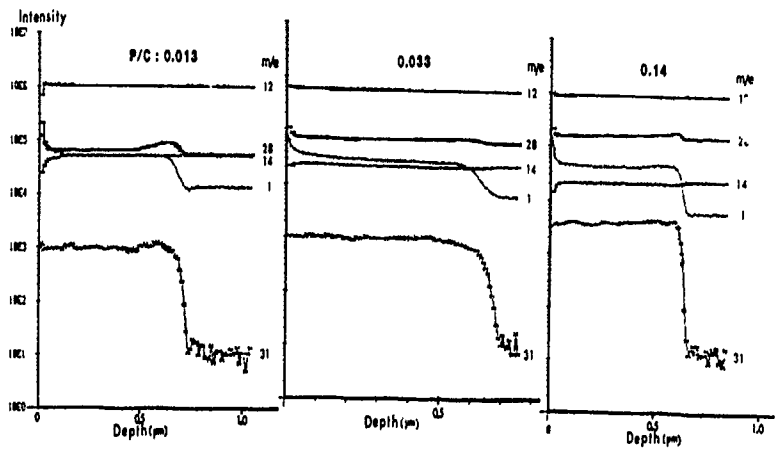



Fig.8 Depth profiles of SIMS analyses of phosphorus-doped diamond films obtained on (110) planes.

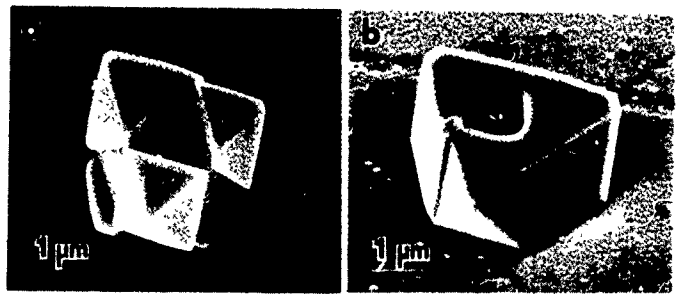



Fig.9 SEM images of typical crystals grown at 500°C[10].

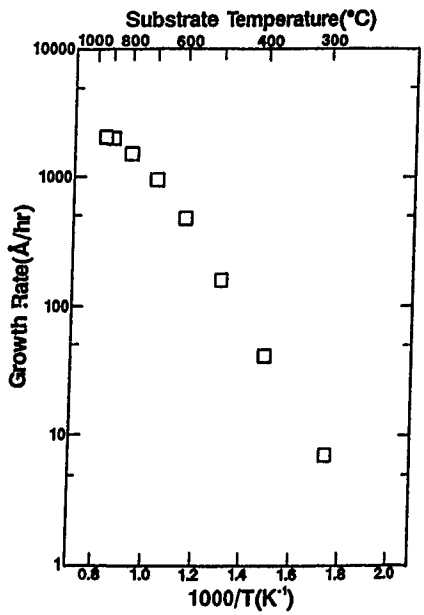



Fig.10 Temperature dependence of growth rate.

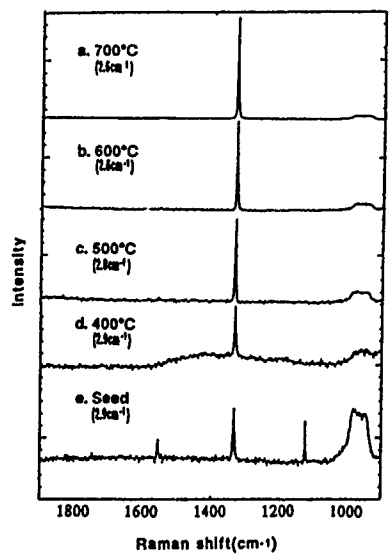



Fig.11 Raman spectra of diamond particles grown at different temperatures[10].

# ALTERNATING CHEMISTRY SYNTHESIS OF DIAMOND

**K.V. Ravi**

**Lockheed Missiles & Space Company, Inc.**
**Research & Development Division**
**3251 Hanover Street, Palo Alto, CA 94304-1191**

## Abstract

By alternating diamond synthesis with the activation of the diamond surface with oxygen it is shown that good quality diamond can be synthesized at methane concentrations up to 15 % in hydrogen. This permits an enhancement of the growth rate of diamond without degrading its quality. It is proposed that the periodic activation of the diamond surface with oxygen results in the creation of surface steps of atomic dimensions that stabalize the diamond phase of carbon even at very high concentrations of methane in the process gas mix.

## Introduction

The conventionally accepted model for the low pressure synthesis of diamond is based on the premise that a supersaturation of hydrogen in the process ambient promotes the formation of diamond and suppresses the formation of non-diamond phases. The most direct inter-relationship between process gas chemistry and diamond quality is the relationship between the methane concentration in hydrogen and the purity of the diamond synthesized. It is well established that as the methane concentration is increased the concentration of non-diamond phases in the diamond increases. This is a direct consequence of the reduction in hydrogen supersaturation as the methane concentration is increased.

In addition to the effects of hydrogen there has been significant interest in the effects of oxygen on process variables such as the growth rate and the quality of diamond. Additions of small quantities of oxygen to diamond forming plasmas has been shown to result in enhanced or reduced growth rates, depending upon the concentration of added oxygen, enhanced quality and the feasibility of synthesizing diamond at temperatures lower than is possible without the addition of oxygen. The effects of oxygen have been attributed to four processes: (a) the formation of additional radicals in the gas phase, (b) the destruction of gas phase pyrocarbon species, (c) the removal of non-diamond phases from the diamond surface and (d) the creation of a more reactive surface. Mucha et. al. (1) have shown that a dominant effect of oxygen addition is to increase the H atom concentration in the discharge. They attribute this increase in H atom concentration to the accelerated removal of amorphous or graphitic carbon allotropes which would otherwise compete with and inhibit diamond growth. Harris and Weiner (2) have shown that the addition of oxygen to non-diamond growing environments, i.e., 7 % methane in hydrogen, reduces the mole fractions of those species not containing oxygen to levels found in diamond growing environments, i.e. 1 % methane in hydrogen. A variation of the process whereby diamond growth is interspersed with a surface etching reaction has been discussed in the literature. Mucha et al.(1) have shown that a marked increase in the growth rate results when the process is partitioned into a diamond

synthesis step involving 4 % methane in a helium discharge with an etching step involving 15% hydrogen and 1 % oxygen in a helium discharge. This process, termed alternating chemistry synthesis, has been suggested as being effective in removing non-diamond bonded surface contaminants during the hydrogen/oxygen cycle, thus activating the diamond surface for more efficient production of diamond during the methane/helium cycle.

In this paper the effects of partitioning the deposition step and surface treatment step are discussed in the light of mechanisms at work on the diamond surface. The effects of surface structure of the diamond have been generally ignored in the literature and it will be shown in this work that the surface structure of the growing diamond plays a very important role in stabilising the diamond phase of carbon during the low pressure synthesis of diamond.

## Experimental

Alternating chemistry synthesis of diamond has been achieved by alternating between a methane-hydrogen discharge and an oxygen-hydrogen discharge. A hydrogen plasma utilizing a gas flow rate of 200 sccm and a pressure of 30 Torr was constantly maintained over an appropriately prepared silicon substrate, at a substrate temperature of ~ 850 °C, in a microwave discharge at a power level of 1.3 KW. Methane and oxygen were alternatively added to the hydrogen discharge to achieve diamond growth (methane cycle) and diamond etching (oxygen cycle) respectively. The concentrations of methane and oxygen as well as the times of the two processes were varied. Typical times, in a cycle, ranged from 2 to 5 minutes for diamond deposition alternated with 0.5 to 2 minutes for diamond etching. Using computer controlled mass flow controllers alternating chemistry synthesis can be achieved for the desired length of time. Typical deposition times reported in this paper were of 5 hours duration each. The substrates used in these experiments were polished silicon wafers which were specially prepared to achieve diamond nucleation in a predetermined matrix. Utilizing a combination of surface damage, created by abrading with 0.25 μm diamond paste, followed by photolithography and selective etching, a square array of damage sites were created with localized damage sites on the silicon surface ranging in size from 1 μm X 1 μm to 10 μm X 10 μm. In this paper the results of the experiments presented involve SEM micrographs of the crystals and films since one of the key results of these experiments is the effect of alternating chemistry on the morphology of diamond crystals and films.

## Experimental Results.

The steady state growth of diamond utilizing mixtures of methane and hydrogen typically results in well cystallized, crystallographically well defined films at methane concentrations typically below 2% in hydrogen. At higher methane concentrations the incorporation of non-diamond phases is accompanied by a degradation in the crystallinity of the material and the development of rounded grains, often called a cauliflower structure. This is shown in Figure 1. 2% methane in hydrogen results in a crystalline film with {111} facets predominating. An increase in methane concentration to 4 % results in a cauliflower structure which is characterized by non-diamond bonded impurities. Utilizing alternating chemistry processing, good quality diamond films can be obtained at methane concentrations at which steady state processes lead to a significant concentration

of non-diamond phases. The bottom electron micrograph in Figure 1 shows the structure of a diamond film synthesized by the cyclic alternation of 4 % methane in hydrogen with 0.5 % oxygen in hydrogen, with a 2 minute duration for each process. Well formed crystals are aggregated together to form a film. This contrasts strongly with the structure of the film obtained with a steady state process.

Increasing the methane concentration in hydrogen during the deposition step and alternating with an oxidation step has been shown to result in good quality diamond with continuing increase in the methane concentration, as evidenced by the surface structure of the crystallites, up to methane concentrations of 15 % in hydrogen. In figure 2 well formed crystals with smooth {100} and {111} faces are observed at a methane concentration of 5% in hydrogen. As the methane concentration is increased, in alternating chemistry processing, the {111} faces get rougher and less well defined. At a methane concentration of 20 % the {100} faces are still observed to be smooth and well formed while the {111} faces are covered with diamond-like carbon phases, as evidenced by the very fine grained, cauliflower-like structure of these faces, as shown in Figure 4.

The growth rate of diamond films increases with increasing methane concentration in hydrogen. However methane concentrations beyond about 3 % lead to the incorporation of increasing amounts of non diamond phases. With alternate chemistry processing, however, diamond quality can be maintained to very high methane concentration levels, as shown above. This leads to the feasibility of significantly enhancing growth rates without degrading the quality of the diamond. A plot of the growth rate as a function of methane concentration is shown in Figure 3. The plot shows the growth rate for a steady state process at low methane concentrations and for cyclical growth for higher methane concentrations. The scanning electron micrographs of the structure of the diamond crystals attest that good quality crystals are observed up to methane concentrations of 15% by periodically interrupting the synthesis process with a surface oxidation step. Growth rates close to 1 μm/hour have been achieved for process gas pressures of 30 Torr. For steady state conditions, the requirement to utilize low methane concentrations to achieve good quality diamond, limits growth rates to values under 0.2 μm/hour at a pressure of 30 Torr (3). Higher pressures can lead to enhanced growth rates but at the expense of deposition area. Alternating chemistry processing permits enhanced growth rates at low pressures and hence on large area substrates.

## Discussion

It has been shown that the stability of the diamond phase of carbon can be considerably enhanced by the use of alternating chemistry processing. Whereas, with steady state synthesis of diamond, the requirement to maintain a supersaturation of hydrogen in the process gas ambient effectively limits the concentration of hydrocarbon that can be utilized, thus severely limiting growth rates, the periodic activation of the growing diamond surface with oxygen permits the use of considerably higher concentrations of methane in hydrogen during the diamond synthesis step of the process. Good quality diamond crystal and films have been synthesized at up to 15 % methane in hydrogen by this process. One explanation for the observations is that during the diamond synthesis step of the process the high methane concentration results in the co-deposition of non-diamond phases and diamond. In the subsequent oxidation step, the non-diamond phases are preferentially removed, leaving behind diamond. However if such a mechanism were operational the net growth rate of diamond is not expected to go

up significantly as the methane concentration is increased. At the higher methane concentrations, the predominant phase of the solid deposited should be non-diamond in nature and thus be removed in the subsequent oxidation step, effectively removing most of the deposited solid with no attendant increase in the net growth rate. Since, up to methane concentrations of 15 %, discussed in this paper, the net growth rate of diamond increases, an alternative mechanism has to be invoked to explain the observations.

It is clear that the nature of the diamond surface plays a crucial role in the stabilization of the diamond phase of carbon. Synthesis of diamond at high methane concentrations is made possible as a result of surface activation by oxygen. Consequently, for stabilizing the diamond surface at low pressures, in addition to atomic hydrogen in the ambient, the nature of the surface on which diamond synthesis occurs appears to be very important. We suggest that oxygen creates atomic sized steps on the diamond surface and these steps promote the stabilization of the diamond phase when carbon is added to the surface during the diamond synthesis cycle of the process. The steps can provide a higher concentration of active surface sites which can be occupied by hydrogen and subsequently replaced by carbon, with $sp^3$ hybridization being promoted between the surface carbon atoms and the arriving carbon atoms. Atomic sized steps on the surface can prevent graphite formation by providing the right environment for diamond formation at the surface, since the steps will have the dimensions of the interatomic spacing (or multiples thereof) of diamond and thus will not readily accommodate graphite or other non-diamond forms of carbon. Steric hindrance effects may be operational in suppressing non diamond formation. This can account for the observations presented here whereby diamond synthesis is achieved at much higher concentrations of methane than is possible with steady state processes. Figure 5 is a schematic illustration of this mechanism.

The finding that the {100} faces of diamond crystals are observed to be of high quality, presenting a smooth well formed surface up to methane concentrations of 20 % in hydrogen, when the surface is periodically activated by oxygen further supports the contention that surface steps, or ledges stabilize the diamond phase. Surface steps are most easily formed on {100} faces and the sideways propagation of these steps can occur to propagate the crystal. It has been shown that at high synthesis temperatures, and in the presence of oxidizing species in the process ambient, {100} faces of diamond crystals predominate (4). This finding is similar to the observation presented here whereby the quality of the {100} faces of diamond crystals is maintained at a high level with increasing methane concentrations while the {111} faces get contaminated by the overgrowth of diamond like carbon phases. These results cast a new light on the mechanism of low pressure diamond synthesis.

## References

1. J.A. Mucha, D.L. Flamm and D.E. Ibbotson, J. Appl. Phys, 65, 3448 (1988)
2. S.J. Harris and A.M. Weiner, " Diamond, Silicon Carbide and Related Wide Band Gap Semiconductors", Materials Research Society Symposium Proceedings, Ed. J.T. Glass, R. Messier and N. Fujimori, Volume 162, p.103 (1989)
3. W. Zhu, R. Messier and A.R Badzian, Proceedings of the First International Symposium on Diamond and Diamond Like Films, Eds. J.P. Dismukes, A.J. Purdees, K.E. Spear, B.S. Myerson, K.V. Ravi, T.D. Moustakas, and M. Yoder, The Electrochemical Society, p. 61 (1989)
4. K.V. Ravi and A. Joshi, Appl. Phys. Lett., 58, 246 (1991)



Figure 1 (a). Steady state growth with 2 % Methane in Hydrogen



Figure 1 (b). Steady state growth with 4 % Methane in Hydrogen

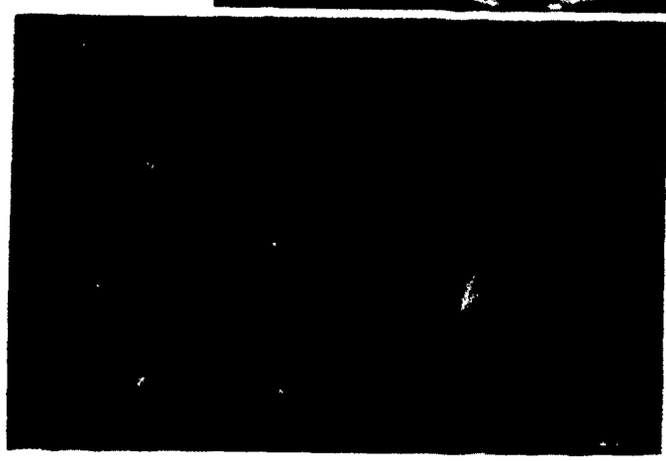


Figure 1 (c). Alternating chemistry synthesis - 4% methane in hydrogen, 2 minutes; 0.5 % oxygen in hydrogen, 2 minutes.

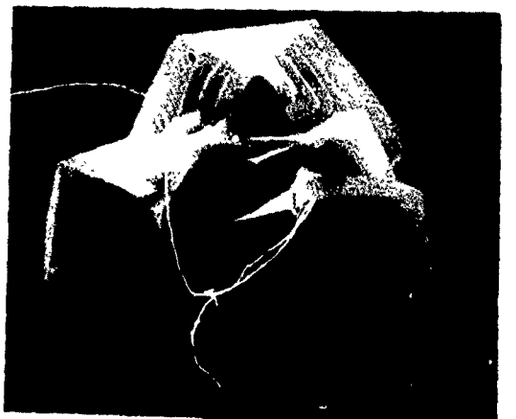


Figure 2 (a). Alternating chemistry synthesis 5 % Methane in Hydrogen ( 2 mins.); 0.5 % oxygen in hydrogen ( 2 mins.)

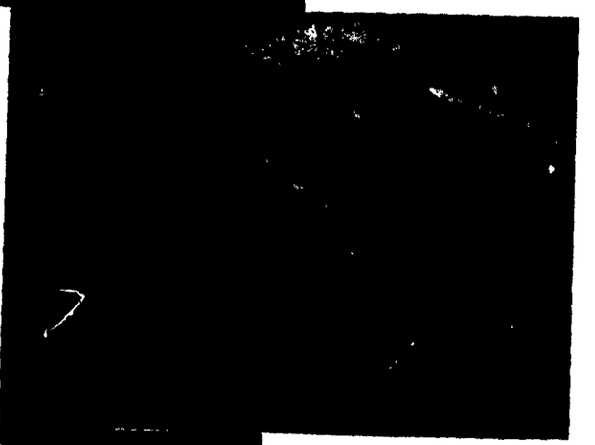


Figure 2 (b). Alternating chemistry synthesis 10 % Methane in Hydrogen ( 2 mins.); 0.5 % oxygen in hydrogen ( 2 mins.)



Figure 2 (c). Alternating chemistry synthesis 15 % Methane in Hydrogen ( 2 mins.); 0.5 % oxygen in hydrogen ( 2 mins.)

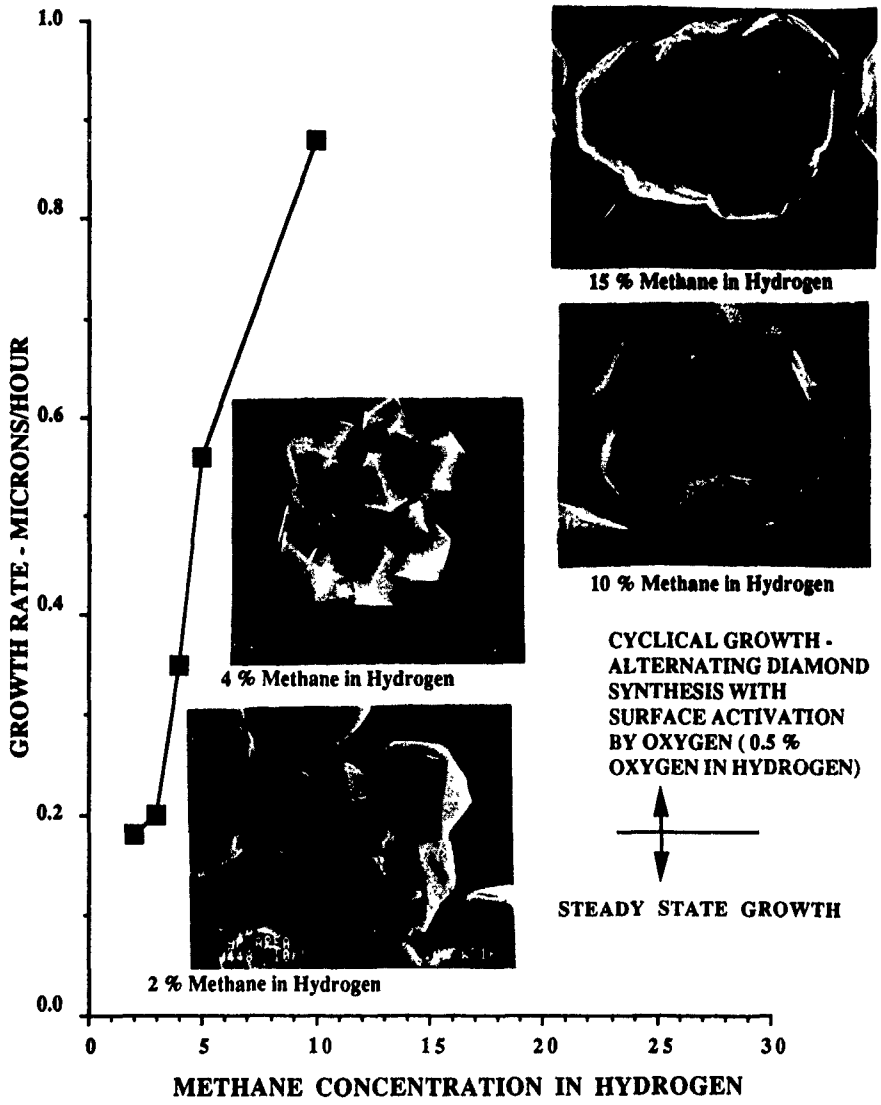



Figure 3. Growth rate as a function of methane concentartion for diamond synthesized by alternating chemistry processing. Electron micrographs of diamond crystals show that high quality, well facetted diamond can be achieved up to methane concentrations of 15% in hydrogen by the use of alternating chemistry synthesis.



Figure 4. Scanning electron micrograph of a cluster of diamond crystals synthesized by the cyclic alternation of 20% methane in hydrogen and 0.5 % oxygen in hydrogen. The {100} faces of the crystals are shooth and well formed whereas the {111} and other more close packed planes are covered with a diamond like carbon layer.

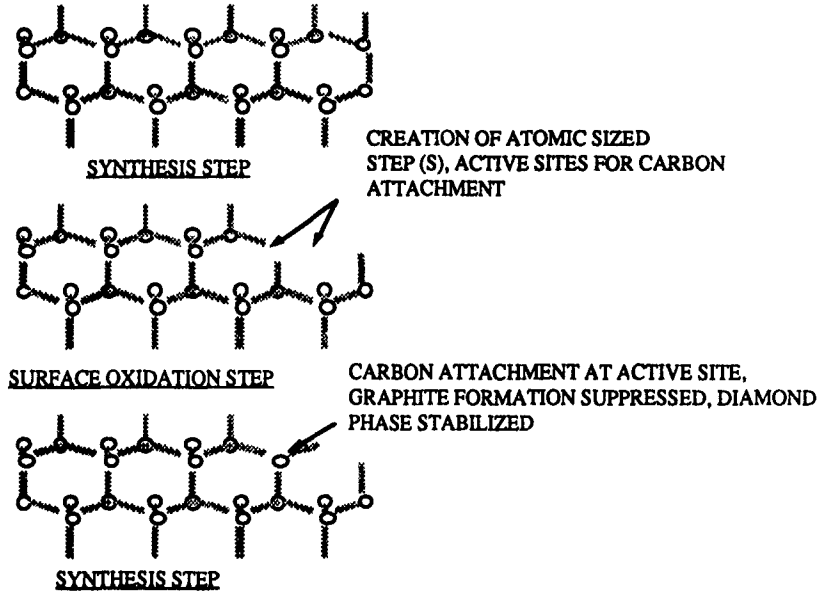



Figure 5. Schematic illustation of the stabilization of the diamond phase of carbon at low pressures by the surface structure of diamond.

# Synthesis of Diamond Films with Pulsed Plasmas

M. Aklufi and D. Brock
Naval Ocean Systems Center, San Diego, CA 92152

Diamond films were grown in plasmas formed with microwaves that were modulated with a pulse generator. Films obtained with the use of pulse periods in the nanosecond, microsecond, and millisecond ranges were compared to baseline films which were obtained with a CW plasma. The deposited films were examined with SEM, XRD and Micro-Raman spectroscopy. For the experimental conditions used, the diamond films' growth rates and quality improved with increasing pulse duration while maintaining a duty cycle at nearly 50 percent, and reached a maximum with CW generated films. This was attributed primarily to an increasing degree of supersaturation of atomic hydrogen at the growth surface with increasing pulse time.

## I. INTRODUCTION

The metastable growth of diamond films has been achieved by a number of continuous plasma-enhanced chemical vapor deposition (CVD) methods [1-4]. Of these, none have gained more attention than the CW microwave plasma-enhanced chemical vapor deposition technique [4]. In this technique the amount of microwave power used is typically limited by the extent of substrate heating induced by plasma and microwave heating. Concomitantly, this restriction in the amount of microwave power that can be used also reduces the amount of reactants that can be dissociated which may adversely effect the film's growth rate as well as quality.

The use of pulsed radio-frequency discharges of very high power to deposit thin films has recently been reported by Scarsbrook et al. [5]. They found that short pulses at high power resulted in increased reactant dissociation rates while simultaneously reducing substate heating. This resulted in higher deposition rates at lower temperatures than previously obtained by steady state conditions. In this paper we investigate the use of microwave induced pulsed plasmas in the CVD growth of diamond films.

## II. EXPERIMENTAL PROCEDURE

A microwave plasma-enhanced CVD system with a dielectric waveguide was used in the deposition of the diamond films. A schematic of the system used is shown in Figure 1. The use of dielectric waveguides to form plasmas has been described previously [6]. The microwave supply was modified by the addition of a Phillips PM5715 pulse generator for pulse operation, and the maximum power output was increased by an order of magnitude to 2.5KW at 7.36 +/- 0.050 GHz from that previously reported, with the use of an Energy Systems 2.5KW, Low X-Band Amplifier.

Deposition was performed on (100) silicon n-type substrates. To aid in the nucleation and reduce the time necessary to nucleate the diamond film, the substrates were seeded by abrading them with diamond crystals that were up to 2 micrometers in size. The dielectric waveguide, located within the inner chamber, is maintained at atmospheric pressure. The silicon substrates were placed horizontally on sapphire tiles that rested on the inner chamber just above the output end of the dielectric waveguide. In addition Grafoil, a graphite sheet product of EGC Corporation, was placed about the substrate. These procedures were used to suppress unwanted plasma reactions and minimize any potential contamination of the diamond film

After the deposition tube was evacuated to less than 100 millitorr, argon was introduced into the reaction chamber and the plasma initiated when the pressure was about 5 torr. Oxygen, and then hydrogen were introduced into the reaction chamber. The deposition pressure was first set by using a throttle valve, and then adjusted with a vernier controlled metering valve. The plasma's intensity was greatest at the surface of the substrate and decreased with distance from the surface. Depositions were performed with and without the use of external heating. When a furnace was not used the substrate was heated only by the plasma and microwave heating. Substrate temperatures were measured with a Chapin Tec, Model ROS-5U two color optical pyrometer. The temperature deposition range was between 800 and 1050$^{o}$C with an average substrate temperature of 925$^{o}$C.

The gas flow rates during deposition were 100 cc/min hydrogen, 0.5 cc/min methane, and 0.5 cc/min oxygen. In addition argon, which acted as a diluent, was added to the gas flow in the amounts of 100 cc/min for CW and 50 cc/min for pulsed-plasmas depositions respectively. The pulse generator was run in the nanosecond, microsecond, and millisecond ranges. The Energy Systems klystron amplifier was set to obtain the system's peak power for all pulsed-plasma depositions. Duty cycles were adjusted to about 50 percent, to obtain an average forward power that was similar to the power used in CW baseline depositions. An effort was made to maintain the substrate at a deposition temperature similar to that of the CW baseline. Deposition times were between 7 and 8 hours.

## III. RESULTS

Some remarks are in order concerning the pulsing of microwaves and the resulting plasmas. Plasmas formed with pulse repetition rates in the nanosecond range were continuous. Plasmas formed in the microsecond and millisecond ranges were pulsed. In addition, the the rise and fall time of the microwave system was approximately 40 nanoseconds, primarily due to the narrow bandwidth of the klystron amplifier. As a result, in nanosecond pulsed experiments the peak microwave power was not reached during the pulse on-time nor was the microwave power completely turned off during the pulse off-time.

In the nanosecond range, with a pulse duration and repetition time of 54 and 100 nanoseconds respectively, the deposited film was not continuous. An SEM micrograph of the discrete crystallites, with poorly defined faceting, is shown in Figure 2a. With the pulse duration and repetition time increased to 5 and 10 microseconds respectively, the deposited film exhibited mostly (111) faceting as can be seen in Figure 2b. Facets, primarily the (111), were reasonably

formed and typically submicrometer in size. However, some of the (100) facets were found to be 2.5 micrometers in length. The average deposition rate was 0.4 micrometers per hour. In the millisecond pulsed-plasma range, with a 5.6 millisecond pulse duration and a 10 millisecond repetition time, the film exhibited well defined (111) and (100) facets. An SEM micrograph is shown in Figure 2c. The largest (100) facet faces measured 5 micrometers in length. The average deposition rate was 0.8 micrometers per hour. For comparison purposes a film was deposited using a continuous plasma. The power used was equal to half of the peak power used in the pulsed mode. The SEM micrograph of this film is shown in Figure 2d. As can be seen very well defined (100) and (111) facets are present. The largest (100) facets faces measured 12 micrometers in length. The average deposition rate was 1.5 micrometers per hour.

If we assume that diamond seeding reduces or eliminates the incubation period the average growth rate may be determined from the thickness of the film and the time of deposition. In Table 1, the thickness and growth rate of the deposited films is shown as a function of the pulse period. For the method chosen to calculate the growth rate, i.e., based on film thickness, no growth rate could be assigned to the non-continuous film grown with a plasma generated with nanosecond pulsed microwaves. As can be seen, the thickness of the deposited films by the pulsed-plasma technique increased with the pulse period and reached a maximum with CW plasmas.

Table 1. Thickness and growth rates of pulsed and CW plasma deposited films.

| MICROWAVE POWER | FILM THICKNESS (μm) | FILM GROWTH RATE (μm/hr) |
|---|---|---|
| ηsec PULSED | NON-CONTINUOUS | —— |
| μsec PULSED | 2.5 | 0.4 |
| msec PULSED | 6.0 | 0.8 |
| CW | 10.2 | 1.5 |

A Rigaku Rotaflex RU 200B X-ray diffractometer was used to determine the structure and nature of the deposits. X-ray diffraction patterns of the continuous deposited films obtained with plasmas formed with microsecond and millisecond pulsed, and CW microwaves are shown in Figure 3. Stick figures of the standard powder pattern of natural cubic diamond are also shown. These define the location and relative intensity of the most prominent cubic diamond crystallographic planes, i.e., (111), (220), (311), (400), and (331) within the diffraction angle of 2 theta that lie between 0 and 140 degrees. The sharp peaks not located at the stick figures are that of the crystalline (100) oriented silicon substrate. Of particular interest is the deviation between the standard powder pattern stick figures relative intensity ratios and that of the intensity rations of the deposited diamond films. These differences indicated that the deposited

diamond film crystal orientation is non-random and exhibits a preferred texture.

The Raman spectra of continuous films deposited with plasmas formed with microsecond and millisecond pulsed, and CW microwaves were generated by Instruments SA on their Raman Microprobe S3000 spectrophotometer and are shown in Figure 4. Excitation was provided with the 514.5 nm line of an argon ion laser. The film grown with the microsecond pulsed plasma exhibits a very broad non-diamond peak about 1600 cm-1 above a luminescent background. The msec pulse film shows a broad diamond peak about 1332.4 $cm^{-1}$ and a broad non-diamond peak about 1500 cm-1. By comparison, the Raman spectrum of the baseline CW plasma film exhibited a sharp diamond peak with a FWHM of 5.5 at 1333.5 cm-1 with no other carbon peaks or fluorescent background present. Sharma et al. [7] found that differences in diamond Raman peak location could be attributed to strain in the diamond.

The pulsed plasma average power levels were nearly equal to those used in the baseline CW plasma, however, the use of pulsed plasmas with long pulse off-times can result in reduced heating of the substrate. Although this study did not specifically address the optimization of temperature, to determine if a temperature effect did exist with pulsed-plasma depositions, the substrates were heated to 600°C before the plasma was ignited. A less than ten percent improvement in film thickness for the microsecond pulsed-plasma case indicated some substrate cooling had occurred. In this case the deposition temperature could have been optimized for maximum growth, but it was not the primary cause for the lower growth rate.

## IV. DISCUSSION

Our present understanding of the chemical vapor deposition of metastable phases, such as diamond, is that large deviations from thermodynamic equilibrium exist within the growth environment, and that the metastable phase is kinetically favored has been discussed [8]. The general chemistry of microwave plasma enhanced chemical vapor deposition of diamond with $H_2$, $CH_4$, and $O_2$ as reacting gases is that H, $CH_3$, $C_2H$, and OH, have been found to be the primary species generated by the plasma.[2] At low $CH_4$ and $O_2$ concentrations the major exiting gas species of include $H_2$, $CH_4$, $C_2H_2$, $H_2O$, and CO [9]. In low pressure diamond growth, the methyl radical and acetylene have been identified as the major carbonic growth species. Using isotopic labeling experiments, Chu et al. [10] found that the methyl radical is the primary growth species. Accordingly, in the discussion only methyl radicals are considered, however similar arguments might be made for acetylene radicals. Martin and Hill [11], have reported that methyl radicals and atomic hydrogen have lifetimes in microseconds and seconds respectively. As previously indicated, the gas flows were maintained at constant flow rates during the deposition, and the microwaves were pulsed with approximately 50 percent duty cycles. Based on this understanding and upon the results of this experiment it is proposed that the extent of dissociation of the reactant gases determined the amount and nature of the deposit.

Diamond deposition with plasmas formed with nanosecond pulsed microwaves had the poorest quality. As previously indicated the forward power rise times were on the same order as the pulse duration. During this period, the microwave power did not reach its maximum value limiting the dissociation of

the incoming reactant gases. Scarsbrook et al. [5] reported that the dissociation of molecular nitrogen into atomic nitrogen did not reach its maximum concentration until 150 microseconds into the pulse, and indicated that reactant dissociation time, within a plasma, may be dependent on its bond strength. Accordingly, the time it takes to dissociate molecular hydrogen into atomic hydrogen and reach its maximum concentration at the given microwave power, may be on the order of 75 microseconds. For nanosecond pulse periods a low concentration of active species may not provide any significant diamond growth.

In the microsecond pulsed case, the increase of pulse duration to microseconds far exceeded the 40 nanosecond rise time of the microwave system. As a result, sufficient time was available for the microwave forward power to reach its maximum value during the pulse on-time. This allowed for an increase in reactant dissociation greater than could be achieved in the nanosecond case. For the 5 microsecond pulse, the reactant gases could still not reach their maximum concentration if dissociation times are in tens of microseconds. Further, the microsecond pulse off-times are sufficiently long to allow the short lived methyl radicals, formed from the dissociation of methane, to recombine with atomic hydrogen. Methyl radicals must now be generated by hydrogen abstraction of methane with atomic hydrogen. This consumption reduces the number of atomic hydrogen formed [12]. However, the the net increase of active species results in an improvement over the nanosecond case.

In the millisecond case, rise time and dissociation time are small compared to the pulse on-time, and the reactants reach their maximum concentration for the given peak power. This maximum concentration of atomic hydrogen coupled with the concomitant increase of atomic hydrogen generated methyl radicals results in an increased growth rate for the film. In the millisecond case, because the generation rate of atomic hydrogen is significantly larger for millisecond than for either nano- or microsecond pulse periods, the amount of atomic hydrogen remaining after recombination is still higher than the other previous pulsed cases. However, the degree of atomic hydrogen supersaturation is dramatically impacted by its recombination during the pulse off-time. As a result, the quality of the film, as represented by the ratio of sp3 to sp2 carbon bonds, only moderately improves.

Baseline films obtained with CW formed plasmas had growth rates and film quality that exceeded any obtained from pulsed-plasmas. The extent of dissociation of the reacting gases was dependent upon the microwave forward power and the resultant plasma density, the time of dissociation, and the recombination rates.

The plasma density is a function of the microwave forward power. Although the average power was approximately the same for both the CW and pulsed cases their peak power was not. Pulsed plasmas were operated at near 50 percent duty cycles and their peak power at 2.5 KW was double of that of the CW case. Due to the rise time, only the microsecond and millisecond pulses reached peak power during the pulse period. As a result the plasma density for pulsed cases would be higher than CW cases. However, the plasma density would not have doubled, since the plasma density increases more slowly than the applied forward microwave power.

The time for dissociation impacted the nanosecond and microsecond

pulsed cases, but was not a factor for either the millisecond pulsed or CW cases. Methyl radical recombination was a factor only for microsecond and millisecond pulsed cases. Atomic hydrogen recombination becomes significant only in the millisecond case. In this case, with the increased pulse off-time proportionately more atomic hydrogen recombines, and more significantly atomic hydrogen is not being generated. From the data reported by Martin and Hill [11], it is estimated that for the 5 millisecond off-time there is an 80 percent recombination of atomic hydrogen into molecular hydrogen. For the experimental conditions used, CW plasmas produced a higher rate of reactant gas dissociation than any of the pulsed cases. As a result the growth rate and quality of CW films were higher than pulsed-plasma films.

As seen in Figure 2, the crystal facets increase in size and appearance as the pulse on-time increases. Crystal faceting can also be considered a measure of film quality. Harker and DeNatale [13], noted that an increase in the oxygen content of the reacting gases resulted in improvements in reactive etching rates, which increased the diamond crystallite size. The possibility of depositing diamond layers with pulse on-times and non-diamond carbon during pulse off-times was considered. However, with subsecond pulse cycles and deposition rates at less than an angstrom per second, atomic layering could not be possible. As a result, it was concluded that diamond and non-diamond carbon are deposited simultaneously .

Because of the fixed composition of the incoming reactant gases, improvements in growth rates could in part be attributed to an increase in dissociation of the carbon precursor methane. However, due to the short lifetime of methyl radicals, the mechanism of hydrogen abstraction is needed to generate these radicals. Although oxygen has been shown to improve both the deposition rate as well as the quality of the film, it requires the presence of atomic hydrogen. Of the roles ascribed to oxygen by Spear and Frenklach [14], only that of promoting the gas phase production of hydrogen would apply to improving the growth rate of diamond films. It was first reported by Spitsyn et al. [15] that atomic hydrogen directly contributes to both the quality as well as the growth rate by stabilizing the diamond surface, preferentially etching sp and sp2 bonded carbon from the growing surface, and activating the growth surface by hydrogen abstraction. The improvement in diamond film growth for increasing pulse periods which reached a maximum for CW grown films, would support the idea that these improvements were attributed primarily to increases of atomic hydrogen. For a given ratio of hydrogen and methane, once the supersaturated level of hydrogen is reached, diamond is deposited. Once diamond growth is achieved, increasing the atomic hydrogen by only a small factor will significantly improve the growth rate and quality. This is in qualitative agreement, for the low pressure regime portion of the theory proposed by Vandenbulcke et al. [16], which concerns the effects of atomic hydrogen supersaturation on the growth of diamond.

## V. SUMMARY AND CONCLUSIONS

Diamond films were grown in plasmas formed with microwaves that were modulated with a pulse generator. Films obtained with the use of cycle times in nanosecond, microsecond, and millisecond ranges with 50 percent pulse on-times were compared to baseline films which were obtained with a CW plasma. For the

experimental conditions used, the diamond films' growth rates and quality improved with increasing pulse duration, and reached a maximum with CW generated films. This was attributed primarily to an increasing degree of supersaturation of atomic hydrogen at the growth surface with increasing pulse duration.

**Acknowledgement**

This research was supported by the Office of Naval Research under project number RR02202.

## REFERENCES

1. S. Matsumoto, J. of Mat. Science Letters, **4**, 600 (1985).
2. K. Kitahama, K. Hirata, H. Nakamatsu, S. Kawai, T. Imai, N. Fujimori, Y. Yoshino, and A. Doi, Appl. Phy. Lett., **49**, 643 (1986).
3. K. Suzuki, A. Sawabe, H. Yasuda, and T. Inuzka, ibid., **50** (12), 728 (1987).
4. M. Kamo, Y. Sato, S. Matsumoto, N. Setaka, J. Crystal Growth, **62** 642 (1983).
5. G. Scarsbrook, I. P. Llewellyn, S. M. Ojha, and R. A. Heinecke, the Proc. of EVAC-88, Vacuum, **8** (8,9), 627 (1988).
6. M. Aklufi and D. Brock, Pro. 1st Internat. Sympos. on Diamond and Diamond-Like Films, Electrochem. Soc., **89** (12), 114 (1989).
7. S. K. Sharma, H. K. Mao, P. M. Bell, and J. Z. Xu, J. Raman Spectras **16**, 350 (1985).
8. R. C. DeVries, Ann. Rev. Mater. Sci., **17**, 161 (1987).
9. T. Kawato and K. Kondo, Japan. J. Appl. Phys. **26** (9), 1429 (1987).
10. C. J. Chu, M. P. D'Evelyn, R. H. Hauge, and J. L. Margrave, J.Mater. Res. **5**, 2405 (1990).
11. L. R. Martin and M. W. Hill, Pro. 1st Internat. Sympos. on Diamond and Diamond-Like Films, Electrochem. Soc., **89** (12), 568 (1989).
12. J. E. Butler and F. G. Celii, ibid., **89** (12), 317 (1989).
13. A. B. Harker and J. F. DeNatale, J. Mater. Res. **5**, 818 (1990).
14. K. E. Spear and M. Frenklach, Pro. 1st Internat. Sympos. on Diamond and Diamond-Like Films, Electrochem. Soc., **89** (12), 122 (1989).
15. B. V. Spitsyn, L. L. Bouilov, and B. V. Deryagin, J. Cryst. Growth, **52**, 219 (1981).
16. L. Vandenbulcke, P. Bou, and G. Moreau, Pro. 1st Internat. Sympos. on Diamond and Diamond-Like Films, Electrochem. Soc., **89** (12), 594 (1989).

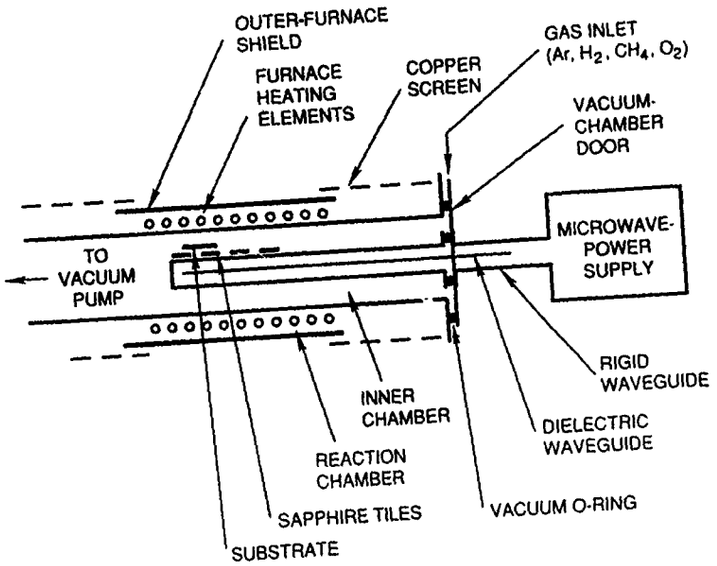



Figure 1. Schematic drawing of the pulse/CW plasma deposition system.

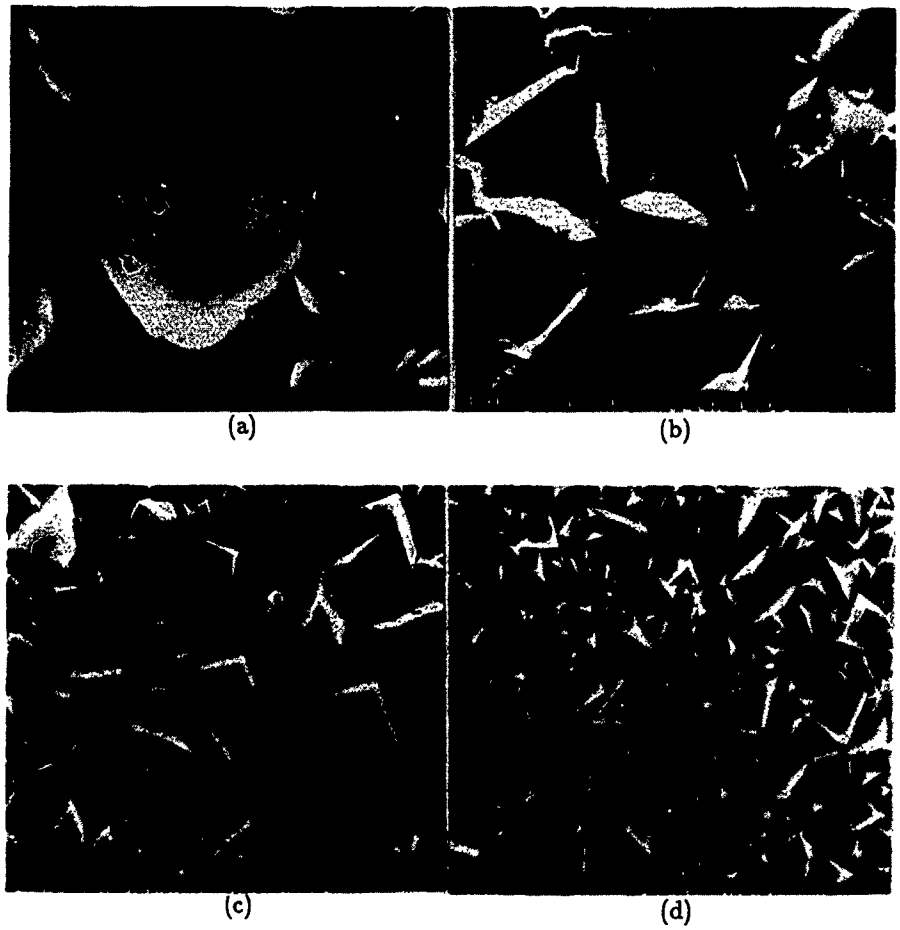



Figure 2. SEM microphotographs of deposited diamond films. (a) nanosecond pulsed-plasma; (b) microsecond-pulsed plasma; (c) millisecond pulsed-plasma; and (d) CW plasma baseline.

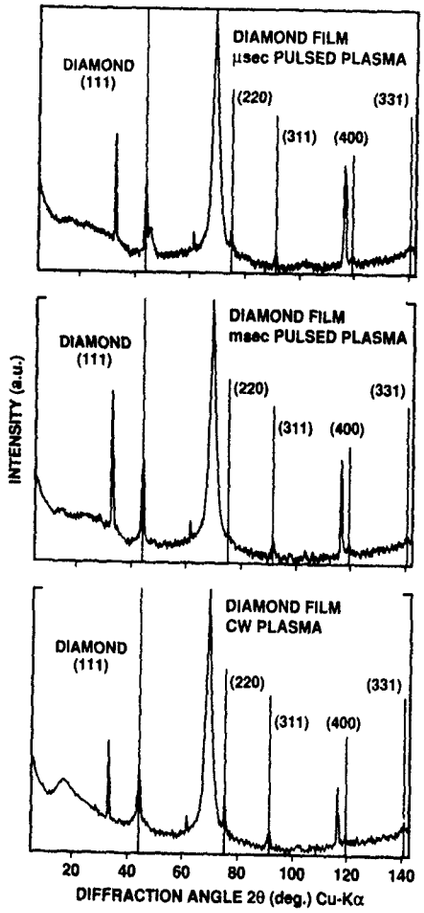



Figure 3. XRD pattern of microsecond and millisecond pulsed, and CW plasma deposited diamond film.

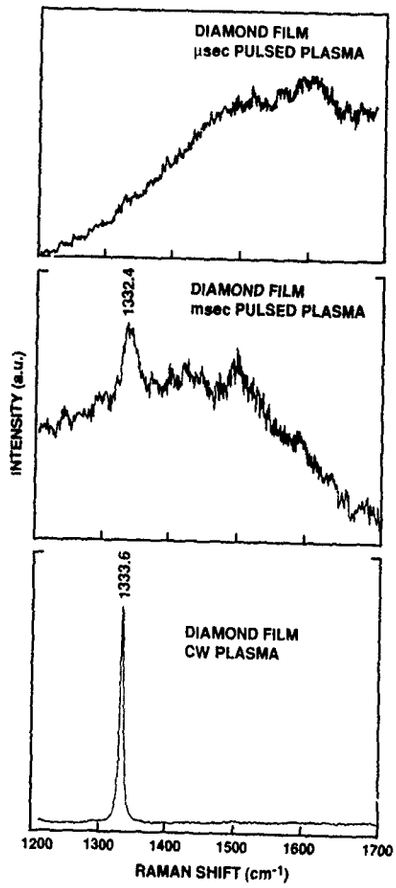



Figure 4. Micro-Raman spectra of microsecond and millisecond pulsed, and CW plasma deposited diamond film.

# MINIMIZATION OF INFRARED ABSORPTION OF FLAME DEPOSITED DIAMOND FILMS BY SEQUENTIAL DEPOSITION AND ETCHING PROCESSES

Y.Tzeng and R.Phillips

Department of Electrical Engineering
Auburn University
200 Broun Hall
Auburn, Alabama 36849

**Abstract**

A computer controlled gas manifold has been used to cycle between oxygen-rich and acetylene-rich combustion flames during diamond deposition in order to achieve higher growth rates without sacrificing diamond quality. The experimental parameters studied include the frequency of cycling between flames and the carbon-to-oxygen (C/O) ratio of the acetylene-rich flame. The acetylene-rich flame used during the deposition part of the cycle has a C/O ratio higher than that used to deposit high quality diamond films with low defect densities. The oxygen-rich flame etches the non-diamond components that are deposited simultaneously with diamond components when using a high C/O ratio. Results show that according to infrared transmittance and Raman Spectroscopy, using a cycling time of less than one minute will result in the deposition of high quality, defect-free diamond films under the experimental conditions for this work. This maximum acceptable cycling time must be decreased for depositing conditions that lead to higher diamond growth rates. These films exhibit intense Raman peaks at 1332 $cm^{-1}$ with no detectable non-diamond peaks and no significant one-phonon band absorption in infrared transmittance measurements.

## 1. INTRODUCTION

The already exciting CVD technologies for the deposition of diamond films on large area substrates at low pressure and low temperature are further promoted by the capabilities of either growing diamond films at high rates

(1) or depositing diamond films of excellent quality (2,3). Unfortunately, it is roughly the rule-of-thumb that a trade-off exists between depositing high quality diamond films and depositing diamond films at high rates. Therefore, it is highly desirable to develop a technology beyond the conventional continuous diamond growth processes for achieving defect-free diamond films at high growth rates. This is especially urgent for applications, i.e. free-standing long wavelength infrared (LWIR) windows, that require thick diamond films with minimum defect densities.

## 2. EXPERIMENTAL

A diagram of the oxy-acetylene torch setup showing two modes of operation is shown in Figure 1. A computer controls a 3-way solenoid valve that is used to either add extra oxygen to the combustion flame thus creating an oxygen-rich "etching" flame or to vent the extra oxygen to air thus increasing the C/O ratio of the combustion gas supplied to the flame. A manual valve is placed at the vent opening of the solenoid valve and is adjusted so that no change in pressure occurs downstream the mass flow controller during the cycling operation. The acetylene flow rate remains fixed during the cycling. The remainder of the torch setup has been described previously (4-7).

To achieve a reproducible high quality diamond film by the oxy-acetylene flame method, the acetylene/oxygen flow ratio must be controlled very accurately. This is further complicated by the fact that acetone present in the acetylene cylinder influences the oxy-acetylene flame to a varied extent depending on the ambient temperature and the acetylene pressure in the cylinder, i.e. the fraction of acetone included in the acetylene flow varies from experiment to experiment. Although activated charcoal is used in our experimental setup, a slight change in the flame is still present from run to run, presumably due to a small temperature induced drift in the electronics of the mass flow controllers and the residual acetone incorporated into the oxy-acetylene flame. In order to compare several experimental runs, we chose to keep the length of the acetylene feather constant for each deposition by slightly adjusting the electronic mass flow controller set-points.

Diamond films deposited on molybdenum become free-standing after cooling down from the deposition temperature due to the thermal expansion mismatch between diamond and molybdenum. These free-standing diamond films are

characterized by means of Raman spectroscopy, Fourier Transform Infra-red (FTIR) absorption measurements, photoluminescence measurements, and scanning electron microscopy. In this paper, we report a sequential deposition and etching process that uses an acetylene/oxygen ratio during the deposition cycle that is higher than what is normally required for achieving high quality diamond films by the conventional continuous deposition method (3). The effects of the cycling frequency on the LWIR absorption spectra and its correlation with the corresponding Raman spectra are discussed.

## 3. RESULTS AND DISCUSSION

The Raman spectra for diamond films deposited under different cycling conditions are shown in Figure 2. Curve (e) in Figure 2 is for the diamond film deposited continuously without cycling between deposition and etching. A broad luminescent background can be seen in this spectrum along with the diamond Raman peak at 1332 $cm^{-1}$. The infrared absorption spectrum for this continuously deposited diamond film is shown in Figure 3 (curve #4*). The one-phonon absorption coefficient for this sample is around 10 $cm^{-1}$ and the maximum "C-H Stretch" absorption peak is around 30 $cm^{-1}$. These are referenced to the absorption coefficient of 12.3 $cm^{-1}$ present at the 5 $\mu m$ wavelength in the two-phonon band which is intrinsic to all diamond and relatively insensitive to defects and impurities in the diamond (8). The infrared absorption coefficients for this sample are too high for LWIR applications that require thick diamond films and high LWIR transmittance.

A sequential deposition and etching process that does repetitive 40 second deposition and 10 second etching is used to deposit diamond films. The corresponding Raman and FTIR spectra for this film are shown in Figure 2 (curve d) and Figure 3 (curve #4), respectively. The dramatic improvement in the optical quality of the diamond film is clearly seen from the sharp diamond Raman peak at 1332 $cm^{-1}$ without any detectable background signals caused by non-diamond in the film. This improvement is further evidenced by the infrared absorption spectrum showing nondetectable one-phonon absorption in the 8 $\mu m$ to 12 $\mu m$ wavelength range. The only extrinsic infrared absorption band detected in this sample is the relatively small "C-H Stretch" absorption that is caused by hydrogen contamination in the diamond film. The nondetectable one-phonon absorption makes this diamond film especially useful for LWIR applications

that require very high transmittance in the 7-12 μm range.

The sequential deposition and etching process must be performed at a sufficiently fast cycling time. If the cycling time is too long, the non-diamonds deposited on the film may accumulate to an extent that they can no longer be removed by the subsequent etching cycle. The quality of the diamond film degrades as the cycling period increases from 40 seconds deposition and 10 seconds etching for the experimental conditions used in this work. This is shown in the increasingly degrading Raman spectra shown in Figure 2 (curves c, b, and a) and the corresponding infrared absorption spectra shown in Figure 3 (curves #3, #2, and #1), respectively. The non-diamonds buried in the fast growing diamond films are obviously responsible for the degradation of the diamond film quality as the cycling time increases. For diamond deposition conditions that lead to higher growth rates than the present work, an even shorter cycling time will be needed to remove the non-diamond components before they are buried beneath the film's surface.

## 4. CONCLUSION

A sequential deposition and etching process using the oxy-acetylene flame method is reported. This dynamic deposition process can either improve or deteriorate the quality of the diamond films depending on the experimental conditions, especially the cycling time. It has been clearly demonstrated that by cycling the deposition and etching periods at an optimal rate, high quality diamond films with few defects as judged by the nondetectable one-phonon absorption in the infrared absorption spectra and the nondetectable non-diamond background signals in the Raman spectrum. This sequential deposition process is therefore promising for further accelerating the production of high quality diamond films for applications that require the best possible diamond films.

## 5. ACKNOWLEDGEMENTS

This work is supported in part by the Office of Naval Research and the SDIO/IST - Naval Surface Warfare Center. Richard Phillips is a NASA graduate fellow supported by NASA Lewis Research Center. The authors would like to express their gratitude to C.B.Willingham and R.P.Miller of Raytheon Company for the FTIR measurements and to B.H.Loo

and P.Wang of the University of Alabama in Huntsville for the Raman measurements.

**REFERENCES**

1. N.Ohtake, H.Tokura, Y.Kuriyama, Y.Mashimo, and M. Yoshikawa, "Synthesis of Diamond Film by Arc Discharge Plasma CVD," ECS Extended Abstracts, Vol.89-1, pp.116-117, 1989.
2. Y.Tzeng, C.C.Tin, R.Phillips, T.Srivinyunon, and Y.Chen, "High Electrical Resistivity Diamond Films Deposited from an Oxyacetylene Flame," Appl. Phys. Lett., Vol.57, No 3, pp.789-791, 1990.
3. Y.Tzeng and R.Phillips, "High Quality Flame Deposited Diamond Films for Infrared Optical Windows," Applications of Diamond Films and Related Materials, edited by Y.Tzeng, M.Yoshikawa, M.Murakawa, and A.Feldman (Elsevier Science Publishers, B.V., Amsterdam, The Netherlands, 1991) pp.189-196.
4. Y.Hirose and N.Kondo, Program and Book of Abstracts, 35th Japan Society of Applied Physics Spring Meeting, 1988 (Japan Society of Applied Physics, Tokyo, 1988), p.434.
5. Y.Hirose, S.Amanuma, N.Okada, and K.Komaki, First International Symposium on Diamond and Diamond-Like Films, Los Angeles, CA (Electrochemical Society, Pennington, NJ, 1989), Vol.89-12, p.80.
6. L.M.Hanssen, W.A.Carrington. J.E.Butler, and K.A.Snail, Mater. Lett., Vol.7, p.289, 1988.
7. Y.Tzeng, C.Cutshaw, R.Phillips, and T.Srivinyunon, "Growth of Diamond Films On Silicon From an Oxygen-acetylene Flame," Appl. Phys. Lett., Vol.56, No.2, p.134-136, 1990.
8. T.M.Hartnett and R.P.Miller, "Potential Limitations for Using CVD Diamond as LWIR Windows," SPIE Proceedings, Vol.1307, 60, 1990.

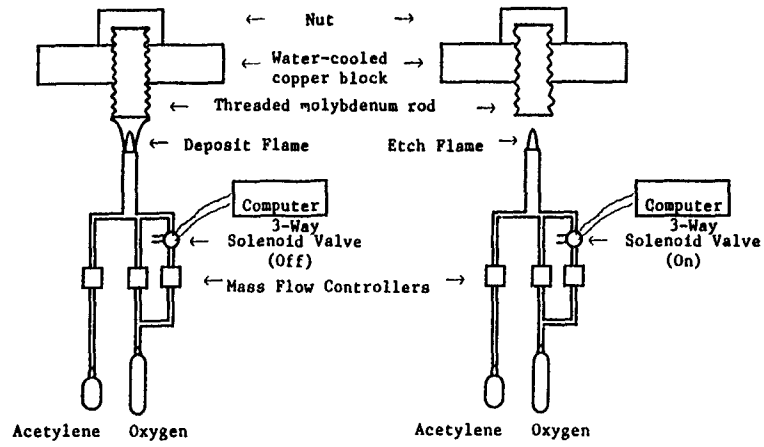



Figure 1. Oxy-acetylene torch setup showing the acetylene-rich (left) and oxygen-rich (right) flames used during sequential deposition and etching processes.

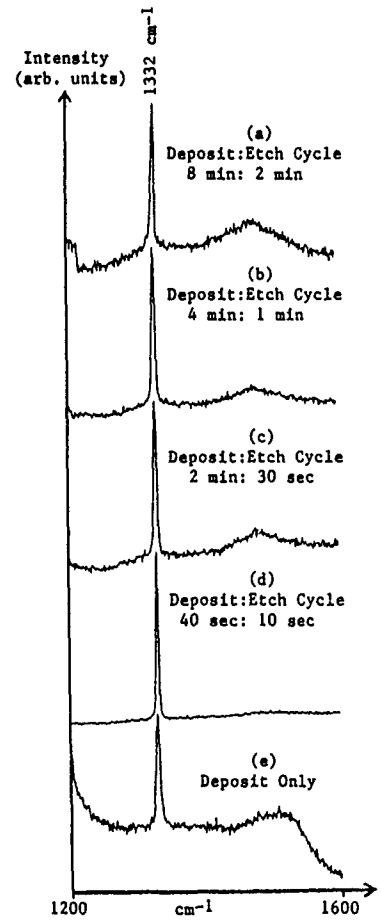



Figure 2. Raman spectra of oxy-acetylene torch deposited diamond films grown by sequential deposition and etching processes. Spectra (a) through (d) were taken from samples grown using four different cycling times. Spectra (e) was taken from a sample that did not use cycling, but used only the deposit flame to grow the film. Spectra (d) shows the optimal cycling time of 40 seconds deposition and 10 seconds etching for this set of experiments according to Raman Spectroscopy.

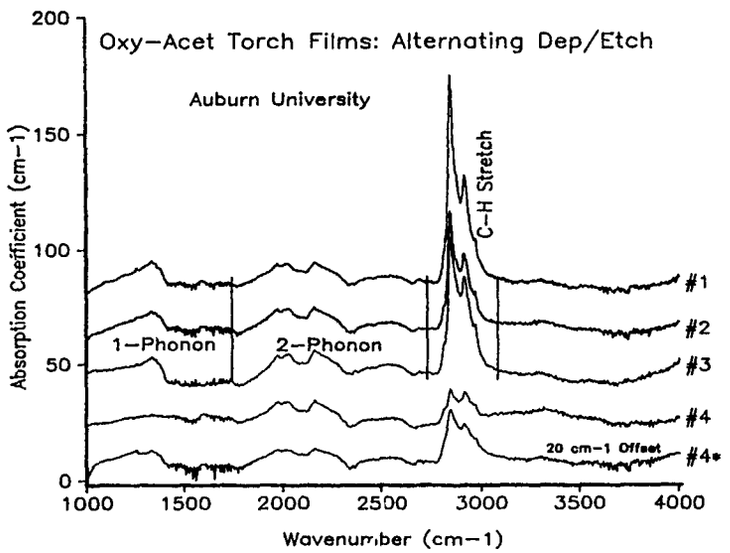



Figure 3. Infrared absorption spectra of diamond films from which Raman measurements in Figure 2 were taken. Spectra #1 was taken from a sample grown by cycling between 8 minutes deposition and 2 minutes etching. Spectra #2 is from a 4 minutes deposition and 1 minute etching sample. Spectra #3 used 2 minutes deposition and 30 seconds etching. Spectra #4 used 40 seconds deposition and 10 seconds etching. Spectra #4* involved no cycling and only the deposit flame was used to grow the diamond film. Again, spectra #4 (40 seconds deposition/ 10 seconds etching) shows the optimal cycling time for this set of experiments according to infrared absorption measurements.

# PARAMETRIC STUDY OF DIAMOND FILM DEPOSITION IN A RADIO-FREQUENCY THERMAL PLASMA

Chiahung Li, Y. C. Lau*, and S. L. Girshick
Dept. of Mechanical Engineering, University of Minnesota
111 Church St. S.E., Minneapolis, MN 55455
*Present address: General Electric R&D Center, P.O. Box 8
Schenectady, NY 12301

## ABSTRACT

Diamond films were deposited on molybdenum substrates in a radio-frequency plasma reactor operating at atmospheric pressure. Continuous 10-μm-thick polycrystalline films were produced in one-hour runs. Cases with a 1% methane-hydrogen ratio consistently produced well-faceted crystallites, while cases with a 5% ratio produced cauliflower-type structures. In either case, crystallite size and morphology tended to be uniform over the deposition area.

## INTRODUCTION

Inductively-coupled radio-frequency (rf) thermal plasmas offer several potential advantages for diamond film deposition. As with direct-current (dc) plasmas the deposition rates are high. However there are several important differences between dc and rf plasmas which affect diamond deposition.

A dc jet typically has higher peak temperatures (~20,000 K) and higher peak velocities (several hundred m/s) than an rf plasma, resulting in thinner substrate boundary layers. While the rf plasma is still hot enough (~10,000 K) to promote complete hydrogen dissociation, the radicals responsible for diamond growth must diffuse across the cold boundary layer. It is thus perhaps not surprising that higher linear growth rates have been reported with dc jets. On the other hand, because a dc jet concentrates its energy into a relatively narrow region along the flow axis, it has extremely steep radial temperature gradients, whereas an induction plasma has a larger, more uniform volume, and is therefore more conducive to coating a large area uniformly. Matsumoto (1) compared his results obtained with dc and rf thermal plasmas, depositing diamond on 20-mm diameter molybdenum substrates. For comparable cases (both at atmospheric pres-

sure, and with similar flow rates of hydrogen and methane), the linear deposition rates were 4 μm/min with the dc jet and 2 μm/min with the rf plasma, while the diameter of the deposited film was 6-7 mm for the dc jet and 20 mm for the rf case. A simple calculation then shows that the *volumetric* deposition rate was approximately five times greater for the rf plasma (~40 $mm^3/h$) compared to the dc jet (~8 $mm^3/h$), indicating a higher carbon conversion efficiency for the rf plasma. In reporting their experiments with dc jet diamond deposition, the SRI group (2) emphasized the highly nonuniform nature of the film, which they attributed to severe radial gradients in the plasma.

Another difference between dc and rf thermal plasmas concerns film contamination. Electrode erosion is inevitable with dc plasmas, and this may pose a serious limitation for certain diamond applications, particularly for electronic devices. In contrast rf thermal plasmas are inductively coupled. There are no electrodes, hence they are inherently cleaner than dc plasmas. Matsumoto (1) reported that his dc jet-deposited film was contaminated with tungsten and copper, whereas little contamination was found in the films produced with his rf reactor. The SRI group found substantial concentrations of impurities in their dc jet-deposited film, including stainless steel constituents and refractory metals attributable to the electrodes.

Thus, while rf thermal plasmas may produce less spectacular linear growth rates than dc plasmas, they are at least competitive regarding carbon conversion efficiency, are more promising regarding film uniformity, and have a definite advantage with respect to film purity. However to our knowledge the only group other than Matsumoto's (3) to have reported diamond deposition using an rf thermal plasma is the group at Stanford (4, 5). Both groups deposited on molybdenum substrates. Matsumoto's group used a stagnation-point flow geometry, and reported the effect of varying the methane flow rate between 0.1 and 1.2 slpm, with a hydrogen flow rate of 12 slpm. The Stanford group compared results with the substrate oriented either for stagnation-point flow or for flat plate parallel flow, but otherwise did not report any variation of operating parameters.

As a first step toward characterizing the parameter space for diamond film deposition in an rf thermal plasma, we conducted a series of experiments involving eight sets of conditions with variation of five operating parameters. This series of experiments was not sufficient to establish clear correlations between film properties and parameter values. However the results provide guidance for the design

of further experiments, which together with appropriate diagnostics and numerical modeling could elucidate the mechanisms for diamond film CVD in a thermal induction plasma.

## EXPERIMENTAL CONDITIONS

In these experiments the plasma reactor was driven by a nominally 20-kW rf generator, supplying current at a measured frequency of 2.93 MHz to a five-turn induction coil. The generator controls were adjusted in each case to provide the same rms coil current, 82 A. Generator plate power was typically 12-14 kW. We have performed numerical simulations (6) which indicate that the actual power coupled to the plasma was 5-6 kW.

The reactor is shown schematically in Figure 1. The plasma tube consisted of water-cooled quartz, with an inner diameter of 46 mm. Argon at 40 slpm was introduced at the top of the tube through a swirl injection ring. Hydrogen (8 slpm) and methane (0.08-0.40 slpm) were introduced coaxially through a water-cooled injection tube with a 1.8-mm inner diameter, inserted directly into the plasma. An important consequence of this injection method is that the reactants emerge into the plasma in the form of a high-velocity jet. Our numerical calculations (6) indicate that the peak jet velocity was ~130 m/s, compared to the background argon velocity of ~10 m/s. The hydrogen/methane jet impinged in stagnation-point flow upon the substrate.

Substrates consisted of 25-mm-diameter molybdenum disks, which were fastened to a stainless steel insert of variable thickness, hereafter referred to as the "thermal insert." The thermal insert in turn was mounted on a water-cooled copper cylinder. By varying the thermal insert thickness the substrate surface temperature could be varied independently of the distance of the substrate from the last induction coil. The temperature of the top surface was measured with a two-color pyrometer (Ircon Modline Series R). Surface temperatures for cases in which diamond was produced were in the range 1090-1250 K, with an average repeatability of ±15 K for given sets of operating conditions.

An initial eight-run sequence of experiments was planned according to a factorial design (7). The following five parameters were varied: distance $z$ of the substrate below the last induction coil (either 2 cm or 6 cm); distance $y$ of the hydrogen-methane injection tube above the last induction coil (either 2.5 cm or 4.5 cm); methane/hydrogen ratio (either 1% or 5%); thickness $d$ of the thermal insert (either 6 mm or 10 mm); and whether or not the substrate was pre-

treated with an application of pump oil, which has been reported to increase nucleation density (8). For this set of experiments all substrates were pretreated by scratching with 1/4-μm diamond paste, and the run duration for each test was one hour. Each experiment was repeated on a separate occasion to test for reproducibility. Samples were examined with scanning electron microscopy (SEM), x-ray diffraction and Raman spectroscopy.

## RESULTS AND DISCUSSION

One outcome of the experiments was the observation that reproducibility was good. In particular, given parameter combinations reproducibly resulted in the formation of either well-faceted crystals or "cauliflower" structures, and the size and density of these were surprisingly reproducible considering that the surface condition prior to deposition inevitably varied from sample to sample. With one exception, however, these experiments did not establish correlations for the parameters tested. We do not believe that this indicates that these parameters are unimportant, only that eight runs are not in general adequate to establish correlations for a five-dimensional parameter space.

The exception was the methane/hydrogen ratio, which was observed to determine whether the crystallite morphology was well-faceted or of the cauliflower type. Regardless of the values of the other four parameters, every case with a 1% ratio resulted in faceted crystallites, while every case with a 5% ratio produced cauliflower-shaped structures. Similar results for the effect of C:H ratio on film morphology were reported by Matsumoto in his rf thermal plasma experiments (3), and have also been reported for diamond CVD using other methods, including microwave discharge (9), combustion flame (10), and hot filament (11).

An example of the results from the 1% case is shown in Figure 4. (SEM micrographs are grouped together on the last page of this paper.) The predominance of octahedral and cubo-octahedral structures, with many (111) faces showing, was quite typical, although in some cases we instead obtained films terminating almost entirely in (100) faces. Micro-Raman spectra obtained from these films produced sharp peaks close to the 1332 $cm^{-1}$ peak of natural diamond. A typical result is shown in Figure 2, which was obtained from the film shown in Figure 4.

Figure 5 shows a typical result obtained with a 5% methane/hydrogen ratio. These structures are seen to be

characterized by a high density of layered crystallites terminating in small (100) facets. The corresponding Raman spectrum, seen in Figure 3, still shows the peak associated with diamond, but it is broader than in the well-faceted cases, and the broad band at higher wavenumbers indicates the presence of non-diamond carbon.

For one-hour runs in which continuous polycrystalline films were obtained, the thickness was typically ~10 μm, as in Figure 6. This linear growth rate is lower than that reported by Matsumoto's group. However it should be noted that their reported film thickness of 6-12 μm (3), for a case cited as producing 1-μm/min growth, implies a deposition time of ~10 minutes, suggesting a high initial nucleation density, perhaps attributable to superior substrate surface conditions. It is not clear whether their initially high growth rates were (or would be) maintained for continued growth of thicker films.

The Stanford group reported linear growth rates of 1-10 μm/h, however in general they did not obtain continuous films. We speculate that the reason we obtained denser films, with higher growth rates, is that the deposition surface in the experiments reported herein was richer in atomic hydrogen than in the Stanford experiments. There are two reasons for this. First, while the hydrogen flow rates are fairly similar--8 slpm in these experiments, ~12 slpm in the Stanford case--the argon flow rates are rather different--40 slpm in these experiments, ~110 slpm in the Stanford case--so that the ratio of hydrogen to argon atoms was at least twice as high in these experiments. Perhaps more significantly, as noted in the preceding section, in our reactor hydrogen and methane are coaxially injected as a high-velocity jet which emerges directly into the plasma core, whereas in the Stanford experiments the reactants were injected either with argon at the upstream end of the plasma torch or radially into the tail flame. The Stanford group argued that their boundary layer was thick enough to allow time for hydrogen atoms to recombine before they diffused to the surface (4). For constant-property stagnation-point flow the boundary layer thickness varies as the inverse square root of freestream velocity (12). Thus the coaxial jet injection method caused our boundary layer to be ~3-4 times thinner than it would have been otherwise, significantly increasing the probability for hydrogen atoms and other radicals to reach the surface.

We usually observed a considerable degree of uniformity over the entire deposition area, typically ~60% of the substrate surface. Regardless of the crystallite morphology we found that in most cases the morphology, cystallite size,

and nucleation density were quite uniform over regions extending from the substrate center to near the edge.

Finally, we also found diamond films on the side surfaces of the molybdenum substrates, as seen in Figure 7. As the boundary layer on the side is fundamentally different than on the top, it is not surprising that we found a greater variety of morphologies on the side, with less uniformity, than on the top of the substrates.

## ACKNOWLEDGEMENTS

J. E. Butler of the Naval Research Laboratory provided the Raman spectroscopy measurements. This work was partially supported by the National Science Foundation Engineering Research Center for Plasma-Aided Manufacturing.

## REFERENCES

1. S. Matsumoto, *Mat. Research Soc. Extended Abstracts* **EA-15**, 119 (1988).
2. K. R. Stalder, R. L. Sharpless, *J. Appl. Phys.* **68**, 6187 (1990).
3. S. Matsumoto, M. Hino, T. Kobayashi, *Appl. Phys. Lett.* **51**, 737 (1987).
4. M. A. Capelli, T. G. Owano, C. H. Kruger, *J. Mater. Res.* **5**, 2326 (1990).
5. T. G. Owano, D. G. Goodwin, C. H. Kruger, M. A. Cappelli, *2nd Intl. Conf. on the New Diamond Science and Technology*, Washington, D.C., 1990.
6. B. W. Yu, S. L. Girshick, in preparation for journal submission.
7. G. E. P. Box, W. G. Hunter, J. S. Hunter, *Statistics for Experimenters: An Introduction to Design, Data Analysis, and Model Building* (Wiley, New York, 1978).
8. P. E. Pehrsson, in *Second Intl. Conf. on the New Diamond Science and Technology* 1990),
9. K. Kobashi, K. Nishimura, Y. Kawate, T. Horiuchi, *Phys. Rev. B* **38**, 4067 (1988).
10. K. V. Ravi, C. A. Koch, H. S. Hu, A. Joshi, *J. Mater. Res.* **5**, 2356 (1990).
11. S. C. Sharma, M. Green, R. C. Hyer, C. A. Dark, T. D. Black, A. R. Chourasia, D. R. Chopra, K. K. Mishra, *J. Mater. Res.* **4**, 2424 (1990).
12. F. M. White, *Viscous Fluid Flow* (McGraw-Hill, New York, 1974).

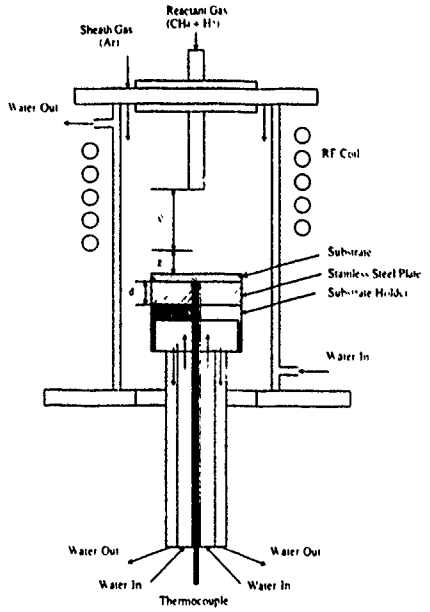



Figure 1
Schematic of rf plasma diamond deposition reactor.

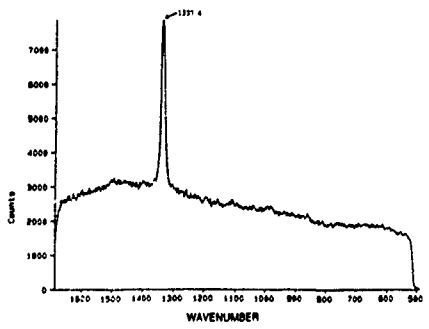



Figure 2. Raman spectrum for a case with a 1% methane/hydrogen ratio.

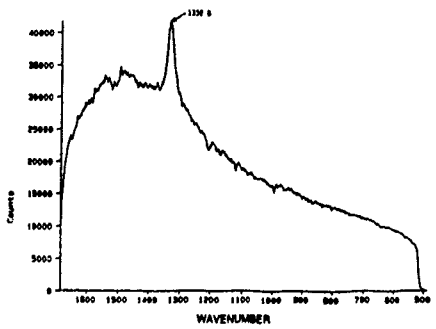



Figure 3. Raman spectrum for a case with a 5% methane/hydrogen ratio.



Figure 4. SEM micrograph for a case with a 1% methane/hydrogen ratio.



Figure 5. SEM micrograph for a case with a 5% methane/hydrogen ratio.

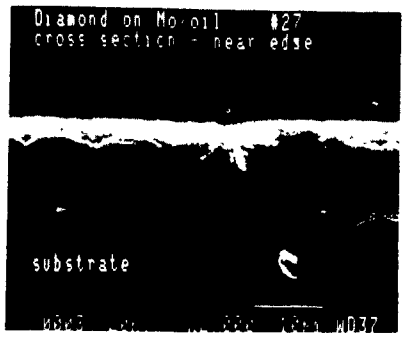



Figure 6. SEM micrograph of a cross-section with 1% methane/hydrogen ratio.

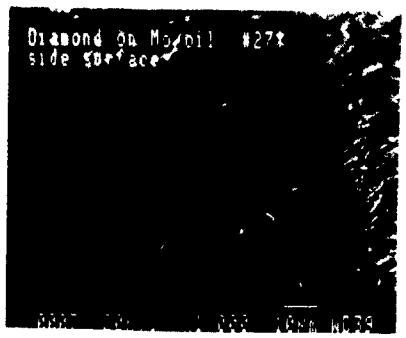


Figure 7. SEM micrograph of film deposited on a substrate side (same substrate as in Fig. 6).

# LASER PLASMA DEPOSITION OF DIAMONDLIKE CARBON FILMS IN VACUUM AND HYDROGEN AMBIENTS

A. Rengan, J. L. Park and J. Narayan
North Carolina State University
Raleigh, N. C. - 27695

J. Hunn
University of North Carolina
Chapel Hill, N. C. - 27675

## ABSTRACT

A laser plasma ablation technique has been used for the deposition of diamondlike carbon films. Systematic studies in the temperature and ambient dependence show a growth and ordering of the bonding components in the films. Raman parameters indicate that the half widths of the 'D'and 'G' bands decrease with increasing T (substrate) suggesting an ordering of the $sp^2$ and $sp^3$ bonding componentsin the film. Hydrogenation is known to promote the formation of $sp^3$ bonds. In a hydrogen ambient the DLC films exhibited a sharp reduction in the halfwidths and an increase in the intensity of the 'D' band. Therefore there appears to be a drect correlation with the $sp^3$ fraction and the 'D' band in the Raman spectra. This conclusion is supported by the presence of octahedral features heterogenously nucleated in the film. TEM observations suggest growth on the <111> facets occur by a step mechanism. Ion implantation studies provides supporting evidence of the ordering and growth in the films as a function of substrate temperature and ambient.

## 1. Introduction

The laser plasma ablation of graphite is a unique technique for the deposition of DLC films [1, 2]. The high temperatures generated in the ablation process (>6000 K ) [3] leads to excited carbon species. These species are quenched on a relatively cooler substrate ( 300 - 1000 K ) depositing metastable structures with interesting and controllable properties.

Raman spectroscopy plays an important role in the analysis of the various allotropes of carbon. The origin of the 'D' and 'G' bands in DLC films is an important issue which is still not resolved conclusively. Yoshikawa [4] proposed that the Raman bands originated from carbon clusters with the $sp^2$ configuration,

however, he also suggested that carbon clusters with $sp^3$ configuration had an indirect influence on the bonding. Schroeder and Nemanich [5] have also attributed the peak positions and narrow half widths to the presence of microcrystalline graphitic domains. Walrafen [6] investigated a variety of carbon materials. His investigations revealed that the width of the 'D' band is a measure of the randomness of the structures involved in $sp^3$ bonding.

We describe a series of systematic experiments using the laser plasma ablation of graphite to elucidate the specific nature of the 'D' and 'G' bands. The variation of spectral parameters as a function of temperature were investigated. The growth of the $sp^2$ and $sp^3$ bonding components of the DLC film were also studied by ion implantaion damage experiments.

## 2. Experimental

In the laser plasma ablation technique a graphite target is ablated using a KrF laser ($\lambda$ = 248 nm) at a fluence of 4 J/cm$^2$. A 50 $\mu$F capacitor discharges simultaneously with the laser pulse through a ring surrounding the grounded target [1]. The films deposited were approximately 1 $\mu$m thick. Raman measurements were taken in the macro and micro mode in the backscatter geometry, using the 5145 Å line af an Argon ion laser. TEM micrographs were obtained by a Hitachi S-800 instrument.

Two sets of experiments were conducted. The first set were deposited in a vacuum ambient ($1x10^{-3}$ Torr) and at substrate temperatures from 25° to 500° C. The second set of experiments were designed to simulate the environment for the CVD growth of diamond thin films. The graphite was ablated in a hydrogen ambient at a partial pressure of 10 mTorr and a substrate temperature of 860° C.

The Raman spectra were deconvoluted into the 'D' and 'G' bands using well defined Gaussian functions. In addition to the deconvolution of the spectra by the Gaussian function, the broad photoluminescent (PL) background was also substracted. A simple quadratic polynomial was used to fit the background [8]. Therefore the total deconvolution consisted of the sum of the Gaussian (D + G) bands plus the quadratic PL background.

## 3. Results and Discussion

### 3.1 Vacuum; T(substrate) = 25° -> 500° C

In this series of experiments the depositions were carried out at substrate temperatures of 25° C to 500° C in 100 deg increments. Representative Raman spectra for the depositions at 25° C is shown in Fig. 1. A featureless assymetric band is observed generally typical of disordered amorphous films. A broad PL background is also present. PL is due to transitions of electrons from filled conduction band states to empty valence band states. The transition may also be from donor bands of impurities or defects to acceptor bands. The broader the defect bands, the broader the the range of states that electrons can make transitions to, and hense the broader the PL. The conduction/donor bands can be filled by the excitation source. The Gaussian deconvoluted spectra show broad 'D' and 'G' bands, the intensity of the 'G" band being much larger than that of the 'D' band.

At a deposition temperature of 500° C the features of the 'D' and 'G' bands are more prominant as shown in Fig. 2. The deconvoluted spectra have narower bands, and the intensities are more or less equal. The broad PL background has decreased substantially suggesting the existence of a much narrower band of defect states. While the Gaussian curve for the 'G' band shows an excellent fit on the high energy side, the 'D' band shows a broad tail at the base of the peak (shaded area). A similar broad tail has been observed in highly defective CVD diamond films. A possible explanation for the tail is that the Raman signal originates from highly disordered regions of diamond adjacent to $sp^2$ bonded defect structures; while the relatively narrow peak originates from regions furthur away from such structures [7]. A similar explanation would be applicable for the DLC films, the degree of disorder being much greater than for the CVD diamond films.

### 3.2 Hydrogen (10 mTorr); T(substrate) = 860° C

In the second set of experiments laser plasma ablation of graphite was conducted in a hydrogen ambient at a substrate temperature of 860° C. It was shown earlier that octahedral shaped particles were heterogenously nucleated [8]. The octahedral morphology suggested the existence of $sp^3$ bonding in the feature.

A TEM brightfield micrograph of one such particle is shown in Fig. 3. The triangular outline of the <111> facets are evident. The interior of the ~ 5μm particle appears electron transparent suggesting a very loosly bonded microstructure. No diffraction pattern was obtained, implying that only local or short range order of ~15-30 Å exists in the feature. The carbon atoms arriving on the surface resemble a "brush" configuration and are perpendicular to the <111>facets suggesting that growth of the <111> surfaces occur by a step mechanism. An atom arriving on the surface migrates to a position of minimum energy. This position would be a kink or corner site bounded on three sides by atoms forming a step.

A typical micro Raman spectra of these features is shown in Fig. 4. The 'D' and 'G' bands are well resolved and do not need any deconvolution. The half widths are much narrower than the previous spectra and the intensity of the 'D' band is now much greater than the 'G' band.

The parameters of the Raman specra for the DLC films deposited in both sets of experiments are plotted in Figs 5, 6 and 7, as a function of substrate temperature. Also included are data obtained from films deposited in vacuum ambient at substrate temperatures of 25°, 100°, 300° and 400° C, as well as data from the planar film deposited in $H_2$ at 860° C. The 'D' and 'G' bands downshift and upshift respectively as can be observed from Fig. 5, approaching a limit of 1350 $cm^{-1}$ for the 'D' band and 1600 $cm^{-1}$ for the 'G' band.

The half widths of both the 'D' and 'G' bands decrease, as shown in Fig. 6, with the 'G' band narrower than the 'D' band in the vacuum deposited films. However the situation is reversed for the hydrogenated films deposited at T(substrate)=860° C. The 'D' band is narrower for the planar film and the octahedral feature. Also the $I_D/I_G$ ratio increases with increasing temperature (Fig. 7).

Studies by Angus and co-workers [9] and by Zou and co-workers [10] have shown that increasing the hydrogen content in the DLC films results in a higher percentage of $sp^3$ bonds. The narrowing in the half widths of the Raman 'D' and 'G" bands suggests an ordering of the $sp^2$ and $sp^3$ structures in the DLC film. The increase in the intensity of the 'D' band suggests that there is a direct correlation with the proportion and of the $sp^3$ bonding component. This conclusion is more apparent by the octahedral morphology of the

particles heterogenously nucleated on the Si <100> substrates.

### 3.3 Ion Implantation

To prove the reverse hypothesis, ie, if we assume the presence of intermediate range ordering in the DLC film, then the task at hand would be to devise an experiment to induce disorder in the film. Ion implantation is a well known technique that damages crystalline surface layers resulting in amorphization of the material.

A DLC film was deposited in a vacuum ambient at a substrate temperature of 500° C. The characteristics of the Raman spectra are shown in Fig. 2. A dose of $3x10^{16}$ ions/$cm^2$ of Boron at an energy of 54 keV and an estimated range of ~ 2500 Å [11],and was implanted into the DLC film. it is expected that the relatively low energy would maximize the damage to the surface layers. The implantation was carried out at room temperature and at normal incidence. The Raman spectra of the ion implanted film is shown in Fig. 8, and can be compared with Fig. 2. The damage to the surface structure, or disordering in the film evidently results in a broad assymetric spectrum. This spectrum is similar to the DLC film deposited at lower substrate temperature (see Fig. 1). Therefore we could conclude that the DLC films deposited at lower temperatures are more disordered. It is of interest to note that the region of the 'D' band is reduced to a greater extent than the 'G' band, implying the metastability of the regions associated with $sp^3$ bonding.

## 4. Conclusion

We have systematically investigated the effect of substrate temperature and ambient conditions on the properties of DLC films deposited by a laser plasma ablation technique. The Raman spectra show systematic changes in the parameters of the 'D' and 'G' bands. Increase in T (substrate) results in a downshift and upshift of the 'D' and 'G' peak positions respectively. The half widths '$\Delta\nu$' of both bands decrease steadily. In vacuum ambient the half width of the 'D' band is always larger than the 'G' band. However in the hydrogenated films the situation is reversed with the the 'D' band being narrower. The intensity of the 'D' band also increases. It is known that the $sp^3$ fraction of the film increases with hydrogen content. Therefore we would conclude that there is a direct relationship with the 'D' band with the ordering and growth of the $sp^3$ fraction in the DLC film.

These results are substantiated by the presence of octahedral features in the hydrogenated films. TEM results suggest a growth of the <111> facets by a step mechanism. Ion implantation studies verify the presence of intermediate range order in the films.

**Acknowledgements**

The authors would like to acknowledge P. Moyer and S. Pramanick for assistance with the Raman measurements Helpful discussions with M. Longo regarding the growth mechanism are also appreciated. Greatful thanks are also due to Dr. N. Parikh for the ion implantation. Part of this research was supported by the Army Research Office under contract No. DAALO3-89-K-0118.

## REFERENCES

1. J. Krishnaswamy, A. Rengan, J. Narayan, K. Vedam and C. J. McHargue., Appl. Phys. Lett. 54, 2455 (1989).
2. F. Davanloo, E. M. Juengrman, D. R. Jander, T. J. Lee and C. B. Collins., J. Appl. Phys. 67 (4) 2081 (1990).
3. D. H. Reitze, X. Wang, H. Ahn and M. C. Downer., Phys. Rev. B 40, 17 (1989).
4. M. Yoshikawa., Mats. Sc. Forum., 52-53, 365 (1989).
5. R.E. Schroeder and R.J. Nemanich., Phys. Rev., B 41, 6, 3738 (1990).
6. G. E. Walrafen., SDIO/IST ONR Diamond Technology Initiative Symposium, Crystal City, VA. July 1988.
7. L. H. Robbins, E. N. Farabaugh and A. Feldman., J. Mater. Res., 5, 1, 2556 (1990).
8. A. Rengan, N. Biunno, P. Moyer and J. Narayan in Diamond, Silicon Carbide and related Wide Band gap Semiconductors, edited by J. T. Glass, R. Messier and N. Fujimori (Sym. Proc. Ser., Mat. Res. Soc., 162, Boston MA 1989), p185.
9. J. Angus and C. Hayman., Science., 241, 913 (1988).
10. J. W. Zou, K. Schmidt, K. Reichelt and B. Dischler., J. Appl. Phys., 67 (1) 487 (1990).
11. VLSI Technology., edited by S. M. Sze., 2nd Edition (1988), p 336.

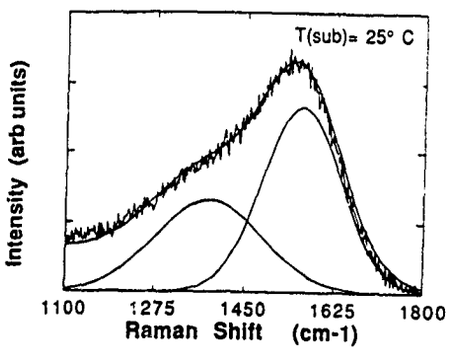



Fig. 1 Raman spectra of DLC film at T(sub)=25° C, in vacuum ambient.Gaussian deconvoluted 'D' and 'G' bands. $I_D < I_G$ and $\Delta\nu_D > \Delta\nu_G$.

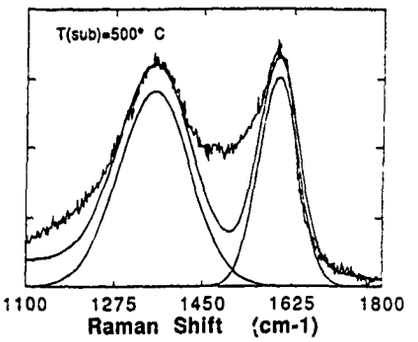



Fig. 2 Raman spectra of DLC film at T(sub)=500° C, in vacuum ambient. Gaussian deconvoluted 'D' and 'G' bands. Broad tail (shaded region) also seen in highly defective CVD diamond films. $I_D = I_G$ and $\Delta\nu_D > \Delta\nu_G$.



Fig. 3 Brightfield TEM micrograph of octahedral shaped feature.

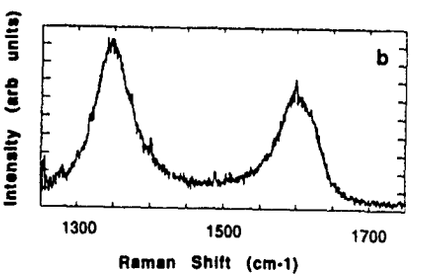



Fig. 4 Micro Raman spectra of octahedral feature heterogenously nucleated at T(sub)=860° C in Hydrogen ambient. 'D' and 'G' bands well defined. $I_D > I_G$ and $\Delta\nu_D > \Delta\nu_G$.

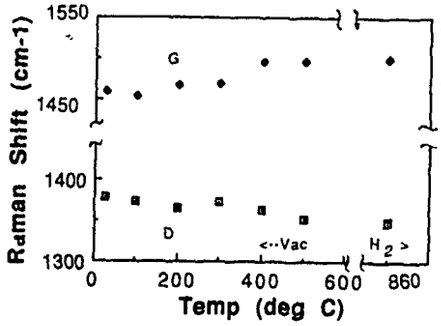



Fig. 5 Raman shift of 'D' and 'G' bands for DLC films deposited in vacuum, T(sub) < 500° C: and hydrogen ambients, T(sub) = 860° C

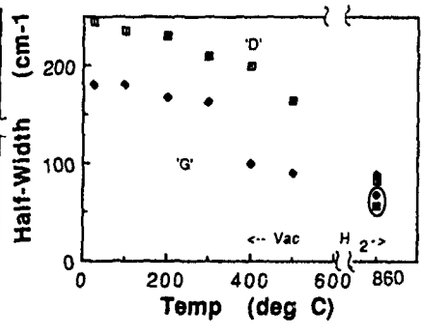



Fig. 6 Raman haf widths of 'D' and 'G' bands for DLC films deposited in vacuum, T(sub) < 500° C: and hydrogen ambients, T(sub) = 860° C.
Data in circle is for octahedral feature.

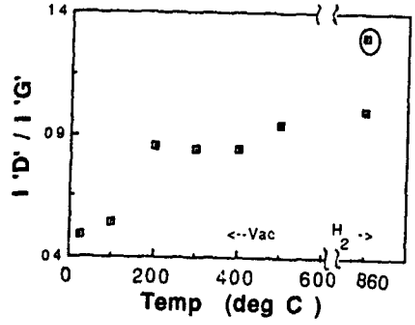



Fig. 7 Raman intensity ratio of 'D' and 'G' bands for DLC films deposited in vacuum, T(sub) < 500° C: and hydrogen ambients, T(sub) = 860° C. Data in circle is for octahedral feature.

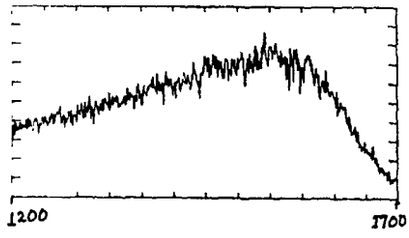



Fig. 8 Raman spectra for DLC film deposited in vacuum at T(sub)= 500° C + Ion implanted with boron. Conditions: Dose: $3x10^{16}$ ions/cm$^2$. Energy: 54 keV.

# HFCVD Of Diamond On Copper Substrate

X.K.Chen, G.Matera, S.Pramanick and J.Narayan

Department of Materials Science and Engineering, North Carolina State University, Raleigh, NC 27695-7916

## Abstract

We have investigated the deposition characteristics of diamond film on copper substrate using hot filament chemical vapor deposition (HFCVD) technique. Deposition parameters (substrate temperature,methane to hydrogen flow ratio and filament temperature ) were systematically varied and the effects of these parameters on diamond nucleation, morphology,growth rate and co-deposition behavior of graphite were studied. A factor of 10 fold increase in the diamond crystal size was observed as increasing substrate temperature from 800°C to 1050°C, with corresponding decrease in nucleation density from $5x10^6/cm^2$ to $0.4x10^6/cm^2$. As the $CH_4/H_2$ ratio is increased, both crystal size and nucleation density were found to increase. With increasing filament temperature, diamond nucleation density was significantly decreased. It was found that diamond growth rate is most sensitive to the substrate temperature. Graphite co-deposition on the copper substrate was found to be much less than that on silicon substrate.

## Introduction

Diamond films have been deposited using hot filament chemical vapor deposition ( HFCVD ) method on a variety of substrates such as silicon,molybdenum,tungsten,nickel,silicon carbide and tungsten carbide[ 1,2,]. All these materials form stable carbides or is already a carbide itself. The CVD of diamond on non-carbide forming materials such as copper has been reported in the early work by Russian researchers [ 3 ] in 1975 and 1981, but only limited description was given on this material and did not seem to attract much attention. Compared to the studies on deposition conditions and techniques, investigation on the effects of different substrate material is much less. As a step toward further understanding the role of substrate material and deposition mechanism, systematic depositions on copper substrate were made in the present work at different experimental conditions. The results are compared to those observed in the case of silicon substrate and possible mechanism of the observed behavior are discussed.

## Experimental

A typical HFCVD system which has been described earlier [ 4 ] was used for diamond deposition. A tungsten filament was placed about 0.9 cm above the substrate surface and substrate temperature was further controlled by an heater placed under the substrate. Polycrystalline oxygen-free copper plates with 2mm thick was used as the substrates. The substrate was cleaned and polished using standard procedure. The depositions were performed systematically at different value of substrate temperatures, filament

temperatures, methane to hydrogen flow ratios and total pressures. In a given series of depositions, one parameter was changed systematically while the other parameters were kept constant. After the first deposition was finished, the substrate was carefully changed without any disturbance to the experimental setup and then deposition was run with the new value of the parameter, which was being investigated. Prior to deposition condition the filament was pre-processed in 5 torr methane atmosphere at working temperature so that a tungsten carbide layer can be formed at the filament surface, leading to minimization 0f tungsten evaporation and substrate contamination. To measure the substrate temperature more accurately, the thermocouple was connected directly to the copper substrate. The filament temperature was measured by an optical pyrometer. .

## Results

### A. Characteristics of HFCVD on Copper Substrate

The SEM pictures shown in Fig. 1 represent a view of deposition results obtained in the present work. The deposition conditions were, substrate temperature 900°C ,filament temperature 1950°C ,total pressure 20 torr and methane to hydrogen flow ratio 1.0/100. After 2 hours deposition well-structured diamond crystals or continuous crystallite diamond film was deposited uniformly over the copper substrate surface. Sharp peak located at 1332cm$^{-1}$ shows diamond phase with very less content of graphite.

From the pictures shown in this paper, the following results were observed.

1) High nucleation density of diamond can be obtained on copper substrate without scratching with diamond paste. This is not consistent with the early work reported by Russian researchers[3 ], where they reported that nucleation density of diamond on non-carbide forming material is 1 to 2 order of magnitude lower than that on carbide-forming materials.

2) Nucleation density of diamond can be controlled by deposition conditions. At different conditions, nucleation densities ranging from very separated particles to continuous diamond film was deposited. In contrast with this, nucleation of diamond on silicon substrate is primarily determined by substrate surface condition such as scratches and is difficult to be related to the deposition parameters.

3) Growth rate of diamond mainly depend upon substrate temperature while being less affected by other deposition parameters. A factor of ten increase in growth rate of diamond was observed as substrate temperature increased from 800°C to 1050°C and seems to further increase at even higher temperatures. Maximum growth rate of about 10 micron/hr was achieved at optimum condition. It was reported that growth rate of diamond grown on silicon substrate shows a maximum, e.g., it initially increases with substrate temperature and then falls. For copper substrate no maximum was observed up to substrate temperature 1050°C.

4) An apparent activation energy of 24 kcal/mol was observed for the growth of diamond phase.

5) At same deposition condition and period, the size of diamond grown on copper substrate was found to be 2 to 3 times bigger than that on silicon substrate.

6) Co-deposition of graphite on copper substrate is less than that on silicon substrate.

7) Strain centers generated by scratching the copper substrate is still an effective method to enhance diamond nucleation density.

8) Generally speaking, the perfection of diamond crystals grown on copper substrate is higher than that on silicon substrate.

9) The adhesion between diamond film and copper substrate is weak. This weakly bonded diamond film peeled off when the substrate temperature was lowered at the end of deposition. The peeled-off film are transparent with light brown color.

## B. Dependence of growth behavior on deposition conditions

In Fig.2, we show systematic results of our deposition on copper substrate. A strong dependence of growth behavior on deposition conditions was observed. Standard deposition conditions used in these systematic depositions were substrate temperature 900°C, filament temperature 1950°C, total pressure 20 torr and methane to hydrogen flow ratio 1.0/100. The deposition parameter being examined was changed in a series of deposition while the others was kept at standard value.

### 1). Growth rate and Activation energy

Growth rate was found to be mostly dependent on substrate temperature than on other parameters as showed in Fig. 2, a to e. About 10 times increase was observed as substrate temperature was increased from 800°C to 1050 °C. The maximum growth rate of about 7μ/hr was obtained at the highest substrate temperature (1050°C ). The data of growth rate from Fig. 2,a to e is plotted in Fig 3a. The trend of the curve shows that growth rate of diamond is still increasing with substrate temperature at Ts>1050°C, which is already very close to the melting point of 1083.4°C for copper. It is noticeable that this result is different from that of HFCVD on silicon substrate where growth rate was found to increase with substrate temperature initially and then falls, when Ts was too high [ 5 ]. Also silicon carbide and graphite can be formed at Ts higher than 1000°C and crystallinity of diamond changed to bad. It is interesting to plot the growth rate data versus substrate temperature in Arrhenius form, as shown in Fig.4. One can see that the curve shows a good linearity and a significantly small apparent activation energy of 24 kcal/mol was observed. This is very close to the result reported by spitsyn et al[3], where they found the activation energy for diamond growth on diamond seeds via pyrolysis of methane is 60 Kcal/mol and it drops down to 25 Kcal/mol when atomic hydrogen was introduced. We note that the growth rate of diamond we are talking here is in terms of "an average size of 20 largest diamond crystals growth per hour". This is approximate in certain degree but,as one can see, the trend of the curve is definitely clear.

The correlation between growth rate and methane to hydrogen flow ratio is plotted in Fig. 3b and the corresponding pictures are shown in Fig.2,i to k. A slight increase in growth rate was observed when flow ratio was increased from 1.0/100 to 3.0/100.

Diamond deposited at different filament temperature are shown in Fig.3c and Fig.2, f to h. The result shows that filament temperature weakly affects diamond growth rate.

### 2). nucleation

From the pictures showed in Fig.2, a to m , it can be seen that nucleation density vary with deposition conditions significantly and thus can be controlled via deposition conditions. This can not be done on silicon substrate because where the nucleation was basically determined by the surface condition such as scratches and adsorbed impurities.

The dependence of diamond nucleation density on substrate temperature is shown in Fig.2,a to e and Fig.3d . Nucleation density of $5x10^6/cm^2$ was observed at Ts=800°C and it dropped down to $0.4x10^6/cm^2$ at Ts=1050°C. Increasing filament temperature was also found to significantly decrease nucleation density of diamond,as shown in Fig.2,f to h and Fig.3f. Nucleation density decreased from $3x10^6/cm^2$ to $0.1x10^6/cm^2$ as filament temperature increased from 1870°C to 2000°C. In the case of Tf=2000°C ,well defined diamond crystals with very low number density was deposited while at Tf=1870°C ,high number density of diamond particles was formed on substrate but no clear faceting was observed. Increasing methane to hydrogen flow ratio was also found to result in increase of diamond nucleation density, as shown in Fig.2,i to k. and Fig.3e .

## Perfection of deposited diamond crystals

The perfection of deposited diamond crystals were found strongly depend upon the deposition conditions, as can be seen in Fig.2 . Since no carbide can be formed on copper substrate, so the disturbance of carbide formation can be ruled out and effects of deposition conditions become more clear than the case of silicon substrate and is helpful to the understanding of deposition mechanism. But, for the reason of limited pages of this paper, this will be discussed later elsewhere.

## Discussion

### 1) Growth rate

Growth rate of CVD diamond ranging from 0.2 to 10 microns per hour has been reported[ 5 ]. Because the data reported are significantly scattered, it is still not clear that which deposition parameter is most important to the growth rate of diamond. From the fact mentioned above, e.g.,the growth rate increase with substrate temperature while being less affected by other parameters, we conclude that at least at Ts<1050°C, the growth rate is mainly controlled by substrate temperature. Activated carbon-containing radicals have to undergo a hydrogen-removing reaction to form diamond or graphite phase. This reaction, although it is still not being clearly understood, must happens at the growing surface because deposition rate of both diamond and graphite are so strongly dependent on substrate temperature. This is also suggested by the Arrhenius plot shown in Fig.4 where the linearity of Ln(D) vs 1/Ts correlation indicates the characteristic of thermally activated surface reaction process. In the normally used condition, say, Ts=800-1000°C, CH4/H2 = 0.5/100-1.5/100 and total pressure 20-100 torr, the growth rate is more dependent upon substrate temperature than upon other parameters. According to Fig.3a, growth rate higher than 10μ/hr can be expected. From the technological point of view, it is of interest to further enhance the growth rate of diamond. But, dependence of growth rate on substrate temperature seems leading to a limitation on low temperature deposition of diamond.

It is noticeable that the value of activation energy for diamond growth observed from this plot is significantly small (24 Kcal/mol ) and,as reported in [3], such a small value is caused by the existence of atomic hydrogen. These facts support the idea that besides etching graphite, atomic hydrogen also directly involved in the diamond-forming reaction. Another interesting result is that the different growth rates of diamond grown on copper and silicon. As has been suggested, the VLS ( vapor-liquid-solid ) growth may be an effective mechanism for diamond growth[ 6]. It can be expected that little amount of copper will be evaporated during deposition and thus provide the condition for VLS growth. Further work is clearly needed to better understand this phenomenon.

### 2) Co-Deposition of Graphite

It has long been realized that excessive growth of graphite hampers the growth of diamond. Where this graphite started and developed should be a interesting question,There are three possibilities: 1) graphite growth on substrate, 2) graphite growth on graphite and 3) graphite growth on diamond. Since the nucleation behavior is expected to vary significantly with different material and phase, thus it can be expected that graphite deposition can appear first on one material while not on the others. From the present work one can see that no graphite was deposited on copper substrate and growing surface of diamond up to Ts=1050°C, but, it was observed on α-alumina and silicon substrates. This fact indicate that diamond itself can nucleate and grow at substrate temperature even higher than 1050°C , as long as this growth is not hampered by the excessive graphite grown from substrate. This should be the main reason for the different behavior of CVD of diamond with different substrate materials,because co-deposition behavior of graphite on different material is very different.

## 3) Nucleation

It is noticeable that diamond can nucleate on copper without scratching the substrate and the nucleation density depend strongly on the deposition conditions. The fact that strain centers generated by scratching the substrate enhance the nucleation density of diamond suggest that different kind of surface defects are still the most effective sites for diamond nucleation. Since polycrystalline copper was used as substrate, the defect density is expected to be much higher than mirror polished single crystal silicon. Note that Fig.2,a to e shows a significant decrease in nucleation density as substrate temperature increase. This can be explained as at high substrate temperature the copper substrate was at least partially annealed . The defects density was reduced and this results in the decreasing diamond nucleation density. This was further confirmed by heating the substrate to melting point for a few seconds so that a mirror- like surface was formed. Diamond nucleation density on this region was found to be further reduced. On the other hand, the nature of the copper material can also play an important role in diamond nucleation. Copper is a non-carbide forming material with very close lattice constant to diamond and the interaction between copper and diamond is weak. These factors could lead to a weakly bonded diamond phase on copper with small elastic energy in copper-diamond interface. This means less energy is needed to form diamond nuclei. Furthermore, absence of graphite nucleation can be expected to favor the formation of diamond nuclei. It should be noted that although surface defects seems to be an effective site for diamond nucleation, dependence of nucleation density on methane to hydrogen flow ratio can not be related to surface defects. This result indicate that the concentration of carbon-containing radicals in gas phase is also an important factor. In fact that diamond nucleation density increases with methane to hydrogen flow ratio, is consistent with the nucleation theory. The reason for nucleation density being strongly dependent on filament temperature can also be related to the gas phase. As filament temperature increases, the concentration of carbon containing radicals relative to atomic hydrogen decrease and the effect of this equals to reducing the methane to hydrogen flow ratio. The reason for this is that methane starts to thermally decompose at 1100°C and at high enough filament temperature such as 1700°C, most of methane molecules that strike the filament surface decomposes, while at this filament temperature hydrogen just starts to decomposes. That is, in the case of low filament temperature, concentration of carbon containing radicals relative to that of atomic hydrogen can be very high. Therefore high nucleation density of diamond will be observed at relative low filament temperature, similar to the effect of increasing methane to hydrogen flow ratio. Another factor that may affect the diamond nucleation is that the composition of methane/hydrogen mixture in a HFCVD chamber changed significantly with filament temperature, as reported recently by Sommer et al[ 7 ]. The importance of filament temperature is clear and further work is needed.

## Conclusions

1) Diamond with high perfection and high nucleation density can be deposited on copper substrate with CVD technique. Diamond can nucleate on non-carbide forming material indicate that strong interaction between carbon and the substrate is not absolutely necessary for diamond nucleation. Strain centers is found still to be the effective site for diamond nucleation.
2) On copper substrate diamond nucleation density can be controlled via deposition condition. Increase in substrate temperature and filament temperature resulting in decrease of diamond nucleation density while it increase with methane to hydrogen ratio.
3) The Co-deposition of graphite on copper substrate is less than that on carbide-forming material.
4) Diamond growth rate was found to be mainly dependent on substrate temperature.

5) The ratio of activated carbon-containing radicals to atomic hydrogen determine the perfection of deposited diamond. Methane concentration and filament temperature are some of the parameters which affect this ratio and therefore changing the quality of the diamond.
6) An apparent activation energy of 24 kcal/mol was observed for diamond growth. The small value of the energy is attributed to the atomic hydrogen - involving reaction that leads to the diamond formation.

## Acknowledgement

We gratefully thank G.Pfeiffer for helping with raman measurements. We also thank Dr. Vijay Godbole and Alessandro Rengan for helpful discussion. This work in part is supported by NSF and Office of Army Research.

## Reference

1. K.Nishjmura, K. Kobashi, Y.Kawate and T.Horiuchi,KOBELCO Technol. Rev., 2, 49-52 (Aug. 1987 )
2. A.R. Badzian,T..Badzian,R.Roy, R.Messier and K.E.Spear,Mater. Res. Bull.,23,531-548(1988)
3. B.V. Spitsyn,L ..Bouilov and B.V.Deryagin, J.Cryst. Growth,52,219-26(1981)
4. S.M.Kanetkar et al, J. Electronics Material,Vol.20,No.2, (1991)
5. Karl E.Spear, J.Am. Ceram. Soc.,72(2) 171 191 ,(1989)
6. B.V.Derjaguin et al, J.Crystal Growth,2,380(1968)
7. M.Sommer and F.W.Smith, J. Mater. Res.,Vol.5, No.11, 2433(1990)

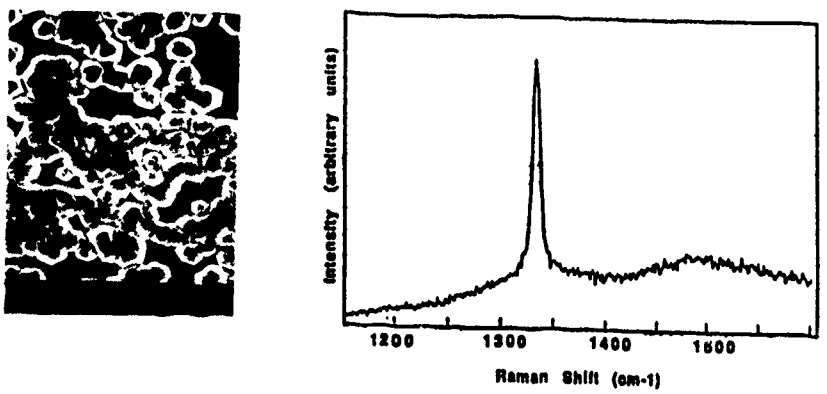



Fig.1 HFCVD of Diamond On Copper Substrate

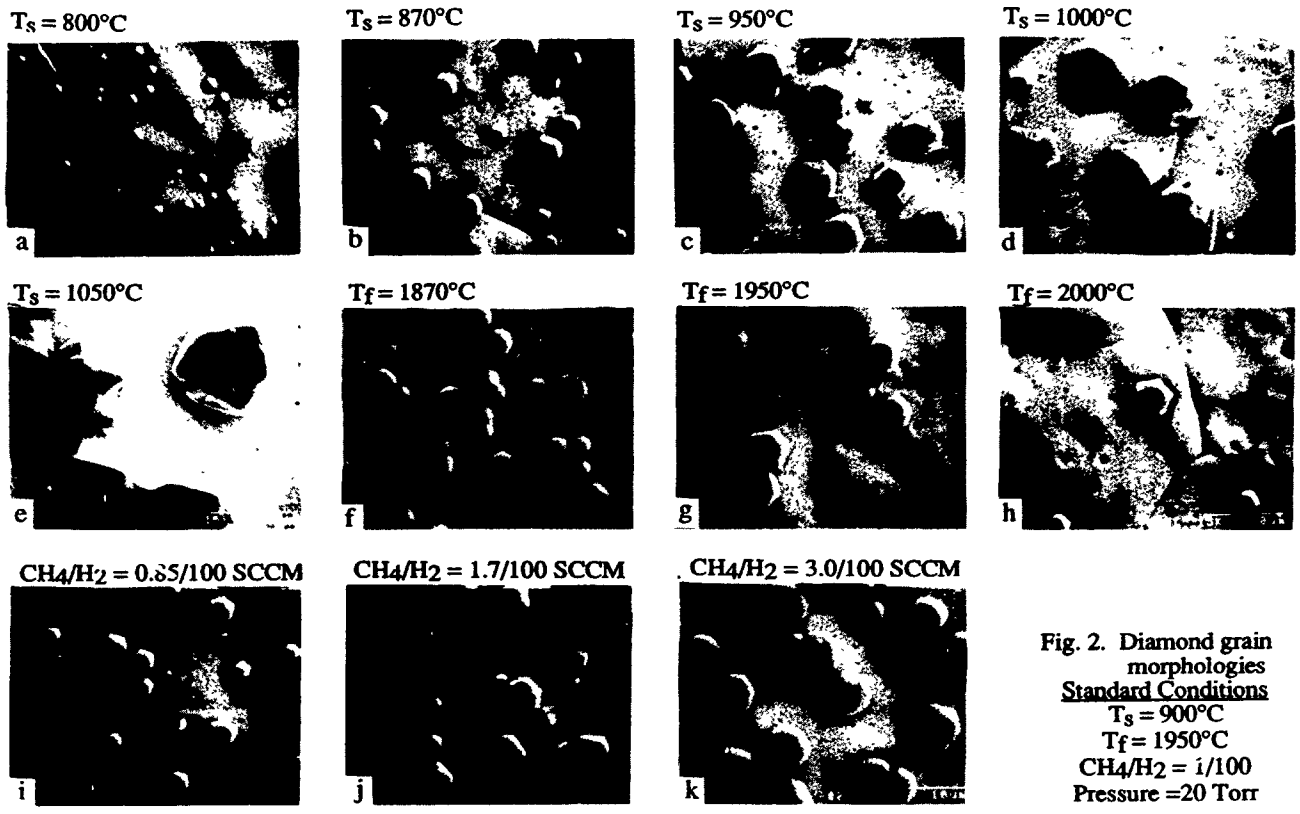



Fig. 2. Diamond grain morphologies
Standard Conditions
$T_s$ = 900°C
$T_f$ = 1950°C
$CH_4/H_2$ = 1/100
Pressure =20 Torr

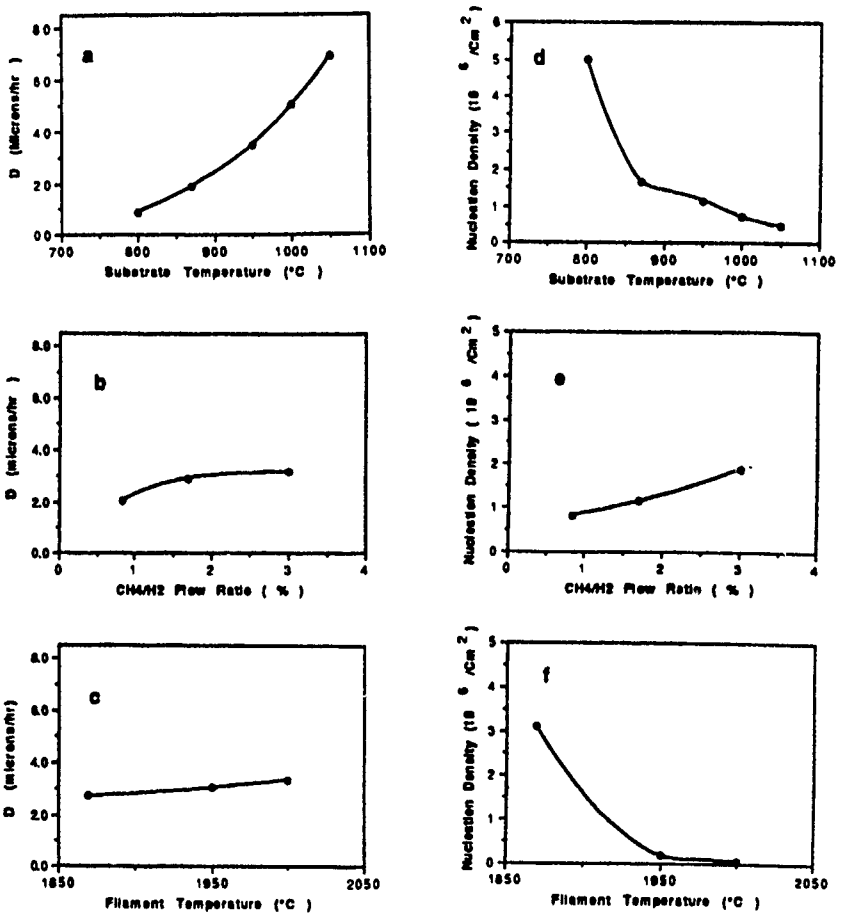



Fig.3 Growth rate (D, crystal size grown per hour) and nucleation density as a function of deposition conditions.

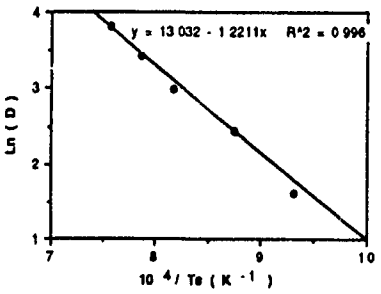



Fig.4 Arrhenius Plot of the Data from Fig.3a

# HIGH RATE HOMOEPITAXIAL SYNTHESIS OF DIAMOND IN A FLAME

K. A. Snail, J. A. Freitas^, C. L. Vold*, and L. M. Hanssen+
Optical Sciences Division, Code 6522
*Material Sciences & Technology Division, Code 6322
Naval Research Laboratory
Washington, DC 20375-5000

^Sachs Freeman Associates
1401 McCormick Drive
Landover, MD 20785-5396

+Current Address: Bldg. 220, Rm. B-306,
National Institute of Standards and Technology,
Gaithersburg, MD 20899, U.S.A.

## Abstract

Homoepitaxial growth of high quality, facetted diamond crystals at rates exceeding 150 microns/hour has been observed on millimeter sized {100} and {110} natural diamond seed crystals, using a laminar, premixed oxygen-acetylene flame in air. The key element in achieving such high growth rates has been a substrate temperature in the 1150-1500°C range. Microscope and naked eye observations show the original cylindrical shaped seed crystals growing into polyhedral shaped crystals with identifiable {100} and {111} faces. Examination under optical and scanning electron microscopes reveals terraces on the {100} faces. The deposited diamond is clear and exhibits Raman spectra almost identical to that of natural diamond. Laue Xray diffraction analyses have confirmed the epitaxial nature of the growth. The deposition temperatures and growth rates reported are the highest ever observed for the homoepitaxial synthesis of diamond crystals at low pressures.

## Introduction

In the fall of 1988 we observed an unusual phenomena during multi-hour diamond depositions with an oxygen-acetylene flame. Frequently,

large (~100-350 microns) single crystals of diamond would begin to grow on Si substrates after about 1-3 hours [1, 2]. These large crystals typically had smooth, oriented {100} faces, and electron channeling measurements [3] indicated that the crystals were monocrystalline and that the strain in the crystal lattice was indistinguishable from natural diamond. The Raman spectra of a typical crystal exhibited a sharp 1332 $cm^{-1}$ peak, no evidence of a-C or graphite, and a very low fluorescence background. The crystals often were found on pedestals which thermally isolated them from the substrate. Capelli [4] has used an energy balance argument to show that diamond crystals in an oxygen-acetylene flame would equilibrate above 1200°C if thermally isolated from their substrate. Unreported in the presentation of previous studies [1, 2, 3] was the observation that during long multi-hour depositions a two color pyrometer always registered temperatures >1250°C (the limit of the instrument) whenever large (>100 μm) single crystals appeared on the substrate, and that the crystals themselves had a visible brightness that was considerably brighter than the 900-1000°C substrate.

Based on these observations, we performed a series of homoepitaxial growths in a laminar, premixed oxygen-acetylene flame at substrate temperatures of 1150-1500°C. The results of these depositions are described in the following sections and in an upcoming publication [5].

## Experimental Setup

The apparatus used in this study is similar to that described in previous work [6,7]. Oxygen and acetylene were metered to a commercial brazing torch with a mass flow control system. The temperature of the substrates was measured with a two-color pyrometer which was insensitive to the flame's emission. The substrates consisted of 0.5 mm thick, natural type I and type IIa diamond heat sinks with circular or square cross sections, polished on the top {100} or {110} faces, and brazed to the ends of 1.5 cm long pieces of threaded molybdenum rod with a Au-Ta compound. Although the braze material melted during the high temperature depositions, no degradation in thermal contact between the seed crystals and the Mo rod was observed during depositions up to 1500°C. Since the thermal conductivity of the seed crystals and braze material is relatively high, the seed crystal is expected to be isothermal and its temperature equal to or slightly greater than the Mo rod temperature. The temperature of the seed crystals was controlled by adjusting the penetration of the Mo rod into a water cooled Cu cylinder. A more detailed description of these procedures can be found elsewhere [5].

## Results

A series of growths on three <100> and one <110> oriented diamond crystal substrates were performed at substrate temperatures of 1150, 1250, 1360, and 1500°C (±30°C), respectively. Depositions at temperatures below 1000°C consisted of small, rectangular shaped, oriented single crystal domains on {100} seed crystals, and rough surface morphologies on {110} seed crystals which were similar to the results reported by Janssen et al. [8]. Growths below 1000°C on both {100} and {110} seed crystals exhibited oriented polycrystalline growth around the perimeter the seed crystals (see Figure 1). A substrate temperature of at least 1150-1200°C appeared necessary to grow a macroscopic facetted crystal which covered the entire top surface of the seed crystal. These results are strongly dependent on the position of the seed crystal in the flame. Growth of macroscopic (e.g. 1.7 mm x 150 μm) polyhedral crystals from 1.5 mm diameter cylindrical seed crystals was observed in ~20-30 minutes at 1250°C on a <100> oriented crystal, and in ~10-15 minutes at 1500°C on a <110> oriented crystal. Large (~100 microns) randomly oriented diamond crystals were also observed to grow at each temperature on the Au-Ta braze covering the top surface of the Mo rod.

Electron micrographs of a cylindrical {100} seed crystal before and after a one hour growth at 1250°C are shown in Figures 2a and 2b, respectively. The thickness of the deposited layer was estimated with an optical microscope equipped with a micrometer; it varied from 100-165 microns depending on position on the {100} face. The deposited material has an octagonal shape when viewed from above (Fig 2b), with the shapes of the side faces alternating between trapezoidal and truncated parallelograms. These are the shapes expected around the 'waist' of a cubo-octahedral crystal which is truncated along a <100> axis which is perpendicular to the plane of the waist (the plane of the waist contains four <100> axes). The trapezoidal and truncated parallelogram shaped faces would thus correspond to the <111> and <100> crystallographic directions, respectively, as shown in Figure 3.

The first order Raman spectrum of the deposited crystal side of the 1250°C sample (see Fig. 2) was measured with a low laser power (40 $W/cm^2$), a 514.5 nm laser line, and a bandpass comparable to the phonon peak's line width, and is shown in Figure 4. Note the absence of graphite and a-C components in the spectra and the low luminescence background. High resolution Raman spectra were also acquired from this crystal. The deposited crystal's diamond peak position was located at 1333.1 ± 0.2 $cm^{-1}$) and it's linewidth (FWHM) was 2.6 $cm^{-1}$. For comparison, we also

measured a natural type IIA diamond; the values obtained were 1333.5 $cm^{-1}$ and 2.4 $cm^{-1}$, respectively.

The increase in the luminescence background observed in the Raman spectrum at higher frequency shifts is due to a defect band which has a zero phonon line (ZPL) at 2.155 eV, as shown in Fig. 5. The low temperature (6K) photoluminescence spectra shown in Figure 5 was excited with a 488 nm laser line and with a power of ~5mW. The two strongest bands (d,e) are located at 2.155 eV and 1.946 eV; these have been assigned (9) to a nitrogen vacancy complex and a nitrogen-vacancy (N-V) pair, respectively. Two weaker bands (a,f) at 2.464 eV and 1.682 eV correspond to the H3 center and a possible Si-related defect (9). A weak band (c) that has not been assigned to any previously observed defect was seen at 2.282 eV. The peak (b) at 2.375 eV is the 1st order Raman peak.

The observation of the polyhedral shape of the deposited crystal shown in Figure 2b and the quality of the deposited crystal's Raman spectra shown in Figure 4 suggested that the growth is monocrystalline. Laue Xray diffraction patterns of both the seed crystal and deposited crystal sides of the 1250°C sample are shown in Figures 6a and 6b, respectively. Analysis of these patterns confirmed that the deposited diamond is monocrystalline with a <100> orientation which is epitaxially oriented with respect to the {100} seed crystal. The optical transparency of the deposited crystal is excellent [5].

At high substrate temperatures in a laminar flame, growth on the {100} surface proceeds mainly via steps which can be many hundreds of microns long. The period of the steps increased with the deposition temperature [5], and ranged from 1-2 microns at 1150°C to 40-60 microns at 1360°C. The seed crystals subjected to higher deposition temperatures had larger misorientations, which would tend to produce a smaller initial step period. This suggests that the step period does increase rapidly with temperature. Under certain conditions, continuous growth across the top surface of the seed crystal is lost, but local well formed domains of epitaxial growth which are 100's of microns on a side are observed to grow at rates exceeding 200 μm/hr in the <100> direction.

A deposition on a cylindrical {110} seed crystal was performed at a temperature of 1500°C. After only 15-20 minutes at this temperature, crystal faces corresponding to the {111}, {110} and {100} directions appeared around the perimeter of the top {110} face of the seed crystal, giving an octagonal shape when viewed from above [5]. A very low growth

rate in the center of the seed crystal's {110} face was observed; the Raman spectra of this area of the face exhibited a strong graphitic character. The Raman spectra of the epitaxially grown faces exhibit a diamond peak height to fluorescence background ratio of >35:1. Poorly formed cubo-octahedral crystals were also observed to grow on the Au-Ta braze material [5]. This is the highest temperature ever reported for both epitaxial and non-epitaxial diamond growth at low pressures.

## Discussion

In 1976 Chauhan et al. [10] reported on a study of carbon deposition on 0-1 micron diamond powders which used methane-hydrogen gas mixtures without activation of the gas phase. Their results showed diamond growth at temperatures of 1140-1475°C (determined from density measurements), and a maximum initial diamond growth rate of <0.02 microns/hour which exponentially decayed with time. The exponential decay of the initial rate was explained by the covering of the diamond surface by graphitic carbon. In 1981 Spitsyn et al. reported [11] on homoepitaxial growth studies in a controlled transport reaction (CTR) environment. They stated, "high perfection single crystalline [diamond] layers were obtained on the {110} face of natural diamond at 750°C... As the temperature is increased further, the growth rate of [the] homoepitaxial film increases ... and reaches a maximum at ~1000°C. Further increase in temperature results in a reduction of the growth rate and in deterioration of the structure of the diamond layers, so that HEED analysis reveals graphite inclusions." As far as we know, no refereed publications reported on the homepitaxial growth of diamond above 1200°C between 1976 and 1990.

Several authors [12,13] have argued that the chemisorption states of hydrogen on diamond surfaces [14], with their desorption peaks at approximately 900 and 1050°C, will prevent a growing diamond surface from maintaining its $sp^3$ hybridization at higher temperatures. The upper temperature limit for CVD diamond growth would then be due to the desorption of atomic hydrogen and the subsequent reconstruction and graphitization of the growing diamond surface. The actual hydrogen coverage of a diamond surface in a CVD environment will depend on a dynamic balance of the flux of hydrogen and other species from the gas phase, as well as the abstraction and desorption kinetics on the surface. Estimates of the hydrogen disassociation fraction in atmospheric pressure oxygen-acetylene flames suggest that the hydrogen flux in a flame environment could be as much as an order of magnitude higher than

in CVD reactors [5]. Thus, the high atomic hydrogen flux in an atmospheric pressure oxygen-acetylene flame could permit a growing diamond surface to remain hydrogen terminated well above the hydrogen desorption temperatures determined under UHV conditions.

A recent U.S. patent application [15] and two publications [16, 17] reported diamond growth at temperatures above 1400°C. Scanning electron micrographs in both publications show a columar type morphology with square, <100> oriented diamond crystals situated on top of the columns. The columns act to thermally isolate the large diamond crystals from the substrate, thus generating the very high crystal temperatures that we first observed in 1988 [1, 2, 3, 5].

The existence of a new high temperature, high rate growth regime for the homoepitaxial synthesis of macroscopic, high quality diamond crystals has been demonstrated by this work. Knowing that DC and RF plasma jets can also induce a high disassociation fraction of hydrogen, we recently initiated a collaboration with the High Temperature Laboratory at the University of Minnesota. The results of this work indicate that monocrystalline diamond can also be grown with a high temperature epitaxy (HTE) type process in a DC triple torch reactor [18, 19]. The work reported in these papers may eventually enable the growth of relatively inexpensive, large (1-10 ct.) single crystals and boules of diamond. Such diamond is not readily available from natural or synthetic sources and is needed to develop diamond-on-diamond electronic devices, heat sinks and bulk optical components.

## Acknowledgements

The authors would like to thank Richard G. Priest and Phillip Klein for many useful discussions on the mechanisms of crystal growth, and Michael Seal for brazing and supplying the diamond seed crystals. James E. Butler is to be thanked for some of the initial Raman characterization of the deposited crystals, and for arranging to have the seed crystals mounted.

## References


[1]L. M. Hanssen, W. A. Carrington, D. B. Oakes, J. E. Butler, and K. A. Snail, Preprints Book, American Chemical Society Yearly Mtg., Vol. **34**, #2, p. 444, April 1989 (Dallas).

[2]L. M. Hanssen, W. A. Carrington, D. B. Oakes, J. E. Butler, and K. A. Snail, Final Prog. & Pres. Summaries, p. T7, SDIO/IST-ONR Diamond Tech. Init. Symp., 11-13 July 1989, (Crystal City, VA).

[3]R. G. Vardiman, C. L. Vold, K A. Snail, J. E. Butler and C. S. Pande, Matls. Ltrs. **8**, 468 (1989).

[4]M. A. Capelli and P. H. Paul, J. Appl. Phys. **67**, 2596 (1990).

[5]K. A. Snail and L. M. Hanssen, "High temperature, high rate homoepitaxial growth of diamond in an atmospheric pressure flame", J. Crystal Growth, in press.

[6]D. B. Oakes, J. E. Butler, K. A. Snail, W. A. Carrington, and L. M. Hanssen, J. Appl. Phys. **69**, 2602 (1991).

[7]L. M. Hanssen, K. A. Snail, W. A. Carrington, J. E. Butler, S. Kellog, and D. B. Oakes, Thin Solid Films **196**, 271 (1991).

[8]G. Janssen, W. J. P. van Enckevort, J. J. D. Schaminee, W. Vollenberg, L. J. Giling, and M. Seal, J. Crystal Growth **104**, 752 (1990).

[9]J. A. Freitas, J. E. Butler, and U. Strom, J. Matl. Res. **5**, 2502 (1990).

[10]S. P. Chauhan, J. C. Angus, and N. C. Gardner, J. Appl. Phys. **47**, 4746 (1976).

[11]B. V. Spitsyn, L. L. Bouilov and B. V. Derjaguin, J. Crystal Growth **52**, 219 (1981).

[12]P. G. Kosky and D. S. McAtee, Matls. Ltrs. **8**, 369 (1989).

[13]B. B. Pate, Surf. Sci. **165**, 83 (1986). See section 9.

[14]S. Matsumoto and N. Setaka, Carbon **17**, 485 (1979).

[15]K. A. Snail, L. M. Hanssen and J. E. Butler, "Epitaxial synthesis of diamond crystals at high growth rates", U.S. Patent Application #548,719, filed July 6, 1990.

[16]Y. Matsui, H. Yabe, and Y. Hirose, Jap. Jrnl. Appl. Phys. **29**, 1552 (August, 1990).

[17]R. Komanduri, K. A. Snail and L. Fehrenbacher, Phil. Mag. Ltrs. **62**, 283 (October, 1990).

[18]Z. Lu, K. Snail, C. Marks, J. Heberlein, and E. Pfender, "High rate homoepitaxial growth of diamond in thermal plasma", late paper, Electrochemical Society Annual Meeting, May 5-10, 1991 (Washington, DC).

[19]K. Snail, C. Marks, Z. Lu, J. Heberlein, and E. Pfender, "High temperature, high rate homoepitaxial synthesis of diamond in a triple torch plasma reactor", subm. to Appl. Phys. Ltrs, Apr. 1991.

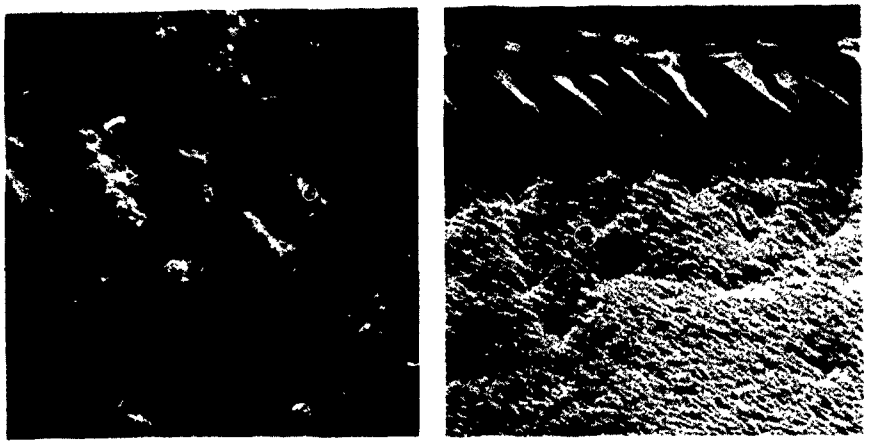



**Figure 1.** Scanning electron micrographs of a) top surface of {110} type IIA seed crystal after 1 hr deposition at 950°C showing rough growth surface similar to that observed by other groups, and b) edge of same seed after deposition showing oriented polycrystalline growth on side of seed.

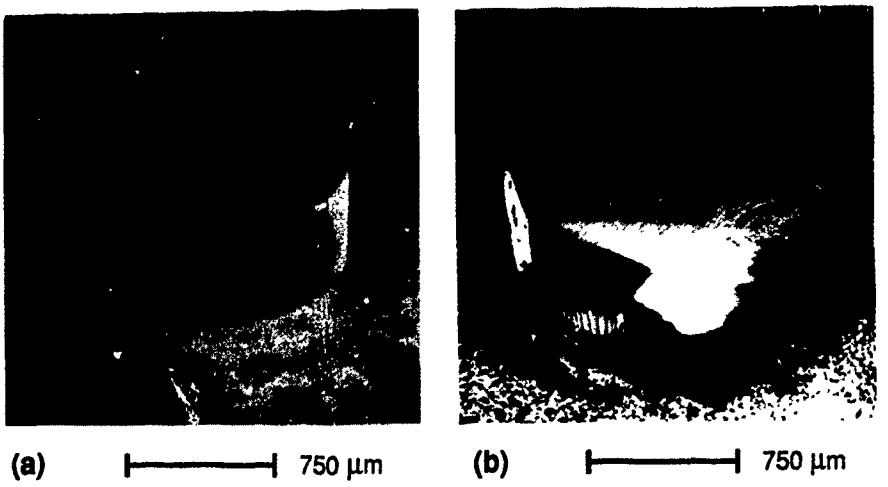



**Figure 2.** Scanning electron micrographs of circular <100> oriented seed crystal grown at 1250±30°C in a oxy-acetylene flame: a) before deposition, and b) after deposition showing faceted growth with octagonal shape.

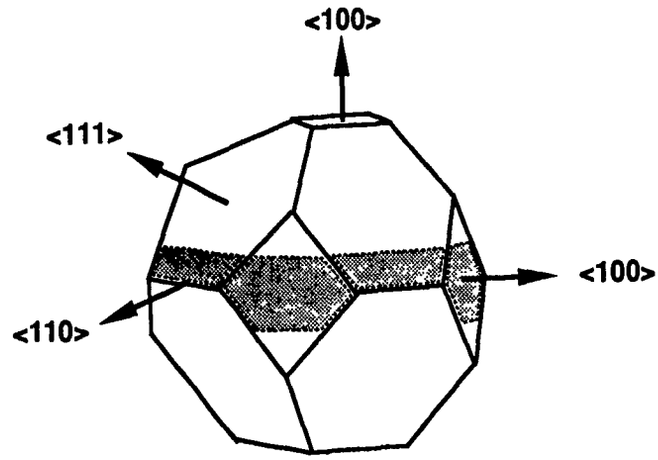



**Figure 3.** Cubo-octahedral crystal showing growth sectors observed (gray) in deposit on {100} seed crystal shown in Fig. 2b.

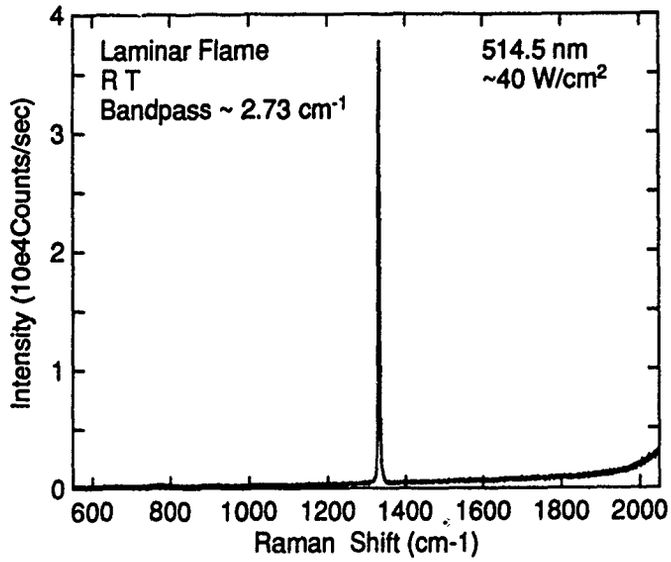



**Figure 4.** Raman spectrum of the diamond crystal shown in Fig. 2b. The diamond peak position and its FWHM are 1333.1 $cm^{-1}$ and 2.6 $cm^{-1}$.

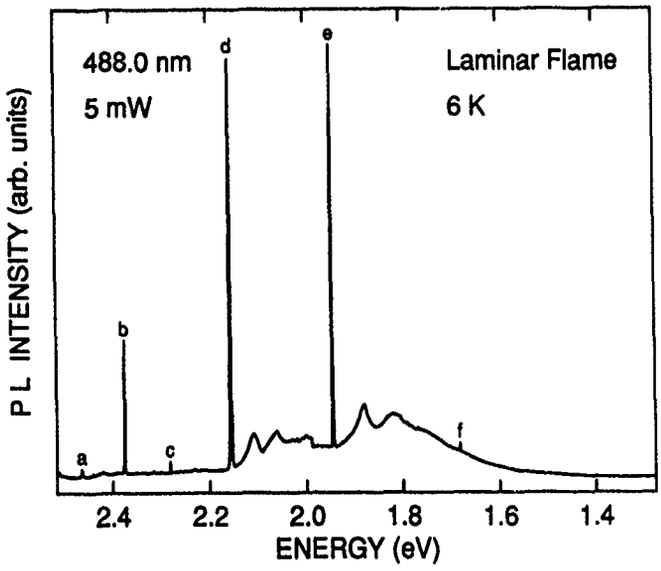



**Figure 5.** Low temperature photoluminescence spectrum of diamond crystal shown in Fig. 2b. Note the peaks at 2.464 (a), 2.282 (c), 2.155 (d), 1.946 (e) and 1.682 (f) eV. The first order Raman peak (b) is at 2.375 eV.

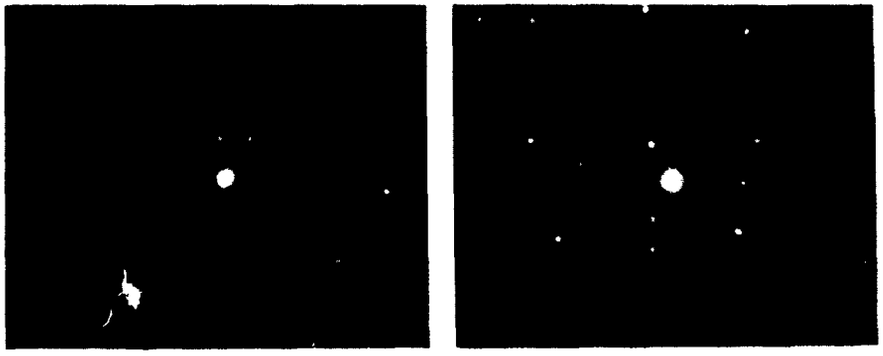



**Figure 6.** Laue Xray diffraction pattern of a) seed crystal side of 1250°C sample after growth, and b) deposited crystal side of same sample. Note that the deposited layer is monocrystalline, of <100> orientation, and epitaxially oriented with respect to the seed crystal.

# GROWTH OF HIGH QUALITY DIAMOND FILMS IN A TURBULENT FLAME

K. A. Snail, C. J. Craigle^, R. G. Vardiman*, C. M. Marks, and J. A. Freitas, Jr.+
Optical Sciences Division, Code 6522
*Materials Science and Technology Division, Code 6325
Naval Research Laboratory
Washington, DC 20375-5000

^Optical Sciences Center
University of Arizona
Tucson, AZ 85721

+Sachs Freeman and Associates
1401 McCormick Drive
Landover, MD 20785-5396

ABSTRACT

High quality polycrystalline diamond films have been synthesized in a turbulent premixed, oxygen-acetylene flame, using a commercial brazing torch. The quality of the films was measured by high resolution Raman spectroscopy, scanning and transmission electron microscopy, hemispherical transmittance measurements in the UV, visible and infrared, and photoluminescence spectroscopy. Turbulence was achieved by operating the torch with a sufficiently high Reynolds number. The presence of turbulence was confirmed by observations of changes in the flame shape, the characteristic sound of the flame, and calculation of the Reynolds number.

Most combustion processes either involve or are dependent on turbulence. While several groups have investigated diamond growth in laminar flames (1,2), none have examined the turbulent case. One of the outstanding features of turbulent flames is that the rates of transfer and mixing can be several orders of magnitude higher than in laminar flames (3). This is due to the presence of eddies, which can have an effective diffusion coefficient which is larger than the molecular diffusion coefficient by one to two orders of magnitude, depending on the Reynolds number (4). Consequently, the transport of molecules, heat and momentum can be greatly enhanced in turbulent, as compared to laminar flow. If the

diamond growth rate in laminar premixed flames is transport limited, then that rate could be significantly increased by the introduction of turbulence. Recently we have reported on the growth of high quality diamond films in a turbulent, premixed, oxygen-acetylene flame (5). In this paper we provide more details about the growth conditions and additional analyses of the quality of the deposited diamond films.

The apparatus used in this study consisted of a commercial oxygen-acetylene brazing torch, a gas mass flow control system, a water cooled copper (Cu) substrate mount, and a two-color infrared (IR) pyrometer that was used to monitor the substrate temperature during growth (see Figure 1). The substrates consisted of ~1.5 cm long sections of 3/8"-16 molybdenum (Mo) threaded rod, slotted on one end and polished with silicon carbide and diamond grit on the other. The temperature of the Mo substrates was controlled by adjusting the penetration of the substrates into a threaded hole in the water cooled Cu substrate mount. A more detailed description of this experimental setup can be found elsewhere (6). High purity oxygen (99.99%) and acetylene (99.6%) were used as source gases, with the acetylene passed through an activated charcoal trap to remove residual acetone (7). For this study the ratio ($R_f$) of the flow rate of oxygen to acetylene was chosen so that a small excess acetylene feather existed just beyond the primary flame front. The substrates were positioned in the feather about 1-2 mm from the primary flame front (see Fig. 1), and adjusted so as to maintain a surface temperature of ~900°C for one hour. Photographs of flame shapes were performed with a Bausch and Lomb StereoZoom7 microscope and a standard polaroid attachment.

Figures 2a and 2b show photographs of premixed oxygen-acetylene flames generated with 0.89 mm and 1.85 mm diameter orifice tips, respectively. The oxygen/ acetylene flow ratio and the average gas velocity at the orifice are the same for both flames. Turbulent flow can cause a rounding and broadening of the primary flame front, as shown in Figure 1b, and introduce a characteristic hissing sound (8). The rounding of the flame front may be due to the rounding of the velocity profile observed when the flow in a tube changes from laminar to turbulent. The broadening occurs when the scale of the turbulence (i.e. the eddy diameter) is significantly greater than the flame front thickness (9). Instantaneous micro-Schlieren photographs have revealed that the thickened flame front seen by the eye is really the time averaged envelope of a fluctuating, corrugated flame front (10). The Reynolds number ($Re = vd\rho/\mu$) of the flow in the tube supporting the flames shown in Fig. 2a and 2b was calculated to be 5,900, and 12,200 respectively, assuming a temperature of 300°K and a 1:1 mixture of oxygen: acetylene. Higher gas temperatures

could lower these Re values (due to the viscosity's $\sqrt{T}$ dependence), but the temperature rise of the gases in the burner tip was estimated to be negligible. The high Reynolds numbers quoted here for flow in the tube supporting a laminar flame may be related to the observation (11) that Bunsen burner flames can appear laminar when the gas flow in the burner tube is turbulent.

The laminar and turbulent operational regimes (12) of a Bunsen burner are shown as a function of the average gas velocity and the burner diameter in Figure 3. We expect that oxygen-acetylene torches will exhibit similar, but not identical, characteristics. Note that both the laminar and turbulent regimes are bounded from below by the flashback limit, and from above by the blow-off limit. These limits correspond to the flame either propagating back down the burner tube or becoming unstable and detaching from the burner tip, respectively. The blow-off and flash back limits are defined semi-empirically in terms of two critical velocity gradients which are expressed in terms of the quenching distance and the average gas velocity. The quenching distance corresponds to the tube diameter below which a flame cannot propagate, due to heat losses to the walls; this sets a lower limit on the burner diameter. For stoichiometric mixtures of oxygen and acetylene, the quenching distance is about 0.1 mm. The laminar and turbulent regimes are separated by a hyperbolic wedge defined by the Reynolds number values corresponding to the laminar-turbulent transition at the flame front. Since these Reynolds numbers are not defined at the flame front, the values may be higher than the normal 2,300-3,200 values that are quoted for turbulent flow in tubes. The velocity profile in the burner tube changes significantly when the flow changes from laminar to turbulent, and hence the critical velocity gradients and slope of the the blow-off and flash-back limits shown in Fig. 3 may also change in passing through the laminar-to-turbulent transition.

The first order Raman spectrum of a polycrystalline diamond film grown at $T_S$ = 900 °C in a premixed ($R_f$ = 1.08), turbulent oxygen-acetylene flame was measured at low power with a bandpass of 2.7 $cm^{-1}$ and is shown in Figure 4. Note the absence of any significant graphite or a-C components in the spectrum and the small luminescence background increases with larger shifts from the excitation wavelength. A measurement of the high resolution Raman spectrum of the same sample was also performed. The film's diamond peak position is located at 1333.3 ± 0.2 $cm^{-1}$ and it's linewidth (FWHM) is 3.0 $cm^{-1}$. For comparison, a natural type IIA diamond sample was also analyzed; the peak position and FWHM were found to be 1333.5 $cm^{-1}$ and 2.4 $cm^{-1}$, respectively.

The low temperature photoluminescence spectra of the polycrystalline sample analyzed in Figure 4 is shown in Figure 5. We have used a 488 nm laser line and a power of 20 mW for this measurement. Note that the spectra exhibits no detectable vacancy and/or nitrogen related complexes that have been observed (12) in diamond grown in laminar oxygen-acetylene flames. The regularly spaced small peaks from 1.4-1.7 eV are due to interference effects in the film. Note that the spectrum is dominated by a strong first order Raman peak at 2.375 eV, and a broad almost featureless luminescence band. The broad band may be due to the recombination of extended defects, as observed in natural diamond. The features at 1.8-1.9 eV and 2.0-2.1 eV are probably due to the spectral response of the spectrometer. A transmission electron micrograph of a film grown under similar conditions is shown in Figure 6a. The grain size is 1-2 μm. Twinning, although frequent, is not as heavy as in FACVD films which were grown and analyzed at NRL. Stacking faults may also be observed, as shown in Fig. 6b.

Diamond crystals grown on Si coated Mo substrates under the proper conditions (i. e. substrate temperature, flow ratio, position in flame) in a turbulent oxy-acetylene flame are transparent enough to allow one to image the substrate through individual crystals with an optical microscope; thin films (~10-30 μm thick) grown on Mo substrates are white and sufficiently transparent to read newsprint through. We have been able to grow well facetted crystals at substrate temperatures of 500-1200°C, depositions outside of this range have not been attempted. The UV, visible and NIR hemispherical transmittance of 10 μm thick diamond films synthesized in a turbulent flame is high throughout the UV, visible and NIR (5). A sharp absorption edge is observed at ~222nm, indicating the absence of the defect center associated with substitutional nitrogen (13). A slightly higher transmittance is observed when the rough side of the film is oriented towards the spectrophotometer's beam. This is due to total internal reflection at the rough surface of the film (14).

The diamond growth rates observed under the conditions reported in this paper are lower than those observed with a laminar oxygen-acetylene flame (2,6). In a turbulent flame, the flux of active species to the growing diamond surface is expected to increase significantly compared to a laminar flame. Recently we have determined that the boundary layer next to a substrate positioned in a flame similar to that shown in Figure 2b is laminar. Hence, the increased species flux associated with turbulent flow may not be fully realized. The increase in quality and lower growth rates for diamond synthesized in a turbulent flame suggests that the flux of growth to etchant species (15) at the substrate surface has shifted in

the direction of etching. If the entrainment of room air increases with flow rate and/or turbulence, then additional etchant species, e.g. OH, may be transported to the substrate. A thinner boundary layer may also change the ratio of growth to etchant species at the substrate if the lifetimes of critical species are close the the transport time across the boundary layer. Finally, if the level of turbulence is sufficiently high, the flame front can be discontinuous, leading to burning in isolated pockets and further changes in the growth chemistry. Previous reports of high quality diamond growth in flames (16,17,18) did not indicate that turbulent flames were employed, and flame shape drawings and/or experimental parameters from these papers suggest that the flames were laminar.

## REFERENCES


[1]Y. Hirose and M. Mitsuizumi, New Diamond 4(3), 34 (1988).

[2]L. M. Hanssen, W. A. Carrington, J. E. Butler, and K. A. Snail, Matls. Ltrs 7, 289 (1988).

[3]H. Tennekes and J. L. Lumley, *A first course in turbulence*, MIT Press, (Boston, 1972).

[4]U. Frisch and S. A. Orszag, Physics Today, p. 24, (January 1990).

[5]K. A. Snail and C. Craigie, Appl. Phys. Ltrs. **58**, 1875 (1991).

[6]L. M. Hanssen, K. A. Snail, W. A. Carrington, J. E. Butler, S. Kellogg, and D. B. Oakes, Thin Solid Films **196**, 271 (1991).

[7]D. C. Manning, Atomic Absorption Newsletter **7**, 44 (1968).

[8]A. G. Gaydon and H. G. Wolfhard, Flames: Their structure, radiation and temperature, Chapman & Hall, p. 14, (London, 1979).

[9]J. A. Barnard and J. N. Bradley, Flame and Combustion, Chapman and Hall, p. 74 (New York, 1985).

[10]M. D. Fox and F. J. Weinberg, Proc. Roy. Soc. A **268**, 222 (1962).

[11]I. Glassman, Combustion, Academic Press, p. 167, (New York, 1987).

[12]J. A. Freitas, J. E. Butler, and U. Strom, J. Matl. Res. **5**, 2502 (1990).

[13]M. Seal, Interdisc. Sci. Rev. **14**, 64 (1989).

[14]T. P. Thorpe, A. A. Morrish, L. M. Hanssen, J. E. Butler, and K. A. Snail, Proc. of the Conf. on Diamond Optics III, SPIE Vol. **1325**, p. 230, Intl. Soc. for Optical Engineering, (Bellingham, WA, 1990).

[15]S. J. Harris and A. M. Weiner, Appl. Phys. Ltrs. **55**, 2179 (1989).

[16]Y. Hirose, S. Amanuma, N. Okada, and K. Komaki, Proc. of the 1st Intl. Symp. on Diamond and Diamond-Like Films, ECS Proc. Vol. **89-12**, p. 80, May 7-12, 1989 (Los Angeles).

[17]K A. Snail, W. A. Carrington, L. M. Hanssen, and A. A. Morrish, Proc. Conf. on Diamond Optics II, SPIE Vol. **1146**, p. 144, Intl. Soc. for Optical Engineering, (Bellingham, WA, 1989).

[18]Y. Tzeng, C. C. Tin, R. Phillips, T. Srivinyunon and Y. Chen, Appl. Phys. Ltrs. **57**, 789 (1990).

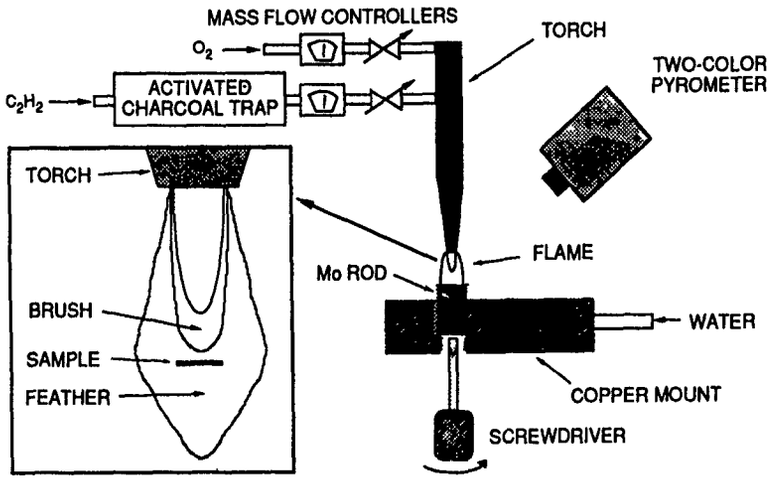



**Figure 1.** Experimental setup showing mass flow controllers, two color pyrometer, brazing torch and substrate mount assembly. The flame shape and sample position are indicated in the inset.

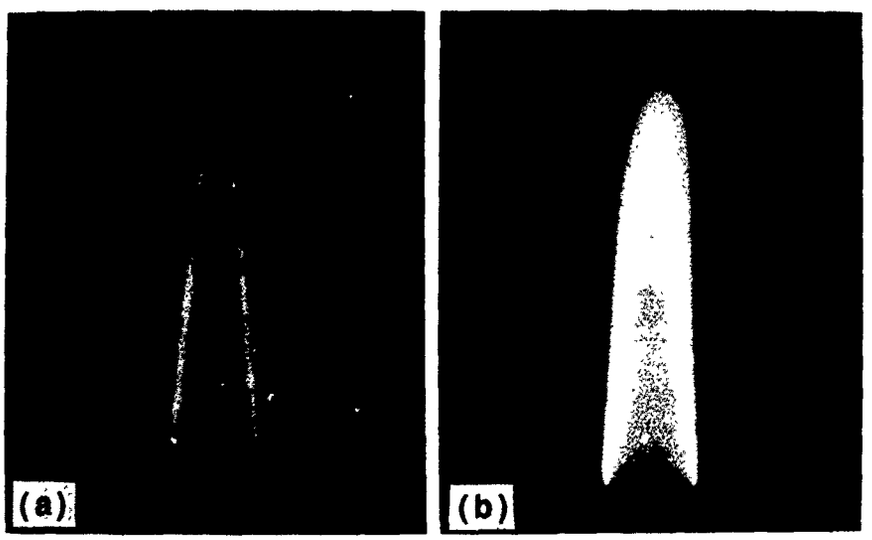



**Figure 2.** Photographs of premixed oxygen-acetylene flames which are (a) laminar and (b) turbulent. Note the rounding and broadening of the flame front in the turbulent case, compared to the thinner conical flame front in the laminar case.

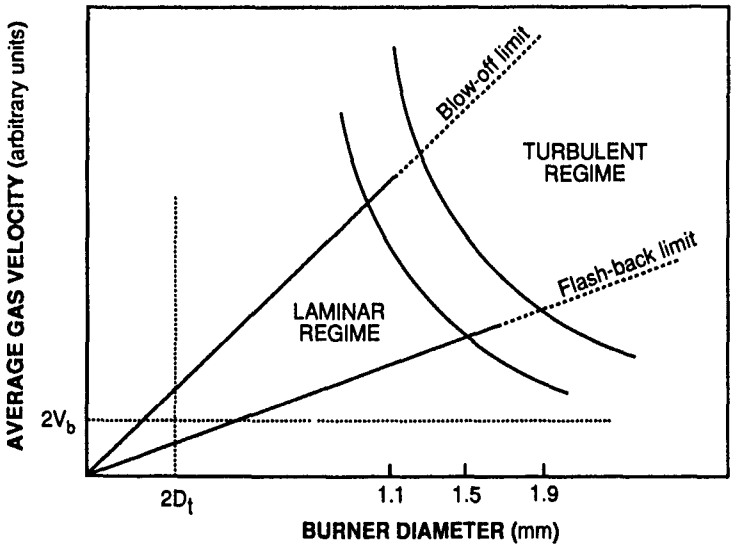



**Figure 3.** Operational regimes of premixed, single orifice torches. Note the flashback limit, the blow-off limit, and the hyperbolic wedge separating the laminar and turbulent regimes.

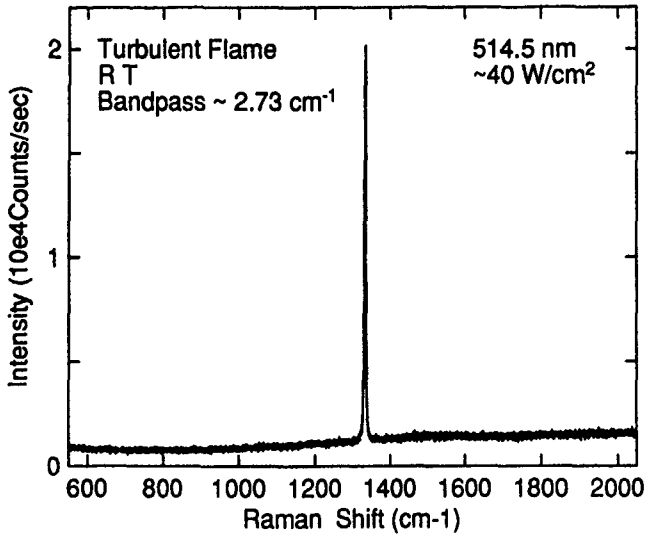



**Figure 4.** Raman spectrum of a polycrystalline diamond film grown in a turbulent, premixed oxygen-acetylene flame at $T_S$ = 900°C.

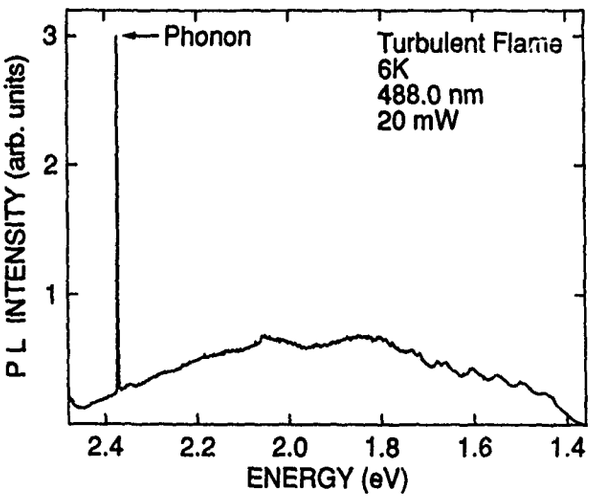



**Figure 5.** Low temperature photoluminescence spectrum of a diamond film grown in a turbulent oxygen-acetylene flame. Note the absence of defect bands associated with vacancies and nitrogen related complexes.




**Figure 6.** TEMs of a diamond film grown in a turbulent flame: (a) bright field, showing twins (b) dark field, showing stacking faults.

# HIGH RATE HOMOEPITAXIAL GROWTH OF DIAMOND IN THERMAL PLASMA

Z.P. Lu[#], K. Snail[*], C. Marks[*], J. Heberlein[#], and E. Pfender[#]

[#] Department of Mechanical Engineering
University of Minnesota
Minneapolis, MN 55455

[*] Optical Sciences Division, Code 6522
Naval Research Laboratory
Washington, DC 20375-5000

## Abstract

Thermal plasma jets were used for high rate homoepitaxial growth of diamond. Coalesced plasma jets impinged on a cylindrical diamond seed crystal which was located at the converging part of the jets. After a typical 30 minute deposition, polyhedral shaped crystals were observed having grown on top of the original seed. The growth rates ranged from 100 to 220 μm/hour, which is highest ever reported for the homoepitaxial growth of diamond.

## Introduction

The many superlative properties of diamond have led to a considerable research and development effort (1) ever since the initial high pressure, high temperature process for making synthetic diamonds has been discovered (2). Polycrystalline diamond films have been deposited on a variety of substrate materials with a multitude of processes (1, 3 - 5). However, the exploitation of the potential of diamond as a high temperature semiconductor material requires the development of processes for epitaxial film deposition.

Homoepitaxial film growth of diamond films has been achieved (1, 6 - 20), however, the growth rate remained on the order of 0.1 μm/hour. Little success has been obtained with heteroepitaxy (17 - 19) except on cubic boron nitride (20).

Two significant studies on high rate homoepitaxial growth of diamond have been reported recently. Both of them used oxygen-acetylene flames. A research group in Drukker International B.V. in the Netherlands has reported successful high rate epitaxial deposition of single crystal diamond on {110} natural diamond substrates with a growth rate of 50 μm/hour (14). A research group at the Naval Research Lab has reported high rate, high quality epitaxial growth on {100} directions of natural diamond seeds at higher temperatures of 1,200 °C with growth rates in the range from 100 to 165 μm/hour (15, 16).

In this paper, we report the high rate homoepitaxial deposition of diamond using the thermal plasma chemical vapor deposition method. High rates of 100 - 220 μm/hour have been obtained on both {100} and {110} planes of diamond seeds. The diamond deposits

have been characterized with scanning electron microscopy (SEM), energy dispersive X-ray analysis (EDX), Laue X-ray diffraction, and Raman spectroscopy.

## Experimental Setup and Conditions

The experiments for the high rate homoepitaxial deposition of diamond have been performed in a Triple Torch Plasma Reactor (TTPR). The reactor consists of three identical plasma torches in which DC electric arcs are utilized to heat the plasma gases. The three plasma torches are mounted in such a way that the plasma jets coalesce forming a convergent plasma volume as shown in Fig. 1 (Only two of the three plasma torches are shown in the illustration).

The plasma gas is a mixture of argon and hydrogen. Methane diluted with hydrogen is injected into the converging plasma jets through a water cooled tube located in the center. The configuration of the plasma volume in this triple torch plasma arrangement ensures a more complete entrainment of the incoming precursors and therefore a more uniform mixture compared to the conventional single torch plasma jet reactor. The plasma envelopes the injected mixture of methane and hydrogen injected and fragments it into activated species before impinging onto the substrate which is located about 10 cm below the nozzles.

Because of the dominance of collisional energy transfer in thermal plasmas, high concentrations of hydrogen atoms and activated hydrocarbon fragments are being generated. Such high concentrations are advantageous for the diamond deposition. Thermal plasma chemical vapor deposition usually results in high deposition rates (21 - 25).

The system is operated in a double wall water-cooled chamber. The optical windows on the sides allow non-contact substrate temperature measurements. The reactor vessel is evacuated before the experiment and filled with argon to a pressure of 270 torr. Hydrogen is gradually added into the torches after the plasma is started. The substrate temperature is usually monitored by a two-color pyrometer as shown in Fig. 1. However, the bright plasma contributes to an error in the reading; therefore, the temperature reading is recorded at the instant of the plasma shut-down. Typical experimental conditions are listed in Table 1.

| | | |
|---|---|---|
| Plasma torches (each): | current: 300 Amps; | voltage: 40 volts; |
| | Ar flow rate: 13 liters/min; | $H_2$ flow rate: 1.3 liters/min; |
| Process pressure: | 270 torr; | |
| Gas feeding probe: | $H_2$ flow rate: 14 liters/min; | |
| | methane flow rate: 5.0 % of the total $H_2$ flow rate; | |
| Substrate: | type IIa natural diamond, {100}, {110} orientation; | |
| Pre-treatment | polished; cleaned with ethanol ultrasonically; | |
| Substrate temperature: | 1,200 - 1,400 °C (±100 °C); | |
| Deposition time: | 30 minutes. | |

**Table 1: Typical Experimental Conditions in TTPR**

The substrates consist of 250 μm thick natural type IIa diamond seed which were laser cut into circular cross sections, polished on the top {100} or {110} faces, and brazed to the ends of 1.5 cm long pieces of threaded molybdenum rod with a Au-Ta layer. The braze materials, which have a melting temperature around 1,300 °C, insured good thermal contact between the diamond seed crystals and the molybdenum rod during deposition. Since the thermal conductivities of the diamond seed crystals and braze material are relatively high, the seed crystal is expected to be isothermal and its temperature equal to or slightly higher than the molybdenum rod temperature. The temperature of the seed crystal has been controlled by varying the penetration of the molybdenum rod into a threaded hole in a water cooled copper substrate assembly.

It has been proposed that high substrate temperatures, which promote sufficiently rapid surface diffusion, is important for the epitaxial growth in chemical vapor deposition processes (26, 27). However, due to the metastable nature of the diamond film, a higher substrate temperature has been believed to result in graphitic carbon formation. This is in part due to the failure of hydrogen termination of the outermost diamond lattice atoms (28) at high temperatures. The limited availability of atomic hydrogen in many CVD systems makes the high temperature epitaxy difficult in many CVD processes. Thermal plasmas, similar to flames, which can offer much more abundant atomic hydrogen compared to other CVD systems, may overcome the shortage of surface terminating hydrogen and enable the successful epitaxial diamond growth at high temperatures.

## Results and Discussion

A series of homoepitaxial growth experiments have been performed on natural type IIa diamond seed crystals. The top surface of the crystals had either <100> or <110> orientation. During half-hour long deposition at substrate temperatures ranging from 1,200 to 1,400 °C (±100 °C), one could observe the specular glint of plasma emissions reflecting off the growing crystal faces after only 5 minutes. Scanning electron micrographs of polyhedral single crystals grown in 30 minutes on an approximately 1 mm diameter, cylindrically shaped {100} crystal at 1,230 °C and on {110} crystal at 1,300 °C are shown in Fig. 2a and 2c, respectively. Note the long range order and step morphology evident on the top surface of the {100} crystal (Fig. 2b), and the vertical plate morphology on the top surface of the {110} crystals (Fig. 2d). The step morphology has been observed at lower temperatures by a number of researchers (29, 30), but the vertical plates observed on the {110} diamond crystals have not been reported before, to our knowledge (although it is common for epitaxy of other crystal systems (31)). If the growth on the {110} face proceeds via a "zipper" growth mechanism (14), then the plates are probably aligned along the <110> directions on the {110} face.

The Raman spectra of the crystals pictured in Fig. 2a and 2c are shown in Fig. 3. Graphite and amorphous carbon peaks are absent in all the spectra, and the fluorescence background is low over the entire surface of the {100} growth (curve a). The {110} growth exhibited a significantly higher fluorescence background on the top corrugated face (curve c) compared to the smooth side faces (curve b). The full width at half maximum (FWHM) of the diamond peaks at 1332 $cm^{-1}$ have been found to be 2.9 $cm^{-1}$ for the {100} growth and 5.1 $cm^{-1}$ for the side face of the {110} growth. A FWHM value of 5.4 $cm^{-1}$ was obtained for the top face of the {110} growth. For comparison, a FWHM of 2 - 3.3 $cm^{-1}$ (14, 32) is common for natural diamond, and 2.6 $cm^{-1}$ (15) has been observed for epitaxially deposited diamond in a oxygen-acetylene flame. Laue X-ray diffraction

measurements have been performed on both crystals and they have confirmed the monocrystalline and epitaxial nature with respect to the underlying seed crystals. A measurement of the impurity levels in both crystals has been performed with an energy dispersive X-ray analysis (EDX) technique. Low levels of copper have been observed in the {110} growth, possibly due to contamination from the plasma torch electrodes.

## Conclusion

A new high temperature epitaxy process (HTE) for growing macroscopic diamond crystals has been demonstrated using thermal plasmas. The results have confirmed and extended earlier reports of the HTE growth of diamond with an oxygen-acetylene flame. One advantage of using plasma over a flame is the total flexibility of the reaction environment. This will permit the use of cheaper fuels such as methane, and improve the economics (33) of growing isotopically enriched, high thermal conductivity diamond (34) using an HTE type process. The high growth rates achieved in plasma or flame processes may prove to be vital for the economic feasibility.

Since only a small region of the parameter space of the deposition process has been investigated, we anticipate further improvement of the observed results by optimizing the process.

## Acknowledgement

The authors would like to thank Dr. L. Stachowicz at the University of Minnesota for taking the SEM images reported here, and Carl Vold at NRL for performing the Laue X-ray analysis of these samples. Professor Robert Glosser and Joe Estrera at the University of Texas at Dallas are to be thanked for measuring and analyzing the Raman characteristics of the crystals.

## REFERENCES

(1) R.C. DeVries, *Ann. Rev. Mater. Sci.* **17**, 167 (1987).
(2) F.P. Bundy, H.T. Hall, H.M. Strong, and R.H. Wentorf, *Nature* **176**, 51 (1955).
(3) W.A. Yarbrough and R. Messier, *Science* **247**, 688 (1990).
(4) R. Pool, *Science* **249**, 27 (1990).
(5) N. Fujimori and A. Hara, in *Proc. of 1st Int. Symp. on Diamond and Diamond-Like Films, The Electrochem. Soc.*, New Jersey, USA, 1989, J.P. Dismukes, A.J. Purdes, K.E. Spear, B.S. Meyerson, K.V. Ravi, T.D. Moustakas, and M. Yoder, eds., (1989), p. 14.
(6) J.C. Angus, H.A. Will, and W.S. Stanko, *J. Appl. Phys.* **39**, 2915 (1968).
(7) S.P. Chauhan, J.C. Angus, and N.C. Gardner, *J. Appl. Phys.* **47**, 4746 (1976).
(8) B.V. Derjaguin and D.B. Fedoseev, *Sci. Am.* **233(5)**, 102 (1975).
(9) B.V. Derjaguin, B.V. Spitsyn, A.E. Gorodetsky, A.P. Zakharov, L.L. Bouilov, and A.E Aleksenko, *J. Crystal Growth* **31**, 44 (1975).
(10) B.V. Spitsyn, L.L. Bouilov, and B.V. Derjaguin, *J. Crystal Growth* **52**, 219 (1981).
(11) B.V. Spitsyn, *J. Crystal Growth* , 1162 (1990).
(12) J.H. Freeman, W. Temple, and G A. Gard, *Vacuum* **34**, 305 (1984).
(13) M. Kamo, H. Yurimoto, and Y. Sato, *Appl. Surf. Sci.* **33/34**, 553 (1988).

(14) G. Janssen, W.J.P. van Enckevort, J.J.D. Schaminee, W. Vollenberg, L.J. Giling, and M. Seal, *J. Crystal Growth* **104**, 752 (1990).
(15) K.A. Snail, E.F. Skelton, J.E. Butler, L.M. Hanssen, and J.A. Freitas, Jr., "High Rate Homoepitaxial Synthesis of Diamond in a Flame," *Extended Abstract for 2nd Int. Symp. on Diamond Materials*, Washington DC, May (1991).
(16) K.A. Snail and L.M. Hanssen, *J. Crystal Growth*, in print (1991).
(17) J. Narayan, A.R. Srivatsa, M. Peters, S. Yokota, and K.V. Ravi, *Appl. Phys. Lett.* **53**, 1823 (1990).
(18) M.W. Geis, *Appl. Phys. Lett.* **55**, 550 (1989).
(19) D.G. Jeng, H.S. Tuan, R.F. Salat, and G.J. Fricano, *Appl. Phys. Lett.* **56**, 1968 (1990).
(20) S. Koizumi, T. Murakami, and T. Inuzuka, *Appl. Phys. Lett.* **57**, 563 (1990).
(21) K. Kurihara, K. Sasaki, M. Kawarada, and N. Koshino, *Appl. Phys. Lett.* **52**, 437 (1988).
(22) S. Matsumoto, in *Diamond and Diamond-Like Materials Synthesis, MRS Extended Abstracts, Materials Research Society*, Pittsburgh, Pennsylvania, 1988, G.H Johnson, A.R. Badzian, and M.W. Geis, eds., (1988), p. 119.
(23) P.K. Bachmann and H. Lydtin, in *Mater. Res. Soc. Symp. Proc., Vol. 165, Characterization of Plasma-Enhanced CVD Processes, Materials Research Society*, Pittsburgh, Pennsylvania, 1989, G. Lucovsky, D.E. Ibbotson, and D.W. Hess, eds., (1989), p. 181.
(24) N. Ohtake and M. Yoshikawa, *J. Electrochem. Soc.* **137**, 717 (1990).
(25) Z.P. Lu, L. Stachowicz, P. Kong, J. Heberlein, and E. Pfender, "Diamond Synthesis by DC Thermal Plasma CVD at One Atmosphere," to be published in *Plasma Chem. Plasma Process.* **11(3)** (1991).
(26) W.A. Bryant, *J. Mater. Sci.* **12**, 1285 (1977).
(27) T.M. Mesmann, D.P. Stinton, and R.A. Lowden, *MRS Bull.* November, p. 45 (1989).
(28) T.R. Anthony, *Vacuum* **41**, 1356 (1990).
(29) K. Kobashi, K. Nishimura, Y. Kawate, and T. Horiuchi, *Phys. Rev. B: Condens. Matter.* **38**, 4067 (1988).
(30) K V. Ravi and A. Joshi, "*Appl. Phys. Lett.* **58**, 246 (1991).
(31) I. Tarján and M. Mátrai, *Laboratory Manual on Crystal Growth*, Akadémiai Kiadó, Budapest, p. 70 (1972).
(32) D.S. Knight and W.B. White, *J. Mater. Res.* **4**, 385 (1989).
(33) The cost of $^{12}C$ pure (99.9%) acetylene is $210/liter in 100 liter quantities, whereas the cost of $^{12}C$ pure (99.9%) methane is only $53/liter. Personal communication, Isotec Inc., July 1990.
(34) T.R. Anthony, W.F. Banholzer, and J.F. Fleischer, *Phys. Rev. B: Condens. Matter.* **42**, 1104 (1990).

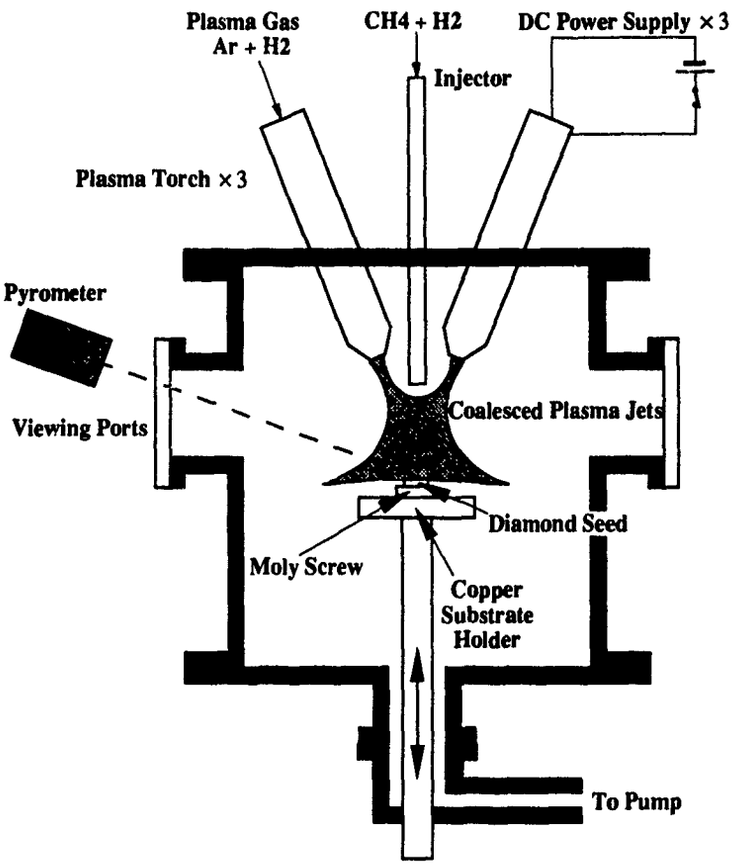



**Fig. 1: Schematic of the Triple Torch Plasma Reactor for the Epitaxial Deposition of Diamond on Natural Type IIa Diamond Seed Crystals.**

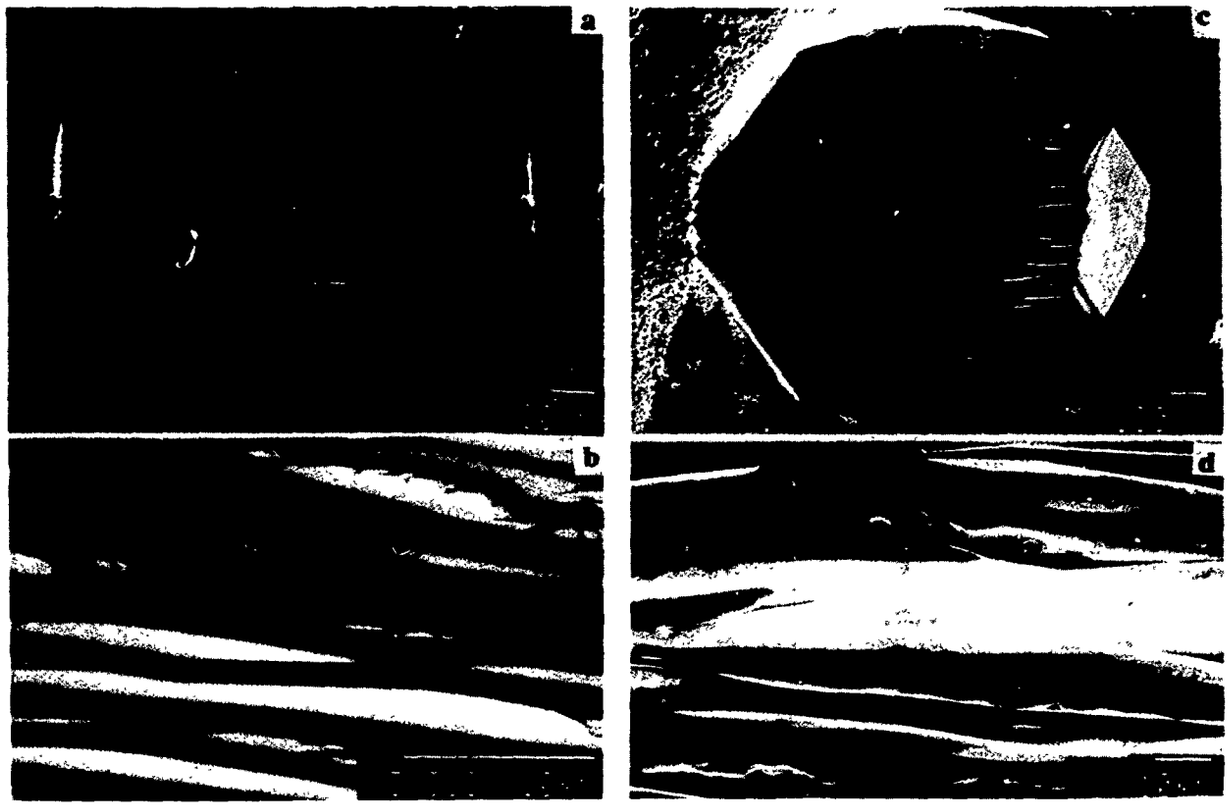



**Fig. 2: Micrographs of Epitaxially Grown Diamond (a) Octagon Formation on Round (100) Seed; (b) Long Range Order on (100) Face; (c) Octagon Formation on (110) Seed; and (d) Zipper Growth on (110) Face.**

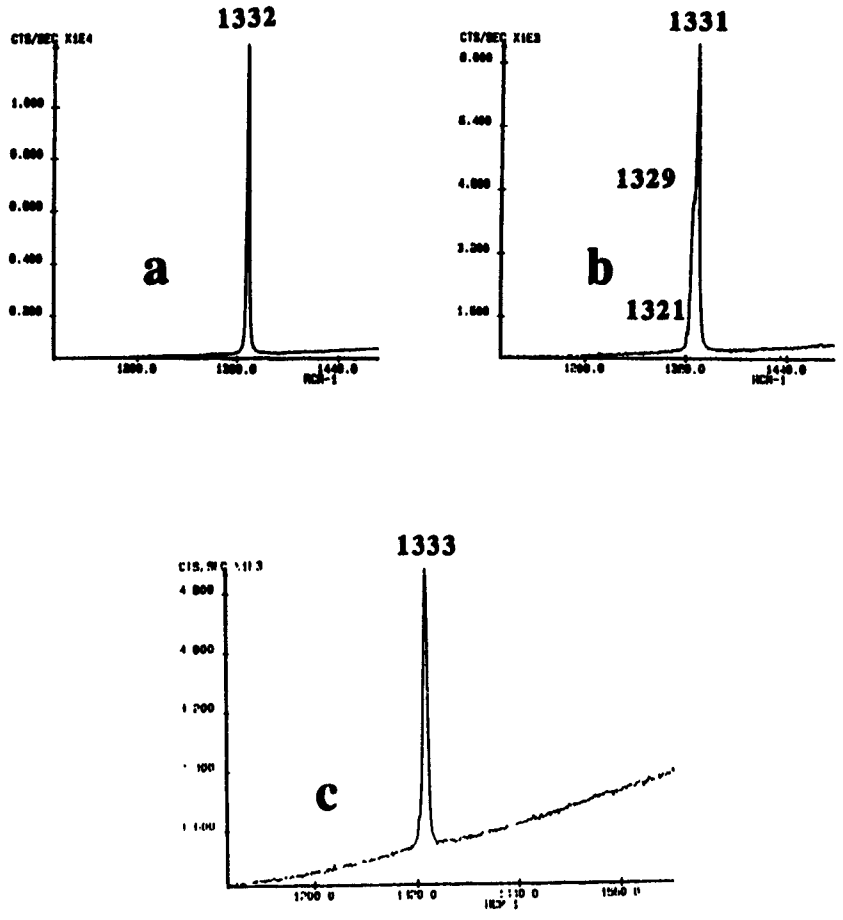



**Fig. 3: Raman Spectra of Epitaxially Grown Diamond (a) Corresponding to Top Face of Fig. 2 (a); (b) Corresponding to Side Smooth Face of Fig. 2 (b); (c) Corresponding to Top Face of Fig 2 (b).**

# EFFECTS OF PROCESS PARAMETERS ON CHEMICAL VAPOR DEPOSITION OF DIAMOND IN THERMAL PLASMAS

**Z.P. Lu, L. Stachowicz, J. Heberlein, and E. Pfender**

Department of Mechanical Engineering
University of Minnesota
Minneapolis, MN 55455

## Abstract

This study has been concerned with thermal plasma CVD of diamond films using methane and hydrogen as precursors and taking several process parameters into account. The properties of the diamond films, including growth rates, growth direction, and crystal sizes are correlated with the governing process parameters. Growth rates of up to 60 μm/hour have been observed on a variety of substrate materials with an optimum pressure of 270 torr at substrate temperatures close to 1,000 °C.

## Introduction

Thermal plasmas have been used for the deposition of diamond in recent years (1 - 10). Because of the dramatically increased growth rates (11) compared to the hot filament or non-thermal plasma CVD processes such as microwave plasmas, thermal plasma CVD processes have attracted increasing attention. However, due to the diversity of the experimental setups used by the different researchers, it is difficult to compare the experimental data. We report the results of an investigation of effects of a number of process parameters on the thermal plasma chemical vapor deposition of diamond. The parameters include substrate material, substrate temperature, methane concentration, process pressure, and the methods for substrate pre-treatment.

## Experimental Setup and Conditions

Experiments have been performed in a Triple Torch Plasma Reactor (TTPR). which is shown schematically in Fig. 1. Three coalescing plasma jets impinge on a water-cooled substrate. Details of this arrangement are discussed elsewhere (9).

Common experimental conditions are summarized in Table 1.

## Experimental Results and Discussion

### a. Effect of Substrate Material

Diamond films have been deposited on various substrates including silicon, molybdenum, tungsten, tantalum, titanium, nickel, palladium, copper, and stainless steel. A typical diamond film is shown in Fig. 2 and corresponding X-ray diffraction pattern in Fig. 3. On the metal substrates, both carbide forming and non-carbide forming, the

deposition has been successful. However, the adhesion of diamond films to the substrate usually is rather poor in case of metal substrates. Cracks (shown in Fig. 4) often develop on the films. This is due to the large differences between the thermal expansion coefficients of diamond and the metals.

| | | |
|---|---|---|
| Plasma torches (each): | current: 300 amps; | voltage: 40 - 45 volts; |
| | Ar flow rate: 10 - 20 liters/min; | $H_2$ flow rate: 1 - 2 liters/min; |
| Process pressure: | 100, 170, 270, 400, 760 torr; | |
| Gas feeding probe: | $H_2$ flow rate: 10 - 15 liters/min; | |
| | methane flow rate: 3.5, 5.0, 6.5, 10, and 40 % of the total $H_2$ | |
| Substrate: | Si, Mo, W, Ta, Ti, Pd, Ni, Cu, and stainless steel; | |
| Pre-treatment | for Si : unscratched or | |
| | scratched with 1 μm or 15 μm grit diamond paste; | |
| | for metals: unscratched or | |
| | sand blasted, or scratched with 1 μm diamond; | |
| | substrates are cleaned with acetone or ethanol ultrasonically; | |
| Substrate temperature: | 800 - 1200 °C; | |
| Deposition time: | 10 minutes to several hours. | |

**Table 1: Typical Experimental Conditions during TTPR Operation.**

### b. Effect of Methane Concentration

The effect of gas composition is depicted in Fig. 6 showing four films deposited on molybdenum substrates with progressively increased methane concentrations (3.5, 5.0, 6.5, and 10 %). The first three micrographs have been taken at the same magnification (× 2,500) for size comparison. Although the first three films show good crystallinity, there is a noticeable difference in sizes of the constituent crystals in the films. The higher the concentration, the smaller the crystal size. This is probably due to the increasing number of secondary nucleations when the methane concentration is increased. The secondary nucleations (shown in Fig. 5) on existing diamond facets prevent the existing crystals from growing before daughter crystals start to form. When the methane concentration exceeds a certain value, a large portion of the film starts to lose its crystallinity dramatically and changes to large cauliflower-type balls with few facets left as shown in the Fig. 6 (d).

### c. Effect of Substrate Temperature

A two-color pyrometer has been employed for temperature measurements. It has been found that the substrate temperature has a pronounced effect on the morphology of the growth surface of the diamond films. Figure 7 (a) shows a film grown on the 1,000 °C substrate and Fig. 7 (b) 1,200 °C. It can be seen that when the substrate temperature is lower most facets facing the growth surface are (111) triangles while when the temperature is higher the surface facets are (100) squares. This observation is in agreement with other investigators' conclusion that at lower temperatures (111) faces dominate the crystallite morphology and at higher temperatures (100) faces are predominant (reviewed in Ref. 12 - 14). It should be noticed that contradictory observations have also been reported (15).

The coverage of the film is about 1.5 inches in diameter. The coverage is not uniform. The growth rate exceeds 60 μm/hour in the center and is about 25 μm/hour close to the fringes. The quality also varies with good crystallinity in the center and ball-like grains close to the edge.

### d. Effect of Process Pressure

Figure 8 shows the relationship between the growth rate vs. pressure (in the range from 100 to 760 torr) at a substrate temperature around 1,000 °C and a methane concentration of 5 %. Among the pressures that have been tested, a pressure of 270 torr results in the highest growth rates. This probably can be understood qualitatively as follows: When the pressure of a plasma is high, the mean free paths of the particles in the plasma are short, and frequent collisions bring the temperature of the heavy species - radicals, molecules, atoms, and ions to about the same level as that of the electrons. When such a plasma is quenched, as inside the boundary layer in front of a cooled substrate, the densities of active species will be much higher than they would be in a thermodynamic equilibrium situation because of the relatively slow chemical reactions. In other words, a deviation from chemical equilibrium prevails. For the kinetically dominated metastable diamond growth process, this deviation caused by quenching a thermal plasma is very beneficial.

If the active species arrive at the substrate surface within a much shorter time than their life spans, as in the case of completely frozen chemical reactions, the situation existing outside the boundary layer would be a very close description for the situation at the substrate surface. However, the diffusion towards the surface requires time and some of the active species vanish because of recombination. Although the high pressure is an advantageous factor for being able to create a plasma with abundant active species because of the equilibria between electrons and heavy particles, it may also cause an increased number of recombinations preventing many active particles from arriving at the surface. The result shown in Fig. 7 seems to suggest that there is an optimum pressure determined by a balance between creating active particles and their survival. Surface recombination has not been included in this calculation which may have a significant effect on the availability of chemically active species for diamond growth. The optimum growth rate reported in microwave plasma system has been 110 torr at 975 °C (15).

### e. Effect of Substrate Pre-Treatment

There have been reports stating that by employing the thermal plasma CVD process, this pre-treatment of the substrate might be eliminated (2, 5). We have investigated this issue and have found that the necessity for the pre-treatment is material dependent.

Both unscratched and highly polished silicon wafers and scratched silicon wafers have been used as substrates. To scratch the silicon wafers, both 1 μm and 15 μm diamond pastes have been used and it has been found that the nucleation density is greatly increased by just several minutes of lapping. Even under thermal plasma conditions, the highly polished silicon wafers do not give satisfactory nucleation density and scratching of the wafer does increase the nucleation density dramatically. This is illustrated in Fig. 9 which shows the diamond nucleation on a partially scratched silicon wafer. It can be clearly seen that the treated half, which is represented on the right part of the micrograph, shows a much higher nucleation density compared to the untreated.

However, for molybdenum, the diamond paste scratching has little effect on the initial nucleation density. Continuous diamond films have been generated within about the same time period no matter whether the metal was scratched or not with the diamond paste. This is probably due to the polycrystalline nature and intrinsic imperfections at the metal surface due to the sheet metal production process. For the molybdenum sheet pre-treated by sand blasting with 325 mesh grit, the surface is very rough and diamond crystals seem to prefer growing on the edges of the pits. Continuous films are difficult to form in this case because of the great surface roughness as a result of sand blasting.

## Conclusions

(1) Diamonds have been deposited on both carbide-forming materials such as silicon, molybdenum, tungsten, and tantalum and non-carbide-forming materials such as palladium, nickel, and copper. The adhesion of diamond films is generally poor on metal substrates.

(2) It has been found that the methane concentration has a pronounced effects on the size of the constituent diamond crystals in the film. The higher the concentration, the smaller the grain size. This observation may be interpreted by the increased number of secondary nucleations at increased methane concentration. When the methane concentration exceeds a certain threshold, crystallinity vanishes and only cauliflower-type balls are produced.

(3) It has been found that the substrate temperature affects the morphology and the direction of growth of crystals and films. At low temperature, the growth surface is dominated by (111) planes while at high temperature by (100) planes.

(4) The non-uniformity of the thermal plasma jets results in uneven deposition of the diamond films across the substrate. The growth rate in the center portion is five times higher than the growth rate in the fringes. The quality of the films also varies. The film in the center is well faceted, but the film close to the fringes shows ball-like features.

(5) The process pressure has been found to affect the growth rate of diamond films. For the TTPR the optimum pressure is about 270 torr at a substrate temperature of 1,000 °C. Above or below that pressure, the deposition rates decrease.

## Acknowledgement

This work has been supported by DCE grant FG02-85ER-13433.

## REFERENCES

(1) S. Matsumoto, M. Hino, and T. Kobayashi, *Appl. Phys. Lett.* **51**, 737 (1987).
(2) K. Kurihara, K. Sasaki, M. Kawarada, and N. Koshino, *Appl. Phys. Lett.* **52**, 437 (1988).
(3) S. Matsumoto, in *Diamond and Diamond-Like Materials Synthesis, MRS Extended Abstracts, Materials Research Society*, Pittsburgh, Pennsylvania, 1988, G.H Johnson, A.R. Badzian, and M.W. Geis, eds., (1988), p. 119.
(4) N. Ohtake and M. Yoshikawa, *J. Electrochem. Soc.* **137**, 717 (1990).

(5) P. Klocek, J. Hoggins, P. Taborek, and T. Mckenna, "CVD Diamond by DC Plasma Torch," Preprint of SPIE Proceedings, Vol. 1325 (1990).
(6) W.K. Kim and K.W. Whang, "Preparation of Diamond Film by DC Thermal Plasma," *Proc. of 2nd Int. Conf. on New Diamond Sci. Technol., Materials Research Society*, Pittsburgh, Pennsylvania, to be published (1990).
(7) M.A. Cappelli, T.G. Owano, and C.H. Kruger, *J. Mater. Res.* **5**, 2326 (1990).
(8) S. Matsumoto, in *Proc. of the 1st Int. Symp. on Diamond and Diamond-Like Films, The Electrochem. Soc.*, New Jersey, 1989, J.P. Dismukes, A.J. Purdes, K.E. Spear, B.S. Meyerson, K.V. Ravi, T.D. Moustakas, and M. Yoder, eds., (1989), p. 50.
(9) Z.P. Lu, L. Stachowicz, P. Kong, J. Heberlein, and E. Pfender, "Diamond Synthesis by DC Thermal Plasma CVD at One Atmosphere," to be published in *Plasma Chem. Plasma Process.* **11(3)** (1991).
(10) M. Kawarada, K. Kurihara, K. Sasaki, A. Teshima, and K. Koshino, in *Diamond Optics II, SPIE Proc. Vol. 1146*, SPIE, Bellingham, Washington, 1989, A. Feldman and S. Holly, eds., (1989), p. 28.
(11) P.K. Bachmann and H. Lydtin, in *Mater. Res. Soc. Symp. Proc., Vol. 165, Characterization of Plasma-Enhanced CVD Processes, Materials Research Society*, Pittsburgh, Pennsylvania, 1989, G. Lucovsky, D.E. Ibbotson, and D.W. Hess, eds., (1989), p. 181.
(12) J.C. Angus and C.C. Hayman, *Science* **241**, 913 (1988).
(13) K.E. Spear, *J. Am. Ceram. Soc.* **72**, 171 (1989).
(14) K.E. Spear and M. Frenklach, in *Proc. of the 1st Int. Symp. on Diamond and Diamond-Like Films, The Electrochem. Soc.*, New Jersey, 1989, J.P. Dismukes, A.J. Purdes, K.E. Spear, B.S. Meyerson, K.V. Ravi, T.D. Moustakas, and M. Yoder, eds., (1989), p. 122.
(15) W. Zhu, R. Messier, and A.R. Badzian, *ibid*, p. 61.

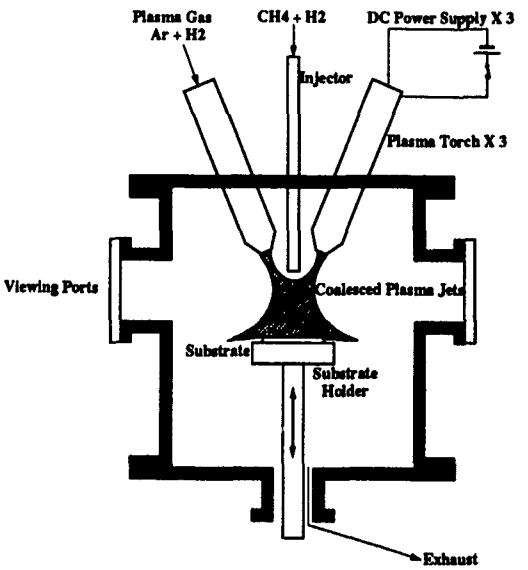



**Fig. 1: Schematic of the Triple Torch Thermal Plasma Reactor for Diamond Deposition.**



Fig. 2: Diamond Film Deposited on (100) Silicon Wafer.

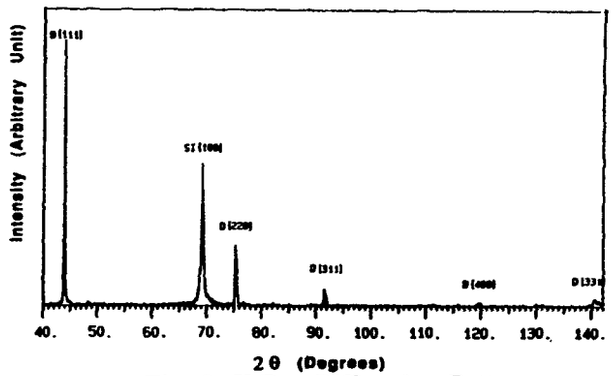



Fig. 3: X-Ray Diffraction Pattern of the Diamond Film.



Fig. 4: Crack Developing on Diamond Film Deposited on Molybdenum.

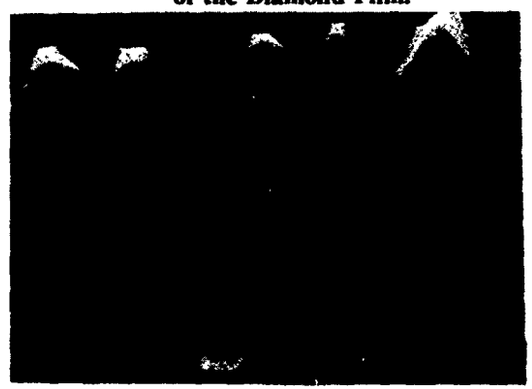


Fig. 5: Secondary Nucleations on Diamond Facets.

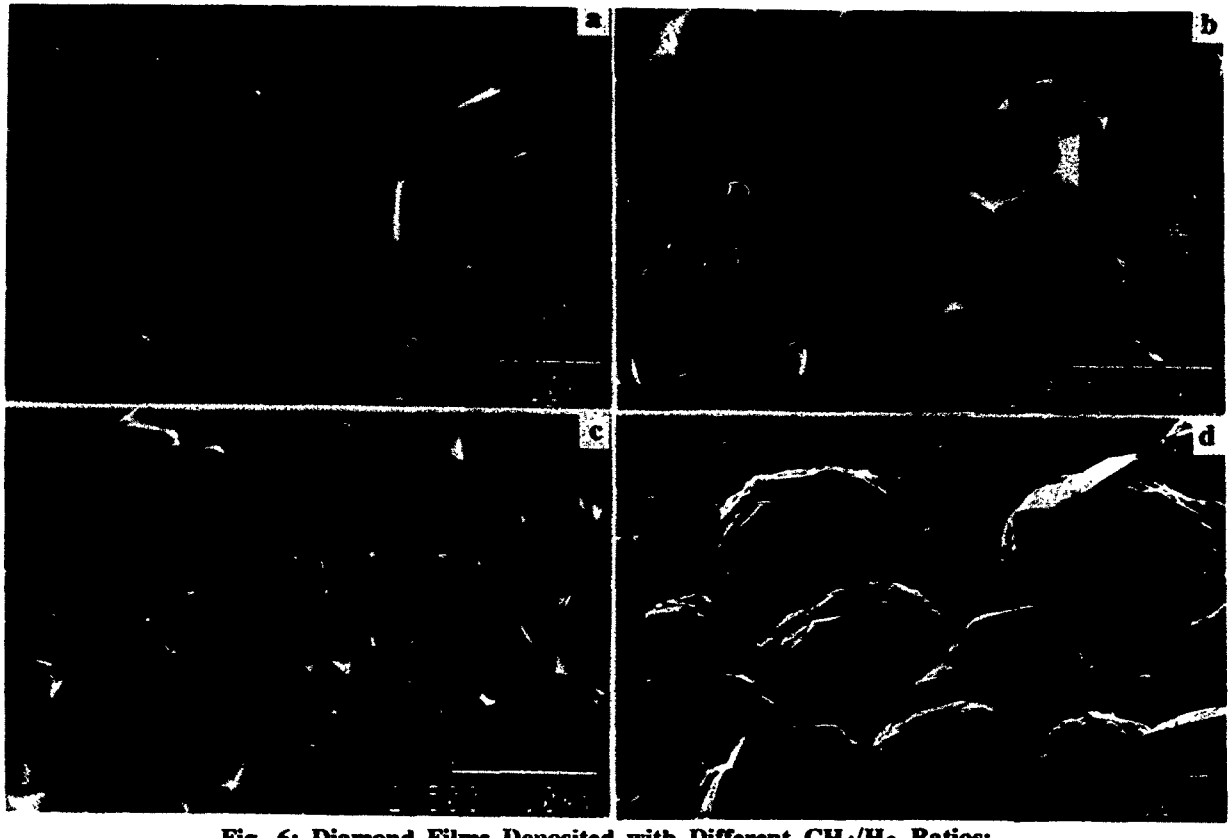



**Fig. 6: Diamond Films Deposited with Different $CH_4/H_2$ Ratios: (a) 3.5 %; (b) 5 %; (c) 6.5 %; and (d) 10 %.**

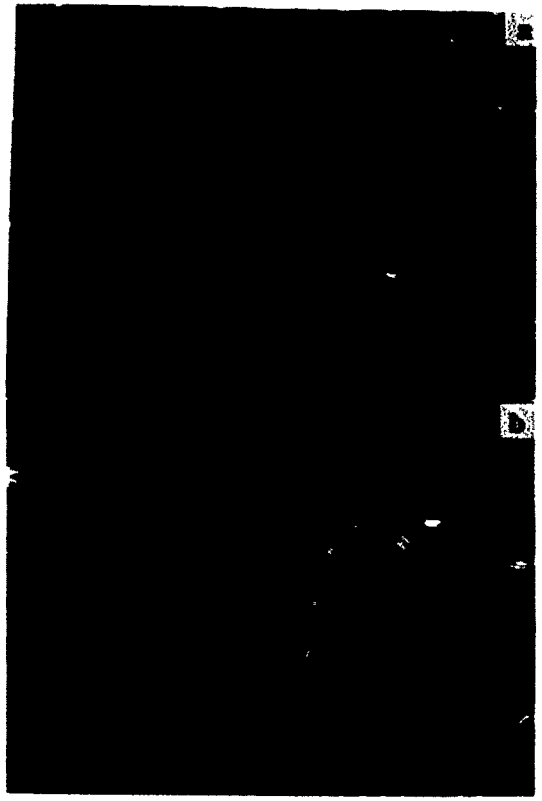


Fig. 7: Diamond Films Deposited at Different Substrate Temperatures: (a) $T_s$ < 1,000 °C and (b) $T_s$ > 1,200 °C.

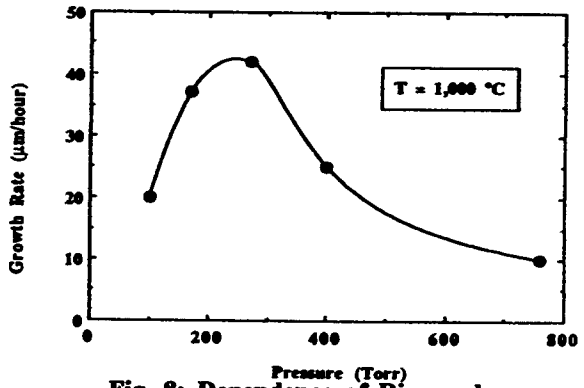



Fig. 8: Dependence of Diamond Growth Rate on Pressure. ($T_s$ = 1,000 °C and $CH_4/H_2$ = 5 %)

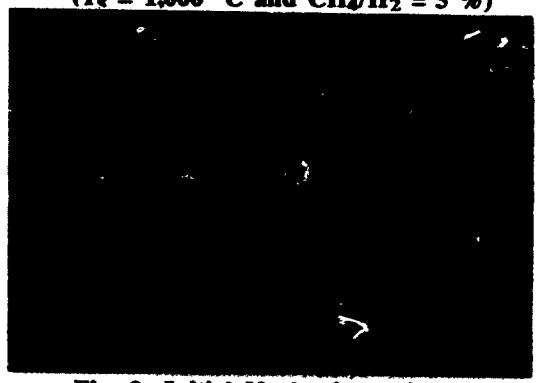


Fig. 9: Initial Nucleations of Diamond on a Partially Scratched (100) Silicon Wafer.

# HIGH RATE DEPOSITION OF DIAMOND USING LIQUID ORGANIC PRECURSORS IN ATMOSPHERIC PLASMAS

**Q.Y. Han, T.W. Or, Z.P. Lu, J. Heberlein, and E. Pfender**

Department of Mechanical Engineering
University of Minnesota
Minneapolis, MN 55455

## Abstract

High rate deposition of polycrystalline diamond films has been achieved by spraying various liquid carbon-containing precursors against a thermal plasma jet operating at atmospheric pressure. The precursors used include (a) alcohols, (b) ketones, (c) halogenated compounds, and (d) aromatic compounds. High deposition rates of up to 1 mm/hour have been observed with acetone and ethyl alcohol. X-ray diffraction results show that diamond is the only crystalline phase present in the deposit. Scanning electron microscopy reveals that the diamond films made from all previously mentioned compounds are well faceted. Raman spectroscopy has confirmed the phase purity of the diamond films.

## Introduction

The many potential applications for diamond films continue to attract new developments of deposition processes. The majority of the diamond film deposition processes being further developed are reduced pressure plasma assisted CVD processes (1 - 3). However, for applications requiring high growth rates, thermal plasma CVD processes offer distinct advantages: high dissociation rates of the carbon containing deposition precursor species in conjunction with a high generation rate of atomic hydrogen which can lead to an abundance of the species which are thought to be crucial for the diamond deposition process, and, therefore, for high growth rates.

Both DC thermal plasmas and RF induction plasmas have been used for high rate deposition of diamond films (4 - 9), and growth rates of up to 930 μm/hour have been reported (5). Because of the high energy density in thermal plasmas, a large variety of carbon containing precursors can be used for the deposition processes. Various organic liquid precursors have been used successfully for the deposition of diamond films (10, 11), and generally higher growth rates have been observed with these precursors (12 - 15) compared to deposition from hydrocarbon precursors. In most cases, these liquid compounds have been introduced into the deposition reactor in vapor form.

We report initial results of a systematic study of thermal plasma CVD of diamond with a variety of liquid precursors which have been injected into the plasma jet as an atomized liquid spray.

## Experimental Setup and Conditions

The DC plasma jet reactor used for these experiments is schematically illustrated in Fig. 1. The liquid precursor is fed into the plasma by a precision metered liquid pump connected to a water cooled stainless steel injection tube. A hydrogen sheath gas is used to atomize the liquid jet at the exit of the injection nozzle. The atomized mist is sprayed against the plasma jet emanating from the plasma torch. The substrate (with a hole in the center to permit the penetration of the precursor jet) is located about 3 - 5 cm from the exit of the nozzle of the plasma torch. The substrate temperature is monitored with a two color pyrometer. Table 1 lists typical experimental conditions. All experiments have been performed at atmospheric pressure. In the experiments with halogen organic precursors, a wet scrubber is used for neutralizing the hydrogen chloride (HCl) which is a by-product of the process.

| | |
|---|---|
| Plasma torch: | power: 16 kW (400 amps and 40 volts)<br>Ar flow rate: 24 *l*/min<br>$H_2$ flow rate: 1.2 *l*/min |
| Pressure: | 760 torr |
| Atomizing gas: | $H_2$ flow rate: 18 *l*/min |
| Precursors flow rate: | 0.5 to 3.0 ml/min (depending on precursors) |
| Substrate: | molybdenum and tungsten |
| Substrate temperature: | ~ 1,000 °C |
| Deposition time: | 10 to 60 minutes |

**Table 1: Experimental Conditions**

The advantages of this counter-flow type arrangement for materials processing have been reported by Paik *et al* (16). It has been found that the high energy content of thermal plasmas, excellent mixing of the two jets, and favorable flow patterns enable a long residence time of the precursor mist in this novel counter-flow thermal plasma reactor.

A number of organic liquid precursors have been used to synthesize diamonds. These organics can be classified into four groups and are listed in Table 2. The flow rates of the liquid organics are between 0.5 to 3.0 ml/min. The flow rates for four compounds have been converted into equivalent carbon input in terms of methane to hydrogen volumetric ratio for a constant hydrogen flow rate. The results are shown in Fig. 2.

## Results and Discussion

The diamond films have been analyzed routinely using scanning electron microscopy, and selected films have been additionally analyzed using X-ray diffraction and Raman spectroscopy. Figures 3, 4, and 5 show representative micrographs demonstrating specific features of this deposition process. Figure 6 shows an X-ray diffraction pattern indicating the match of the observed lines with the ASTM XRD standard for diamond. Figure 7 shows a Raman spectrum indicating complete $sp^3$ bonding which is the diamond structure. No graphitic or amorphous structures are detected in the Raman spectrum. However, the fluorescence background is high at higher energies. From the SEM micrographs, the following observations are made:

| Chemical Groups | Liquid Precursors | Chemical Formulas | Density (g/ml) |
|---|---|---|---|
| alcohols | methanol | $CH_3OH$ | 0.793 |
| | ethanol | $CH_3CH_2OH$ | 0.789 |
| | 1-propanol | $CH_3CH_2CH_2OH$ | 0.804 |
| | isopropyl alcohol | $(CH_3)_2CHOH$ | 0.785 |
| | 1-butanol | $CH_3(CH_2)_3OH$ | 0.810 |
| ketones | acetone | $CH_3COCH_3$ | 0.786 |
| | methyl ethyl ketone | $CH_3CH_2COCH_3$ | 0.805 |
| halogen compounds | dichloromethane | $CH_2Cl_2$ | 1.325 |
| | chloroform | $CHCl_3$ | 1.492 |
| | carbon tetrachloride | $CCl_4$ | 1.595 |
| aromatic compound | benzene | $C_6H_6$ | 0.879 |
| other compound | cyclohexane | $C_6H_{12}$ | 0.775 |

**Table 2: Liquid Precursors Used for Diamond Synthesis**

(1) Diamond films with clear facets have been obtained with all liquid organic precursors which have been used. There has been no conclusive evidence about differences in morphology with different precursors, although differences in growth rate have been observed.

(2) The highest growth rates have been reproducibly observed with ethanol and acetone. At present it is unclear if the chemical composition or the fluid properties are mainly responsible for this effect. The molecular structure may lead to fragmentation and/or recombination rates resulting in the most favorable mixture of radicals, whereas the fluid properties may produce the optimal droplet size for the mass transport to the vicinity of the substrate.

(3) The growth rates vary strongly with radial distance from the spray injection tube. Close to the injection tube, a ring-shaped region with the highest growth rate has been observed. During a one hour experiment using ethanol or acetone, a typical diamond film in this region consists of an initial dense layer 100 to 500 μm thick from which individual columnar crystals grow (see Fig. 3) with very high growth rates (more than 1 mm/hour have been observed). This ring of very high growth rate has a width of approximately 2 mm and is surrounded by a region in which film growth is more similar to that observed in other thermal plasma vapor deposition experiments (see Fig. 4). The film thickness is uniform over a region of 5 to 10 mm wide, and growth rates range from 50 to 100 μm/hour. Beyond this region, towards the edge of the 40 mm diameter substrate, individual crystals are observed.

(4) The very large crystals making up the columns in the high growth rate region show a large number of defects. However, occasionally, under conditions of high carbon concentrations and at higher than normal temperature, the columns are topped by very distinct (100) planes (see Fig. 5). This observation indicates that under such conditions the growth proceeds preferentially in directions other than <100>. This condition typically precedes the formation of graphite which starts in the central portion of the substrate and rapidly spreads towards the substrate fringes.

A qualitative explanation for these results can be provided if the temperature and flow profiles in this reactor are considered. The substrate temperature drops continuously from the central region to the rim. However, in the central region we expect the evaporation of the droplets occurring very close to the substrate surface, thus providing the mixture of radicals which is favored for high growth rates. We also have to consider that in thermal plasma CVD, the surface heat fluxes are sufficiently high to allow a significant temperature drop from the diamond film surface to the substrate interface (e.g. a 5 $kW/cm^2$ heat flux will result in a temperature difference in the order of 100 °C for a 1 mm thick diamond layer). Thus the growth conditions vary during the deposition process unless the deposition parameters are changed.

## Conclusion

The injection of atomized liquid sprays into a thermal plasma jet can lead to high growth rates of diamond films. It is believed that mass transport in the form of liquid droplets to a location very close to the substrate surface is responsible for this high growth rate. All organic precursors have led to diamond film growth, however, the highest film growth has been observed with acetone and ethanol. For films of 1 mm thickness, the increase of the surface temperature during the deposition process has to be considered.

## Acknowledgement

The authors acknowledge contributions by Dr. L. Stachowicz who performed X-ray diffraction and some SEM analysis. Dr. J. Butler at the Naval Research Laboratory is acknowledged for the Raman analysis of some samples. This work has been supported by the Blandin Foundation and by DOE under grant FG02-85ER-13433.

## REFERENCES

(1) B.V. Spitsyn, L.L. Bouilov, and B.V. Derjaguin, *J. Crystal Growth* **52**, 219 (1981).
(2) W.A. Yarbrough and R. Messier, *Science* **247**, 688 (1990).
(3) C.V. Deshpandey and R.F. Bunshah, *J. Vac. Sci. Technol. A* **7**, 2294 (1989).
(4) P.K. Bachmann and H. Lydtin, *Mater. Res. Soc. Symp. Proc., Vol. 165, Characterization of Plasma-Enhanced CVD Processes, Materials Research Society*, Pittsburgh, PA, 1989, G. Lucovsky, D.E. Ibbotson, and D.W. Hess, eds., (1989), p. 181.
(5) N. Ohtake and M. Yoshikawa, *J. Electrochem. Soc.* **137**, 717 (1990).
(6) S. Matsumoto, M. Hino, and T. Kobayashi, *Appl. Phys. Lett.* **51**, 737 (1987).
(7) M.A. Cappelli, T.G. Owano, and C.H. Kruger, *J. Mater. Res.* **5**, 2326 (1990).

(8) S. Matsumoto, in *Diamond and Diamond-Like Materials Synthesis, MRS Extended Abstracts, Materials Research Society*, Pittsburgh, PA, 1988, G.H Johnson, A.R. Badzian, and M.W. Geis, eds., (1988), p. 119.
(9) Z.P. Lu, L. Stachowicz, P. Kong, J. Heberlein, and E. Pfender, "Diamond Synthesis by DC Thermal Plasma CVD at One Atmosphere," to be published in *Plasma Chem. Plasma Process.* **11(3)** (1991).
(10) Y. Sato, M. Kamo, and N. Setaka, in *Proc. of the 8th Int. Symp. on Plasma Chem. Vol. 4*, Tokyo, Japan, 1987, K. Akashi and A. Kinbara, eds., (1987), p. 2447.
(11) Y. Hirose and Y. Terasawa, *Jpn. J. Appl. Phys.* **25**, L519 (1986).
(12) T. Kawato and K. Kondo, *Jpn. J. Appl. Phys.* **26**, 1429 (1987).
(13) C.P. Chang, D.L. Flamm, D.E. Ibbotson, and J.A. Mucha, *J. Appl. Phys.* **63**, 1744 (1988).
(14) Y. Saito, K. Sato, H. Tanaka, K. Fujita, and S. Matuda, *J. Mater. Sci.* **23**, 842 (1988).
(15) T.W. Or, Q.Y. Han, Z.P. Lu, J. Heberlein, and E. Pfender, "Thermal Plasma Deposition of Diamond Using Liquid Organic Precursors at One Atmosphere," to be presented in the 10th Int. Symp. on Plasma Chem., Bochum, Germany, August 4 - 9, (1991).
(16) S.H. Paik, Xi Chen, P. Kong, and E. Pfender, *Plasma Chem. Plasma Process.* **11**, 229 (1991).

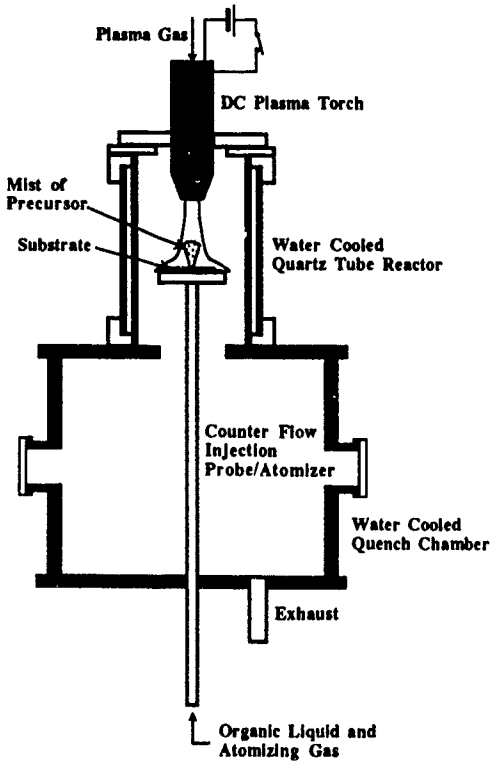



**Fig. 1: Schematic of the Counter-Flow Liquid Injection Thermal Plasma Reactor for Diamond Deposition.**

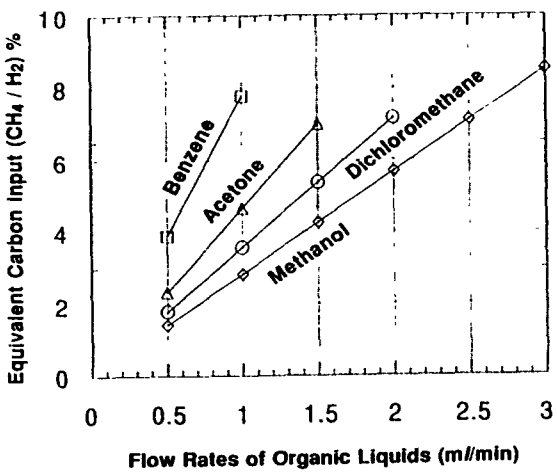



**Fig. 2: Equivalent Carbon Input by Injecting Various Liquid Precursors.**




**Fig. 3: Cross Sectional Views of High Rate Deposited Diamond: (a) Diamond Deposited on Molybdenum from Ethanol (Deposition Time: 1 hour); and (b) Formation of Large Diamond Columns.**

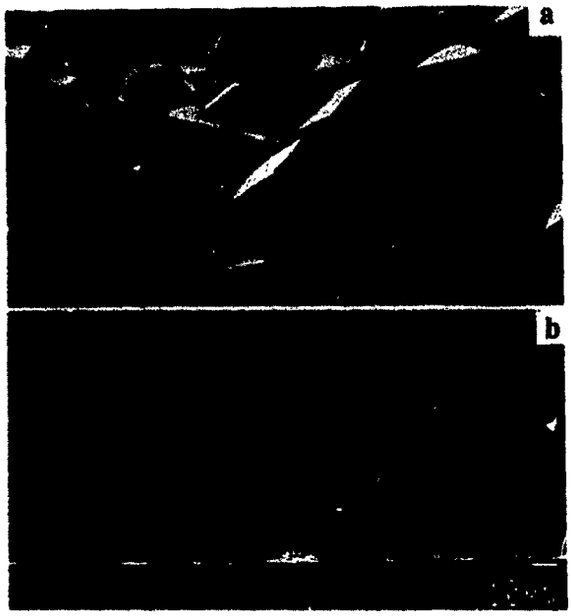
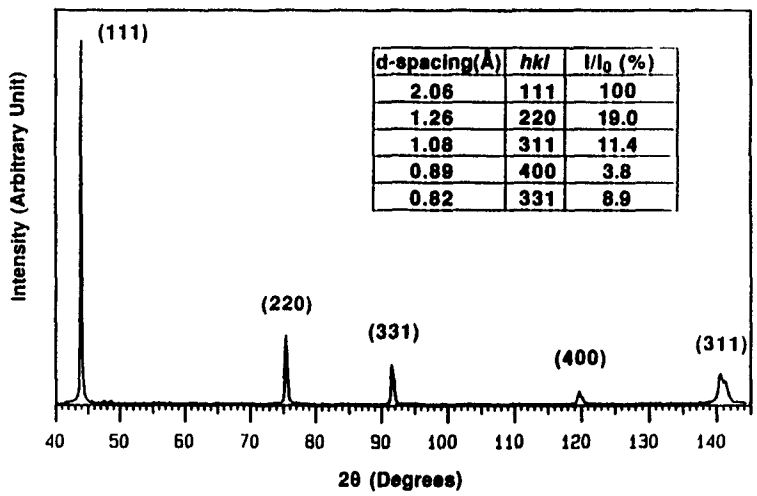



**Fig. 4: Typical Diamond Film Deposited on Molybdenum: (a) Top View, and (b) Cross Sectional View.**



**Fig. 5: Diamond Deposited on Tungsten from Carbon Tetrachloride.**




| d-spacing(Å) | *hkl* | $I/I_0$ (%) |
|---|---|---|
| 2.06 | 111 | 100 |
| 1.26 | 220 | 19.0 |
| 1.08 | 311 | 11.4 |
| 0.89 | 400 | 3.8 |
| 0.82 | 331 | 8.9 |

**Fig. 6: X-Ray Diffraction Pattern of a Diamond Film Made from Methanol.**

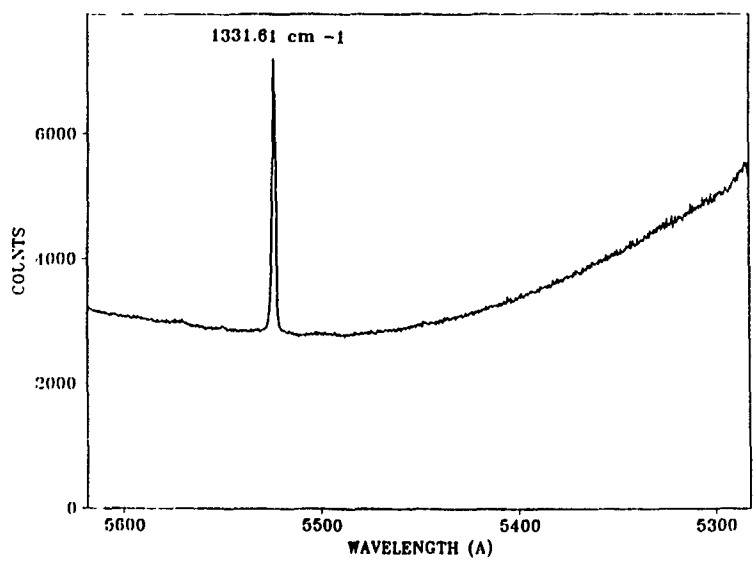



**Fig. 7: Raman Spectrum of a Diamond Film Made from Methanol.**

# PART II: GROWTH MECHANISMS

# Nucleation and Growth Processes in Chemical Vapor Deposition of Diamond

John C. Angus, Zhidan Li, Mahendra Sunkara, Roy Gat,
Alfred B. Anderson, Satya P. Mehandru and Michael W. Geis*

Case Western Reserve University
Cleveland, Ohio 44106

*Lincoln Laboratory, Massachusetts Institute of Technology
Lexington, Massachusetts 02173

## ABSTRACT

Diamond nucleation was enhanced by the addition of powdered graphite and non–volatile graphite–like compounds to silicon substrates. In addition, preferential nucleation of diamond was found along the edges of the basal planes of highly oriented pyrolytic graphite. The (111) diamond planes appear to be approximately parallel with the (0001) graphite basal plane. Computer simulation confirms the enhanced growth rate of multiply–twinned nuclei compared to un–twinned nuclei. The five– and twenty–fold twinned diamond crystals can arise from the intersection of two and three stacking errors on non–parallel (111) planes. Molecular orbital studies confirm that atomic hydrogen can hydrogenate aromatic molecules and the edges of graphite planes. The results are consistent with a nucleation mechanism in which high molecular weight aromatic or graphitic precursors are hydrogenated to saturated ring compounds. The multiply–twinned, e.g., boat–boat conformers, which can rapidly add carbon atoms, are the most likely immediate precursor to diamond formation.

## INTRODUCTION

It is now well established that diamond can nucleate from the vapor phase without the presence of a pre–existing seed crystal. The *de–novo* nucleation of a metastable phase in such a harsh growth environment is not easy to explain. It is also well known that scratching the substrate prior to deposition greatly enhances nucleation rates. This enhancement is greatest if diamond powder is used, but other abrasives enhance nucleation, although to a lesser extent.

The mechanism by which scratching enhances nucleation rates is not understood in detail. Several effects may be operating simultaneously. These include: 1) diamond detritus left on the surface, 2) pyrolysis of adsorbed

hydrocarbons to high molecular weight, non–volatile graphitic structures, 3) formation of convex edges and corners to which mass transfer from the gas phase is more rapid, 4) formation of defects, e.g., dislocations, at which nucleation is enhanced. One might even advance the hypothesis that extreme local temperatures and pressures obtained during scratching transform adsorbed hydrocarbons into very small diamond crystallites.

Matsumoto and Matsui proposed a series of hydrocarbon cage compounds as the diamond precursors (1). These included adamantane, tetracyclo–dodecane and hexacyclopentadecane. Badziag et al. showed that very small hydrogen terminated diamonds, less than 3 nm in diameter, are stable with respect to graphitic nuclei of the same size (2). This implies that diamond nucleation in hydrogen–rich environments may, in fact, be thermodynamically favored over nucleation of polyaromatic hydrocarbons.

A class of compounds has been proposed by one of the investigators (JCA) as possible precursors to diamond nucleation. These are the multiply twinned, fully saturated polycyclic hydrocarbons. The simplest example is boat–boat bicyclodecane. It was proposed that these and related molecules are formed by the hydrogenation of unsaturated graphite–like deposits in the atomic–hydrogen rich environment (3,4). A certain fraction of the hydrogenated polycyclic compounds will have the multiply twinned structure that promotes rapid growth of the nucleus. The compounds that are more closely related structurally to diamond, e.g., adamantane and its derivatives, would not be expected to be efficient nucleation promoters because they have no easy sites for atom addition. The multiply twinned precursors, on the other hand, have re–entrant surfaces which are continually renewed as growth proceeds. These reentrant surfaces provide an efficient point for nucleation of new {111} layers. The structures of the proposed precursors are shown in Figure 1.

## NUCLEATION EXPERIMENTS

To test the hypothesis that graphitic–like structures are precursors to diamond nucleation a series of seeding experiments were performed. In these experiments a specific molecule or seed material is added to the substrate surface before the deposition takes place. The nucleation density is determined by scanning electron microscopy. The results, which are summarized in Table 1, are still somewhat preliminary in nature, but do provide insights into the nature of diamond nucleation.

### Experimental Procedure

The diamond nucleation experiments were conducted in what are now considered conventional hot–filament diamond deposition reactors. The reactor at the MIT Lincoln Laboratory utilized tantalum filaments, while the CWRU reactor employed tungsten filaments. In the latter reactor a shutter and a rotating, translatable substrate holder were employed to provide reproducibility

and uniformity of deposition conditions.

The filament was first turned on (~ 2000° C) in flowing $H_2$ (100 sccm at 20 Torr) with the shutter positioned between the tungsten filaments and substrate. After 15 minutes the $CH_4$ flow (0.5 sccm) was started. After another 10 minutes the shutter was removed and the substrate moved to within 0.8 cm of the filaments. This procedure insured that adsorbed contamination from the filaments did not reach the substrate during start–up. It also provided a reproducible, carburized filament surface for each run. Total run time after removal of the shutter was 7 hours. The estimated surface temperature of the substrate was 830° C. The rotation speed of the substrate was 1/3 rpm throughout the deposition.

All substrates were undoped (100) Si wafers. Before addition of seeding agents, the wafers were given a standard RCA cleaning. Except for one control sample, the wafers were not scratched or polished with diamond.

The nucleation densities were determined using a scanning electron microscope. A representative area was examined and diamond crystals manually counted. Only faceted crystals of approximately 1.0 $\mu$m in maximum linear dimension were counted. This procedure gives only a relative nucleation density since sub–micron particles were excluded.

Seeding Experiments

Several species were found to have a positive effect on nucleation density. This effect appears to arise from several factors including chemical structure and relative volatility. The ability to form bonds with the substrate to reduce volatility may also play a role.

Graphite powder and graphite–related compounds, i.e., 3,4,9,10 perylene tetracarboxylic acid di–anhydride (PTCDA), enhanced nucleation rates. The perylene derivative contains five condensed aromatic rings, and may be thought of as a partially oxidized fragment of a graphite sheet.

The PTCDA enhanced nucleation when it was physically spread on the surface as a powder. A greater and more uniform nucleation density was achieved when the perylene was dissolved in tetra methyl ammonium hydroxide (TMAH), a standard etching solution for silicon. The wafer was soaked overnight in the PTCDA/TMAH solution at room temperature. The wafer was removed from the solution, rinsed lightly with methanol and placed in the deposition system. The graphite flakes were dispersed in isopropanol and the wafer coated with the resulting slurry. The isopropanol was allowed to dry and the wafer placed in the deposition system.

It is not possible to unambiguously separate out all of the effects taking place during these seeding experiments. For example, the TMAH solution alone proved to be an effective seeding agent. We speculate that this effect may arise

from Si–C or Si–O–C bonds formed between the TMAH and the silicon substrate. The bound TMAH remains on the surface long enough to undergo graphitization and subsequent hydrogenation.

Several experiments were performed to determine whether the enhanced nucleation density was simply caused by an increased supply of carbon on the surface, or whether the seed materials were acting as true nucleation agents. In one experiment part of the wafer was covered with graphite particles and the other part was not. A very sharp demarcation line between the region of high nucleation density and the unseeded region was observed after the run. This result is suggestive that the graphite flakes are acting as true nuclei. If the graphite particles were acting solely as an additional source of carbon, the rapid gas phase transport of carbon containing species would have caused greater nucleation in the unseeded area.

A further test was obtained by measuring the relative orientations of the graphite flakes and the diamonds that grew on them. Graphite flakes were dispersed in acetone and spun onto a silicon substrate at 3000 rpm. This provided a thin coating of HOPG flakes that were preferentially oriented with their basal planes parallel to the substrate surface. The orientation of the flakes before deposition and the orientation of the diamond crystals after deposition were determined by x–ray diffraction. The distribution of intensities is shown in Figure 2. The (111) planes of the diamond crystals are preferentially oriented in the same plane as the (0001) basal planes of the graphite flakes. This suggests that the graphite is serving as a true nucleation seed and not just as an additional source of carbon.

Depositions were also performed on large pieces of highly oriented pyrolytic graphite (HOPG). Greatly enhanced nucleation densities were found along the edges of the basal planes.

A series of experiments were also conducted using the diamondlike hydrocarbons as (a–C:H) seed materials. The diamonds grown using the diamondlike films as seeds showed a ball–like morphology with very poorly developed faceting and a weak Raman signal for diamond. On the other hand, the diamonds grown under the same conditions using graphite as the seed were well faceted and had a sharp, Raman line at 1332 $cm^{-1}$. It is surprising that the diamond crystals are still influenced so strongly by the original substrate after growing to micrometer–size dimensions.

One particularly interesting seed is buckminster fullerene, $C_{60}$. These spherical molecules present no edges for attack by atomic hydrogen and therefore would be expected to be less susceptible to hydrogenation and thus less likely to serve as precursors for diamond nucleation. No enhancement in nucleation density was found when $C_{60}$ was used as the seed.

It was also observed that the nucleation density was the highest along the convex corners of etched grooves on silicon substrates. We interpret this effect as resulting from an enhanced carbon concentration on the exposed, convex corner

TABLE 1. Nucleation Densities

| SUBSTRATE DESCRIPTION | NUCLEATION DENSITY, $CM^{-2}$ |
|---|---|
| Untreated (100) Si wafer | 8,500 |
| Untreated (100) Si wafer | 14,500 |
| Diamondlike film (a–C:H) | 4,700 |
| Graphite powder | 120,000 |
| Highly oriented pyrolytic graphite (near edge) | 220,000 |
| 3,4,9,10 perylene tetra–carboxylic acid dianhydride | 83,000 |
| Buckminster fullerene | 14,000 |
| Scratched with diamond powder | continuous film |

because of the enhanced mass transfer of carbon from the gas phase. These sites would first become supersaturated with carbon and hence would first provide graphitic precursors which could be hydrogenated by the atomic hydrogen.

Atomic Force and Scanning Electron Microscopy

In some cases small hexagonally shaped platelets were observed using scanning electron microscopy. Several of these, along with their Raman spectrum, are shown in Figure 3. Similar hexagonally shaped platelets have been observed by Tamor using scanning tunneling microscopy (5).

The morphology of diamond crystals was also studied by atomic force microscopy (AFM). An example of a hexagonal platelet is shown in Figure 4a. In some cases the AFM showed evidence of terraced crystals, which were much larger than other crystals in the same region on the surface. See Figure 4b. The terraced crystals may have grown by a screw dislocation mechanism. However, no direct observation of the presence of a screw dislocation by high resolution transmission electron microscopy was attempted.

We speculate that the hexagonally shaped platelets arise from the growth of nuclei with two (or more) parallel twin planes. A computer model of this type of

crystal is shown in the next section.

## MODELLING STUDIES

### General Description of Computer Program

We compare the observed morphologies of diamond crystals grown in the laboratory to the morphologies of crystals "grown" on the computer with known stacking errors. Correlation of experimentally observed morphologies with morphologies obtained with known atom addition rules on the computer can give important clues about nucleation and growth mechanisms.

All carbon atoms are assumed to have tetrahedral, $sp^3$, coordination. An ad-atom bonded once to the surface has limited rotational freedom about the bond axis, i.e., its orientation can be either staggered or eclipsed. These two orientations correspond respectively to chair or boat six-membered rings. The eclipsed orientation (boat conformation) is a stacking error in the diamond-cubic lattice. The relative probabilities of the staggered and eclipsed orientations can be fixed by the program user. Also, if desired, stacking errors at specific points in the precursor nucleus can be introduced.

The program makes provision for atom removal as well as atom addition. The relative overall probability of atom removal can be adjusted so that it is less than, equal to, or greater than the probability of atom addition. These three conditions correspond to growth, equilibrium and evaporation of the crystallites.

A basic assumption of the modelling is that the atom addition and removal events occur randomly on the crystal surface according to a Poisson process. Multiple atom events are not normally allowed. It is possible, however, to provide for simultaneous two-atom addition events. This is necessary, for example, to simulate acetylene addition at step sites.

Several complex affects can arise from the interaction of stacking errors. For example, some atoms that are not fully bonded to four other carbon atoms, will be buried in the crystal as the simulation proceeds. These buried free bonds must be automatically removed from the table which contains the free surface bonds. Also, intersections of growth fronts arising from different stacking errors will sometimes lead to bond distances and bond angles that are "close" but not equal to the single carbon-carbon bond parameters. In this case, the program permits a bond to be formed if the bond length and bond angles are within a pre-set range of values. The most common situation when this occurs is the formation of five-membered rings.

### Modelling Results

Simulations were performed using several twinned and un-twinned molecules as starting nuclei and various probabilities for stacking errors and for

relative atom addition and removal rates. A general discussion of the method will be given elsewhere (6). Here we describe some results of relevance to the present experimental studies.

Flat, hexagonally shaped crystals arise naturally from nuclei with two parallel stacking errors, e.g., the boat–boat bicyclodecanes shown in Figure 1a and 1b. A computer–grown crystal arising from this nucleus is shown in Figure 6. The crystal shown in Figure 6 is, in fact, a thin crystal of Lonsdaleite (hexagonal diamond) with the ABA . . . stacking sequence clearly visible. Also visible are several adatoms starting the next layers on the large exposed crystal faces. These adatoms have the staggered orientation and will give rise to a new layer of the correct cubic diamond stacking. The probability of nucleating a new layer will increase as the area of the hexagonal platelet increases. The net result, after much longer simulations will be a crystallite of hexagonal shape but, apart for the initial few layers, of the diamond cubic structure.

The rapid lateral growth of the original bicyclodecane nucleus into a hexagonal platelet arises because of the relative probabilities chosen for atom addition and removal. In this simulation, after chosing a surface site, the ratio of the probability for removal of a single bonded carbon atom to the probability of addition of a carbon atom to the surface site was 496/4. Also, atoms that are bonded only once to the surface had a much higher probability for removal than atoms that are bonded twice to the surface. Along the re–entrant surface defined by the two parallel stacking errors, only two atoms are required to form a stable structure. This is shown graphically in Figures 1a and 1b, where the first two adatoms are shown. On a smooth (111) surface or on the basal plane of the hexagonal crystal, however, the stable nucleus is a three atom bridge. The probability of finding two carbon atoms adjacent to each other is much larger than the three carbon atom process and, hence, the platelet will grow more rapidly within the plane of the stacking errors than normal to the plane.

The relative growth rates of computer grown crystals starting from boat–boat bicyclodecane, boat–boat–boat tricyclotetradecane and chair–chair bicyclodecane (which has no stacking errors) are shown in Table 2. A dramatic difference in growth rates of the twinned and un–twinned nuclei is evident.

Simulation runs were also performed with starting nuclei having forced stacking errors on non–parallel (111) planes. Growth from the doubly–twinned nucleus shown in Figure 1c gives rise to a decahedral crystal with apparent five–fold symmetry. The resulting computer–grown crystal is shown in Figure 6. The five–member rings at the center of the crystal closed according to the allowed bond–length and bond–angle ranges specified initially. Closure of the bonds was not achieved further from the center and the growth of a grain boundary between two of the five sectors of the crystal is starting.

If a crystal is grown on the computer from a nucleus with three non–parallel twin planes, an icosahedral crystal with twenty intersecting twin planes is generated. A partially grown icosahedral crystal grown from such a nucleus is shown in Figure 6c.

TABLE 2. Growth Rate Simulations

| PRECURSOR | N+ | N– | ΔN | RELATIVE GROWTH RATES |
|---|---|---|---|---|
| Two boats[a] | 19,558 | 18,558 | 1,000 | 1.0 |
| Three boats[b] | 12,823 | 11,823 | 1,000 | 1.457 |
| Two chairs[c] | 7,000 | 6,980 | 20 | <0.01 |

N+ = Number of atom additions

N– = Number of atom removals

ΔN = Net atom additions

Note: After choice of surface site, the ratio of probabilities of removal of single bonded atom to addition of an atom is 496/4.

a) boat–boat bicyclodecane ($C_{10}H_{18}$)

b) boat–boat–boat tricyclotetradecane ($C_{14}H_{24}$)

c) chair–chair bicyclodecane ($C_{10}H_{18}$)

The formation of the complex central cores of the five–fold and twenty–fold twinned crystals often seen in vapor–grown diamond arises naturally during growth from the sequential occurrence of two and three stacking errors respectively. These stacking errors are propogated by layer growth and the complex central core is formed where they intersect. This sequential process appears far more likely than the spontaneous generation of the central core structure from the reaction mixture.

## MOLECULAR ORBITAL STUDIES

The mechanism proposed above for diamond nucleation involves the hydrogenation of graphitic materials to saturated polycyclic ring compounds. Gill et al. (7) investigated the reaction of atomic hydrogen produced at a hot tungsten filament with graphite, lamp black and diamond at 77 K. Gaseous carbon species ($C_1$ to $C_4$) were produced and an unidentified higher molecular weight compound was formed from graphite. Furthermore, graphite was found to be more reactive

with atomic hydrogen than diamond. Rye studied the reaction of atomic hydrogen with carbon film held at 340°C and identified a number of ring compounds including cyclohexane, though methane was the major gaseous hydrocarbon product (8).

Using the extended Hückel method and a rigid cluster model for the graphite sheet, Chen and Yang investigated the adsorption of a single H atom to the basal plane and the $(10\bar{1}0)$ and $(11\bar{2}0)$ edges of graphite (9). They concluded that only the edge planes can adsorb hydrogen. Subsequently, Pan and Yang used the same theoretical technique and proposed a mechanism for methane formation from the reaction between atomic hydrogen and the $(11\bar{2}0)$ edge face (10). Other theoretical investigations for H atom interaction with graphite are limited to the basal plane of graphite (11,12). All of these studies were done from the perspective of understanding graphite etching.

In the present work, we have investigated the structures and stabilities for the sequential addition of atomic hydrogen to benzene, naphthalene, and perylene molecules to form the corresponding saturated ring systems. The semiempirical atom superposition and electron delocalization molecular orbital (ASED–MO) technique has been used for all calculations. Some preliminary results for the chemisorption of atomic hydrogen to the edges and corners of a graphite sheet are also presented. The C and H parameters used in the calculations are the same as used earlier (13,14).

Addition of H Atoms to Benzene, Naphthalene, and Perylene

Various configurations for the sequential addition of H atoms to benzene are investigated with full structure optimizations. The binding energies are given in Table 3, and structures are shown in Fig. 7. It may be seen that the first, third, and fifth H addition is relatively weak compared with the second, fourth, and sixth H addition. This is due to the formation of a destabilized radical orbital for the odd–electron systems as shown in Fig. 8. The average binding energy per H for complete hydrogenation is 4.40 eV. Our calculated energy difference between the chair and boat conformers is 6.2 kcal/mole, with the chair form more stable than the boat form. This compares well with the literature estimate of 5–6 kcal/mole.

The sequential addition of H atoms to naphthalene molecule is essentially similar to the benzene hydrogenation, except that the H chemisorption commences from the outer C atoms and proceeds inwards, until fully saturated bicyclodecane is formed. The average binding energy per H atom on going from naphthalene to the fully saturated bicyclodecane is 4.41 eV which is the same as for the benzene hydrogenation. The structures and relative energies for various conformers of bicyclodecane are in Table 4. The chair–chair bicyclodecane is calculated to be more stable by 10.8 kcal/mole compared with the cis boat–boat form which in turn is more stable than the trans boat–boat form by about

TABLE 3. Sequential Binding Energies, BE(eV), for H Additions to Benzene, i.e., $H_n/C_6H_6$ (n = 1–6).

| | Configuration | BE(eV) |
|---|---|---|
| 1st H | — | 2.80 |
| 2nd H | 1,2 | 5.21 |
| | 1,3 | 2.66 |
| | 1,4 | 5.15 |
| 3rd H | 1,2,3 | 3.08 |
| | 1,2,4 | 2.93 |
| 4th H | 1,2,3,4 | 5.46 |
| | 1,2,4,5 | 1.88 |
| 5th H | 1,2,3,4,5 | 3.25 |
| 6th H | chair | 5.99 |
| | boat | 5.72 |

2.4 kcal/mole. The energy difference between the chair and boat forms of bicyclodecane is approximately twice that for the cyclohexane. This suggests that each saturated ring contributes about 5 to 6 kcal/mole to the energy difference between the chair and boat conformers. Thus, based on these results, multiple ring saturated systems are expected to be more stable in the all–chair configuration than any combination of chairs and boats.

Next we consider the hydrogenation of perylene with atomic hydrogen. This molecule (Fig. 9) may be imagined as two naphthalene molecules fused together at 1,8 positions with the elimination of 4 H atoms and the formation of two CC bonds. Hydrogen atom additions to this molecule were carried out in two steps. In the first step, 10 H atoms were added to a naphthalene fragment comprising half of the molecule while retaining the rigid planar structure for the other half. All bond lengths and angles for the hydrogenated half were fully optimized. The average binding energy per H addition for this step is 4.39 eV and the favored chair–chair configuration is also shown in Fig. 9. The cis boat–boat configuration (Fig. 9) is 0.47 eV less stable. In the second step, 10 more H atoms

TABLE 4. Calculated CC and CH Bond Lengths and Relative Energies for Various Ring Isomers of Bicyclodecane.

| Isomer | $r_{CC}$(Å) | $r_{CH}$(Å) | E(eV) |
|---|---|---|---|
| Chair–chair | 1.573 | 1.104 | –0.573 |
| Cis boat–boat | 1.583 | 1.102 | –0.106 |
| Trans boat–boat | 1.585 | 1.102 | 0.0 |

were added to the planar half of the molecule and all CC and CH bonds were reoptimized using tetrahedral angles. The fully saturated structure is shown in Fig. 9. The calculated average binding energy per H for the second step is 4.41 eV. Thus, the average CH bond strength for the hydrogenation of perylene to the fully saturated multiple ring chair configuration is 4.40 eV, which is the same as for similar reactions for benzene and naphthalene.

The above results for the reaction of atomic hydrogen with unsaturated ring systems suggest that the formation of fully saturated analogues is favored in the atomic hydrogen–rich environment. However, the actual outcome of such processes will perhaps be determined by kinetic factors.

Interaction of H Atoms with Graphite Edges

A graphite sheet may be imagined as an extremely large unsaturated hydrocarbon. The experiments of Rye have shown that atomic hydrogen reacts with graphite even at 77 K to produce a variety of hydrocarbon species (8). The mechanism of formation of such products is not known. The reaction of atomic hydrogen with graphite is most likely to start at the edges and corners of the sheet since these carbon atoms possess maximum un–saturation as well as the flexibility for distorting the neighboring CC bonds as a result of increased coordination.

Using large cluster models (see Fig. 10) for the monohydrogen terminated zigzag $\{10\bar{1}0\}$ and armchair $\{11\bar{2}0\}$ edge faces for the graphite sheet, we have investigated the binding of a second H atom to the outermost C atom on the edge site. The calculated CH bond strengths are 3.74 and 3.83 eV, respectively, for the zigzag and armchair faces (calculated as the average value when two H atoms were simultaneously added to two neighboring outermost C atoms on the edges).

Next, we have investigated the possibility of saturated ring formation from the reaction of atomic hydrogen with a graphite sheet. On the zigzag face each

hexagonal ring is bonded to five C atoms of the basal plane, whereas on the armchair face there are four carbon bonds with the rest of the sheet. At the corner between the zigzag and armchair faces the hexagonal ring is bonded to three C atoms of the sheet and one can also imagine a corner ring with only two CC bonds with the rest of the sheet. Lastly, a pendant benzene ring bonded to the graphite sheet through one C atom is possible. Complete hydrogenation of a planar ring will lead to large distortions resulting in a highly strained structure. The lesser the coordination of a ring with the rest of the basal plane, the larger will be the flexibility of the ring toward distortion. Thus the corners are more likely to form fully saturated rings than the edges. We have considered one such corner for our H addition calculations where the corner ring is attached to the rest of the sheet through two CC bonds (Fig. 11). In the first step we added 7 H atoms to the outer C atoms of the corner ring. The structure of the ring and its immediate vicinity was completely optimized. In the most stable structure, the corner ring assumes the chair configuration (Fig. 11). The average binding energy per H atom is calculated to be 4.38 eV, which is about the same as for benzene or naphthalene hydrogenation processes. Thus, the hexagonal ring bonded through two C atoms to the graphite basal plane has essentially complete flexibility to distort to the tetrahedral structure. Next, we added five more H atoms to the neighboring C atoms and reoptimized the structure of the two corner rings. The two corner rings distort to the chair–chair bicyclodecane structure bonded to the rest of the sheet through three CC bonds (Fig. 11). The average binding energy for the second addition of H atoms is reduced to 3.93 eV. The decrease in the bond strength is due to the fact that the second ring is bonded to the rest of the sheet by three CC bonds which leads to larger strain due to distortion. Further addition of H atoms may also be possible but we have not considered it in this work. From the above calculations we may conclude that fully saturated multiple ring systems can be formed on the corners of a graphite sheet.

We are presently investigating the H insertion reactions into the edge CC bonds on the zigzag and armchair faces of graphite to devise mechanisms for the formation of $C_1$ and higher hydrocarbons.

## SUMMARY

The above results indicate that unsaturated aromatic ($sp^2$) compounds and graphite can serve as sites for diamond nucleation. In order to serve as a nucleation site, the precursor must be sufficiently non–volatile and thermally stable to remain in the reaction environment long enough to be hydrogenated to the saturated ($sp^3$) structures. In some cases the ability of a seed compound to serve as a nucleation site may be enhanced by the formation of Si–C or Si–O–C bonds with the surface, which would reduce volatility. The multiply twinned ring compounds, e.g., boat–boat bicyclodecane, will grow most rapidly to achieve small stable diamond crystallites.

## ACKNOWLEDGEMENTS

The Case Western Reserve University portion of this work was sponsored by a National Science Foundation Materials Research Group Grant and by the Defense Advanced Research Projects Agency. The Lincoln Laboratory portion was sponsored by SDIO/OST, through the Office of Naval Research. The atomic force microscopy was performed by Thomas Altshuler, Advanced Materials Laboratory, Concord, Massachusetts, 01742.

## REFERENCES

1. S. Matsumoto and Y. Matsui, *J. Mat. Sci.* **18**, 1785 (1983).

2. P. Badziag, W.S. Verwoerd, W.P. Ellis and N.R. Greiner, *Nature* **343**, 244 (1990).

3. J.C. Angus, R.W. Hoffman, and P.H. Schmidt, *Proc. First Intl. Conf. on the New Diamond Science and Technology*, Tokyo, October 24–26, 1988, KTK Scientific Publishing, Tokyo, 1991.

4. M. Sunkara, J.C. Angus, CC. Hayman, and F.A. Buck, *Carbon* **28**, 745 (1990).

5. M. Tamor, *J. Vac. Sci. Tech.* **9** (May/June) 1570 (1991).

6. M. Sunkara, Ph.D. Thesis, Case Western Reserve University, 1992.

7. P.S. Gill, R.E. Toomey and H.C. Moser, *Carbon* **5**, 43 (1967).

8. R.R. Rye, *Surface Sci.* **69**, 653 (1977).

9. J.P. Chen and R.T. Yang, *Surf. Sci.* **216**, 481 (1989).

10. Z.J. Pan and R.T. Yang, *J. Catal.* **123**, 206 (1990).

11. V. Barone, F. Lelj, C. Minichino, N. Russo, and M. Toscano, *Surf. Sci.* **189/190**, 185 (1987).

12. R. Dovesi, C. Pisani, and C. Roetti, *Chem. Phys. Lett.* **81**, 498 (1981).

13. K. Nath and A.B. Anderson, *Solid State Commun.* **66**, 277 (1988).

14. S.P. Mehandru and A.B. Anderson, *J. Mater. Res.* **5**, 2286 (1990).

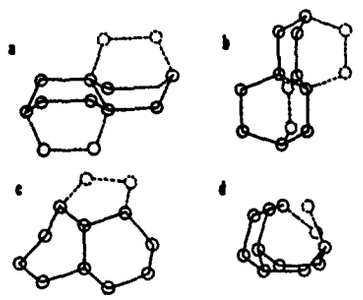


Figure 1. Four "boat–boat" conformers of bicyclodecane. Positions of first two ad–atoms are shown as dashed lines. a) and b) conformers with two parallel twin planes, c) conformer with two twin planes at angle of 70°53′, d) conformer that leads to an incoherent boundary.

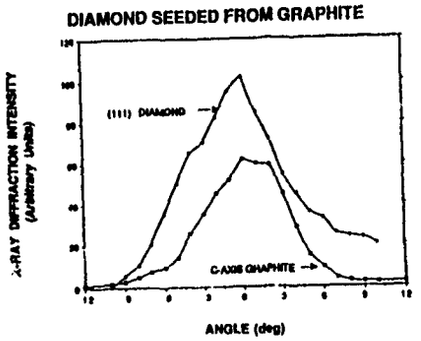



Figure 2. Distribution of x–ray intensities from oriented graphite seed crystals and from diamond crystals grown on the seeds. The original graphite seeds show a strong (0001) texture and the diamond crystals show a strong (111) texture.

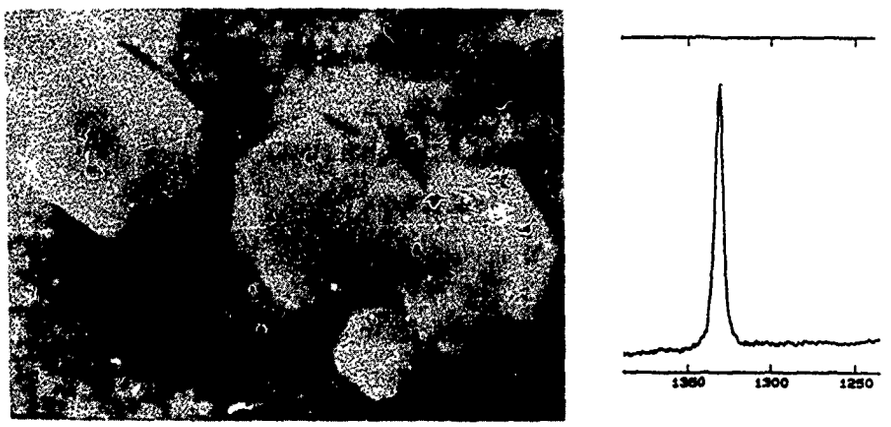



Figure 3. Scanning electron micrograph of a cluster of hexagonally shaped diamond crystals along with their associated Raman spectrum. Maximum linear dimension of the large platelets is approximately 4 $\mu$m; Raman peak at 1331.1 $cm^{-1}$.

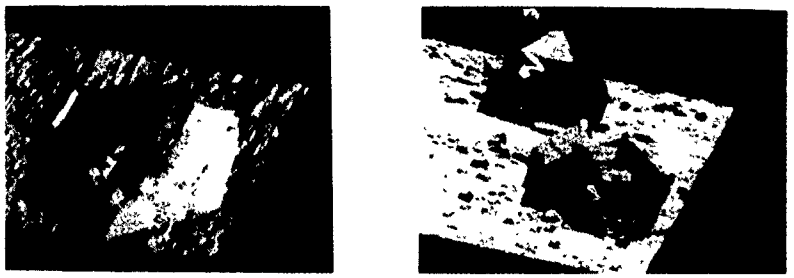


Figure 4. a) Atomic force micrograph of a single hexagonally shaped diamond platelet. Maximum linear dimension is approximately 30 $\mu$m; b) Atomic force micrograph of diamond crystals showing terraced morphology. Maximum linear dimension is approximately 4 $\mu$m.

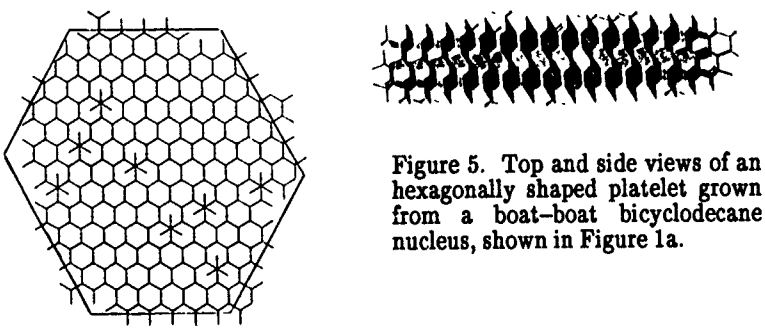


Figure 5. Top and side views of an hexagonally shaped platelet grown from a boat–boat bicyclodecane nucleus, shown in Figure 1a.

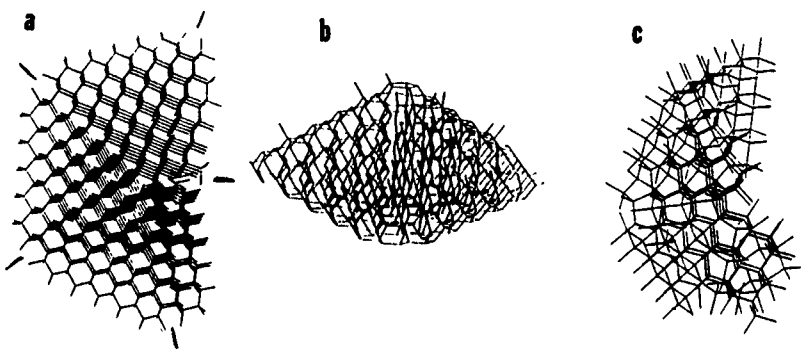



Figure 6. a) and b) Top and side views of a decahedral, five–fold twinned crystal grown from a nucleus with two stacking errors inclined at 70°53′. See Figure 1c; c) A partially grown icosahedral crystal arising from a nucleus with three intersecting stacking errors.

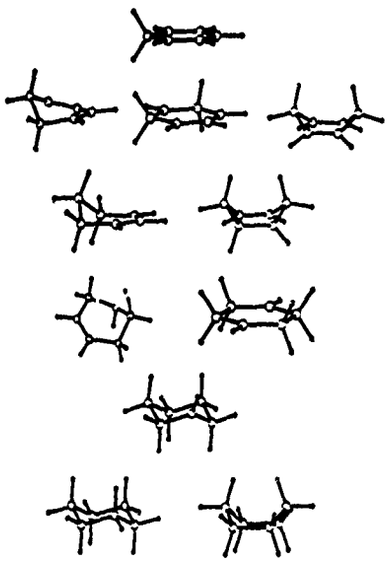


Figure 7. Various configurations during the sequential addition of hydrogen to benzene.

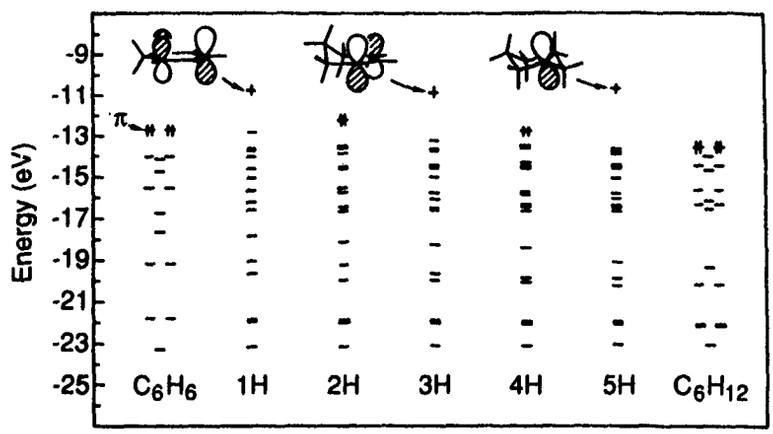



Figure 8. Energy levels for structures shown in Figure 7.

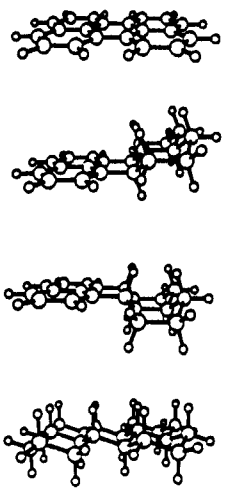


Figure 9. Perylene, the chair and boat conformers of partially hydrogenated perylene, and fully hydrogenated perylene.

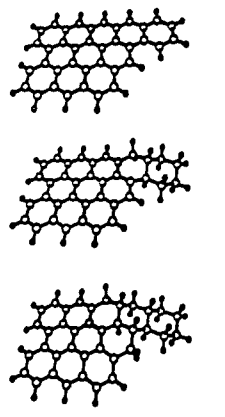


Figure 10. Cluster models for monohydrogen terminated edges of graphite.

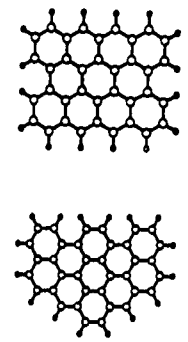


Figure 11. Successive hydrogenation of a corner of a graphite sheet.

# MOLECULAR PROCESSES IN DIAMOND FORMATION

Michael Frenklach
Department of Materials Science and Engineering
The Pennsylvania State University
University Park, PA 16802

Diamond formation in gas-activated deposition processes is discussed in terms of elementary chemical processes. The discussion is based on a recently developed detailed kinetic model. The model does not support the theory of preferential etching advanced to explain the kinetic competition between diamond and non-diamond phases, but instead, establishes the critical role of aromatics condensation and interconversion of $sp^2$ and $sp^3$ carbon phases mediated by hydrogen atoms.

## INTRODUCTION

Diamond film deposition at low pressures is rapidly moving towards technological applications. Most challenging applications among them — heteroepitaxial deposition of single-crystal films, low-temperature deposition of high quality films, and high-rate–high-quality film growth — require a more thorough understanding of the fundamental processes governing the process. Several macroscopic approaches — phenomenological, thermodynamic, and those based on classical nucleation theory — have been used in the past and new microscopic descriptions begin to appear. A detailed review of the pre-1990 theories and models of nucleation and growth of diamond films was given recently elsewhere (1). The objective here is to discuss the principal mechanistic issues of diamond chemical vapor deposition (CVD) in terms of elementary phenomena and to present some new results on the subject.

## ETCHING THEORY OF DIAMOND CVD

Diamond is a metastable form of carbon with respect to graphite at low pressures. This manifests itself in that the growth of graphite (more generally, $sp^2$ carbon) always accompanies the growth of diamond, and this co-deposition is what presents the principal technological difficulty. Russian scientists (2) provided a persuasive argument that the competition between diamond and graphite growth is controlled by kinetics and not thermodynamics. The kinetic factor was suggested (2–4) to be the preferential etching of graphite over diamond by hydrogen atoms: both diamond and graphite are formed simultaneously but graphite (or, more generally, graphitic component) is destroyed by reactions with H atoms whereas diamond is not, or at least not to the same extent.

## AROMATICS THEORY OF DIAMOND CVD

The preferential etching theory has been recently challenged. Analyzing why micron-an-hour deposition rates of diamond were obtained only when a large excess of hydrogen was employed, it was suggested (5) that it is not necessarily due to hydrogen *atoms*, but rather due to the large concentration of hydrogen *molecules* which suppress the formation of aromatic species in the gas phase thereby preventing their condensation on the growing surface. That is, along with molecular precursors for diamond growth, gas-phase reactions produce higher molecular weight compounds. Among them are particularly stable and "sticky" aromatic hydrocarbons, the smallest of them being benzene. When present in the deposition zone, these aromatic species condense on the growing surface thereby covering the diamond $sp^3$ carbon with $sp^2$ carbon phases.

This proposal was further supported by a subsequent detailed kinetic modeling study (6), where the entire deposition process — gas-phase reactions occurring in the activated gas above the deposition surface, diffusion of chemical species to the deposition surface, and reactions occurring on the growing surface by which the diamond growth takes place — was described, for the first time, in elementary terms. The development of this model was based on the postulate, first suggested several years ago (5,7,8), that chemical reactivity of solid carbonaceous materials is localized on the carbon sites in a manner similar to that of the corresponding hydrocarbon gaseous species. In other words, the kinetics of analogous elementary chemical reactions on a per site basis is the same for all forms of carbon. Following this assumption, specific surface reactions for diamond $sp^3$ and non-diamond $sp^2$ surface sites were postulated and corresponding rate parameters evaluated (6). The model was tested by simulating diamond film deposition in a hot-filament reactor and was found to correctly predict the concentrations of major gaseous species and to reproduce the general experimental trends observed for the growth rate and film quality: the effects of temperature, pressure, initial methane concentration, and the addition of oxygen. At temperatures of diamond deposition, the model predicted that the rate of gasification of $sp^2$ carbon by H atoms is much too slow compared to the rates of other processes. The slow rate of $sp^2$ gasification may be further supported by a recent molecular-dynamic study of Brenner *et al.* (9), which showed no formation of hydrocarbon fragments upon H-atom attacks on diamond surfaces.

### Principal mechanism and kinetics of diamond growth

Analysis of the computational results in Ref. (6) revealed the existence of three basic factors governing the deposition process: epitaxial growth of diamond, diamond surface graphitization, and condensation of aromatics on the growing surface.

The principal growth of diamond occurs by the formation of an active site — a surface carbon $sp^3$ radical — followed by the addition of a carbonaceous gaseous species, referred to as the growth species, to the surface radical formed. The number density of the surface radicals is determined primarily by the balance between the following

reactions: abstraction of hydrogen atoms from the surface C–H bonds, denoted here as $C_dH$, by gaseous hydrogen atoms thereby producing the surface radicals, denoted by $C_d\bullet$,

$$C_dH + H \longrightarrow C_d\bullet + H_2\,; \tag{1}$$

the reverse of this reaction,

$$C_d\bullet + H_2 \longrightarrow C_dH + H\,; \tag{-1}$$

combination of the surface radicals with free gaseous hydrogen atoms,

$$C_d\bullet + H \longrightarrow C_dH\,; \tag{2}$$

addition of the growth species to the surface radicals,

$$C_d\bullet + C_nH_m \longrightarrow \text{products}\,; \tag{3}$$

and thermal decomposition of the surface radicals (and its reverse),

$$C_d\bullet \longrightarrow C_gH + H\,, \tag{4}$$

where $C_gH$ denotes an $sp^2$-hybridized carbon site. Assuming a steady state for $C_d\bullet$, we obtain

$$\chi_{C_d\bullet} = \frac{k_1[H]}{k_{-1}[H_2] + k_2[H] + k_3[C_nH_m] + k_4}\,\chi_{C_dH}\,, \tag{5}$$

where $\chi$ denotes the number density of the corresponding surface sites, square brackets the concentrations of gaseous species, and $k$ the rate coefficients of the corresponding reactions.

Under typical deposition conditions, the term $k_2[H]$ dominates the denominator of Eq. (5), which leads therefore to expression

$$\chi_{C_d\bullet} = \frac{k_1}{k_2}\chi_{C_dH}\,. \tag{6}$$

From Eq. (6) follows that the number of available surface radicals $C_d\bullet$ increases with temperature because reaction (1) has a substantial activation energy whereas reaction (2) does not. Another important prediction of Eq. (6) is that the number density of surface active sites, and hence the rate of diamond growth, should *not* depend on the gas-phase concentration of hydrogen atoms. We expect this behavior in the main growth regime under typical deposition conditions: hot-filament or thermal-plasma reactors, highly diluted in hydrogen hydrocarbon mixtures, about 800 to 1000 °C substrate temperature,

and large superequilibrium of H atoms. In the deficit of hydrogen atoms, the term $k_{-1}[H_2]$ becomes dominant and then

$$\chi_{C_d\bullet} = \frac{k_1[H]}{k_{-1}[H_2]}\chi_{C_dH} = K_1\frac{[H]}{[H_2]}\chi_{C_dH}, \qquad (7)$$

where $K_1$ is the equilibrium constant of reaction (1). That is, under these conditions, the number density of active sites is determined by the "equilibrium position" of reaction (1) and hence by the concentration of H atoms.

With the increase in the substrate temperatures, the rate coefficient of reaction (4) is rapidly increasing, reaching a point when $k_4$ dominates the denominator of Eq. (5). Thus, at these high temperatures, the thermodynamic stability of $C_d\bullet$ radicals becomes the limiting kinetic factor: the $sp^3$-hybridized $C_d\bullet$ sites decompose forming an $sp^2$ graphitic phase. And the latter is gasified (etched) by reactions with hydrogen atoms.

At low substrate temperatures, the condensation of benzene from the gas phase onto the growing surface competes with the growth of diamond by covering the available $sp^3$ diamond sites, i.e., decreasing $\chi_{C_dH}$. The condensing aromatic molecules are presumably converted, by thermal decomposition or by the addition of hydrogen atoms, into an amorphous $sp^2/sp^3$ carbonaceous network.

## Major experimental trends

The model discussed above offers the following explanations for the trends observed in experiments:

GAS ACTIVATION: Without activating the gas by thermal, plasma or other energetic sources, the concentration of H atoms is low and hence the number density of active sites and consequently the film growth rate are low.

SUBSTRATE TEMPERATURE: At low temperatures, the formation of active sites is slow as it is limited by the low rate of reaction (1). With the increase in temperature, this rate is increased. However, at high enough temperatures, the number density of active sites decreases due to their thermal decomposition and graphitization. The $sp^2$ carbon formed at these high temperatures is rapidly etched away by hydrogen atoms. These phenomena explain the bell-shaped dependence of the film growth rate on substrate temperature. The diamond film quality is predicted to be the highest at temperatures of the peak deposition rate. At higher substrate temperatures, when graphitization occurs, the film should contain increasingly large amounts of graphitic component; and at lower substrate temperatures, the condensation of benzene leads to an amorphous $sp^2/sp^3$ carbonaceous network.

ROLE OF HYDROGEN: There are two main roles that hydrogen plays. First, molecular hydrogen suppresses the formation of aromatics in the gas-phase; and second, the atomic hydrogen activates the surface by the H-abstraction, reaction (1), thus creating surface radicals. Also important are the combination of H atoms with the surface radicals, and addition of H atoms to unsaturated carbon-carbon bonds thereby converting aromatics into amorphous carbon at low temperatures and gasifying graphite at high temperatures.

INITIAL HYDROCARBON CONCENTRATION: The main factors affecting the deposition characteristics with the increase in the initial hydrocarbon concentration are: higher concentrations of the film growth species and therefore larger film growth rates in highly diluted mixtures; increased formation of aromatics which reduces the film quality; and lower H atom concentrations that, among other things (6,10), shifts the peak of the deposition rate to higher substrate temperatures. For a fixed deposition temperature, at low initial $CH_4$ concentrations, the deposited film consists of diamond. At higher methane concentrations, when benzene condensation catches up with diamond deposition, the film begins to contain amorphous carbon, formed by the H addition to benzene condensed on the surface. At even higher methane concentrations, as the $sp^2 \rightarrow sp^3$ transformation by the H addition can no longer follow the benzene condensation, the depositing film should consist of predominantly graphite.

EFFECT OF PRESSURE: The effect of pressure on diamond deposition is essentially the concentration effect: the absolute concentrations of the key hydrocarbon species are increased with the increase in pressure, thus following the phenomena described in the point above.

ADDITION OF OXYGEN: The addition of small amounts of oxygen does not necessarily increase the deposition rate of diamond but substantially improves the film quality, especially at low temperatures. This improvement in film quality results from the decrease in the concentration of benzene, caused by the oxidation of key hydrocarbon precursors in the gas phase, and gasification (etching) of $sp^2$ surface carbon by OH radicals.

## Improved deposition of diamond

Our model suggests two factors for improvement in deposition characteristics of diamond films at lower substrate temperatures: a higher temperature gradient and a larger concentrations of OH in the deposition zone. The high gas temperatures in the deposition zone prevent the formation of aromatics in the gas phase, and the OH radicals remove the non-diamond $sp^2$ component from the growing surface. These factors should improve the quality of diamond films but not necessarily increase the deposition rate of diamond. A possible strategy for increasing the rate of diamond film deposition is to separate the growth and etching processes by a cyclic operation, in which after a period of growth, the

non-diamond component is removed by oxidation (11), as first suggested by the Russian scientists (2).

## Effect of florine on diamond growth

The presence of halogens in the reaction system is known to promote the production of various forms of solid carbon [see, e.g., Refs. (12–14) and references cited therein]. Of particular interest are the recent results of Patterson *et al.* (14) who reported deposition of diamond films at substrate temperatures as low as 250 °C and relatively mild gas activation when florine was added to the mixture. These observations can be rationalized by the abstraction of the surface H atoms by gaseous F atoms,

$$C_dH + F \longrightarrow C_d\bullet + HF. \qquad (8)$$

The rate coefficient of this reaction is likely to be substantially larger and essentially temperature independent by comparison to reaction (1), as evidenced by analogy to known gas-phase reactions (see Fig. 1). Thus, the presence of F atoms will lead to an increased activation of surface, especially at low temperatures. An additional factor affecting the deposition characteristics may be the preferential etching of $sp^2$ component by F atoms, as suggested by Patterson *et al.* (14).

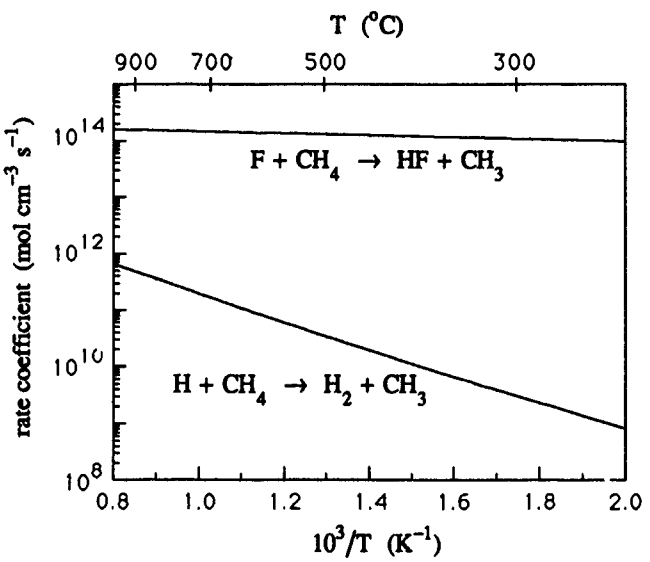



Figure 1. Comparison of rate coefficients of the F- and H-abstractions by hydrogen atoms; the data are from Ref. (15) and (16), respectively.

## THE GROWTH SPECIES

It should be noted that the above discussion did not invoke a specific growth species. Assuming the growth species to be either $C_2H_2$ or $CH_3$, the two most likely candidates at typical deposition conditions, would predict the same qualitative trends and produce in both cases near quantitative agreement with experiment for an appropriate choice of rate parameters. However, as the controversy over $C_2H_2$-versus-$CH_3$ mounts, it is pertinent here to examine the criticism advanced against the acetylene hypothesis.

### Experimental arguments

MARTIN AND CO-WORKERS (17) have synthesized diamond films in a flow tube reactor in which hydrocarbon was added downstream from a microwave discharge in 10%$H_2$–Ar mixtures. They reported that more diamond is formed and of higher quality when methane is used as the initial hydrocarbon compared to acetylene. They concluded therefore that methyl radicals and possibly methane are more effective diamond precursors than acetylene.

However, starting with acetylene should not necessarily be a better environment for diamond growth in Martin *et al.*'s experimental system because at high acetylene concentrations the production of benzene is increased and this, according to the aromatics theory of diamond CVD presented here, suppresses diamond deposition. It should be noted that while the growth rate of diamond is first order in acetylene concentration, the formation rate of aromatics in the gas phase is second to third order in the concentration of acetylene. Therefore, increasing acetylene concentration should tilt the kinetic competition towards production of aromatics, and hence away from the growth of diamond.

CHU ETAL. (18) presented a clever idea of diamond deposition from a mixture of isotope-labeled hydrocarbons. They used a hot-filament technique; though, their reactor was different from those typically used in diamond chemical vapor deposition. Only hydrogen gas was sent through the hot filament region and the hydrocarbons, mixed in hydrogen, were injected into post-filament stream near the substrate. The hydrocarbons were $^{13}CH_4$ and $^{12}C_2H_2$, mixed in the molar ratio of 2 to 1, whereby creating a gaseous environment containing equal amounts of $^{13}C$ and $^{12}C$ atoms. Comparing the isotopic ratios of the deposited film with those of the gas-phase species, Chu *et al.* arrived at a conclusion that methyl radical is the dominant growth precursor.

However, in their experiments only methane and acetylene could be analyzed, and the concentration as well as the isotope ratio of methyl radicals — the critical data for their conclusion — were deduced through a series of highly-questionable assumptions. For example, one of the key assumptions is that "$^{13}C_2H_2$ and $^{12,13}C_2H_2$ remain in quasiequilibrium with $^{13}CH_3$ and $^{12}CH_3$ even though the latter species are *not* in equilibrium with $^{13}CH_4$ and $^{12}C_2H_2$, respectively" (18). Supposing that the kinetics and

thermodynamics of the $^{13}C$-labeled hydrocarbons is about the same as those of their nonlabeled analogs, as Chu *et al.* also accepted in their analysis, the assumption that $^{13}C_2H_2$ is in equilibrium with $^{13}CH_3$ and $^{12,13}C_2H_2$ in equilibrium with $^{13}CH_3$ and $^{12}CH_3$ is inconsistent with the assumption that $^{12}C_2H_2$ is not in the same state of equilibrium with $^{12}CH_3$.

Actually, it is very unlikely that an equilibrium between methyl radicals and acetylene molecules in the deposition zone is attained at all. This is exemplified in Fig. 2, which depicts the results obtained in detailed calculations performed for a typical hot-filament reactor (6). As can be seen in this figure, the products-to-reactants ratio for $CH_3 + CH_3 \leftrightarrows C_2H_2 + 2H_2$ is removed by about five orders of magnitude from the equilibrium.

Making a different assumption that methyl radicals are in partial equilibrium with methane molecules via reaction $CH_4 + H \leftrightarrows CH_3 + H_2$, leads to a conclusion that methyl radicals and acetylene molecules contribute about equally to the growth of diamond [see also Ref. (1)]. However, the above reaction is not exactly in the state of partial equilibrium at temperatures below about 1200 K (see Fig. 2), i.e., at the Chu *et al.*'s reaction temperatures.

Another viable possibility for isotope exchange in the system is through formation of $C_3H_X$ species, e.g.,

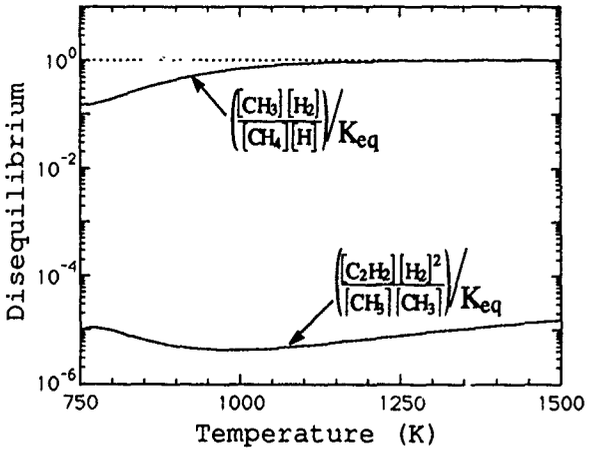



Figure 2. Disequilibrium ratios calculated for $CH_4 + H = CH_3 + H_2$ and $CH_3 + CH_3 = C_2H_2 + 2H_2$ at the conditions modeled in Ref. 6.

$$
\begin{array}{lcl}
{}^{13}CH_3 + {}^{12}C_2H_2 & \rightleftharpoons & {}^{13}CH_3\text{–}{}^{12}C{\equiv}{}^{12}CH + H \\
 & & \uparrow\downarrow \\
 & & {}^{13}CH_2{=}{}^{12}C{=}{}^{12}CH_2 \\
 & & \uparrow\downarrow \\
{}^{12,13}C_2H_2 + {}^{12}CH_3 & \rightleftharpoons & {}^{13}CH{\equiv}{}^{12}C\text{–}{}^{12}CH_3 + H\,.
\end{array}
$$

Assuming partial equilibrium and neglecting the isotope effect on the reaction rates, the concentrations of the methyl and acetylene isotopes can be related by

$$2[{}^{13}CH_3]\,[{}^{12}C_2H_2] \;=\; [{}^{12}CH_3]\,[{}^{12,13}C_2H_2]\,, \tag{9}$$

where the factor of 2 on the left-hand side of Eq. (9) appears due to the symmetry of H–$^{12}$C≡$^{12}$C–H versus the lack of such for H–$^{12}$C≡$^{13}$C–H. Analogously, for reactions between $^{12}CH_3$ and $^{13}C_2H_2$, the following relationship is derived

$$2[{}^{12}CH_3]\,[{}^{13}C_2H_2] \;=\; [{}^{13}CH_3]\,[{}^{12,13}C_2H_2]\,. \tag{10}$$

From Eqs. (9) and (10), we obtain

$$[{}^{12,13}C_2H_2] \;=\; 2\sqrt{[{}^{12}C_2H_2]\,[{}^{13}C_2H_2]} \tag{11}$$

and

$$\frac{[{}^{13}CH_3]}{[{}^{12}CH_3]} \;=\; \sqrt{[{}^{13}C_2H_2]/[{}^{12}C_2H_2]}\,. \tag{12}$$

Upon substitution of the experimental values from Ref. 18 of 0.53 and 0.18 for the fractions of $^{12}C_2H_2$ and $^{13}C_2H_2$ in the gaseous acetylene molecules, respecuvely, the fraction of $^{13}CH_3$ in the methyl radicals, is calculated by Eq. (12) equal to 0.37. This would imply that the $^{13}$C fraction of methyl radicals is about the same as the $^{13}$C fraction of the acetylene molecules, 0.32 – 0.35, and both being lower than the fraction of $^{13}$C in the deposited film, 0.50–0.51. A possible explanation of this difference may be that the gas sampled by the probe does not have the same composition as the gas in the diamond deposition zone. However, the fraction of $^{12,13}C_2H_2$ calculated according to Eq. (11) results in a value of 0.62, much higher than its experimental counterpart, 0.29, which indicates that the partial equilibria expressed by Eqs. (9) and (10) are not attained.

It is thus demonstrated that the data collected by Chu *et al.* (18) on isotope ratios of methyl radicals, acetylene molecules, and diamond films are inconclusive without direct measurements of the isotope composition of $CH_3$.

## Theoretical and computational arguments

Our detailed-kinetic (6) and quantum-chemical analyses (19) indicated that the main growth under the conditions typical of diamond hot-filament and plasma reactors is dominated by the addition of acetylene molecules to surface radical sites, created by the H-abstraction on microscopic surface steps, kinks and ledges The growth by other species — methyl, ethyl, ethylene and vinyl — was computed to be much slower.

"Common-sense" arguments that adding one carbon at a time or that the growth species must be radical in nature have been refuted by the results of a quantum-chemical study (19) showing that diamond growth by the addition reaction of acetylene, a nonradical species with two carbon atoms, is favorable on energetic grounds. This result was confirmed by Mehandru and Anderson (20). Another frequently expressed opinion is that the growth of (111) diamond can be explained by one or two carbon-atom species but the growth of (100) diamond can be accommodated only by a one-carbon-atom species. It should be noted however, that both surfaces are not smooth on the atomic scale, and therefore their growth can be envisioned by either growth species. In other words, the morphology of diamond films alone cannot serve as an indicator of the precise nature of the growth species.

A counter-argument against the acetylene hypothesis was recently expressed by Harris (21), who argues that the energetic advantage of the acetylene-addition reaction step is counterbalanced by the decrease in entropy, making the reverse direction — decomposition of the surface complex forming during the reaction — more favorable at temperatures of diamond growth. His argument is founded on the principle of detailed balancing, which states that the ratio of the forward and reverse rate coefficients is equal to the equilibrium constant. The latter was estimated based on ideal-gas-law and ideal-mixture assumptions. However, it is not clear to what extent the principle of detailed balancing can be applicable to a chemically-activated gas-surface reaction as a whole, and whether acetylene activity, the actual property required in the calculation of the equilibrium constant for the acetylene-addition reaction, can be replaced by the partial pressure of acetylene in the gas phase. Although the answers to these questions cannot be given at the present state of knowledge, there is an evidence supporting our hypothesis: assuming the change in the Gibbs free energy at 1200 K equal 1.1 kcal/mol, as estimated by Harris (21), we calculate that (111) diamond should be *etched* with the rate of 80 μm/h! This clearly disagrees with available experimental facts, thus indicating that the reverse rate of our proposed acetylene addition should be much lower than the rate suggested by Harris.

As an alternative, Harris (22) proposed a $CH_3$-based mechanism, and most recently Goodwin (23) reported that this mechanism can quantitatively account for diamond growth rate in hot-filament, flame and arcjet environments. However, as discussed earlier in the text, any methyl or acetylene based reaction mechanism would be capable of

similar predictions upon appropriate choice of rate parameters, and certainly calculations with only one of the possible mechanisms does not prove its dominance or uniqueness.

Furthermore, the numerical predictions of the Harris' mechanism may be lower than reported. The reaction rate formalism and the rate coefficient values of Ref. 22 (and used also in Ref. 23) are those of the *gas-phase* reaction kinetics. We recalculated these rate coefficients, following the formalism that expresses the postulate of the chemical similarity, i.e., using Eq. (5) in Ref. (6) [see (24)]. Simulating then diamond growth for the conditions of a hot-filament reactor with the Harris' mechanism but using the recalculated rate coefficients and treating the growth kinetics by a Monte Carlo algorithm which properly accounts for the formation frequency of adjacent surface radical sites, the growth rate of diamond was calculated to be 0.01 μm/h, in contrast to the experimental values of 0.1 to 1.0 μm/h. Taking into account the repulsion between methyl groups should lower the calculated value further, by one to two orders of magnitude.

## CONCLUDING REMARKS

Summarizing the above discussion, not only that there is presently no evidence disproving the acetylene hypothesis, but there is also no evidence to claim that methyl radical is a more efficient growth species than acetylene. At the same time, the results of theoretical and modeling studies comparing the two growth species on similar grounds favor acetylene. It does not however imply that methyl radicals do not or cannot play a role in diamond CVD. On the contrary, the reaction sequence comprised of addition of $CH_3$ to a surface radical, abstraction of an H atom from this chemisorbed $CH_3$, and addition of $C_2H_2$ to the radical formed was suggested by us (8) to be a likely nucleation step in homoepitaxial diamond deposition. Subsequent kinetic analysis (6) showed that this process is the second fastest under typical hot-filament deposition conditions, being slower than the acetylene-addition reaction by merely one to two orders of magnitude. This means that the presence of some amount of $CH_3$ is *necessary* for epitaxial growth of diamond, and if the $CH_3$-to-$C_2H_2$ concentration ratio is substantially increased, as probably achieved in the experiments of Martin and Hill (17) and Chu *et al.* (18), the growth by $CH_3$-driven reactions may become more prominent. Obviously, when other reactive chemical species are present in substantial concentrations, such as C atoms in arcjet reactors [see e.g. (23)], they may contribute to and even dominate the growth of diamond.

***Acknowledgements.*** *The computations were performed using the facilities of the Pennsylvania State University Center for Academic Computing. The work was supported in part by Innovative Science and Technology Program of the Strategic Defence Initiative Organization (SDIO/IST) via the U.S. Office of Naval Research, under Contract No. N00014-86-K-0443. The author thanks David Goodwin and Mark D'Evelyn for providing their manuscripts prior to publication.*

## REFERENCES


1. M. Frenklach, "Theory and models for nucleation and growth of diamond films," in *Diamond and Diamond-Like Films and Coatings*, J. C. Angus, R. E. Clausing, L. L. Horton, and P. Koidl, Eds., Plenum, in press.
2. D. V. Fedoseev, B. V. Deryagin, I. G. Varshavskaya, and A. S. Semenova-Tyan-Shanskaya, *Surf. Coatings Technol.* **38**, 1 (1989).
3. J. C. Angus and C. C. Hayman, *Science* **241**, 913 (1988).
4. B. V. Spitsyn, L. L. Bouilov and B. V. Derjaguin, *Prog. Crystal Growth and Charact.* **17**, 79 (1988).
5. M. Frenklach, *J. Appl. Phys.* **65**, 5142 (1989).
6. M. Frenklach and H. Wang, *Phys. Rev. B.* **43**, 1520 (1991).
7. M. Frenklach, M., in *Carbon in the Galaxy: Studies from Earth and Space*, edited by J. Tarter, S. Cheng, and D. J. DeFrees (NASA Conference Publication 3061, Moffett, CA, 1990), p. 259.
8. M. Frenklach and K.E. Spear, *J. Mater. Res.* **3**, 133 (1988).
9. D.W. Brenner, B. I. Dunlap, J. W. Mintmire, R. C. Mowrey and C. T. White, "Molecular-dynamics simulations of the reaction of atomic hydrogen with diamond surfaces," Proceedings of the Second International Conference on the New Diamond Science and Technology, in press.
10. There is an error in the first sentence on p. 1539 of Ref. 6; it should say that "at low methane concentrations, the decrease in the H concentration leads to an increase in the [production rate] of $C_d$ surface sites ..." The number density of $C_d$ is actually decreasing following the decrease in the number density of the available $C_dH$ sites.
11. H. Wang and M. Frenklach, "Analysis of cyclic deposition of diamond," to be published.
12. M. Frenklach, *Combust. Sci. Technol.* **74**, 283 (1990).
13. M. Frenklach, R. Kematick, D. Huang, W. Howard, K. E. Spear, A. W. Phelps, and R. Koba, *J. Appl. Phys.* **66**, 395 (1989).
14. D.E. Patterson, B. J. Bai, C. J. Chu, R. H. Hauge, and J. L. Margrave, "Halogen-assisted chemical vapor deposition of diamond," Proceedings of the Second International Conference on the New Diamond Science and Technology, in press.
15. W.B. DeMore, S. P. Sander, D. M. Golden, M. J. Molina, R. F. Hampton, M. J. Kurylo, C. J. Howard, and A. R. Ravishankara, *Chemical Kinetics and Photochemical Data for Use in Stratospheric Modeling*, NASA JPL Publication 90–1, 1990.
16. M. J. Rabinowitz, J. W. Sutherland, P. M. Patterson, and R. B. Klemm, *J. Phys. Chem.* **95**, 674 (1991).
17. L.R. Martin and M.W. Hill, *Appl. Phys. Lett.* **55**, 2248 (1989); S.J. Harris and L. R. Martin, *J. Mater. Res.* **5**, 2313 (1990).
18. C. J. Chu, M. P. D'Evelyn, R. H. Hauge, and J. L. Margrave, *J. Mater. Res.* **5**, 2405 (1990); "Mechanism of diamond growth by chemical vapor deposition on diamond (100), (111), and (110) surfaces: carbon-13 studies," *J. Appl. Phys.*, submitted.
19. D. Huang, M. Frenklach, and M. Maroncelli, *J. Phys. Chem.* **92**, 6379 (1988); D. Huang and M. Frenklach, *J. Phys. Chem.* **95**, 3692 (1991).
20. S. P. Mehandru and A. B. Anderson, *J. Mater. Res.* **5**, 2286 (1990).
21. S. J. Harris, personal communication, 1990.
22. S. J. Harris, *Appl. Phys. Lett.* **56**, 2298 (1990).
23. D.G. Goodwin, "Simulations of high-rate diamond synthesis: methyl as growth species," *Appl. Phys. Lett.*, submitted.
24. There is a typographical error in Eqs. (5) and (6) of Ref. 6: it should be $m_g/m_p$, not $m_p/m_g$, in the denominators of these equations.

# MOLECULAR BEAM EPITAXY OF DIAMOND WITH CARBON ATOMS $^1D$: A THEORETICAL EXPERIMENT BASED ON QUANTUM CHEMISTRY

M. Tsuda, S. Oikawa, C. Sekine, and S. Furukawa

Laboratory of Physical Chemistry
Faculty of Pharmaceutical Sciences
Chiba University
Chiba 260, JAPAN

A mechanism of the diamond synthesis in hydrocarbon plasmas were investigated in the case where carbon atoms in the lowest singlet state $^1D$ are the reactive species and the epitaxial growth takes place on the (001) surfaces. The results obtained are as follows: (i) Two types of the $S_B$ step are generated in the $S_B$ step growth; i.e., the $S_B$ step type I and $S_B$ step type II. ii) The $S_B$ step growth is the dimer row growth. The dimer row on the (001) surface grows independently. This situation explains the ragged line of the $S_B$ step. iii) The $S_A$ step growth is a complex process. It is initiated by the nucleation at the $S_A$ step edge and followed by the dimer row propagation. iv) The nucleus is a dimer which has the reactivity like a $\sigma$-type dangling bond which propagates a dimer row to the both sides of the nucleus along the $S_A$ step edge. This situation explains the straight line of the $S_A$ step. v) The propagation process of the dimer row in the $S_A$ step growth follows exactly the same mechanism as the $S_B$ step growth does.

## 1. Introduction

There is no report on the experiment of molecular beam epitaxy(MBE) of diamond. However, an imaginary experiment on MBE of diamond by means of the method of quantum chemistry is able to be carried out prior to a real experiment since Schrödinger equation is written even on imaginary materials and imaginary reaction systems. Such a research as presented here will give theoretical predictions of results which may be obtained by real experiments.

In this paper, elementary processes of MBE of diamond with carbon atoms in the lowest singlet state $^1D$ were investigated on reconstructed (001) surfaces. There is an intimate relationship between this theoretical research and real experiments of homoepitaxial growth of diamond crystals by chemical vapor depositions (CVD) in the following points. One is that carbon atoms in the lowest singlet state $^1D$ may be produced by decompositions of $CH_4$ molecules in $CH_4$ plasmas, which are used for diamond syntheses, in the the similar manner that $Si(^1D)$ atoms are generated in $SiH_4$ plasmas which has been proved already [1, 2]. A carbon atom in the lowest singlet state $^1D$ may have a long life time as observed in the case of $Si(^1D)$[2] or *ortho*-He($^3$He), although the ground state of a carbon atom is the triplet one. Another point is that the (2×1) reconstructed structures were observed by the scanning tunneling microscope(STM) experiments on (001) surfaces of diamond crystals produced in $CH_4$ plasmas. The two types of steps, $S_A$ and $S_B$ named by Chadi on reconstructed Si(001) surfaces[11] were clearly observed on the diamond(001) surfaces[3].

There are many reactive species which are the candidates of the ultimate species for the diamond crystal growth in $CH_4$ plasmas; i.e. $^2CH_3$, $^1CH_2$, $^3CH_2$, $^2CH$, $^4CH$, $C(^1D)$, $C(^3P)$. These neutral species are important than the ionic, the excited or the secondary generated species because of their higher concentrations. Since the real mechanism of diamond formations in CVD processes is not established yet, all the possibilities must be investigated on these reactive species. The author have proposed a diamond formation mechanism where a methyl radical $\cdot CH_3$ contributes as the ultimate species to the epitaxial growth of diamond[4, 5]. However, this mechanism does not exclude another mechanism where other reactive species than a methyl radical serves as the ultimate species.

In this paper, we tried to construct one of other diamond formation mechanisms where the ultimate species is $C(^1D)$ atoms. Successful results were obtained and will be described here.

## 2. Method

The Schrödinger equation on a reaction system was solved by ab initio molecular orbital(MO) method[6]. On large reaction systems, a semiempirical MO method with MNDO approximation[7] was used. Chemical structures were determined by the full optimization at minima and maxima of the potential energy hypersurface of a reaction system[8]. The potential energy values were elabolated by the method of configuration interactions(CI) or the Moeller-Plesset perturbation theory[6].

In the calculations of large reaction systems, all the underlayer atoms are fixed in order to take account of the characteristic of the crystal. The carbon atoms which is expressed by an open circle also fixed in the same reason, eve.. when they occupy the utmost surface.

## 3. The Structure of (001) Surfaces of Diamond Crystals

### 3.1. Model Molecular System

Fig. 1 represents the unreconstructed diamond(001)-(1×1) surface whose bond distances and bond angles are postulated identical with those of the inner structures of diamond crystals. No one knows whether the growing surface of diamond crystals in hydrocarbon plasmas at 800°C is bared or terminated with hydrogen which forms C-H bonds. We postulated bared (001) surfaces in this research because the theoretical experiment on MBE of diamond crystals has to be discussed here. In order to describe the reconstruction process of diamond(001) surface, we must take notice of the two top C atoms denoted as solid spheres in Fig. 1. The first, second and third underlayers also have to be considered. For these reasons, the construction of the smallest model molecular system for ab initio calculations was performed in the following way: i.e., the C atoms designated by the solid spheres in Fig. 1 were remained and those of the open spheres were replaced by hydrogen atoms. Consequently, a $C_9H_{12}$ model was obtained as shown in Fig. 2(a).

### 3. 2. The Reconstructed Structure of Diamond(001) Surfaces

Starting from the (1×1) structure, the potential energy of the model molecular system(Fig. 2(a)) in the lowest electronic singlet state was minimized at the Hartree-Fock level. The fully optimized structure obtained at the minimum of the potential energy hypersurface in the lowest singlet state of the model reaction system was shown in Fig.

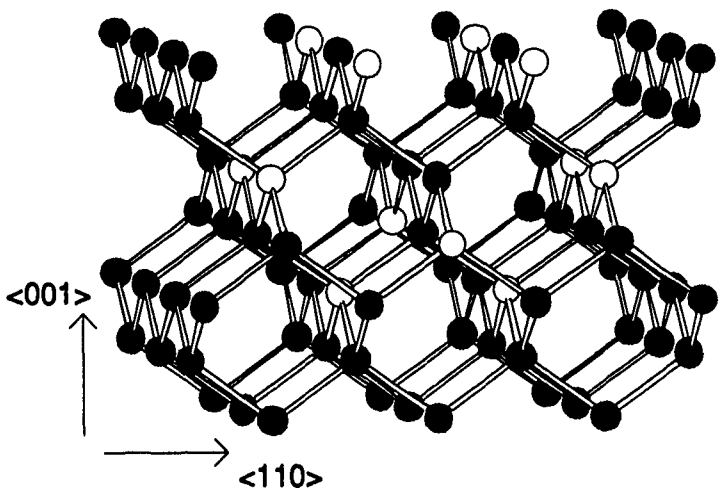



Fig. 1. Unreconstructed diamond (001)-(1×1) surface.

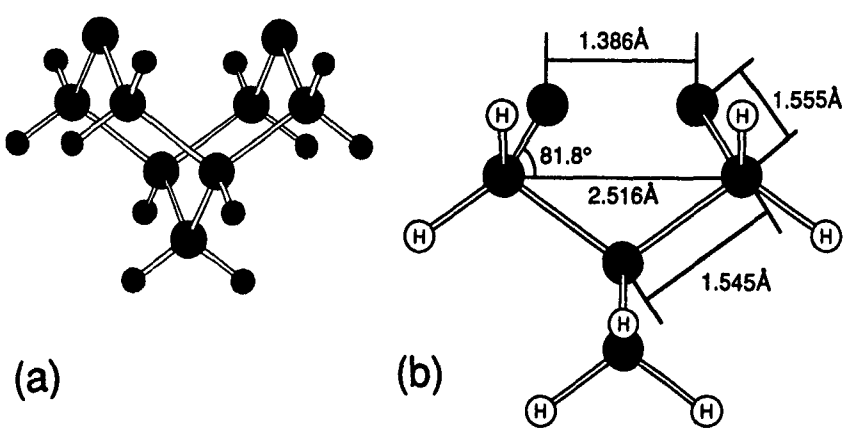



Fig. 2. A model molecular system for ab initio calculations. (a) the intial (1×1) structure, (b) the optimized strucure.

2(b). The $C_1$-$C_2$ distance which was 2.185Å in the (1×1) structure(Fig. 2(a)) became 1.386Å in Fig. 2(b) which shows formations of the reconstructed (2×1) dimer structures. The dimer produced is symmetric and not buckled.

This result is very similar to the case of Si(001) surfaces reported in the previous paper[9]. The (2×1) symmetric dimer structures of reconstructed Si(001) surfaces are well established by STM experiments[10]. Quite recently, the (2×1) symmetric dimer structure was observed by STM experiments on (001) surfaces of diamond crystals produced in $CH_4$ plasmas[3]. This experiment supports the theoretical results presented here. As mentioned in section 1., the STM image of diamond(001) surfaces clearly shows the two kinds of steps, $S_A$ and $S_B$, which are always observed on Si(001) surfaces.

## 4. The $S_B$ Step Growth on (001) Surfaces of Diamond Crystals with Carbon ($^1D$) Atoms

### 4.1. The Steps of (001) Surfaces of Diamond

From the theoretical result on the reconstructed (001) surfaces of diamond crystals shown in section 3 as well as the STM experiment on the Si (001) [10], we can imagine the structures of (001) surfaces of diamond where homoepitaxial growth takes place in hydrocarbon plasmas. A sketch of the imagined (001) surface of diamond crystals are drawn in Fig. 3. The structure is identical with Si(001) surfaces in the meaning that the two kinds of steps, $S_A$ and $S_B$, exist there. The dimerization direction of the (2×1) structure on an upper terrace near a step is normal to the step edge in the $S_A$ step and parallel in the $S_B$ step, respectively, as shown in Fig. 3. In the STM image of Si (001) surfaces, the $S_A$ step stands in a straight line but the $S_B$ step has a ragged edge [3]. This fact means that each of the dimer rows grows independently at the $S_B$ steps. For this reason, the $S_B$ step growth will be elucidated if the elementary growth process of a single dimer row could be clarified.

The $S_A$ step growth was found to begin with a nucleation on the lower terrace at the $S_A$ step edge as shown later. Once a nucleus has been formed at the $S_A$ step edge, the same structure as the $S_B$ step type I (see section 4.3.) is generated at both sides of the nucleus as shown in Fig. 8(II). Then, a dimer row growth starts from the nucleus along the $S_A$ step edge in the same mechanism that operates in the $S_B$ step growth (see sections 4.3 and 4.4 for the $S_B$ step growth). This dimer row formation is corresponding to one step growth of the $S_A$ step. In other words, the $S_A$ step growth is a complex process, i.e., a nucleation followed by a dimer row growth whose propagating direction is normal to the direction of the $S_A$ step growth as shown in details in section 5 and 6. Therefore, the elementary processes of the $S_A$ step growth are identical with those of the $S_B$ step growth except its initial process for the nucleation. Consequently, the $S_B$ step growth was investigated in details at first in terms of the elementary process in this paper.

### 4.2. A Model Reaction System for the $S_B$ Step

A model reaction system which represents the $S_B$ step on diamond(001) surfaces, the large model, was constructed by replacements of the carbon atoms shown by open circles at the $S_B$ step in Fig. 3 with hydrogen atoms. The constructed model reaction system was shown in Fig. 4(a).

### 4.3. The $S_B$ Step Structures Appearing during the Epitaxial Growth

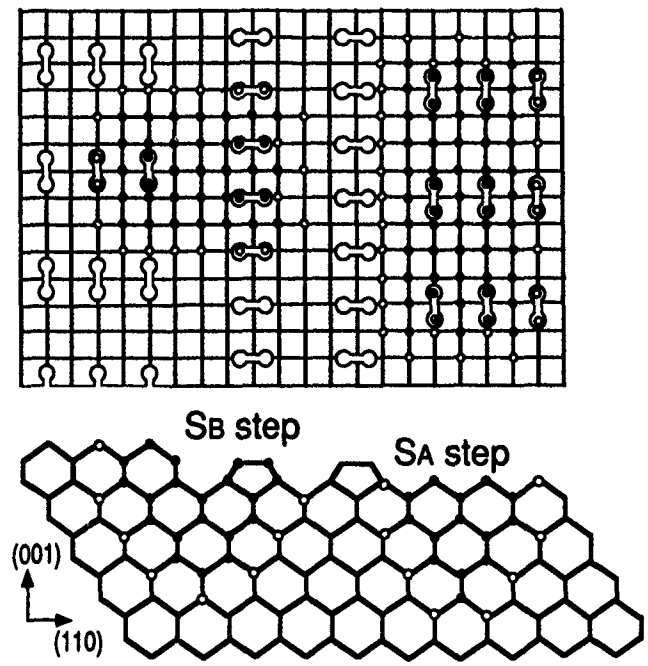



Fig. 3. $S_A$ and $S_B$ steps of (001) surfaces. Model molecular systems for the $S_B$ and $S_A$ steps are constructed by the replacement of the open circles with hydrogen atoms. The lower figure shows the top view and the upper one is the side view.

Table I. State functions of C atom by full CI calculation with 3-21G+ [a,b]

| | |
|---|---|
| $^1D$ | $\Psi_1$=0.75(222000000)–0.37(220200000)–0.37(220020000)+0.23(221000100)+... |
| | $\Psi_2$=0.65(220020000)–0.65(220200000)–0.20(220010001)+0.20(220100010)+... |
| | $\Psi_3$=0.92(220110000)+0.20(220010010)–0.20(220100001)–0.16(210111000)+... |
| | $\Psi_4$=0.92(221010000)+0.20(221000001)–0.20(220010100)–0.16(211011000)+... |
| | $\Psi_5$=0.92(221100000)+0.20(220100100)–0.20(221000010)–0.16(211101000)+... |
| $^1S$ | $\Psi_6$=0.51(222000000)+0.51(220200000)+0.51(220020000) |
| | +0.20(221000100)+0.20(220100010)+0.20(220010001)+... |

a) (222000000), (221000100), etc. are the electronic configuration functions of C atom. The numerals in parentheses are the occupation number of electron in each AO, 1s, 2s, 2px, 2py, 2pz, 3s, 3px, 3py, and 3pz in this order, where 3s and 3p AOs are Rydberg ones.

b) Contributions from the other configurations are small (less than 1%).

The structures of the $S_B$ step generated during the process of a dimer row growth were shown in Fig. 4. The atomic distance between the neighboring carbon atoms of the utmost diamond(001) surfaces changes from 2.522Å at the initial (1×1) structure, to ~1.5Å at the (2×1) structure after the dimer formation. With careful examination of Fig. 4, we can find that there are two types of $S_B$ steps on diamond (001) surfaces; i.e., (a) and (c) belong to the same type of $S_B$ steps but (b) to another different type. At these $S_B$ steps, the dimers belonging to the utmost surfaces are on the same position as the crystal lattice for both cases of (a) and (c), but the position of the dimers for the case(b) is slid to the right hand side from the crystal lattice. Hereafter, we call the $S_B$ step type I and the type II for the former and the latter, respectively.

4.4. Elementary Process of the $S_B$ Step Growth

The electronic state functions for a carbon($^1$D) atom were calculated, because the elementary process of the $S_B$ step growth by diamond($^1$D) atoms generated from the decomposition is investigated in this research. The five state functions representing the $^1$D state have the same forms as the d atomic orbitals of H atom (Table 1). The spatial distributions of the square values of the highest occupied MO(HOMO) and the lowest unoccupied MO(LUMO) as well as the second HOMO are shown in Fig. 5 on the structure(a) of Fig. 4. The MO energies of the HOMO and the second HOMO are substantially degenerated. It is well known that HOMO and LUMO control an initial stage of chemical reactions significantly[7]. In Fig. 5, the HOMO is localized at the dimer part of the lower terrace next to the $S_B$ step, but the second HOMO and the LUMO are localized at the $S_B$ step edge of the upper terrace. It should be noted that the LUMO and the second HOMO have the spatial distribution very similar to a σ-type dangling bond at the step edge. A carbon($^1$D) atom interacts with the LUMO or the second HOMO at the initial stage of the growth reaction at the $S_B$ step. The carbon atom makes a bridge between the carbon atom having the LUMO as well as the second HOMO and the other carbon atom of the dimer which is next to the $S_B$ step and belongs to the lower terrace (the first carbon bridge formation; Fig. 6). This situation corresponds to the reaction of a so-called dangling bond at the step edge with a carbon ($^1$D) atom. The dimer row propagates one dimer at the $S_B$ step edge as is shown in Fig. 4(b) immediately after the second carbon bridge was formed at the neighbor position in the same way as the first carbon bridge (Fig. 6).

The potential energy stabilization following this $S_B$ step growth (a)→(b) is 13.66eV (Fig. 7). It should be noted that the two dimers at the lower terrace in the structure(a) hold their dimer characters considerably even after the structure(b) has been formed; i.e., the bond length of 1.436Å in the dimer of structure(a) changed to 1.730Å in the structure(b). This lengthening of the dimer bond distance means the unstabilization of the dimer. But, one should remember that this bond length of 1.730Å is very short, when comparing it with 2.522Å of (1×1) structure of diamond(001) surfaces. Because of holding a dimer structure at the lower terrace, the position of the dimer newly produced at the $S_B$ step edge in the structure(b) moves to the direction of the right hand side from the corresponding crystal lattice.

The next $S_B$ step growth occurs when two carbon($^1$D) atoms insert to the unstabilized dimers at the lower terrace in the structure(b). In this way, the dimer row propagates one more dimer at the $S_B$ step edge as shown in Fig. 3(c). The potential energy stabilization by this step growth (b)→(c) is 20.60eV and larger than the step growth (a)→(b), as shown

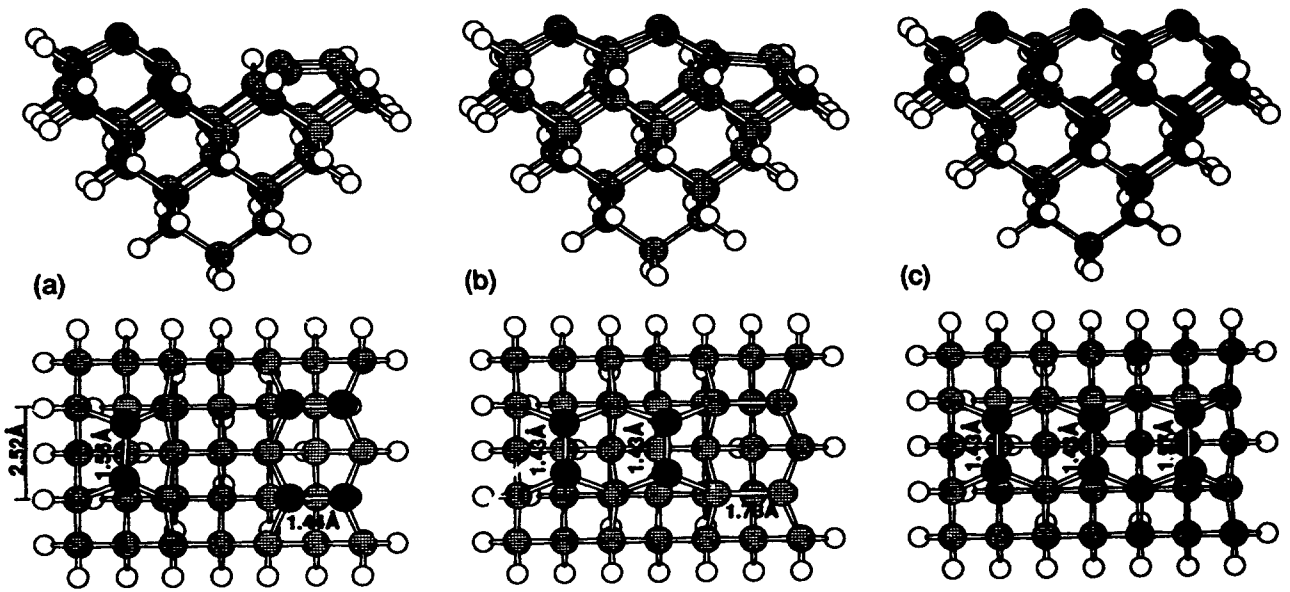



Fig. 4. The structual changes following the $S_B$ step growth, (a)→(b)→(c).

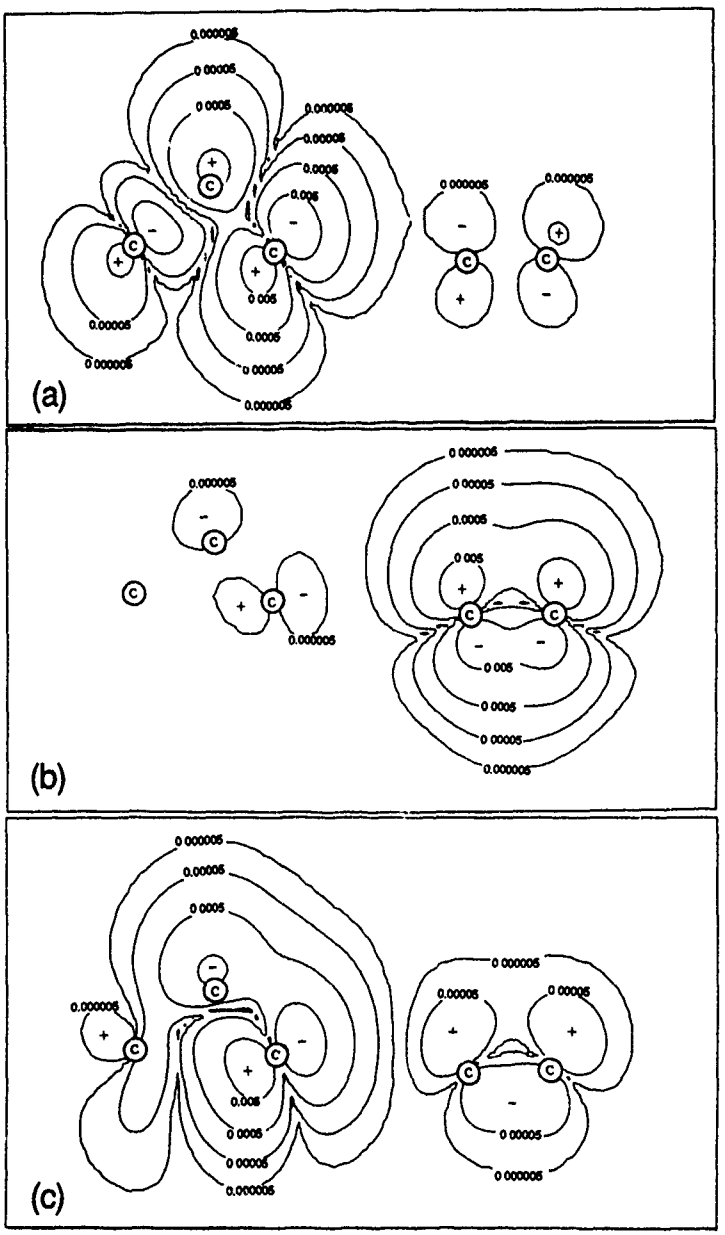



Fig. 5. The spatial distributions of molecular orbitals of the structure (a) in Fig. 4. (a) LUMO, (b) HOMO, (c) the second HOMO.

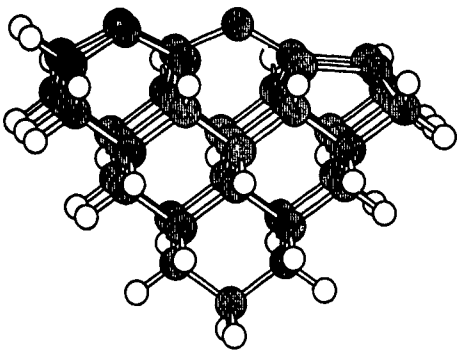


Fig. 6. The first carbon bridge formation in the elementary process of the $S_B$ step growth.

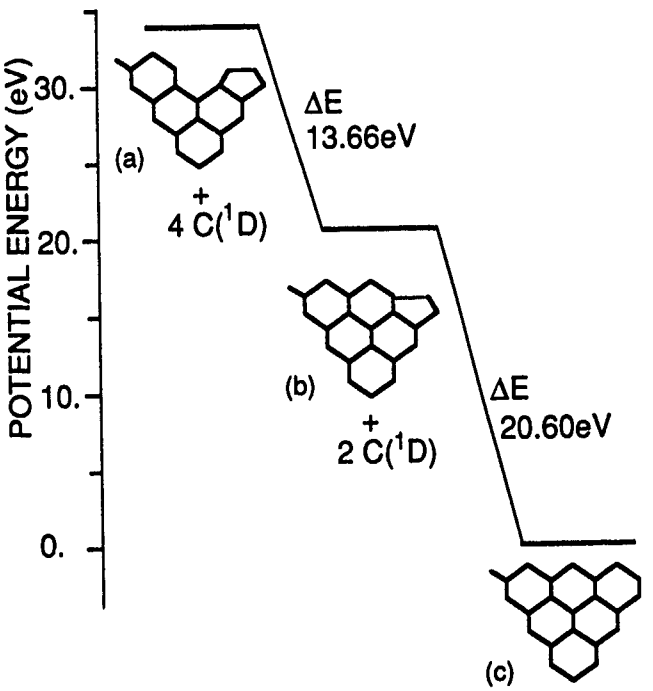



Fig. 7. The potential energy stabilization following the $S_B$ step growth.

in Fig. 7. Remember that the structure(c) and the structure(a) belong to the same type(type I) as mentioned in section 4.3.

It is concluded that the $S_B$ step growth by carbon($^1D$) atoms on diamond (001) surfaces takes place by repeat of a series of reactions (a)→(b)→(c) in Fig. 4, or by the alternative dimer formations at the type I and the type II of $S_B$ steps.

## 5. The Nucleation with Carbon($^1D$) Atoms on Diamond(001) Surfaces

### 5.1. A Model Reaction System for the $S_A$ Step

A model reaction system which represents the $S_A$ step on the diamond (001) surfaces, the large model, was constructed by replacements of the carbon atoms shown by open circles with hydrogen atoms at a $S_A$ step in Fig. 3. The constructed model reaction system was shown in Fig. 8(I).

### 5.2. Elementary Porcess of the Nucleation at the $S_A$ Step

The nucleation process at the $S_A$ step initiates as a dimer formation on the model reaction system of Fig. 8(I). The dimer is successfully produced at the center of the reaction system (Fig. 8(II)) as the minimum of the potential energy hypersurface of the system. The structure of the newly produced dimer in Fig. 8(II) is very similar to that of the dimer at the $S_B$ step edge in Fig. 3(a); i.e., these dimers have the same bond distance 1.559A.

The spatial distributions of the HOMO and the LUMO of the newly generated dimer of Fig. 8(II) are very similar to each other (Fig. 9). They look like σ-type dangling bonds standing at both sides of the dimer. This spatial distribution like a σ-type dangling bond of the LUMO and the second HOMO of the structure in Fig. 4(a) contribute to the $S_B$ step growth as presented in section 4.4. For these reasons, we can consider that the newly formed dimer at the central part of the reaction system in Fig. 8(II) is the nucleus which serves as the $S_B$ step type I. The spatial distributions of the HOMO and the LUMO in Fig. 9 indicate that the $S_B$ step type I of a dimer row is generated at the both sides of the nucleus. Therefore, the dimer row growth, which takes place at the $S_B$ step edge investigated in section 4, starts from the nucleus along the $S_A$ step edge to both sides as shown in section 6. This is the mechanism of the $S_A$ step growth.

The potential energy stabilization following the nucleation process is 13.81eV (Fig. 10) which is very similar to the stabilization energy 13.66eV obtained in the growth of $S_B$ step type I, but smaller than the mean value (17.13eV) of the stabilization energies generated in the successive growths of $S_B$ step type I and type II (Fig. 6).

## 6. The $S_A$ Step Growth on (001) Surfaces of Diamond with Carbon ($^1D$) Atoms

### 6.1. The $S_A$ Step Structures Appearing during the Epitaxial Growth

In the model reaction system of Fig. 8(I), the bond lengths of the dimers of the top layer have substantially the same value althoughs the center dimers are 0.004Å shorter than others. The value of 1.436Å is the same one that appeared in the dimers on the lower terrace at the $S_B$ step type I in Fig. 4(a). The nucleus produced on the center dimers of the reaction system is a dimer whose bond length is 1.559Å (Fig. 8(II)). This bond length is the same value as that in the $S_B$ step type I of Fig. 4 (a).

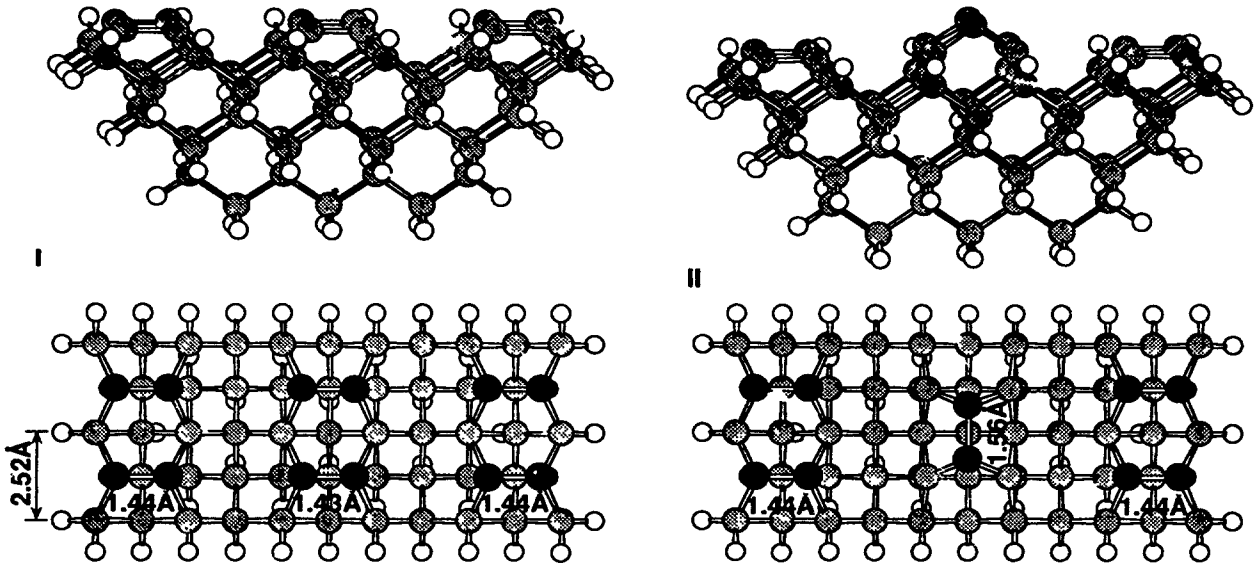



Fig. 8. The structual changes following the $S_A$ step growth.

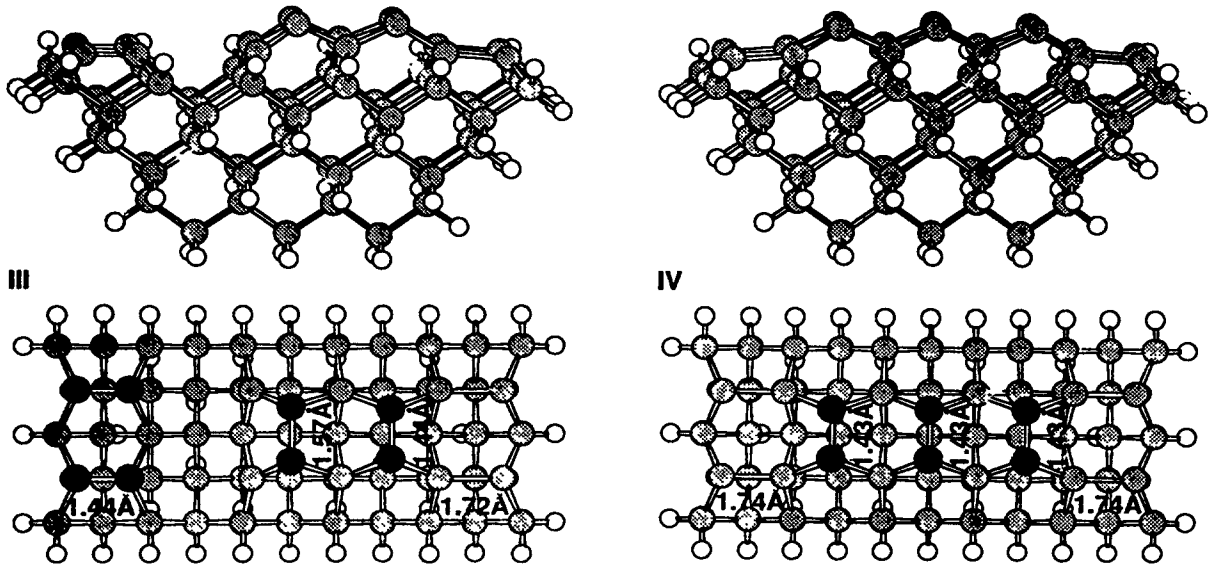



Fig. 8. (Continued)

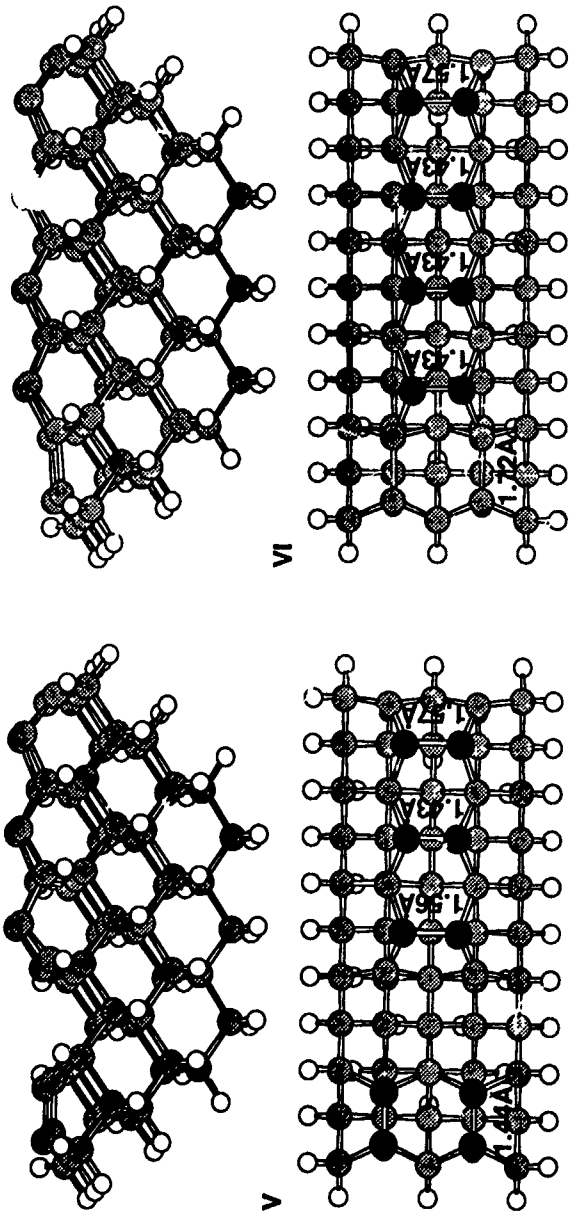



Fig. 8. (Continued)

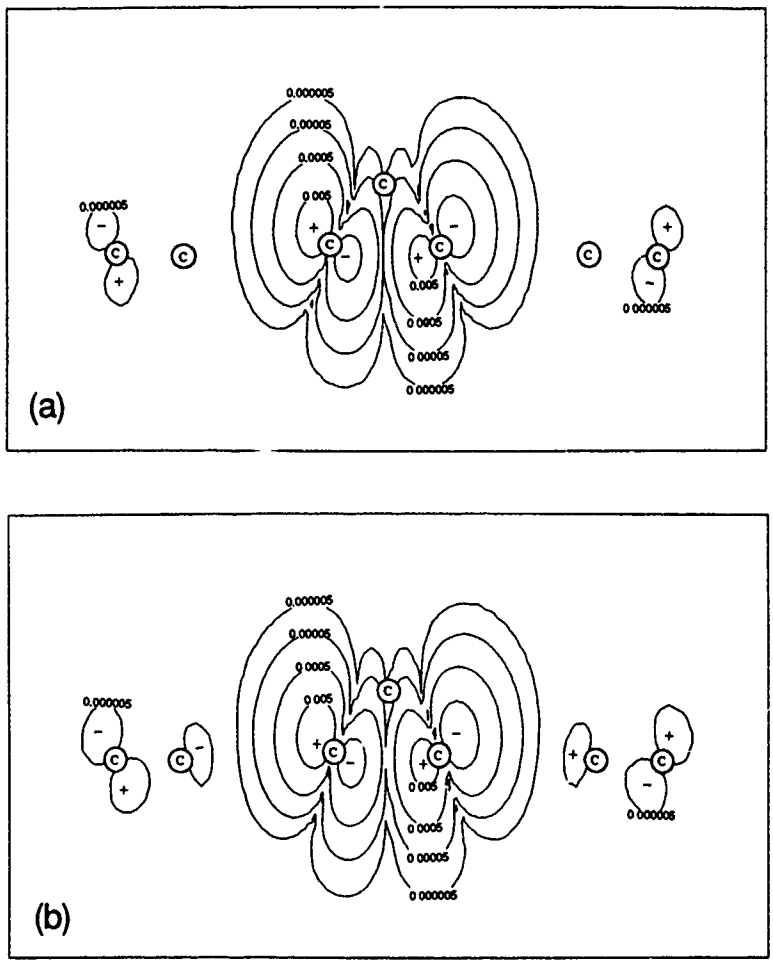



Fig. 9. The spatial distributions of molecular orbitals of the structure I in Fig. 8. (a) LUMO, (b) HOMO

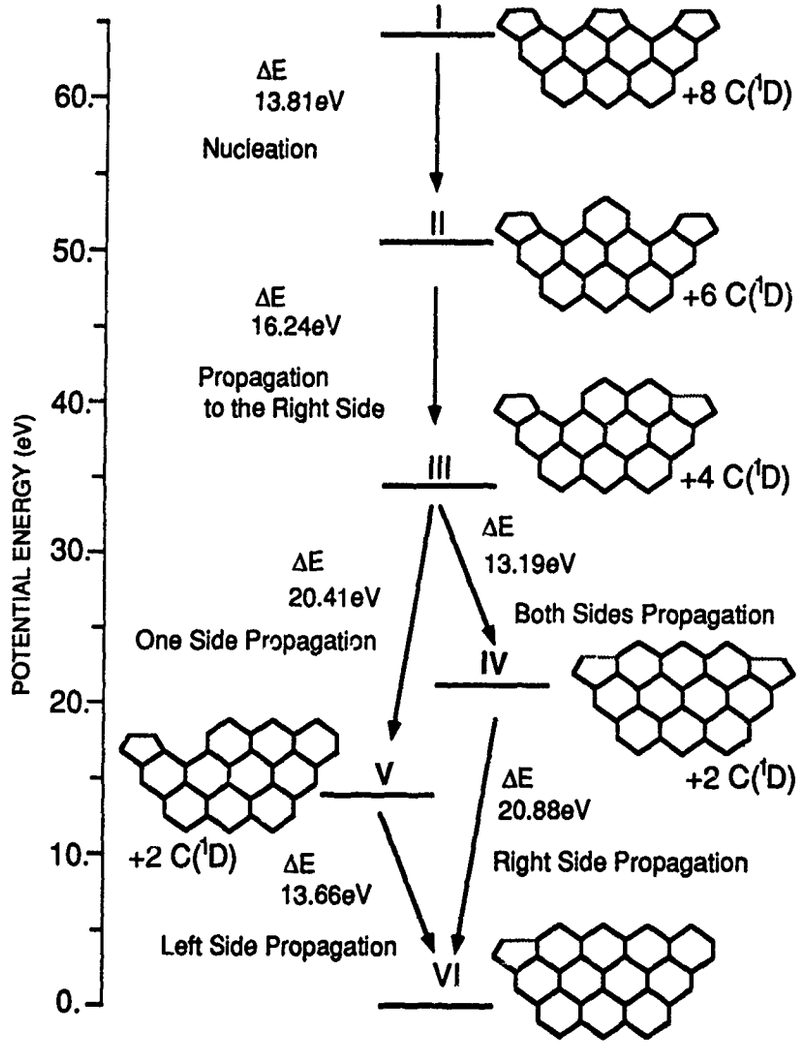



Fig. 10. The potential energy stabilization following the $S_A$ step growth.

One step propagation from the nucleus generates the $S_B$ step type II as shown in Fig. 8(III). Here, we can find the characteristic of the $S_B$ step type II of Fig. 4(b) in the structures of the newly produced dimer and the dimers on the lower terrace. One more step propagation to the left hand side generates two step edges of the $S_B$ step type II as shown in Fig. 8(IV). The bond length of the dimer at the $S_B$ step type II is ~1.43Å and those of the dimers on the lower terrace is ~1.7Å. This rule is true in the structures of Fig. 8(III), (IV), (VI) as well as Fig. 4(b). The dimer of the $S_B$ step type I has a longer length (~1.56Å) than that (~1.43Å) of the $S_B$ step type II. This rule is verified in the structures of Fig. 8(II), (III), (V), and (VI) as well as Fig. 4(a) and (c).

6.2. Elementary Process of the Dimer Row Growth Starting from the Nucleus.

The first step of the dimer row growth starting from the nucleus is followed by the remarkable stabilization of the reaction system as shown in Fig. 10. The stabilization energy of 16.24eV is much larger than the usual $S_B$ step growth of type I (13.66eV in Figs. 7 and 10). This remarkable stabilization originates from the large displacement of the utmost layers from the crystal lattice as shown in Fig. 8(III). A strain energy arisen from keeping the crystal structure is relaxed in this structure. For this reason, the next propagation to the left side releases a small amount of energy (13.19eV; Fig. 10) where the crystal structure is recovered in the utmost layer (Fig. 8(IV))

The one side propagation in two steps to the right hand side from the nucleus (Fig. 10(V)) produces the real $S_B$ step type I of Fig. 4(a). The stabilization energy from the structure V to VI in Fig. 10 is 13.66eV which exactly equals the energy released in the growth of $S_B$ step type I (see Fig. 7). The bond lengths of the dimers corresponding to the $S_B$ step type I in the structure of Fig. 8(V) have also exactly the same value as that of the $S_B$ step type I in Fig. 4(a).

The both sides propagations from the nucleus produce two step edges of the $S_B$ step type II (IV in Fig. 10). One side propagation from the structure IV to VI generates the stabilization energy of 20.88eV which is slightly larger than the energy liberated in the growth of the $S_B$ step type II of Fig. 7(b). However, the growth of the $S_B$ step type II from the structure III to V in Fig. 10 generates smaller stabilization energy (20.41eV) which may be affected by the remarkable stabilization of 16.24eV in the formation of the structure III.

Acknowledgement

This work was supported by Grants-in Aid on Priority-Area Research on "Photo-Excited Process" from the Ministry of Educaiton, Science and Culture.

References

[1] M. Tsuda, S. Oikawa and K. Sato, J. Chem. Phys., **91** (1989) 6822
[2] M. Sakakibara, M. Hiramatsu and T. Goto, J. Appl. Phys., **69** (1991) in press
[3] T. Tsuno, T. Imai, Y. Nishibayashi, K. Hamada, and N. Fujimori, The 38th Spring Meeting of The Japan Society of Applied Physics, The Extended Abstracts, **2** (1991) 422
[4] M. Tsuda, M. Nakajima and S. Oikawa, J. Am. Chem. Soc., **108** (1986) 5780
[5] M. Tsuda, M. Nakajima and S. Oikawa, Jpn. J. Appl. Phys., **26** (1987) L527
[6] For example, A. Szabo and N.S. Ostlund, Modern Quantum Chemistry, Macmillan (1982)
[7] M. J. S. Dewar and W. Thiel, J. Am. Chem. Soc., **99** (1977) 1685
[8] J. A. Pople, Applications of Electronic Structure Theory, H. F. Schaefer III,et al., Plenum (1977)pp.1
[9] M. Tsuda, T. Hoshino, S. Oikawa, and I. Ohdomari, Phys. Rev. **B**, to be published.
[10] For example, R. J. Hammers, Phys. Rev. Lett., **59** (1987) 2071
[11] D. J. Chadi, Phys. Rev. Lett., **43** (1979) 43

# Growth from Acetylene on the Diamond (110) Surface

David N. Belton and Stephen J. Harris
Physical Chemistry Department, General Motors Research Labs
P.O. Box 9055, Warren, MI 48090-9055

## Abstract

We have proposed a detailed chemical kinetics mechanism for addition of $C_2H_2$ to a (110) diamond surface, which is the fastest-growing face. The model contains no adjustable parameters and is based on the hypothesis that diamond surface chemistry may be understood in analogy with gas phase hydrocarbon chemistry. We calculated a growth rate of 0.03 $\mu$m/hour, which gives approximate agreement with experiments suggesting we have a feasible mechanism for growth on (110) surfaces.

## Introduction

Recently, we proposed an approach for modeling and predicting the growth rate of diamond[1] which assumes that the chemistry of diamond surfaces is fundamentally similar to the very well-known chemistry of hydrocarbon molecules. We then proposed a simple chemical kinetics mechanism[1] with $CH_3$ as the growth species[2,3,4] which accurately predicts the growth rate[1] as well as its pressure- and composition-dependence[5] in filament-assisted CVD systems. In this paper we examine growth on the (110) diamond surface, which is the fastest-growing surface[6]. Sites with (110) character are also found at steps and kinks on other low index faces. Noting that there is now direct experimental evidence showing that diamond can be grown from acetylene[4], we analyze growth on the (110) surface with the assumption that $C_2H_2$ is the growth species. Huang, Frenklach, and Maroncelli (HFM) previously proposed[7] a different mechanism to describe the conversion of $C_2H_2$ to diamond, but our thermochemical analysis showed that the proposed HFM mechanism does not lead to diamond formation[8]. In this

work we propose a new mechanism which is consistent with the thermochemical principles observed with gas phase hydrocarbon chemistry and which can account for a significant fraction of diamond growth in cases where the $C_2H_2$ concentration is relatively high[4].

## Analysis

To construct a detailed kinetics mechanism that describes diamond growth we need a series of elementary reaction steps making up a mechanism, rate constants $k$ for each step in the mechanism, an estimate for the Gibbs free energy change $\Delta G$ for each reaction in the mechanism in order to calculate rate constants for reactions proceeding in reverse directions, and gas phase species concentrations.

**Table I**

| REACTION | $k_s$ | $\Delta G_{1200K}$ |
|---|---|---|
| 1. $H_4 + H_{(g)} \rightleftharpoons RH_3 + H_{2(g)}$ | $5.0 \times 10^{14} e^{-7300/RT}$ c | −20.1 |
| 2. $RH_3 + H_{(g)} \rightleftharpoons H_4$ | $1.0 \times 10^{13}$ | −53.1 |
| 3. $RH_3 + H_{(g)} \rightleftharpoons R_2H_2 + H_{2(g)}$ | $1.3 \times 10^{14} e^{-7300/RT}$ | −15.7 |
| 4. $R_2H_2 + H_{(g)} \rightleftharpoons RH_3$ | $2 \times 10^{13}$ | −58.1 |
| 5. $R_2H_2 + C_2H_{2(g)} \rightleftharpoons VH_2$ | $8.1 \times 10^{10} e^{-7700/RT}$ | −40.0 |
| 6. $VH_2 + H \rightleftharpoons VRH + H_{2(g)}$ | $2.5 \times 10^{14} e^{-7300/RT}$ | −21.0 |
| 7. $VRH + H_{(g)} \rightleftharpoons VH_2$ | $1.0 \times 10^{13}$ | −52.8 |
| 8. $VRH + H_{(g)} \rightleftharpoons VR2 + H_{2(g)}$ | $1.3 \times 10^{14} e^{-7300/RT}$ | −20.4 |
| 9. $VR2 + H_{(g)} \rightleftharpoons VRH$ | $2 \times 10^{13}$ | −53.4 |
| 10. $VR2 + C_2H_{2(g)} \rightleftharpoons V_2$ | $8.1 \times 10^{10} e^{-7700/RT}$ | −23.7 |
| 11. $V_2 + H_{(g)} \rightleftharpoons VE$ | $9.5 \times 10^{12} e^{-2100/RT}$ | +5.1 |
| 12. $VE \rightleftharpoons C_4R$ | $1 \times 10^{13} e^{-7700/RT}$ | −22.9 |
| 13. $C_4R + H_{(g)} \rightleftharpoons C_4$ | $1 \times 10^{13}$ | −53.2 |

## Reactions and Structures

In order to calculate strain energies and steric repulsions on the diamond (110) surface, we took as our model compound a 3.8 Å thick diamond slab containing 130 carbon atoms with a hydrogenated 11.5 by 11.5 Å(110) face. Use of large model compounds is a requirement if strain energies are to be calculated accurately. This is because the calculation must take into account the fact that lattice atoms close to a surface reaction site may move somewhat to relieve steric repulsions, but it must also take into account that the crystal as a whole is extremely rigid. As large as our model compound is, we found that it would flex when the surface was strained by reactants with a great deal of steric repulsion. Therefore, the 67 carbon atoms at the edges of the crystal were fixed at their lattice positions, which prevented any overall flex of the model compound; the remaining 63 carbon atoms were allowed to move in response to steric repulsions. To calculate entropies we used a smaller crystal consisting of 15 carbon atoms because of limitations in the computer program. Since changes in the entropy depend only on changes in vibrational frequencies, which are hardly affected by the size of the model compound, use of this smaller model for the entropy calculations has almost no effect on the results.

For our mechanism we imagine dividing the (110) surface into units containing 4 surface carbon atoms and assume growth occurs at all such units in parallel. The mechanism begins with fully hydrogenated surface units called $H_4$. In the first step of the mechanism a surface $H$ is abstracted by a gas phase $H^{gas}$ giving a surface radical $RH_3$. ($R$ denotes a $R$adical site.) $RH_3$ can recombine with a gas phase $H^{gas}$ atom, Reaction 2, or a second surface $H$ can be abstracted, Reaction 3, to give $R_2H_2$. $C_2H_2$ adds to one of the radical sites of $R_2H_2$, and the free radical end of the added $C_2H_2$ quickly attaches to the other radical site. The result is an adsorbed vinyl structure called $VH_2$, where the two added carbons from $C_2H_2$ are now connected to each other by a double bond. An analogous series of steps leads to the addition of the second vinyl group giving $V_2$. The final series of reactions then connects the two vinyl groups, resulting in 4 carbon atoms bound to each other with single bonds: In Reaction 11 an $H^{gas}$ adds to one end of one of the vinyl groups which changes it to an $E$thyl-like secondary radical and makes the surface structure into $VE$. This ethyl radical attacks the nearer end

of the remaining vinyl group in Reaction 12, joining all four carbons in a butyl radical-like structure which can add a $H^{gas}$ to give the final hydrogenated 4-carbon structure $C_4$. Following Goodwin[9], we note that formation of $C_4$ is equivalent to forming a new $H_4$ structure. $C_4$-type structures form in parallel all across the surface, and these $C_4$ groups rapidly link, giving a new (110) layer, through a series of hydrogen abstraction and radical recombination reactions, which are very fast compared to the acetylene addition reactions required to form $C_4$. Therefore, completion of a new diamond "layer" proceeds at the rate at which $C_4$ is formed.

**2. Thermochemical quantities**

**Table II**

| SPECIES | $E_{strain}$ kcal/mole | $H_{bond}$ kcal/mole | $S$ cal/mole-K |
|---|---|---|---|
| $H_4$ | 0.0 | 0.0 | 0.0 |
| $RH_3$ | −0.6 | 41.6 | 2.8 |
| $R_2H_2$ | 1.45 | 83.3 | 3.7 |
| $VH_2$ | 9.7 | 33.9 | 14.4 |
| $VRH$ | 7.9 | 75.6 | 16.5 |
| $VR_2$ | 6.5 | 117.2 | 18.4 |
| $V_2$ | 28.9 | 68.0 | 27.4 |
| $VE$ | 40.8 | 86.8 | 35.9 |
| $BR$ | 32.6 | 65.4 | 30.3 |
| $C_4$ | 35.7 | 22.3 | 28.4 |
| $H^{gas}$ | — | 56.6 | 34.3 |
| $H_2^{gas}$ | — | 6.4 | 41.1 |
| $C_2H_2^{gas}$ | — | 66.6 | 67.1 |

According to the principle of group additivity[10], the heat of formation $H_f$ of a species can be decomposed into a bond enthalpy $H_{bond}$ and a strain energy $E_{strain}$, which comes from steric repulsion between the atoms. We used the group additivity scheme of Benson[10], corrected for more recent values of the $C$–$H$ bond

dissociation energies[11], to estimate changes in bond enthalpy for each reaction at 1200 K; and the MM3 molecular mechanics force field[12] to estimate $E_{strain}$ for each of the structures we used. Results are shown in Table II.

Since only changes in enthalpy are important, all quantities are referenced to $H_4$. We estimate the uncertainty in the calculation for $\Delta H$ which is defined as $\Delta H_{bond} + \Delta E_{strain}$, at about 1 kcal/mole[12].

Calculated entropies for each compound in our mechanism are shown in Table II, with an estimated uncertainy of around 0.3 cal/mole-deg[12]. The change in the Gibbs free energy for each reaction, shown in Table I, is calculated from

$$\Delta G = \Delta H - T\Delta S. \tag{1}$$

Uncertainty in $\Delta G$ is estimated at less than 2 kcal/mole, which corresponds to an uncertainty in a reverse rate constant of around a factor of 2. We note that although $\Delta G$ is evaluated at 1200 K, $\Delta G$ can be estimated at nearby temperatures using Eq. 1 because the temperature dependences of $\Delta H$ and $\Delta S$ tend to cancel in that equation.

### 3. Rate constants

Rate constants used in our analysis are shown in Table I. Since there are no experimental measurements for these gas-surface reactions, we assume that we can use data from gas phase alkane chemistry in order to estimate values for gas-surface reactions. Our critical assumption is that the reaction cross section $\sigma_s$ per surface site is equal to reaction cross section $\sigma_g$ *per equivalent site* in a prototype gas phase reaction.

This method for estimating $k_s$ differs importantly from that proposed previously by Frenklach and Wang[13] who assumed that the reaction *probability*, $\gamma$, rather than the reaction *cross section*, is transferable from gas phase to gas-surface reactions. $\gamma$ is defined as the reaction rate divided by the collision rate. Therefore, evaluating $\gamma_g$ and $\gamma_s$ involves estimating the collision cross section or "size" of a molecule or of a surface site. However, the size of a molecule depends on the prototype reaction chosen, and the size of a surface site is not necessarily a well defined concept. Frenklach and Wang[13] define the size of a surface site to be the inverse of the surface site density. This implies that the reactivity of, for example,

a given $C$–$H$ bond depends sensitively on how far away neighboring $C$–$H$ sites are. Although in principle this is conceivable, there is no precedent in alkane chemistry for such a dependence. In fact, experiment shows that the rate constant per site does not depend on the density of reactive sites in those molecules. That Frenklach and Wang calculate values for $k_s$ about two orders of magnitude smaller than ours is due primarily to the particular choices they made for molecular and surface site sizes.

### 4. Concentrations

In this work we use $[C_2H_2] = 2.7 \times 10^{-10}$ moles/cm$^3$, which was determined by Harris and Weiner[14] from measurments and from modeling of their filament assisted growth system. By assuming that $CH_4 + H = CH_3 + H_2$ is in partial equilibrium they estimated $[H] = 3.5 \times 10^{-9}$ moles/cm$^3$. However, Goodwin[9,15] has pointed out that our mechanism predicts that gas-surface reactions undergone by $H^{gas}$ are so fast that its concentration at the surface is lowered by around a factor of 7. Thus, we take $[H^{gas}] = 5.0 \times 10^{-10}$. However, we will also examine the dependence of the growth rate on $[H]$ and $[C_2H_2]$ over several orders of magnitude.

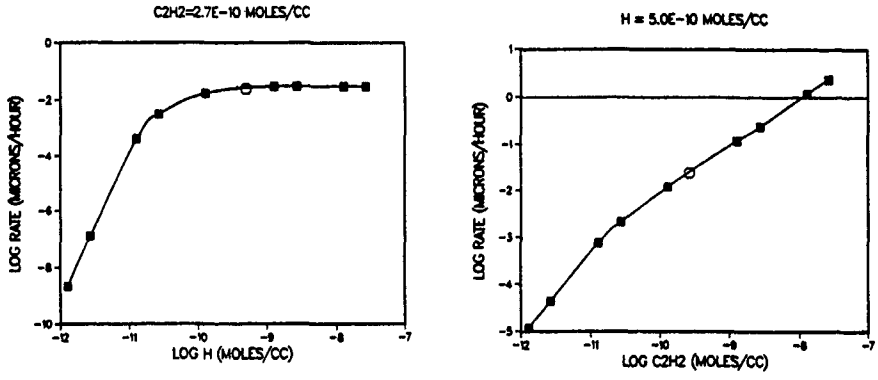
## Discussion

### 1. Results of the Model

The hydrogen abstraction and addition reactions reach steady state in about 50 microseconds, but steady state growth is not reached for about 20 seconds. The long induction time is the result of the relatively slow reactions involved in acetylene addition. Because the hydrogen abstraction and addition reactions are so fast compared to the acetylene addition reactions, reactions which link neighboring B groups are fast compared to their rate of formation. Once steady state is reached, our calculations predict a growth rate of 0.03 $\mu$m/hr with an estimated uncertainty of around an order of magnitude. Considering that experimentally measured growth rates in filament-assisted systems are typically in the range 0.1 - 1.0 $\mu$m/hr, we have shown that our mechanism is a feasible pathway for contributing significantly to diamond growth on (110) faces or at other (110)-like sites which can be present at step and kink sites on other faces.

Our model allows us to predict the relative amounts of different species on the (110) surface under steady state growth conditions. We find that about half of the topmost surface C atoms are hydrogenated, with a hydrogen atom coverage $\theta_H$ of 0.53 monolayers (ML), while the total surface radical coverage is $\theta_R = 0.20$ ML. Of these, about 20% have a neighboring radical site, making $\theta_{R2} = 0.04$ ML. These results contrast with suggestions sometimes made that finding two neighboring radical sites is very unlikely. Interestingly, there is a very high coverage of adsorbed vinyl groups ($\theta_V = 0.26$ ML). Since each vinyl occupies two surface H sites, this value represents roughly 1/2 of the maximum amount of vinyl which could adsorb on the surface. This high coverage, which is due in part to the strong bonds formed by $sp^2$ carbons, may well be observable spectroscopically.

There is no simple steady-steady formula which describes the growth rate over a significant range of possible $C_2H_2$ and $H$ concentration ranges. Instead, we plot the calculated growth rate vs. $[C_2H_2]$ (Fig. 1a) and $[H]$ (Fig. 1b). The growth rate is first order in $C_2H_2$ over a very wide range of $C_2H_2$ concentrations, but at the relatively high H atom concentrations which are prevelant in filament assisted growth system, the reaction is zero order in H. There is a very strong dependence on H atom concentration below about $10^{-10}$ moles/cc.




## 2. Comparison to Previous Models

Diamond growth has been modeled by several other groups beginning with Tsuda et al.[16,17], who examined an ionic mechanism. Neutral mechanisms, appropriate for filament-assisted systems, have been proposed by Frenklach and co-

workers[7,13,18] for $C_2H_2$ addition and by Harris[1] for $CH_3$ addition. The $C_2H_2$ addition mechanism of HFM[7] has some similarities with the one proposed here. Both mechanisms propose $C_2H_2$ as the growth species, and both propose addition to (110)-like sites. However, there are also critical differences (beyond the use by HFM of reaction probabilities rather than reaction cross sections[13]).

1. The individual steps are completely different. The HFM mechanism begins with $C_2H_2$ addition to $RH_3$ followed by a complex series of atom rearrangements on the surface to give a secondary surface radical with only single bonds. There is then a short radical chain mechanism as a second $C_2H_2$ adds at the radical site. The chain ends when a hydrogen atom is expelled. In contrast, the mechanism proposed in Table I adds $C_2H_2$ at the di-radical site $R_2H_2$; there are no atom rearrangements on the surface; the mechanism for $C_2H_2$ addition is not a radical chain; and the mechanism ends with $H$ atom recombination.

2. $C_2H_2$ addition is taken by HFM[13] to be irreversible; that is, the rate constant for $C_2H_2$ desorption is set identically to zero. (In contrast, HFM assign a large rate constant to $CH_3$ desorption, which explains their conclusion that $C_2H_2$ addition is more effective for diamond growth than $CH_3$ addition.) According to our method of analysis, the HFM mechanism is not a feasible pathway to diamond formation because the addition step, in which $C_2H_2$ adds to a surface radical site yielding a another surface radical site, is only mildly exothermic but has a very negative $\Delta S$. As a result, $\Delta G$ is not sufficiently favorable to permit the HFM mechanism to proceed. In contrast, our mechanism adds $C_2H_2$ to a *di*-radical, which is a very high energy species, and the addition reaction replaces the di-radical site with a stable structure. This step is so exothermic that the negative $\Delta S$ is overcome and the growth process becomes favorable.

3. The HFM mechanism provides a model not only for diamond growth but also for formation of $sp^2$ carbon. We have not attempted to incorporate $sp^2$ chemistry in our models.

## Conclusions

We have proposed a detailed chemical kinetics mechanism for addition of $C_2H_2$ to a (110) diamond surface. The model contains no adjustable parameters and is

based on the hypothesis that chemistry on the diamond surface may be understood in analogy with the chemistry of gas phase hydrocarbon molecules. We have calculated a growth rate of 0.03 $\mu$m/hour, which is within about an order of magnitude of experimentally measured growth rates. We conclude, therefore, that this is a feasible mechanism to account for growth on this surface or at steps or kinks on other surfaces where 110-like sites may be found. The critical surface species in this mechanism is the di-radical $R_2H_2$, which is present at significant concentrations, according to our model. We find that growth is first order in $C_2H_2$ and near-zero order in $H$ over a wide range of concentrations and that addition of the second $C_2H_2$ molecule is the rate limiting step. The rate that we calculate is most sensitive to the rate constant for $C_2H_2$ addition, but also depends strongly on the ratio of the $H$ abstraction and recombination rate constants. Thermodynamics is most important for the $C_2H_2$ addition reactions. The rate falls by an order of magnitude when the calculated value for $E_{strain}$ in $V_2$ is increased by 10 kcal. Steady state is reached in 20 seconds, at which point the surface has a surprisingly high (0.25 ML) concentration of adsorbed vinyl groups.


### Acknowledgements

We gratefully acknowledge many valuable discussions with Professor David Goodwin of Caltech.


## References


[1] S. J. Harris. A mechanism for diamond growth from methyl radicals. *Applied Physics Letters*, 56:2298, 1990.

[2] L. R. Martin and M. W. Hill. Diamond film synthesis in a chemically simplified system. *Applied Physics Letters*, 55:2248, 1989.

[3] C. J. Chu, M. P. D'Evelyn, R. H. Hauge, and J. L. Margrave. Mechanism of diamond film growth by hot-filament CVD: Carbon-13 studies. *Journal of Materials Research*, 5:2405, 1990.

[4] S. J. Harris and L.R. Martin. Methyl vs acetylene as diamond growth species. *Journal of Materials Research*, 5:2313, 1990.

[5] S. J. Harris, A. M. Weiner, and T. A. Perry. Filament-assisted diamond growth kinetics. Journal of Applied Physics, accepted.

[6] M. Geiss. Homoepitaxial diamond films. In *Materials Research Society, Fall Meeting*, Boston, MA, December 1989. Paper F4.1.

[7] D. Huang, M. Frenklach, and M. Maroncelli. Energetics of acetylene-addition mechanism of diamond growth. *Journal of Physical Chemistry*, 92:6379, 1988.

[8] S. J. Harris and D. N. Belton. Thermochemical kinetics of a proposed mechanism for diamond growth from acetylene. Japanese Journal of Applied Physics, accepted.

[9] T. G. Owano, D. G. Goodwin, C. H. Kruger, and M. A. Cappelli. Diamond synthesis in a 50 kw inductively coupled atmospheric pressure plasma torch. In *Second International Conference on the New Diamond Science and Technology*, Washington, DC, September 1990. Paper 7.2.

[10] S. W. Benson. *Thermochemical Kinetics*. John Wiley and Sons, New York, 1976.

[11] D. Gutman. The controversial heat of formation of the t-butyl radical and the tertiary C-H bond energy. *Accounts of Chemical Research*, 23:375, 1990.

[12] J.-H. Lii and N. L. Allinger. Molecular mechanics. The MM3 force field for hydrocarbons. *Journal of the Americal Chemical Society*, 111:8551, 1989.

[13] M. Frenklach and H. Wang. Detailed surface and gas-phase chemical kinetics of diamond deposition. *Physical Review B*, 43:1520, 1991.

[14] S. J. Harris and A. M. Weiner. Methyl radical and H atom concentrations during diamond growth. *Journal of Applied Physics*, 67:6520, 1990.

[15] D. G. Goodwin. Simulations of high-rate diamond synthesis: methyl as growth species. Applied Physics Letters, accepted.

[16] M. Tsuda, M. Nakajima, and S. Oikawa. Epitaxial growth mechanism of diamond crystal in $CH_4 - H_2$ plasma. *Journal of the Americal Chemical*

*Society*, 108:5780, 1986.

[17] M. Tsuda, M. Nakajima, and S. Oikawa. The importance of the positively charged surface for the epitaxial growth of diamonds at low pressure. *Japanese Journal of Applied Physics*, 26:L527, 1987.

[18] M. Frenklach and K. E. Spear. Growth mechanism of vapor-deposited diamond. *Journal of Materials Research*, 3:133, 1988.

# NEGATIVE ION MASS SPECTROMETRY IN A FILAMENT ASSISTED CVD DIAMOND GROWTH APARATUS

P.A. Sullivan#, F.P. Doty*, J.W. Boring#, W.A. Jesser*, R.A. Baragiola#*
#Department of Engineering Physics; *Department of Materials Science
School of Engineering and Applied Science
University of Virginia, Charlottesville, VA 22903-2442

We have studied gas phase chemistry during diamond growth using hydrocarbon/hydrogen mixtures in a filament-assisted CVD reactor. A mass spectrometer was used to find the ions present during diamond growth. Three negative ion peaks resulting from ionization of the gas on the filament surface were discovered at masses 1, 26, and 27 amu.

## I. INTRODUCTION

Low pressure CVD diamond growth has many applications (1). Knowledge of the chemistry during the diamond growth process could lead to improvement in diamond quality. Hot filament CVD (HFCVD) growth of diamond on a variety of substrates in $H_2/CH_4$ mixtures at low pressure exhibits a growth rate that depends upon the electrical bias of the substrate (2-4). For example, it was found (2) that a positively biased substrate produced the best diamond growth results, suggesting that diamond growth is dependent on a charged species. It is possible that molecular ions are an important participant in the gas phase chemistry. The research goal here was to determine the ion species present during HFCVD to better understand the diamond growth process.

## II. EXPERIMENTAL

An EXTREL Mass Spectrometer was connected to an HFCVD chamber for ion measurement. The arrangement geometry is shown in figure 1. The mass spectrometer was operated in a secondary ion mass spectrometer (SIMS) configuration in order to select charged species only. A mixture of 1% $CH_4$ in $H_2$ was leaked into the chamber at pressures limited by the

SIMS apparatus: $10^{-6}$ to $10^{-5}$ Torr. A 0.10 by 0.005 by 5.08 cm tungsten filament was resistively heated to temperatures ranging from 1300 to 2000 C.

The energy analyzer portion of the ion mass spectrometer selects the energy of detected ions. The filament and energy analyzer voltage level were matched in order to insure that the ions detected were from the region at or near the surface of the filament.

Three negative ion peaks were discovered (figure 2) at mass 1, 26, and 27 amu. We assign these peaks as $H^-$ and $C_2H_2^-$ : the peak at mass 27 having a $^{13}C$ instead of $^{12}C$ at one of the $C_2$ sites. No positive hydrocarbon ions were detected. The $C_2H_2^-$ peak intensities were constant over the pressure range of $10^{-6}$ to $10^{-5}$ Torr. The intensity was strongly dependent on the filament temperature and peaked at around 1430 C (figure 3).

## III. DISCUSSION

Simple surface ionization theory suggests that the collected ion counts should follow an exponential increase with increasing temperature and then an ion count saturation. The plot of log intensity vs 1/T , however, seems to indicate two competing processes leading to ion formation: one increasing and the other decreasing the ion yield (figure 3).

The production of negative ions at or near the filament surface has been shown in two ways: the ion production has a large dependence on filament temperature , and the ion signal peaked when the potential of the filament and acceptance energy of the analyzer were matched. According to surface ionization theory, the ion density created by the filament should saturate at a given temperature that depends on the pressure of ionizable gas available. The fact that the signal is independent of the gas pressure suggests that the rate of $C_2H_2^-$ formation is determined by a stable concentration of hydrocarbon at the surface. We believe that at least one other process is competing with surface ionization, perhaps molecular breakdown.

In conclusion, we found $H^-$ and $C_2H_2^-$ during a simulated diamond growth process. We think these ions are important in the gas phase chemistry during diamond growth and certainly in the hot filament region in HFCVD. Identification of the predominant negatively charged species helps in developing a model for diamond growth.

## REFERENCES


1. R.N. Boggs, Design News, p.70 (4/10/89).
2. F.P. Doty and W.A. Jesser, J. Elect. Materials, *20*, No.2 (1991).
3. M. Tsuda, M. Nakajima and S. Oikawa, Jpn. J. Appl. Phys. pt. 2 *26*, 1527 (1987)
4. M. Sokolowski, A. Sokolowski, B. Godieli, A. Michalski, A. Rusek and Z Zomanowski, J. Cryst. Growth, *54*, 519 (1981).
5. M. Tsuda, M. Nakajima and S. Oikawa, J. An.. Chem. Soc. *108*, 5780 (1986).

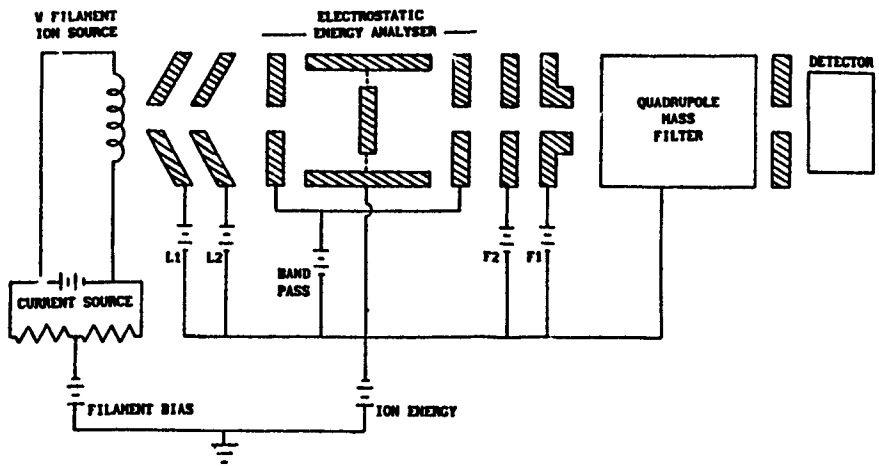



Fig. 1 - Mass spectrometer on a filament assisted CVD chamber. The negative ions are created at the filament, extracted by a lens, energy analyzed, focused, mass analyzed, and finally detected with a dynode/electron multiplier arrangement.

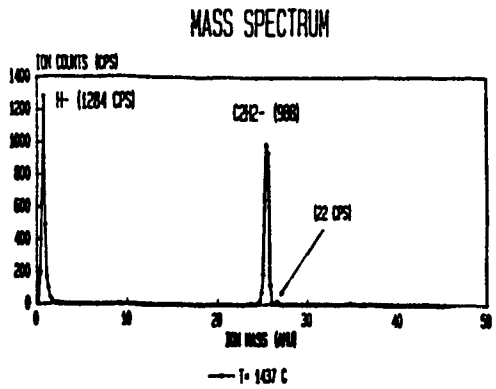



Fig. 2 - Ion counts per second when the spectrometer was swept over a 50 atomic mass unit range. The $C_2H_2$- counts per second peaked at around a filament temperature of 1430 $^0$C. We believe the peak at 27 amu is $C_2H_2$- with one of the Carbons having a mass of 13 amu.

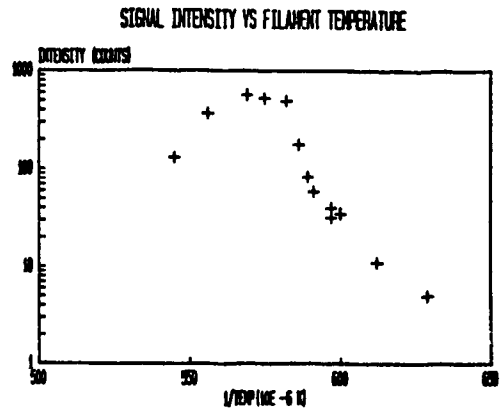



Fig. 3 - Total ion counts over the inverse filament temperature. The plot seems to have distinct linear portions. Raw data is included from several experiments.

# THERMAL DESORPTION FROM HYDROGENATED DIAMOND (100) SURFACES

R.E. Thomas, R.A. Rudder, R.J. Markunas
Research Triangle Institute, Research Triangle Park, NC 27709

## ABSTRACT

Thermal desorption spectroscopy and low energy electron diffraction (LEED) have been used to study the interaction of atomic hydrogen with the diamond (100) surface. Heating a diamond crystal in-vacua readily reconstructs the surface from a (1x1) configuration to a (2x1) structure. Unlike the case for silicon, exposure to atomic hydrogen does not easily convert the surface back to the (1x1) structure. Hydrogen thermal desorption peaks from the (2x1) surface exposed to atomic hydrogen at $1x10^{-6}$ Torr are seen at approximately 950°C for heating rates of 20°C/sec. After exposure of the surface to atomic hydrogen in amounts in excess of that required to terminate the surface, $10^{-2}$ Torr, thermal desorption peaks associated with methyl radicals and acetylene are observed in addition to hydrogen. Upon further exposure at 10 Torr the surface appears to be partially converted to a (1x1) structure and acetylene desorption features are no longer observed.

## Introduction

Hydrogen plays a key role in most diamond growth processes developed to date. However, the details of the behavior of hydrogen on the diamond surface are not well understood. It is thought to both etch non–$sp^3$ bonded carbon, which may be deposited during the growth process, and to stabilize the cubic structure on the growing diamond surface by terminating dangling bonds. Previous studies of hydrogen interactions on diamond indicate that hydrogen desorbs from the surface at approximately 900°C (1,2). Typically, researchers find that heating the diamond to approximately 1000°C results in the (1x1) surface structure converting to the (2x1) surface structure (2,3). One might expect, as in the case of silicon, the surface would convert back to the (1x1) state upon exposure to atomic hydrogen. Hamza et al. have observed the transition back to a (1x1) configuration on exposure to atomic hydrogen but find that on subsequent annealing the (2x1) surface is not recovered (2).

In the present work thermal desorption spectroscopy and LEED were used to study interactions of atomic hydrogen with the diamond (100) surface. Transitions from the (1x1) phase to (2x1) phase upon annealing and from the (2x1) phase to the (1x1) phase upon exposure to atomic hydrogen were studied with LEED. Thermal desorption spectroscopy was used to determine desorption kinetics and products from hydrogen terminated surfaces.

## Experimental

Thermal desorption spectroscopy and LEED observations were performed in a stainless steel UHV system. Base pressure was $5x10^{-10}$ Torr for the sample chamber and $1x10^{-10}$ Torr for the quadrupole chamber. The sample chamber was separated from the quadrupole chamber by a 2mm diameter aperture. Sample heating was accomplished by clipping the crystals to a 0.25mm thick molybdenum resistive strip heater. All parts associated with the heater stage, including the clamps and current leads were manufactured from molybdenum. The sample temperature was measured by a 0.125mm diameter chromel/alumel thermocouple in intimate contact with the crystal. The thermocouple was threaded through a hole in one corner of the crystal, and the thermocouple bead then held in tension against the crystal. Two (100), 5mmx5mmx0.25mm, diamond crystals were used in the course of the present study. One of the crystals had approximately .5 microns of homoepitaxial diamond deposited prior to insertion into the system. Diamond polishing of the substrates leaves fine scratch marks on the surface, which previous work has shown can be covered by deposition of a homoepitaxial film (4). The homoepitaxial diamond was grown with an rf discharge plasma CVD process using $CH_4$ in $H_2$ as feedstock. The uncoated samples were cleaned by hand-polishing with 0.25 micron diamond grit and water. Following the polishing, the samples were ultrasonically cleaned in two series of baths of TCE, acetone, and methanol. Between solvent bath series the samples were vigorously swabbed to remove particulates. Once the samples were introduced to the chamber, no additional cleaning was performed aside from thermal desorption of adsorbed species. Several pressure regimes were used in dosing with atomic hydrogen, which necessitated slightly different procedures. For samples dosed at pressures from $1x10^{-7}$ Torr to $1x10^{-5}$ Torr, the hydrogen was flowing through the system. Samples were also dosed at pressures of $10^{-3}$ Torr-$10^{-2}$ Torr and 1-10 Torr. For these samples the main chamber was sealed and hydrogen was admitted to the desired pressure. In all cases atomic hydrogen was generated via a tungsten filament operating at a temperature of approximately 1500 °C. The sample was positioned approximately 2 cm. from the filament during dosing. The sample was not actively cooled and at the lowest dosing pressures remained at room temperature. At dosing pressures in the 1-10 Torr range the sample temperature rose to approximately 125 °C. All thermal desorption spectra were taken with a heating rate of 20 °C/sec.

## Results

The surface structure of the samples was monitored with LEED immediately after introduction to the chamber, after dosing, and after thermal desorptions. All samples exhibited a LEED pattern without annealing. For most samples this was a (1x1) configuration. The one exception was the homoepitaxial sample which gave a (2x1) pattern. Since this sample remained at the growth temperature, 800-900 °C, while the plasma and the gasses were shut off, it is likely that surface hydrogen simply desorbed and consequently the surface reconstructed before the sample was removed from the growth chamber. Upon annealing to 800 °C-1000 °C and for times ranging from 5 seconds to 120 seconds, all samples exhibited some degree of reconstruction to the (2x1) configuration. Annealing at temperatures greater than approximately 1100 °C usually resulted in a degradation of the LEED pattern. Typically, the second order spot intensity was

reduced, and the background intensity increased. In these cases first order spot intensity usually remained strong. The quality of the (2x1) LEED patterns obtained upon annealing samples varied considerably, and no consistent trends were observed to account for the variability.

Samples exhibiting good reconstructions were then exposed to atomic hydrogen in an attempt to convert the surface back to a (1x1) configuration. Three pressure regimes were investigated: $10^{-6}$-$10^{-5}$ Torr, $10^{-3}$-$10^{-2}$ Torr and 1-10 Torr. Only at the highest pressures studied were we able to partially convert the surface back to a (1x1) state. Samples exposed to atomic hydrogen at the maximum pressure showed only very faint second order spots. Annealing of these samples to 1000 °C restored the (2x1) configuration. At the two lower pressure regimes studied little if any change was seen in the (2x1) LEED patterns upon addition of atomic hydrogen.

Given the difficulty in converting the surface back to a (1x1) configuration, all thermal desorption spectra were, perforce, from surfaces that had an indefinite degree of surface reconstruction. The three dosing regimes used in the LEED study were also used in the thermal desorption studies. Of the masses monitored during the course of the study, (2,13,14,15,16,18,26,27,28, and 44), desorption peaks were seen only for masses 2,15, and 26.

Figure 1 shows a series of hydrogen desorption spectra taken from a hydrogen dosed natural diamond surface. The sample was subjected to atomic hydrogen doses at fixed pressures and for a series of increasing times. A single desorption peak is evident at 900 °C. Figure 2 shows a similar series of hydrogen thermal desorption traces for the CVD homoepitaxial sample dosed at a pressure of $3x10^{-6}$ Torr. In this case two closely spaced hydrogen desorption peaks can be seen at 900 °C and at 1000 °C. It is apparent from both figures that extending the dosing time does not result in dramatically increased amounts of hydrogen desorbing from the surface. We also do not see any evidence for a shift in the desorption temperature as the coverage increases. The next series of figures shows thermal desorption spectra from the CVD diamond film after exposure to atomic hydrogen at the three pressure regimes used in the LEED study. Figure 3 shows that after exposure to atomic hydrogen at $1x10^{-5}$ Torr, hydrogen desorbs at 900 °C and perhaps a small amount of $CH_3$, but little evidence of $C_2H_2$. Figure 4 shows the sample after dosing at $2x10^{-3}$ Torr, a dosing pressure far higher than what is required to terminate the (2x1) surface. At this dosing pressure we now see clear evidence of desorbing methyl radicals (700 °C) and acetylene (600 °C). Although the sample has received an atomic hydrogen dose far in excess of what is required to saturate the (2x1) surface, LEED indicates the sample is in fact still in a (2x1) configuration. These two species are desorbing in significant quantities compared to the hydrogen desorption. The hydrogen desorption peak has broadened considerably after dosing at this pressure but the peak desorption temperature has not shifted. Figure 5 shows the sample after dosing at 3 Torr for 2700 seconds. In this case the sample has lost much of the (2x1) structure as seen in LEED but has not fully regained the (1x1) surface structure. The hydrogen desorption peak has remained at 950 °C. The methyl peak has shifted to approximately 800 °C and the acetylene peak has virtually disappeared

**Discussion**

Surface reconstruction on the diamond (100) face has been reported previously (2,3). As noted by these authors, the reconstruction process was not always reproducible. For all of the newly polished surfaces used in the present study, some reconstruction was noted upon annealing. However, as indicated in the results section, not all surfaces fully reconstructed. Field emission SEM indicates the starting morphology for all the hand-polished surfaces was quite similar. If surface morphology is influencing the reconstruction, it is at a scale of less than 1000Å. Hamza et al. have suggested that adsorbed oxygen can affect the ability of the surface to reconstruct (3). Ex-situ measurements of samples show the presence of oxygen on the surface, some or all of which may have been added to the surface during the air transfer to the XPS system. No clear trend connecting the quantity of adsorbed oxygen and the quality of the reconstruction was observed. Other contaminants below the detection limit of XPS remain a possibility. Annealing at temperatures higher than required to establish the (2x1) structure appears to degrade the surface. The (1x1) pattern is still apparent but, as an increase in the background is observed, it is likely that the surface is becoming disordered and the (1x1) pattern is from the bulk.

Conversion of the (2x1) surface structure back to the original (1x1) structure appears very difficult. Extended dosing at high pressures is only partially successful at restoring the surface. In contrast, silicon (100) samples in the same chamber and under identical dosing conditions readily convert from the (2x1) state to the (1x1) state at dosing pressures of $1x10^{-6}$ Torr and at dosing times on the order of 1000 sec. For diamond samples in this pressure regime, we do not see conversion even after 2000 seconds at $5x10^{-6}$ Torr; a dose 10 times at great as used on silicon. This is not too surprising as the C-C bond strength at 83 kcal/mole is much greater than the Si-Si bond of 46 kcal/mole. Cluster calculations by Verwoerd indicate the diamond surface dimer bond is very resistant to attack by atomic hydrogen (5). The apparent stability of the dimer bond may also help explain results of the thermal desorption experiments described next, particularly the appearance of acetylene.

It appears difficult to maintain a well characterized surface during the course of thermal desorption experiments. The surface structure is evidently a function of sample history and it is difficult to return to a standard starting point. In the case of the thermal desorption experiments there may be several sites which are contributing to the hydrogen observed. LEED in this case is a very rough measure of surface characteristics. On a nominally (2x1) surface we find the hydrogen uptake saturates. By comparing this with data obtained from silicon samples under identical conditions, we find the quantity of hydrogen desorbed is consistent with monohydride coverage, or 1 hydrogen per carbon atom. Extended dosing does not significantly increase the hydrogen yield from the surface. The substrate which had received the homoepitaxial film showed two hydrogen desorption peaks only after film deposition. Before the film was deposited, a single peak is observed at 900°C. The desorption temperature does not appear to be coverage dependent. This indicates a first order reaction with fixed activation energy. A simple calculation using a standard frequency factor of $10^{13}$ gives an activation energy of 74 kcal/mole, which is considerably smaller than the C-H dissociation energy of 104 kcal/mole. First order kinetics are also found by Sinniah et al. for hydrogen desorption

from the monohydride phase on the silicon (100) surface (6). Along with first order kinetics, an activation energy was found which was much less than the dissociation energy for the Si-H bond.

As additional hydrogen is added to the saturated (2x1) surface we see the appearance of LEW desorption products, methyl radicals and acetylene. Since the dimer bonds resist attack by atomic hydrogen it may be possible for the dimer back bonds to be hydrogenated. If one or two of the back bonds were broken on the dimer unit, it would then be possible for the two carbon atoms to desorb as a unit, perhaps resulting in the acetylene production seen. Methyl radicals are also seen desorbing from the surface, but at a higher temperature. Since the two species desorb at different temperatures, one expects evolution from different sites. Mass 15 could be a fragmentation product of either ethylene or ethane. Mass 28 was monitored for ethylene species but given the large background seen at this mass it is difficult to discern a peak. No significant desorption products were seen at mass 27 either, which one would expect if large quantities of ethylene or ethane were desorbing. Given the size of the hydrocarbon desorption peaks relative to the hydrogen peak, it is clear that an appreciable fraction of a monolayer of carbon is desorbing from the (2x1) surface after extended dosing. It is not clear what sites the methyl radicals may be desorbing from. It seems likely that the methyl radicals are desorbing from dihydride sites.

If breaking of back bonds is occurring during hydrogen dosing, it seems likely that etching of the dimer units is also occurring on a continuous basis. If completed, we should see a reduction in amount of acetylene desorbed from the surface. At the highest hydrogen doses studied, the acetylene does in fact diminish dramatically. Methyl radicals, however, are still seen. Although the sample has moved closer to the (1x1) configuration as a result of the hydrogen dosing, the hydrogen desorption peak remains at 950°C. If desorption is occurring by processes similar to that on silicon, one would expect a peak to appear at a lower temperature corresponding to the desorption from the dihydride phase. Hamza et al. have results which indicate that both on the (100) and the (111) face of diamond, the surface reconstructs after the hydrogen desorbs (2,7). If there was little energy to be gained by formation of the dimer bonds on the surface, one would expect the desorption from the dihydride and the monohydride to occur near the same temperature.

## Conclusions

The clean surface appears to saturate quite readily in the (2x1) configuration and hydrogen desorption from this phase follows first order kinetics. Conversion of a diamond (2x1) surface back to the (1x1) configuration by the addition of atomic hydrogen is difficult. It appears this is accomplished by hydrogenation of dimer back bonds and subsequent desorption of acetylene from the surface rather than by breaking of dimer bonds. Surfaces which show substantial reduction in the (2x1) surface phase after hydrogenation also show considerably reduced desorption of acetylene.

**Acknowledgements**

The authors wish to thank the Strategic Defense Initiative Organization/Innovative Science and Technology Office through the Office of Naval Research (N-00014-86-C-0460) for the financial support of this work.

## REFERENCES

1. S. Matsumoto, Y. Sato, and N. Setaka, Carbon 19, 232 (1981).
2. A.V. Hamza, G.D. Kubiak, and R.H. Stulen, Surf. Sci. 237 35 (1990).
3. P.G. Lurie, and J.M. Wilson, Surf. Sci. 65, 453 (1977).
4. J.B. Posthill, R.A. Rudder, G.C. Hudson, D P. Malta G.G. Fountain, R.E. Thomas, R.J. Markunas, T.P. Humphries, R.J. Nemanich, and D.R. Black, this proceedings.
5. W.S. Verwoerd, Surf. Sci. 108 153 (1981).
6. K. Sinniah, M.G. Sherman, L.B. Lewis, W.H. Weinberg, J.T. Yates, and K.C. Janda, Phys. Rev. Lett. 62 567 (1989).
7. A.V. Hamza, G.D. Kubiak, and R.H. Stulen, Surf. Sci. 206 L833 (1988).

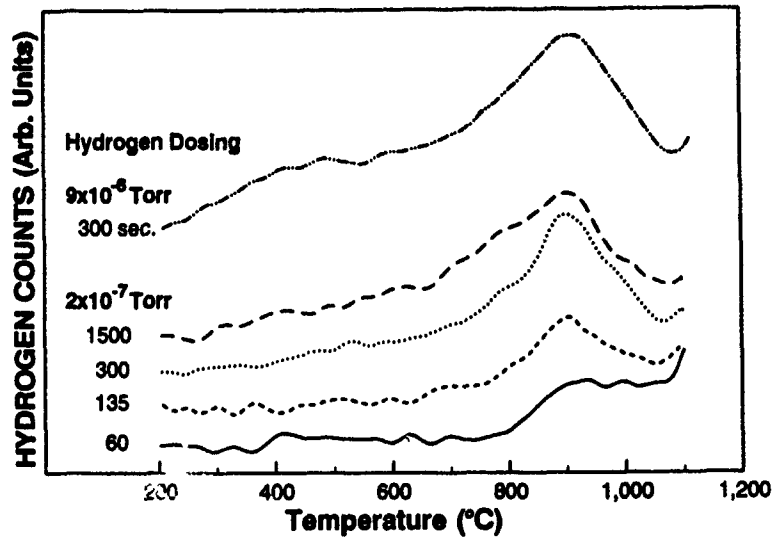



Figure 1. Thermal desorption spectra from natural diamond surfaces. An additional spectra was taken after dosing the sample at $9x10^{-6}$ torr with atomic hydrogen. The higher pressure is comparable to the dosing pressure used on the samples in Figure 2. Note that although the dose has increased by a factor of 3.5 between the sample exposed at $9x10^{-6}$ and the sample exposed for 1500 seconds at $2x10^{-7}$ torr, the magnitude of the desorption peaks is very close.

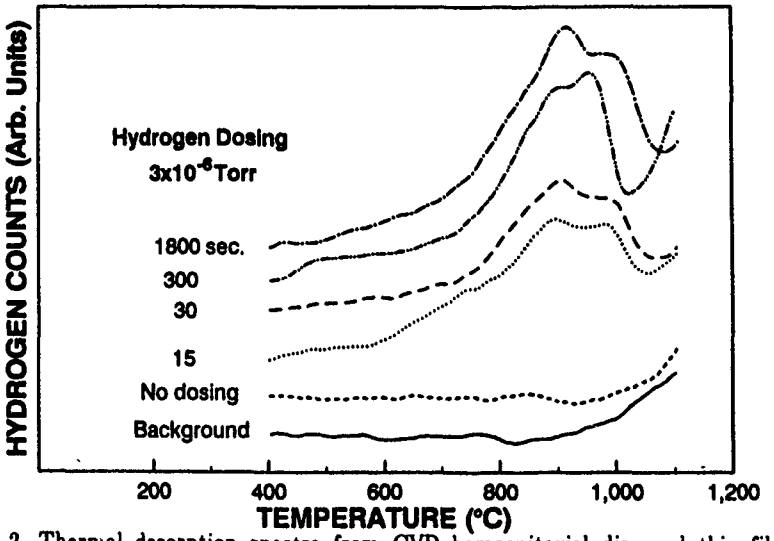



Figure 2. Thermal desorption spectra from CVD homoepitaxial diamond thin films deposited on natural diamond substrates. In addition to the hydrogen desorption spectra after dosing, a background spectrum is included where the sample was dosed but not placed adjacent to the aperture.

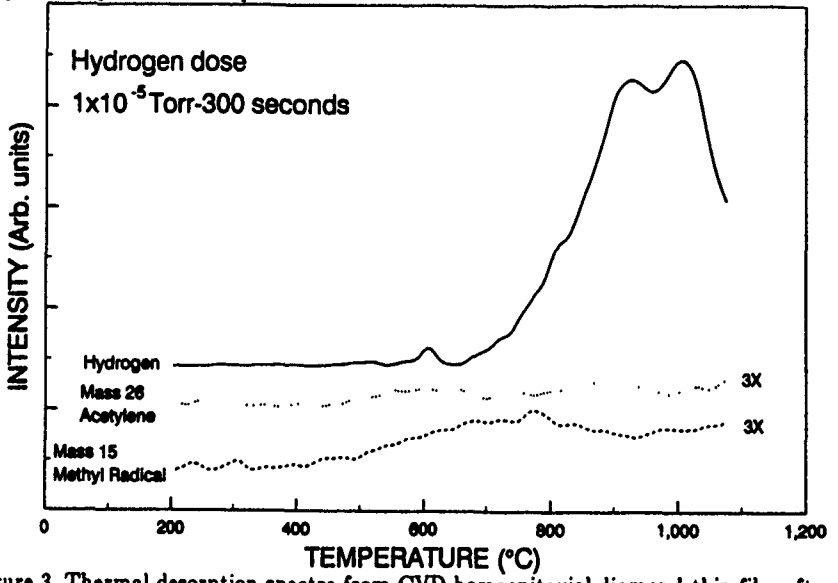



Figure 3. Thermal desorption spectra from CVD homoepitaxial diamond thin films after dosing at $1x10^{-5}$ torr. The vertical scale on masses 15 and 26 has been magnified by a factor of 3 to show detail.

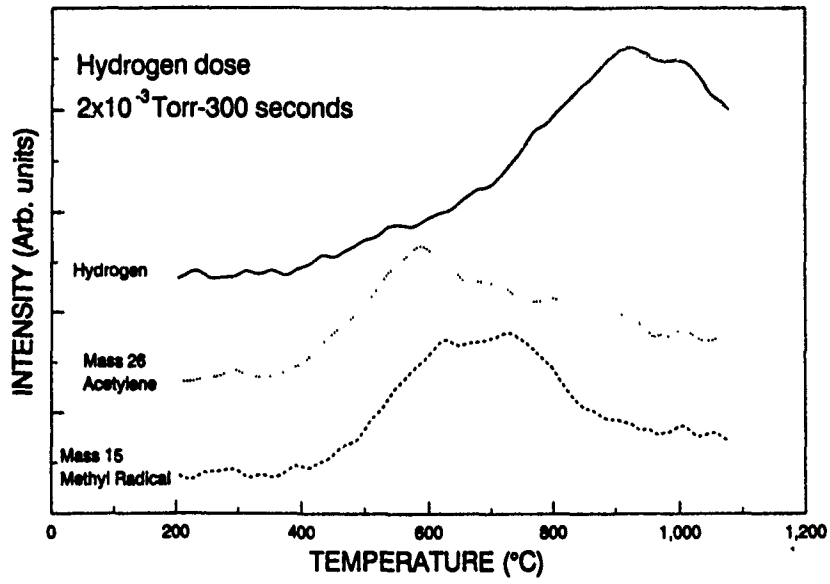



Figure 4. Thermal desorption spectra from CVD diamond film after hydrogen dosing at $2x10^{-3}$ torr. Note the large increase in methyl and acetylene production compared to Figure 3.

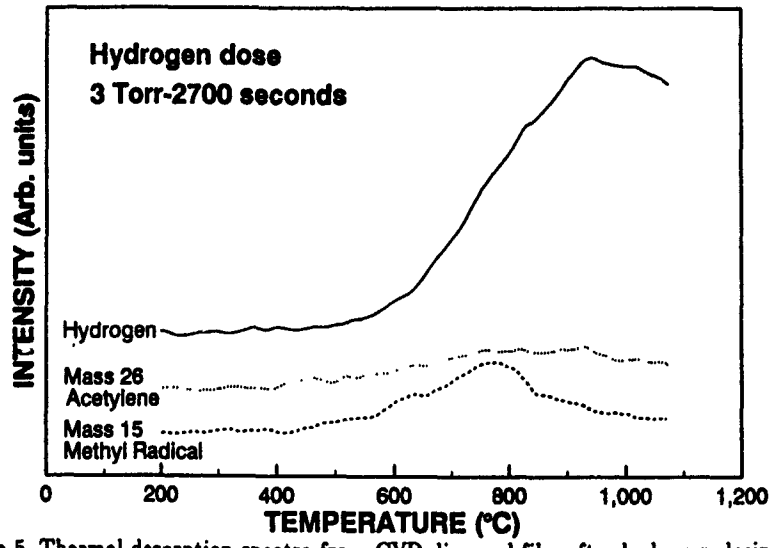



Figure 5. Thermal desorption spectra from CVD diamond film after hydrogen dosing at 3 torr. In this case the acetylene production is considerably reduced.

# GAS PHASE CHEMISTRY IN A DIAMOND-DEPOSITING dc-ARC-JET*

Gregory P. Smith and Jay B. Jeffries
Molecular Physics Laboratory
SRI International
Menlo Park, CA 94025

A model of the gas phase chemistry of diamond deposition in an arc-jet plasma is presented. The model does not predict a large enough methyl radical concentration to account for the observed diamond growth rate from $CH_3$ alone. Large superequilibrium concentrations of atomic carbon are found. More than half of the total carbon in the feedstock is found in polyatomic hydrocarbon molecules.

## Introduction

Diamond thin films have been produced in dc-arc-jet plasmas with reported growth rates which approach 1 mm/hr (1-6). Such rates are as much as four orders of magnitude faster than the typical growth rates attained in dc, microwave, and hot filament reactors. Recent experiments with hot filament (7) and flow (8,9) reactors have indicated that methyl radical concentrations above the growing diamond surface can account for the observed growth rate. Harris (10) has developed a mechanism for growth of the diamond 100 surface via methyl addition. The hot filament chemistry has been extensively modelled (11-13); these results show that the methyl radical flux to the surface can support growth rates between 0.06 and 0.6 μm/hr with the Harris mechanism. Such values are consistent with the observed values.

It is tempting to believe that understanding the differences in the growth environment between the dc-arc-jet and hot filament reactors will elucidate strategies to increase the growth rate for all the diamond growth methods. Crucial to this understanding is the determination of the mechanism of the diamond film growth. We have modelled the gas phase chemistry in the dc-arc-jet plasma in order to discern if the methyl radical flux at the substrate surface is sufficient for the Harris mechanism to predict the measured growth rate.

We have modelled the dc-arc-jet of Stalder and Sharples (5) to take advantage of the laser-induced fluorescence measurements of the gas phase temperature by Raiche, et al. (13). This measured gas temperature is used as a boundary condition for our chemical mechanism. We find that the reactions of atomic carbon are quite important in this environment. The primary reaction path for the loss of carbon atoms is addition to molecules with carbon-carbon double bonds to form hydrocarbon molecules with three or more carbon atoms. A surprisingly large fraction of the carbon feedstock is converted to

these polyatomic hydrocarbon molecules even though the gas residence time in this reactor is quite short. We do not predict enough methyl radicals at the substrate surface to account for the measured growth rate with the Harris mechanism. However, Goodwin (14) has recently considered this same environment. His results lead him to the opposite conclusion; he finds enough methyl radicals at the surface for a growth rate consistent with the measured value. Differences between the two models will be discussed after presenting the results of our calculations.

## Chemical Model

For the purpose of calculating spatially-resolved species concentrations in the plasma torch system, we assembled a chemical mechanism of 15 species with 42 elementary chemical reactions whose interconnecting rate expressions are integrated integrated using the CHEMKIN code (15). Ion chemistry in the arc, diffusion in the jet and boundary layer, and gas surface chemistry at the substrate are not included. To solve this constant pressure, varying temperature problem, a temperature distribution is imposed. Our temperature profile begins with 300 K feedstock gas, rises to a constant 5000 K in the plasma arc itself, falls to 2100 K at the boundary layer (13), and 1200 K at the substrate surface (5). The temperature in the arc is estimated from emission measurements and is consistent with the temperature expected in a fast flow 1 kW arc. At the position of the boundary layer above the substrate, 1 cm down stream from the nozzle exit of the arc, Raiche et al. (13) measured the gas temperature by CH laser-induced fluorescence. Linear cooling is assumed between the arc and the boundary layer and between the boundary layer and the substrate surface.

Figure 1 shows a schematic view of the gas flow, temperatures, and estimated the residence times. The measured flow rate of 0.45 moles/min, 235 Torr gas pressure, and the geometry of the arc leads to an estimate of 1.5 μs residence time in the arc. The pressure drop across the arc is 15 Torr, and the hot gas exits with an estimated velocity of $2 \times 10^5$ cm/s. Optical emission measurements show that the diameter of the jet expands from 0.2 cm at the orifice to 0.3 cm at the substrate. The mean axial velocity between the nozzle and substrate is $1.7 \times 10^5$ cm/s, and the transit time from the arc to the boundary layer at 2100 K is an additional 6 μs. Although these velocities are large, they are subsonic in the hot hydrogen gas.

Near the stagnation point, we estimate the thickness of the boundary layer $\delta \sim \sqrt{\mu_\infty/\rho_\infty a}$ where $\mu_\infty$ and $\rho_\infty$ are the gas viscosity and density, respectively; $a \sim 2u/R$ where u is the mean axial jet velocity and R the jet radius. (This estimate for the boundary layer is identical to that of Goodwin (14), although we find $a \sim 4 \times 10^6$/s where he used $a \sim 10^6$/s.) This leads to a boundary layer thickness of 0.007 cm for this fast flow condition. We estimate a diffusion time of 22 μs from the top of the boundary layer to the substrate.

It should be emphasized that the purpose of this calculation is not to simulate the precise physics and chemical profiles in the boundary layer. It is rather to determine

which carbon-containing species could be present in sufficient quantities at the surface of the substrate to account for the observed diamond growth rate. Thus, our goal is to assess whether significant gas phase reactions are likely in the boundary layer region when the time scale involved is dominated by thickness and diffusion.

The reactions and their rate constants used in the mechanism are given in Table 1. The basic mechanism is that used by Frenklach (17) to describe hot-filament reactor chemistry. We have supplemented this with chemistry of less hydrogenated species, drawn from other sources and our own rough estimates. The extensive polycyclic aromatic hydrocarbon(PAH) mechanism of Frenklach (11) has been omitted. However, we have represented formation of PAH precursors by including a single, irreversible reaction between carbon atoms and acetylene to form $C_3H$ (referred to as "pre-PAH"). Carbon atoms are then allowed to irreversibly add to the pre-PAH to form molecules with up to six carbon atoms. All other reverse rates are calculated from the Sandia thermodynamic data base (18) through equilibrium constants. For the critical hydrogen dissociation/recombination reactions, the recommendation of Cohen and Westberg (19) was followed. Hydrogen atom abstraction of hydrogen from vinyl, present in low equilibrium amounts from the major species acetylene and H, forms a second (chaperon) mechanism for this recombination.

## Results and Discussion

Calculated mole fractions versus reaction time for selected species are shown in Figure 2. In the arc, methyl radical are rapidly produced and consumed, and have a 0.1% mole fraction at the beginning of the jet region; note that the total methane in the feedstock only has a mole fraction of 0.5%. The extent of the decomposition in the arc is exemplified by the CH which has a concentration exceeding $CH_3$ at the nozzle. Both CH and $CH_3$ decline in the jet to 30 ppm levels at the beginning of the boundary layer. Atomic carbon and acetylene concentrations increase in the jet to significant 0.1% levels, with the subsequent pre-PAH growth also evident. These trends, particularly for pre-PAH growth, persist into the boundary layer simulation. Calculated concentrations of carbonaceous species other than C, $C_2H_2$, PAH, and $CH_4$ are relegated to sub-ppm levels at the substrate surface. No kinetic trends from the jet portions of the model appear to be significantly reversed in the boundary layer region. The general features observed are not qualitatively altered if we use a temperature of 3500 K for the arc region instead of 5000 K.

Table 2 lists calculated mole fractions for many of the species at the boundary layer and substrate surface, as well as the equilibrium concentrations at the appropriate temperatures. The persistence of nonequilibrium concentrations of radicals, particularly atoms, clearly shows kinetic control of the gas phase chemistry. In particular, there are very large nonequilibrium concentrations of hydrogen atoms due to the slow rate of termolecular atomic recombination. The decay lifetime in the boundary layer region is roughly 100 μs. This high hydrogen atom concentration in turn controls the carbon chemistry.

Because carbon atom reactions are often neglected in models of both combustion and diamond CVD, its high concentration may appear surprising. Carbon is produced by the H + CH reaction, but the reverse loss reaction is 23 kcal/mole endothermic. We predict large conversion of the methane to carbon atoms in the superequilibrium of hydrogen atoms. At cooler temperatures removal by the endothermic reaction with $H_2$ will be slow. Superequilibrium amounts of carbon atoms persist, removed mainly by the postulated reaction with acetylene and further addition reactions which lead to PAHs.

Acetylene itself is observed to rise through the jet region. It is important to include many combination reactions between the various carbon radicals, steps not normally found in many combustion or pyrolysis mechanisms. The decline observed in the boundary layer is from pre-PAH formation. A more precise prediction of both acetylene and larger species requires a more complex mechanism (11). PAHs with 4 to 5 rings have been observed (21) in the arc jet plasma by laser-induced fluorescence, and thus the predicted growth of the pre-PAHs in the model is satisfying.

Methyl radicals are often considered the key diamond growth species, but according to the arc torch chemistry model their concentration declines continuously beyond the arc. Production rates remain low because the high concentrations of superequilibrium carbon atoms are unreactive. Since equilibrium in the system favors methane, there is a strong driving force converting whatever methyl is formed in the boundary layer irreversibly to methane. (Calculated methane concentrations increase through the boundary layer region.) Also, the superequilibrium hydrogen atoms destroy methyl by the H + $CH_3$ reaction.

A 100 μm/min growth rate over our area is an atom deposition rate from the torch of $1.5 \times 10^{-6}$ mole/min. For our flow, this requires the active species have at least .001 of the total carbon, or greater than 5 ppm of the total flow. Atomic carbon, acetylene, pre-PAH and methane are the only other species at the substrate which meet this criterion. Methyl radicals have a concentration a factor of 20 too low. Since we neglect important diffusion effects, we might estimate an upper bound of that simplification by averaging the calculated methyl throughout the boundary layer. The resulting 5 ppm average concentration requires a unity probability for the conversion of $CH_3$ to diamond carbon. Thus, we conclude that our model does not predict sufficient methyl radical concentration for the Harris mechanism to account for the measured diamond growth rate.

These results strongly suggest carbon atoms could contribute to diamond growth in the arc-jet plasma. There is a chemical precedent; carbon atoms are known to react with hydrocarbons by insertion into C-H bonds (20). Except for acetylene, and perhaps some of the larger species grouped together as pre-PAH, no other carbon species carries enough carbon to the surface to account for the observed growth rates from our arc under these conditions.

Goodwin (14) has recently reported modeling calculations on the same plasma torch experiment. His results indicate enough methyl (100 ppm) is present at the

substrate surface to account for the observed growth rates. We do not understand the origin of the differences between our predictions and Goodwin's. His model has a much better treatment of the fluid flow, diffusion, and surface reactions. However, it is not clear that the improved fluid mechanics is the source of the difference in our conclusions. We find that the chemical mechanism has profound impact on our prediction; for example, the use of our conventional flame mechanism which neglects atomic carbon predicts 20 ppm methyl at the substrate. We are unable to assess the differences in the chemical mechanisms, as Goodwin could not list his chemical mechanism within the length restrictions of a letter.

We draw five conclusions. First, our gas phase chemistry model does not predict enough methyl radicals at the substrate to account for the observed growth rate using the Harris mechanism. Second, if our chemical mechanism is equivalent with Goodwin's, then fluid dynamics and surface chemistry can increase the $CH_3$ concentration by a factor of 500. Third, omission of the additional chemistry from the mechanism increases the methyl radical concentration by more than a factor of 100. Fourth, in the arc-jet-plasma, carbon atoms are present in such excess that their addition to C-H bonds on the surface must be considered. Fifth, a surprising amount, more than half, of the carbon in the feedstock grows into polyatomic hydrocarbon molecules.

*Supported by the Army Research Office.

## REFERENCES

1. K Kuarihara, K. Sasaki, M. Kawarada, and N. Koshino, Appl. Phys. Lett. **52**, 437 (1988).
2. N. Koshino, K. Kurihara, M. Kawarada, and K Sasaki, in *Diamond and Diamond-Like Materials Synthesis*, ed. G. H. Johnson, A. R. Badzian, and M. W. Geis, Materials Research Society, Pittsburgh, PA **EA 15**, 1988, pp 95-98.
3. S. Matsumoto, in *Diamond and Diamond-Like Materials Synthesis*, ed. G. H. Johnson, A. R. Badzian, and M. W. Geis, Materials Research Society, Pittsburgh, PA **EA 15**, 1988, pp 119-122.
4. N Ohake, H. Tokura, Y. Kuriyama, Y. Mashimo, and M Yoshikawa, *Proceedings of the 1st Int. Conf. on Diamond and Diamond-Like Films*, ed J. P. Dismukes, The Electrochemical Society, Pennington, NJ, 1989, pp 93-105.
5. K. R. Stalder and R. L. Sharpless, J. Appl. Phys. **68**, 6187 (1990).
6. C. J. Chu, M. P. D'Evelyn, R. H. Hauge, and J. L. Margrave, J. Mater. Res. **5**, 2405 (1990).
7. L. R. Martin and M. W. Hill, J. Mat. Sci. Lett. **9**, 621 (1990).
8. S. J. Harris and L. R. Martin, J. Mater. Res. **5**, 2313 (1990).
9. S. J. Harris, Appl. Phys. Lett. **56**, 2298 (1990).
10. S. J. Harris, J. Appl. Phys., **65**, 3044 (1990).
11. M. Frenklach and H. Wang, Phys. Rev. B **43**, 1520 (1991).
12. D. G. Goodwin and G. G. Gavillet, J. Appl. Phys., **68**, 6393 (1990).

13. G. A. Raiche, G. P. Smith, and J. B. Jeffries, Proceedings of the 2nd Int. Conf. on the New Diamond Science and Technology, ed. R. Messier and J. T. Glass, Materials Research Society, Pittsburgh, PA, in press.
14. D. G. Goodwin, preprint, Appl. Phys. Lett., submitted 1991.
15. R. J. Kee, J. A. Miller, and T. H. Jefferson, Sandia Report SAND80-8003, 1980.
16. A. W. Phelps and K. R. Stalder, Appl. Phys. Lett. **57**, 1090 (1990).
17. M. Frenklach, J. Appl. Phys. **65**, 5142 (1989).
18. R. J. Kee, F. M. Rupley, and J. A. Miller, Sandia Report SAND87-8215, 1987.
19. N. Cohen and K. Westberg, J. Phys. Chem. Ref. Data **12**, 531 (1983).
20. P. B. Shevlin and S. Kammula, J. Amer. Chem. Soc. **99**, 2627 (1977).
21. G. A. Raiche and J. B. Jeffries, unpublished data.

Table 1
**Reaction Mechanism**

| Reaction | A | n (cc/mole) | E (cal/mole) | Source |
|---|---|---|---|---|
| $CH_4 + M \leftrightarrow CH_3 + H + M$ | 1.300E + 33 | -3.73 | 106600. | F |
| $CH_3 + H_2 \leftrightarrow CH_4 + H$ | 2.800E + 04 | 2.50 | 9400. | F |
| $CH_3 + M \leftrightarrow CH_2 + H + M$ | 1.000E + 16 | 0.00 | 90500. | F |
| $CH_3 + H \leftrightarrow CH_2 + H_2$ | 1.800E + 14 | 0.00 | 15000. | F |
| $CH_2 + H \leftrightarrow CH + H_2$ | 4.000E + 13 | 0.00 | 0.00 | F |
| $CH_2 + CH_2 \leftrightarrow C_2H_2 + H + H$ | 1.000E + 14 | 0.00 | 0.00 | F |
| $CH_3 + CH_2 \leftrightarrow C_2H_4 + H$ | 5.000E + 13 | 0.00 | 0.00 | F |
| $CH_3 + CH_3 \leftrightarrow CH_4 + CH_2$ | 1.700E + 09 | 0.56 | 12600. | F |
| $CH_3 + CH_3 \leftrightarrow C_2H_5 + H$ | 5.000E + 12 | 0.10 | 10600. | F |
| $C_2H_6 + M \leftrightarrow CH_3 + CH_3 + M$ | 2.500E + 37 | -04.6 | 98500. | SJ |
| $C_2H_6 + M \leftrightarrow C_2H_5 + H + M$ | 7.700E + 35 | -4.43 | 107000. | SJ |
| $C_2H_6 + H \leftrightarrow C_2H_5 + H_2$ | 5.400E + 02 | 3.50 | 5200. | F |
| $C_2H_6 + CH_3 \leftrightarrow CH_4 + C_2H_5$ | 5.500E-01 | 4.00 | 8300. | F |
| $C_2H_6 + CH_2 \leftrightarrow C_2H_5 + CH_3$ | 6.500E + 12 | 0.00 | 7900. | F |
| $C_2H_5 + H \leftrightarrow C_2H_4 + H_2$ | 3.000E + 13 | 0.00 | 0.00 | F |
| $C_2H_5 + M \leftrightarrow C_2H_4 + H + M$ | 2.400E + 36 | -5.36 | 41800. | F |
| $C_2H_4 + CH_3 \leftrightarrow C_2H_3 + CH_4$ | 4.400E-04 | 5.00 | 8300. | F |
| $H + H + H \leftrightarrow H_2 + H$ | 3.200E + 15 | 0.00 | 0.00 | CW |
| $H + H + H_2 \leftrightarrow H_2 + H_2$ | 9.700E + 16 | -0.60 | 0.00 | CW |
| $C_2H + M \leftrightarrow C_2H + H + M$ | 4.200E + 16 | 0.00 | 107000. | TG |

Table 1
(Continued)
**Reaction Mechanism**

| Reaction | A | n (cc/mole) | E (cal/mole) | Source |
|---|---|---|---|---|
| $C_2H + C_2H_3 \leftrightarrow C_2H_2 + C_2H_2$ | 1.000E + 13 | 0.00 | 0.00 | SJ |
| $C_2H_3 + M \leftrightarrow C_2H_2 + H + M$ | 4.000E + 35 | -6.17 | 50700. | SJ |
| $C_2H_3 + H \leftrightarrow C_2H_2 + H_2$ | 3.000E + 13 | 0.00 | 0.00 | SJ |
| $C_2H_3 + C_2H_3 \leftrightarrow C_2H_4 + C_2H_2$ | 1.000E + 13 | 0.00 | 0.00 | SJ |
| $C_2H_4 + M \leftrightarrow C_2H_3 + H + M$ | 2.500E + 17 | 0.00 | 96600. | W |
| $C_2H_4 + M \leftrightarrow C_2H_2 + H_2 + M$ | 2.500E + 17 | 0.00 | 79350. | W |
| $C_2H_4 + H \leftrightarrow C_2H_3 + H_2$ | 1.500E + 14 | 0.00 | 10200. | W |
| $C_2H_4 + C_2H \leftrightarrow C_2H_3 + C_2H_2$ | 2.000E + 13 | 0.00 | 0.00 | SJ |
| $C_2H + H_2 \leftrightarrow C_2H_2 + H$ | 4.100E + 05 | 2.40 | 860. | MB |
| $C + CH_3 \leftrightarrow C_2H_2 + H$ | 5.000E + 13 | 0.00 | 0.00 | MB |
| $CH + CH_2 \leftrightarrow C_2H_2 + H$ | 4.000E + 13 | 0.00 | 0.00 | MB |
| $CH + CH_3 \leftrightarrow C_2H_3 + H$ | 3.000E + 13 | 0.00 | 0.00 | MB |
| $C + CH_2 \leftrightarrow C_2H + H$ | 5.000E + 13 | 0.00 | 0.00 | MB |
| $CH + H \leftrightarrow C + H_2$ | 1.500E + 14 | 0.00 | 0.00 | MB |
| $C + CH \leftrightarrow C_2 + H$ | 5.000E + 13 | 0.00 | 0.00 | SJ |
| $C_2 + H_2 \leftrightarrow C_2H + H$ | 4.000E + 05 | 2.40 | 1000. | SJ |
| $CH + CH \leftrightarrow C_2 + H_2$ | 5.000E + 12 | 0.00 | 0.00 | SJ |
| $CH + CH \leftrightarrow C_2 + H + H$ | 5.000E + 13 | 0.00 | 19000. | SJ |
| $C + C + M \leftrightarrow C_2 + M$ | 3.000E + 14 | 0.00 | -1000. | SJ |
| $C + H + M \leftrightarrow CH + M$ | 3.000E + 14 | 0.0 | -1000. | SJ |
| $C + C_2H_2 \rightarrow$ "pre-PAH" + H | 2.000E + 13 | 0.0 | 0.00 | SJ |
| C + "pre-PAH" → "pre-PAH" | 2.000E + 13 | 0.0 | 0.00 | SJ |

W 22 J. Warnatz, in *Combustion Chemistry*, ed by W. C. Gardiner Jr., Springer, New York, 1984, pp 1773.
SJ This work.
MB 23 (Miller & Bowman, Prog.En.Comb.Sci. 15, 287 (1989)).
F 17 (M.Frenklach, J.Appl.Phys. 65, 5142 (1989). (main text)).
CW 19 (N.Cohen & K.Westberg, J.Phys.Chem.Ref.Data 12, 531(1983) (main text)).
TG 24 (T.Tanzawa & W.C.Gardiner, 17th Comb.Symp. 563 (1979)).

Table 2
**Calculated Mole Fractions**

| Species | Boundary Layer | Substrate Surface | %C | Equilibrium 2100 K | Equilibrium 1200 K |
|---|---|---|---|---|---|
| H | .406 | .355 | | .005 | 400 ppb |
| $H_2$ | .590 | .643 | | .992 | .995 |
| C | .0021 | 890 ppm | .22 | 1 ppb | |
| $C_2$ | 1 ppm | 10 ppb | 5 ppm | .1 ppb | |
| CH | 42 ppm | 500 ppb | 120 ppm | 2 ppb | |
| $CH_2$ | 22 ppm | 150 ppb | 35 ppm | .1 ppm | |
| $CH_3$ | 24 ppm | 240 ppb | 60 ppm | 15 ppm | 40 ppb |
| $CH_4$ | 9 ppm | 21 ppm | .005 | 110 ppm | .005 |
| $C_2H$ | 30 ppm | 15 ppb | 10 ppm | .4 ppm | |
| C2H2 | 670 ppm | 428 ppm | .11 | .0024 | 150 ppb |
| "pre-PAH" | 125 ppm | 720 ppm | .67 | | |

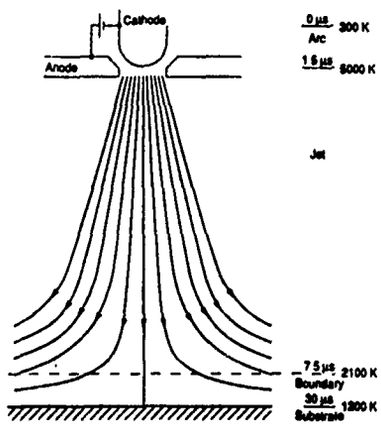



Fig. 1. Schematic of the gas flow through the arc-jet plasma including gas temperatures and residence times.

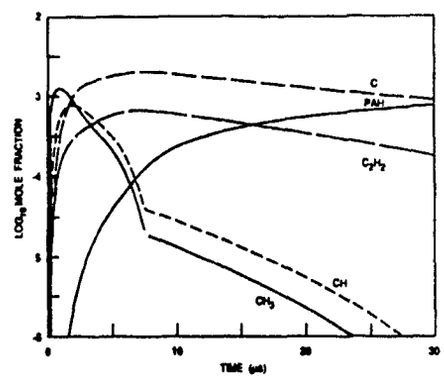



Fig. 2. Predicted concentrations of selected species in the arc-jet plasma environment as a function of reaction time. PAH represents the precursor formation of large hydrocarbon radicals as described in the text.

# OBSERVATION OF OH RADICALS IN A FILAMENT-ASSISTED DIAMOND GROWTH ENVIRONMENT*

Ulrich E. Meier,** Lukas E. Hunziker,
David R. Crosley, and Jay B. Jeffries
Molecular Physics Laboratory
SRI International
Menlo Park, CA 94025

The first observations of the hydroxyl radical in a hot filament assisted diamond growth environment are presented. Laser-induced fluorescence (LIF) is used to make *in situ*, nonintrusive, measurements of the spatial distribution of OH concentration near the filament as a function of feedstock composition, reactor pressure, and filament temperature. LIF measurements of the OH rotational level population distribution are used to determine spatially resolved gas temperature.

## Introduction

The addition of oxygen to the feedstock gases for diamond CVD can have a profound effect on the quality of the resulting diamond film. Kawato and Kondo (1) found the deposition of graphitic or amorphous carbon could be suppressed. Several studies (2-5) of microwave diamond CVD have found that oxygen addition can extend the range of conditions which produce diamond film. For example, Liou et al. (5) found that the addition of oxygen allowed them to significantly reduce the substrate temperature. All these studies (1-5) find that the diamond growth rates can be varied and the quality of the film significantly improved by the addition of $O_2$.

The influence of oxygen on the gas composition of hot filament diamond CVD has been investigated using *in situ* mass spectrometry by Harris and Weiner (6). They find that oxygen addition can convert a significant fraction of the hydrocarbons to CO and $H_2$. They model the gas chemistry with added oxygen and find good agreement with their measurements of CO, $C_2H_2$, and $CH_4$. They postulate that the addition of oxygen produces "sufficient gas phase OH to remove the nondiamond (pyrolytic) carbon from the film (6)." Frenklach and Wang (7) have introduced oxygen into their detailed model of hot filament assisted diamond growth. They find the oxygen addition has two significant effects: 1) formation of aromatics is suppressed by the oxidation of the carbon to CO and 2) the gasification of deposited $sp^2$ phase carbon by OH radicals.

We have observed hydroxyl radicals in our hot filament reactor using laser-induced fluorescence (LIF). LIF has four principal advantages for the detection of chemically reactive radical species like OH. First, the LIF measurement is selective, each species has its own definitively characteristic excitation and detection spectra. Second, the measurements can be performed *in situ* without inserting physical probes into the plasma or extracting any of the plasma gases. Third, LIF is quite sensitive: ppb detection limits of OH are quite feasible. Fourth, the measurement is spatially resolved; signal is observed only from the intersection of the laser beam and fluorescence collection viewing region.

LIF measurements of the rotational population distribution in OH are used to determine gas temperatures as a function of pressure and distance from the filament. The OH concentration is measured as a function of reactor pressure, feedstock composition, and filament temperature. These measurements show that OH is indeed present in hot filament diamond CVD reactors which use $H_2$-$CH_4$-$O_2$ mixtures.

## Experimental Method

The hot filament reactor is constructed inside a 30 cm vacuum chamber with a feedstock inlet 5 cm above the filament and gas exhaust 10 cm below. Figure 1 is a schematic drawing of the experimental arrangement showing the hot filament and the optical collection geometry. A 0.04 cm diameter, 3.3 cm long tungsten wire is mounted on molybdenum posts and is heated by direct current to temperatures 2300-2800 K as measured by an emission corrected optical pyrometer. The filament and gas inlet is mounted on a vacuum manipulator which allows us to alter the laser beam to filament distance with fixed optical collection. The laser enters the chamber through Brewster angle windows, and the fluorescence is collected f/5 at right angles to the laser beam. The excitation laser is aligned along the filament. Fluorescence from molecules excited by the laser is collected, and passes through a spatial filter which limits the field of view to a region 0.5 cm along the laser beam and 0.1 cm perpendicular to the beam. The light is then spectrally filtered with a uv pass filter (Schott UG5) and a 0.25 m monochromator, and detected on a photomultiplier, whose signal is integrated on a boxcar integrator and linearly averaged by a laboratory computer. The spatial filter eliminates much of the emission from the hot filament. At positions near the filament, significant scattered laser light is observed. To avoid much of this scattered light and improve the signal/noise ratio of the LIF measurements, the 40 ns wide boxcar gate is delayed 50 ns with respect to the laser pulse.

To obtain an LIF signal, the laser wavelength is tuned to a hydroxyl absorption in the 0-0 band of the $A^2\Sigma^+$-$X^2\Pi_i$ electronic transition near 308 nm. When the laser wavelength coincides with a specific rotational transition, OH radicals absorb a laser photon and are excited to the A state. These excited molecules can radiate, undergo energy transfer collisions to other rotational levels which subsequently radiate, or be collisionally quenched. The fraction that radiate is called the quantum yield, and this fluorescence is the LIF signal. An example of the OH LIF signal in the hot filament

reactor is shown in the upper panel of Figure 2. The laser wavelength is scanned through a series of transitions; the wavelength of the observed features and their identification (8) shown above the upper panel unambiguously identify the LIF signal as originating from OH radicals.

Quantitative relative OH concentrations can be inferred from the signal intensity, gas temperature, density, and composition. The LIF signal is the product of the excited state number density $N_e$ and the quantum yield $\Phi$. The laser excites molecules with a rate $dN_e/dt = BI_L N_g f$, where $N_g$ is the ground state concentration, f the Boltzmann fraction of population in the absorbing rotational level, B the Einstein absorption coefficient, and $I_L$ the laser intensity. The quantum yield for the LIF is $\Phi = A/(A+Q)$, where A is the Einstein A coefficient and Q is the collisional quenching rate. $Q = \Sigma k_{Qi} n_i$ where the sum is over all the species in the gas, $k_{Qi}$ is the quenching rate constant for the ith species, and $n_i$ the species concentration. Rate constants for OH quenching as a function of temperature for a variety of colliders including atomic hydrogen have been measured in our laboratories (9-12). The quenching rate constants for $O_2$, $CH_4$, and $H_2$ differ less than a factor of two and that for atomic hydrogen is at most a factor of five larger at 1200 K. Harris and Weiner (13) find that less than 1% of the gas in the hot filament reactor is atomic hydrogen. Thus, to calculate Q we use $k_Q$ for $H_2$ and n equal to the total density.

Gas temperature is an important parameter in the conversion of the LIF signal to OH concentration. Both the excitation rate $dN_e/dt$ and the quantum yield $\Phi$ are temperature dependent. The laser excites molecules from a single rotation level from the Boltzmann population distribution over all the rotational levels. Thus, $dN_e/dt$ depends directly on f(T). The quantum yield has temperature dependence in both $k_Q$ and n. The pressure is constant in the hot-filament reactor, so n is simply proportional to 1/T. $k_Q$ for hydrogen declines ~25% over the temperature range in the hot filament reactor; we calculate the quenching corrected relative concentrations from high temperature quenching measurements (11).

The gas temperature is deduced from LIF measurements of the rotational distribution; this distribution is deduced from a laser excitation spectrum like that shown in Figure 2. The signal intensity for each transition is divided by the degeneracy and rotational line strength, and ln(I/Bg) is plotted versus the rotational energy of the ground state rotational level. The lower panel of Figure 2 shows such a Boltzmann plot for the spectrum in the upper panel. The straight line indicates that the distribution is well described by a temperature, and the slope of the line is proportional to 1/T. The 0-0 band of OH extends over a broad spectral range near 308 nm. This broad bandwidth requires the photo detector to have a uniform response over the 306-321 nm to avoid spectral bias errors in the temperature. We construct a spectral filter with a trapezoidal bandpass from a small (0.25 m f.l.) monochromator by setting a narrow (0.05 cm) front slit and the broad (0.5 cm) exit slit. Systematic errors in OH LIF temperature determination from spectral bias are discussed in detail in Ref. 14.

Results and Discussion

The gas temperature measured by LIF is significantly lower than the temperature of the hot filament. The data in Figure 2 are taken at 30.9 Torr, 1.1 mm from a filament at 2750 K. The slope of the Boltzmann plot in the bottom of Figure 2 gives a best fit of 1541 ± 88 K. The feedstock gas is $H_2$ with 0.5% $CH_4$ and 0.5% $O_2$. This temperature difference is slightly greater than observed with thermocouple measurements by Harris et al. (15). They measured 1800 K in the gas 1 mm from a 2600 K filament. The thermocouple measurements were not corrected for radiation. One would expect radiative heating of a thermocouple in close proximity to the brightly glowing hot filament, and thus a lower actual gas temperature.

The gas temperature depends on the reactor pressure. Figure 3 shows the OH LIF temperature as a function of distance from a 2600 K filament at hydrogen pressures of 4.4, 10.4, and 30.9 Torr. Again the added methane and oxygen are 0.5% each. The temperature gradient is in good agreement with Harris et al. (15). Both of these experiments measured the gas temperature without a substrate. With a substrate at 800-1200 K temperature and a distance from the filament of 0.5-2 cm we would expect an even steeper temperature gradient than shown in Figure 3. A temperature gradient which depends on substrate distance has been observed (16).

The relative OH concentration versus distance from the filament is shown in Figure 4. These data at 30.9 Torr are representative of the data over the entire range 4-30 Torr. The OH falls rapidly for 4-6 mm to 10-20% of the peak OH observed. The lower concentration is then nearly constant to distances of 1 cm. Note that the data in Figure 4 have been corrected for temperature dependent quenching of $H_2$ and the variation in Boltzman fraction, using the temperature gradient in Figure 3.

The OH concentration is strongly dependent on reactor pressure. The OH intensity exciting the $R_1(3)$ line falls by a factor of 40 from 4-25 Torr. The LIF signal depends on the product of OH number density and quantum yield. In the limit $Q>>A$, $\Phi \sim 1/Q$ and Q is proportional to gas pressure. Thus, for a constant mole fraction of OH in the limit where most of the excited molecules are collisionally quenched, the OH LIF signal is independent of pressure. Thus, the rapid drop in OH intensity is surprising and indicates that the mole fraction of OH declines with reactor pressure. Using the data in Figure 3 to predict the gas temperature as a function of pressure and correcting for quenching by $H_2$, the we find the OH mole fraction declines by a factor of 30 as the reactor pressure rises from 4 to 25 Torr.

Figure 5 shows the variation in the relative OH concentration as a function of added $CH_4$ and $O_2$. The OH concentration does not depend on the amount of added $CH_4$, as shown by the triangles in the figure for 0.7% of added $O_2$. However, the OH is quite dependent on the amount of added $O_2$; increasing the $O_2$ by a factor of four increased the OH by a factor of 14. This large variation is expected; Harris and Weiner (6) predict a factor of 5 increase in the OH at 7% $CH_4$ when the $O_2$ is increased from 1-3%.

Summary

We have observed LIF from OH radicals in a hot filament diamond CVD reactor in a mixture of $H_2$, $CH_4$, and $O_2$. We find the gas temperature is significantly cooler than the filament temperature. The gas temperature increases with increasing pressure. The OH mole fraction declines significantly with increasing reactor pressure. The OH concentration does not depend on the amount of added methane, but is strongly dependent on added oxygen.

## REFERENCES

1. T. Kawato and K. Kondo, Jpn. J. Appl. Phys. **26**, 1429 (1987).
2. C. Chen, Y. C. Huang, S. Hosomi, and I Yoshida, Mater. Res. Soc. Bull. **24**, 87 (1989).
3. C-P Chang, D. L. Flamm, D. E. Ibbotson, and J. A. Mucha, J. Appl. Phys. **63**, 1744 (1988).
4. J. A. Mucha, D. L. Flamm, and D. E. Ibbotson, J. Appl. Phys. **65**, 3448 (1989).
5. Y. Liou, R. Weimer, D. Knight, and R. Messier, Appl. Phys. Lett. **56**, 437 (1990).
6. S. J. Harris and A. M. Weiner, Appl. Phys. Lett. **55**, 2179 (1989).
7. M. Frenklach and H. Wang, Phys. Rev. **B43**, 1520 (1991).
8. G. H. Dieke and H. M. Crosswhite, J. Quant. Spectrosc. Radiat. Trans. **2**, 97 (1962).
9. P. W. Fairchild, G. P. Smith, and D. R. Crosley, J. Chem. Phys. **79**, 1795 (1983).
10. R. A. Copeland and D. R. Crosley, J. Chem. Phys. **84**, 3099 (1986).
11. G. P. Smith and D. R. Crosley, J. Chem. Phys. **85**, 3896 (1986).
12. J. B. Jeffries, K. Kohse-Höinghaus, G. P. Smith, and D. R. Crosley, Chem. Phys. Lett. **152**, 160 (1988).
13. S. J. Harris and A. M. Weiner, J. Appl. Phys. **67**, 6520 (1990).
14. K. J. Rensberger, J. B. Jeffries, R. A. Copeland, K. Kohse-Höinghaus, M. L. Wise, and D. R. Crosley, Appl. Opt. **28**, 3556 (1989).
17. S. J. Harris, A. M. Weiner, and T. A. Perry, Appl. Phys. Lett. **53**, 1605 (1988).
16. S. J. Harris, D. N. Belton, A. M. Weiner, and S. J. Schmieg, J. Appl. Phys. **66**, 5353 (1989).

* Supported by the Army Research Office

** On leave from DLR, Stuttgart, Germany

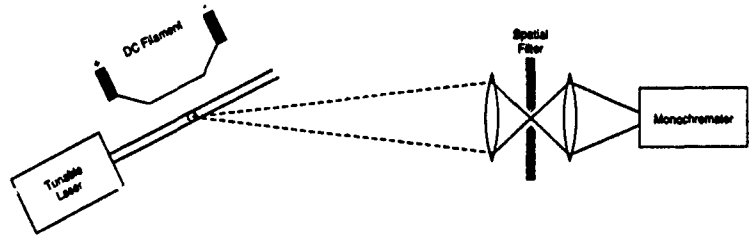



Fig. 1. Schematic diagram showing the orientation of the laser beam, hot filament, and optical collection.

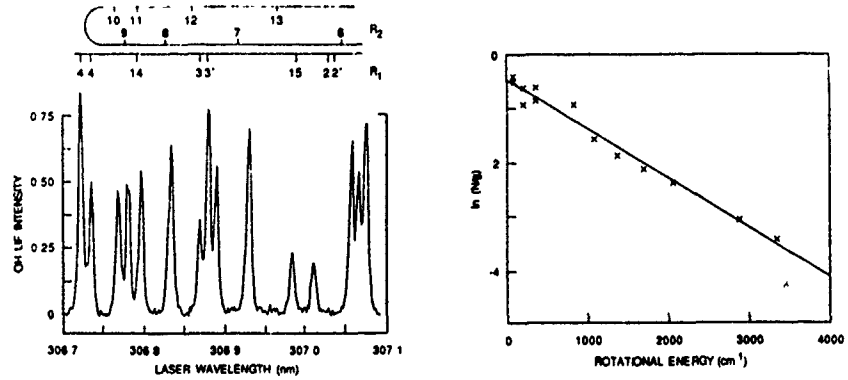



Fig. 2. Left: OH LIF rotational excitation spectrum taken 1.1 mm from a 2750 K filament in 30.9 Torr $H_2$ with 0.5% $CH_4$ and 0.5% $O_2$.

Right: Boltzmann plot of the relative rotational level populations determined from peak height analysis of the spectrum in the top panel. The best fit slope gives T = 1541 ± 88 K.

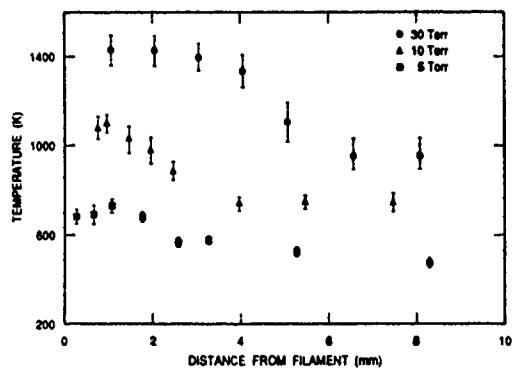



Fig. 3. Gas temperature determined from OH rotational excitation spectra versus distance from the filament for 30.9, 10.4, and 4.3 Torr pressure of $H_2$ with 0.5% $CH_4$ and 0.5% $O_2$ with a 2600 K filament temperature.

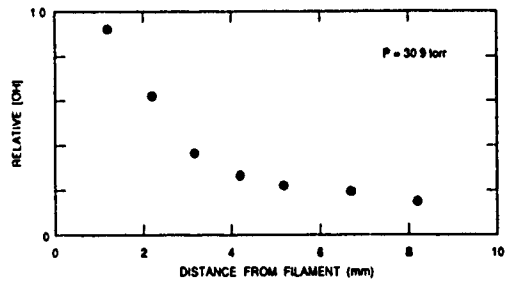



Fig. 4. Relative OH concentration versus distance from a 2600 K filament at 30.9 Torr from quenching corrected LIF measurements.

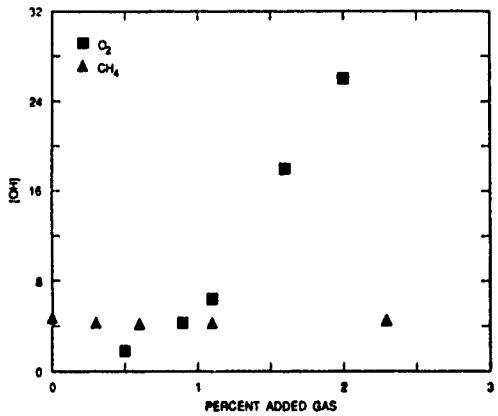



Fig. 5. Relative OH concentration from quenching corrected LIF measurements versus added $CH_4$ and $O_2$ at 4.4 Torr of $H_2$ 1.0 mm from a 2700 K filament. $CH_4$ variation (triangles) at 0.7% added $O_2$ and $O_2$ variation (squares) at 0.6% added $CH_4$.

# ACETYLENE PRODUCTION IN A DIAMOND-PRODUCING LOW PRESSURE rf-PLASMA ASSISTED CHEMICAL VAPOR DEPOSITION ENVIRONMENT

R.A. Rudder, G.C. Hudson, J.B. Posthill, R.E. Thomas, and R.J Markunas
Research Triangle Institute, P.O.Box 12194, Research Triangle Park, NC 27709

R.J. Nemanich, Y.M. LeGrice, and T.P. Humphreys
Department of Physics
North Carolina State University, Raleigh, NC 27695-8202

## ABSTRACT

We have examined using quadrupole mass spectroscopy the production of acetylene molecules under diamond growth conditions wherein no acetylene was introduced. There are two pathways available for the production of acetylene. One path for acetylene production is through conversion of $CH_4$ into $C_2H_2$ in the high temperature plasma region. The other path for acetylene production is through gasification of the graphite. In the pressure range from 1 - 10 Torr using a rf plasma discharge, the graphite gasification is the dominant path and the diamond deposition rate appears to correlate fairly well with the acetylene concentration in the reactor. The correlation can be understood by considering the acetylene production rate to be proportional to the atomic hydrogen flux to the graphite susceptor and, hence, to the atomic hydrogen flux to the diamond growth surface.

## Introduction

Many workers are studying the importance of acetylene and methyl radicals in the vapor phase growth of diamond. Techniques such as infrared diode laser absorption spectroscopy and multiphoton ionization have been used to examine the gaseous environment of the diamond deposition(1). Other workers have used isotopic labeling to identify the parentage of carbon atoms deposited as diamond(2). In this work, we have used quadrupole mass spectroscopy to monitor acetylene production during diamond deposition in a low pressure rf-plasma chemical vapor deposition environment. We find that there are two channels for acetylene production, one via conversion of $CH_4$ into $C_2H_2$ and second via gasification of graphite into $C_2H_2$. By realizing that a requirement for graphite gasification is the atomic hydrogen flux to the graphite surface, mass quadrupole spectroscopy of the gasification products has been able to demonstrate that the diamond deposition rate is proportional to the atomic hydrogen flux.

## Experimental Approach and Results

Diamond depositions have been accomplished in a low pressure rf plasma assisted chemical vapor deposition system using 1% $CH_4$ in $H_2$ gas at pressures from 1 - 10 Torr. Details of that reactor and the growth process have been previously reported(3). The vacuum system for diamond deposition is shown schematically in Figure 1. It consists of a stainless steel 150 mm conflat flange 6-way cross upon which the reactor tube, pumps, control orifice valve, vacuum gauges, quadrupole mass spectrometer, and load lock are appended. Samples are introduced into the reactor on a graphite carrier/susceptor through a vacuum load lock, transferred horizontally onto a heater stage, and raised vertically into the quartz reaction tube. The reaction tube consists of a double-walled 50 mm inside diameter quartz tube sealed to the stainless chamber by compression viton o-ring seals. The reactor tube is water cooled through the use of a heat exchanger which maintains the water temperature at 15 °C. A 8 mm water-cooled copper tube formed into a 3-turn helix 100 mm long provides the inductive coupling from the rf generator to the discharge. The rf power output from a power amplifier tube couples to the plasma using a LC resonant circuit with the plasma coil constituting the inductive component. The vacuum system is evacuated by a Balzers 500 l/s corrosive series turbomolecular pump. The pressure of the reactor is $1.0 \times 10^{-7}$ Torr prior to introducing the reactant gasses.

Conditions for diamond growth are given in Table I over the presure range from 1 - 10 Torr. Note that the temperature of the hydrogen plasma has been calculated from the relative emission intensities of the atomic hydrogen Balmer series assuming a Boltzman distribution and collisionless lifetimes. These assumptions may be in error, but this calculation allows some internal standard for the power input to the plasma.

Table I

| Pressure | Flow rate (sccm) | Estimated rf power (w) | $T_{plasma}$ (K) |
|---|---|---|---|
| 1 | 1.3 | 400 | 3420 |
| 3 | 3.8 | 660 | 3350 |
| 5 | 6.3 | 1000 | 3200 |
| 7 | 8.8 | 1800 | 3200 |
| 10 | 12 5 | 2400 | 3270 |

One notices that the pressure in this series is varied by maintaining a constant pumping speed and reducing the gas flow into the reactor. The estimated plasma temperature remains constant throughout this pressure range despite

the 6-fold increase in power input. Without this increase in power at the higher pressures, it would not be possible to maintain the atomic hydrogen emission. This increase in applied power also increases the substrate temperature. The substrate temperature varies from ≈650 ° C at 1.0 Torr to ≈850 ° C at 10 Torr.

Following deposition, films were analyzed using scanning electron microscopy (SEM) and Raman scattering spectroscopy. Cleaved sectional analysis in the SEM was used to ascertain diamond deposition rates at the different pressures. We assumed the deposition rate was linear in time. The silicon substrates used in this work were diamond polished prior to introduction into the reactor to provide immediate nucleation sites.

SEM micrographs show that the deposited films are polycrystalline showing well-defined faceting. The crystallite sizes vary from 0.5 - 2.5 $\mu$m. The crystallites appeared to have nucleated at point sites upon which growth proceeded 3-dimensionally into a continuous film. Raman spectra for the complete series are given in Figure 2. All samples display a 1332 $cm^{-1}$ diamond Raman line. Samples grown at lower pressures show more non-diamond bonding. It is not clear at this point if the appearance of the non-diamond bonding components (i.e. the appearance of Raman features between 1500 and 1600 $cm^{-1}$) is due to a reduction in pressure or a reduction in substrate temperature. It is clear that all conditions produced diamond from the gas phase using the low pressure rf-plasma system.

The environment of the diamond g th was probed by mass spectroscopic analysis of gasses downstream from the . sma region. Samples were positioned near the rf coil on a graphite susceptor. By comparing the $C_2H_2$ production observed with the graphite susceptor removed from the discharge tube to the $C_2H_2$ production when the susceptor was positioned near the rf coil, one can distinguish $CH_4$ conversion to $C_2H_2$ in the gas phase from gasification of the graphite to $C_2H_2$ at the susceptor surface. (It should be noted that these experiments were performed when the plasma tube was fairly clean of carbon deposits. The graphite susceptor represents the largest source of solid carbon exposed to the plasma.) Figure 3 shows the conversion of $CH_4$ to $C_2H_2$ as a function of total pressure when the graphite susceptor is *not* present in the reactor. This figure shows a nearly constant ratio of $CH_4$ to $C_2H_2$ across the pressure series. Given that two $CH_4$ molecules are necessary for $C_2H_2$ production, we conclude that approximately 60% of the $CH_4$ is converted into $C_2H_2$. Figure 4 shows the observed $C_2H_2$ production when the graphite susceptor is inserted 3.0 mm below the rf coil with 1% $CH_4$ in $H_2$ discharge. There is a pronounced pressure dependence to the $C_2H_2$ production. At 3 Torr, there is approximately 4 times more $C_2H_2$ partial pressure in the reactor with the graphite susceptor present than there was with the graphite susceptor absent. More $C_2H_2$ is produced at 3 Torr by graphite gasification than is produced by $CH_4$ conversion into $C_2H_2$.

It is interesting to compare the diamond deposition rate with the $C_2H_2$ production rate. Figure 5 shows the growth rate as a function of pressure for this series. We find that the deposition rate is a maximum for a pressure of approximately 3 Torr. A comparison with Figure 4 shows that the deposition rate and the $C_2H_2$ production rate both show a similar dependence on reactor pressure with the highest deposition rate and the highest $C_2H_2$ production rate occuring at 3 Torr.

**Discussions and Conclusions**

This work shows an apparent correlation between the deposition rate of diamond and rate of gasification of the graphite susceptor into $C_2H_2$. Perhaps, the growth rate of diamond is inhibited by graphitic sites which must be removed before diamond can propagate. Hence, growth conditions which rapidly gasify graphite, remove graphitic sites from the diamond surface allowing diamond growth to propagate. Mucha et al.(4) used similar arguments to explain higher effective growth rates in microwave CVD experiments when alternating cycles of $H_2$ and $CH_4$ were introduced into the reactor. Alternatively, the $C_2H_2$ radical may be promoting diamond growth as Frenklach et al.(5) have suggested. Thus, higher concentrations of $C_2H_2$ in the gas phase may be responsible for the higher growth rate.

The work of Balooch and Olander(6) yields considerable insight into the data presented in this paper. Balooch and Olander showed that the gasification products observed when atomic hydrogen interacts with pyrolytic graphite are distinctly different depending on the temperature of the graphite. At temperatures below 550°C, the primary product was $CH_4$. At temperatures above 900°C, the primary product was $C_2H_2$. Balooch and Olander argued that in the intermediate temperature range H atoms recombined on the pyrolytic graphite surfaces without substantial graphite gasification. In the pressure series reported in this paper, the graphite susceptor is certainly above 550°C. We, as Balooch and Olander, do observe $C_2H_2$ as a by-product of atomic H with graphite. We are able to deposit diamond films in the intermediate temperature range where atomic hydrogen is not as efficient in dissolving graphite. It should be noted that the flux of atomic hydrogen present to a diamond CVD growth surface is orders of magnitude higher than the fluxes used by Balooch and Olander. Consequently, graphite removal from a diamond CVD growth surfaces with atomic H is undoubtedly possible.

The production of $C_2H_2$ from a graphite surface at elevated temperatures will be proportional to the atomic hydrogen flux. If one interprets the $C_2H_2$ production rate shown in Figure 4 as proportional to the atomic hydrogen flux to the graphite surface and hence to the diamond CVD growth surface, then one

concludes that the atomic hydrogen flux to the growth surface is a strong function of pressure. Hence, the correlation between diamond growth rate and acetylene production is more concisely a consequence of the differing atomic hydrogen fluxes. The higher fluxes of atomic hydrogen dissolve graphite and promote diamond bonding. These results are strong support for the work of Yarbrough(7) showing that at high atomic hydrogen concentrations diamond precipitated as the stable phase.

*Acknowledgements* The authors wish to thank the Strategic Defense Initiative Organization/Innovative Science and Technology Office through the Office of Naval Research (N-00014-86-C-0460) and the Office of Naval Research (N00014-90-J-1707) for the financial support of this work.

## REFERENCES

(1) F.G. Celii, P.E. Pehrsson, H.-T. Wang, and J.E. Butler, Appl. Phys. Lett. 52 , 2045 (1988).

(2) C. Judith Chu, Mark P. D'Evelyn, Robert H. Hauge, and John L. Margrave, J. Mat. Res. 5, 2405 (1990).

(3) R.A. Rudder, G. C. Hudson, Y. M. LeGrice, M.J. Mantini, J.B. Posthill, R.J. Nemanich, and R.J. Markunas, Mat. Res. Soc. EA-19 , 89 (1989).

(4) J.A. Mucha, D.L. Flamm, and D.E. Ibbotson, J. Appl. Phys. 65, 3448 (1989).

(5) Michael Frenklach and Hai Wang, Phys. Rev. B 43, 1520 (1991).

(6) M. Balooch and D.R. Olander, J. Chem. Phys. 63, 4772 (1975).

(7) Walter A. Yarbrough, Mat. Res. Soc. Symp. Proc. 162, 75 (1990).

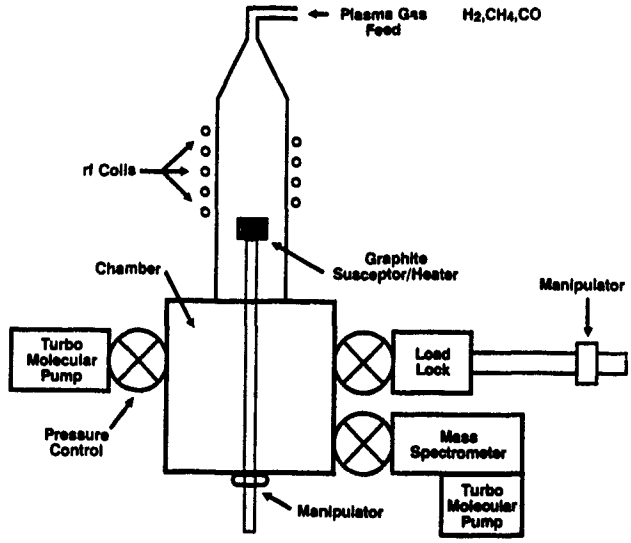



Figure 1. Schematic of low pressure rf-plasma assisted chemical vapor deposition system.

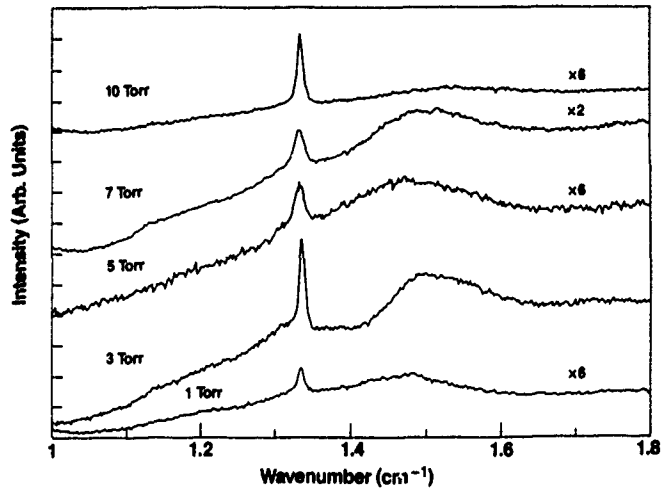



Figure 2. Raman spectra for diamond films deposited from 1 to 10 Torr using 1% $CH_4$ in $H_2$.

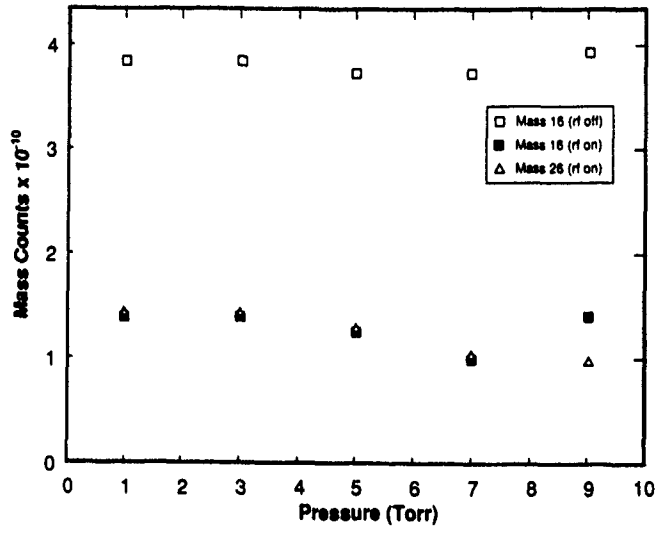



Figure 3. Conversion of $CH_4$ into $C_2H_2$ without the graphite susceptor in the reactor.

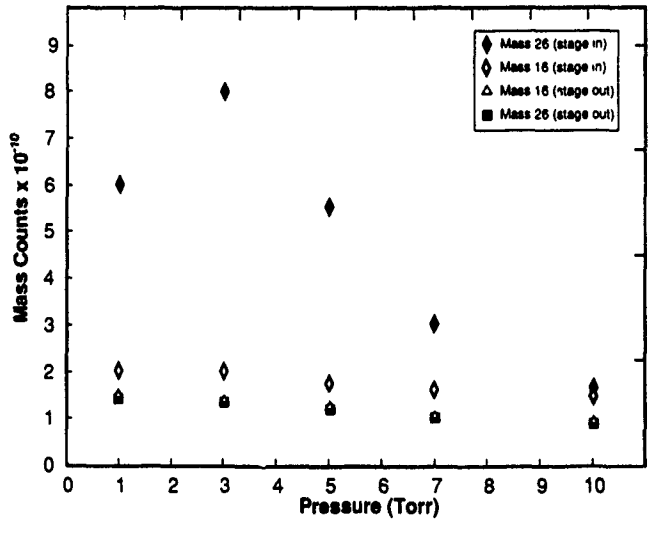



Figure 4. Production of $C_2H_2$ in the growth reactor as a function of pressure with the graphite susceptor in place.

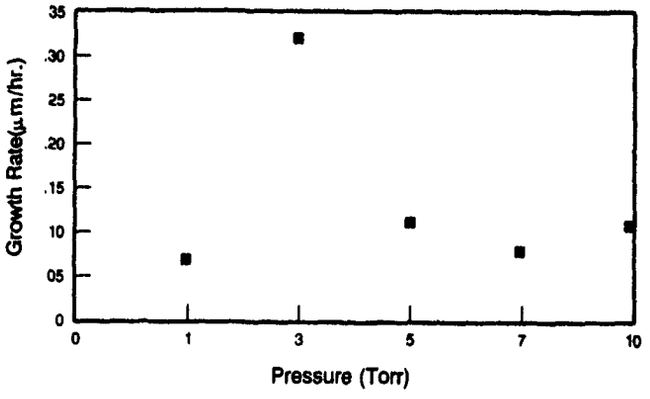



Figure 5. Diamond deposition rate as a function of pressure. Thickness values were obtained from SEM micrographs of cleaved sections.

# QUANTITATIVE ANALYSES OF THE GASEOUS COMPOSITION DURING FILAMENT-ASSISTED DIAMOND GROWTH

W. L. Hsu
Sandia National Laboratories
Livermore, CA 94551-0969

## ABSTRACT

The concentrations of H, $CH_3$ and other stable species in a hot-filament reactor have been measured quantitatively under diamond growth conditions. The two radical species have mole fractions in the range of $10^{-4}$ - $10^{-3}$, while $CH_4$ and $C_2H_2$ have significantly higher levels. As the methane percentage in the feed gas was increased up to 7.5%, the concentration of H decreased by an order of magnitude. Under the same conditions, the rate of film growth was found to increase. This divergence of results suggests that H-induced surface reactions are not the rate-limiting steps for film growth.

## INTRODUCTION

Quantitative measurements of some gaseous species in diamond growth reactors have been reported in the past.[1-3] These measurements are generally limited to to a small set of species. In a previous paper we demonstrated the use of a molecular beam mass spectrometry system which has the ability to detect a wide range of species.[4] For this paper we will present quantitative measurements of H, $CH_3$, and other species in a hot-filament reactor under diamond growth conditions.

## EXPERIMENTAL PROCEDURE

Gas from the process chamber is extracted through a 300-μm diameter orifice. The gas undergoes free-jet expansion and forms a molecular beam in which chemical reactions amongst the molecules cease. This "freezing" process is necessary to ensure that the composition in the beam remains as it was before the extraction. The beam is allowed to pass unobstructed to the ionization chamber where the species are ionized, mass analyzed, and then detected. Ions formed by direct ionization of the radical species can be distinguished from those formed by dissociative ionization of the parent molecules by using the threshold ionization technique.[4]

A more detailed description of the procedure for deriving mole fractions is given elsewhere[5]; suffices it to say that all signals are normalized to that of argon, which is present as a diluent. The signal ratios, $I_i/I_{Ar}$, are related to the mole fraction ratios, $X_i/X_{Ar}$, by the sensitivity factor, $S_{i,Ar}$. For stable species, the sensitivity factors are determined by calibrating the signal ratios with known

mixtures. For radical species, we use reported ionization cross sections to determine the sensitivity factors.

In this paper we will show how the mole fractions of H, $CH_3$, $CH_4$, and $C_2H_2$ vary with increasing addition of methane to the feed gas. Two types of experiments were conducted: one in which the feed gas was pure hydrogen (data shown in Fig. 1), another in which the feed gas was a mixture of $H_2$, Ar, and $CH_4$. The methane percentage, $f=100 \times (CH_4)_{flow\text{-}rate}/\{(CH_4)_{flow\text{-}rate}+(H_2)_{flow\text{-}rate}+(Ar)_{flow\text{-}rate}\}$, ranged from 0.4% to 7.5%. The filament was a single strand of uncoiled tungsten wire 0.25 mm in diameter. The filament temperature was monitored by a Williams 8120 two-color pyrometer and the substrate temperature by a K-type thermocouple. During the experiment we discovered that the resistance of the filament changed as we changed the methane percentage. In order to obtain repeatable results we allowed 15 minutes for the resistance to stabilize every time we changed the operating conditions. We also subjected each new tungsten filament to a carburization procedure prior to data taking by heating the filament to 2700 K in a 7.5% methane mixture for one hour.

## RESULTS

Shown in Fig. 1 are the H mole fractions measured when only $H_2$ was fed into the reactor. The results are plotted as a function of the filament temperature while the substrate was kept fixed at 1073 K. Also shown is a solid curve which is the equilibrium H mole fractions calculated at the filament temperature. The measured values are at least one order of magnitude less; however, when compared to the equilibrium value at the substrate temperature, the data are at least two orders of magnitude larger. In this sense, H in the vicinty of the substrate surface is in "superequilibrium".

Now, let us add methane to the system. Shown in Fig. 2 are the mole fractions of H, $CH_3$, $CH_4$, and $C_2H_2$ as a function of the methane percentage in the feed gas. The mole fractions of $H_2$ and Ar remained essentially constant at 0.9 and 0.07, respectively, and are not shown. The experiments were performed at a fixed pressure (20.25 Torr), a fixed filament temperature (2600 K), and a fixed substrate temperature (1073 K).. The flow rate of $H_2$ and Ar was fixed at 170.6 and 13.2 Pa-l/s, respectively, and only the feed rate of methane was varied.

One of the most interesting features is the large decrease in the H-atom concentration. At f=0.4%, the concentration was as high as when methane was absent. When the methane percentage was increased to 7.5% the H mole fraction dropped by an order of magnitude . Even more pronounced decreases were observed at lower filament temperatures. At 2273 K, the H concentration decreased by nearly two orders of magnitude over the same range of methane percentage. Similar effects have been reported by Celii and Butler;[6] we concur with their explanation that this behavior was caused by filament poisoning.

Both methyl and acetylene are observed to behave similarly; the concentration first increased and then leveled off at high methane percentages. At low levels of methane feed methane has concentrations lower than that of acetylene, but it became the dominant hydrocarbon species as more methane was fed into the system. The mole fractions have also been measured when three parallel filaments, separated 0.5 cm apart, were used.[5] This geometry was used to simulate a planar filament source. The primary effect has been the further reduction of $CH_4$ relative to acetylene at low levels of methane feed. We believe that in the single filament case, methane from the feed gas can flow around the filament and remain unpyrolyzed. As one pulls the single filament further away from the gas sampling pin-hole, one would expect to see an increasing $CH_4/C_2H_2$ concentration ratio; this behavior was indeed reported by Harris and Weiner.[2] When the filament source approximated that of a planar geometry, it was less likely for the methane that flowed around the edges of the plane to reach the sampling orifice. Gas transport from the filaments to the substrate thus approaches that of a one-dimensional flow problem.

The concentration of the three hydrocarbon species discussed has been measured by Celii et al.[1] using infrared absorption spectroscopy. To derive a local concentration they divided the signal by an absorption pathlength given by the diameter of the chamber, which is substantially wider than the extent of the filament. For the two stable species, acetylene and methane, their values agree with ours to within a factor of four. However, for methyl, their value is less by nearly a factor of twenty. Since methyl is a radical species, it is probable that it was more localized around the filaments than assumed.

Using the measured hydrocarbon species shown in Fig. 2 we can perform an inventory analysis for carbon atoms. The mole fraction of carbon atoms that have been detected is given by $[CH_3] + [CH_4] + 2*[C_2H_2]$, where the [ ] indicate the mole fraction; the results are shown in Fig. 3. We see that we can essentially account for all the carbon fed into the system and that the bulk of it resides in the form of methane and acetylene. All other hydrocarbon species, including those not yet detected, can only exist in trace amounts.

We have conducted a series of film-growth experiments. The experimental conditions were identical to those set during the mole fraction measurements. The films were deposited on Si <111> with the surface scratched by 1/8-μm diamond paste. After growth the wafers were fractured and observed under a scanning electron microscope to obtain the film thickness. The film growth rate was determined by dividing the thickness by the 24-hr growth period. Examination of the film texture showed that the crystalline facets became less pronounced at higher percentages. From our past experience this feature is generally associated with a higher content of amorphous or graphitic carbon.[7] In our growth rate calculations we made no attempt to differentiate between diamond and non-diamond materials.

The growth rate is plotted as a function of the methane percentage in Fig. 4; it rises initially and then levels off. This behavior is in sharp contrast with the trend for the H concentration curve, which is replotted in Fig. 4. The divergence of the two curves implies that the deposition of carbon (diamond and non-diamond) is not rate-limited by H-induced surface reactions. Recent studies by Raman spectroscopy have concluded that graphite inclusion in vapor deposited diamond films is rather low,[8] especially when the methane percentage is less than 1% (our films deposited at 1% still showed a high degree of crystallinity). If this is the case, then Fig. 3 would further imply that the deposition of diamond is not rate-limited by H-induced surface reactions.

Frenklach and Wang[9] have recently described a model of diamond growth. In their studies the rate-limiting step for film growth was acetylene addition (surface reaction step s5 in their model). However, they arrived at this conclusion because they used substantially lower $C_2H_2$ and somewhat higher H concentrations then what we actually measured. If our measured values are used instead, their model would predict the rate-limiting step for film growth to be the formation of $sp^3$ radical sites by H abstraction (step s1 in their model). Our results show that this step cannot be rate-limiting. This disagreement, however, does not necessarily mean that the basic structure of the model is wrong, it can simply arise from an improper estimation of the magnitude of the involved rate coefficients.

We know from experience that the films grown at the higher methane percentages have higher graphitic content and the observed decrease in H concentration is consistent with the view that H is necessary to remove graphite from the deposits.[10]

The trend of the growth-rate curve bears strong resemblance to the methyl and acetylene mole fraction curves. However, the total change for growth rate is less than x2, while that for acetylene is x3, and methyl more than x5. The growth rate therefore does not scale linearly with any of the hydrocarbon species.

We can determine the flux impinging on the growth surface from our measured results. For each hydrocarbon species with concentration, n, the flux is given by $n\bar{v}/4$, where $\bar{v}$ is the average velocity of the species at a temperature given by that of the substrate. If the measured film growth were due solely to each of the three measured hydrocarbon species, the required effective sticking coefficient can be calculated. At f=0.4%, the sticking coefficients would be: $CH_3$ ~$1x10^{-3}$, $CH_4$ ~$1.7x10^{-4}$, and $C_2H_2$ ~$1x10^{-4}$. Since the growth rate does not rise as rapidly as the concentrations, all the calculated sticking coefficients decrease at higher methane percentages.

## SUMMARY

Absolute concentrations of H, $CH_3$, $CH_4$, and $C_2H_2$ have been measured under realistic diamond growth conditions in a hot-filament reactor. The results are shown as a function of methane percentage in the feed gas, which was varied within the range of 0.4% - 7.5%. Both acetylene and methyl showed an initial rise and then leveled off at higher methane percentages. The H-atom concentration showed an order of magnitude drop over the same range. This behavior, in conjunction with the knowledge that the content of non-diamond material within the film rises, is in agreement with the view that H atoms assist in graphite removal. The film growth rate was observed to increase with methane percentage. At least at low levels of methane percentages, where the films are expected to contain primarily diamond, the results would imply that H-induced surface reactions are not the rate-limiting steps for diamond growth.

## ACKNOWLEDGEMENT

The author wish to thank David Tung for his assistance in the experiment and Bert Brown for operating the scanning electron microscope. This work was supported by the U.S. Department of Energy under contract #DE-AC0476DP00789 and DARPA/DSO-Material Science Program.

## REFERENCES:

1. F.G. Celii, P.E. Pehrsson, H.-t. Wang, H.H. Nelson, and J.E. Butler, Proceed. 1st Int. Conf. on New Diamond Science and Technology, (Tokyo, Japan, 1988).
2. S.J. Harris and A.M. Weiner, Appl. Phys. Lett. **53** 1605 (1988).
3. U. Meier, K. Kohse-Hoinghaus, L. Schafer, and C.-P. Klages, J. Appl. Optics, 29 4993 (1990).
4. W.L. Hsu and D.M. Tung, Proceed. 2nd Int. Conf. on New Diamond Science and Technology (Washington, D.C., USA, 1990).
5. W. L. Hsu, submitted to Appl. Phys. Lett..
6. F.G. Celii and J.E. Butler, Appl. Phys. Lett. **54** 1031 (1989).
7. D.M. Tung, W.L. Hsu, and K.F. McCarty, Proceedings of the 1st International Symposium on Diamond and Diamond-Like Films at the 175th Meeting of the Electrochemical Society, Los Angeles, CA, May 7 - 12, 1989, editors J. P. Dismukes et al., Vol. 89-12, published by the Electrochemical Society, Inc. Pennington, NJ, p 500.
8. R.E. Schroder, R.J. Nemanich, and J.T. Glass, Phys. Rev. B **41** 3738 (1990).
9. M. Frenklach and H. Wang, Phys. Rev. B **43** 1520 (1991).
10. B.V. Spitsyn, L.L. Bouilov, B.V. Derjaguin, J. Crystal Growth **52** 219 (1981).

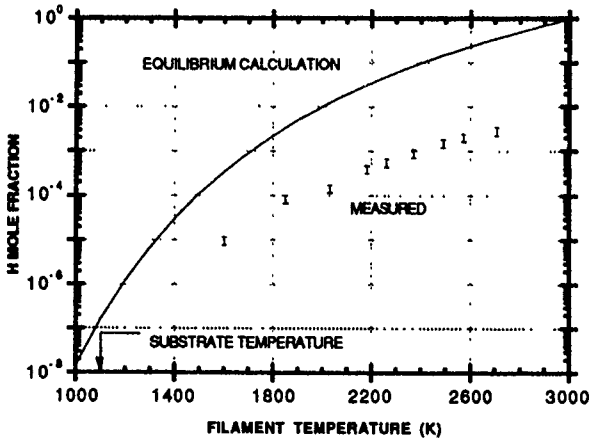



Fig. 1 Measured and calculated H mole fractions in a hydrogen-only system.

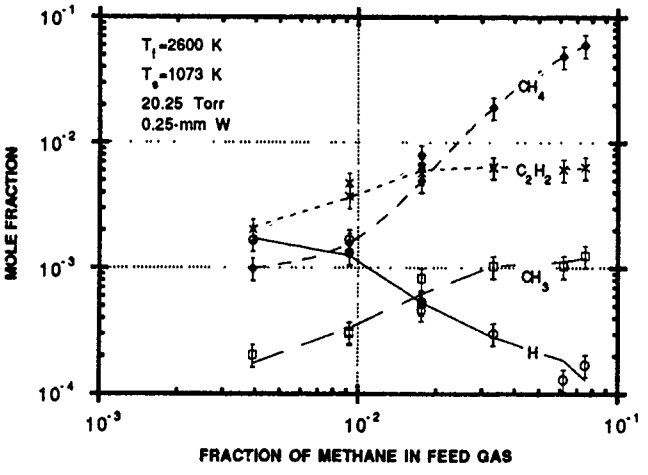



Fig. 2 Mole fractions of H, $CH_3$, $CH_4$, and $C_2H_2$. The lines are drawn to guide the eye. Indicated are the filament temperature, $T_f$; substrate temperature, $T_s$; process pressure; and diameter of the tungsten wire.

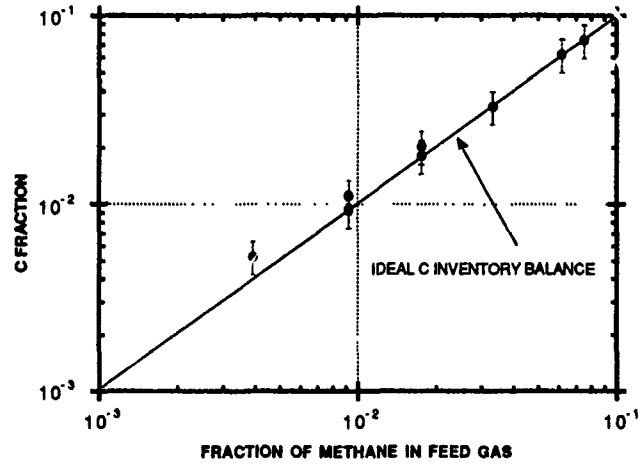



Fig. 3 Carbon atom inventory analysis.

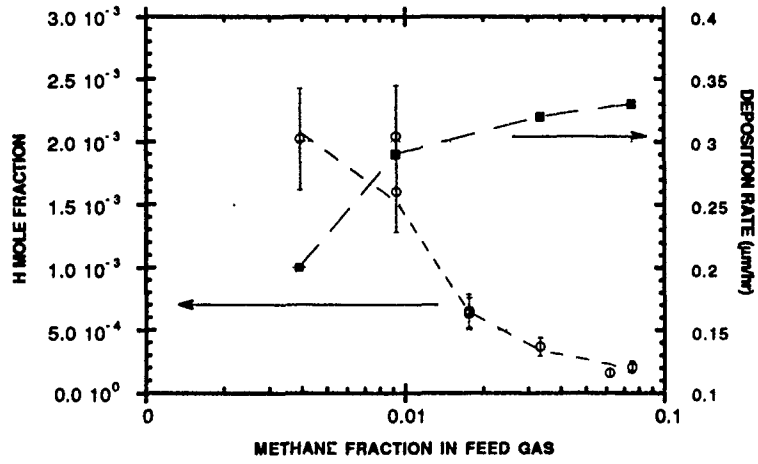



Fig. 4 Film deposition rate and H mole fraction at different methane percentages.

# TEXTURED GROWTH AND TWINNING IN POLYCRYSTALLINE CVD DIAMOND FILMS

C. Wild, P. Koidl, N. Herres, W. Müller-Sebert, T. Eckermann

Fraunhofer-Institut für Angewandte Festkörperphysik (IAF),
Tullastr. 72, D-7800 Freiburg, Germany

## Abstract

The morphology and structure of polycrystalline diamond films have been investigated for various growth conditions as a function of film thickness. Samples exhibiting pronounced <100>, <110> and <111> fibre textures have been studied. It is shown that growth starts from randomly oriented nuclei with the texture developing in the course of film growth due to the competition between differently oriented grains. Growth models are discussed relating the observed textures to the relative growth rates of {100} and {111} faces and to twin formation during the nucleation stage.

## I. Introduction

The deposition of diamond from the gas phase has found tremendous interest during the recent years (1, 2, 3). To date thin polycrystalline diamond films and several 100 $\mu$m thick free standing wafers are currently prepared using a variety of chemical vapour deposition (CVD) techniques. The deposition rate, film uniformity, crystalline structure and surface morphology of these diamond films depend strongly on the growth technique and growth conditions. The correlation between growth parameters and film properties has been the subject of many investigations.

It is known that one reason for the structural variability of polycrystalline diamond films is the non-random orientation of the crystallites. Textured growth has been observed by evaluating the surface morphology and the Bragg peak intensities in X-ray diffraction (4-11). However it is only recently that attention has been paid to the growth mechanisms leading to specific textures (8-11).

In the present paper we report on the growth of CVD diamond films exhibiting pronounced fibre textures. By varying the growth conditions, texture axes with different orientations (<100>, <110>, <111>) can be obtained. It will be shown

that there are three basic parameters influencing the texture and thus the morphology of CVD diamond films:

i.) the ratio between film thickness and average nuclei distance,

ii.) the ratio between the normal growth velocity on {100} and {111} faces, and

iii.) the formation of twins on {111} faces.

## II. Experimental

The samples under investigation were prepared either by hot filament assisted CVD (HFCVD) or by microwave plasma assisted CVD (MW-PACVD). Additional samples were provided by T. Anthony, General Electric, who used a combination of both techniques (7). In the case of the hot filament assisted CVD we use a stainless steel vacuum chamber with water cooled walls. The substrate is located on a molybdenum holder, which contains an ohmic heater and a thermocouple to control the deposition temperature. For the microwave plasma deposition a tubular reactor with a 40 mm diam. silica tube has been used similar to the system described by Kamo et al. (12). The substrate temperature is measured by a two colour pyrometer. Diamond films were deposited on 100 Si substrates pretreated with diamond grit to enhance the nucleation density.

For the characterization of the diamond films several techniques were employed most important being Raman scattering, optical absorption spectroscopy, angular resolved optical reflection, scanning electron microscopy, X-ray diffraction and X-ray texture analysis. The experimental details are described in Refs. (7, 8, 13, 14).

In this paper emphasis is put on the X-ray texture analysis, which was performed with a four circle diffractometer equipped with a curved germanium monochromator. The measurements were carried out in reflection geometry using $CuK_{\alpha 1}$ radiation. Fig. 1 shows the scattering geometry. To analyze the distribution of crystal orientations, the position of the detector is fixed at a specific reflection angle $2\Theta$ of diamond. In this configuration only lattice planes perpendicular to the scattering wave vector **k** (shown in Fig. 1) contribute to the diffraction of the incident beam into the detector. By varying the angles $\chi$ and $\varphi$ the sample can be rotated in any orientation relative to **k**. Since the X-ray intensity measured at the detector is approximately proportional to the number of diffracting lattice planes this technique in effect measures the orientational distribution of specific lattice planes {hkl}.

Additional measurements were carried out using a high resolution diffractometer equipped with a four reflection germanium monochromator, which reduces the divergence of the primary beam to less than 0.0035° (in the plane of dispersion).

## III. Observed Textures

Fig. 2 depicts the {111}, {220}, {311} and {400} pole figures of a <100> textured CVD diamond film. The preferred orientation of the <100> directions parallel to the growth direction is evident from the pronounced peak in the center of the {400} pole figure. All other features in Fig. 2 result from this <100> texture. While the pole density depends strongly on the polar angle $\chi$, no dependence on the azimuthal angle $\varphi$ can be observed in Fig. 2. The distribution of crystal orientations exhibits a rotational symmetry with respect to the substrate normal. Thus the diamond film exhibits a so-called fibre texture and a plot of the pole density vs. the polar angle $\chi$ is sufficient to describe the texture. From the rotational symmetry it is evident that the texture does not result from an interaction of the diamond nuclei with the lattice of the silicon substrate.

The distributions of the {111}, {220} and {400} pole densities of CVD diamond films with <111>, <110> and <100> texture (sample a, b and c respectively) are shown in Fig. 3. The growth conditions for these films are summarized below.

| sample<br>texture axis | a<br><111> | b<br><110> | c<br><100> |
|---|---|---|---|
| thickness | 30 $\mu$m | 300 $\mu$m | 150 $\mu$m |
| dep. technique | HFCVD | HFCVD | MW-PACVD |
| gas composition | 0.7 % IPA* | 0.7 % IPA* | 2.0 % $CH_4$ |
| growth temp. | 800°C | 800°C | 880°C |
| filament | Ta, 1 mm ∅ | W, 0.125 mm ∅ | |

*IPA=Isopropyl alcohol

The surface morphologies of the samples b and c are shown in Fig. 4. Sample b exhibits roof shaped structures penetrated by vertical twin planes. The surface consists entirely of {111} faces. This has been confirmed by angular resolved optical reflection measurements (8), which revealed that the faces at the surface are inclined by an angle of 35° - i.e. the angle between the <110> and <111> direction.

In contrast to sample b, the surface of sample c is covered with rectangular or square {100} faces which are aligned almost parallel to the substrate surface. Due to this alignment, the sample exhibits a very flat surface - a feature which is very important when thinking about applications. The angular distribution of the optical reflection measured at 633 nm is shown in Fig. 5. The distribution exhibits a sharp peak superposed on a somewhat broader background. The full width at half maximum (FWHM) of the background signal amounts to 1.5°.

In order to determine precisely the tilt of the <100> directions relative to the surface normal, rocking curves were measured with a high resolution X-ray diffractometer. Fig. 6 shows the rocking curve ($\omega$-scan) of the 400 reflection of a <100> textured diamond film and for comparison the 400 reflection profile of the silicon substrate. The FWHM of the silicon profile amounts to 0.36°. Since the divergence of the indicent beam (0.0035°) is negligibly small, the peak width observed is mainly due to a bending of the silicon substrate which influences the shape of the silicon profile. In the case of the diamond 400 reflection the FWHM amounts to 2.7°. Taking into account the broadened silicon profile, it can be concluded that the FWHM of the {100} distribution function in sample c is below 2.5°.

In order to clarify the mechanism responsible for the formation of the observed fibre textures, we studied the dependence of the film texture on the film thickness. This was achieved by successively etching a 190 $\mu$m thick, <110> textured CVD diamond film in an oxygen discharge (8). The etching was performed in an asymmetric, capacitively coupled rf glow discharge system, which provides an intense and strongly anisotropic flux of energetic oxygen ions.

After different etching periods, i.e. at different film thicknesses, the powder diffraction pattern of the film was analyzed. In Fig. 7 the ratio of the 220 and 111 reflection intensity, $I_{220}/I_{111}$, is plotted as a function of the film thickness. At large film thicknesses the 220 reflection dominates, in accordance with the pronounced <110> texture of the present sample. The decrease of the film thickness leads to a strong decrease of the relative intensity of the 220 reflection. When extrapolating the experimental data towards zero film thickness, an intensity ratio $I_{220}/I_{111}$ of 0.4 is obtained. This value corresponds to a random distribution of crystal orientations. Thus it can be concluded, that film growth starts from randomly oriented nuclei and that the texture develops progressively in the course of film growth.

## IV. Discussion

### A. Mechanism of texture formation

The dependence of the film texture on the film thickness clearly shows that the texture formation is due to evolutionary selection (15), i.e. the texture results from the growth competition between differently oriented crystallites. This mechanism is illustrated in Fig. 8. During film growth, the crystallites grow larger. As a consequence, some of them are burried by adjacent crystallites and the number of crystallites extending to the surface decreases successively. Due to the anisotropy of the growth velocity only those crystals with the direction of fastest growth oriented parallel to the substrate normal survive. As a consequence, a fibre texture develops with increasing film thickness. The direction of the texture axis equals the direction of fastest growth.

### B. Direction of fastest growth

Since the direction of fastest growth determines the axis of the film texture, an important question is, what are the parameters influencing the direction of fastest growth ? For a specific nucleus, the direction of fastest growth is given by its longest dimension. The shape of the nucleus, on the other hand, is determined by the relative growth rates of the individual faces and eventually by the formation of twins. CVD diamond crystals generally grow in the form of cubo-octahedra. The influence of the relative growth rates on the shape of cubo-octahedra is illustrated in Fig. 9. The parameter $\alpha$ equals the ratio of the normal growth velocity on {100} and on {111} faces multiplied with the square root of 3. By varying $\alpha$ from 1 to 3, the shape of the crystallite varies from a cubic over a cubo-octahedral to an octahedral. The direction of fastest growth varies from <111> over <110> to <100> (see Fig. 10). These are exactly the texture axes observed experimentally. However, unfortunately reality is not that simple. Only the <100> texture can be fully explained by this simple model.

### C. The <100> fibre texture

In order to explain the <100> fibre texture, it is sufficient to assume that the diamond film grows from cubo-octahedrally shaped nuclei, with $\alpha$ slightly below 3. In this case, the nuclei form octahedra with very small {100} faces at the tips. The direction of fastest growth is almost perpendicular to these {100} faces. For that reason, evolutionary selection leads to a preferred alignment of these {100} faces parallel to the substrate surface. In the course of the film growth, these {100} faces grow larger and larger and one ends up with a surface which is completely covered with more or less parallel {100} faces.

This process has been simulated in two dimensions with a computer program, which calculates the temporal evolution of a growing surface. As a two-dimensional analog of an octahedron with truncated tips, squares with truncated corners were used as nuclei. The nuclei were randomly oriented and distributed with an average distance $d_0$. Fig. 11 shows typical examples for simulated two dimensional films grown from those nuclei. The film thickness is $3 \cdot d_0$ (Fig. 11a), $30 \cdot d_0$ (Fig. 11b) or $300 \cdot d_0$ (Fig. 11c). To discriminate between the two types of "faces", the side of the squares are plotted as thick lines, whereas the truncated corners are plotted as thin lines.

The computer simulations clearly reproduce the experimental findings: i.) the alignment of the {100} faces parallel to the substrate and ii.) the disappearance of the {111} faces at the surface. For comparison, Fig. 12 shows cleaved edges of a <100> textured diamond film. They exhibit the same columnar structures as predicted in Fig. 11b and 11c.

Another aspect also supports the present model. The ratio between the size of the square faces at the surface of a <100> textured film and the film thickness depends directly on the growth parameter $\alpha$. In Fig. 4 the typical dimension of the {100} faces is about 5 $\mu$m, the film thickness is 150 $\mu$m. From these values a growth parameter of $\alpha$=2.95 can be derived. On the other hand, the tilt of the <100> directions from the surface normal also allows one to determine $\alpha$. From Fig. 5 and Fig. 6 it can be concluded that the tilt angle is $\approx$ 1°. This value corresponds to an $\alpha$ of $\approx$ 2.95 in agreement with the value derived above.

One of the most imporant features of sharply <100> textured diamond films is the smooth surface. The analysis of the optical reflection profile shown in Fig. 5 revealed that the surface roughness of this particular sample is about 150 nm. Another property of <100> textured diamond films also deserves mentioning. When the <100> texture is fully developed, the surface is covered completely with {100} faces. Thus the growth of <100> textured films occurs on {100} faces which are much less susceptible to twin and defect formation as compared to {111} faces (16). In Ref. (14) we showed, that the defect induced one-phonon absorption in the IR absorption spectrum is considerably reduced in the case of <100> textured diamond films.

It should be noted, that for $\alpha$ somewhat smaller than 3 the present model predicts a texture axis that deviates from <100>. Clausing et al. (9, 10) reported on fibre textured diamond films with the texture axis tilted by about 10° from <100>. This growth morphology is consistently explained assuming $\alpha \approx 2.6$.

An independent way of determining $\alpha$ may be the characterization of crystallite shape during the nucleation phase (10). However, care must be taken, since $\alpha$ may be influenced by the presence of the uncovered Si surface due to surface diffusion.

## D. <110> textured films

From Fig. 10 one would expect that the <110> texture corresponds to an $\alpha$ of 1.5. However there are two reasons which contradict this assumption:

i.) The surface of <110> textured diamond films consists completely of {111} faces. This has been shown by angular resolved optical reflection measurements and by SEM micrographs (8). For $\alpha$=1.5, however, one would expect both, {111} and {100} facets at the surface.

ii.) The <110> texture is a very common texture. A variety of diamond samples prepared under different growth conditions were found to exhibit this texture. It is not reasonable to assume that $\alpha$ equals exactly 1.5 for all those samples.

In an earlier publication we have proposed and discussed a possible mechanism for the growth of <110> textured diamond films. In brief, it is assumed that $\alpha$ is larger than 3 and that the growth of octahedra is suppressed due to the preferred formation of twins at the tips of octahedra. These assumptions are supported by various experimental findings:

i.) As mentioned above, <110> textured diamond films do not show {100} faces at the surface. The formation of only {111} faces suggests that $\alpha$>3.

ii.) To our knowledge octahedrally shaped nuclei have never been observed in SEM micrographs. Sometimes SEM micrographs show structures which resemble octahedra tips. However, a closer look always shows that these tips are terminated by small {100} faces.

iii.) SEM micrographs of the diamond nuclei at the beginning of film growth often show multiply twinned particles with surfaces consisting entirely of {111} faces. These particles often exhibit five-fold corners. The twins forming such a corner have a common <110> axis which equals the direction of fastest growth of the corner. This example shows that twinning can lead to surface structures which consist only of {111} faces and where <110> is the direction of fastest growth.

The surface of <110> textured diamond films consists of {111} faces with a high density of twin planes normal to the surface. This polysynthetic growth morphology leads to a large number of roof-shaped and re-entrant 110 edges (see Fig. 4). Angus et al. (17) have pointed out that carbon attachment at the re-entrant 110 edge of a twinned bi-crystal will lead to an increased growth rate in the direction of the common <110> direction.

All these arguments demonstrate that frequent twinning may change the direction of fastest growth from <100> (expected for $\alpha > 3$) to the common <110> direction of the twinned material.

## E. Twin formation

Twinning is a very common phenomenon associated with the growth of diamond from the gas phase. Especially {111} faces are very susceptible to twin formation since the energy required to grow an incorrectly stacked monolayer is very low (18). To study the formation of twins without paying attention to the irregularities of polycrystalline diamond films, it is interesting to investigate twinning under homoepitaxial growth conditions.

In a preliminary investigation we analyzed the amount of twinned material in a 350 $\mu$m thick homoepitaxial diamond film grown on a {111} diamond substrate. The substrate thickness was 1 mm. The analysis was performed with the X-ray diffractometer used for the texture measurements. To discriminate between twinned and untwinned material, the detector was positioned at $2\Theta$ of the 220 reflection of diamond and the sample was oriented such, that the reflection condition was fulfilled for one of the {220} lattice planes inclined 35.7° against the {111} surface. If the sample is rotated about its <111> normal, the reflection condition will be re-established every 120°. The lattice of a twin can be obtained by rotating the original lattice by an angle of 60° about the <111> stacking direction. For that reason one expects that the 220 reflections of twinned regions of the homoepitaxial film appear at the intermediate angles. This is exactly what we observed experimentally. Fig. 13 shows the diffracted intensity (plotted on a logarithmic scale) as a function the rotation angle. The {220} lattice planes of the substrate and of untwinned regions of the homoepitaxial film show up in the form of pronounced peaks which are indeed separated by an angle of 120°. At the intermediate angles the weak reflection lines of the twinned regions can be clearly observed. The relative integrated intensity of these additional reflection lines is about $2 \cdot 10^{-3}$. Taking into account that the diamond substrate constitutes 75 % of the sample, we estimate that about 1 % of the homoepitaxial film consists of twinned material.

## V. Conclusions

It has been shown that the crystalline structure and the morphology of polycrystalline CVD diamond films generally depend on the growth conditions *and* the film thickness. Starting from randomly oriented nuclei, a preferred orientation of the crystallites will develop with increasing film thickness (unless secondary nucleation is enforced to inhibit textured growth). Growth competition between differently oriented grains and evolutionary selection will lead to the development of a fibre texture with the fibre axis given by the direction of fastest growth of the diamond crystallites. By varying the growth conditions, textured films with the texture axis parallel to <100>, <110> or <111> have been prepared.

A model has been proposed, where for the general case of cubo-octahedral crystallite morphology the texture axis is determined by the relative growth rate parameter $\alpha=\sqrt{3}\cdot v_{100}/v_{111}$. For $\alpha$ slightly below 3, <100> textured growth will occur, with the surface terminated by {100} faces. <110> textured growth with the surface formed by {111} faces requires $\alpha>3$ plus additional twinning to generate the maximum growth velocity along <110>.

The various growth schemes and resulting textures have immediate implications for the application of the films. Textured growth leads to an increase in grain sizes with increasing film thickness and finally to a columnar structure. For the <110> texture this goes parallel with an increase in surface roughness. However, in the case of <100> textured films the surface roughness can be limited due to an increasing alignment of {100} faces parallel to the sample surface. It is evident that this "self polishing" growth mechanism is important for any application where a smooth surface is required.

## Acknowledgments

We would like to thank T.R. Anthony, General Electric, for providing part of the <110> textured samples and R. Dian for technical assistance.

## References

1. *Diamond and Diamond-like Films*, J.P. Dismukes, A.J. Purdes, B.S. Meyerson, T.D. Moustakas, K.E. Spear, K.V. Ravi, M. Yoder, Eds., Electrochem. Soc. Proc. Vol. 89-12 (1989)

2. *Diamond, Silicon Carbide and Related Wide Bandgap Semiconductors*, J.T. Glass, R. Messier, N. Fujimori, Eds., Mat. Res. Soc. Symp. Proc., Vol. 162 (1990)

3. *Diamond and Diamond-like Films and Coatings*, R.E. Clausing, L.L. Horton, J.C. Angus, and P. Koidl, Eds., Nato-ASI Series B, Vol. 266, Plenum, New York (1991)

4. W.A. Yarbrough and R. Roy; Proc. Mat. Res. Soc. EA-15, 33 (1988)

5. K. Kobashi, K. Nishimura, Y. Kawate and T. Horiuchi; Phys. Rev. B38, 4067 (1988)

6. Y. Sato and M. Kamo; Surface and Coatings Technol. 39/40, 183 (1989)

7. C. Wild, N. Herres, J. Wagner, P. Koidl and T.R. Anthony; Electrochem. Soc. Proc. 89-12, 283 (1989)

8. C. Wild, N. Herres and P. Koidl; J. Appl. Phys. 68, 973 (1990)

9. E.D. Specht, R.E. Clausing and L. Heatherly; J. Mater. Res. 5, 2351 (1990)

10. R.E. Clausing, L. Heatherly, and E.D. Specht; in Ref. 3

11. R.E. Clausing, L. Heatherly, E.D. Specht and K.L. Moore; Proc. 2nd Int. Conf. *New Diamond Science and Technology*, Washington D.C. (1990), in print

12. M. Kamo, Y. Sato, S. Matsumoto, and N. Setaka; J. of Crystal Growth 62, 642 (1983)

13. J. Wagner, M. Ramsteiner, C. Wild and P. Koidl; Phys. Rev. B40, 1817 (1989)

14. C. Wild, W. Müller-Sebert, T. Eckermann and P. Koidl; in Proc. of the *Applied Diamond Conference 1991*, Auburn, Alabama, to appear

15. A. Van der Drift; Philips Res. Rep. 22, 267 (1967)

16. M.W. Geis; in Ref. 2, p. 15

17. J.C. Angus, R. Gat, Z. Li, M. Sunkara and M.W. Geis; Electrochem. Soc. Extended Abstracts 91-1, 130 (1991)

18. A.R. Lang, in *The Properties of Diamond*, J.E. Field ed., Academic Press, London (1979)

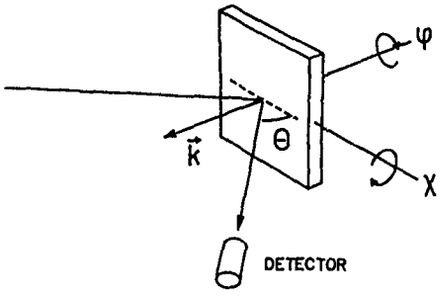



Fig. 1: Diffraction geometry for X-ray texture measurements

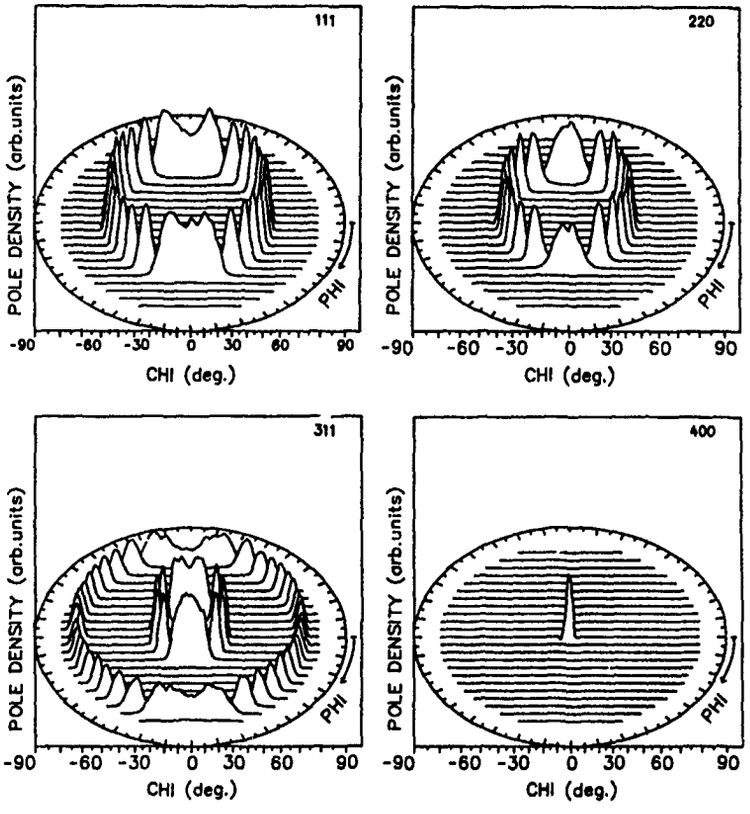



Fig. 2: X-ray pole figures of a 150 $\mu$m thick diamond film (sample c) showing sharp <100> fibre texture

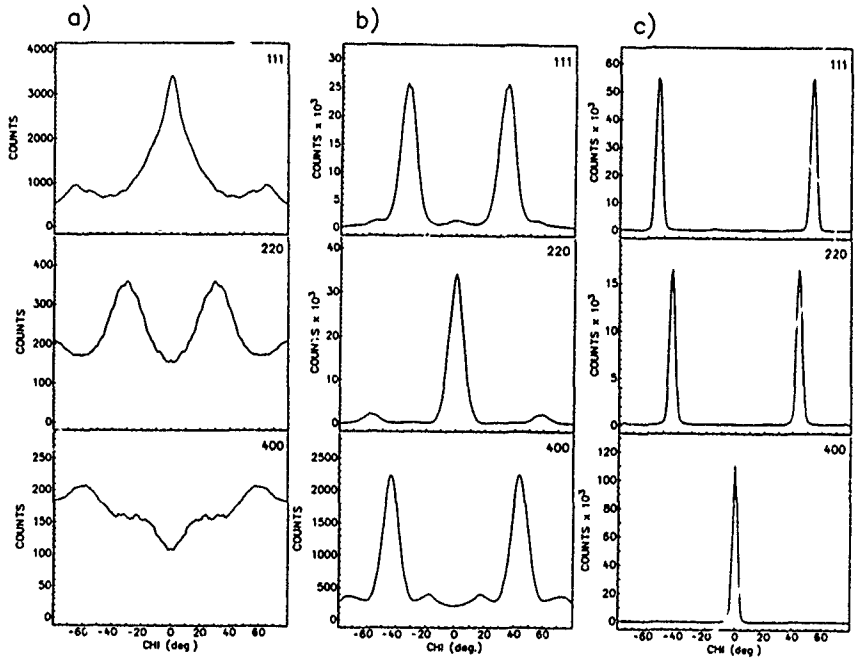



Fig. 3: {111}, {220} and {400} pole densities vs. polar angle $\chi$ for sample a, b, and c which exhibit <111>, <110> and <100> fibre textures, respectively

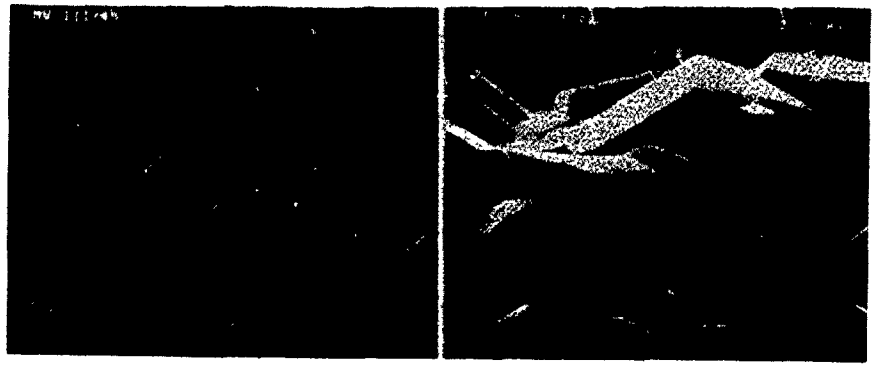


Fig. 4: SEM micrographs of sample c (left) and b (right) showing 100 and 111-faceted surface morphology, respectively

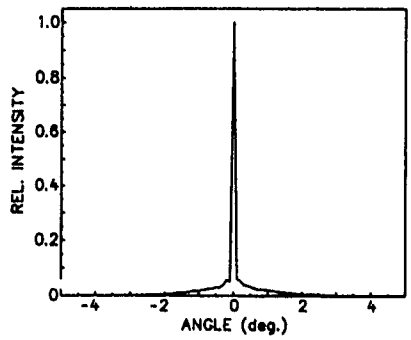



Fig. 5: Angle resolved optical reflection of sample c; zero degrees corresponds to specular reflection

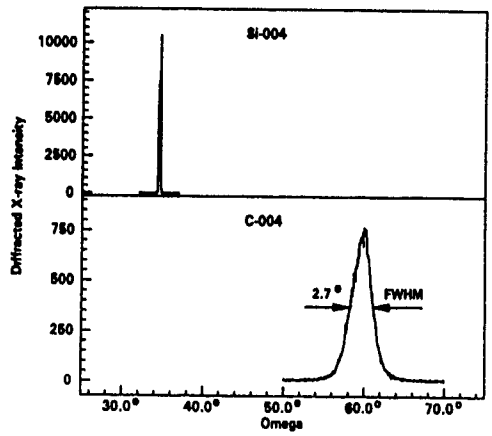



Fig. 6: X-ray rocking curve (004 reflection) of Si substrate and diamond film (sample c)

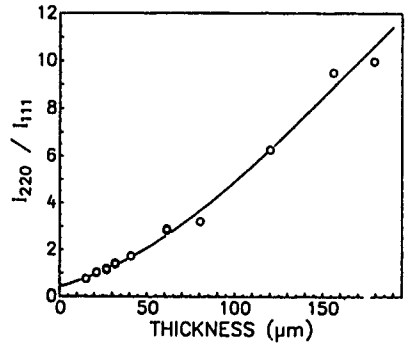



Fig. 7: Intensity ratio of the 220 to 111 X-ray diffraction peak as a function of film thickness for <110> textured sample b

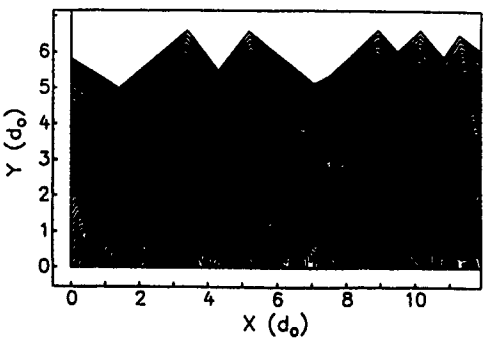



Fig. 8: Computer simulation of two-dimensional crystal growth from randomly oriented square nuclei. Distances are normalized to average nuclei distance $d_0$

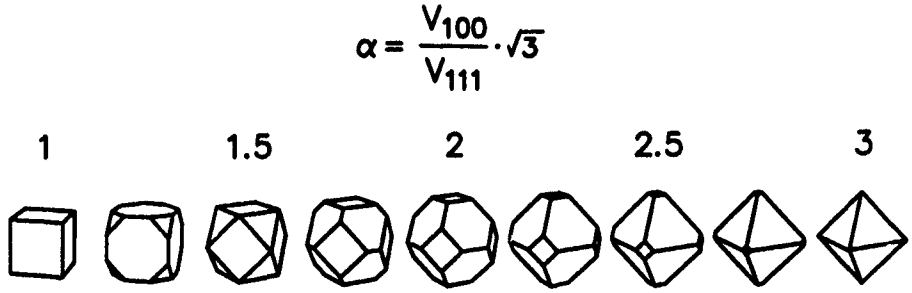



Fig. 9: Morphology of diamond crystallites as a function of relative growth rate parameter $\alpha = \sqrt{3} \cdot V_{100}/V_{111}$

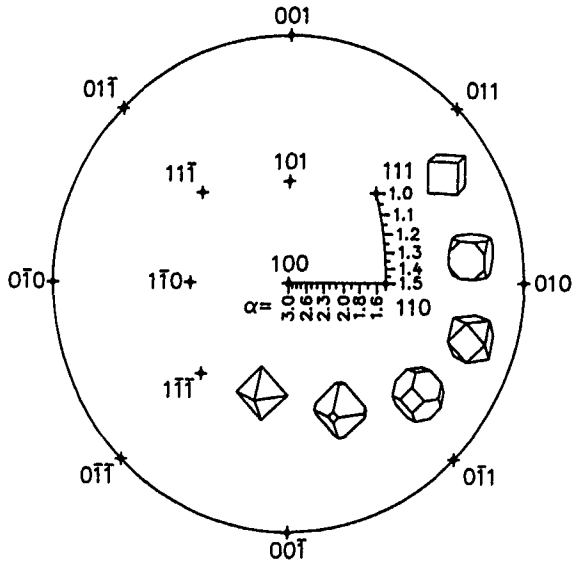



Fig. 10: Pole figure showing expected texture direction for $1 \leq \alpha \leq 3$. Values of $\alpha$ and corresponding particle shapes are indicated

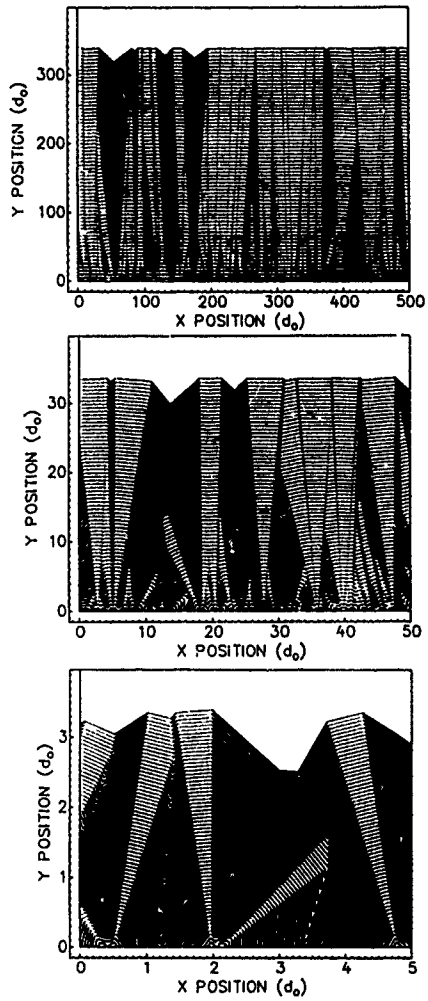



Fig. 11: Two dimensional simulation of crystal growth from "cubo-octahedral" nuclei. Texture development is shown for film thicknesses of $3 \cdot d_0$, $30 \cdot d_0$ and $300 \cdot d_0$

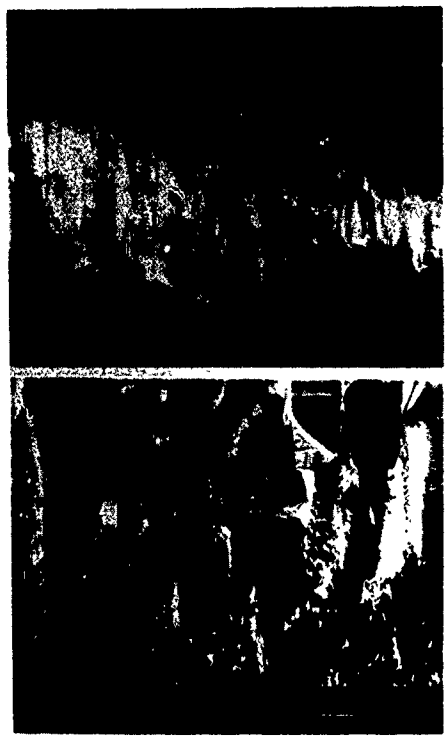


Fig. 12: SEM micrographs of fracture edge of <100> textured sample c evidencing evolutionary selection and columnar growth with flat surface

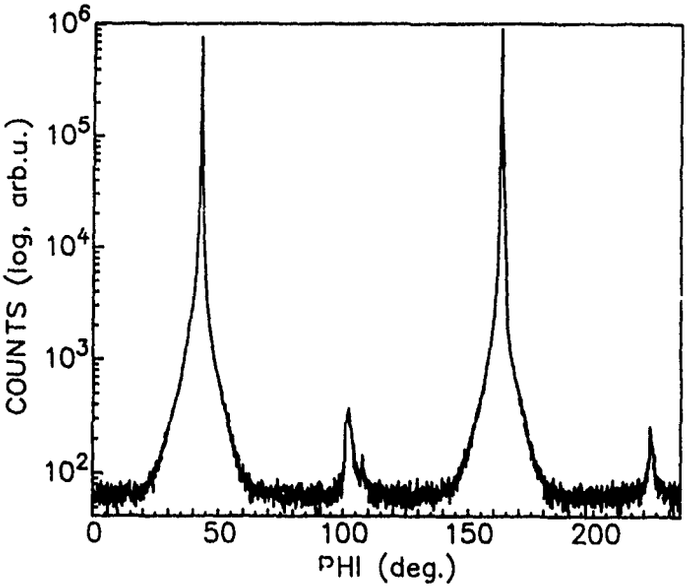



Fig. 13: X-ray 220-diffraction intensity of epitaxial diamond film on 111-oriented substrate. Azimuthal angle $\varphi$ describes sample rotation about <111> normal

# AGGREGATE PROCESS MODEL OF DIAMOND FILM GROWTH

**A.K. Miller and K.V. Ravi**

**Lockheed Missiles & Space Company, Inc.**
**Research & Development Division**
**3251 Hanover Street, Palo Alto, CA 94304-1191**

**ABSTRACT**

A graphics-output computer model of combustion flame synthesis of thick diamond structures starts with small statistical "intrinsic" variations in the growth rate of individual crystallites in the film. The model simulates "competitive shadowing" (large differences in growth rates among neighboring crystallites due to nutrient redistribution), a phenomenon which has been shown to strongly influence the microstructure of thick diamond structures. The same model also simulates suppression of the morphological instabilities characteristic of steady state synthesis of thick diamond by periodic renucleation using very thin layers of diamond-like carbon (DLC). Relations between the DLC deposition time and the thick film density can be calculated.

## Introduction

One critical phenomenon which accompany high rate growth of diamond is morphological instability (1). Increasing film thicknesses, at high growth rates, results in extremely rough surfaces, the trapping of voids and discontinuities and the incorporation of non diamond phases in the growing film. These characteristics are typical of morphological instabilities when surface diffusion and re-evaporation processes are absent and instability is promoted by the high rate arrival of the appropriate species from the flame ambient to the surface. As certain of the crystallites grow slightly faster than their neighbors, they project out ahead topographically and consume the gas stream nutrients before those nutrients can reach the neighbors. This causes the initially faster-growing crystallites to accelerate in growth rate by "nutrient overfeeding", and the initially slower-growing crystallites to decelerate by "nutrient starvation". The result is the classic instability termed "competitive shadowing".

Recently, a strategy for defeating competitive shadowing in the growth of thick diamond films has been demonstrated experimentally (2). By periodically changing the flame chemistry, in the combustion flame synthesis of diamond, to a more carbon-rich mixture, a thin layer of diamond like carbon (DLC) can be deposited on top of the already-grown diamond. Upon resumption of the original flame chemistry, new diamond crystallites nucleate on the just-deposited DLC layer. Since these new crystallites are not epitaxially related to the underlying diamond crystallites, their orientations and growth rates are again random. Each single fast-growing crystallite is replaced by a group of crystallites of random orientations, as is each slow-growing crystallite.Thus, on the average the growth rates of the fast-growing regions are reduced and those of the slow-growing regions are increased. While providing the above benefit, periodic deposition of DLC is not without cost. Most importantly, DLC contamination can lead to reduced thermal conductivity and increased electrical conductivity of the diamond; accordingly the volume fraction of DLC must be minimized while still retaining the beneficial effects of

DLC in renucleating diamond crystallites. Accordingly, it is desireable to be able to rapidly predict the effects of DLC deposition on the control of morphological instability during the diamond growth process. The model described below is an initial attempt to do so.

## Model for morphological instability in thick diamond film growth

Many researchers have investigated film growth from the vapor phase. For example, Bales et al. (3) studied competitive shadowing using analytical techniques. The "first-principles" models which have been developed from such studies provide a rich base of knowledge. However the present problem, involving periodic changes and spatial variations in the gas chemistry and resulting diamond film structure, as well as an eventual requirement for real-time process control, was judged to be more conveniently treated in an "aggregate" manner, by lumping the physically-relevant behavior into a small number of state variables. This permits a model which is computationally simpler and can be run in a microcomputer environment. By using a programming language (in this case, Microsoft BASIC on a Macintosh) which contains built-in graphics commands, such a modelling environment permits graphical depiction of the morphology integrally with the predictions, which assists in rapid assimilation of the predictions, their comparison against experiment, and improvement of the model. With modern microcomputers such as the Macintosh II, the computational speed is high enough that simulations can be run in seconds despite the simplicity of the programming language.

The aggregate model tracks the growth of a thick diamond film by numerically simulating crystal growth using an approximate, but physically-meaningful, representation of the growth process itself. The logic of the model is summarized in Figure 1 and described in the following sections. "Crystallites" are nucleated on the substrate. Random variables are used within the program to select the orientation and intrinsic growth rate of each crystallite. This simulates the modest initial growth variations observed experimentally. The crystallites are then permitted to grow in numerical increments, with a fixed geometric aspect ratio. At each step the growth rate of each crystallite depends not only on its intrinsic growth rate, but also on its current height relative to the average height of all of the crystallites. This simulates competitive shadowing. If periodic DLC nucleation is utilized, then after a specific growth time, new crystallites are nucleated (by random variable selection) on the tops of the previous generation of crystallites, and the entire cycle is repeated.

Discussion of the actual numerical scheme, program flowchart, user inputs and outputs, etc. is beyond the scope of the present paper.

### A. Statistical nucleation and growth of crystallites

#### *1. Statistical nucleation of crystallites*

Initially the surface area available for nucleation is a single region (the substrate) but at later steps will consist of multiple regions, namely the top surface area of each of the already-grown crystallites. A number of crystallites can be nucleated within each area, and the probability of successful nucleation will depend on the area as well as the amount of DLC deposited. To model this process, each such area ($A_S$) available for nucleation is divided into a number ($N_S$) of discrete sites. Thus the area of each site is $A_S/N_S$. The DLC deposition time is $t_{DLC}$. For each site, the probability ($P_n$) of nucleating a new

crystallite within that site depends on its surface area and the DLC deposition time, according to the equation:

$$P_n = 1 - \exp\left(-t_{DLC} * \left(A_s/N_s\right) / K_1\right) \qquad (1a)$$

where $K_1$ is a constant. This equation was selected to meet the limiting behavior requirements such as $P_n = 0$ for $t_{DLC}=0$ or $A_s=0$, and $P_n = 1$ for $t_{DLC} = \infty$ or $A_s = \infty$.

Each site is interrogated to determine whether or not nucleation has occurred. To do this, a random trial number $N_{t1}$ between 0 and 1 is selected using the RND function. Comparison of the nucleation probability from eq. (1) against this random number generates the actual prediction of nucleation/no nucleation at that site:

If $P_n < N_{t1}$ then nucleation is deemed to have occurred on that site (1b)
If $P_n > N_{t1}$ then nucleation has not taken place on that site. (1c)

By this scheme, nucleation will occur (on the average) at $P_n$ of the similar sites.

If nucleation occurs at a site, the area of the "bottom" of the crystallite thus formed is assumed to equal a given fraction of the area of that site.

*2. Statistical orientation of crystallites*

For each crystallite which is successfully nucleated, an orientation is chosen. At present, to keep the model simple, the orientation is assumed to fall into one of two discrete populations, either {100} or {111}. The orientation of each crystallite is determined by selecting another random number $N_{t2}$ and comparing this random number against the total fraction of grains within a given population. The fraction of {100} oriented grains is input as $F_{100}$. Thus:

If $N_{t2} < F_{100}$, then the crystallite is of {100} orientation (2a)
If $N_{t2} > F_{100}$, then the crystallite is of {111} orientation. (2b)

This scheme can be extended to any number of orientations by inputting additional population fractions.

In the graphical simulations which follow, a square pattern represents {100} oriented crystallites, while a large triangular pattern represents {111}. Although at this stage in the model development no effect of orientation on growth rate has been invoked, the patterns are useful to help discern the individual crystallites. For graphical illustration purposes (only) a value of 0.9 for $F_{100}$ has been selected, i.e., on the average 90% of the grains will be {100}.

*3. Statistical "intrinsic" growth rate of crystallites*

The growth rate of any given crystallite is determined by its orientation and the chemical environment. For growth of diamond by the flame technique, it is postulated that at high temperatures (> 1000 °C) this process involves the preferential growth of {100} faces by selective etching of ledges by oxidizing species (OH, CO, $CO_2$) in the flame followed by lateral propagation of these ledges to grow the film (4). This process

accounts for both the vertical growth (eventually dominated by {100} faces) and lateral growth which produces densification between the crystallites. At lower temperatures, ledge creation on {100} faces by oxidation does not occur and {111} growth dominates. With this physical picture, the appropriate state variables for the process model include the local ledge density at each point on each crystallite, and the model should calculate the geometric extent to which each facet grows as carbonaceous material deposits on that ledge, the geometric extent to which each facet can be etched (in a temperature-dependent manner) by oxidizing species, and the changes in crystallite morphology due to such deposition and etching. These steps depend in turn on the overall crystal orientation. Modelling the growth rate in this way would have the considerable advantage of being able to predict the detailed effects of local temperature and flame chemistry (via oxidation and deposition) on crystallite growth.

At present, this rather complicated picture has been collapsed into a much simpler model in which the "intrinsic" growth rate is assumed to vary statistically, but with a shape chosen to reproduce the intrinsic variations in growth rates observed in experiments. To do this, a base growth rate $R_{g,b}$ is selected (corresponding to the current average temperature and average flame chemistry). For each nucleated crystallite, a third trial variable $N_{t3}$ is selected as a random number. The effect of this random number on the growth rate is "shaped" with a growth rate exponent $n_g$ such that the net intrinsic growth rate $R_{g,i}$ of that crystallite is:

$$R_{g,i} = R_{g,b} * \left(N_{t3}\right)^{n_g} \qquad (3)$$

For the present calculations, $n_g = 0.03$ and the intrinsic growth rate variations are quite small, but are large enough to trigger the larger variations in growth rates due to competitive shadowing. This will be seen in the predictions which follow.

Each crystallite grows with a specified aspect ratio. In reality this aspect ratio depends on the local temperature and flame chemistry, via the ledge formation and deposition process described above. In the present model, for simplicity the growth aspect ratio is the same for all crystallites; it determines the ratio between the initial "bottom" area and the larger "top" area which each crystallite has after it has grown for a finite time. Physically this represents the manner in which the crystallites grow together to fill what would otherwise be voids between them, and thereby form a dense diamond film. In the present model, no attempt is made to prevent any one crystallite from filling the space already occupied by another crystallite. Thus, in the graphical output which follows, as the triangular pattern from {111} grains overlaps the square pattern from {100} grains, a mixed pattern appears which resembles small triangles with squares inside them.

B. Competitive shadowing

If each crystal saw the same local external environment, then it would continue growing according to the prescription given in the preceding sections, and differences in growth rates among the crystals would not be particularly severe. However this is not the case. As certain crystals grow, they project out ahead of their neighbors; the faster-growing crystals shield the slower-growing neighbors from the carbon-rich gases, i.e., the "nutrients." This process accentuates the differences in growth rates and ultimately leads to growth instabilities in which growth is dominated by a small number of narrow

crystals, with large voids between them. This effect is "competitive shadowing." In the present numerical model, this phenomena is modelled by tracking the distance $d^i$ of each crystal from a reference point (corresponding to the hot portion of the flame). The average distance $d_{avg}$ for all of the crystals is computed by summation:

$$d_{avg} = (1/N)\sum_{N} d^i \qquad (4)$$

where N is the total number of crystals.

Corresponding to the physical concept that individual crystals suffer in growth rate (because of nutrient starvation) if they are further from the reference point than the average, and that individual crystals excel in growth rate (because of nutrient overfeeding) if they are closer to the reference point than the average, the growth rate is made to depend upon both $d_i$ and $d_{avg}$, according to the equation:

$$R_g = R_{g,i} * \left( \frac{d_{avg}}{d_i} \right)^p \qquad (5)$$

A value for p of 2 causes relatively mild initial variations in growth rate to cascade into large differences, as shown in the predictions which follow.

C. Stabilization of growth by periodic DLC deposition on growing crystals

The experiments to date have shown how periodic deposition of DLC (diamond-like carbon) on the growing crystals can stabilize growth. The physical mechanism at work appears to be statistical averaging. By renucleating with a new distribution of crystals, fast-growing crystals are replaced by slower-growing crystals (on the average), and conversely. This prevents the fast-growing crystals from taking over and permits the slower-growing crystals to catch up. It is sort of a welfare state.

Renucleation is modelled as followed: After each specified growth time interval, growth of all crystals is stopped and the top of each currently-growing crystal is divided into a finite number of sites. Renucleation using DLC is attempted at each site. The same nucleation law as described in section A.1 above is used. Renucleation occurs at some fraction of the sites available on top of the crop of currently-growing crystals. Because renucleation is via DLC deposition, it is assumed that there is no relationship between the orientation or growth rate of the "old" crystal and the probability of nucleation, orientation, or growth rate of any "new" crystals which are nucleated on it.

It is also assumed that growth of the old crystals stops when renucleation is imposed, so that the only crystals which grow after each renucleation step are those successfully nucleated during that step. This assumption could be tested by experimental examination of thick films so grown.

The cycle of growth/renucleation/growth, etc. is repeated until the largest crystal exceeds a specified size, at which point the calculation stops.

## Predictions

A. Growth without renucleation -- Competitive shadowing effects

Figure 2 shows a simulation of continuous film growth (i.e., without renucleation by DLC deposition). Because there is no renucleation, individual grains preserve their characteristics such as orientation (indicated by the square or triangular pattern) and intrinsic growth rate for the entire film growth. At the early stages (Fig. 2, left) the film grows with only minor variations in growth rates among the individual grains, reflecting the small growth rate exponent $n_g$ (0.03) in eq. (3). However at the later stages (Fig. 2, right) these small "intrinsic" variations grow into large differences in crystallite height, as the effects of competitive shadowing (eq.(5)) become more pronounced. In such a film, substantial voids are still left above the slowest-growing crystallites at the time growth would have to be stopped because of the length of the fastest-growing crystallites. This simulation corresponds well to experimental thick films grown without renucleation (e.g., Figures 4, 5, and 6 of reference 1), which show extensive voids.

B. Growth with renucleation -- Stabilization of morphology

Figure 3 shows a simulation of interrupted film growth, in which renucleation by DLC is imposed after each increment of growth. The initial stages (Fig. 3, left) are similar to the initial stages of Figure 2. However during the later stages (Fig. 3, right) the benefits of renucleation with DLC's become clear: Large differences in the extent of growth are suppressed by the renucleation process. The output shows graphically how the growth of "old" grains stops and is replaced by the nucleation and growth of "new" grains on top of the old grains. For example, the two {111} grains (triangular pattern) which were initially nucleated in the simulation have stopped growing and have been replaced by {100} grains (square pattern) which have nucleated on top of them. The output also shows new {111} grains nucleating on top of {100} grains. Due to this renucleation, voids above the slower-growing crystallites are filled in as they are replaced by faster-growing crystallites, and excessive growth by fast-growing crystallites is arrested. The result is a simulated film which is much more dense than that produced without renucleation, and with a much lower surface roughness. This simulation corresponds well to the experimental observations of thick films grown with renucleation (e.g. Figure 12 of reference 1 and Figures 4 and 5 of reference 2), in which dense thick films have been grown.

In the simulation of Figure 3, a "long" DLC deposition time was used, which causes extensive renucleation between diamond growth stages. Figure 4 illustrates the effect of shorter DLC deposition times. As the DLC deposition time is decreased, the renucleation probability after each growth stage decreases (eq. 1a) , leading to an increasingly "voidy" film. Thus, some minimum DLC deposition time will be required in order to produce dense diamond films. However (as mentioned above) the DLC deposition time cannot be made too long, otherwise there will be an excessive fraction of non-diamond phases in the film. Modelling should be useful in determining the optimum renucleation time.

Figure 4 showed one trial for each deposition time. Figure 5 summarizes the results of a number of trials for each condition. The output for each trial is a "uniformity parameter" calculated from the final morphology. As can be noted from Figure 4, values greater than about 5 for this parameter correspond to a dense film appearance. Figure 5

shows that due to statistical variations, if a number of films were to be grown using fixed growth procedures, then in order to ensure that the "worst case" still produces a dense film, the DLC deposition time would have to be almost twice the average deposition time required for a dense film. As noted above, the excess DLC deposited by such a procedure could compromise the thermal conductivity of the diamond film. These results emphasize the potential value of in-process monitoring and intelligent process control, in which the DLC deposition time during any one film growth could be tailored to the film which is actually evolving, rather than having to be prescribed in advance to cover the worst case.

## Concluding remarks

The present model is clearly only a first attempt at simulating morphological instability ("competitive shadowing") and its suppression in diamond film growth by flame deposition. While the model is not as fundamental as atomistic models (instead relying on aggregation of the controlling physical mechanisms by internal state variables), it is capable of treating more complex situations (for example, periodic renucleation ) and eventually of being used in real-time process control.

Areas in which improvement of the model for the present purposes would be appropriate include: (1) a more physical representation of the manner in which crystallite growth occurs by ledge etching (by oxidative species in the gas) followed by deposition of carbonaceous species on these active ledges, (2) prediction of the growth rates and aspect ratios/densification rates produced by this ledge activation process, and (3) prediction of the effects of flame chemistry, temperature, and history on this ledge growth process.

## REFERENCES


1. K.V. Ravi, J. Materials Science (In Press)
2. K.V. Ravi, A. Joshi and H.S. Hu, Proc. 2 nd International Conference on The New Diamond Science and Technology, Washington DC, Sept. 1990 ( In Press)
3. G.S. Bales, R. Bruinsma, E.A. Eklund, R.P.U. Karunasari, J. Rudnick and A. Zangwill, Science, 249, 264 (1990)
4. K.V. Ravi and A. Joshi, Appl. Phys. Lett, 58,246 (1991)

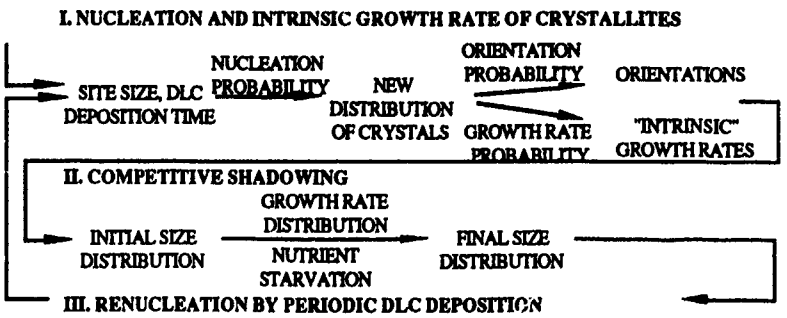




Figure 1. Schematic of Model

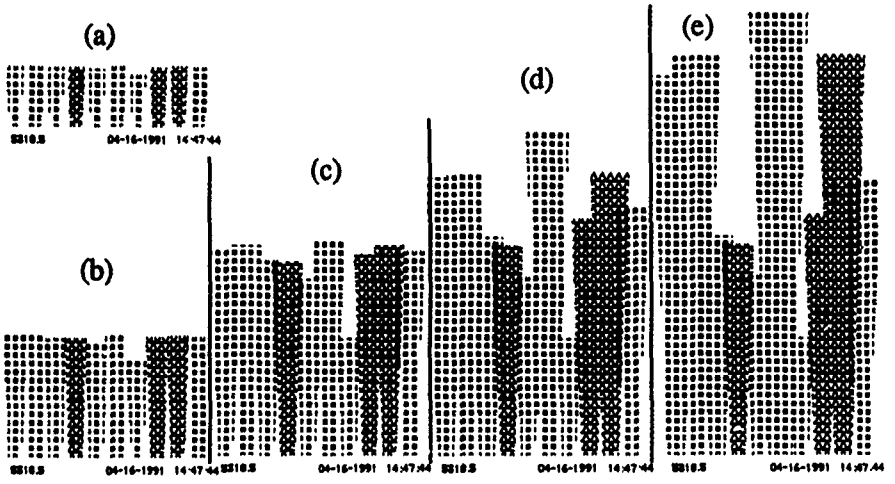



Figure 2. Model simulations, showing cross sectional structure, of 5 stages in the growth of a thick diamond film without renucleation."Competitive shadowing" causes initial minor variations in growth rate (left) to be amplified into major morphological instabilities (right).

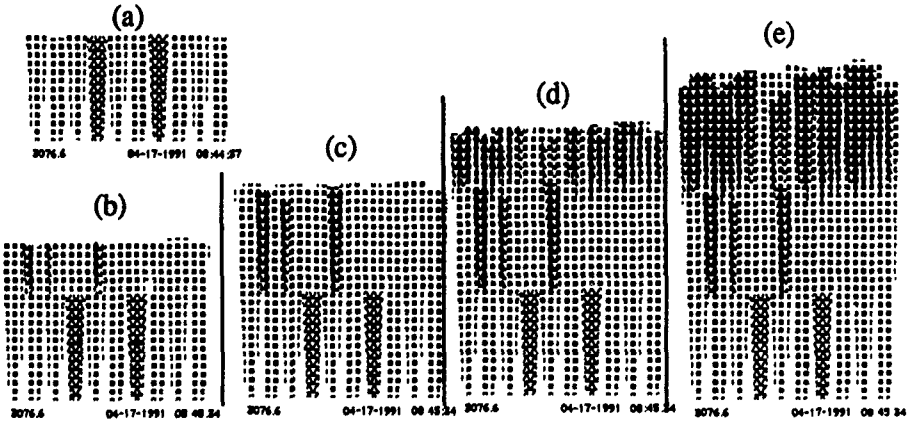



Figure 3. Model simulations of 5 stages in the growth of a thick diamond film with periodic renucleation by DLC deposition at the end of each stage. The periodic renucleation suppresses morphological instability and leads to a much more dense simulated thick film.

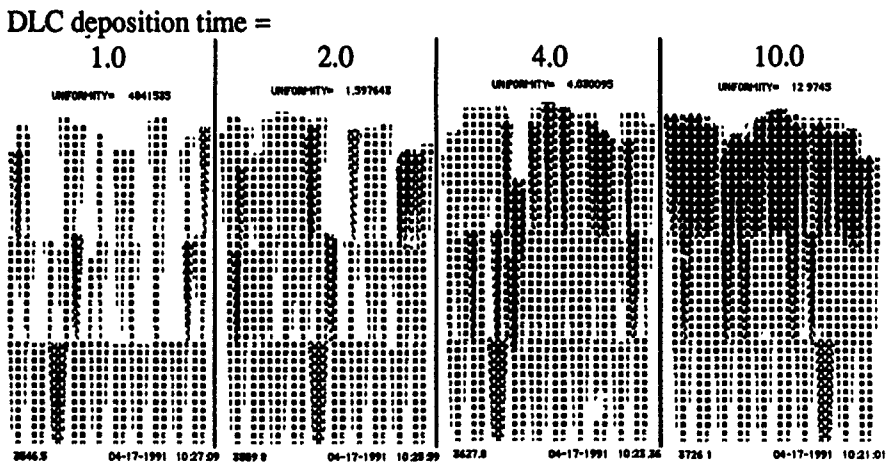



Figure 4. Model simulations of the final film produced using periodic renucleation by DLC deposition, for various times. The longer the DLC deposition time, the denser the film.

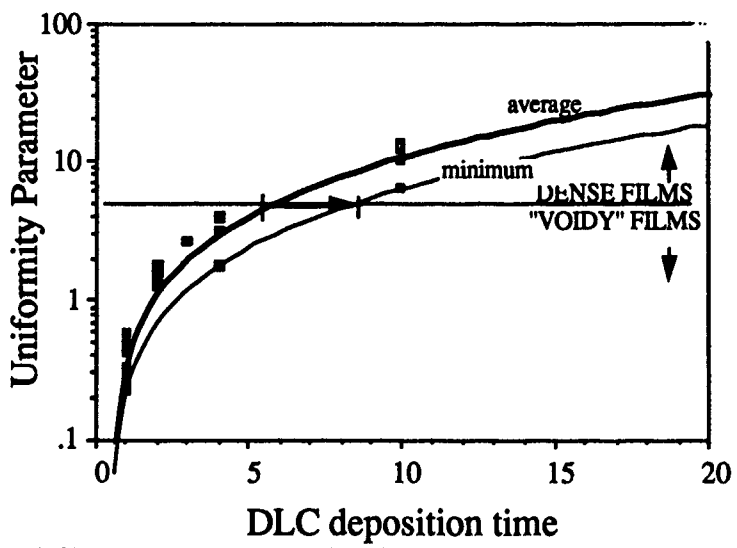



Figure 5. Simulated effect of DLC deposition time upon the "uniformity parameter" (measure of film density). Statistical variations in nucleation and growth cause the minimum DLC deposition time required to produce dense films to be almost twice the average.

# The Effect of Gas-Phase Residence Time on Microwave Plasma Diamond CVD

F. G. Celii, D. White, Jr.[a] and A. J. Purdes

Texas Instruments, Inc.
Central Research Laboratory, M. S. 147
P. O. Box 655936, Dallas, TX 75265

## ABSTRACT

The effects of gas-phase residence time on the properties of chemical vapor deposited (CVD) diamond films are reported. Films were prepared by microwave plasma CVD at various gas flow rates, while keeping other process parameters constant. Depositions were repeated at 40 Torr and 23 Torr, and on either diamond-abraded Si wafers or a microcrystalline diamond (MCD) layer. The diamond films were analyzed using scanning electron microscopy, x-ray diffraction, electrical resistivity, Raman and infrared spectroscopies. Some films displayed preferred crystal orientations and surface morphologies. The invariance of the deposition rate with gas flow is rationalized using flow modeling. We argue that the flow-dependent variation in film properties is caused by changes in gas-phase concentrations, which are due to differences in plasma residence time.

## INTRODUCTION

X-ray lithography membranes are a potential near-term application for CVD diamond. Diamond films are attractive because of an extremely high Young's modulus, thermal conductivity and radiation hardness.[1-5] Using microwave plasma CVD, we have deposited diamond films which are under tensile stress. The free-standing membranes have high visible and IR transmission, and are stable under extended x-ray irradiation.[5] Control of the structural properties of the diamond films may be important for increasing the tensile strength and/or Young's modulus of the membranes. In efforts to manipulate CVD diamond film properties, we have investigated the effect of reactant residence time, and, to a lesser extent, substrate preparation and gas pressure, on diamond film morphology and texture.[6]

## EXPERIMENTAL

Diamond films were deposited in an AsTEX 2.45 GHz microwave plasma system, with a chamber i.d. of 140 mm. Substrates were mounted on an inductively heated graphite susceptor. The substrate temperature was regulated using a thermocouple embedded in the susceptor. An uncorrected one-color (2.0-2.6 $\mu$m) pyrometer registered growth temperatures of ~760 C. A constant ratio of 1% $CH_4/H_2$ was metered by separate flow controllers to 25–800 sccm. The microwave power was 1.45 kW at 40 Torr or 1.10 kW at 23 Torr. Because of the chamber geometry, our results are substantially different from the study of Zhu, *et al.*[7]

Samples were prepared either on diamond-abraded 50 mm diameter Si wafers,

or onto an intermediate layer of microcrystalline diamond (MCD). Each Si wafer was HF-dipped after abrasion, pumped to $\sim 10^{-4}$ Torr, then etched for 5 min with a hydrogen plasma at the growth pressure. For films deposited directly on Si, diamond growth conditions at a chosen flow rate would then ensue. The growth time was chosen to yield films of nominal 2 $\mu$m thickness suitable for x-ray lithography membranes: 5 hours at 40 Torr or 7 hours at 23 Torr. For films grown on MCD, the diamond growth step was preceded by deposition with 4% $CH_4/H_2$ for 60 min, followed by a 30 min etch in pure $H_2$, both at 200 sccm. Continuous diamond films were deposited, due in part to the high nucleation density provided by the diamond abrasion process.

The films were analyzed *ex situ* with scanning electron microscopy (SEM), x-ray diffraction (XRD), Raman scattering, photoluminescence (PL) and infrared (IR) transmission spectroscopies. Electrical measurements were made at 1 and 10 V, between a masked region on the Si and Al dots evaporated onto the diamond film. The deposition plasma was monitored with optical emission spectroscopy. Assuming an average gas temperature of 300 C, the residence time for gas flows of 800 to 25 sccm ranged from 3 to 100 sec or from 0.3 to 9 sec, considering either the chamber volume above the susceptor or the plasma volume, respectively, at 40 Torr. The apparent residence times were a factor of $\sim 2$ shorter at 23 Torr.

## RESULTS AND DISCUSSION

The electrical resistivity was similar for all 40 Torr samples, ranging across the wafer from $10^8$-$10^{11}$ $\Omega$-cm, as grown, and $10^{12}$-$10^{13}$ $\Omega$-cm, after annealing at 900 K under 1 atm $N_2$ for 2 hrs. No variation with respect to flow rate or surface preparation (on Si or MCD) could be discerned. Analysis of the PL spectra will be presented elsewhere.[6] The optical emission spectra varied little between the range of 40 Torr growth conditions. Most bands were due to excited states of atomic or molecular hydrogen.[8] Excited-state CH and $C_2$ emission bands were not detected under the 1% $CH_4/H_2$ conditions.

### 1. Film Morphology

The crystalline film morphology (Figure 1) showed a strong dependence on flow rate. For the 40 Torr samples on Si, smooth (100) and (111) facets of $\sim 1$ $\mu$m size were dominant for 100 and 200 sccm conditions, respectively, with most oriented approximately parallel to the growth surface. Random, but distinct, crystal facets occurred at higher flow rates, while a rough, small-grain matrix was observed between the larger grains at low flows. The morphology of the 40 Torr deposits on MCD was similar, but small, facetted grains were present under all flow conditions.

The diamond films deposited on Si at 23 Torr showed: $\sim 1$ $\mu$m (111) facets at 25 sccm; smooth, randomly-oriented $\sim 2$ $\mu$m (100) faces at 100 and 200 sccm, with finer intergranular growth in the latter; $<0.5$ $\mu$m grains at 800 sccm flow. All the 23 Torr growths on MCD displayed small grain sizes ($\sim 0.5$ $\mu$m at 25 sccm, $<0.3$ $\mu$m at 800 sccm), with some 1 $\mu$m (100) faces imbedded in the 100 sccm film.

## 2. Crystal Structure

The XRD spectra of the deposited films showed the diamond (111), (220), (311) and (400) reflections, but often with relative intensities different from those predicted from a powder pattern, for randomly distributed grains. While only a pole figure can provide a complete description of preferred orientation, significant deviation from predicted intensities provides (limited) information on the film texture.[9] In our case, the texture reflects the preferred orientation of those grains whose (hkl) planes are parallel to the substrate surface, since only those contribute to the spectra in the $\theta/2\theta$ coupled scan mode.

Many of the 40 Torr diamond films exhibited a preferred orientation (Figure 2a). The films on MCD had a (110) texture, as indicated by the intensity ratio I(111)/I(220) < 4, which was independent of flow rate. The films prepared on Si mostly had (111) preferred orientations, with the strongest texturing at 25 and 50 sccm. Interestingly, the 100 sccm films, which displayed dominant (100) facets, showed no evidence of an enhanced (400) reflection; one sample had a non-random I(111)/I(220) value (~8). Specht, *et al.*,[10] observed a [17,3,0] texture for a sample with square facet morphology, in which the intense (400) scattering was observed out of the normal scattering plane ($\chi \neq 0$).

Under the 23 Torr conditions (Figure 2b), the films on MCD exhibited a greater [110]-preferred orientation than the 40 Torr films, and the extent of the texturing increased at higher flow rates. The films on Si and on MCD both showed flow-dependent changes in preferred orientation. As at 40 Torr, the 25 and 200 sccm films on Si exhibited a [111] texture. The 800 sccm flow, however, induced a [110]-texturing of the diamond films on Si.

The texture of films deposited directly on Si has been shown to be dependent on deposition temperature.[10] For the 40 Torr depositions, we found that substrate temperature variation of ~10 C did not give rise to significant changes in film morphology.[6] Interestingly, the films in our study showed little correlation between surface morphology and crystal texture, unlike the filament-assisted growths reported by Kaae, *et al.*[11]

The observation of [110]-oriented diamond films deposited on MCD layers is consistent with the microwave plasma study of Kobashi, *et al.*,[12,13] who found that the extent of [110]-texturing depended sensitively on both $CH_4/H_2$ ratio and deposition time. A [110]-preferred orientation was also observed in films deposited with combined microwave-filament activation.[14,15] A [110]-textured diamond film was reported for the case of dc plasma deposition on Si,[16] but the nucleation details were not given, and may have employed an MCD or DLC layer. The film morphology was shown to be sensitive to the conditions of initial layer formation in microwave[17] and combustion flame[18] depositions.

In the study of Wild, *et al.*,[15] the [110]-texturing parallel to the growth direction increased continuously with film thickness. A model of evolutionary selection was used to explain the tendancy toward increased texture with increasing film

thickness or decreasing separation of diamond nuclei.[15] In light of this model, the increased [110]-texturing we observed in films on MCD may be explained by the smaller grain sizes present in those films.

### 3. Deposition Rate

It is important that the film thicknesses be similar so that comparisons are made between samples at the same stage of growth. The deposition rate was gauged either from the weight gain on the entire wafer, or from the interference fringes in the IR transmission spectra. The film thickness showed little variation with flow rate among the 40 Torr samples (Figure 3), indicating growth rates within 20% of ~0.25 $\mu$m/hr. The difference in thickness between the films grown on Si and on MCD is due solely to the MCD layer, and does not represent an increase in growth rate of the 40 Torr samples. At 23 Torr, the deposition rate increased with the flow rate: ~0.20 $\mu$m/hr at 25 sccm, ~0.30 $\mu$m/hr at 800 sccm.

### 4. Raman Spectra

All films prepared in this work showed the sharp (~8 $cm^{-1}$) crystalline diamond peak at 1334 $cm^{-1}$, a broad (~100 $cm^{-1}$) amorphous carbon band near 1530 $cm^{-1}$, and a luminescence background.[19] For the 40 Torr films (Figure 4), the intensity ratio, $I_{1334}/I_{1530} = I_D/I_{AC}$, varied with flow rate on Si ($I_D/I_{AC} \sim 2$ to 5) and on MCD (0.8 to 1.6), and exhibited maxima at moderate flows (400 sccm and 100 sccm, respectively). In the case of the 23 Torr films, the amorphous carbon component was larger, and the $I_D/I_{AC}$ ratio generally decreased with increasing flow rate, both on Si ($I_D/I_{AC} \sim 2.2$ to 0.5) and MCD (0.5 to 0.3).

### 5. Flow Modeling

To help interpret the observations, numerical simulations of the flow geometry were performed which demonstrated the importance of convective flow in our reactor. Temperature contours were calculated by assuming a fixed temperature susceptor, and were found to be insensitive to flow rate. Neglect of the plasma as a heat source is warranted in low pressure (<1 Torr) plasmas. Temperature measurement of a 30 Torr dc discharge diamond CVD plasma showed gas kinetic temperatures of 1200-1300 K, slightly above the susceptor temperature.[20] Addition of the plasma as heat source would serve to *enhance* the vortex structure in the center of the chamber.

Flow velocities were determined using finite difference techniques.[21] Vortices above the growth surface are predicted at all flows, and are shown in Figure 5 for the low and high flow rate cases at 40 Torr. The presence of recirculation cells complicates the concept of residence time in our reactor. Because of the increased downward momentum, the flow velocities through the plasma region actually decrease by ~34% as the flow is increased from 25 to 800 sccm.

The insensitivity of the 40 Torr deposition rate on gas flow rate can be rationalized by the flow pattern: as the flow rate increases, a larger portion of the gas bypasses the growth surface and is shunted directly to the chamber exhaust.

The increase of the deposition rate at high flows at 23 Torr may be a result of increased gas residence time near the surface, and is being investigated.

To understand the significant flow-dependent changes in diamond film morphology and texture, we performed separate experiments in which a decrease in plasma power was found to affect the film morphology, whereas an independent decrease in substrate heating (~10-30 K, the same change as resulted from the decrease in plasma power) caused little change.[6] Thus, we believe that changes in the concentrations of diamond-growth species, perhaps from subtle variations of the residence time in the plasma, are responsible for the flow dependence of the film properties. Mass-dependent reactant diffusion through the vortex may also alter the effective carbon fraction above the growth surface.

## CONCLUSIONS

We have studied the effect of gas flow rate and substrate preparation on microwave plasma-assisted diamond deposition. The diamond film texture and morphology can be influenced by both the gas flow rate and the deposition surface. Films of ~2 $\mu$m thickness can be prepared with varying degress of [111] texturing by altering the flow rate. An initial MCD layer induces a [110]-oriented diamond film, even under the same growth conditions that produce [111]-oriented films on Si. This fact suggests that the texture variations for diamond films on Si are to some degree determined by the nucleation step, perhaps through an effect on the grain size. Lower pressure growth conditions enhanced the [110] texturing. Flow modeling showed recirculating vortices under the 40 Torr conditions.

## ACKNOWLEDGEMENTS

We acknowledge the technical assistance of Ray Stinedurf and valuable discussions with Hung-Yu Liu.

## REFERENCES

a) Semiconductor Process & Design Center, M. S. 944.

1. H. Windischmann, *Proc. SPIE Conf. on Electron-Beam, X-Ray, and Ion-Beam Technology: Submicrometer Lithographies IX,* **1263** (1990) 241.
2. H. Windischmann and G. F. Epps, *J. Appl. Phys.*, **68**, 5665 (1990).
3. B. S. Berry, W. C. Pritchet, J. J. Cuomo, C. R. Guarnieri and S. J. Whitehair, *Appl. Phys. Lett.*, **57**, 302 (1990).
4. Y. Vladimirsky, J. R. Maldonado, O. Vladimirsky, A. Starikov, R. Fuentes, C. R. Guarnieri, S. J. Whitehair and J. J. Cuomo, *J. Vac. Sci. Technol. B*, **8**, 1579 (1990).
5. G. M. Wells, S. Palmer, F. Cerrina, A. Purdes and B. Gnade, *J. Vac. Sci. Technol. B*, **8**, 1575 (1990).
6. F. G. Celii, D. White, Jr. and A. J. Purdes, *J. Appl. Phys.*, submitted for publication.

7. W. Zhu, R. Messier and A. R. Badzian, *Proc. 1st Intl. Symp. on Diamond and Diamond-Like Films,* Eds., J. P. Dismukes, A. J. Purdes, B. S. Meyerson, T. D. Moustakas, K. S. Spear, K. V. Ravi and M. Yoder, **89-12** (The Electrochemical Society, 1989), p. 296.

8. R. W. B. Pearse and A. G. Gaydon, *"The Identification of Molecular Spectra"* (Chapman and Hall, London, 1976).

9. B. D. Cullity, *"Elements of X-ray Diffraction,"* 2nd ed. (Addison-Wesley Pub. Co., Inc., Reading, 1978).

10. E. D. Specht, R. E. Clausing and L. Heatherly, *J. Mater. Res.*, **5**, 2351 (1990).

11. J. L. Kaae, P. K. Gantzel, J. Chin and W. P. West, *J. Mater. Res.*, **5**, 1480 (1990).

12. K. Kobashi, K. Nishimura, K. Miyata, K. Kumagai and Y. Kawate, *Proc. 1st Intl. Symp. on Diamond and Diamond-Like Films,* Eds., J. P. Dismukes, A. J. Purdes, B. S. Meyerson, T. D. Moustakas, K. S. Spear, K. V. Ravi and M. Yoder, **89-12** (The Electrochemical Society, 1989), p. 296.

13. K. Kobashi, K. Nishimura, K. Miyata, K. Kumagai and A. Nakaue, *J. Mater. Res.*, **5**, 2469 (1990).

14. Ch. Wild, H. Herres, J. Wagner, P. Koidl and T. R. Anthony, *Proc. 1st Intl. Symp. on Diamond and Diamond-Like Films,* Eds., J. P. Dismukes, A. J. Purdes, B. S. Meyerson, T. D. Moustakas, K. S. Spear, K. V. Ravi and M. Yoder, **89-12** (The Electrochemical Society, 1989), p. 283.

15. Ch. Wild, H. Herres and P. Koidl, *J. Appl. Phys.*, **68**, 973 (1990).

16. J. Narayan, A. R. Srivatsa, M. Peters, S. Yokota and K. V. Ravi, *Appl. Phys. Lett.*, **53**, 1823 (1988).

17. R. Meilunas, M. S. Wong, K. C. Sheng, R. P. H. Chang and R. P. VanDuyne, *Appl. Phys. Lett.*, **54**, 2204 (1989).

18. K. V. Ravi and C. A. Koch, *Appl. Phys. Lett.*, **57**, 348 (1990).

19. D. S. Knight and W. B. White, *J. Mater. Res.*, **4**, 385 (1989).

20. H. N. Chu, A. R. Lefkow, E. A. Den Hartog, J. Jacobs, P. Sandstrom, L. W. Anderson, M. G. Lagally and J. E. Lawler, in *"Diamond, Boron Nitride, Silicon Carbide and Related High Bandgap Semiconductors,"* Mater. Res. Soc. Symp. Proc., **162**, 1990, 163.

21. FLUENT software is a product of creare.x Inc., Hanover, NH.

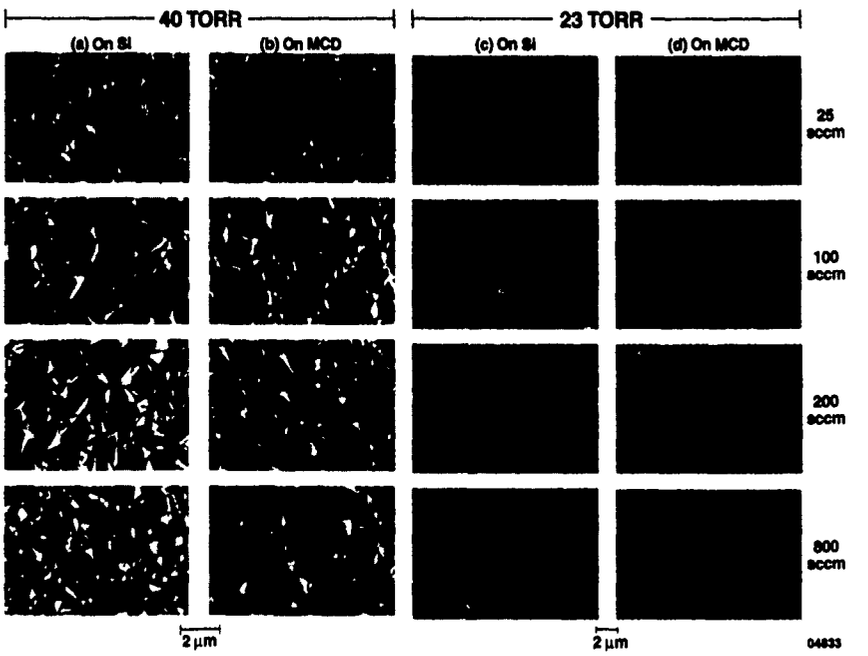



**Figure 1.** SEM of diamond films deposited at: (a,b) 40 Torr; (c,d) 23 Torr. The 40 Torr films grown on Si show dominant facets at intermediate flow, but random faceting at high and low flow. The 40 Torr films grown on MCD show similar features, plus small grains under all flow conditions. The 23 Torr films show grain sizes of $< 0.5$ $\mu$m, except for samples deposited on Si at intermediate flow conditions.

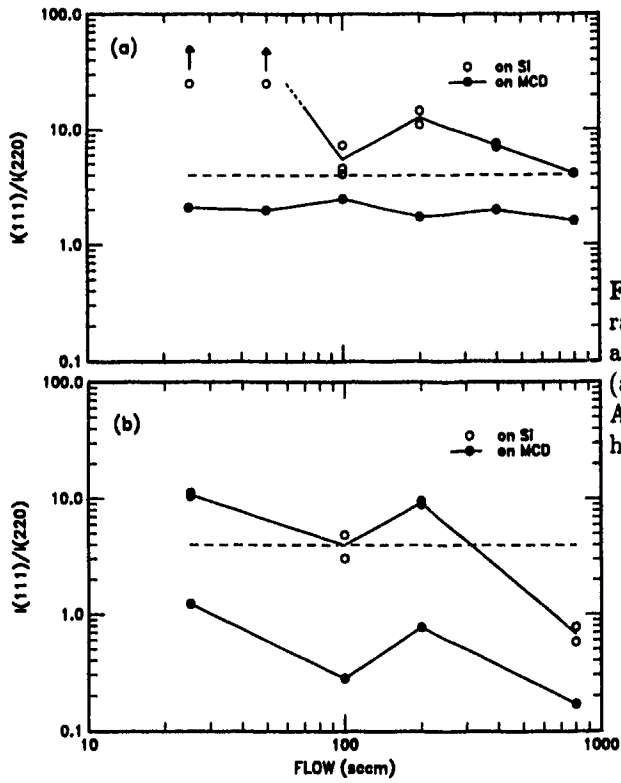



**Figure 2.** XRD intensity ratio *vs.* flow rate for diamond films deposited at: (a) 40 Torr; (b) 23 Torr. A randomly-oriented film has $I_{111}/I_{220} = 4$.

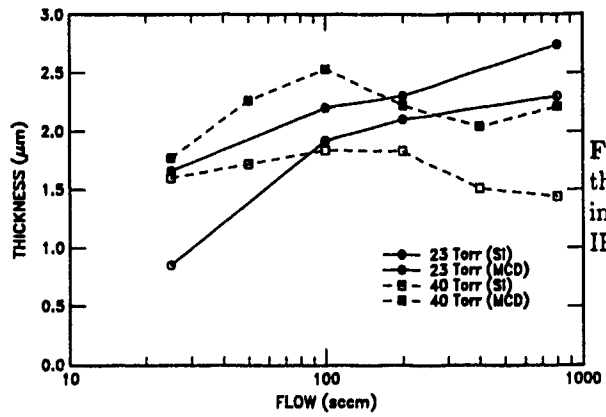



**Figure 3.** Diamond film thickness, measured from interference fringes in the IR transmission spectra.

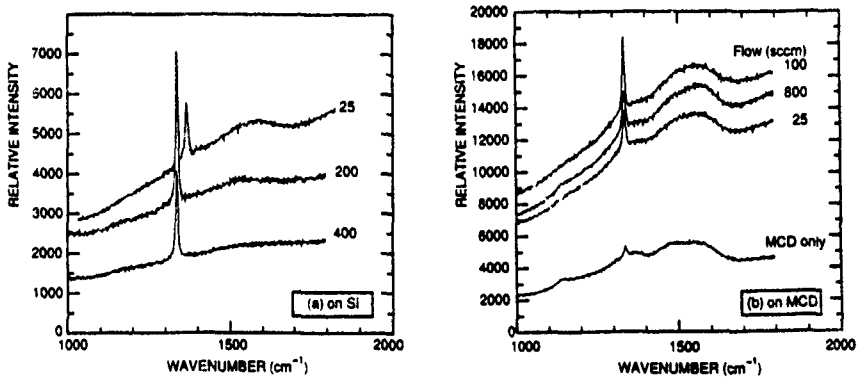



**Figure 4.** Raman spectra of diamond films: (a) on Si; (b) on MCD. The Raman signature of diamond at 1332 $cm^{-1}$ is evident in the spectra of all films. The 25 sccm spectrum in (a) was shifted horizontally for clarity. The Raman spectrum of an MCD layer on Si is also shown in (b).

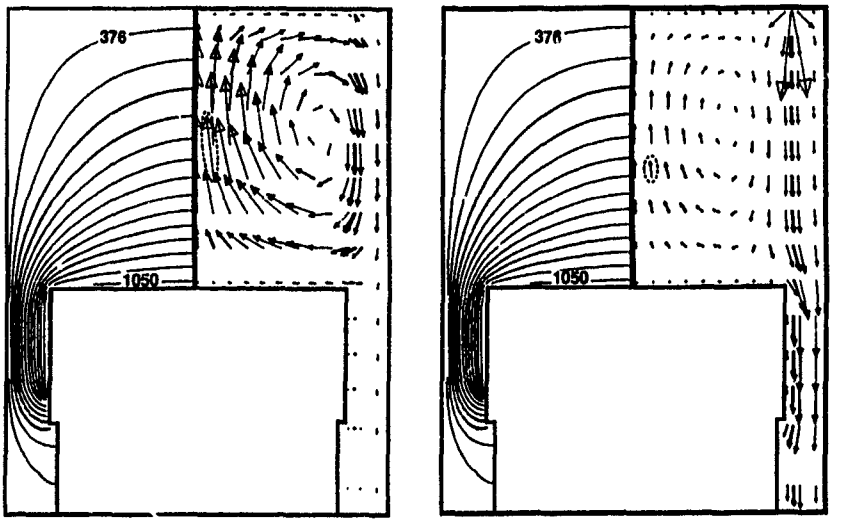



**Figure 5.** Simulation results for our reactor geometry and an assumed susceptor temperature of 800 C, wall temperature of 60 C, and gas flow rate of: (a) 25 sccm; (b) 800 sccm. The calculated temperature profiles are given on the left side of (a) and (b) with a contour spacing of 52 C. The lengths of the flow field vectors (on the right) correspond to gas velocity. The two velocity plots are scaled differently, with the circled vectors representing: (a) 7.4 cm/sec; (b) 4.9 cm/sec. Note that the velocity in the vortex region is *lower* at the higher flow rate.

# INVESTIGATIONS OF NUCLEATION AND CRYSTAL GROWTH OF CVD DIAMOND USING THE SENTAXY TECHNIQUE

Hiroyuki Yagyu, Jing Sheng Ma, *Hiroshi Kawarada, **Takao Yonehara, and Akio Hiraki

Department of Electrical Engineering, Osaka University, Suita-shi, Osaka 565, Japan.
*School of Science and Engineering, Waseda University, Shinjuku-ku, Tokyo 169, Japan.
**Canon Inc., R/D Headquarters, Hiratsuka-shi, Kanagawa 254, Japan.

We have investigated the initial stage of crystal growth and growth processes of chemical-vapor-deposition (CVD) diamond with a scanning electron microscope (SEM) and a transmission electron microscope (TEM), making use of the SENTAXY (Selective Nucleation Based Epitaxy) technique by which it is possible to control the nucleation sites and therefore to fabricate CVD diamond array. The growth of the same particle has been pursued by SEM observation. Overgrowth and preferential growth have been observed. Removal of a small particle during crystal growth has also been observed. Moreover, an investigation concerning with nucleation has been done by plane-view and cross-sectional TEM. It has been clear that the defects near the surface of the substrates with high concentration have close relation to diamond nucleation sites.

## INTRODUCTION

The applications for semiconducting or optical devices have been expected of the chemical-vapor-deposition (CVD) diamond synthesized from gas phase at low pressure. However, because of random nucleation of diamonds on hetero-substrates, CVD diamond thin films are polycrystalline, which restricts to make good use in devices. The diamond SENTAXY (Selective Nucleation Based Epitaxy) technique makes a great approach to applications since single-crystal-diamond array, as shown in Fig.1(a) can be fabricated(1),(2),(3). The SENTAXY technique has been carried out in the field of silicon first, and a success in device has been made(4),(5). The diamond SENTAXY is a novel technique not only in applications but also in fundamental research, e.g. elucidation of nucleation and crystal growth, because the

technique enables to grow crystals separately and to control nucleation sites artifitially. This makes it much easy to study diamond nucleation sites on the substrates and crystal growth of CVD diamond. In addition, it is very important for the SENTAXY diamond itself to make it clear whether the particle synthesized separately with this technique is a single crystal or not. In this paper, we have investigated the initial stages of crystal growth and the growth processes of CVD diamond by pursuing the growth of a same particle with a scanning electron microscope (SEM). A transmission electron microscope (TEM) studies, from both plane-view and cross-sectional view, has also been carried out.

## EXPERIMENTAL

[1] Procedure of the diamond SENTAXY:

The substrates used here were Si wafers patterned with square dots or stripes as shown in Fig.2(a) and (b) respectively. The dots and stripes are made from Si itself. The dot size is 1.2 μm × 1.2 μm with 0.2 μm in height and the interval between the dots is 10 μm. The stripes are 1.2 μm in width and 0.2 μm in height and 10 μm separated each other.

Before deposition, a two-step process for substrate treatment has been done. First, the substrates were pretreated by abrasive powders (diamond powders of about 30μm in diameter) using an ultrasonic generator for 3 minutes.

Then, after the pretreatment, an oblique irradiation by an argon beam to the substrates was carried out. The argon beam was produced by a D.C.ion source. The pressure of the argon gas was $10^{-5}$ Torr and the accelerated voltage of the beam was 5kV with current of 50 μA. By irradiating obliquely, diamond nucleation sites are selectively localized on the dot edges opposite to the incident direction of the beam. We call this edge "the opposite edge" and the effect of the nucleation on the opposite edges "the edge effect"(1),(2). The argon beam was irradiated perpendicularly to the stripes when stripe-patterned substrates were employed.

Finaly, a microwave plasma CVD system was employed for fabrication of diamond. CO(15 vol.%)/$H_2$ mixture was used and the reaction pressures were 30-35 Torr. Substrate temperatures were 900-1000 ℃.

[2] SEM observation:

After a certain growth time by the microwave plasma CVD

mentioned above, the sample was taken out of the CVD apparatus, observed by SEM, then returned to the apparatus for further growth. This procedure was repeated several times. The SEM observations were aimed on the same Si dot patterned on the Si wafer in order to pursue the crystal growth process.

[3] TEM observation:

A High-Voltage TEM operated at 200 kV (H-800) and an Ultra-High-Voltage TEM operated at 2000 kV (UH-3000) in Research Center for Ultra-High-Voltage Electron Microscopy of Osaka University have been used. Both plane-view and cross-sectional view were observed. The plane-view TEM specimens were prepared by thinning the substrates with $HF:HNO_3:CH_3COOH$. The cross-sectional TEM specimens were prepared by slicing, lapping, and then thinning by an argon ion milling. The stripes-patterned substrates were employed for the cross-sectional observation because it was difficult to obtain cross-sectional images of the dots and the diamonds forming on their opposite edges.

## RESULTS AND DISCUSSION

[1] Observations by SEM:

Fig.3 shows a growth process of CVD diamond observed by SEM. Due to the pretreatment of the abrasive powders and the oblique irradiation of the argon beam, the Si dot is no longer a square. Two diamond particles (A and B) are formed on the opposite edge of the Si dot at the initial stage. As growth time passing, the particle at right hand (A) grows preferentially while the left one (B) seems no growth. In addition, after 50 minutes, B dissapears from the dot. It is not clear whether because of the overgrowth under A or because of being removed by the discharge. This kind of preferential growth has often been observed. After 1-1.5 hours, A grows large to be identified as a twinned crystal of 1-2 μm. Astonishingly, a small particle (C) begins to grow on the opposite edge, and grows large. It burys gradually under A due to the overgrowth. Finally, it almost burys at all in A except a small protruding part on {100} facet of A. This kind of particles are often observed in SEM images and usually considered as second-order nucleations. In fact, it is "the head" of a particle hiding behind or burying under a large particle.

[2] Observations by TEM:

Three plane-view TEM (UH-3000) images are shown in Fig.4. The Si dot appears in shape of square. Some defects of

dislocations are formed in the specimen due to the pretreatment by abrasive powders and during the deposition process with high temperature. The incident beams is illustrated by the arrows, and diamonds are formed on the opposite edges of the dots. In Fig.4 A, it is recognized that defects are created densely along the four edges on the square dot instead of the center part. This is because the dots protrude on the surface and the abrasive powders are much bigger (30μm in diameter) compared with the dots. The diamond particle is formed on the area where the defects concentration is high. On the edge at left hand, no diamond is formed in spite of high defect density. It is considered that the argon beam affected only onto the surface of the dot rather than the inside, and so the inside defects, being revealed by the high penetration TEM, remained. However, though there are high density defects in Fig.4 B, no particle is formed here. This is a special example, in most cases, diamond particles grow on the opposite edges of the dots. In Fig.4 C, two diamond particles are formed on one corner of the dot. The overgrowth of one particle has been observed in this figure also with TEM as well as observed with SEM mentioned above. From this observation, it is obvious that there is a close relation between diamond nucleation sites and the defects, though it cannot conclude that diamond nucleation sites are formed by the defects until a much high resolution observation is carried out.

The cross-sectional TEM (H-800) images, Fig.5, show how the diamond particles grow on the edges of the stripes. The original Si stripes are not so sharp at the edges, and are made duller by the pretreatment and mainly by the beam irradiation. The arrows indicate the incident beam direction. Diamond particles are formed on the opposite edges. The dark line (Fig.5 A) seen under the diamond particles is corresponding to the difference in thickness of Si, not to defects. Inside the Si stripes, no defect is observed except on the left edge of the stripe shown in Fig.5 B. Associating with the result of the plane-view TEM shown in Fig.4, however, it is considered that the defects exist almost on the surface of the substrates (or the dots). On the other hand, although the deep defect can be seen on the left edge of the stripe shown in Fig.5 B, no diamond is formed there. This is because the area of the defect appearing on the stripe surface was changed to amorphous by argon beam irradiation, which was made sure by RED (Reflection Electron Diffraction) (1). On the other hand, the nucleation site is retained on the opposite edge where the beam irradiation is shadowed or weekened.

It has been clear that the defects which exist on the

surface of the substrates with high concentration have close relation to diamond nucleation sites. Even though there is a defect to the deep level, it is not able to work as a nucleation site if the surface is changed into amorphous.

## SUMMURY

We have investigated the initial stage of crystal growth and growth processes of CVD diamond with SEM and TEM making use of the SENTAXY technique. It has been obseved that one particle grows over others to form a "single crystal" which is sometimes missed as a second-order nucleation. At the early stage of the crystal growth, a small-size particle can be removed off and vanished. It has also been found that the high density defects near the surface of substrates have close relation to diamond nucleation sites.

## ACKNOWLEDGEMENT

The authors thank for Professor H. Mori and the staff at Research Center for Ultra-High-Voltage Electron Microscopy of Osaka University, and thank for the support by a Grant-In-Aid for Developing Research (B) from Ministry of Education Science and Culture of Japan.

## REFERENCES

(1) J.S.Ma, H.Kawarada, T.Yonehara, J.Suzuki, J.Wei, Y.Yokota, and A.Hiraki : Proceeding of "1st International Symposium on Diamond and Diamod-Like Films." 175th Meeting of the Electrochemical Society, 149 (1989)
(2) J.S.Ma, H.Kawarada, T.Yonehara, J.Suzuki, J.Wei, Y.Yokota, and A.Hiraki : Applied Physics Letters 55,1071 (1989)
(3) H.Kawarada, J.S.Ma, T.Yonehara, and A.Hiraki : Proceeding of Symposium, the Materials Research Society, 162,195 (1990)
(4) T.Yonehara, Y.Nishigaki, H.Mizutani, S.Kondoh, K.Yamagata, T.Noma, and T.Ichikawa : Applied Physics Letters 52 (15),1231 (1988)
(5) T.Yonehara, Y.Nishigaki, and H.Mizutani : Oyo Buturi, 57, 1387 (1988) (in Japanese)



Figure 1. Typical scanning electron microscope image of
(a) a diamond array fabricated with the SENTAXY (Selective Nucleation Based Epitaxy) technique,
(b) a diamond thin film fabricated by random nucleation.

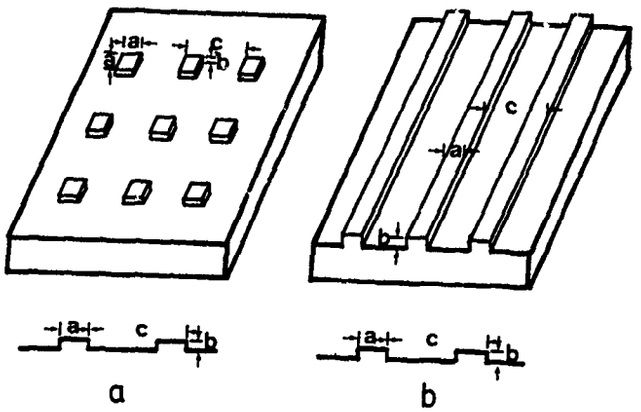



Figure 2. Schematic of the patterned Si substrates.
(a) The dots-patterned substrate : a=1.2μm, b=0.2 μm, c=10μm in this experiment.
(b) The stripes-patterned substrate : a=1.2 μm, b=0.2 μm, c=10μm in this experiment.

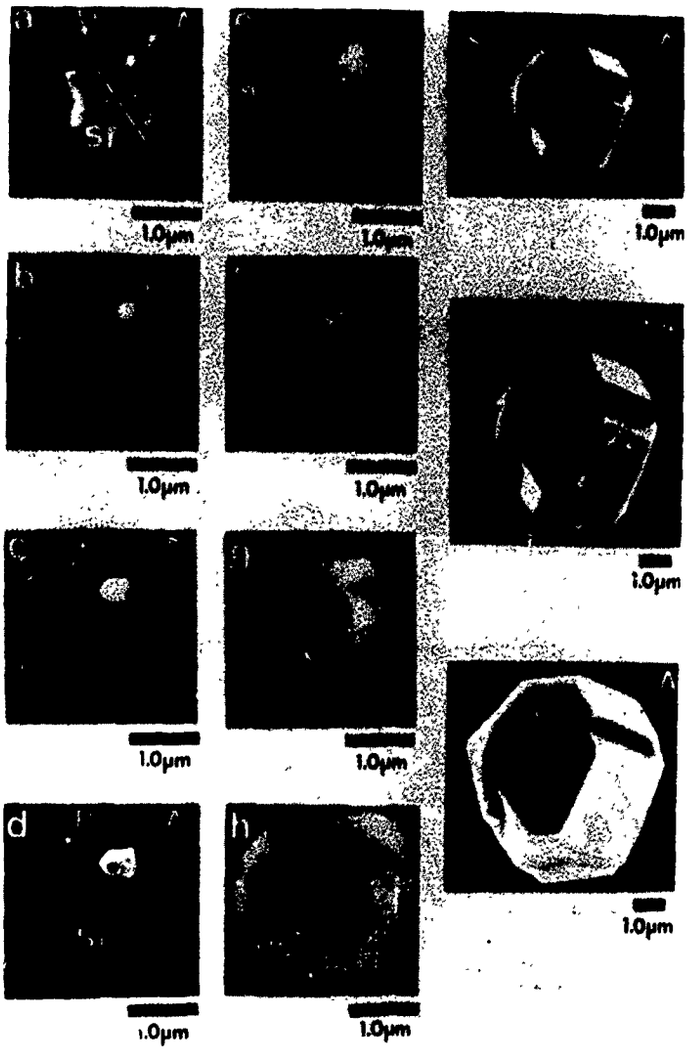



Figure 3. Growth process pursued with scanning electron microscope. Growth times are : a.10min. b.20min. c.30min. d.40min. e.50min. f.1hr. g.1.5hr. h.2hr. i.3hr. j.4hr. k.5hr.
The particle marked with A grows preferentially. After the particle B disappeared (at e.), the particle C is formed newly (at f.) and then buried under A (at j,k).

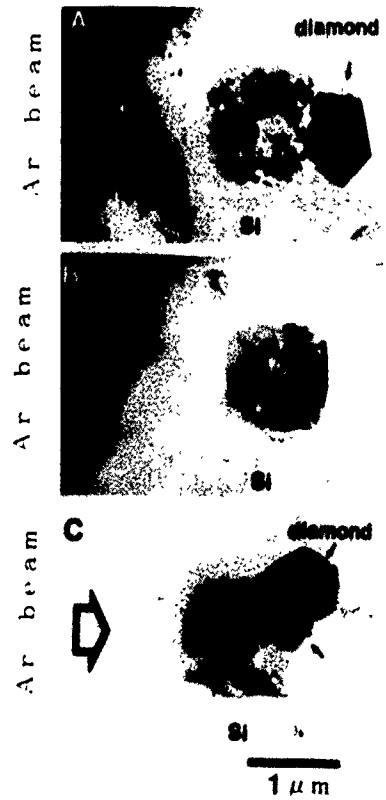



Figure 4. Plane-view observations with transmission electron microscope. The incident direction of an argon beam is indicated by arrows. (A) A dimond particle is formed on the opposite edge of the Si dot. The high density defects exist along the four edges of the dot. (B) No diamond particle is formed in spite of high density defects. (C) Two diamond particles are formed and the bigger one grows over the smaller one.

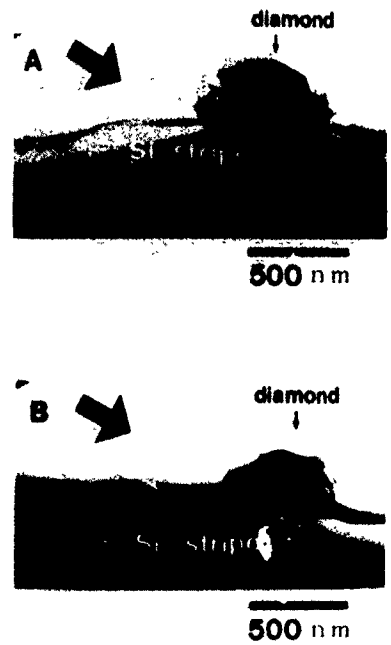



Figure 5. Cross-sectional view observations with transmission electron microscope. The incident direction is indicated by arrows. Diamond particles are formed on the opposite edges of the stripes. (A) No defect is seen inside the Si stripes. (B) At the left edge, a little defects are seen , however no diamond is seen there.

# DIAMOND ON SILICON : A HOT FILAMENT CVD STUDY OF NUCLEATION.

P. Ascarelli, S. Fontana §
E. Molinari, R. Polini, M.L. Terranova $
E. Cappelli *
§ Istituto di Metodologie Avanzate Inorganiche, C.N.R.
via Salaria Km 29,300 I-00016 Monterotondo S. (Roma)
$ Dipartimento di Scienze e Tecnologie Chimiche
II Università di Roma "Tor Vergata" I-00173 Roma
* Enricerche - SCISU
Via Ramarini, 32 I-00015 Monterotondo S. (Roma)

## ABSTRACT

The diamond nucleation time evolution can be reconstructed analysing the data obtained from the examination of a single deposited sample surface, once the single diamond particle growth rate is assumed to be known and the particle size distribution is measured. In this way it is possible to get information on the initial stage of the diamond nucleation. We found that the nucleation rate exhibits a maximum after a certain time which is longer the lower is the deposition temperature. This suggests the existence of an induction period of slow nucleation.

## INTRODUCTION

The main purpose of this work is to get information about the initial stage of diamond nucleation on a substrate surface. To achieve this goal we devised a kinetic scheme that relates the single diamond particle growth rate and the particle size distribution to the nucleation rate.
We analysed several diamond deposits made on Si (111) and on Si (100) substrates. The nucleation density and the particle growth were observed as a function of the deposition time and temperature, at a constant gas composition. The particle size distribution has also been recorded for each sample.
The complete nucleation time evolution can be reconstructed by the analysis of the data contained on a single sample, once the single particle growth rate is assumed to be known and the particle size distribution is measured.
We consider (1) that a nucleus of average radius r at the time $t_g$ derives from a nucleus which has nucleated at a previous time $t_b$. The time $t_b$ can be determined from the size r and the time $t_g$ when the law of growth is known.

We consider the distribution function $F(r,t_g)$ such that

$$F(r,t_g)dr \qquad (1)$$

equals the number $dN(t_b)$ of nuclei which granulated at the earlier time $t_b$ in an interval of time $dt_b$ corresponding to dr, then:

$$-F(r,t_g)\frac{dr}{dt_b} = \frac{dN}{dt_b} \qquad (2)$$

The distribution function $F(r,t_g)$ can be derived directly by counting on a sample surface, where a deposition has been made for a time $t_g$, the number of particles associated to each particle size r.
Many particle growth phenomena may be approximated by a single particle growth law of the type

$$r(t) = \alpha t^n \qquad (3)$$

where $\alpha$ is a time constant (which is a function of temperature) and n is an exponent related to the way the particle grows by acquiring matter from the outside source. In our case the experimental data suggest that a linear approximation (i.e. n=1) may be a reasonable first guess.
A constant growth rate may be simply justified assuming that the particle volume growth rate is proportional to its surface.
This for a spherical particle would give

$$\frac{dV}{dt} = \alpha\, 4\pi r^2 \qquad (4)$$

where V is the particle volume, $\alpha$ is the rate constant, then

$$4\pi r^2 \frac{dr}{dt} = \alpha\, 4\pi r^2$$

and

$$r = \alpha t \qquad (5)$$

Considering this particle size growth function and according to the previous definitions:

$$r(t_g,t_b) = \alpha(t_g - t_b) \qquad (6)$$

and

$$\frac{dr}{dt_b} = -\alpha \qquad (7)$$

thus from (2), (6) and (7) we get:

$$\frac{dN}{dt_b} = \alpha\, F(r,t_g)\Big|_{r=\alpha(t_g-t_b)} \qquad (8)$$

where $r = \alpha (t_g - t_b)$ has been substituted in the function $F(r,t_g)$, $t_g$ is the duration of the deposition experiment and $t_b$ is the running time from the beginning of the deposition.
We notice that if the distribution function $F(r,t_g)$ shows a maximum for a certain size r occurring between $r \neq 0$ and the maximum observable r, also the rate of nucleation shows a maximum for a certain time t.
Finally the nucleation density as a function of the deposition time $t_b$ is found by integrating (8):

$$N(t_b) = \int_0^{t_b} \frac{dN}{dt_b} dt_b = \alpha \int_0^{t_b} F(r,t_g) \Big|_{r=\alpha (t_g - t_b)} dt_b \qquad (9)$$

## EXPERIMENTAL RESULTS

The result of a typical deposition obtained on a Si(100) substrate surface kept at the temperature of 850°C with a Ta filament set at a distance of 5 mm at a temperature of 2100°C with a gas composition of 1% $CH_4$ and 99% $H_2$, a gas flux of 100 sccm, a dynamic pressure of 30 torr, is shown in figure 1 and 2 as seen by SEM.
The particle size distributions have been obtained from similar pictures; typical distributions are plotted in figs. 3 and 4.
Depositions carried out for different times allowed the determination of the particle size growth rate. An example of particle size growth rate, occurring at substrate deposition temperature of 950°C, is shown in figure 5, where it is possible to appreciate the nearly linear growth law.

## DISCUSSION AND CONCLUSION

It is possible to appreciate from fig. 3 and 4 the presence of a maximum occurring for certain particle size $r_o$. This maximum shifts toward higher size with increasing deposition temperature. From these distributions the nucleation density evolution as a function of time can be derived by the formula (9). The results are shown in figs. 6 and 7. The time evolution of the nucleation density shown in fig. 6 exhibits clearly a sigmoid behaviour. The sigmoid flexus shifts toward the time origin when the temperature is increasing (fig. 7).
For a tentative explanation of the presented evidence, let us consider a simplified nucleation model, according to which the nucleation occurs on a certain number of "active sites" present on the substrate surface. The nucleation

rate is therefore proportional to the number of "active sites" still present at each time.
Hence

$$\frac{dN}{dt_b} = v_d \left( N_o - N(t_b) \right) \qquad (10)$$

where $v_d$ is the rate constant for nucleation and $N_o$ the total number of active sites.
Integrating we find

$$N(t_b) = N_o \left(1 - e^{-v_d t_b}\right) \qquad (11)$$

and

$$\frac{dN(t_b)}{dt_b} = N_o \; e^{-v_d t_b} \qquad (12)$$

recalling (6) and (8) and substituting in (12) we get:

$$\begin{aligned} F(r) &= A \, e^{v_d r/\alpha} \quad \text{for } r/\alpha \leq t_g \\ F(r) &= 0 \qquad\qquad \text{for } r/\alpha > t_g \end{aligned} \qquad (13)$$

and $$A = \frac{N_o}{\alpha} v_d \, e^{-v_d t_g}$$

This simple exponential function provides a suitable fitting of the data at high temperatures, however it does not predict a maximum in the particle size distribution at values of r between the minimum and the maximum values observed, as required by the low temperature distributions. It can be shown that a more detailed treatment which allows the description also of the lower temperature data requires the introduction in the model of an induction time for nucleation. This point will form the subject of a forthcoming paper.

ACKNOWLEDGEMENT

It is a pleasure to acknowledge the help of Mr. P. Alessandrini for the SEM analysis.
We are grateful to Eniricerche for granting dr. S. Fontana a fellowship.

## REFERENCES

(1) We have adapted the general Avrami kinetic scheme to our analysis.
M. Avrami, J.Chem.Phys. 9, 177, 1941

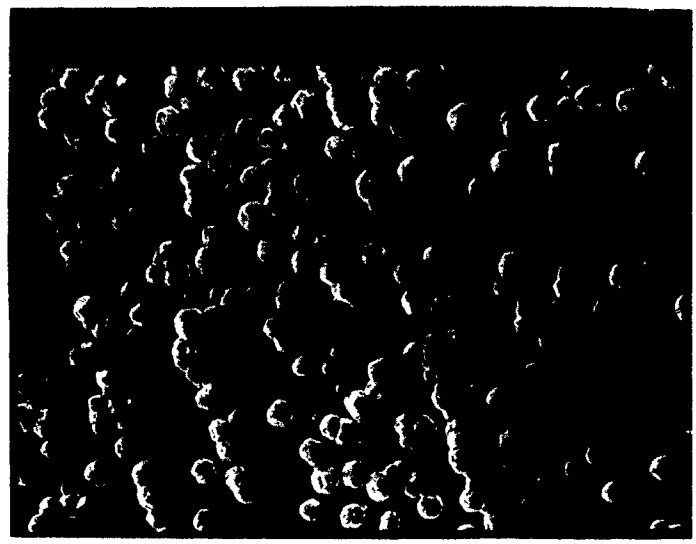
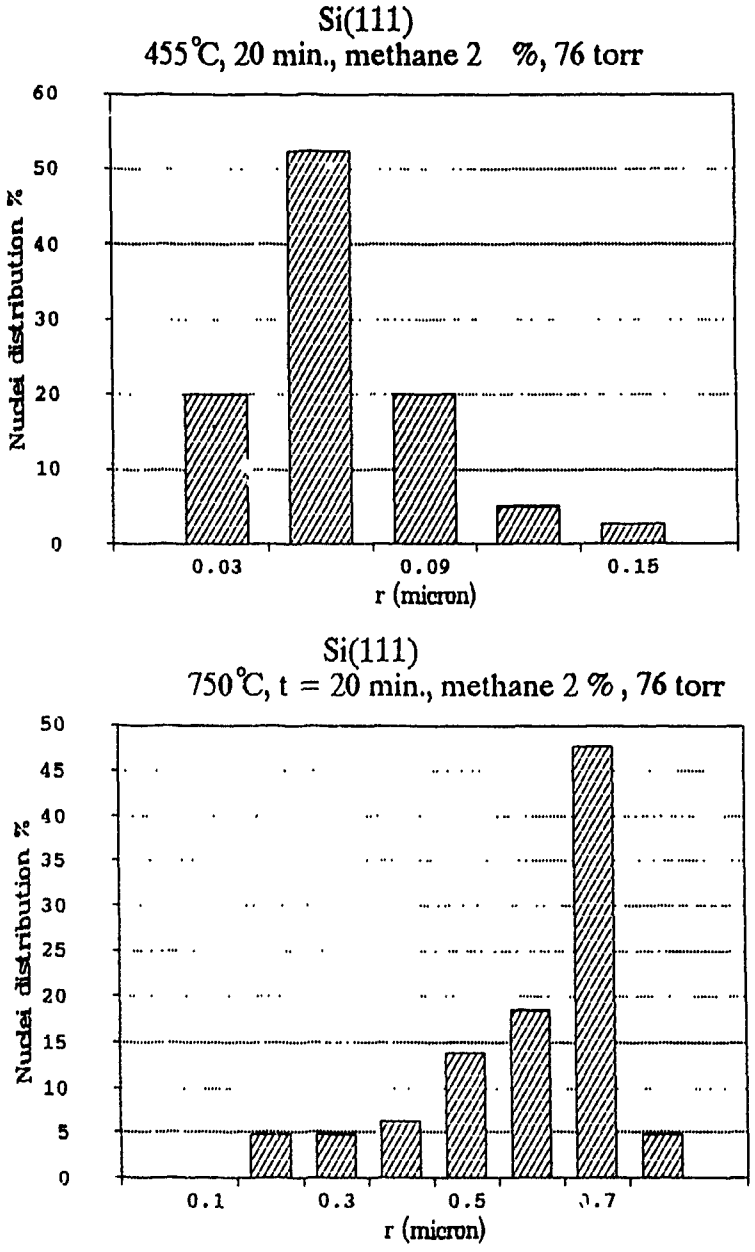


fig. 1 SEM picture of diamond crystallites on Si (100), T = 850 °C, 30 torr, 2% $CH_4$.



fig. 2 A higher magnification of fig. 1.




figs. 3, 4 Nuclei distribution versus crystallites dimension.

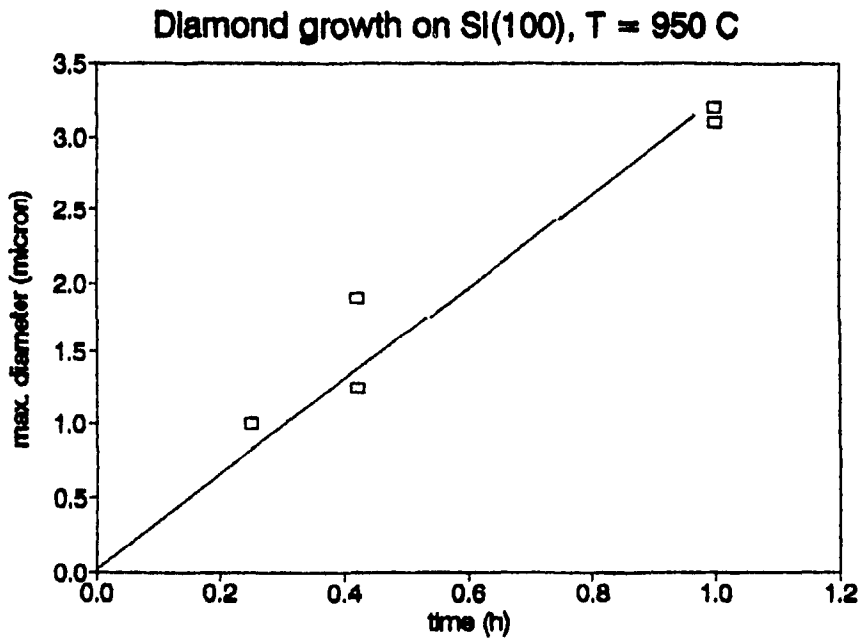
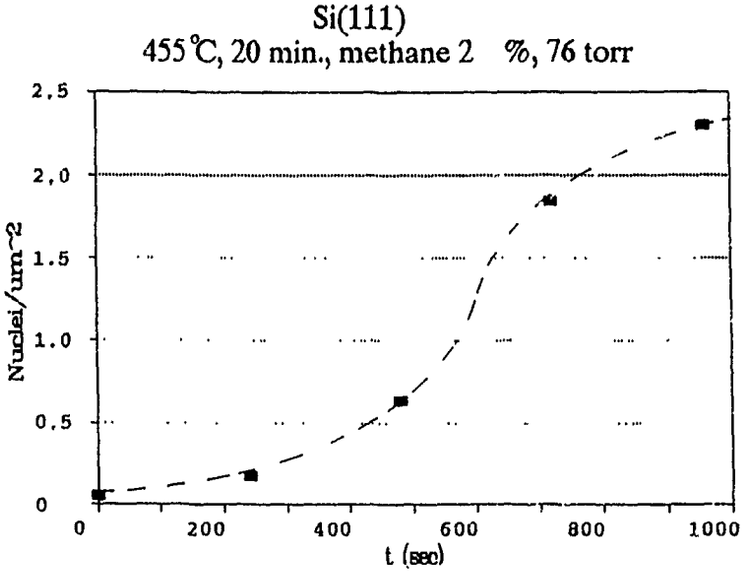
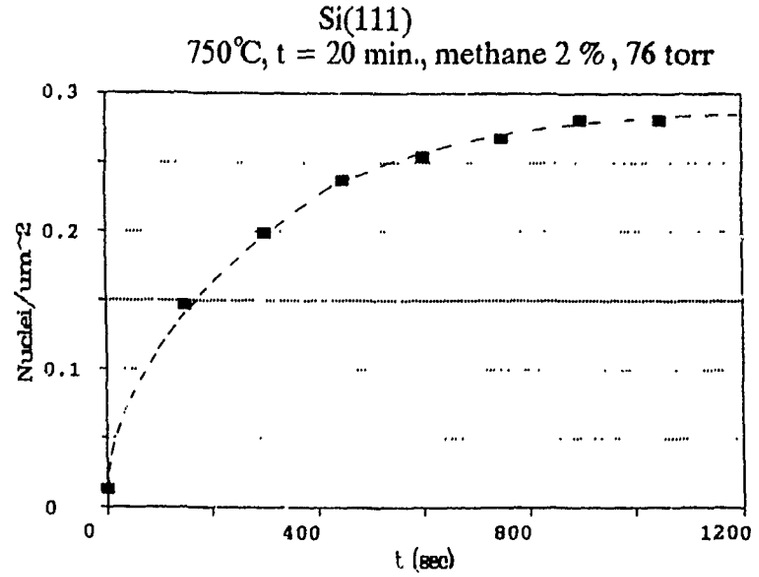



fig. 5 Diamond growth on Si (100), T = 950 °C, 2% $CH_4$, 76 torr.




figs. 6, 7 Nucleation density versus deposition time.

# SUBSTRATE EFFECTS AND THE GROWTH OF HOMOEPITAXIAL DIAMOND (100) LAYERS USING LOW PRESSURE rf PLASMA-ENHANCED CHEMICAL VAPOR DEPOSITION

J.B. Posthill, R.A. Rudder, G.C. Hudson, D.P. Malta,
G.G. Fountain, R.E. Thomas, and R.J. Markunas
Research Triangle Institute, Research Triangle Park, NC 27709-2194

T.P. Humphreys and R.J. Nemanich
Department of Physics
North Carolina State University, Raleigh, NC 27695-8202

D.R. Black
National Institute of Standards and Technology, Gaithersburg, MD 20899

## ABSTRACT

The technological evaluation of commercially-available, single crystal diamond substrates for homoepitaxial diamond growth is presented. Surface topographies of insulating diamonds (types Ia, IIa, and Ib) are shown, and microstructural comparisons are examined with X-ray topography. Wet chemical and mechanical cleaning procedures are briefly reviewed. The effect of the starting substrate on the resultant homoepitaxial diamond film can be partially mitigated by the proper choice of substrate, appropriate cleaning protocol, and the use of a well-qualified diamond deposition technology.

## Introduction

The thermal and electrical properties of diamond make it an excellent candidate for electronic applications. A number of significant problems must be overcome before the potential of diamond can be realized. While suitable heteroepitaxial substrates have not been developed yet, the fabrication of diamond transistors on natural diamond substrates allows testing and evaluation of diamond electronics [1]. One problem arising in the fabrication of diamond devices on diamond is the quality of the natural diamond substrates. Recent studies indicate that X-ray topography is a potentially valuable technique for characterizing structural defects in diamond single crystal substrates [2]. Selection of high quality diamond substrates is imperative to the growth of high mobility homoepitaxial diamond layers. In order to achieve the highest electrical quality diamond films, growth techniques may have to be developed which deposit epitaxial layers without replicating the crystalline defects commonly found in diamond single crystals.

This paper presents technological results accumulated over the last two years that pertain to the quality of commercially-available single crystal

diamond substrates, the cleaning of these substrates, and the resultant homoepitaxial diamond growth by low pressure rf plasma-enhanced chemical vapor deposition (PECVD). Both uniform coverage and selective-area diamond homoepitaxy are described.

**Experimental Procedures**

Natural type Ia and IIa and synthetically-produced type Ib diamond single crystals have been evaluated for their suitability for diamond homoepitaxy. Cutting and polishing to nominal (100) orientation were performed commercially by the vendors, and analysis has included scanning electron microscopy (SEM) [equipped with a field emission gun] on uncoated diamond substrates. X-ray topography [3], using near-parallel and monochromatic X-rays prepared from synchrotron radiation, has been used to evaluate the microstructure of selected type Ia, IIa, and Ib single crystal diamonds (not necessarily cut and polished to a specific orientation).

Two different chemical cleaning methods were utilized. Diamond substrates were cleaned with the RCA cleaning technique [4], which has found wide-spread use in silicon integrated circuit fabrication, or with sequential exposure to boiling $CrO_3/H_2SO_4$ solution (glass cleaning solution) for 15 minutes followed by boiling aqua regia for 15 minutes followed by a dip in 10:1 $H_2O$:HF solution and complete deionized water rinse. The efficacy of swabbing to remove particulates has also been evaluated. Cotton-tipped swabs were used in deionized water.

Homoepitaxial diamond growth was accomplished using a 13.56 MHz inductively-coupled plasma-enhanced chemical vapor deposition (PECVD) system as described in more detail elsewhere [5]. Briefly, the system is UHV-compatible and the nominal conditions used were: 1% $CH_4$ in $H_2$ or 1:2 mixture of 2% CO in $H_2$ and 1% $CH_4$ in $H_2$, total gas flow = 20-30 sccm (32.2-48.3 Pa-L-$s^{-1}$), pressure = 5.0 Torr (667 Pa), temperature = 500-800 °C, and rf power $\simeq$ 1.5kW. The homoepitaxial diamond films have been characterized with SEM and Raman spectroscopy.

**Results and Discussion**

Diamond Substrates

Features have been observed on the surfaces of commercially-supplied diamond substrates which might inhibit high quality epitaxial growth. Figure 1 shows a series of SEM micrographs from several as-received natural Type IIa diamond (100) substrates (size: 4 × 4 × 0.25 mm). It can be seen that the surface topographies do vary from substrate to substrate, and some are clearly "better" than others. However, the fine unidirectional scratches are observed on all substrates of this size. Commercially-produced synthetic, type Ib diamonds can also have surface topographies that may influence subsequent

epitaxy (Figure 2). However, it must be borne in mind that a less than perfectly smooth surface topography only indicates that the polishing process needs optimization and does not necessarily imply that the bulk of the substrate is microstructurally defective. This has been shown by electron-beam-induced current (EBIC) imaging of natural semiconducting type IIb diamonds in the SEM, where it has been seen that the surface scratches bear no relationship to subsurface microstructural defects that are nonradiative recombination sites [6].

The extent of microstructural defects in a diamond substrate is perhaps a more crucial issue pertaining to the attainment of low-defect-density homoepitaxial diamond films for electronic evaluation. To begin to examine this issue, X-ray topographs have been taken of natural and synthetic diamond single crystals. X-ray topography has revealed differences in the internal structure of type Ia [7] and type IIa diamonds (Figure 3). Although the type Ia diamond appears to show planar defects in projection, there appear to be fewer defects and defects with a lower degree of strain and/or crystallographic misorientation than the type IIa crystals. This is qualitatively consistent with the observations that type Ia diamond crystals tend to exhibit superior axial ion channeling characteristics than type IIa crystals [8]. While these results appear to indicate a trend, variations between different natural diamond crystals may not permit these results to be generally applicable to all diamond substrates of a given type. Also shown is an X-ray topograph of a synthetically produced type Ib diamond which has defects that appear to have propagated radially from the center of the crystal.

Substrate Cleaning

Both of the chemical cleaning procedures described above have been used, and both techniques have met with successful homoepitaxial growth. Unfortunately, the success has not been uniform and unequivocal. The reason for this has been that residual particulates remain on the surface of the diamond substrate. The effect of particulates on the surface is the nucleation of sporadic regions of polycrystalline diamond material interspersed throughout the homoepitaxial film. The particulates are believed to result from the commercial polishing processes, and apparently are not removed with wet chemical cleaning. Mechanically cleaning the substrates by swabbing with cotton-tipped swabs in deionized water will remove most of the particulates. This effect is shown dramatically in Figure 4 where a diamond substrate, which had been intentionally contaminated with particulates and then chemically cleaned (particulates still remain adherent), is shown to be free of these particulates after a short time ($\sim$ 1 min.) of swabbing.

Diamond Homoepitaxy

Figure 5 shows the change in surface morphology after 1 $\mu$m of diamond deposition on a diamond substrate. Before deposition the surface shows pits

and polishing scratches present. After deposition, the surface finish is greatly improved as little surface topography is visible. This planarization is an important feature for development of electronic devices in diamond.

The effect of surface planarization during homoepitaxial growth can also be illustrated using selective homoepitaxial deposition. Epitaxial lateral overgrowth (ELO) has been demonstrated using this low pressure rf-driven PECVD technique [9]. A lithographically patterned 200 nm thick Si mask, which substantially inhibits diamond nucleation, has been used to define the diamond "seeds" for homoepitaxial diamond growth. The overgrowth was best revealed by chemically etching the Si from the diamond. Figure 6 shows SEM of a cleaved cross-section showing diamond ELO. The sample has been sputter-coated with 10 nm of Pt to prevent charging during SEM examination. Growth of homoepitaxial diamond was observed to be approximately isotropic, extending over the Si mask by 0.45 $\mu$m and above the mask by 0.50 $\mu$m. There is evidence for smooth epitaxial growth above the diamond seed windows and faceting on the overgrowth. Comparing the surface of the epitaxial layer to the surface of the substrate, the initial substrate topography has been planarized by this diamond homoepitaxial deposition process.

Both macro- and micro-Raman spectroscopy have been routinely employed to assess the crystalline quality of the homoepitaxial diamond films. Spectra were excited using the 514.5 nm line of an $Ar^+$ ion laser with a micro-Raman spot size at the sample surface of $< 5$ $\mu$m. Shown in Figure 7 are micro-Raman spectra showing the 1332 $cm^{-1}$ diamond LO phonon line taken from the selective-area homoepitaxial film and taken off the film where scattered and isolated polycrystalline diamond crystals have grown on the Si mask. The full-width at half-maximum (FWHM) values from these spectra differ by 1.6 $cm^{-1}$ - with the homoepitaxial film having the narrower peak. This is consistent with the fact that the Raman signal from polycrystalline diamond films have greater FWHM than from single crystal diamonds. Another homoepitaxial diamond film with uniform coverage that was grown on a (100) type IIa substrate was examined with micro-Raman spectroscopy by focusing on the surface of the homoepitaxial film. The corresponding 1332 $cm^{-1}$ diamond LO phonon line was found to have a FWHM of 2.1 $cm^{-1}$. Because of the small depth of focus of the micro-Raman system, it was also possible to focus into the bulk of the type IIa substrate. In this case, the FWHM increased to 2.4 $cm^{-1}$. Although this technique cannot completely isolate the Raman signals from the epitaxial film and the substrate, it shows qualitatively that this homoepitaxial diamond film is of greater perfection than the substrate. This same trend has been seen for homoepitaxial diamond grown on (100) type Ia diamond substrates, but the differential between the FWHM of the epitaxial film and the type Ia substrate is less (on the order of 0.1 $cm^{-1}$).

**Summary**

From the point of view of commercial availability, type Ia diamond substrates currently appear to be microstructurally superior for homoepitaxial growth. Although there remains diamond substrate surface topography concerns, if the substrates are mechanically and chemically cleaned properly and an adequate diamond deposition technique is used, the surface can be planarized for device fabrication. The evidence accumulated thus far indicates that homoepitaxial diamond films grown with rf PECVD are superior to the starting substrates. The ability to grow homoepitaxial diamond selectively with ELO allows for the possibility of creating films that are less microstructurally defective than the starting substrate.

*Acknowledgements:* The authors gratefully acknowledge the support of this work by the SDIO/IST through ONR, Contract No. N00014-86-C-0460. TPH and RJN gratefully acknowledge the support of this work by SDIO/IST through ONR, Contract No. N00014-90-J-1707.

## REFERENCES

1. G.G. Fountain, R.A. Rudder, D.P. Malta, S.V. Hattangady, R.G. Alley, G.C. Hudson, J.B. Posthill, R.J. Markunas, T.P. Humphreys, R.J. Nemanich, V. Venkatesan, and K. Das, this proceedings.
2. Andrew R. Lang, 2nd Intl. Conf. on the New Diamond Science and Technology, Washington, DC, September 23-27, 1990, in press.
3. B.K. Tanner, *X-ray Diffraction Topography*, Pergamon Press, Oxford (1976).
4. W. Kern and D.A. Puotinen, RCA Rev., 31, 187 (1970).
5. R.A. Rudder, G.C. Hudson, Y.M. LeGrice, M.J. Mantini, J.B. Posthill, R.J. Nemanich, and R.J. Markunas, Mater. Res. Soc. Symp. Proc., EA-19, 89 (1989).
6. D.P. Malta, S.A. Willard, R.A. Rudder, G.C. Hudson, J.B. Posthill, R.E. Thomas, and R.J. Markunas, Proc. 49th Annual Meeting of the Electron Microscopy Society of America, (1991) in press.
7. The type Ia crystal examined in this study had a thin $\sim 0.5\mu$m epitaxial film grown selectively on it. The film was not visible, and its presence did not affect the X-ray topography images of the substrate microstructure.
8. G.S Sandu, N.R. Parikh, and M.L. Swanson, private communication of unpublished results, University of North Carolina, Chapel Hill, 1989.
9. R.A. Rudder, J.B. Posthill, G.C. Hudson, D.P. Malta, R.E. Thomas, R.J. Markunas, T.P. Humphreys, and R.J. Nemanich, 2nd Intl. Conf. on the New Diamond Science and Technology, Washington, DC, September 23-27, 1990, in press.



Figure 1. Surfaces of different as-received (100) type IIa diamond substrates.



Figure 2. Surface of representative as-received (100) type Ib diamond substrate.

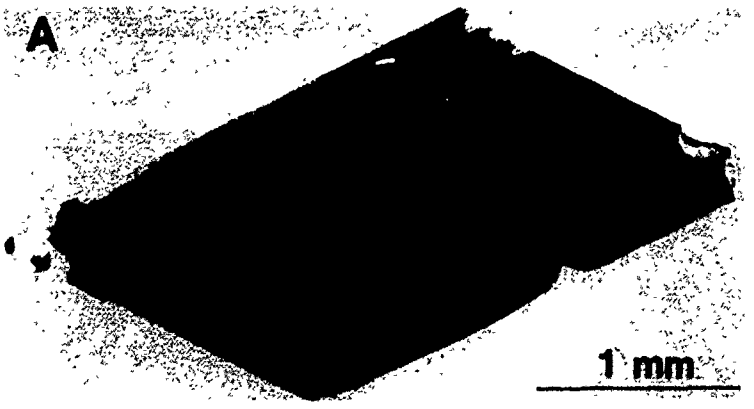



Figure 3. Representative X-ray topographs from: (A) type Ia diamond, $(0\bar{4}0)_{ST}$ [the radial defects are believed to have been created when the diamond was cleaved prior to analysis];

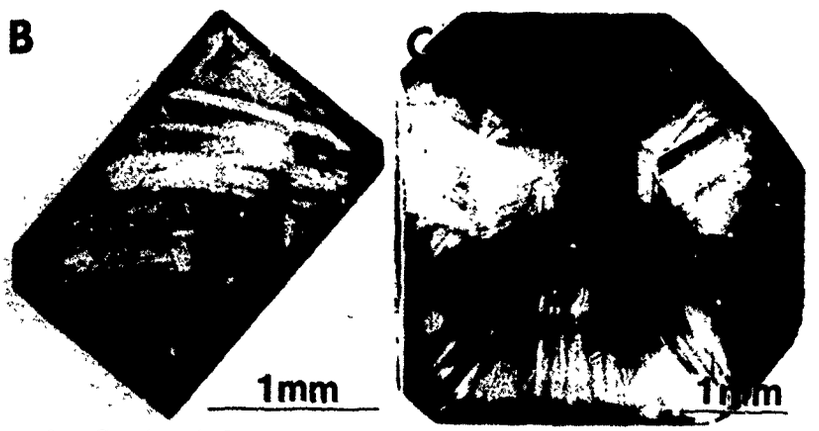



Figure 3. *Continued:* Representative X-ray topographs from: (B) type IIa diamond, $(\bar{1}\bar{1}1)_{AT}$; and (C) type Ib diamond, $(\bar{1}\bar{1}1)_{AT}$.

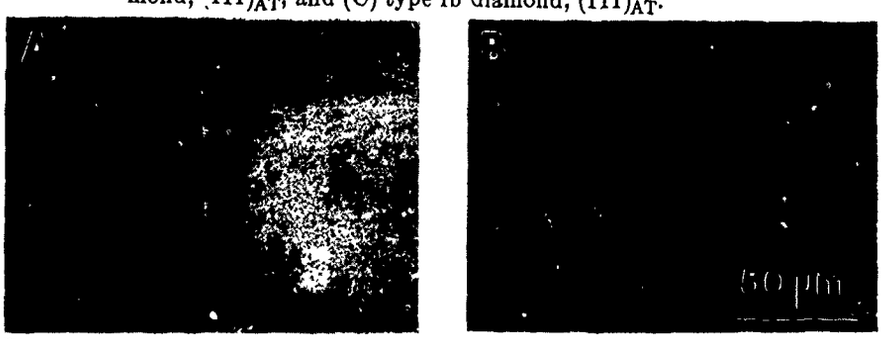



Figure 4. Surface of diamond: (A) after intentional particulate contamination and (B) after swabbing.




Figure 5. Surface of homoepitaxial diamond film grown on (100) type Ia diamond substrate. Compare with as-received diamond in Figure 1.



Figure 6. Cleaved cross-section showing ELO of diamond over a Si mask that has been chemically removed: (A) inclined view and (B) edge-on view.

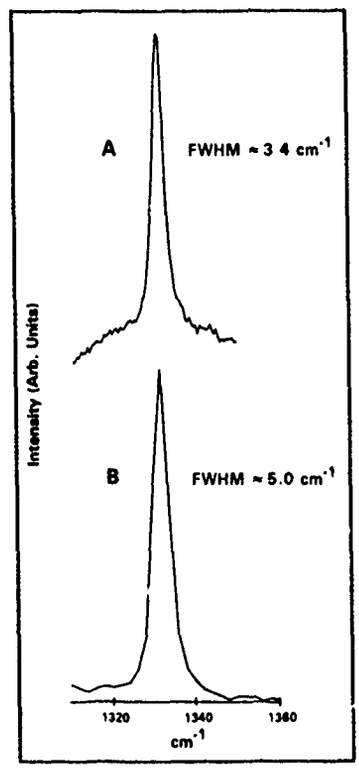



Figure 7. Micro-Raman spectra from: (A) selective-area homoepitaxial diamond (shown in Figure 6) and (B) polycrystalline diamond nucleated on mask (not shown in Figure 6 because it was etched off).

# INVESTIGATION OF LOW PRESSURE DIAMOND GROWTH BY ELASTIC SCATTERING OF LIGHT AND REFLECTANCE SPECTROSCOPY

A.M. BONNOT, T. LOPEZ-RIOS, B. MATHIS and J. LEROY
Laboratoire d'Etudes des Propriétés Electroniques des Solides, CNRS, BP 166X
38042 Grenoble Cedex, France

## ABSTRACT

The growth of diamond on silicon by the use of a hot filament and methane hydrogen was monitored by reflectivity and elastic scattering of 1.96 eV He-Ne laser radiation. It will be shown that the development of the elastic scattered light and reflectivity with diamond growth give insight into the diamond nucleation and growth rates. In particular, a start of diamond growth manifests itself by a strong increase of the scattered light followed by structures which can be correlated to the size of isolated diamond crystals.

## INTRODUCTION

The ability to synthesize diamond films by assisted chemical vapor deposition (CVD) at low pressure where diamond is in its metastable phase is now well stated. However, the film morphology on substrates other than diamond precludes, up to now, their uses in the fields of optic and electronic : the continuity of the films arises from the juxtaposition of micrometer-sized diamond crystals randomly oriented to the substrate and as a consequence, their roughness limits their transparency and the joints between crystals deteriorate the electrical properties. In order to progress, one has to succeed in synthesizing heteroepitaxial diamond films. The question raised is, whatever the technique used, the low pressure diamond growth which takes place tridimensionally with a slow nucleation rate. This type of growth seems to preclude epitaxial growth, for which an increase in the nucleation rate and bidimensional growth would be more favorable. From a fundamental point of view, one has to acquire a better understanding of the nucleation and growth mechanisms by employing characterization techniques sensitive to the first diamond growth.

In this spirit, in-situ optical measurements are very attractive because they can give insight into the diamond growth mechanisms without perturbing the experimental synthesis conditions. Considering that whatever the assisted CVD technique (plasma, hot filament...) and the carbon source (methane, acetylene... bourbon) are, the resulting diamond morphology is the same; the optical techniques becoming very interesting when probing the diamond surface growth. In that sense, in-situ variations of elastic scattering of light and reflectivity with deposition time of low pressure diamond on silicon substrates has been undertaken.

## EXPERIMENTAL DETAILS

- Synthesis technique

Diamond films have been synthesized by a hot filament CVD technique. Details of the experimental arrangement have been described elsewhere (1). Typical synthesis conditions were a 0.5-2 at.% methane proportion in hydrogen with a 3000 Pa total pressure and a 20 sccm total flowrate, a 2000 °C heated tungsten filament and a 800 °C substrate temperature. In order to increase the nucleation rate, the silicon substrates were scratched with 1 µm diamond paste. The deposition have been made either with a grounded substrate, or electron assisted with a 100-200 V positive substrate potential. This forward bias presents the advantage of increasing the nucleation rate.

- Optical technique

Elastic scattering of light and reflectivity measurements have been undertaken in-situ, in the CVD apparatus. The incident 1.96 eV He-Ne laser radiation was linearly polarized with the electric field parallel to the substrate with a 45° incidence angle. The elastic scattered light was detected in a direction normal to the substrate. In order to suppress the spurious signal due to the light emitted by the hot filament, the incident radiation was modulated by a chopper and scattered light and reflectivity were simultaneously measured with Lock-in amplifiers.

## EXPERIMENTAL RESULTS

Figure 1 shows the development of scattered light and reflectivity with diamond deposition time. The synthesis has been interrupted three times : at 30 mn, 120 mn and 450 mn, in order to allow the observation of the final morphology at the end of each stages of the diamond growth. Same experimental synthesis conditions were used at each stages : a 1 at% methane proportion in hydrogen, a 100 V forward dc bias and a 800 °C substrate temperature. The general trend with deposition time is an increase in the scattered light and a decrease in the reflectivity. However, part (a), (b) and (c) evidence three different variation domains of the scattered light :

- Part (a) in figure 1 corresponds to the first 30 mn deposition time. At these first steps of the diamond growth, there is a monotonic rise in the scattered light which takes place after about 15 mn experimental synthesis conditions are well established. At the end of this first stage, observation with an optical microscope with a 1000 magnifying power did not yet evidence any diamond crystals.

- Part (b) in figure 1 corresponds to the next 90 mn diamond growth. The development of the scattered light at this stage of the growth shows strong structures. At the end of this second stage, SEM micrographies presented in Figure 2 (a) and (b) showed isolated well faceted diamond crystals of about 800 nm in size.

- Finally, part (c) in figure 1 corresponds to the last 330 mn deposition period. During this last diamond deposition period, the scattered light first continues to increase but finally saturates at long deposition times with weak and more or less regular oscillations superimposed. These weak oscillations are also observed in the

reflectivity. At the end of this last deposition period, micrography in figure 2 (c) shows a fully covered film with micrometer sized diamond crystals

Figures 3 shows the development of relative scattered light intensity with deposition time for two methane proportion in hydrogen : (a),1 at. % and (b), 0.5 at. %, all other experimental conditions being the same : a 100 V forward dc bias and a 800 °C substrate temperature. It can be seen that for both conditions the general trend is the same but that the overall relative scattered light intensity is even more delayed from the beginning of the growth that the methane concentration is lower. From the very first steps of the growth, the scattered light first increases monotonically, then presents structures which, for a 0.5 at.% methane concentration, occur at about twice the deposition time than that for a 1 at.% one. It can be inferred that this time delays are related to the diamond growth rate which is even slower that the methane concentration is lower. The same argument is reflected by the dependence of the relative reflectivity with deposition time (figure 4) : the decrease of the reflectivity is even more pronounced than the methane concentration is high.

Although the behavior of the scattered light with deposition time is the same for the same methane concentration and the same substrate temperature, its overall relative intensity increase varies strongly from one sample to another. For example, the scattered light development with deposition time of two diamond deposits with same experimental synthesis conditions, are shown in figure 5 (a) and (b). The relative scattered light had increased by a factor of about 100 in case (a) while it is only about 5 in case (b). Micrographies of these two samples show isolated diamond crystals of a same size but with a very different nucleation density : $Na = 2\ 10^7\ cm^{-2}$, and $Nb = 1.710^6\ cm^{-2}$. This result indicates that the relative increase of the scattered light is proportional to the number of diamond crystals which are probed by the laser light. This is confirmed by curve (b') which corresponds to the scattered signal (b), but normalized to that of (a) by multiplying it by Na/Nb. This non-reproducibility from one sample to another could be attributed to different scratching of the silicon substrate before to the deposition.

## DISCUSSION

Roughly speaking we can describe the optical response of our samples during diamond deposition as follow :

At the earlier stage of the diamond formation, tiny crystals give rise to Rayleigh scattering of intensity proportional to the number of nucleation sites and to the square of the volume of the diamond crystals. The Rayleigh scattering by N isolated spheres of radius a is proportional to $N\ a^6/\lambda^4$, $\lambda$ being the wavelength of the light. This formula applies for values of $x < 1$, where $x = 2\pi a/\lambda$, that is to say for radius of the particles smaller than 60 nm (if $\lambda = 632.8$ nm (He-Ne radiation)). Afterwards, light scattering increases and Mie scattering takes place.

The intensity of scattering by a single sphere, for a 45° scattering angle and for the impinging and scattered light polarized with the electric vector on the sagital plane (as is the case in the experiments), has been computed with an exact formalism (2). Figure 6 shows the results obtained for two values of the index of refraction : $n = 2.4$

corresponding to bulk diamond and n = 2 corresponding to a more diamond-like film. For both cases, the extinction coefficient k has been set to 0.005 so as to take into account some absorption. It can be seen that the intensity of scattering first increases monotonically for small sphere radii (a < 60 nm ) and then presents Mie resonances for a = 100-300 nm. These Mie resonances are even more shifted to greater sphere radii than the index of refraction is lower.

From this model and considering figure 1, the extremely abrupt increase of the light scattering from the beginning of the diamond growth at t ~ 15 mn, up to t ~ 50 mn, can be inferred to Rayleigh scattering of diamond crystals whose size is inferior to 100 nm. Afterwards Mie resonances are observed (see part (b) in figure 1). By a simple inspection of the curve, Rayleigh scattering and Mie resonances draw a very easy and straight forward way of estimating the mean dimension of the diamond crystals at this stage of the growth . It is important to underline that the sharp increase of the scattering light at t = 15 mn is indicative of a narrow size distribution of our diamond crystals, otherwise the curves would be smoothed out.

It is clear that even for relatively thin deposits our samples cannot be described by a single particle model. At this end the sample must be considered as a rough thin film presenting, eventually, interference effects as are probably observed for t > 300 mn in figure 1 labeled (c). The general shape of the experimental curves and, in particular, the noticeable decrease of the reflectivity as a function of the deposition time can be understood in the frame of a scalar scattering approximation correct for roughness larger than the wavelength. Within this approximation the scattering of light does not depend on the correlation function and the change of reflectivity due to roughness is just given by $R=R_0 \exp-(4S/\lambda)^2$, $R_C$ being the reflectivity of the smooth surface and S the amplitude of the roughness (3).

A realistic description of our optical measurements must take into account the electromagnetic interaction of particles and the contribution of the substrate. These effects are at present under investigation.

## CONCLUSION

These preliminary results indicate that, in-situ measurements of the scattering of light is a well adapted technique to investigate the diamond nucleation and growth mechanisms. The start of diamond growth manifests itself by a steep increase in the scattering of light which is attributed to Rayleigh scattering by tiny particles (with radii inferior to 600 nm if $\lambda$ = 632.8 nm, but with even more smaller radii for the incident light in the UV range). From Rayleigh scattering, which is proportional to the number of tiny particles and to the square of the volume of a particle, the nucleation rate can be determined. For diamond particles with radii of the order of 100-400 nm, the Mie resonances, which occur for characteristic values of $x = 2\pi a/\lambda$, allow to evaluate the cristal size during the diamond growth. By correlation with the reflectivity measurements, the absorption can be estimatedand; and thus the diamond "quality". But, also, measurements of the scattering of light is a suitable method of substrate preparation, before diamond growth takes place, because it is very sensitive to roughness modifications of the substrate when establishing the experimental synthesis conditions (for example increase of the roughness due to $SiO_2$ desorption).

Currently, we are setting up a more elaborate analysis of the data, which would take into account the electromagnetic interaction between the diamond crystals and the influence of the substrate. We are also extending the measurements of light scattering and reflectivity as a function of the wavelength.

## ACKNOWLEDGEMENT

We are indebted to Dr. F. Cyrot-Lackmann for his enthousiastic support to this project and to Dr. J. Mercier for stimulating discussions. The support of this research by the Ministry of Research and Technology, KODAK and THOMSON is also gratefully acknowledged.

## REFERENCES

(1) A.M. Bonnot, Phys. Rev. B, 41, 6040, (1990)
(2) Light Scattering by particles : Computational methods, P.W. Barber and S.C. Hill, Advanced series in applied physics, World Scientific Publishing (1990)
(3) P. Bechman and A. Spizzichins, The Scattering of Electromagnetic Waves from Rough Surfaces, Pergamon, New York (1963)

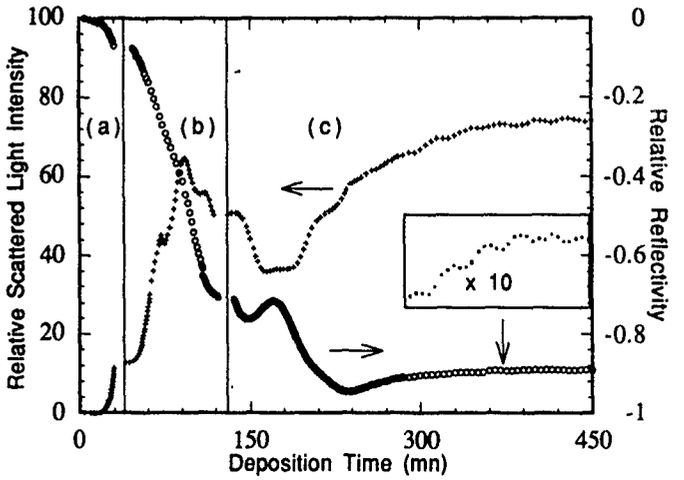



Figure 1 : Development of the elastic scattered light intensity and reflectivity with total deposition time t : (a), t = 30 mn; (b), t = 120 mn; (c), t = 450 mn.

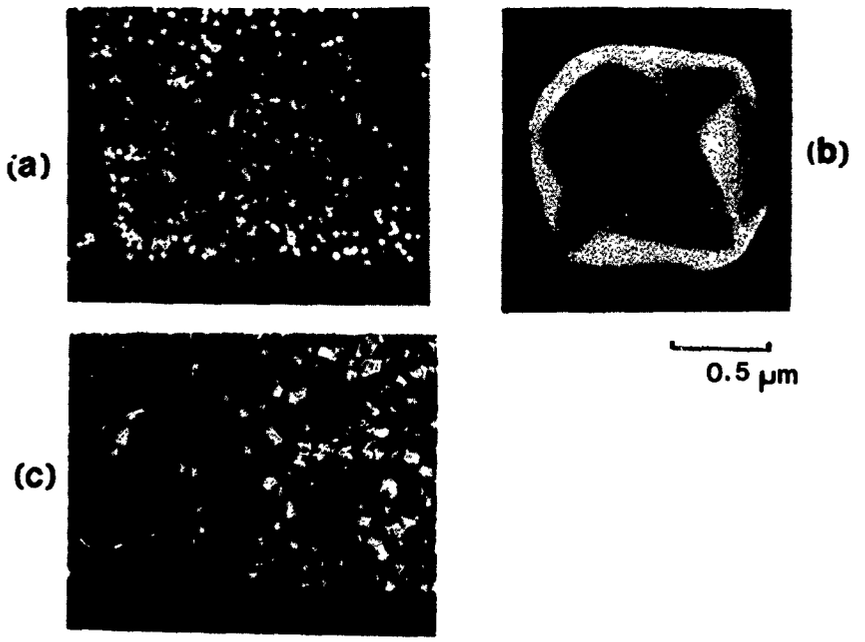



Figure 2 : SEM micrographs of a diamond film after : 120 mn : (a) and (b) ; 450 mn : (c) total deposition time (same film as in Figure 1)

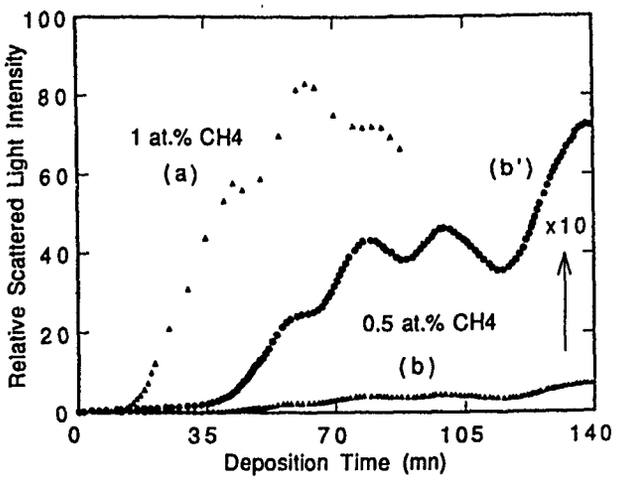



Figure 3 : Development of elastic scattered light intensity with deposition time for two diamond films prepared with same experimental conditions except the methane proportion in hydrogen : (a), 1 at.% and (b) and 0.5 at.% correspond to relative values; (b'), 0.5 at.% with a 10 times amplification of (b).

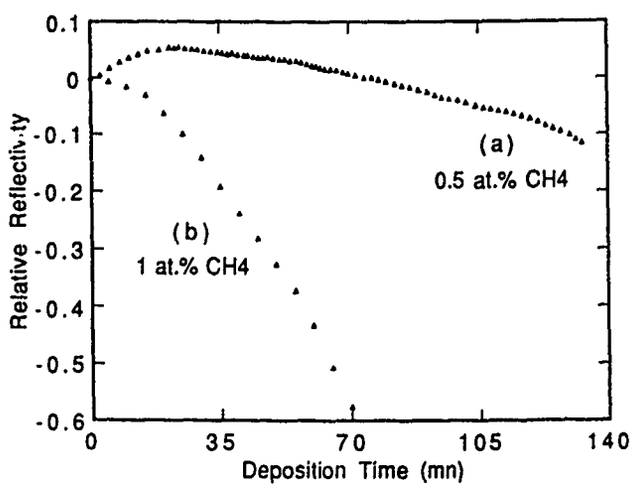



Figure 4 : Development of relative reflectivity with deposition time for two diamond films prepared with same experimental conditions except the methane proportion in hydrogen : (a), 1 at.%; (b), 0.5 at.% (same films as in Figure 3).

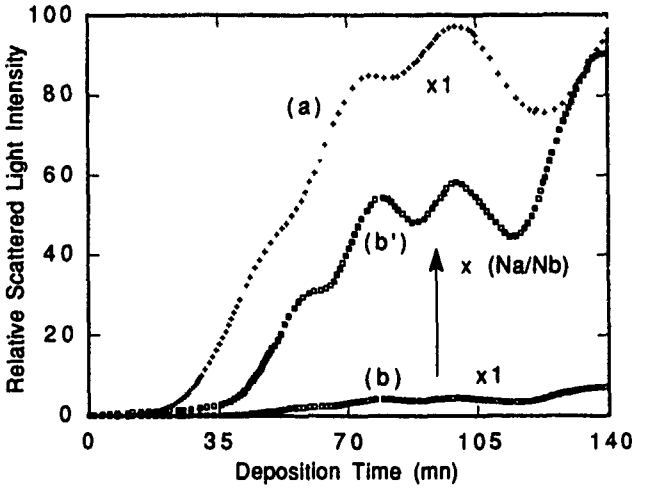



Figure 5 : Development of relative scattering of light for two diamond films prepared with same experimental conditions but the nucleation rate : (a), Na = 2 $10^7$ $cm^{-2}$ and (b), Nb = 1.7 $10^6$ $cm^{-2}$; (b') with a Na/Nb times amplification factor of (b).

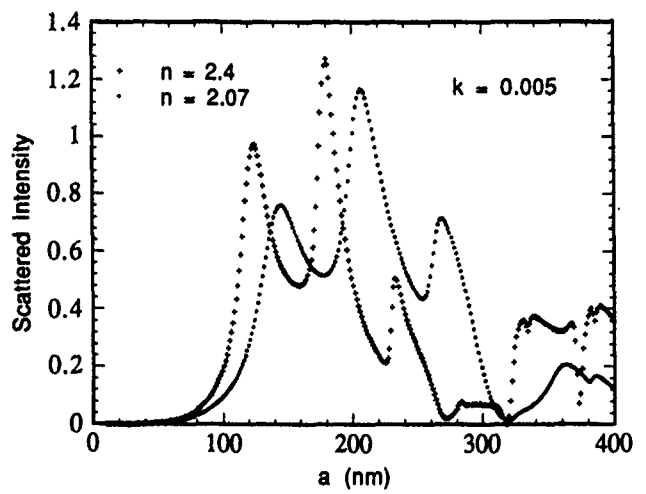



Figure 6 : Development of scattered light intensity with radius a of a sphere computed from (2). + : n = 2.4, k = 0.005, • : n = 2, k = 0.005.

# CHARACTERIZATION OF DC PLASMAS FOR THE CONTROL OF DIAMOND DEPOSITION

Linda S. Plano,* David A. Stevenson,** and John R. Carruthers†

*Crystallume, Menlo Park, CA
**Stanford University, Stanford, CA
†Intel Corp., Santa Clara, CA

## ABSTRACT

DC plasmas provide a unique opportunity to study the diamond deposition process. Since they are less complex than other plasma techniques such as microwave, they lend themselves well to a variety of diagnostic techniques, including optical emission spectroscopy, Langmuir probe, and mass spectrometry. These techniques have been applied to diamond producing DC plasmas to establish correlations between plasma processes and resulting film characteristics for process control purposes. Relationships between plasma electrical structure and film properties will be discussed.

## 1.0 INTRODUCTION

Since the discovery in 1976 of the importance of superequilibrium concentrations of atomic hydrogen in enhancing the chemical vapor deposition of diamond-bonded carbon [1], a wide array of potential applications of these films has been proposed. However, relatively few of these applications have been realized because good quality films can not be reliably produced. Although CVD growth of diamond is relatively straightforward in most deposition systems, it is difficult to grow coalesced films with the appropriate growth rate, uniformity, carbon bonding state, and other qualities required for diamond film applications. The empirical approach used in many studies of diamond CVD has led to an understanding of the main effects of many variables on resultant film properties. However, *in situ* studies have not yet been able to describe the deposition process to the point where control mechanisms can be established. A combined empirical and theoretical approach is needed to develop effective process control in diamond CVD systems.

The objective of the present study is to establish a correlation between the electrical and chemical aspects of the deposition environment and the film characteristics. To achieve this objective, both the deposition environment and the resulting films were analyzed. Statistical experiment design was used to establish the deposition parameters for thirty experiments in a low current (1 - 2 A) DC plasma diamond deposition environment. These plasmas were used for film growth and were analyzed with *in situ* diagnostic instruments.

In this paper, the relationship between the electrical characteristics of the plasma and film properties is discussed. (Correlations between the results of plasma chemical analysis and diamond film properties and the process used to empirically establish a process

window will be published elsewhere [2].) In particular, the spatial variation in potential (referred to hereafter as the potential profile or electrical structure) near the anode was found to be a critical parameter in determining bonding state in the growing film. This result indicates that the instrument used to measure potential, the Langmuir probe, can be of use as an *in situ* process control tool.

## 2.0 EXPERIMENTAL DETAILS

### 2.1 Overall Approach

To correlate the electrical characteristics of the deposition environment and properties of the resulting films, thirty carbon films were deposited using the same set of parameters used for *in situ* analysis. These experiments were developed using statistical experiment design, which allows a parameter space to be more quickly and thoroughly investigated than is possible with the more commonly employed approach in which one factor is varied at a time [3].

The experimental parameters selected for this study were the system pressure, the methane concentration, the DC current, and the electrode spacing. The ranges of these parameters were selected so that diamond, diamondlike carbon, and graphitic films were produced and were as follows:

| | |
|---|---|
| pressure | 18 - 38 torr |
| methane concentration | 0.2 - 0.6 % in hydrogen |
| DC current | 1 - 2 A |
| electrode spacing | 1 - 3 cm |

The flow rate and substrate temperature were held constant at 100 sccm and 725 °C, respectively. The films grown with these plasmas were characterized for bonding state by Raman spectroscopy while the growth rate was calculated from SEM cross section measurements.

Prior to implementing the statistically designed experiments, the *in situ* diagnostic instruments were used to analyze pure hydrogen plasmas as a function of each of the non-chemical deposition parameters, *i.e.*, current, pressure, and electrode spacing. From these data, it was possible to deconvolve the individual effects of these parameters on the plasma characteristics. When not being varied, each parameter was held at the midpoint of its above range.

### 2.2 Deposition and Analysis Reactors

Separate reactors were used for film growth and plasma analysis by *in situ* diagnostic instruments. Analysis was performed in a separate reactor to minimize contamination of the various probes from extended exposure to deposition conditions. The internal components of the two reactors were designed to be as nearly identical as possible. The major differences were the chamber wall materials- quartz for the deposition reactor and aluminum for the analysis reactor- and the anode material which was silicon for deposition and molybdenum for analysis. No detectable effects of these differences were observed.

## 2.3 *In Situ* Plasma Diagnostic Instrumentation

Three instruments were used to analyze the plasma: a Hiden mass spectrometer; an EG&G Princeton Applied Research optical emission spectrometer; and a Langmuir probe based on a design developed by M. Surendra [4]. Only the Langmuir probe and optical emission spectrometer were used for the work presented here. These instruments are shown schematically in Figure 1.

The optical emission spectrometer was employed primarily as a monitor of signal intensity for an emission peak corresponding to excited molecular hydrogen (603 nm) as a function of interelectrode spacing (an indication of the visible structure of the plasma). The Langmuir probe was used to acquire current-voltage characteristics (as shown schematically in Figure 1) as a function of interelectrode spacing. The characteristics were produced by inserting a platinum wire into the plasma, then biasing it with respect to the plasma such that currents were induced in the platinum wire. The zero current condition of the characteristics was used as an indication of plasma potential.

# 3.0 RESULTS AND DISCUSSION

## 3.1 Physical Processes in Diamond-Producing Plasmas

To ignite a DC piasma, one electrode (in this case the anode) is held at ground while the other is biased until partial ionization of the gas takes place. For the diamond-producing plasmas discussed here, the cathode is maintained at -300 to -400 V. The potential difference is distributed through the plasma as shown in Figure 2a: most of the potential change from the driven cathode to the grounded anode occurs over a fairly short distance near the cathode. Through most of the plasma, the potential is relatively constant and negative. Near the anode, the potential increases to ground, producing a significant electric field in this region.

The potential remains negative throughout the plasma because of the high neutral gas density in these plasmas. At 28 torr and 725 °C (typical for diamond deposition), the neutral gas density is ~ $10^{17}$ $cm^{-3}$, about an order of magnitude higher than that of classical glow discharges. The increased density results in increased frequency of electron-neutral collisions which in turn result in decreased electron mobility and diffusivity:

The equation governing total electron flux has two components, one for electrically driven drift and one for electron diffusion:

$$J_e = - \mu_e N_e E - D_e \frac{dN_e}{dx}$$

where $J_e$ is the total electron flux, $\mu_e$ is the electron mobility, $N_e$ is the electron density, E is the electric field, and $D_e$ is the electron diffusivity. Since the electron diffusivity is very low in these plasmas, an electric field must develop to supply the electron flux needed to maintain the plasma. It is the need for such a field that leads to the potential gradients present in the bulk of the plasma and at the anode shown in Figure 2a.

The potential gradients determine the visible structure of the plasma. As the electrons are accelerated by the strong fields near each electrode, they acquire sufficient energy to participate in inelastic electron-neutral reactions such as excitation, dissociation, and ionization. As the excited species relax, they may emit visible light as illustrated by Figure 2b, which can be detected by optical emission spectroscopy. Modelling [5] has shown that dissociation occurs in the same regions as excitation and that dissociation dominates near the anode and ionization near the cathode [2]. Dissociation leads to the production of atomic hydrogen and other radicals near the growth surface. Ionization, coupled with the large electric field near the cathode results in energetic ion bombardment of the cathode, inhibiting the growth of diamond. The presence of an anode glow and the electric field which causes it have been found to be a necessary but insufficient requirement for diamond growth, as discussed below.

### 3.2 Hydrogen Plasmas

The individual effects of current, pressure, and electrode spacing on the electrical and visible structure of pure hydrogen plasmas were studied. Current was found to have little effect on potential profile since current does not affect electron diffusivity. The visible structure was affected because increased current results in increased inelastic processes, including excitation.

Pressure was found to have a strong influence on electrical structure because electron diffusivity is affected through neutral gas density (see Figure 3). As the pressure was increased, the gradient in potential in the bulk of the plasma increased. This led to an increase in the magnitude of the potential change at the anode (dashed line in Figure 4 indicates extrapolated variation in potential). The magnitude of the potential change adjacent to the anode (hereafter referred to as the anode field) proved to be a good predictor of film bonding state as is discussed more fully in §3.4. Variations in visible structure were difficult to evaluate as a function of pressure because of effects such as self-absorption of emitted light which are also affected by pressure.

Electrode spacing does not affect electron diffusivity but it does affect the total number of collisions each electron encounters while moving from cathode to anode. As the spacing increases, the number of collisions also increase and the resistivity must also increase. For this reason, the potential gradient in the bulk of the plasma was strongly dependent on electrode spacing (Figure 4). Extrapolation of this gradient to the anode (dashed lines near anode in Figure 4), however, indicates that the magnitude of the anode field is not strongly affected by the spacing. This observation is supported by results published elsewhere [2], namely, that there is relatively little correlation between spacing and carbon bonding state. Because electrode spacing has no influence on electron diffusivity or density, it also had little effect on the visible structure of the plasma for a moderate to high pressure.

In summary, pressure, which directly affects electron diffusivity, had a strong effect on both the magnitude of the anode field and on the potential gradient in the bulk of the plasma. Electrode spacing, which affects plasma resistivity, had a large effect on the potential gradient in the bulk of the plasma but only a small one on the anode field. Current, which affects only electron density but not diffusivity or resistivity, had no detectable effect on anode field or potential gradient in the plasma.

### 3.3 Diamond-Producing *vs.* Graphite-Producing Plasmas

From the thirty films grown from the parameters established by experimental design, the plasmas which produced the most highly diamond bonded and least diamond bonded (*i.e.*, most highly $sp^2$ bonded) were analyzed in terms of their visible and electrical structures. The two plasmas had the same current (2 A) but different methane concentrations, pressures and electrode separations. The graphite-producing plasma had a low neutral gas density and resistivity (18 torr and 1 cm spacing) and high methane concentration (0.6%) while the diamond-producing plasma had a high neutral gas density and high resistivity (38 torr and 3 cm spacing) and low methane concentration (0.2%). Methane concentration, like current, has little effect on electrical structure and will be neglected in this discussion.

The optical emission profiles for the two plasmas are shown in Figure 5a. The cathode sheaths of the two plasmas are similar. The anode profiles are quite different in the two cases. The diamond-producing plasma exhibits an anode glow while the graphite-producing plasma has none; instead, the emitted light intensity in this region is due simply to the tail of the cathode sheath.

The observed lack of an anode glow in the graphite-producing case implies that electrons are not being accelerated to sufficient energies to participate in inelastic electron-neutral collisions which in turn suggests that there is no significant anode field to accelerate the electrons. This prediction is consistent with the potential profiles shown in Figure 5b. The graphite-producing plasma has a flat potential gradient through the bulk of the plasma and a magnitude of approximately 0 V, so there is no anode field. The diamond-producing plasma has a strong gradient through the plasma and a potential change of more than 30 V near the anode. These results suggest that the presence of an anode field and the resulting anode glow are necessary for the production of diamond films.

### 3.4 *In Situ* Control of Diamond Film Growth by DC Plasma Enhanced CVD

The floating potential results displayed in Figure 5b indicates that either the magnitude of the potential change near the anode or the gradient of the potential through the bulk of the plasma may correlate with carbon bonding state. To verify this trend, the potential profiles for all thirty of the plasmas were categorized by the type of film each plasma produced- diamond, diamondlike carbon, or graphite- so that variations in potential profile could be observed. General trends were apparent from this analysis, but electrode spacing had a strong effect on potential gradient in the bulk of the plasma which interfered with interpretation of the anode field, therefore the plasmas were subdivided again according to narrow (1 - 1.5 cm) and wide (2 - 3 cm) electrode spacings. These profiles are shown in Figures 6a and b for graphite- and diamond-producing plasmas.

The increase in magnitude of the anode field with increased diamond bonding is particularly apparent for the narrow spacing cases. The wider spacings show some departures from this trend, but these can be attributed to plasma instabilities. Such instabilities are more apparent at wide spacings because it is more difficult to accommodate the destabilizing effects of low currents and high pressures. Nonetheless, the general trend is apparent in both cases. These results indicate that a Langmuir probe located near the anode of a DC plasma could be used as an *in situ* indicator of film bonding state and

therefore provide a useful sensor to improve the reproducibility of DC diamond deposition processes.

## 4.0 SUMMARY AND CONCLUSIONS

Spatially resolved Langmuir probe and optical emission measurements of diamond- and graphite-producing plasmas combined with film characterization have yielded a correlation between plasma structure and film bonding state. This relationship arises from the high neutral gas density of the plasmas used to grow diamond. The high neutral gas density reduces the electron diffusivity so that electric fields must develop in the plasma to drive the electrons out of the plasma to maintain the plasma current. The electric field at the anode accelerates the electrons to sufficient energies to produce dissociation, excitation, and, to a lesser extent, ionization by inelastic electron-neutral collisions. Electron impact dissociation yields atomic hydrogen and methyl radicals, both of which are believed to be important species for diamond growth [2,6]. These observations could be exploited for a control system for DC plasma diamond deposition; the potential near the anode can be monitored with a Langmuir probe and optimized by controlling the deposition pressure.

## 5.0 ACKNOWLEDGEMENTS

The authors gratefully acknowledge support for this work through AFOSR Phase II SBIR Contract No. F49620-89-C-0009. We also thank I. Mikheyeva for the growth and Raman spectroscopy of the carbon films, C. Bailey for construction of the Langmuir probe, and M. Surendra and D.B. Graves for many useful discussions.

## 6.0 REFERENCES

1. B.V. Deryagin, D.V. Fedoseev, N.D. Polyanskaya, and E.V. Statenkova; Soviet Physics- Crystallography, **21** (2), p. 239 (April 1976).

2. L.S. Plano; "Structure and Chemistry in Diamond-Producing DC Plasmas;" Ph.D. Thesis, Dept. of Materials Science and Engineering, Stanford University; Stanford, CA (1991).

3. The Experiment Strategies Foundation, Box 27254 Seattle, WA 98125.

4. M. Surendra; "Langmuir Probe Theory and Its Application in Radio-Frequency Excited Plasmas;" S.B. Thesis, Dept. of Chemical Engineering; Massachusetts Institute of Technology, Cambridge, MA (1985).

5. M. Surendra, D.B. Graves, and L.S. Plano; to be submitted to Journal of Applied Physics.

6. S.J. Harris; Appl. Phys. Lett., **56** (23), p. 2298 (1990).

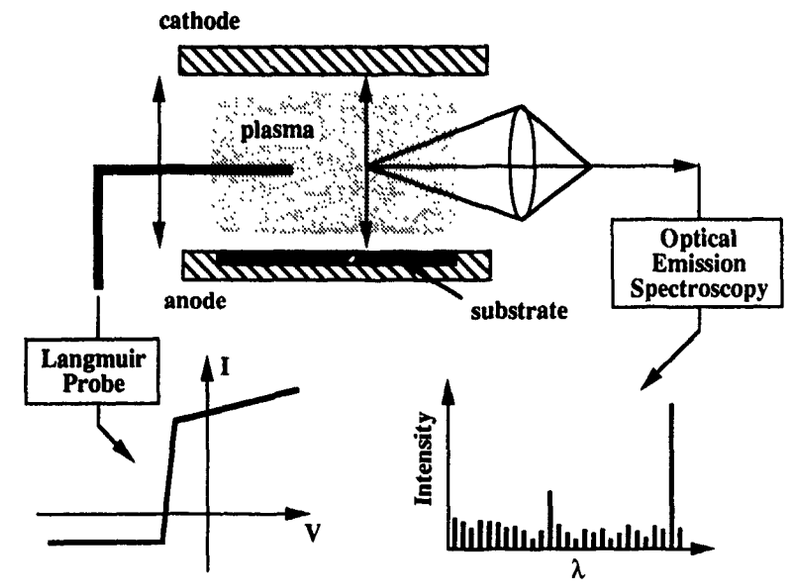



Figure 1: Schematic diagram of two plasma diagnostic instruments. Left: Langmuir probe with typical probe characteristic. Right: Optical emission spectrometer with typical wavelength spectrum.

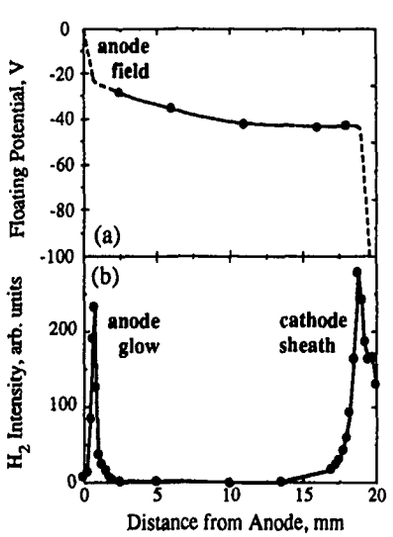



Figure 2:
(a) Electrical and (b) visible structrue of plasma. Note correlation between large potential gradients and emitted light intensity.

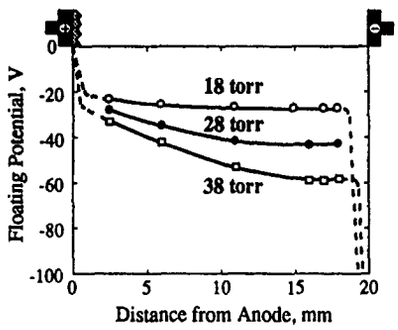



Figure 3: Dependence of floating potential profile on deposition pressure.

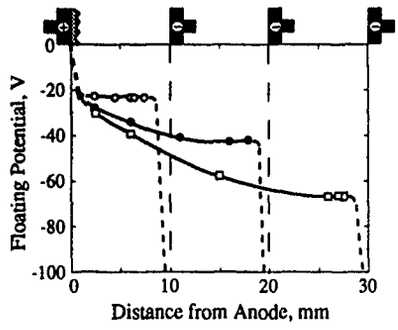



Figure 4: Dependence of floating potential profile on electrode spacing.

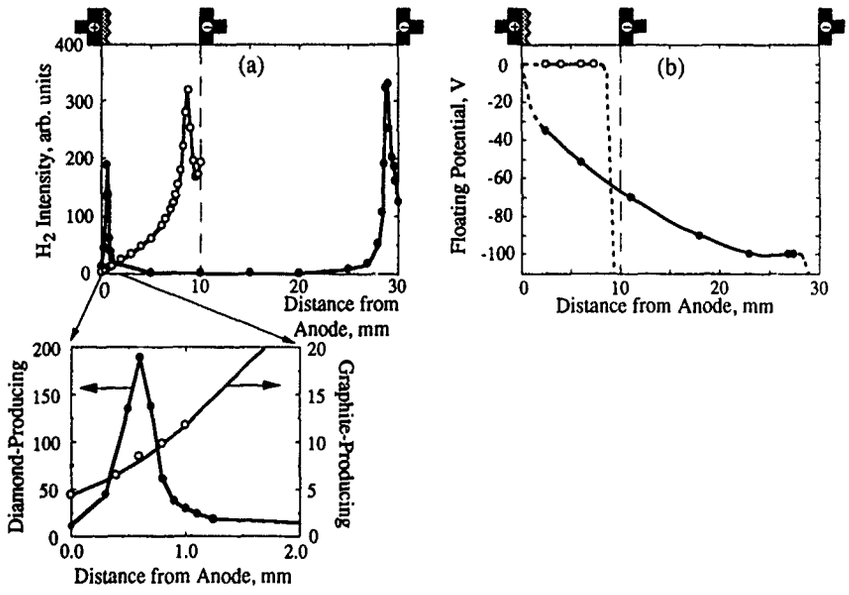



Figure 5: (a) Optical emission and (b) potential profiles for diamond- and graphite-producing plasmas. Closed circles: diamond; open circles: graphite.

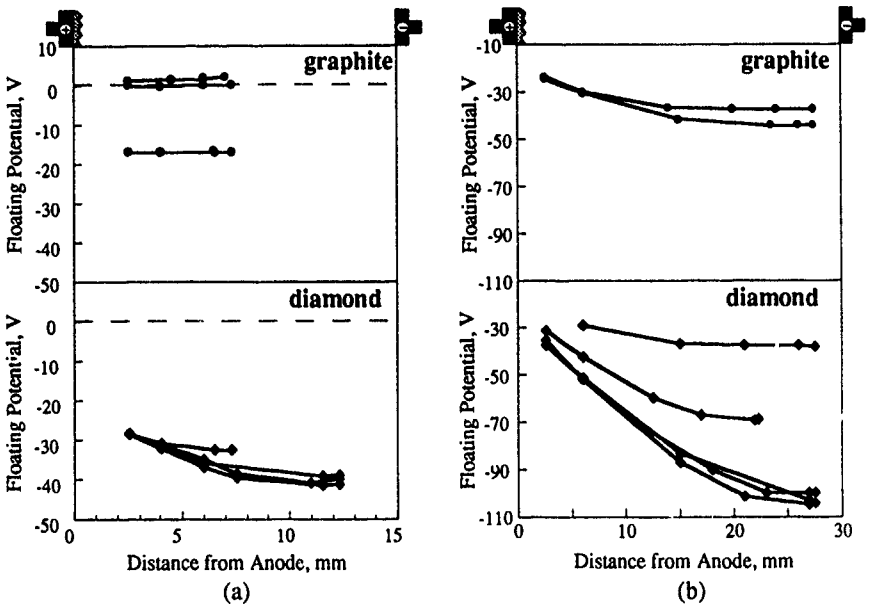



Figure 6: Potential profiles for (a) narrow and (b) wide electrode spacings. Top plots are from plasmas which produced graphite films while bottom plots are from plasmas which produced diamond films.

# PART III: DIAMOND FILM PROPERTIES

# STRUCTURE-PROPERTY RELATIONSHIPS AND APPLICATIONS OF DIAMOND FILMS

**K.V. Ravi**

**LOCKHEED MISSILES & SPACE COMPANY, INC.**
**RESEARCH & DEVELOPMENT DIVISION**
**3251 HANOVER STREET, PALO ALTO, CA 94304-1191**

## ABSTRACT

The interrelationships between synthesis, processs, the structure and selected applications of low pressure synthesized diamond are discussed. Optical and electronic applications are explored and the required structural characteristics and processes that determine these characteristics explored.

## Introduction

The potentially vast range of applications for diamond crystals, films and thick diamond structures, synthesized by low pressure activated techniques, derive from the unsurpassed physical properties of this material. These properties are by now very familiar to practitioners in the field and, briefly, include the exceptional thermal conductivity (20 w/cm-K for isotopically mixed diamond structures and a demonstrated 30 w/cm-K for isotopically enriched diamond), the low coefficient of friction and the high wear resistance, the superior transmission to radiation over a very broad spectrum of wavelengths, the high band gap attended by high resistivities and high breakdown electric field strengths, and a low work function.

The transition of a new technology from the research laboratory into manufactured products is a function of a number variables, not all of which are technology driven. Since the initial discovery of the low pressure diamond synthesis process significant progress has been made in developing an understanding of the process /property relationships. Applications of diamond films in various forms are beginning to emerge. The situation is such that sufficient knowledge has been developed regarding process flexibility, materials properties and fabrication approaches that preliminary product applications are becoming a reality. However for deriving the full benefit of diamond in the very large number of potential applications significant further work remains. The fundamental requirement is a knowledge of structure/property/process relationships for the various approaches utilized to synthesize diamond at low pressures. A significant body of information has been developed relating the process variables in diamond synthesis to the micro structure of the resulting material. The relation of these variables to physical properties of importance have, however, not yet received the attention they deserve. The relationships between structure/process/properties and the operational characteristics of diamond based products is at an even more primitive stage of understanding. Consequently a fundamental requirement is the coupling of the various stages of process knowledge with structure, properties and product performance.

In this paper the relationship of applications of low pressure synthesized diamond to structure/properties and the synthesis process is discussed. By defining the requirements of the applications the microstructural characteristics of the diamond can be defined which, in turn, will determine the process variables that have to be developed, understood and controlled. These interrelationships can be depicted as in figure 1. The current understanding of the key requirements of structural properties are related to selected applications of diamond in optics and electronics.

For the purposes of this discussion structure is defined broadly to include phase purity; microstructure involving grain size, morphology and orientation; geometrical factors including surface smoothness, thickness uniformity, selectivity of growth on substrates of interest; and defect structure and impurities. Clearly the relative importance of these various factors would be a function of the particular application. The process requirements/ capabilities depicted in Figure 1 are related closely to the structural requirements.

**Phase purity**

The most extensively investigated processes in low pressure diamond synthesis deals with phase purity. The ability to synthesize diamond at low pressures is based on the use of kinetically driven processes whereby a supersaturation of hydrogen is utilized to stabilize the diamond phase as well as to selectively remove any graphite formed. Among the process variables that have been shown to affect phase purity the most important is the ratio of hydrocarbons ( such as methane) to the hydrogen. It has been well established that increasing this ratio leads to increasing concentrations of non-diamond bonded phases in the films and the maintenance of high purity, in terms of minimisation of non-diamond contamination, requires a low methane to hydrogen concentration in the typical CVD of diamond. Figure 2 shows the relationship between the ratio of the diamond to non-diamond bonded phases as a function of methane concentration in hydrogen (1). This ratio drops rapidly as the methane concentration is increased. Although this behaviour is generally observed with all the low pressure synthesis techniques, the specific details of the concentrations of hydrocarbons at which unacceptable amounts of non-diamond phases get included in the growing material are technique and process specific.

As reported elsewhere in these proceedings (2) it is found that the relationship between the concentration of hydrocarbons in the process gas mix and the phase purity of the resulting diamond is also a strong function of the surface characteristics of the diamond during synthesis. Diamond films and crystals have been synthesized at methane concentrations as high as 15% by periodically activating the diamond surface by oxygen. The ability to alter the phase purity of the diamond during growth is a technique that is available to manipulate the microstructure of the diamond film. This is discussed further in a later section.

Phase purity effects are very important in determining the properties of diamond and the opportunities for incorporating non-diamond bonded phases in diamond films and thick diamond structures exist which do not only depend upon the mix of process gases in the reaction chambers or the diamond synthesis ambient. Local effects at the surface of the diamond play a strong role in local material incorporation phenomena and thus on the properties of the diamond. Although further research is required to better understand the relationships between process variables and the phase purity of diamond

films, for the purposes of this paper it will be assumed that diamond films of the required purity can be synthesized by the use of supersaturations of hydrogen in the process gas mix and that the concentrations of non-diamond phases can be maintained at a negligibly low level so as not to affect the physical properties of diamond. Selected applications of low pressure synthesized diamond will now be discussed and the interrelationships between the required properties, the structure and the process explored.

## Optical applications of diamond

Diamond is transparent over a very wide rang of the electromagnetic spectrum. This property leads to a large range of potential applications in the form of windows for radiation ranging from X-rays to the far infrared. Among the first commercial applications of low pressure synthesized diamond are X-ray windows for utility in analytical instrumentation. The combination of the low atomic number and the superior mechanical properties of diamond enables the fabrication of very thin diamond windows to replace beryllium windows in energy dispersive X-ray analysis instruments. The attractions of diamond windows lie in the superior transmission to X-rays that thin ( < 1 μm) diamond windows afford. In Figure 3 the X-ray transmission characteristics of conventional beryllium and thin diamond ( carbon ) windows are compared in a plot of the percent transmission of characteristic X-rays for various light elements (3). 0.5 and 1 μm thick diamond windows are more transmissive than the typical 8 and 12.5 μm beryllium windows. The detection of light elements with atomic numbers below that of sodium is not possible with the beryllium windows whereas diamond windows permit the detection of elements of atomic number down to boron. Beryllium windows below ~ 8 μm are not easy to fabricate without pinholes and other flaws. Since these windows have to withstand pressure differentials up to 2 atmospheres and have to be helium leak tight, thin beryllium windows are not practical for this application. Thin diamond windows, however can be fabricated without pinholes and other flaws and have the requisite mechanical properties to withstand pressure differentials encountered in the typical operation of X-ray analysis instruments.

The structural requirements for the fabrication of windows of this type as well as allied products such as X-ray lithography mask membranes can be ennumeratued as follows:

• Since windows and membranes for X-ray applications have to be very thin, ranging from < 0.5 μm to > 2 μm a primary requirement is that the grain size of the films be smaller than the thickness.

•Since such windows have to be mechanically robust, being able to withstand pressure differentials greater than one atmosphere as well as handling requirements associated with further processing such as absorber deposition and patterning in the case of X-ray lithography mask membranes, the windows have to be defect and flaw free. Defects such as pinholes, incompletely consolidated triple points between grains, etc. cannot be tolerated. This is particularly true for the case of X- ray windows for analytical instrumentation since such windows have to be vacuum leak tight.

• The stress state of diamond membranes is important for X-ray lithography applications. Utilizing microwave enhanced chemical vapour deposition techniques thin ( ~ 2 μm) diamond films have been fabricated which have been measured to display a

tensile stress of the order of 5 X $10^9$ dyn/$cm^2$ (4), a tensile stress value that is entirely acceptable for the intended application. The finding that diamond films with a built in tensile stress component that more than compensates for the differences in the coefficient of thermal expansion between diamond and silicon substrates on which the diamond films are deposited is an important finding that enables the development of taught membranes, in a state of tension for lithography mask fabrication. Although the specific reasons of this behaviour of diamond membranes have not been discussed in the open literature it is clear that the stress state of polycrystalline diamond films is a function of a number of deposition variables including the synthesis temperature, the deposition rate and the resulting microstructure of the films.

The fundamental process requirement for the fabrication of diamond windows for X-ray applications is the need to synthesize films with a small grain size and uniform distribution of grain size over the area of the window. To achieve a small grain size the nucleation density has to be enhanced such that a high density of crystallites are nucleated and these crystallites aggregate to form a film of the desired thickness, without any pin holes or other discontinuities. For thin windows this requires considerable enhancement of nucleation density. The most commonly used approach to promote nucleation of diamond on foreign substrates is to abrade the surface with a suitable abrasive to generate surface mechanical damage which promotes diamond nucleation. An alternative approach involves the deposition of thin diamond like carbon films by the use of a higher concentration of hydrocarbons in the process gas mix than that required to synthesized diamond. This technique has been reported for the case of nucleation enhancement of diamond utilizing DC glow discharge CVD, RF excited CVD and combustion flame synthesis (5-7).

## Passive electronic applications of diamond

Passive electronic applications entail the use of diamond in conjunction with active electronic materials such as silicon and gallium arsenide. The properties of diamond that make it particularly attractive in passive electronics include its exceptional thermal conductivity, the very high electrical resistivity, the low dielectric constant and chemical non-reactivity. These characteristics find use in electronic packaging, as dielectrics in conjunction with other semiconductors such as silicon and for protecting electronic circuits from environmental effects. The near term application of low pressure synthesized diamond in passive electronics is likely to occur in electronic packaging and, specifically, in its use as a heat sink for thermal management in electronics.The attraction of diamond as a substrate for electronic devices and circuits can be demonstrated by comparing the thermal conductivity and the dielectric constant of a number of candidate packaging materials with those of diamond. This is shown in Figure 4.

Diamond exhibits the highest thermal conductivity and the lowest dielectric constant of all electronic ceramics with only $SiO_2$ and the polymeric materials exhibiting lower dielectric constants. This combination of properties has important implications in the use of diamond as a substrate for high speed and microwave devices.

For the development of diamond substrates that effectively utilize all the desirable attributes of this material thick diamond structures are required. Thin films of diamond deposited on other substrates such as silicon or metals may serve the purpose of spreading locally generated heat but lack of sufficient material in the thickness direction

effectively limits the use of thin films. For applications such as the development of diamond based multi-chip modules it is necessary that free standing diamond substrates of thicknesses of 0.5 to 2 mm be synthesized. In order to achieve this, high growth rate techniques have to be developed and scaled. The economics of manufacturing thick diamond structures are very closely related to the growth rate. In figure 5 the time required to produce diamond structures 1 mm and 2 mm thicknesses, respectively, is plotted as a function of growth rate. The demarcation in the growth rate between the low growth rate CVD techniques and the high growth rate thermal techniques is indicated at ~ 10 μm/hour. For achieving practical production times, and hence economics of manufacture, growth rates in excess of 30 μm/hour and, preferable, in excess of 50 μm/hour have to be achieved over large areas. For addressing this application the high rate thermal techniques have to be used.

In the growth of thick diamond structures a particularly important issue is that of morphological instabilities attending the high rate synthesis of diamond. In the growth of diamond one of the sought after objectives is that the interface between the gas phase and the solid be planar and advance smoothly in a direction normal to itself as growth proceeds. However, in real crystal growth processes, and particularly at high growth rates, such quiescent interfaces are the exception rather than the rule. Typically, small, random fluctuations at the interface can grow with time leading to morphological instabilities (8,9). This can lead to extremely rough surfaces, the trapping of voids and discontinuities and the incorporation of impurities and second phases in the growing material.

The modeling of interface instabilities has been treated in the literature. For CVD processes the early work of van den Brekel and Jansen (10) examined the stability of planar gas-solid interfaces utilizing first order perturbation calculus. They showed that vapour growth is essentially an unstable process whereas vapour etching in an essentially stable process.

Recently Palmer and Gordon (11) have combined the ideas of van den Berkel and Jansen (10) and Mullins (12) to develop a continum description of the CVD process. In essence this model invokes three processes at work in the growth of films. The appropriate chemical specie for the synthesis of the solid is created in the gas phase and diffuses to the interface by gas phase diffusion. Once the specie arrives at the interface it is either, (a) incorporated into the surface, (b) it can move over the surface by surface diffusion or, (c) it can be re-evaporated into the gas phase.These processes are described by a system of partial differential equations with the final result that Palmer and Gordon arrive at being the following:

$$\omega = -\frac{\Omega^2 \nu D_s \gamma}{k_B T} k^4 - \frac{\gamma c^o_{eq} \Omega^2 D_O}{(1+sk) k_B T} k^3 + \frac{\Omega D_O (n_O - c^o_{eq})}{(1+sk)(L+s)} k$$

where $\omega$ is the stability parameter, $\Omega$ is the atomic volume in the bulk, $\nu$ is the concentration of surface particles, $\gamma$ is the surface tension, Ds is the surface diffusion coefficient, $D_O$ is the gas phase diffusion coefficient, $c^o_{eq}$ is the equilibrium concentration of the active specie in contact with a flat interface, s is the sticking parameter, L is the

thickness of the boundary layer above the surface, k is the mean curvature of the interface, $n_o$ is a constant and T and $k_b$ are the absolute temperature and the Boltzmann's constant.

The first term in the equation is related to surface diffusion which is a result of chemical potential gradients, the second term is due to desorption or re-evaporation of surface particles and the third term represents the net flux of particles to the surface and is governed by the gas phase diffusion coefficient. The first two terms in the equation work in such a manner as to stabilize and smooth out the interface, whereas the third term is destabilizing and causes morphological instabilities.

For the case of diamond synthesis one can show that the first two terms in the stability equation are reduced to zero (13). The first term, the surface diffusion term, is largely a function of $D_s$, the surface diffusion coefficient. $D_s$ is expected to be negligible for diamond. The second term in the stability equation is the re-evaporation or desorption term and this is also expected to be negligible since in the diamond synthesis ambients the diamond phase of carbon is very stable and gassification of the diamond, once it has been formed, will occur very slowly, if at all.

From the above it is clear that high rate deposition of diamond is accompanied by surface instabilities and these instabilities are magnified with time of growth. With sustained growth certain regions of the film grow at a higher rate than neighbouring regions. A finger like morphology develops with the taller regions shadowing the shorter regions as well as getting closer to the source of nutrients. Such instability effects have been termed competitive shadowing and nutrient starvation processes. These mechanisms are a dramatic feature of high rate diamond synthesis as demonstrated below.

Figure 6 is an example of this effect in thick diamond structures grown at high growth rates. Morphological instabilities manifest themselves in the form of columnar growth of indvidual crystals, the development of voids and very rough surfaces. The larger crystallites screen the smaller crystallites from the source of nutrients, further accelerating the instabilities. It has also been shown that non-diamond phases, such as DLC, can be trapped in an uncontrolled manner in the material as a result of the instability phenomena (13).

To avoid such instabilities processes that permit periodic interruption and renucleation of the diamond have to be developed. One such technique is to periodic deposit very thin layers of diamond like carbon on the growing diamond surface followed by recommencing diamond growth. Such an approach has been reported and figure 7 is an example of the cross sectional structure of a composite structure achieved by the alternate deposition of diamond and DLC (14). This is achieved by cycling the process gases between diamond synthesis conditions ( a high ratio of oxygen to acetylene in the combustion flame synthesis process ) and DCL synthesis conditions ( a reduced ratio of oxygen to acetylene). By appropriately controlling the relative deposition time of diamond and DLC it is feasible to achieve dense structures without morphological instabilities while minimizing the DLC content of the completed structure.

## Active electronic applications of diamond

Active electronic applications of diamond include the fabrication of devices whereby carrier transport occurs in the diamond and mechanisms of rectification,

switching, transistor action and current gain are promoted. The wide band gap, high thermal conductivity and the high carrier mobilities are the driving force for the exploitation of diamond in active electronic applications. A fundamental technology that has to be developed is the growth of diamond single crystals on non- diamond, larger area, low cost substrates. Although homoepitaxy of diamond is feasible this process does not meet the requirements enumerated above and as such is not economically viable. Heteroepitaxy continues to be an elusive goal. Consequently, techniques such as grapho-epitaxy and syntaxy have to be developed to achieve single crystal growth.

It has been demonstrated that diamond single crystals can be grown on non-diamond surfaces by promoting lateral growth of {100} oriented faces of diamond (15). It has been proposed that lateral growth occurs as a result of the creation of atomic sized ledges on the diamond surface by active specie such as oxygen or OH radicals, which are ingredients of combustion flames that can be utilized to synthesize diamond, followed by the sideways propagation of the ledges. This approach dispenses with the need to have lattice matched substrates and diamond growth is promoted on diamond nucleated on a foreign, non-lattice matched substrate. Figure 8 is an example of a diamond single crystal ~ 50 μm X 50 μm in dimension synthesized by the combustion flame synthesis technique. Growth ledges are observed on the surface of the crystal. The electron channeling pattern shows that the crystal exhibits a {100} orientation and the Auger spectra shows that the crystal is of high quality as compared with a natural diamond single crystal.

For the practical utilization of such single crystals it is necessary that the spatial location of such crystals be controlled on a convenient, low cost substrate such as silicon. For this purpose selective nucleation techniques can be applied. Selective nucleation of diamond has been demonstrated and it should be feasible to combine selective nucleation with lateral epitaxial growth techniques to achieve arrays of diamond single crystals on non -diamond substrates for further processing, in wafer form, into devices. These technologies require further development of selective nucleation processes and approaches to control the orientation and structure of diamond single crystals.

Selective nucleation processes can also be utilized to synthesize micron sized diamond crystals to function as local field emission sources in the fabrication of vacuum microelectronic devices. Elsewhere in these proceedings the attractions of diamond as a field emitter have been discussed (16). The combination of negative electron affinity, near zero work function and the high thermal conductivity makes diamond a very attractive candidate for the fabrication of field emitter structures. Figure 9 is an example of arrays of diamond crystals, selectively nucleated on a silicon wafer showing the potential of such processes for the fabrication of vacuum miocroelectronic devices.

## Conclusions

The interrelationships between structure, process and selected applications of low pressure synthesized diamond have been discussed. It is clear that further knowledge of processes and their relationships to physical properties is required to successfully utilize diamond in the large range of potential applications of this material. This paper has attempted to discuss some of the pertinent, current issues in structure -property relationships and applications of diamond films.

## REFERENCES


1. L.S.Plano and K.V.Ravi, SPIE Proceedings on Raman Scattering, Luminescence, and Spectroscopic Instrumentation in Technology, Vol 1055 (1989)
2. K.V. Ravi, "Alternating Chemistry Synthesis of Diamond", These Proceedings.
3. M.Peters, J.M. Pinneo, L.S. Plano, K.V. Ravi, V. Versteeg, and S. Yokota, SPIE Proceedings, 877, 79 (1988)
4. B.S. Berry, W.C. Pritchet, J.J. Cuomo, C.R. Guarnieri and S. J. Whitehair, Appl. Phys. Lett., 57, 302 (1990)
5. K.V.Ravi, L.S.Plano, M.Pinneo, M.Peters, and S.Yokota, First International Conference on the New Diamond Science and Technology - Tokyo, Program and Book of Abstracts, Paper 1.06 (1988)
6. D.E.Meyer, R.O.Dillon and J.A.Wollman, J.Vac. Sci. Tech. A (7), 2325 (1989)
7. K.V. Ravi, C.A. Koch, H.S. Hu and A. Joshi, Journal of Materials Research, 5, 2356 (1990)
8. G.S. Bales, R. Bruinsma, E.A. Eklund, R.P.U. Karunasari, J. Rudnick and A. Zangwill, Science, 249, 264 (1990)
9. A. Mazor, D.J. Srolovitz, P.S. Hagan and B.G. Bukiet, Phys. Rev. Lett., 60, 424 (1988)
10. C.H.J. van den Brekel and A.K. Jansen, J. Crystal Growth, 43, 364 (1978)
11. B.J. Palmer and R.G. Gordon, Thin Solid Films, 158, 313 (1988)
12. J.W. Mullins, J. Appl. Phys., 28, 333 (1957)
13. K.V. Ravi, J. Materials Research, In Press
14. K.V. Ravi, A. Joshi and H.S. Hu, Proceedings of the 2nd. International Conference on the New Diamond Technology, Washington, D.C. Sept. 1990 ( Proceedings in press)
15. K.V. Ravi and A. Joshi, Appl. Phys. Lett, 58, 246 (1991)
16. M.W. Geis, N.N. Efremow, J.D. Woodehouse and N.D. McAleese, "Diamond Cold Cathodes", These Proceedings.

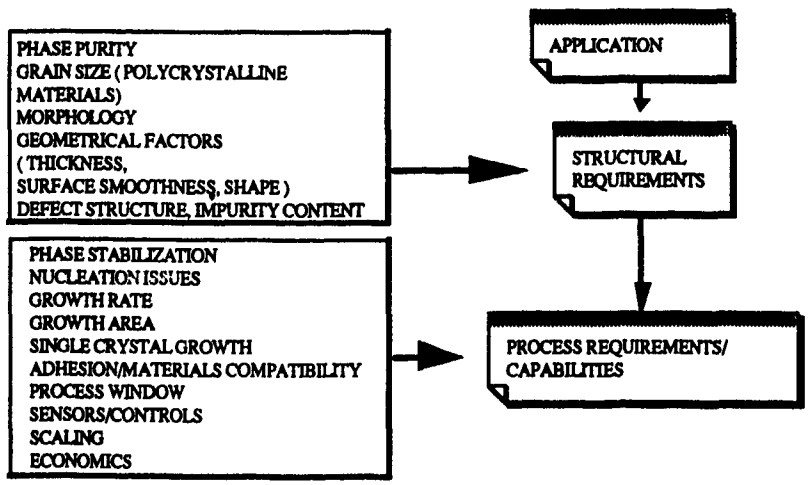




Figure 1. Interrelationships between applications, structural requirements and process requirements in the low pressure synthesis of diamond

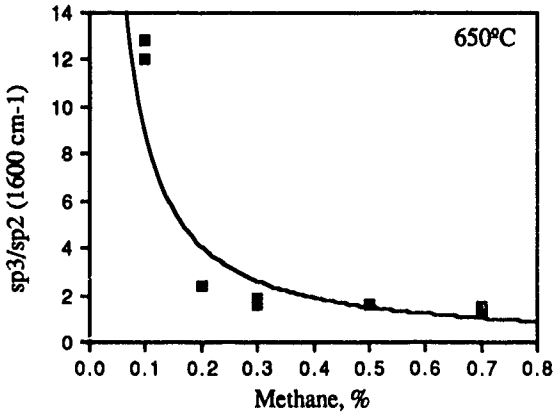



Figure 2. Relationship between the ratios of diamond to non-diamond bonded phases as a function of methane concentration in hydrogen (1).

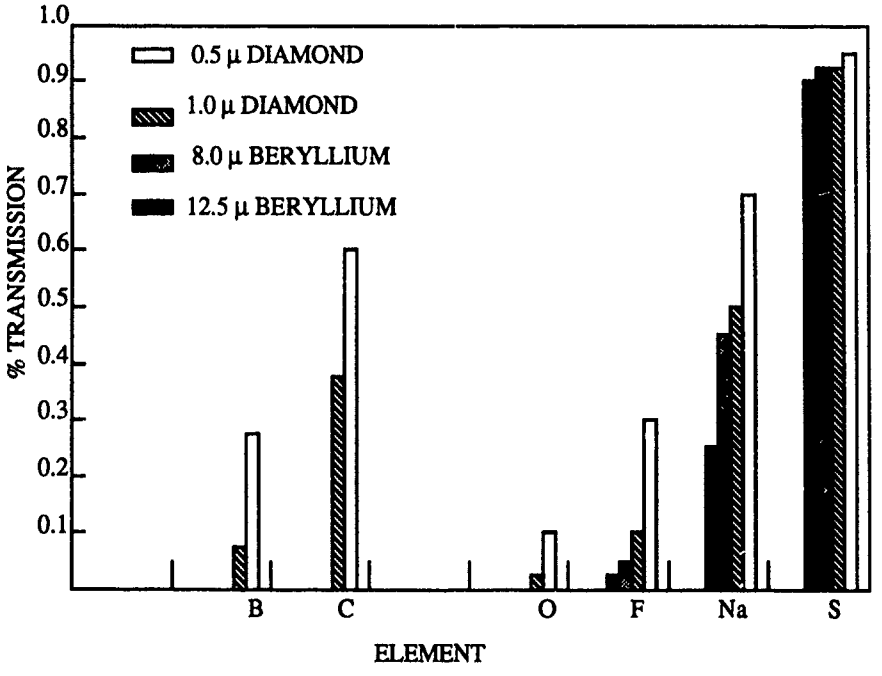



Figure. 3. Transmission of characteristic X-rays through Beryllium and Diamond windows (3).

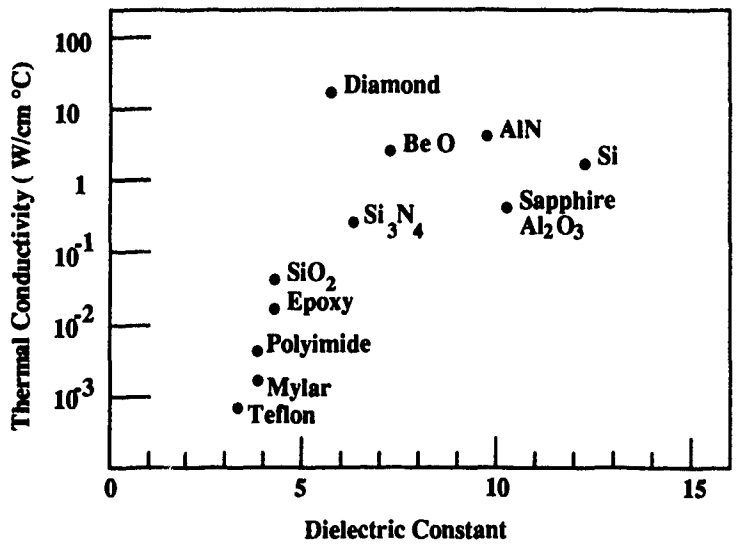



Figure 4. Thermal conductivity/ Dielectric constant of selected packaging materials

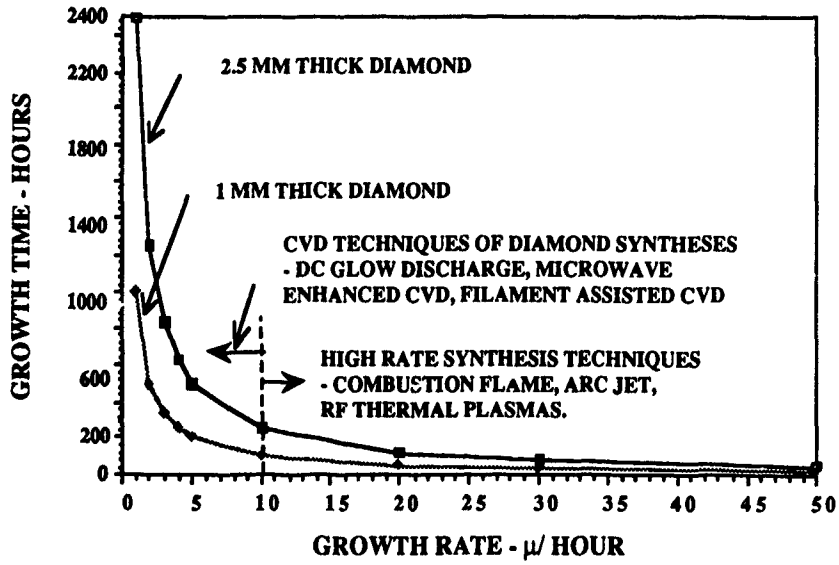



Figure 5. Effect of growth rate on time required to fabricate 1 and 2 mm thick diamond structures.



Figure 6. SEM micrograph of a cross section of a thick diamond structure demonstrating morphological instabilities attending the steady state, high rate growth of diamond (13).




Figure 7. Cross sectional structure resulting from the alternate deposition of diamond and thin DLC layers. Morphological instabilities are eliminated (14).

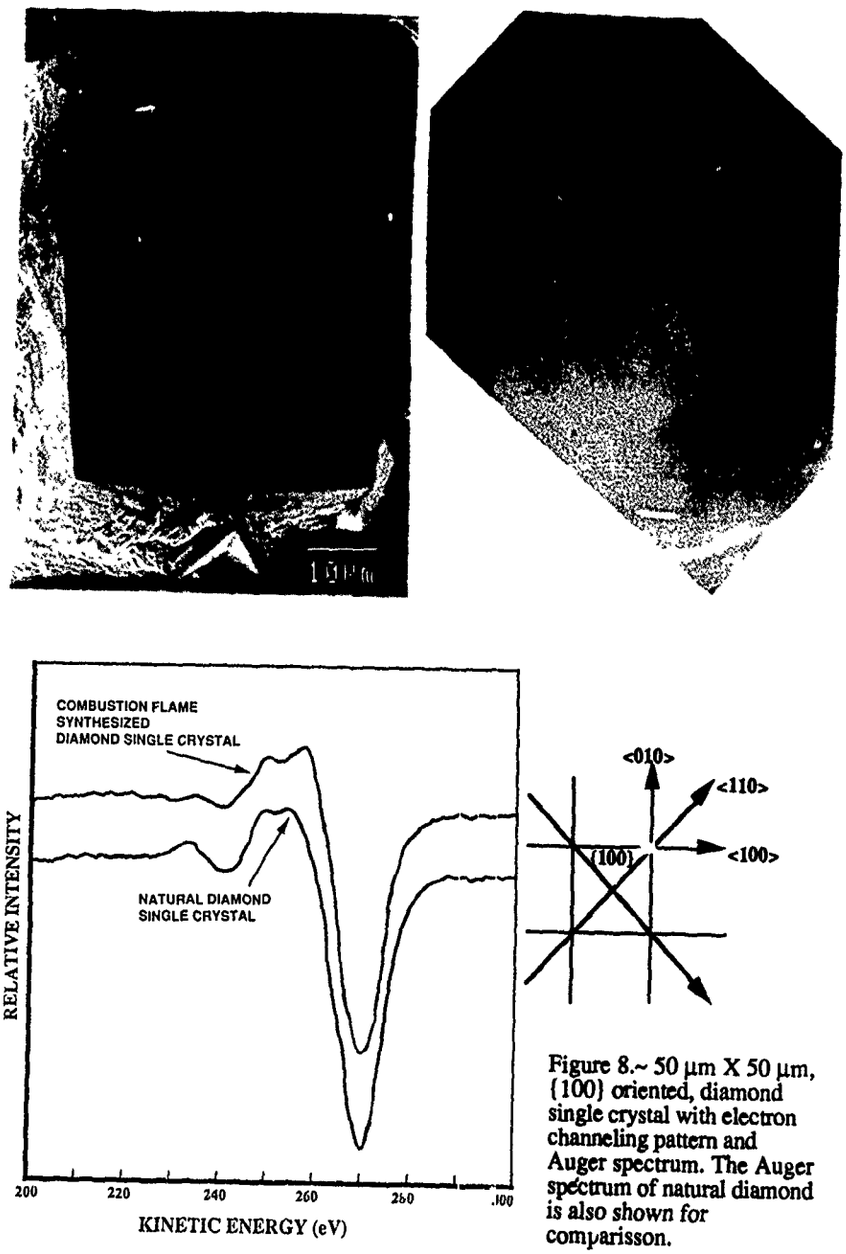



Figure 8.~ 50 μm X 50 μm, {100} oriented, diamond single crystal with electron channeling pattern and Auger spectrum. The Auger spectrum of natural diamond is also shown for comparisson.

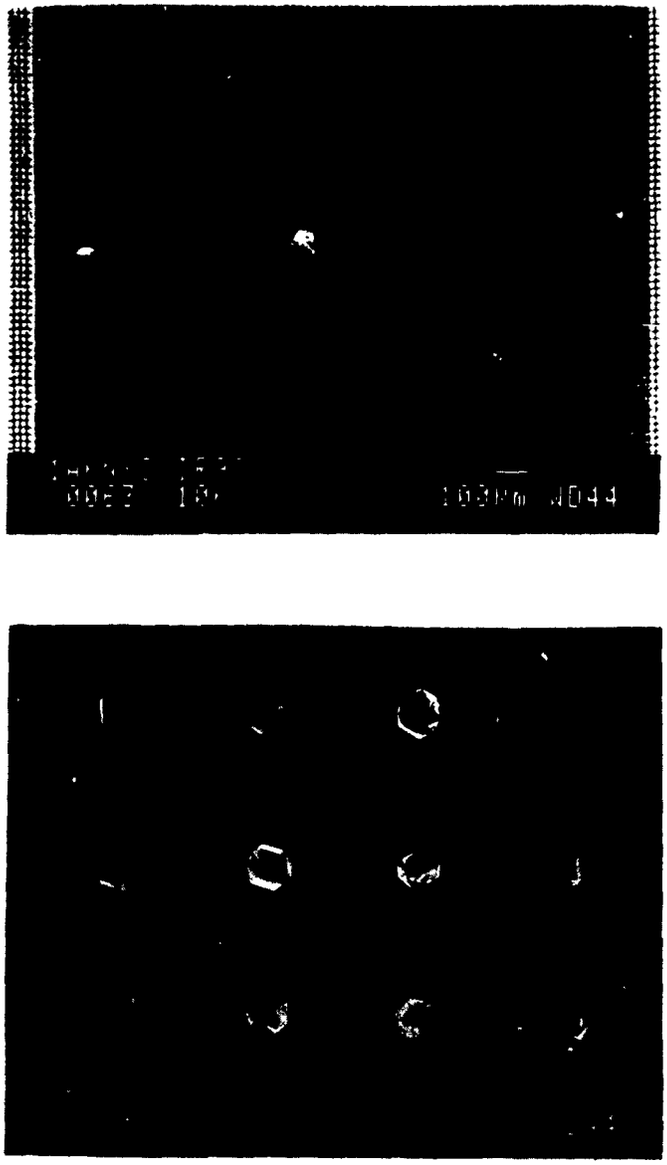


Figure 9. Examples of arrays of diamond crystals nucleated on a silicon wafer for application as field emitter arrays in vacuum microelectronics.

# NUCLEATION AND GROWTH OF WEAR-RESISTANT DIAMOND COATINGS

Benno Lux and Roland Haubner, Institute for Chemical Technology of Inorganic Materials, Technical University Vienna, Getreidemarkt 9/161, A-1060 Vienna, Austria

**ABSTRACT**

Freestanding low-pressure diamond sheets bonded to tools or wear parts and CVD diamond-coated products are now on the market for testing. Their cutting performances approach those of commercial wear-resistant products.
Low-pressure diamond grits and new composite powders (e.g. diamond-coated superhard c-BN powders) could provide new and extraordinary grinding properties.
These "simple" applications will soon lead to competitive commercial products, if the process upscaling - now under development - can make low-cost and reliable fabrication possible.

## 1. INTRODUCTION

Protective hard coatings are used industrially for purposes ranging from maintaining the aesthetical appearance of scratch-resistant watches or jewelry to improving the performance of wear-resistant tools. Typical examples for tool applications are dies for wire and tube drawing, punching edges, sliding friction parts, cutting tools, etc. For about 20 years, CVD coatings of refractory carbides, nitrides and oxides have improved cutting performances and lifetimes of cemented carbide tools which are used mainly for metal cutting /1/.
Natural as well as high-pressure diamond has long been used for a variety of tools. It is either brazed directly onto the surface of the tool or previously-formed thin sintered PCD (= Poly-Crystalline Diamond) compacts are bonded to the surface of a tool substrate /2/.

### 1.1. Low-pressure in situ diamond coatings vs. soldering of freestanding films

The low-pressure diamond synthesis makes in situ diamond as a tool coating feasible /3/. It is also possible to produce thin, freestanding diamond layers which are bonded to the tool surface, as done for PCD products. Depending on the specific technical application, both techniques have proven successful /4/. The freestanding layer

application is however much simpler as the diamond layer growth and its adhesion are carried out in separate product steps. The substrate material for in situ coating cannot be chosen freely. It must fulfill certain specific needs for diamond nucleation and growth, and good adhesion must also be assured.

## 1.2. Typical tool substrate materials

Normally the substrate bulk material for tools must have high toughness, stiffness, mechanical and thermal shock resistance, hot hardness, high heat conductivity, etc. For a tool to be effective, strong coating adhesion is essential, whereby apparently at least a partial chemical bonding between the coating and the refractory carbides of the hard metal is needed for perfect adherence /5/.
Cemented carbides, the traditional bulk materials for such applications, seem to be a good choice for diamond-coated tools as well. They can withstand high local pressures and temperatures, including those occurring at cutting edges during chip formation. Other promising candidates are the so-called cermets (Ni-bonded TiC and TiN), as well as some special oxides and nitrides ($Al_2O_3$, $Si_3N_4$, SiAlON). Refractory metals are of interest as intermediate layers /6/.
Both diamond nucleation and growth can be strongly influenced by the substrate surface and its chemistry /3/. Uncontrolled interface reactions during the deposition can be detrimental, as when causing changes of the diamond crystal growth mode or even graphite formations due to excess Co binder at the cemented carbide surface /3/.

## 1.3. Performance obtained so far

Cutting tests with diamond-coated tools on hypoeutectic AlSi alloys confirm that the adhesion problems can be controlled. The performance of low-pressure diamond-coated tools now approaches that of commercial PCD products /3,6/. The automotive industry will be one of the principal users of such tools /7/. Since for very complex tools only the traditional low-performance tool materials are now competitive, diamond-coated tools, which are hardly feasible with today's PCD technology, represent a significant market potential.

## 1.4. Abrasive low-pressure diamond powders

Another typical application which has long held an appreciable share of the market is the use of diamond grits for grinding and polishing. Pure diamond and composite powder particles were recently produced by the low-pressure method /8,9/. Due to their particular structure, composite powders can be expected to be suitable for specific grinding and polishing applications

as well as for revolutionary uses yet to be developed. One of these new products is a composite powder with a superhard c-BN core surrounded by a diamond shell /10/. Special PCD products, made by compacting composite powders into the required shapes, will open up new dimensions for the fabrication of specialized high-performance tools.

## 2. NUCLEATION OF DIAMOND

The usual pre-nucleation steps for diamond nucleation are illustrated in Fig.1. Surface diffusion and subcritical cluster formation should precede the stable growth stage. Yugo et al. /11/ suggested the size of a homogeneous diamond nucleus to be about 30 A.
The nuclei are difficult to observe but the early growth stages of diamond can be easily seen by SEM /12/. Assuming that each of the visible tiny crystallites originates from a surviving, supercritical diamond nucleus, the nuclei number is easy to count.
Clusters of subcritical size should form continuously from the incoming flux on the substrate surface which does not react with carbon. Stable nuclei develop and grow to crystals, which then grow together, resulting finally in the coating /13,14/.

### 2.1. Kinetics during diamond deposition

Although the basic low-pressure diamond synthesis differs little from a normal CVD process except in its need for gas activation, a comparison of its chemistry with "normal CVD processes" reveals both differences and similarities /3/. Various carbon species are supposedly involved in the atomic attachment /15-20/. The presence of atomic hydrogen leads to a "selective etching". Under "super-equilibrium" conditions and at certain temperatures, pressures, etc., the appearance of $sp^2$-bonded carbon (graphite) is prevented and the $sp^3$-bonded carbon (diamond) is stable. These kinetic reactions are essential for the CVD diamond formation /21,22/.

### 2.2. Substrate/reaction gas interactions

The main reason for the long incubation times frequently observed for diamond nucleation is the occurrence of chemical interactions at the substrate surface with the synthesis gases, e.g.:
- atomic and molecular hydrogen
- hydrocarbides or $CH_x$ radicals
- oxygen, dopants, etc., as applicable

Depending on the nature of the substrate, different chemical reactions and/or diffusion with hydrogen and/or

carbon are possible. Chemical reactions occur normally with compounds such as oxides, nitrides, sulfides, etc. /23/.

Obviously the formation of new compounds on the substrate surface can be beneficial or detrimental for the diamond nuclei formation as such. Gas formation can also strongly interfere with the nuclei formation. Both can prolong the time needed to develop the early growth stages and can also influence the adhesion of the final diamond coating /3,23/.

Regarding the carbon/substrate interactions only, metals, alloys and pure elements can be classified in three groups:

1. Little or no solubility or reaction: diamond, graphite, Cu, Ag, Au, Sn, Pb, etc.

2. C diffusion only, whereby C dissolves in Me(C) mixed crystals: Pt, Pd, Rh, Fe, Ni, etc. /24/.

3. Carbide formation /25/
   metallic: Ti, Zr, Hf,
   V, Nb, Ta,
   Cr, Mo, W, etc.
   Fe, Co, Ni (metastable), etc.
   covalent: B, Si, etc.
   ionic : Al, Y, rare earth metals, etc.

Besides the surface modifications discussed above, which lead to compounds promoting heterogeneous diamond nucleation, certain substrate materials (2 and 3) delay diamond nucleation by acting as carbon sinks. At deposition temperatures, large amounts of carbon are transported into the bulk, where it forms either carbides or solid solutions. This leads to a temporary decrease in the carbon surface concentration, which delays the onset of nucleation. For substrates with very high C diffusion rates their thickness becomes a relevant parameter for the onset of nucleation. Thin foils reach their carbon saturation more rapidly than bulky crystals /26,27/. If the carbon solubility decreases with temperature, formation of metastable carbides or precipitation of graphite (Me+C) usually occurs during cooling /24/.

## 2.3. Nucleation on different substrates

If nucleation were independent of the substrate, the weight increase during the nucleation period would be identical for all substrates. Experiments showed however that the weight change during the early stage of diamond

deposition depends on the substrate used (Fig.2) /23/. Only after the surface is completely covered with diamond did the weight increase with time become constant for most of the substrates investigated.

Not only the weight change but also the nuclei number and the time to obtain full coverage of the surface (= layer formation) depend strongly on the chemical nature of the substrate and its surface condition /12,23,28,29/.
The C oversaturation needed for heterogeneous nucleation to occur obviously depends on the chemical nature of the substrate. If the substrate surface itself cannot nucleate the diamond, but must first undergo a chemical reaction to produce a suitable basis for heterogeneous nucleation, then the longer incubation time is logical (Fig.3,4). For example, it takes hours for diamond crystals to become visible on the clean surface of a Si wafer, while nucleation on single-crystalline SiC takes place rapidly /23/. As known for the refractory metals /30,31/, apparently Si must also form its carbide before nucleation can occur /32,33/.

2.3.1 Diamond nucleation and growth on SiAlON substrates
Diamond deposits readily on SiAlON substrates, resulting in high nucleation densities /23/. After the layer is formed, further growth is influenced only by the diamond deposition parameters. These effects can be explained by the high resistivity against the activated $H_2/CH_4$ gas mixture during diamond deposition.

2.3.2 Cemented carbide substrates and nucleation
Bichler /34/ reported that the diamond nucleation rate on cemented carbides without prior diamond polishing treatment of the surface decreases with increasing Co concentration (3-10% Co). At a Co concentration above 6% the diamond nucleation rate reached the minimum. A negative influence of Co on diamond nucleation on cemented carbide surfaces was reported by Matsubara and Kihara /35/. They obtained a graphitic carbon deposition on the Co phase, which was later overgrown by diamond, leading to poor adhesion of the diamond coatings. Although this is difficult to observe for the fine-grained cemented carbides normally used, the same basic principles still apply /36/.

The Co concentration clearly influences the diamond crystal growth and its morphology as well. At low concentrations (0 to 0.3 % Co) and short deposition times no nucleation effect or growth changes due to Co were observed. At a higher Co content (3%) branching due to surface nucleation occurred and smaller crystals were

grown on top of the larger ones. Co diffusion to the layer surface led to a secondary nucleation of new diamond crystals. A similar influence of diffusing Co on CVD depositions other than diamond have already been investigated for $Al_2O_3$ coatings using Auger analysis /37/.

## 3. MANIPULATIONS TO ENHANCE DIAMOND NUCLEATION

The scratching and polishing of Si wafers with diamond grits or other hard particles such as SiC, $B_4C$, c-BN, etc. /11,29,38-41/, precoating with diamond-like carbons /41/, or even fingerprints on refractory metals /42/, were reported to promote diamond nucleation on Si wafers. They avoid the long exposure times required on smooth Si /32/. Nucleation enhancement by surface treatment is however specific for neither diamond nucleation nor for Si substrates. Various refractory metals showed analogous enhanced diamond nucleation as well as rapid film formation after polishing or scratching with diamond, SiC, $Al_2O_3$ or other particles (Fig.5) /12/.
The comparison of various polishing and grinding materials and their interaction with different substrates should also yield valuable information about the mechanisms involved /12/. Thin corners are prone to be carburized more rapidly than flat surfaces, which could explain the early nucleation on exposed groove walls or fracture surfaces. Remaining fragments of the grinding materials are also possible nucleation sites, as the critical homogeneous nuclei size for fractured diamond particles to act as nuclei can be expected to be rather small.

## 4. DIAMOND GROWTH

### 4.1. Nucleation number and layer growth rates

For the coating formation two growth regimes must be distinguished /28/. During the early growth period the nuclei grow as isolated crystals. The crystals grow, form larger islands and finally completely cover the substrate surface. The initial rapid increase in size of the isolated crystals and islands is due to abundant surface diffusion of carbon from the relatively large diamond-free areas surrounding them /43/. After layer formation, the increase in thickness is proportional to the incoming carbon flux. The time needed to form a continuous film depends not only on the growth parameter chosen but also on the number of nuclei formed. As outlined above, the substrate and its surface condition are important additional parameters for this. Usually the growth rate of the coating itself is independent of the substrate.

## 4.2. Formation of layers and coatings

The mechanism described above is also valid for other facetted crystals. As well known from various CVD coatings on tools ($Al_2O_3$, TiC, etc.) /44/ preferred growth directions can lead to "columnar" structured layers which are also observed with CVD diamond /3,45-47/.

Outward diffusion of impurities from substrates can be undesirable since facetted crystal growth is usually very sensitive to foreign elements /37/. This was an early problem with $Al_2O_3$ coatings on cemented carbides /44/. As seen above, Co binder diffusion also has negative effects during diamond coating /36,48,49/. Proposed solutions to the problem include intermediate layers /50/, removal of excess Co by etching /36/, and using substrates with low Co contents /48,51/.
A "beneficial" effect of such diffusion is the faster layer growth rate on BN substrates, most likely caused by an "outwards" diffused boron "impurity" which accelerates the diamond growth /52/.

## 5. SPECIFIC PROBLEMS ENCOUNTERED DURING DIAMOND CVD

For industrial production, even after the problems of nucleation, growth, interface reactions and interface bonding are solved, the specifics of technical reactors must also be well understood /3,7/. During CVD growth the reactants must diffuse through different types of boundary layers /53/. The growth kinetics are closely linked with this boundary layer transport mechanism in conjunction with the specific chemical reaction kinetics /53-55/.
Additional "CVD diamond" problems:
- The convection is strongly influenced by an atomic hydrogen wind /56/.
- In hot-filament reactions the Sorret effect can become unusually important /53/.
- The metastable nature of the atomic hydrogen complicates reactor upscaling, etc.

## 6. CONCLUSION

Today, product development for diamond cutting applications is already in a relatively advanced state, since a perfect diamond crystal lattice and single crystallinity are not primary requirements for their proper functioning. Their technical feasibility has already been demonstrated in different wear applications.
The rapid advancement in these "simpler" application areas has already led to industrial products based on

freestanding diamond.
However, the production of technically and economically feasible products for superhard applications is still only in its early stages. Some of the major problems remaining to be solved are
- higher diamond growth rates
- better carbon and energy yield
- better adhesion between substrate and diamond coating
- upscaling for diamond deposition reactors for continuous production of wear parts
- better tool lifetimes during wear operations
- perfection of in situ coatings

## 7. ACKNOWLEDGEMENTS

The authors would like to thank the Austrian "Fonds zur Förderung der Wissenschaftlichen Forschung" for financial support (Projects P6031, P7274) and the management of Sandvik Stockholm, for so many years of actively sponsoring low-pressure diamond research work.

## REFERENCES

1. B.Lux, R.Haubner, C.Wohlrab: Surface and Coating Technology, 38 (1989) 267-280
2. P.J.Heath: VDI Ber. Nr.762 (1989) 37-59
3. B.Lux, R.Haubner: Proc. of NATO ASI, Il Ciocco, Castellveccio Pascoli, Italy, July 22-Aug.3, 1990, Plenum Press
4. B.Lux, R.Haubner: J.Ref.Met.-Hard Mat., 8 (3) (1989) 158-174
5. P.C.Jindal, D.T.Quinto, G.J.Wolfe: Thin Solid Films, 154 (1987) 361-375
6. B.Lux, R.Haubner: 2nd Int.Conf.on the New Diamond Science and Techn., ICNDST-2, Washington DC Sept.23-27, 1990 (in press)
7. "Diamond Films and Coatings" edited by R.Davis and J.Glass (in preparation)
8. B.Lux: European Patent, EP 0226898 A2 (03.12.86)
9. R.Litos, R.Haubner, B.Lux: High Temp.- High Press., Vol.22 (1990) 99-118
10. R.Haubner: J.Ref.Met.-Hard Mat. 9, (2)(1990) 70-77
11. S.Yugo, T.Kimura, H.Kanai: 1st Int.Conf Diamond Sci.and Techn. (JNDF) Oct.24-26, 1988, Tokyo, Japan, P2-20, pp.130-131
12. A.Lindlbauer: Doctoral Thesis, TU-Vienna, in preparation
13. T.R.Johansson, J.N.Lindström: J.Vac.Sci.Technol., 12 (1975) 854

14. M.Kornmann, H.Schachner, R.Funk, B.Lux: J.Cryst.Growth 28 (1975) 259-262
15. S.Matsumoto, Y.Matsui: J.Mater.Sci. 18, (1983) 1785
16. M.Frenklach, K.Spear; Manu.Dept.Mater.Res.Lab., Pennsylvania State Univ. Park PA 16802
17. M.Tsuda, M.Nakajima, S.Oikawa: J.Am.Chem.Soc. 108(9)(1986) 5708
18. M.Tsuda, M.Nakajima, S.Oikawa: Jap.J.App.Phys. Part 2, 26(5) (1987) 527-529
19. J.Angus: Workshop on the Science and Techn. of Diamond Thin Films, May 20-24, 1990, Cleveland, Ohio
20. J.Harris: 2nd Int.Conf.on the New Diamond Science and Techn., ICNDST-2, Washington DC Sept.23-27, 1990, presentation 7.1 (in press)
21. B.V.Derjaguin, D.V.Fedoseev, I.G.Varshavskaya: Journal de Physique, Colloque C5, suppl. to no5, Vol.50, May 1989, 893-900
22. A.R.Badzian, R.C.DeVries: Mat.Res.Bull., Vol.23, (1988) 385-400
23. A.Lindlbauer: Diploma Thesis, TU-Vienna, 1989
24. W.G.Moffatt: "Binary Phase Diagrams Handbook", Vol.1-3 Genium Publ.Corp., New York, 1984
25. H.Holleck: Fischmeister/Jehn; Hartstoffschichten zur Verschleißminderung, pp.25-45, Publ.DGM, Oberursel, BRD, 1987
26. D.N.Belton, S.S.Schmieg; J.Appl.Phys. 66 (9), (1989) 4223-4229
27. S.J.Harris, D.N.Belton, A.M.Weiner, S.J.Schmieg; J.Appl.Phys. 66, Dec.1989, 5353-5359
28. R.Bichler, R.Haubner, B.Lux: High Temp.-High Press., Vol.22 (1990), 99-118
29. P.K.Bachmann, W.Drawe, D.Knight, R.Weimer, R.F.Messier: Diamond and Diamond-Like Mat. Synth., April 5-9, 1988, Reno, 99-103
30. P.O.Joffreau, R.Haubner, B.Lux: J.Ref.Met.-Hard Mat., Vol.7, Nr.4 (1988) 186-194
31. P.O.Joffreau, R.Bichler, R.Haubner, B.Lux: J.Ref.Met.-Hard Mat., Vol.7, Nr.2 (1988) 92-97
32. B.E.Williams, J.T.Glass, R.F.Davis: SPIE, Vol.877, Micro-Optoelectronica Materials (1988) 56-63
33. B.E.Williams, D.A.Asbury, B.R.Stones, J.T.Glass: Proc. of NATO ASI, Il Ciocco, Castellveccio Pascoli, Italy, July 22-Aug.3, 1990, Plenum Press
34. R.Bichler: Doctoral Thesis, TU-Vienna, 1988
35. H.Matsubara, J.Kihara: 1st Int.Conf.Diamond Sci.and Techn. (JNDF) Okt.24-26, 1988, Tokyo, Japan, P2-12, pp.114-115
36. X.X.Pan: Doctoral Thesis, TU-Vienna, 1989
37. C.Colombier, B.Lux, A.Riahi, M.Puchhammer, H.Störi: Fresenius Z.Anal.Chem., 329 (1987) 355-360

38. A.R.Badzian, T.Badzian, L.Pilione: 3rd Int.Conf.on Surf.Mod.Techn., pp.51-61, Aug.28-Sept.1, 1989, Neuchatel, Switzerland
39. K.Hirabayashi, K.Ikoma, Y.Taniguchi, N.I.Kurihara: 1st Int.Conf.Diamond Sci.and Techn. (JNDF) Oct.24-26, 1988, Tokyo, Japan, P2-03, pp.96-97
40. L.Vandenbulcke, P.Bou, R.Herbin: Journal de Physique, Colloque C5, supp. to no5, Vol.50, May 1989, 177-188,
41. W.A.Yarbrough: MRS 1987, Nov.30-Dec.5, N3.8, Boston MS
42. B.DeVries, T.Anthony, R.Haubner: private communication
43. T.Anthony: MRS 1987, Nov.30-Dec.5, N3.8, Boston MS
44. B.Lux, R.Haubner, H.Altena, C.Colombier: Fischmeister/ Jehn; Hartstoffschichten zur Verschleißminderung, pp.71-112, Publ.DGM, Oberursel, BRD, 1987
45. H.Altena, C.Colombier, B.Lux: Proc. of 4th EURO-CVD, Eindhoven 1983, pp.435-443
46. C.Wild, N.Herres, P.Koidl: J.Appl.Phys. 68(3)(1990) 973-978
47. M.W.Geis: Diamond Technology Initiative Symposium; July 11-13, 1989, Virginia, USA
48. R.Haubner, B.Lux: Journal de Physique, Colloque C5, suppl. to no5, Vol.50, May 1989, 169-176
49. H.Matsubara, J.Kiahari: 1st Int.Conf.Diamond Sci.and Techn. (JNDF) Oct.24-26, 1988, Tokyo, Japan, P2-12, pp.114-115
50. H.Schachner, H.Tippmann, B.Lux, K.Stjernberg, A.Thelin: Swedish Patent 8403428 (1984)
51. K.Saijo, M.Yagi, K.Shibuki, S.Takatsu: 1st Euro.Conf.on Diamond and Diamond-like Carbon Coatings, DIAMOND FILMS 90, Sept.17-19, 1990, Crans-Montana, Switzerland, presentation 16.2
52. S.Matsumoto: ISPC Eindhoven (July 1985) Paper A-1-10
53. J.O.Carlsson, M.Boman: 9th Int. CVD Conf.1984, 129-149
54. C.A.M.Mulder, W.H.M.M.Van de Spijker, J.Jensma, G.Vespui, G.H.C.Heijnen: Journal de Physique, Colloque C5, suppl. to no5, Vol.50, May 1989, 241-248
55. Van der Breckel: Philips Res. Repts 32, 118-146, 1977
56. T.Anthony: Proc. of NATO ASI, Il Ciocco, Castellveccio Pascoli, Italy, July 22-Aug.3, 1990, Plenum Press

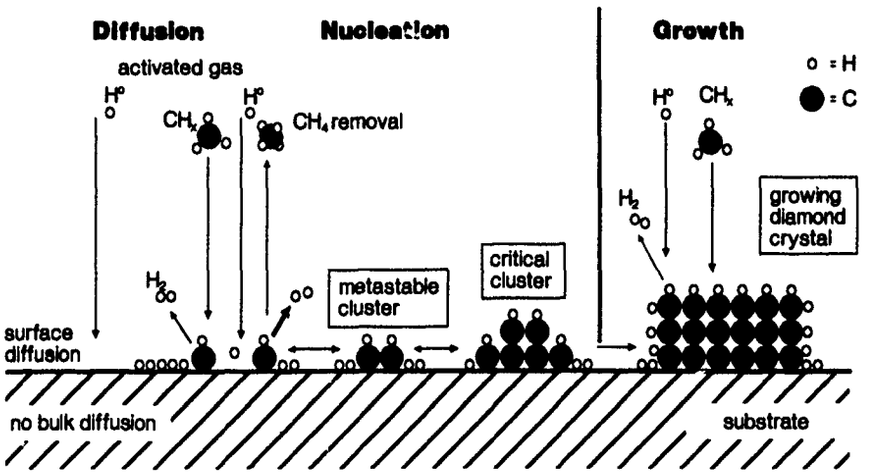



Fig.1: Nucleation and growth kinetics of low-pressure diamond deposition on a non-reacting surface

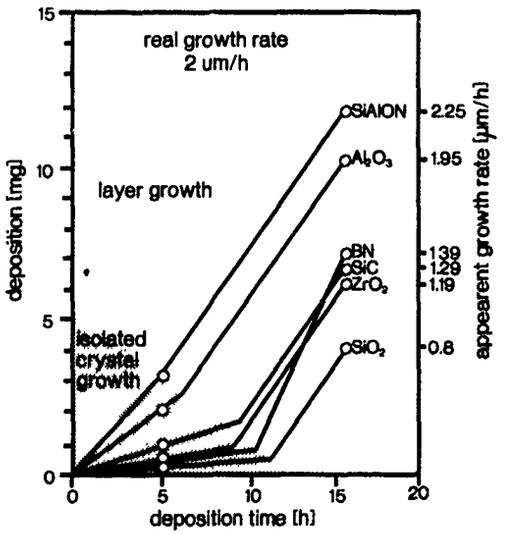



Fig.2: Nucleation and growth of low-pressure diamond on different substrates /64/

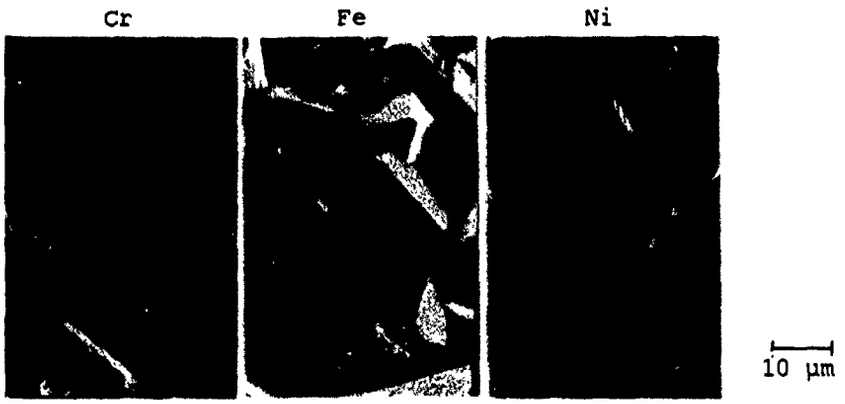



Fig.3: Diamond deposition on Cr, Fe and Ni substrates /12/

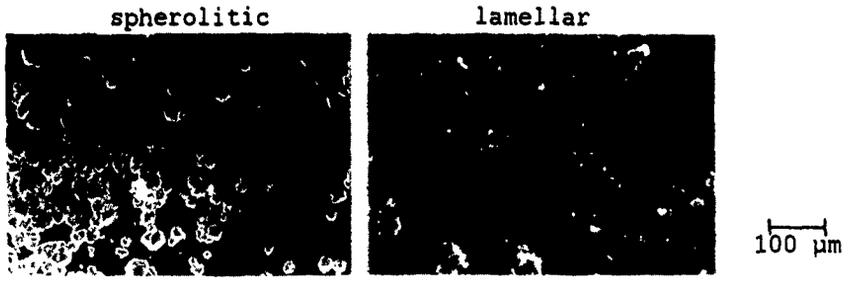



Fig.4: Diamond deposition on spherolitic and lamellar cast iron /12/

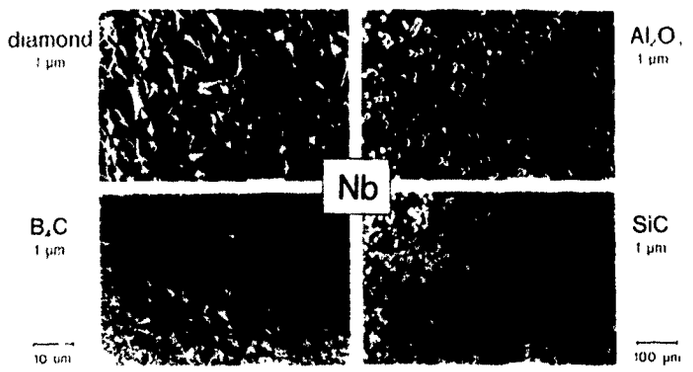



Fig.5: Influence of substrate surface treatment on diamond deposition using Nb substrates /12/

# THE MECHANICAL PROPERTIES OF CVD DIAMOND

M. D. Drory[1], C. F. Gardinier[1], J. M. Pinneo[1], and J. S. Speck[2]

[1]Crystallume, 125 Constitution Drive, Menlo Park, CA 94025

[2]Materials Department, College of Engineering, University of California, Santa Barbara, CA 93106

## ABSTRACT

The fracture toughness of CVD diamond is measured by the Vickers indentation method. Free-standing diamond films of 400 μm thickness are produced with plasma-enhanced chemical vapor deposition, and highly polished for indentation testing. Indentation testing was performed with a microhardness tester using a load range of 500-800g. The average fracture toughness is measured as 5.3 MPa$\sqrt{m}$.

## INTRODUCTION

There is now considerable interest in the commercializing diamond film technology produced by chemical vapor deposition (CVD). Numerous applications have been identified which exploit the superior material properties of diamond; such as, detector windows, heat sinks and tooling. Despite the enormous potential of CVD diamond, the mechanical properties are largely unknown. This study focuses on the fracture toughness of CVD diamond using the indentation method to measure $K_c$.

## EXPERIMENTAL PROCEDURES

A diamond film was grown using plasma-enhanced chemical vapor deposition at 2.45 GHz. The necessary conditions for diamond deposition were achieved at 1.5-2.0 KW and a total gas pressure of 80-90 Torr. Reactant gasses, $H_2$, $CH_4$, and CO were premixed and metered with flow controllers at flow rates of 250-200 sccm. The substrate was a two inch diameter, one quarter inch thick [100] silicon wafer. To enhance nucleation, the wafer was polished with diamond powder followed by rinsing in isopropyl alcohol and deionized water to remove all diamond powder from the surface. After deposition a free standing diamond film was obtained by back etching the silicon using $HF:HNO_3$:HAc in a 2:2:1 ratio.

The diamond film used in this investigation had a maximum thickness of 400 μm unpolished with an approximate 50μm grain size. The grains are {100} form with [111] perpendicular to the plane of the film. In addition twinning is observed on {111} (Fig. 1). The film was characterized by Raman spectroscopy (Jobin Yvon spectrometer) scanning from 1200 to 1700 $cm^{-1}$ to determine the presence of diamond, nondiamond carbon and graphite. The Raman spectrum taken from the top surface of the diamond film shows the characteristic diamond peak at 1331$cm^{-1}$ (Fig. 2). The lack of broad peaks at 1355 and 1560 $cm^{-1}$ indicates a low concentration of $sp^2$ bonded nondiamond carbon and graphite.

After characterization, the free standing film was polished using a cast iron scaife and 4-12 μm diamond grit. Surface roughness of the polished film was obtained by contact profilometery using a 5 μm radius stylus scanning 3 mm. The peak-to-valley surface roughness was found not to exceed 400 Å.

The hardness and fracture toughness of the polished film was measured with a Zwick microhardness tester using a Vickers diamond indenter under 500-800g (4.9-7.8N) load. As described in the next section, the hardness is determined from the impression size, while fracture toughness follows from the radial crack length[1,2]. Measurements of the impression size and crack lengths were made with optical microscope under 1000x (dry lens) magnification. The sample was sputter coated with a thin gold-palladium layer to enhance light reflection. The load range was selected to allow measurable indentation features with optical

microscopy while reducing the tendency for indenter failure. Indentations at loads of 800g or higher caused failure with fewer than five tests for a given Vickers indenter.

## RESULTS AND DISCUSSION

Eleven Vickers indentations of the polished diamond surface were made in the 500-800g load range (Fig. 3), producing a hardness impression and radial crack lengths measurable in the optical microscope (Fig. 4). The hardness, H, is related to the impression size, 2a, by[1]

$$H = 0.47P / a^2 \quad (1)$$

where P is the applied load. Hardness was measured in the range of 57.5 to 108 GPa, with the average H=80.6 GPa and standard deviation of 17.6 GPa. The size of the impressions, 2a, was 5 to 10μm which is smaller than the average grain size. The wide variation in hardness is due to the difficulty in measuring the impression size under low loads, and the incidence of damage at the edge of impressions at high loads. Despite the large variation in hardness, the mean value is within about 10% of the 90 GPa value measured in other studies.[3,4] A narrower range of values of hardness values is likely to occur with Vickers indentations at higher loads (> 1 Kg), however indenter damage occurs with these loads after a single test.

The fracture toughness, $K_c$, is determined from the Vickers indentation by measuring the radial crack lengths emanating from corners of the hardness impression. The crack length, c, hardness, and Young's Modulus, E, is related to fracture toughness by[2]

$$K_c = \xi (E / H)^{1/2} (P / c^{3/2}) \quad (2)$$

where ξ (=0.016) is a calibration constant determined in a previous study of indentation fracture[2]. Fracture toughness values were determined using equation (2) with the E=1000 GPa reported in the literature,[4] and are summarized in Fig. 3. $K_c$ varied from 3.5 to 7.4 MPa$\sqrt{m}$ with an average value of 5.3 MPa$\sqrt{m}$ and a standard deviation of 1.3 MPa$\sqrt{m}$.

The average $K_c$= 5.3 MPa$\sqrt{m}$, is an *upper bound* value of the fracture toughness, since the resolution of crack length in this study is

limited by 1000x magnification. Higher resolution microscopy may reveal longer crack lengths thereby reducing $K_c$ for a given load. In addition to optical microscopy, crack length measurements were also attempted with scanning electron microscopy (SEM) using a relatively low accelerating voltage of 5 KV to maximize the secondary electron yield. However, the crack lengths measured by SEM were shorter than those measured by optical microscopy. Additional work is needed to further resolve crack length measurements. This is particularly important for indentation experiments with low loads which is necessary for reasonable penetrator life.

Cracks lengths in this study were a maximum 25μm which gives the total crack length, 2c, on the order of the average grain size. Fracture toughness in this case may represent a mixture of intergranular and intragranular failure which requires microstructure analysis to quantify the fracture path. Ideally, the method for measuring $K_c$ that was used here should use sufficient load to create radial cracks much longer than the grain size. However the load necessary to create long indentation cracks in polycrystalline diamond far exceeds the fracture strength of the Vickers indenter. Further determination of fracture toughness may use traditional methods such as double cantilever beam specimens with long pre-cracks.

## SUMMARY

The fracture toughness of CVD diamond was determined by the indentation method as about 5.3 MPa$\sqrt{m}$. This represents the first report of fracture toughness for PECVD diamond and should be considered an upper bound value for $K_c$ where indentation crack lengths are on the order of the grain size. Additional work is needed to further resolve crack lengths, particularly under low indentation loads. Fracture toughness measurements should also be made with other methods using long pre-crack lengths.

## REFERENCES

1. A. G. Evans and E. A. Charles, "Fracture Toughness Determinations by Indentation," *J. Am. Ceram. Soc.*, **59** [7-8] 371-72 (1976).

2. G. R. Anstis, P. Chantikul, B. R. Lawn, and D. B. Marshall, "A Critical Evaluation of Indentation Techniques for Measuring Fracture

Toughness: I, Direct Crack Measurements," *J. Am. Ceram. Soc.*, **64** [9] 533-38 (1981).

3. D. M. Jassorwski. "Investigation of Applications of Diamond Film," Aerojet TechSystems Final Report of Air Force contract #F04611-88-C-0074, August 1989.

4. M. E. Hearn, C. J. McHargue, R. E. Clausing, W. C. Oliver, and R. H. Parrish, "Determination of the Mechanical Properties of Diamond and Diamond-Like Films by the Ultra-Low Load Indentation Technique," Proc. Mat. Res. Soc., 1989.



Fig. 1 Scanning electron micrograph of the diamond film surface prior to polishing.

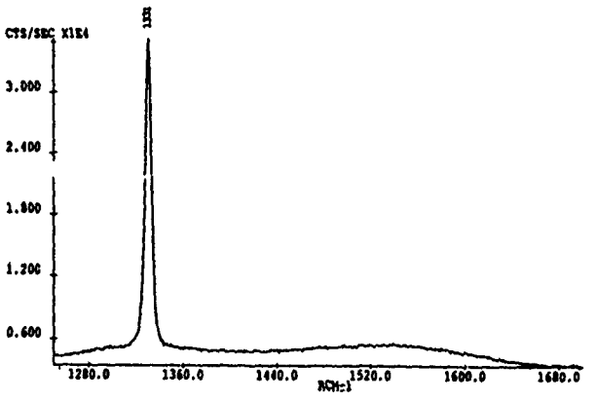



Fig. 2 Raman spectra of diamond film revealing strong characteristic peak.

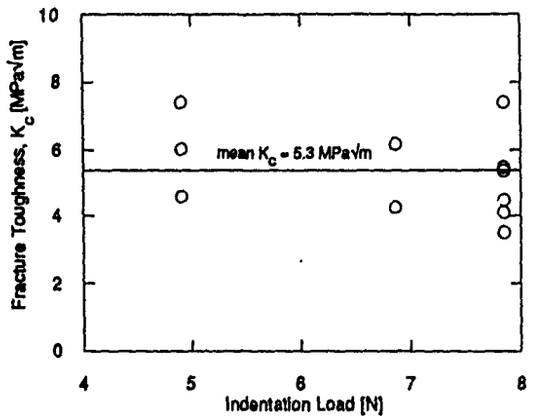



Fig. 3 Plot of Fracture toughness data vs. load showing an average $K_C$=5.31 MPa√m.



Fig. 4 Optical micrograph of Vickers indentation under 700g load.

# ULTIMATE TENSILE STRENGTH OF POLYCRYSTALLINE DIAMOND FILMS

J. L. Davidson, X. Cao

Vanderbilt University
P.O. Box 99-B
Nashville, TN 37235

## Abstract

Diamond films grown by microwave plasma CVD, thicknesses approximately 5 - 20 microns, were patterned into tensile test specimens. Using conventional tensile test techniques, the diamond was stressed in tension to fracture and the load recorded. The cross sectional area at separation was measured and the tensile strength observed to be nominally 1.5 ($10^5$) psi, best case. Fracture characteristics were examined by SEM.

## Introduction

Although the fact that diamond is "hard" is a well-established point of fact, lay and scientific, the actual "conventional" mechanical properties such as the modulus of elasticity, tensile strength and compressibility are much less quantified. This is especially true of the interesting polycrystalline diamond films, PDF, resultant from the synthesis work with filament and plasma growth techniques of the last decade. The potential mechanical applications for diamond, which are numerous, suggest more property characterization would be useful.

The Young's modulus of PDF has been found to be 1.20($10^7$) kg/cm$^2$ [1] as compared to 1.15($10^7$) kg/cm$^2$ for natural, single crystal, diamond. As regards tensile strength, experimentation was performed, monitoring deflection as a function of pressure and the pressure to rupture PDF membranes, resulting in estimates of tensile strength [2]. However, complications in the model selection for membrane approach (e.g., should the PDF be treated as a membrane or a plate?) led to wide variations in the estimates.

Ideally, a more conventional specimen of PDF could be fabricated for true orthagonally loaded tensile stress testing. In this work, we attempted to "shape" such PDF tensile specimens fabricated by HPMWCVD (high pressure microwave chemical vapor deposition) PDF processing. PDF deposition was performed in an ASTEX (TM) HPMW DDS-6 system, Figure 1, this process of achieving diamond films, most typically on silicon substrates, has been described elsewhere[1]. Raman spectra and visual inspection indicate films with very low $sp^2$ content. The surface morphology of PDF typically obtained is shown in Figure 2 and a typical Raman spectra of these films is shown in Figure 3.

For PDF stripes, the diamond was deposited on silicon and the silicon was then etched away in a conventional silicon etch solution which has no effect on the diamond. Analytical techniques, e.g., SIMS, indicated all of the silicon was removed. For some specimens the silicon substrate was shaped to result, directly from the deposition, in a stripe of diamond suitable for tensile testing. Other diamond specimens were deposited as a film and a patterning process, described elsewhere [3], used to achieve the desired specimen shape. Figure 4 is a photograph of a free standing PDF tensile specimen.

*Two* forms of tensile specimens were pursued, stripes, as just described,and *filaments*. Filaments were formed by depositing diamond on free standing sections of small (nominally 10-25 $\mu$ diameter) fibers of tungsten, molybdenum, graphite and aluminum oxide. See figures 5 and 6. The molybdenum core fibers were selected to attempt filament tensile testing.

## Mechanical Testing

Free standing PDF structures are fragile and brittle, easily broken by macroscopic bending loads. Large compressive grips are unsuitable for gripping the films or fibers in the tensile machine. Employing an MTS model 5002 tensile test machine, specially designed connectors and a specimen mounting technique using a supporting aperture card for pre-loading, successful tensile tests were performed. Successful is defined as pulling the tensile specimens apart and achieving a clear separation at or near the middle (gauge length) of the specimen.

The plastic frame aperture card that was used in some instances enabled placement of the tensile specimen in readiness for load. The ends of the specimen were "super glued" to the frame which had holes centrally located into which universal hooks to connect to the load cell and base of the tensile machine were attached. A typical arrangement is shown in Figure 7, and typical machine and load conditions are indicated.

PDF structures were loaded to fracture and the maximum load noted. A typical load:time output is shown in Figure 8. The calibrated load cell signal as f(t) was processed through a PC based data recording system for storage, plotting, etc. Due to unquantifiable "give" in the entire arrangement, no attempt at accounting for strain in the PDF is made. The first, smaller peak in the example represents a shifting in the hooks as the load began to build up.

By noting the maximum load sustained to failure and measuring the width and thickness (area) of the cross section that fractured under that load, the tensile strength is estimated. It is noted that only data where the PDF failed (separated) clear of the plastic frame "grips", i.e., preferably at or near the middle of the length of PDF stripe, was used in these estimates. Slightly less than half of specimens tensile tested to date fractured in a "good data" zone.

Figure 9 is an SEM of the fracture surface of the cross section of PDF that failed at maximum load. The fracture surface resembles that of other fractured PDF, characterized by Hoff [4], although loading conditions in that work may be different in application and unknown in magnitude.

Figure 10 is a table summarizing the tensile test data. All data is from stripes. More specimens are under evaluation. Processing deposition conditions for these samples were: Substrate Temperature = 850°C, hydrogen flow = 500 sccm, methane flow = 5 sccm, microwave power = 1500 Watts. Samples nominally 8 - 10 microns thick were deposited for 20 hours. Samples nominally 15 microns thick were deposited for 36 hours. It was presumed that negligible plastic flow occurred (none was observed) during tensile load, and thus the area at fracture cross section measured was taken as the area that carried the load at failure.

No load data is available for poly diamond fibers. No successful handling technique is yet achieved for "zero" or start conditions of the load testing on the size instrument and fixtures used without first breaking the fiber specimens by cross loading.

## Discussion

Even the highest value observed for tensile strength, 166 ksi, is smaller than expected based on the very high Young's modulus of diamond and based on the membrane rupture data [2]. There are several possible explanations: (a) loading in these experiments is still not perfectly axial and bending moments are present, (b) microcracks (notches/stress risers) exist at the edges or surfaces of the specimens, or (c) intergranular fracture is occurring through material inferior to pure diamond. Also, the small number of samples successfully tested thus far do not allow statistical assessment.

We are continuing to refine the techniques and are exploring different PDF. As reported by others [5,6] grain size and $sp^3$:$sp^2$ of the polydiamond can be influenced by, e.g., deposition temperature, $H_2$:$CH_4$ ratio, and the presence of oxygen during deposition. Using techniques described in this paper, and their refinements, the tensile strength of diamond films will be further examined with these parameters as variables.

## Summary

Free standing polycrystalline diamond films have been subjected to tensile testing and the load to pull them apart determined. An estimate for the tensile strength and the morphology of the tensile fracture surface were presented.

## Acknowledgements

This work was supported in part by the NASA Office of Commercial Programs, Grant No. NAGW-810 and the Vanderbilt Microelectronics Laboratory. Invaluable technical support by M. Howell, T. Keller, M. Languell and A. Strauss is noted.

## References


1. J. L. Davidson, et. al., "Synthetic Diamond Micromechanical Membranes, Cantilever Beams, and Bridges", J. Electrochemical Society, 137, No. 10, (1990).
2. Air Force Report AL-TR-89-044, CN F04611-88-C-0074, Edited by D.M. Jassowski, Nov. 1989.
3. J. L. Davidson, et. al., "Diamond as an Active Microelectronic Material", Proceedings of the Advanced Materials Symposium, International Society of Hybrid Microelectronics, Dallas, Texas, April, 1991.
4.H. A. Hoff, et. al., "Fracture Characteristics of Chemical Vapor and Combustion Deposited Diamond", Second International Conference on the New Diamond Science and Technology, Washington, D.C., Sept. 1990.
5. W. Zhu, et. al., Proc. First Intl. Symp. on Diamond and Diamond-like Films, 175th Electrochemical Society Meeting, May, 1989.
6. M. Yoshikawa, et. al., Appl. Phys. Lett., 55, 2608 (1989).


## Figures

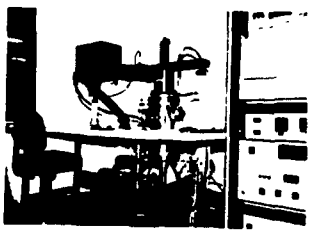


Figure 1. Diamond Deposition System




Figure 2. SEM of PDF Surface

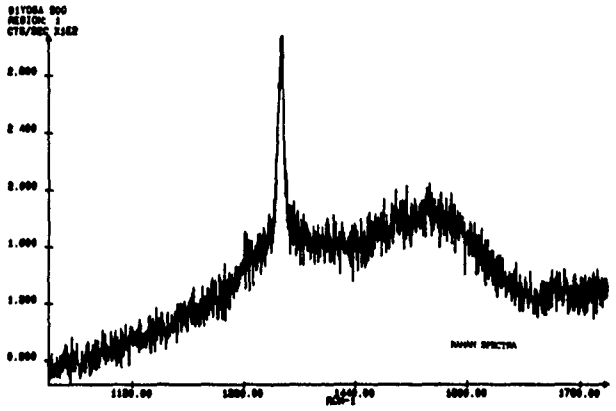


Figure 3. Raman Spectra of PDF




Figure 4. Photograph of PDF Tensile Specimen
Length = 2.5 cm.



Figure 5. PDF Coated Molybdenum Fiber

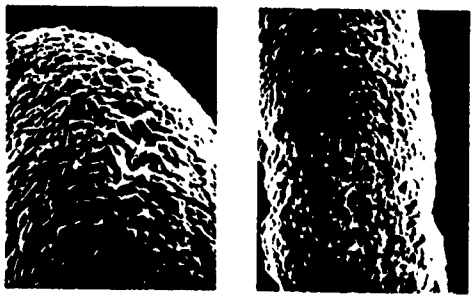


Figure 6. PDF Coated Tungsten

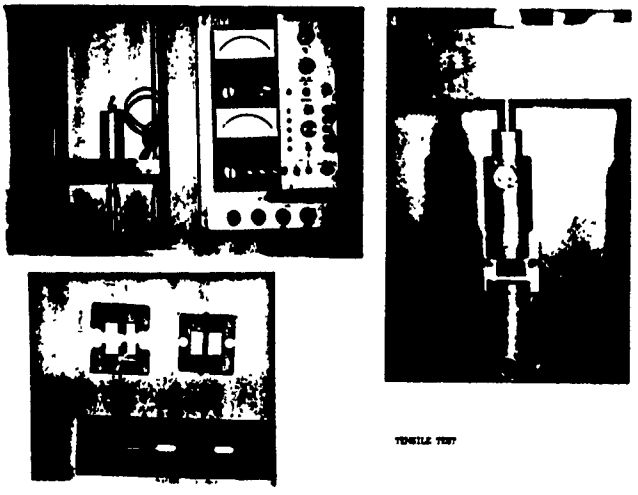


Figure 7. Tensile Machine and Specimen Loading
crosshead speed = 6mm./min.
50N Load Cell

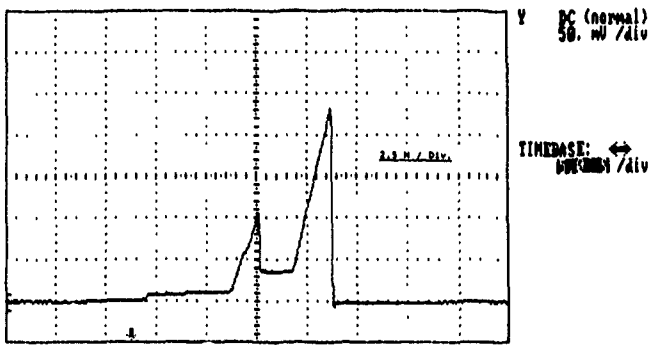



**Figure 8. Tensile Test Load Output**
**vertical scale,load calibration:**
**1V = 50 N**

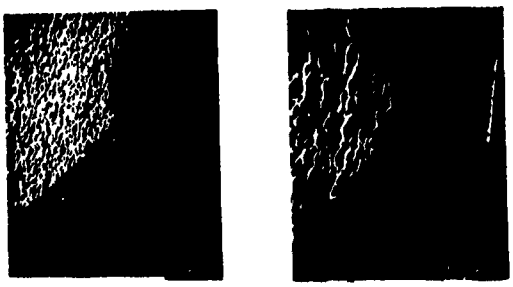


**Figure 9. SEM of Fractured Tensile Specimen**
**[the vertical surface was the**
**load bearing interface]**

| SPECIMEN | w(mm.) | t(μ) | L(N) | T.S.(psiX10$^5$) |
|---|---|---|---|---|
| 1 | 1.0 | 10 | 11.5 | 1.66 |
| 2 | 2.0 | 5.7 | 10.5 | 1.33 |
| 3<1> | 1.0 | 15 | 3.0 | .29 |
| 4 | 3.0 | 8 | 12.5 | .75 |
| 5<2> | 2.2 | 8 | 6.0 | .49 |
| 6<1> | 4.1 | 16 | 13.5 | .30 |

w = width in mm. (± .1 mm.)
t = thickness in microns (± .1 μ)
L = Load in Newtons
T.S. = Tensile Strength in psi (est. ± 20%)

notes <1> broke "near" grip
<2> "hourglass" shape

**Figure 10. Tensile Test Summary Results**

# INDENTATION BEHAVIOR OF DIAMOND FILMS ON CEMENTED CARBIDE

M. D. Drory and M. G. Peters

Crystallume
125 Constitution Drive
Menlo Park, California 94025

## ABSTRACT

Successful development of diamond coated tooling requires a quantitative measurement of adhesion between diamond and cemented carbide. The brale indentation method is explored whereby a circular interface crack is created under applied load. A model is presented which focuses on the plastic deformation near the indenter that results in mode I loading of the film. In particular, an Obreimoff-type analysis is used to relate interface toughness to the plastic deformation near the indenter, film thickness, Young's modulus, and applied load.

## INTRODUCTION

There has been considerable effort focused in recent years towards the development of CVD diamond as a hardcoating for tool inserts[1]; an application which takes advantage of some of the superior material properties of diamond, namely, that is has the highest hardness and a very low friction coefficient. Substrates for this purpose have been

ceramics such as SiAlON, and tungsten carbide/cobalt cermets. The latter is the traditional tool insert material and is preferred in some cases over ceramic inserts because of its higher fracture toughness. However, a critical issue remaining for diamond-coated WC/Co substrates is maintaining adequate adhesion.[2]

An important ancillary issue for the development of diamond coated tool inserts is adhesion testing, where a rapid and quantitative test of adhesion allows feedback for deposition development without the use of more costly and possibly time consuming machining tests. Several *quantitative* adhesion tests have been proposed for this purpose including: scratch,[3] scraping,[4] indentation,[5,6] and four-point bending tests.[7] However, one or all of these methods encounter a number of difficulties as a simple and quantitative test for adhesion that is appropriate for diamond-coated tool inserts. For example, stylus wear greatly affects the scratch test,[8,9] and the four-point bending test is not appropriate for the tool insert geometry. To avoid these difficulties, the brale indentation test is of considerable interest because it is a simple and rapid test which is easily transferred to the production environment.

The brale indentation test involves indenting a coated substrate under a 15-150 $K_f$ load using a Rockwell hardness tester. Under sufficient load, a region of interface cracking and film buckling is readily seen in the optical microscope (Fig. 1). A *qualitative* assessment of adhesion is easily made by comparing interface crack diameters for a given load,[2] however, a *quantitative* measure of the interface toughness is not yet available. This issue is addressed here by presenting a first order analysis of the brale indentation test.

## INDENTATION ANALYSIS

An estimate of the interface toughness, $G_c$, can be obtained from the brale indentation test by considering the plastic deformation in the WC/Co substrate near the indenter. Under load, *uplift* and *lateral* displacement of substrate material occur adjacent to the indenter, and result in mixed-mode loading of the diamond film. Although a detail analysis should consider mode I and II contributions, a first order prediction for $G_c$ can be made by only considering mode I loading induced by the uplift displacement, $\Delta$ (Fig. 2). In this case, crack extension takes place along the interface when the indentation load is sufficient to increase the mode I loading to $G_c$.

A simple fracture mechanics model for the process shown schematically in Figure 2 follows from an Obreimoff analysis of the uplift displacement of the diamond film.[10] For a two-dimensional (planar) geometry the strain energy release, G, is related to the variation in strain energy, U, with crack length, a:[11]

$$G = -\frac{1}{b}\frac{\partial U}{\partial a} \tag{1}$$

where b is the out-of-plane dimension (Fig. 3). The strain energy is easily found for a diamond beam of length, a, under a force, P:[12]

$$U = \frac{P^2 a^3}{6EI} \tag{2}$$

where E is the Young's modulus of the film, h is the film thickness, and I (=$bh^3/12$) is the section modulus. Similarly, the uplift displacement, $\Delta$, is given by:

$$\Delta = \frac{Pa^3}{3EI} \tag{3}$$

Combining equations (1) - (3), the normalized strain energy release rate is found by as a function of the uplift displacement, film thickness and crack length:

$$\frac{G}{Eh} = \frac{1}{32}\left(\frac{\Delta}{h}\right)^2\left(\frac{a}{h}\right)^{-4} \tag{4}$$

## RESULTS AND DISCUSSION

The strain energy release rate is found by equation (4) to strongly decrease with the inverse of crack length, and increase with uplift displacement (Fig. 4). The sharp decrease in normalized G with increasing crack length indicates that the brale indentation test should provide a sensitive measure of interface toughness.

The substrate material properties are not explicitly given in equation 4, but are reflected in $\Delta$. Thus, the uplift displacement is a critical parameter for this analysis because it relates G to material properties of the substrate and the indentation load. $\Delta$ is a complex function of the indentation load, yield stress, and elastic properties and is determined by surface profile measurements or finite element computations.

The determination of $\Delta$ for WC/Co remains for future work, however, interface toughness can be explored for a range of displacement values (Fig. 4). Specifically, values of $G_c$ can be determined with typical value of Young's modulus[13] and film thickness for a deposited diamond film (E=1050 GPa, h=1 $\mu$m). For example, a brale indentation test providing a normalized displacement of $\Delta/h=1$ results in a 10 $\mu$m interface crack radius with an interface toughness of 1 J/m$^2$ (Fig. 4).

Further work is needed to refine the calculation by accounting for the axisymmetric indentation geometry, residual film stress, and buckling.

## CONCLUSIONS

A first order analysis of the brale indentation test for film adhesion is presented in which film decohesion is driven by uplift displacement of the substrate. Trends in interface toughness are predicted as a function of the substrate displacement, crack length, and film thickness. Additional work is needed to refine the model for the axisymmetric geometry, and provide values of the displacement, $\Delta$.

## ACKNOWLEDGMENTS

This work is supported by the National Center for Manufacturing Sciences (Ann Arbor, Michigan).

## REFERENCES


1. B. Lux and R. Haubner, "CVD-Beschichtung von Werkzeugen mit polykristallinem Diamant," CIRP/VDI Conference "Cutting Materials and Tools" Sept. 19-20, 1989 VDI Bericte 762, pp. 61-84 (In English).

2. K. Saijo, M. Yagi, K. Shiburi and S. Takatsu, "The Improvement of the Adhesion Strength of Diamond Films," *Surface and Coatings Technology*, **43/44** [1-3] 30-40 (1990).

3. A. J. Perry, "Scratch Adhesion Testing of Hard Coatings," *Thin Solid Films*, **107**, 167-180 (1983).

4. M. Murakawa and S. Takeuchi, "Quantitative Adhesion Strength Measurement of Diamond Coatings," *Thin Solid Films*, **181**, 443-50 (1989).

5. P. K. Mehrotra and D. T. Quinto, "Techniques for Evaluating Mechanical Properties of Hard Coatings," *J. Vac. Sci. Technol. A*, **3** [6] 2401-05 (1985).

6. C. T. Kuo, T. Y. Yen, and T. H. Huang, "Adhesion and Tribological Properties of Diamond Films on Various Substrate," *J. Mater. Res.*, **5** [11] 2515-23 (1990).

7. P. G. Charalambides, J. Lund, A. G. Evans, and R. M. McMeeking, *J. Appl. Mechanics*, **56**, 77-82.

8. M. Alam, D. E. Peebles, and D. R. Tallant, "Adhesion Between CVD Diamond Films and Tungsten," This Proceedings.

9. P. C. Jindal, D. T. Quinto, and G. J. Wolfe, "Adhesion Measurements of Chemically Vapor Deposited and Physically Vapor Deposited Hard Coatings on WC-Co Substrates," *Thin Solid Films*, **154**, 361-75 (1987).

10. J. W. Obreimoff, "The Splitting Strength of Mica," *Proc. Royal Soc. (London)* **127A**, 290-97 (1930).

11. R. W. Hertzberg, Deformation and Fracture Mechanics of Engineering Materials, 3rd Ed., Wiley, New York, 1989.

12. E. P. Popov, Introduction to Mechanics of Solids, Prentice-Hall, New Jersey, 1968.

13. D. M. Jassorwski. "Investigation of Applications of Diamond Film," Aerojet TechSystems Final Report of Air Force contract #F04611-88-C-0074, August 1989.

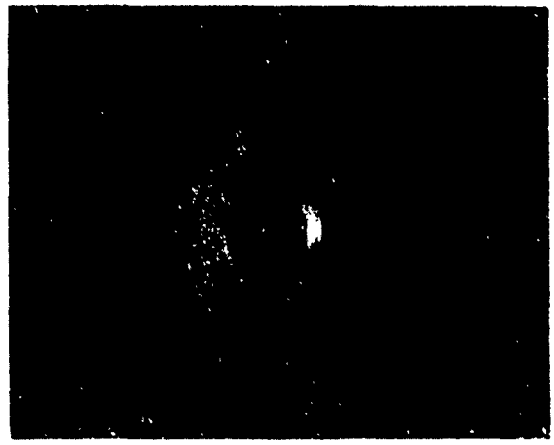


Fig. 1 Optical micrograph of a brale indentation at 100 Kg load of diamond deposited on WC/Co.

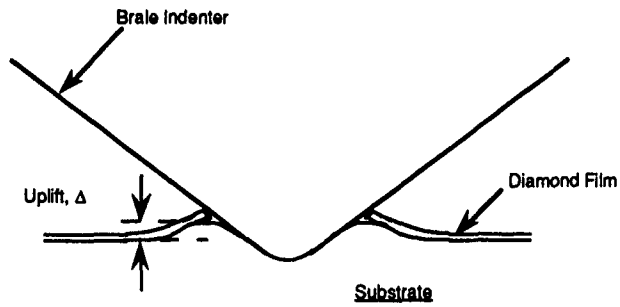



Fig. 2 Schematic of brale indentation with uplift displacement near the indenter.

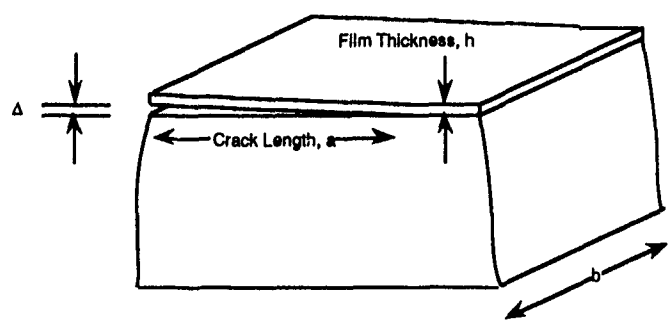



Fig. 3 Schematic of Obreimoff analysis of film decohesion with uplift displacement causing mode I loading.

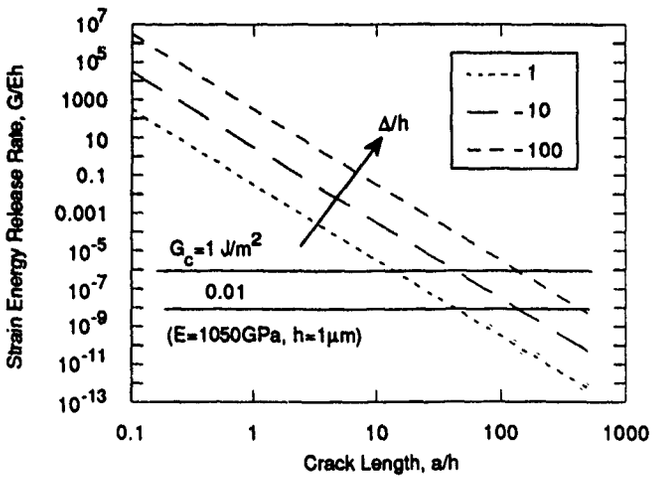



Fig. 4 Trends in interface toughness with uplift displacement and crack length.

# ADHESION BETWEEN CVD DIAMOND FILMS AND TUNGSTEN

M. Alam
New Mexico Institute of Mining and Technology
Socorro, New Mexico 87801

D.E. Peebles and D.R. Tallant
Sandia National Laboratories
Albuquerque, New Mexico 87185

## ABSTRACT

Adhesion between diamond films synthesized by a CVD method and tungsten has been investigated by pull testing method. Diamond films have been deposited at temperatures from 1173 to 1323 K with a growth rate ranging from 0.2 to 0.45 μm/hour. The films are highly crystalline and are dominated by (100) faces at low temperatures, changing to (111) at higher temperatures. Grain size and residual stress in the films increase with increasing deposition temperature. X-ray diffraction shows the expected diamond diffraction peaks plus peaks attributed to WC and $W_2C$. Raman spectroscopy shows a sharp diamond band for all of the films, with a small broad peak attributed to amorphous carbon. There is no distinct correlation between diamond/amorphous carbon intensity with deposition temperature. Sebastion pull testing shows that the failure mode of the films correlates with deposition temperature, but specific adhesion strength values do not.

## INTRODUCTION

Chemically vapor deposited polycrystalline diamond films are potential candidates as wear resistant coatings on cutting tools, bearings and other high wear surfaces. A pre-requisite in this regard is good adhesion between the diamond film and the substrate, because any protective coating is useful only as long as it adheres to the substrate. Despite its importance, the adhesion of diamond films to various substrates has received only limited interest in the past (1-5). An understanding of the adhesion of diamond films to substrate materials and how it can be improved is of considerable importance. This paper deals with the measurement of adhesion of

CVD diamond films and its correlations with substrate temperature, growth rate and film characteristics. Such correlations are necessary to arrive at some general guidelines for synthesizing good quality diamond films at high growth rates and with good adhesion.

## EXPERIMENTAL

Diamond films were deposited on a 22 mm diameter area on 25 x 25 x 1.6 mm polycrystalline tungsten substrates from $CH_4$-$H_2$ gas mixtures by a hot filament assisted CVD technique in a bell jar system, using tungsten ribbon filaments (0.762 mm wide by 0.0762 mm thick). The films were prepared at 1173, 1223, 1273 and 1323 K. All other deposition parameters were kept constant: filament temperature = 2273 K, system pressure = 30 torr, gas flow rate = 100 sccm, $CH_4$ content of the input gas = 0.5% by volume, distance between the filament and the substrate = 5 mm. Prior to deposition the substrates were polished down to 5 μm size alumina powder, ultrasonically cleaned with methanol and seeded by scratching the tungsten with 43 μm diamond powder. Typical film thickness ranged from 5 to 10 μm.

The films were characterized with regard to morphology by scanning electron microscopy (SEM), structure by Raman spectroscopy, crystallinity and residual stress by x-ray diffraction and adhesion by tensile pull testing. Raman spectra were taken from a 2 mm by 0.1 mm area of the sample using both the 514.5 nm and the 457.9 nm lines of an argon ion laser with a monochromator resolution of 6 $cm^{-1}$. The tensile pull adhesion testing was performed with a Quad Group Sebastion tester using 3.175 mm diameter studs. The epoxy-bonded studs were cured at 423 K for 1 hour after mounting on the samples.

## RESULTS AND DISCUSSION

### Growth Rate

The average growth rates in terms of film thickness per unit time were measured from the knowledge of the weight gained by the samples during the deposition period (22.25 hrs), diameter of the deposited film area (2.22 cm) and assuming a film density equal to bulk diamond (3.52 gm/cc). The dependence of film growth rate on temperature is shown in Fig. 1. The growth rate reaches a maxima at about 1223 K. The apparent activation energy upto 1223 K is 95 kJ/mole. The decline in the growth rate beyond this

temperature may be attributed to the increased thermal desorption of hydrogen and carbonic species at the growth surface.

Morphology

Typical morphologies of diamond films synthesized at different substrate temperatures are shown in Fig. 2. At 1173 K the film is dominated by (100) surfaces and the crystallites are rather small. At 1223 K, the predominant morphology is still cubic, however the individual grains are relatively larger. At 1273 K, (111) surfaces begin to appear. At 1323 K the film is dominated by octahedral faces. Cubo-octahedra can also be seen.

Structure

X-ray diffraction measurements indicated the presence of all three diamond peaks, (111), (220) and (311) in the 2θ range scanned. An internal standard was used to measure the precise peak positions. No shift in the positions of the peaks was observed. Signals from non-diamond carbon phases were not observed. X-ray diffraction however, did indicate the presence of WC and $W_2C$.

Raman spectra of the diamond films are presented in Fig. 3. The peak intensities are normalized with respect to the broad band. All samples show a good sharp diamond band at 1333 $cm^{-1}$. For all of the samples, this band is broader and shifted to higher wavenumber, relative to a gem quality natural diamond standard. The broadening is most likely a result of non-uniform strain in the deposited diamond films. The shift in the peak is probably due to a shortening of the bond length, relative to the diamond standard, as a result of compressive stresses in the film. The broad band near 1550 $cm^{-1}$ represents an amorphous type carbon. These effects are in agreement with the x-ray diffraction results presented below. The ratio of the intensity of the diamond band relative to the amorphous carbon band varies with the sample and substrate temperature and is summarized in Table 1 for two sets of samples. It can be seen that there is a large difference from sample to sample that overshadows the differences as a function of temperature. This difference between repeat samples is largest at each of the temperature extremes; much closer values are obtained for the intermediate temperatures.

Residual Stress

Diamond films produced by the CVD process on any substrate are under strain due to a variety of reasons. The strain is either uniform or non-uniform. In terms of x-ray diffraction patterns, each type of strain has a distinct affect. Uniform strain causes a shift in peak

Table. 1 Ratio of the intensity in the Raman diamond band relative to the intensity in the amorphous carbon band as a function of deposition temperature, using the 457.9 nm laser line. Values are reported for two different sets of samples.

| Samples | Temperature (K) | Diamond/Amorphous C |
|---|---|---|
| 1 | 1173 | 13.5 |
| 2 | 1173 | 5.1 |
| 3 | 1223 | 3.6 |
| 4 | 1223 | 4.3 |
| 5 | 1273 | 8.2 |
| 6 | 1273 | 5.8 |
| 7 | 1323 | 18.4 |
| 8 | 1323 | 2.2 |

positions. Since no shift was observed, the strain in the films is not uniform. Non-uniform strain leads to peak broadening. Broadening is also caused by fine particles in the film (<0.1 μm) and the instrument itself. In all films, particles are larger than 0.1 μm. So measured peak widths have no contribution from particle size effect. Instrument assisted broadening was assumed negligible. Therefore, measured peak widths (full width at half maximum) are attributed to non-uniform strain alone. Non-uniform strain was calculated from peak width and peak position data utilizing standard procedure (6). Since the films had different thicknesses, the measured strain values were normalized with respect to thickness. The data is presented in Fig. 4 as a function of substrate temperature. The strain in the films increases with substrate temperature. The higher thermal expansion of tungsten relative to diamond causes the films to be in compression once the samples are cooled down to room temperature.

Adhesion

Scratch adhesion testing was used at first to measure adhesion. The tests produced clear acoustic emission of the failure of the diamond film. However, reproducible and quantifiable critical normal loads could not be obtained because of extensive damage to the Rockwell C diamond stylus. The previous successful results for diamond on silicon (4) were obtained with thin diamond films (2.5 μm) consisting of a very small grain size (< 100 nm). The present films are much thicker and have a much larger grain size, with sharp faceted features. Therefore an alternative Sebastion pull testing technique was used to test the adhesion of the diamond film. This testing showed three distinct failure modes of the film. The first failure mode resulted in a clean pull of the film

from the epoxied-stud surface area, leaving a circular area of the substrate free of the diamond film. This type of failure mode was observed most often for the films deposited at the lower temperatures. As the temperature was increased, the amount of film pulled free of the sample decreased, leaving substrate areas which had only partial removal of the film. At the highest temperatures, a second failure mode was typically observed, which resulted in only very small spots of the film being removed. This range of film removal is illustrated in the photographs in Fig. 5. In Figure 5(a), the circular dark area in the center shows where the diamond film has been completely removed from the substrate. The light regions surrounding the center zone show areas where the diamond film has delaminated from the substrate, but has not been removed. The other panels of Figure 5 show the decreasing areas of film removal as the deposition temperature is increased. In Figure 5(d), it can be seen that only very small, limited portions of the film have been removed from the substrate. A small number of the samples exhibited a third failure mode which resulted in total delamination of almost the whole diamond-film coated area from a single adhesion pull test. The samples exhibiting this total delamination did not share a common deposition temperature, film thickness or diamond/amorphous carbon Raman intensity, suggesting that poor surface preparation may be the problem with the few samples. The measured film adhesion ranges from $1.8 \times 10^6$ Pa to $> 7.0 \times 10^7$ Pa and does not appear to correlate with deposition temperature, film thickness (growth rate), or the diamond/amorphous carbon Raman intensity. In fact, the variation in the adhesion values from one location to another on a single sample far outweighs the differences observed from sample to sample. This adhesion data is summarized in Table 2.

Table 2. Adhesion testing values as a function of deposition temperature. Values are reported for two different sets of samples. The multiple adhesion values listed for each row of the table result from multiple pull tests on the same sample, in the order that the repetitive tests were performed.

| Sample | Temperature (K) | Adhesion Values (Pa x $10^{-5}$) | | | |
|---|---|---|---|---|---|
| 1 | 1173 | delaminated | | | |
| 2 | 1173 | 31.0 | 454.4 | 46.9 | |
| 3 | 1223 | 111.7 | 347.5 | | |
| 4 | 1223 | 17.9 | 695.0 | 58.6 | |
| 5 | 1273 | 466.8 | 126.2 | 704.6 | |
| 6 | 1273 | 83.4 | 552.3 | | |
| 7 | 1323 | 638.4 | 670.2 | 314.4 | 459.2 |
| 8 | 1323 | 619.8 | 705.3 | | |

## SUMMARY

Temperature dependence of film growth rate exhibit parabolic behavior with a maxima at 1223 K. The films are dominated by (100) surfaces at low temperatures and change to (111) surfaces as the temperature increases. The ratio of the diamond to amorphous carbon intensities as measured by Raman spectroscopy do not appear to be a strong function of the deposition temperature. The residual stress in diamond films increases as the deposition temperature increases. Sebastion adhesion testing shows that the failure mode of the films varies with deposition temperature. The amount of film removal over the surface area of the stud decreases with increasing temperature. No strong correlations of adhesion strength with deposition temperature, film thickness, residual stress, or diamond/amorphous carbon intensity have been observed.

## ACKNOWLEDGEMENTS

Funding for the research performed at New Mexico Institute of Mining and Technology was provided by Sandia National Laboratories. A portion of this work was performed at Sandia National Laboratories, supported by the United State Department of Energy under contract number DE-AC04-76DP00789. The authors would like to thank R.L. Morrison for taking the Raman spectra, J.A. Ohlhausen for doing the scratch adhesion testing and taking the optical photographs, C.H. Sifford for doing the Sebastion adhesion testing, and M.E. Smith for taking some of the SEM micrographs.

## REFERENCES

1. H. Suzuki, H. Matsubaro and N. Horie: J. Jpn. Soc. Powder Metall., v. 33, p. 262, 1986.
2. M. Murakawa, S. Takeuchi, H. Miyazawa and Y. Hirose: Surf. Coat. Technol., v. 36, p. 303, 1988.
3. S. Scaglioni and G. Emiliani: J. Vac. Sci. Technol., v. A7, p. 2302, 1989.
4. D.E. Peebles and L.E. Pope: J. Mater. Res., v. 5, p. 2589, 1990.
5. C.T. Kuo, T.Y. Yen and T.H. Huang: J. Mater. Res., v. 5, p. 2515, 1990.
6. B.D. Cullity: Elements of X-ray Diffraction, Addison-Wesley, Reading, MA, 1978.

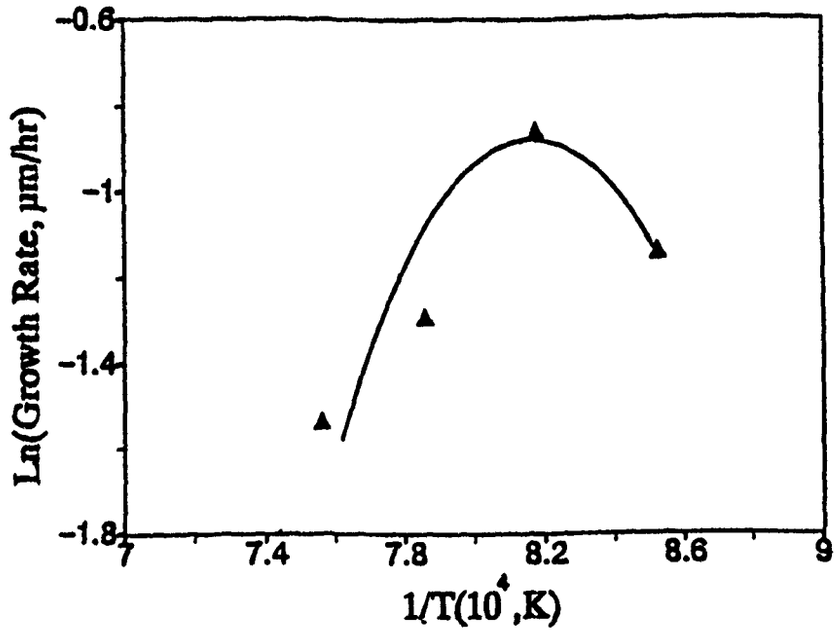



Fig. 1 Arrhenius plot of the rate data

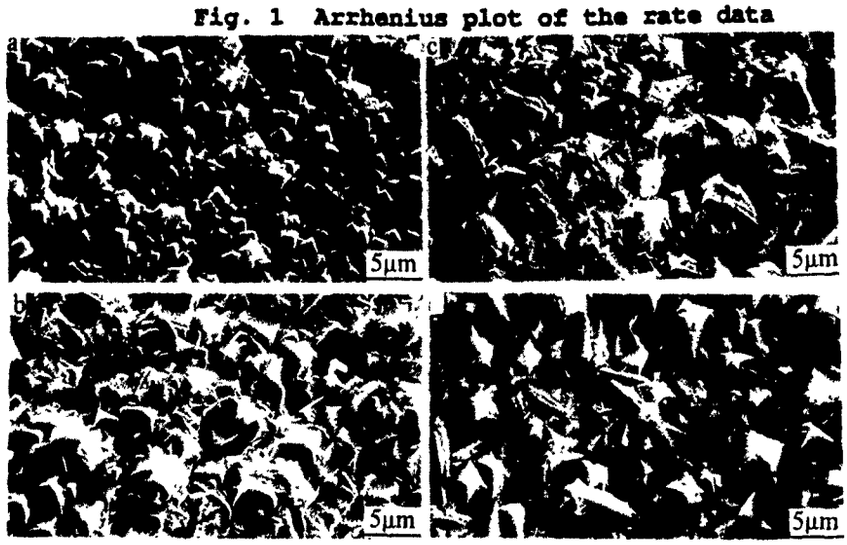



Fig. 2 Typical SEM micrographs of diamond films prepared at (a) 1173K (b) 1223K (c) 1273K and (d) 1323K

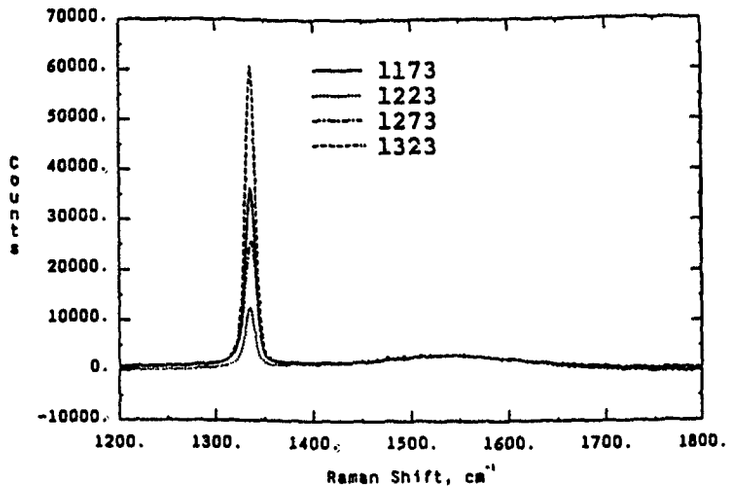



Fig. 3 Raman spectra of diamond films with intensity of each spectrum normalized to the broad band peak near 1550cm$^{-1}$

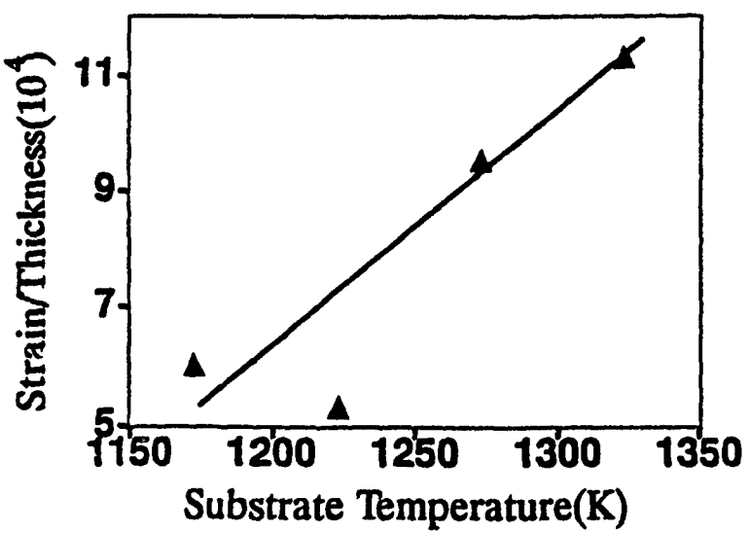



Fig. 4 Strain in the films versus substrate temperature

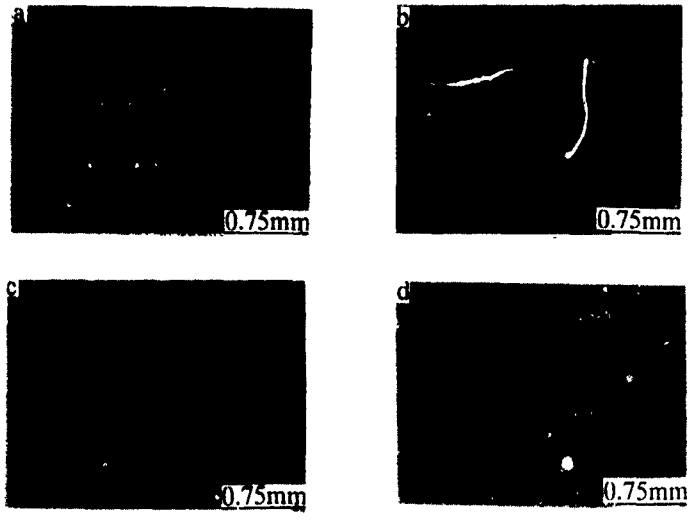



Fig.5 Photographs of typical Sebastion Pull-testing scars from films deposited at (a) 1173K (b) 1223K (c) 1273K and (d) 1323K

# EXCIMER LASER ETCHING AND POLISHING OF DIAMOND FILMS

A. Blatter and U. Bögli.
L.L. Bouilov, N.I. Chapliev, V.I. Konov, S.M. Pimenov, A.A. Smolin, I.V. Spitsyn.

Institute of Applied Physics, Sidlerstr. 5, CH-3012 Berne, Switzerland.
General Physics Institute and Institute of Physical Chemistry, USSR Academy of Sciences, Moscow, USSR.

Diamond films of various microstructures were prepared on W substrates by arc-discharge plasma CVD at different temperatures. The films were irradiated with KrF excimer laser pulses of fluences 1 - 9 J/cm$^2$. The irradiation-induced surface modification and etching of the films were studied. Etch rates between 10 and 300 nm/pulse were measured. During etching the surface roughness was observed to diminish by an order of magnitude. However, both the etching and polishing properties of the films depended on their growth conditions. The results indicate that etching is correlated with the purity of the films while polishing is limited by the grain size and growth morphology. In the case of pronounced columnar microstructures there was a particular distinctive polishing process. Smoothening and roughening processes were observed to occur simultaneously.

The benefits of using polycrystalline diamond films (DF) for applications in microelectronics and optics, as hard coatings, substrates and other purposes are apparent. For the realization of such applications it is necessary to develop methods for machining of the DF surfaces. The UV radiation of excimer lasers has been demonstrated to be an effective means for the micro-chemical dry etching of natural diamond (1) and DF (2). Etch rates as high as 300 nm/pulse with pulse repetition rates up to 40 Hz were reported. This must be compared with the 200 nm/min achieved with alternative ion etching (3). Furthermore, the laser induced etching was found to diminish simultaneously the surface roughness. Excimer lasers have therefore been considered as a valuable tool for the polishing of DF (2). In this paper we study processes and effects induced by KrF laser irradiation of diamond films. Films were prepared under different deposition conditions resulting in a variety of microstructures. We begin with the microstructural characterization of the DF. We then present results of laser induced etching and polishing, and discuss the dependence of these processes on the microstructures.

Polycrystalline diamond films of thickness 20 - 30 μm were grown from a methane hydrogen mixture on W substrates by use of the dc discharge plasma CVD-technique. The deposition temperature was varied by heating the substrates to 900, 1050, 1150, and 1200 $^{o}$C. All other deposition parameters were kept constant. The methane concentration was 3% and the deposition gas pressure 100 Torr.

The deposited DF were irradiated in air with 15 ns pulses from a KrF excimer laser ($\lambda$ = 248 nm). The laser radiation was apertured and slightly focused onto the DF surface to form uniform spots of size (60 x 120) $\mu m^2$. Each spot was irradiated with 1 to 1000 pulses at fluences ranging from 1 to 9 J/cm$^2$. The repetition rate was kept sufficiently low (1-10 Hz) in order to exclude any thermal interference of subsequent pulses. The photon energy of KrF (5 eV) is slightly lower than the band gap of diamond (5.4 eV). Absorption is therefore via non-diamond impurities and at high fluence via nonlinear effects.

The DF were analyzed before and after laser irradiation using scanning electron microscopy (SEM) and thin film x-ray diffractometry (Cu $K\alpha_1$). Microprobe Raman spectra were taken in the range from 1200 to 1700 cm$^{-1}$ with an accuracy of 1 cm$^{-1}$. Excitation was by means of the 488 nm line of an argon ion laser. The probe spot size was 2 μm. The low power of about 2 mW at the sample surface ruled out any laser effects on the films. Surface profiles were recorded using a stylus profilometer with a diamond tip of radius 1 μm.

The SEM analysis showed that DF grown below 1200 $^{o}$C consisted of partially twinned particles. The particle sizes were between 5 μm (deposition at 900 $^{o}$C) and 10 μm (1050 $^{o}$C). Planar octahedral and cube faces were visible. The DF deposited at 1200 $^{o}$C showed plate-like particles of widely varying sizes (0.5 - 10 μm) implying a dominant (100) morphology. Cross sections revealed a columnar growth type. The speckled contrast of the flat faces (which was also faintly visible at 900 $^{o}$C) marked the presence of graphitic impurities. We conclude that the best quality DF with the largest and most perfect grains resulted near 1050 $^{o}$C while the least quality was achieved at 1200 $^{o}$C.

The x-ray diffraction pattern of a film grown at 1050 $^{o}$C is shown in Fig. 1. It is dominated by the diamond peaks. The peaks due to the W substrate are also visible. All other peaks can be attributed to (WC)2H and ($W_2C$)12O. It substantiates the formation of an interfacial carbide layer in the beginning of the deposition process. The positions of the diamond peaks, though slightly shifted with

respect to those of diamond powder, did not obviously depend on deposition temperature. The relative intensities, however, did depend on the growth conditions, revealing a change in growth morphology. The line intensities of DF grown at 900 $^{o}$C were similar to the standard pattern of diamond powder. Only the (220) line, being somewhat too intense, reflected a slight deviation from random crystal orientations. The (111) line increased with deposition temperature indicating that the growth tendency changed from (110) to (111) morphology. The DF grown at 1200 $^{o}$C displayed an exceptionally strong (400) line, implying a marked (100) morphology. In comparison with the pattern shown in Fig. 1, some DF grown at 1200 $^{o}$C exhibited a weak and broad additional diffraction line identified as the 100% line of graphite structures. The presence of a substantial fraction of non-diamond carbon phases in such films was also evidenced by Raman spectroscopy.

In Fig. 2 are presented the Raman spectra of DF grown at 1050 $^{o}$C (a) and 1200 $^{o}$C (b). Both spectra display the diamond line (at 1327.4 and 1324.5 cm$^{-1}$, respectively) superimposed on a rising background.The background is due to photoluminescence arising from lattice defects and impurities. It was approximated by a quadratic polynomial, allowing better discrimination of the other components of the Raman spectra. Broad bands centered at 1350 and 1570 cm$^{-1}$ (b) reveal the presence of microcrystalline graphite and forms of disordered carbon in DF grown at 1200 $^{o}$C - in agreement with the x-ray data. Films grown at lower temperatures, on the other hand, showed only a faint band around 1580 cm$^{-1}$.

The shifts of the diamond lines to lower wavenumbers with reference to the 1332 cm$^{-1}$ standard line position can be attributed to tensile stresses in the DF of the order of 2 GPa (4). In contrast, a precise analysis of the x-ray patterns revealed that the diamond lattice constants were smaller than that of natural diamond by 0.075 - 0.2 %. Using the elastic moduli of diamond such contractions imply compressive stresses of the order 1 - 2 GPa. These opposing results can be reconciled if it is assumed that the bulk of the DF (seen by x-rays) is under compressive thermal stress while the surface (examined by Raman spectroscopy) is under tensile growth stress. It was recently shown that DF may in fact grow under tensile stress (5). During cooling after growth a thermal strain is generated due to the misfit of the thermal expansion coefficients. The expansion coefficient of diamond ($3 \cdot 10^{-6}$) is lower than those of W and WC (both about $4.9 \cdot 10^{-6}$) causing a compressive stress of the order of 2 GPa when cooled by 1000 $^{o}$C. While the thermal stresses mainly develop in the interface region and the bulk, it is likely that the tensile growth stresses survive at the surface.

The Raman spectrum shown in Fig. 2(c) is from the same DF as that of Fig. 2(a) after irradiation with 200 pulses of 7 J/cm$^2$. The characteristic diamond line has disappeared. Instead there are the two broad bands centered at 1360 and 1570 cm$^{-1}$. These show that the irradiated surface is covered by a microcrystalline graphite layer. When heated in air this layer sublimes. The results are strong evidence in favor of the two-stage process recently proposed for laser etching (1). The laser irradiation first induces a diamond to graphite conversion in a depth of the order 100 - 200 nm. Once formed, the graphite layer strongly absorbs the incident radiation, heats up and sublimes.

For the determination of etch rates the DF were irradiated with different numbers of laser pulses at various fluences. The etched depths were determined with the profilometer. At constant laser fluence they were found to increase linearly with the number of laser pulses. The etch depth divided by the number of laser pulses was taken to represent the etch rate. In fact the etched depths varied slightly across the irradiated area because the laser beam shape was not perfectly uniform. However, etch rates were identical whether determined by taking the maximum depth or an average depth inferred from the removed volume. The etch rates as a function of laser fluence for the various films are presented in Fig. 3. At higher fluences, linear fits serve as a guide to the eyes. It is seen that the etch rates at constant fluence are lowest for DF grown at 1050 and 1150 $^{o}$C. The extrapolation of the curves to zero etch rate gives an estimate for the threshold fluences of etching. Though the curves do not extend linearly into the low fluence regime - rather, they are the sum of Arrhenius-type functions - a rough estimate of the thresholds leaves no doubt about their variation with deposition temperature. The threshold is lowest (below 1.2 J/cm$^2$) for DF grown at the highest temperature. For films grown at 900 $^{o}$C, graphite formation but no etching occurred at 1.4 J/cm$^2$. The related threshold therefore is between 1.4 and 1.8 J/cm$^2$. The lower bounds for the DF grown at 1050 and 1150 $^{o}$C are 1.8 and 2.3 J/cm$^2$ respectively. In summary, the higher quality DF have higher thresholds and lower etch rates. In line with this, type IIA monocrystalline diamond exhibits even higher thresholds and lower etch rates (1).

The results suggest that the laser induced etching is limited by the purity of the DF. On the basis of the two-stage model for etching it is conceivable indeed that the non-diamond material contained in the DF governs the etching behavior. Absorption is similar for all DF as well as the diamond due to the surface graphite layer. The diffusion of the generated heat, on the other hand, is limited by the thermal conductivity of the sub-surface material. The thermal conductivity of microcrystalline and disordered carbon phases is significantly lower than that of diamond. It therefore is highest for the single-crystal dia-

mond, and it is higher for purer DF obtained at 1050 and 1150 $^{o}$C than for those grown at 900 and 1200 $^{o}$C. A higher conductivity means a lower rise of surface temperature at a constant fluence. This explains the variation of the thresholds for etching as a higher fluence is required to heat the graphite surface to its sublimation temperature. It also implies that the duration and hence the rate of sublimation is lower as the heat is extracted more rapidly from the graphite layer.

Surface profiles of a film grown at 900 $^{o}$C are shown in Fig. 4. The upper trace is from the non-irradiated surface. The lower trace is taken across an irradiated spot. A significant flattening of the irradiated surface is evident. In the SEM the irradiated surface appeared homogeneous and smooth. The origin of the smoothing process is not yet clear. Possible mechanisms resulting in polishing during laser-induced solid state evaporation are discussed in Ref. 6.

We quantify the roughness in terms of the roughness parameter $R_a$. For the determination of $R_a$ we limited the bandwidth of the surface profile data by means of Fourier methods. Spatial periods larger than 50 μm were discarded. This left the profiles of the virgin surface unchanged while some waviness of the irradiated surface due to the non-uniformity of the laser beam was largely removed. For the virgin surfaces $R_a$ parameters in the range of 0.5 - 0.65 μm (deposition at 900 $^{o}$C), 0.9 - 1.05 μm (1050 $^{o}$C), 0.65 - 0.8 μm (1150 $^{o}$C), and 0.5 - 1 μm (1200 $^{o}$C) were deduced. The values simply correlate with the grain sizes and their distribution. The true roughness of the non-irradiated surfaces is slightly underestimated because there are narrow cracks between the grains which are not fully resolved by the profilometer.

An inverse relationship between the $R_a$ parameter and the etched depth, which is given by the product of fluence and number of pulses, was found for all but the DF grown at 1200 $^{o}$C. The $R_a$ parameter decreased at a steadily lower rate with increasing etch depth At an etch depth of the order of 10 μm the polishing process virtually terminated. The $R_a$ parameter changed only marginally with further etching. It suggests that a minimum depth of the order of the particle size must be etched to achieve the smoothest surface. $R_a$ values of 0.1 - 0.12 μm (deposition at 900 $^{o}$C), 0.14 - 0.2 μm (1050 $^{o}$C), and 0.13 - 0.17 μm (1150 $^{o}$C) were typically obtained. The parameters achieved seem to correlate with the original roughness, i.e. with the grain size. However, further investigations with a greater variability of grain sizes are required to clarify and quantify this point.

The polishing behavior of DF grown at 1200 °C was entirely different. Rather than progressive polishing of the film with irradiation, an intermittent smoothening and roughening process was observed. The roughness parameter oscillated between 0.15 and 0.3 μm. This behavior is likely to be related to the particular growth morphology. In DF of columnar (100) morphology the inter-columnar spacing is filled with non-diamond material (7). This material is preferentially etched. Because of the preferential etching there is no uniform lateral polishing. Because there are several rows of columns there is also no uniform polishing through the film. This irregular polishing leads to the oscillatory smoothening/roughening procedure.

In conclusion we have found that KrF excimer laser induced dry etching and polishing of polycrystalline diamond films is dependent on their microstructures which are related to the conditions of deposition. Etching was observed in all films investigated. The process involves a diamond to graphite phase transformation followed by sublimation. Etch rates increase with laser fluence. Both the rate and threshold of etching are related with the purity of the diamond films. The purer the films the higher the thresholds and the lower the rates. During etching down to a depth of the order of a particle size the surface roughness decreased progressively by an order of magnitude. The final smoothness achieved seems to depend on the original grain size. An oscillatory behavior rather than continued polishing was found, however, in case of a pronounced (100) columnar growth morphology. This may be rationalized by the spatially inhomogeneous chemical and physical properties pertinent to such a microstructure.

This work was partly supported by the Swiss Commission for the Encouragement of Scientific Research.

(1) M. Rothschild, C. Arnone, D.J. Ehrlich, J. Vac. Sci. Technol. **B4**, 310 (1986).
(2) V.P. Ageev, L.L. Builov, V.I. Konov, A.V. Kuzmichev, S.M. Pimenov, A.M. Prokhorov, V.G. Ralchenko, B.V. Spitsyn and N.I. Chapliev, Sov. Phys. Dokl. **33**, 840 (1988).
(3) N.N. Efremow, M.W. Geis, D.C. Flanders, G.A. Lincoln, and N.P. Economou, J. Vac. Sci. Technol. B **3**, 416 (1985).
(4) D.S. Knight and W.B. White, J. Mater. Res. **4**, 385 (1989).
(5) B.S. Berry, W.C. Pritchet, J.J. Cuomo, C.R. Guarnieri, and S.J. Whitehair, Appl. Phys. Lett. **57**, 302 (1990).
(6) V.I. Konov and V.N. Tokarev, Sov. J. Quant. Electronics, 1991 (to be published).
(7) W.A. Yarbrough and R. Messier, Science **247**, 688 (1990).

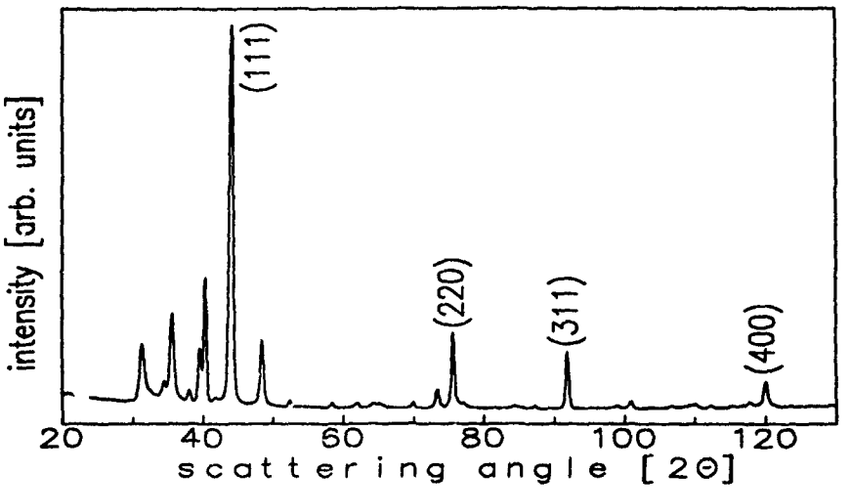



Fig. 1 X-ray diffraction pattern of a DF grown at 1050 °C. The diamond peaks are labelled.

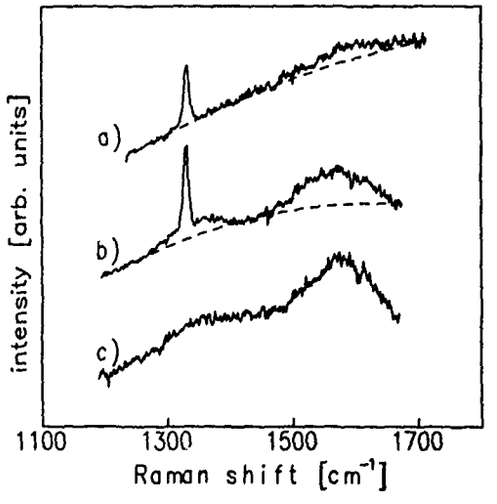



Fig. 2 Microprobe Raman spectra of DF. (a), deposition at 1050 °C; (b), deposition at 1200 °C; (c), same as (a) after laser irradiation. The broken curves approximate the photoluminescence background.

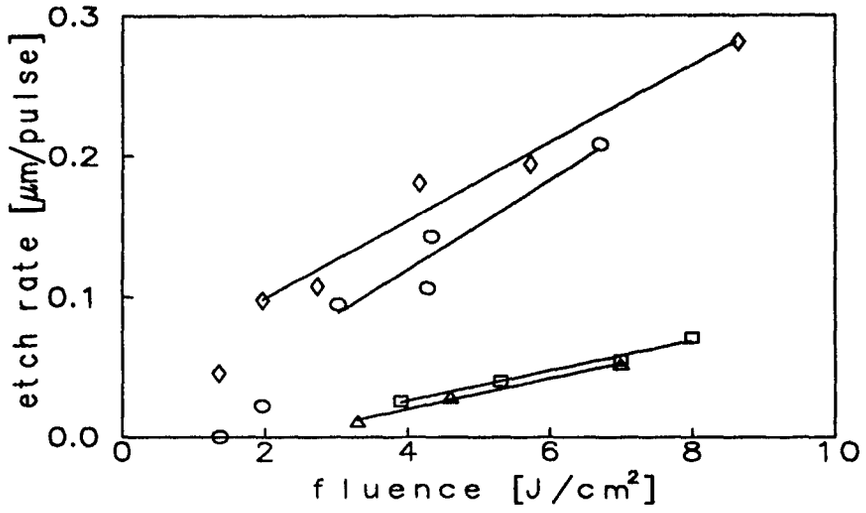



Fig. 3 Etch rates of DF grown at 900 °C (○), 1050 °C (□), 1150 °C (△), and 1200 °C (◇) as a function of laser fluence.

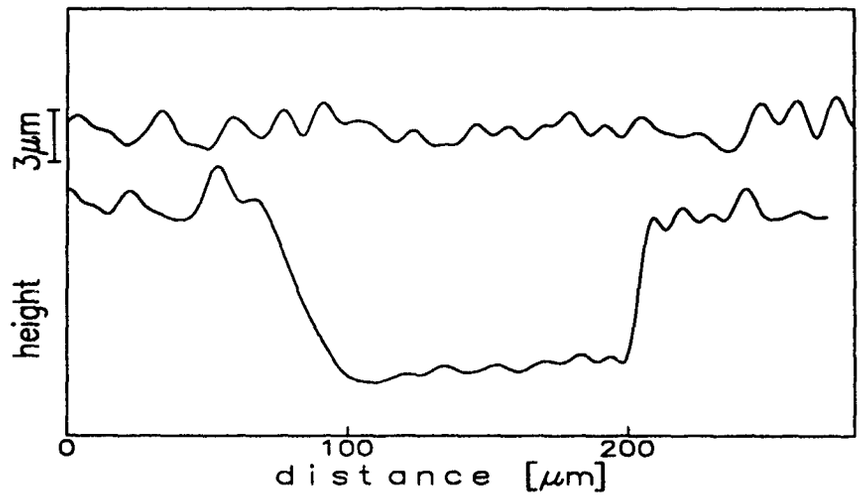



Fig. 4 Surface profiles of a DF grown at 900 °C. Top: non-irradiated surface, $R_a$ = 0.6 μm. Bottom: across an irradiated spot with $R_a$ = 0.1 μm.

# SEM TRIBOMETRY OF FLUORINATED CVD DIAMOND COATINGS

M. N. Gardos, B. L. Soriano
Hughes Aircraft Company, El Segundo, CA 90245
and
D. E. Patterson, R. H. Hauge,
J. L. Margrave
Rice University, Houston, TX 77251

## ABSTRACT

Polycrystalline CVD diamond films were fluorinated by direct fluorination and plasma techniques. SEM tribometry and surface chemical analysis were performed to characterize the thin fluorine-absorbate layers generated on the diamond films by (a) high temperature and UV-assisted $F_2$ gas and (b) $CF_4$/Ar plasma treatments. Direct fluorination achieved only partial coverage and did not result in significant chemical reaction between fluorine and carbon. No polytetrafluoroethylene (PTFE)-like $[-(CF_2)-]_n$ bonds could be found on the surfaces. The SEM tribometer test data indicated that direct fluorination did not significantly improve the tribological behavior of diamond; plasma fluorination was somewhat more promising. The more pronounced tribological enhancement, in terms of reduced friction, resulted from mechanically polishing the rubbing surfaces prior to testing and further run-in of the mating surfaces during testing.

## INTRODUCTION

Chemically vapor deposited (CVD) polycrystalline diamond films are excellent candidates for use in harsh tribological environments due to their reported hardness, low wear rate, high thermal conductivity and inert chemical nature. Furthermore, the potential applications have increased dramatically due to their reported superior or even "Teflon-like" frictional behavior (1, 2). Contrary to these reports, in extreme environments where CVD diamond is considered most promising, the frictional behavior may be far from ideal. In high temperature vacuum tests, the coefficient of friction (COF) of CVD diamond pairs was as high as 0.8 (3). These data suggest that surface modifications are necessary to enhance the tribological behavior before diamond can be used successfully in many harsh environments.

Our previous SEM tribometer data indicate that the adhesion, friction and to some extent, wear of diamond at high temperatures is controlled by the surface chemistry of the exposed crystallites (3). Desorption of surface species upon heating in vacuum under the electron beam create dangling bonds on the surfaces. Mechanically, dangling bonds are also generated when the respective materials are sheared tangentially under load. If these bonds did not reconstruct or were not satisfied (capped) by hydrogen or other benign adsorbates, then they interact with the sliding counterface to generate high (COF~ 0.8) friction forces. Enhanced adsorption of such adsorbates (e.g., on cooling the tribosystem in the relatively hydrogen-rich atmosphere of the turbomolecular-pumped SEM tribometer) annihilates unreconstructed dangling bonds, lowering the friction (COF~ 0.1). The friction trends also indicate that at high temperatures, in vacuum, the friction

may also become reduced by graphitization and by bond reconstruction on the sliding surfaces.

In light of the large effect of surface chemistry on the tribological behavior of CVD diamond, the objective of this work was to investigate surface modification techniques, namely polishing and fluorination, which would enhance the inert and tribochemically stable nature of the CVD diamond film surface in a wide range of environments. The effectiveness of fluorination in enhancing tribological behavior was evaluated by the following techniques:

1) X-ray photoelectron spectroscopic (XPS) analysis of certain samples to determine the degree of $[-(CF_2)-]_n$ bonding (if any) found on the surface; and
2) pin-on-flat SEM tribometry to measure the friction values of the fluorinated diamond vs. diamond test combinations.

## SAMPLE PREPARATION

Direct current (DC)-CVD diamond, ~1.5 μm thick with primarily {111} texture, was deposited on polished triboflats of bare, polycrystalline α-SiC, single crystal silicon (100) and single crystal sapphire. The sapphire was coated with a 100 μm Ti primer layer to promote adhesion prior to diamond deposition. The second side of each α-SiC flat was coated with an ~10 μm thick microwave (MW)-CVD diamond film of similar texture. This thick film was polished in air (by mechanical means, with diamond paste) to a ~0.15 μm RMS surface finish. The hemispherically tipped polycrystalline α-SiC tribopin (2 mm dia., 10 mm long) counterfaces were also coated with either an ~1.5 μm DC- or ~10 μm MW-CVD diamond, with no polishing treatment. After the diamond deposition and mechanical polishing (where applicable) was completed, the samples were fluorinated by one of the following techniques:

- direct, high temperature fluorination in $F_2$ gas; 340° to 530°C, 4 to 8 hours.
- UV-assisted fluorination, with 10 percent $F_2$ in He; 2 hours.
- plasma fluorination in 5 to 10 percent $CF_4$ in Ar plasma, 1 to 3 hours.

The harmful effects of fluorination are shown in Figure 1. The diamond layers extensively delaminated from the majority of the triboflats, indicating considerable substrate/diamond interface attack by fluorine through the microcracks and pinholes in the films. Most of the tribopin tip diamond coatings themselves suffered from microcracking during the treatment, although gross and catastrophic delamination was not observed. Some of the pins were still usable, microcracks notwithstanding. A description of the fluorination parameters and sample combinations is given in Table 1.

The SEM photomicrographs of the cracked but not delaminated diamond on the tip of the α-SiC pin indicated that the fluorination process may have indeed weakened the interface, via the cracks. The best explanation for diamond film delamination from the various substrates is based on fluorine attack of the DLC-like interfacial layer through cracks and pinholes in the film and not the underlying substrate since both atomic and molecular fluorine etches $sp^2$-bonded carbon components in diamond (4).

## X-ray Photoelectron Spectroscopic (XPS) Analysis

Prior to the tribotests, XPS analysis of one fluorinated diamond-coated α-SiC triboflat was performed on Sample B described in Table 1. For comparison, both the polished (Side 1) and unpolished (Side 2) surfaces were analyzed. We looked for the characteristic C and F binding energy shifts, which might indicate PTFE-like [-$(CF_2)_n$-] bonding between the diamond substrate and fluorine. Note that the binding energy of carbon (C1s) in this structure would be just below 292 eV; the equivalent energy of fluorine (F1s) is close to 689 eV.

The XPS survey of the unpolished Side 1 (Figure 2) showed a fluorine (F1s) binding energy of 687, below the characteristic 689 eV binding energy of the [-$(CF_2)_n$-] structure. The meager 8.9 percent F concentration on the surface dropped to 3.82 percent after a 15 second Ar ion etch, indicating ready desorption. There was some minimal shift of the binding energy peaks of the carbon peak (C1s) to higher eV values after argon etching, possibly due to some additional C-F bonding induced by the ion-etching process itself.

One very significant observation was that XPS verified the presence of both oxygen and fluorine on the polished and unpolished fluorinated diamond surfaces. In other XPS work, it was seen that the relative amount of oxygen decreases linearly with the increase in fluorine (5). This suggests that hydrogen directly bonded to carbon may not be as prominent on the diamond surface as previously believed, since fluorine should preferentially attack hydrogen, relative to oxygen, to evolve very stable HF. In that case, there would be no observable decrease of oxygen as the fluorine content increased. Also, there was no reported C-H stretching frequencies around 2900 $cm^{-1}$ in any of the IR spectra, unless the diamond was treated with $H_2$ in some fashion. The data suggest that oxygen and hydroxyl groups are the most predominant species on an untreated diamond surface. Peebles and Pope have confirmed the observation that hydrogen is not as prevalent there as originally believed (6). They reported that the bulk hydrogen content of these films is as low as 1 to 3 atomic percent, with near surface values typically only 1 atomic percent higher than the bulk. These finding are extremely significant, especially in view of the high starting friction of CVD diamond films in air, at room temperature. It is suspected that the oxidized diamond surface attracts moisture to a certain extent by hydrogen bonding and the surface is different from the bulk.

The XPS results on the polished side of the same triboflat confirm the substantive lack of reaction between C and F (Table 2, Figure 2b). However, there are some significant differences caused apparently by the polishing of diamond prior to fluorination:

1. Fluorine was present in greater concentration on the polished side (11.87 percent) compared to the unpolished side (8.9 percent), as shown in Table 2.
2. The oxygen content of the surface was also far greater (20.01 percent) than that of the unpolished surface (6.94 percent). One may attribute the larger F and O content of the surface to activation by polishing.

3. The cast iron polishing plate transferred some Fe to the diamond which must have penetrated the microcracks indicated by the increase in Fe content on Ar etching.

Fluorine's unwillingness to react with the diamond surface has been recently substantiated by Freedman and Stinespring's research (7). They fluorinated diamond (100) substrates with atomic (F) and molecular ($F_2$) fluorine in ultrahigh vacuum and found that (a) atomic fluorine reacts with an initial accommodation coefficient of 0.25 ± 0.1 at 300K, resulting in a saturation coverage of ~3/4 of a monolayer stable to 700K without desorption, and (b) molecular fluorine reacts even slower, with a saturation coverage of less than 1/5 monolayer, even at the exposure temperatures as high as 700K. In addition to fluorine's unwillingness to form [-$(CF_2)_n$-], it was shown by Hauge, et al (5), that the bond strength of fluorine to carbon was only incrementally higher than that of hydrogen during thermal desorption studies.

**SEM Tribometry**

The tribological behavior of the fluorinated diamond films was evaluated using an oscillating pin-on-flat tester. The test apparatus, a specially designed Knudsen-cell-type tribometer built into a SEM, is described elsewhere (3). The data are recorded and stored by VCR and a computerized data acquisition system. The procedure was similar to that previously utilized for testing as-deposited diamond films (3, 8). The SEM tribometer tests were performed with the following test parameters: a 50 g. normal load (0.49 N) and a 4.66 $mm \cdot s^{-1}$ oscillatory speed with an up-and-down temperature ramp (850°C maximum ). The tests were performed in 1.33 X $10^{-3}$ Pa ($10^{-5}$ torr) vacuum. When the samples did not delaminate rapidly, the tests were repeated in a partial pressure air ($P_{air}$) atmosphere of 13.3 Pa (0.1 torr).

The coefficient of friction traces, in vacuum and $P_{air}$, of the fluorinated-polished diamond (Sample B, Side 2) are shown in Figure 3. Similar to that of the as-deposited surfaces shown in Figure 4, the COF of fluorinated diamond also increases on heating in both vacuum and in $P_{air}$. However, due to the high shear stresses resulting from the increasing COF as the temperature increased, the film delaminated from the substrate (~ 900 cycles). Once delamination occurred, this combination became diamond versus α-SiC. The rapid increase in the COF during heating is presumably due to the progressive desorption of fluorine (and other residual adsorbates) and the simultaneous generation of dangling bonds, similar to what happens hydrogen desorption from the as-deposited surfaces. Spin-pairing of increasing numbers of unreconstructed dangling bonds on the respective contact surfaces results in higher adhesive friction forces (3).

Generally, in $P_{air}$, the fluorine-desorbed polished diamond exhibits higher friction than the unpolished, as-deposited sample. One exception, however, was the behavior of the polished-fluorinated sample at room temperature. Interestingly, the equilibrium COF at room temperature was lower (substantially below 0.1) and less variable than the unpolished, as-deposited films. We believe that the initially lower COF is mainly attributed to the worn-in nature (i.e., progressively smoother surface) of the as-grown diamond on the reused α-SiC pin during the second ($P_{air}$) test, sliding on a new wear

track of the same polished diamond flat. Because the tribopin surface was worn-in prior to the start of the second test, the contribution of Coulomb friction, caused by the climbing of the asperities on one surface over those on the counterface, was lower. This resulted in an overall decrease in the initial COF. This means that the COF is heavily affected by significant roughness and morphology differences between polycrystalline, CVD diamond films, resulting from different deposition techniques. For example, recent tribometry revealed (9) that rough diamond surfaces produced COF values up to an order of magnitude greater than smooth ones, when sliding against various solids, in air.

The COF results of unpolished-fluorinated diamond on Si (100) flat (Sample A) are shown in Figure 5 a, b and c. Similar to the as-deposited samples tested in vacuum, the room temperature equilibrium COF stabilized around 0.1. However, even at this low friction, the diamond film delaminated rapidly in the first and second test runs, as indicated by SEM observation. In the first test run, delamination occurred near 300 cycles, indicating that the smooth Si substrate exhibited lower friction than the rougher, diamond surface. During the second test run, the diamond began to peel around the 300th cycle also, followed by a COF increase characteristic to dehydrogenated (i.e., dangling bond-containing) diamond or silicon.

As compared to the high temperature UV assisted fluorinated sample B (Figure 3), the relatively greater tenacity of the $CF_4$/Ar plasma-generated, fluorine-containing film (Figure 6) is apparent in both runs 2 and 3 on the Si(100) flat. In test run 2, the COF does not substantially increase until 400 °C when the film begins to delaminate at ~ 300 to 400 cycles. This is compared to the immediate increase in COF upon heating for sample B which was fluorinated with a UV assisted process. The high tenacity of the fluorinated top layer was even more remarkable in the third test run. Here, the test combination was preheated prior to the onset of sliding (Figure 5c) to mitigate thermal ramp induced delamination and improve in-situ SEM imaging. At high temperatures, the COF remained low (COF $\cong$ 0.13), even though the temperature of the flat ranged from 600 °C to 850 °C to 600 °C during sliding. The diamond film did not delaminate until it was cooled down near 100 °C, as indicated by the drastic increase in COF at ~1560 cycles. No $P_{air}$ test was performed on this flat.

## CONCLUSIONS

Direct fluorination from the gas phase was unsuccessful in lowering the coefficient of friction or lengthening the wear life of polycrystalline CVD diamond films deposited on various substrates. Film adhesion was severely reduced by attack of the substrate-diamond interface by the fluorine gas, through the pinholes and cracks in the layers. Furthermore, XPS indicated a lack of substantive reaction between C and F on the sliding surfaces. The $CF_4$/Ar plasma-treated diamond may exhibit better resistance to desorption and rubbing then the UV-assisted treatment. A more pronounced effect is associated with that of polished versus unpolished rubbing surfaces. Polished diamond may thus serve better than the unpolished counterpart, at least at room-to-moderate temperatures, provided fluorine-containing (or hydrogen-hydrocarbon) species are continuously replenished on the sliding interfaces.

**ACKNOWLEDGEMENTS**

The authors would like to thank those people who have contributed their time and effort to this work. P.S. Davis, G.L. Meldrum and B. Buller of Hughes Aircraft performed SEM tribotests. D. Demeo, also of Hughes Aircraft Co. provided the XPS services. This work was performed under the auspices of the "Determination of Tribological Fundamentals of Solid Lubricated Ceramics Program", DARPA Order No. 5177, WRDC Contract No. F33615-85-C-5087, with B.D. McConnell acting as the WRDC Project Engineer. The specimens were coated by Crystallume, Menlo Park, CA, by L.S. Plano, S. Yokota and J. M. Pinneo.

## REFERENCES

1. A. Brown, Aerospace America, 25 (11), p. 12 (1987).
2. E. Corcoran, Sci. Amer., 261 (8), p. 62 (1989).
3. M. N. Gardos, and B. L. Soriano, J. Mater. Res., 5, pp. 2599-2609 (1990).
4. R. A. Rudder, J. B. Posthill and R.J. Markunas, "Thermal CVD of Homoepitaxial Diamond using $CF_4$ and $F_2$", Electr. Lett., 25, pp. 1220-1221 (1989).
5. D. E. Patterson, R. H. Hauge and J. L. Margrave, "Fluorinated Diamond Films, Slabs and Grit", Mater. Res. Soc. Symp. Proc. Vol 140, New Materials Approaches to Tribology: Theory and Applications, Eds. L. E. Pope, L.L Fehrenbacher and W.O. Winer, pp. 351-356 (1989).
6. D. E. Peebles and L. E.Pope, J. Mater. Res., 5, pp. 2589-2598 (1990).
7. A. Freedman and C. D. Stinespring, "Fluorination of Diamond (100) by Atomic and Molecular Beams", paper submitted to Appl. Phys. Lett., Apr.1990.
8. M. N. Gardos, and K. V. Ravi, in Proc. 1st. Symp. on Diamond and Diamond-Like Coatings (The Electrochem. Soc. Proc.), Vol. 89-12, pp. 475-493 (1989).
9. P. J. Blau, C. S. Yust, and R. E. Clausing, in Mechanics of Coatings, Proc. 16th Leeds-Lyon Symp. on Trib., Lyon, France, Trib. Ser. 17, Elsevier, Paper XVIII, pp. 399-407 (1989).

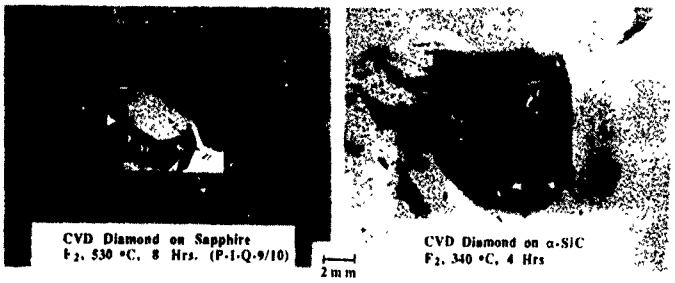



Figure 1. The appearance of fluorinated CVD diamond films on sapphire and α-SiC.

| TRIBOFLAT | FLAT | PIN | Evaluation Technique |
|---|---|---|---|
| Sample A | DC-CVD Dia. on Si (100) unpolished, ~1.5 μm thick 10% $CF_4$, Ar Plasma, 3 hrs. | DC-CVD Dia. on α-SiC unpolished, ~1.5 μm thick $F_2$, 350 °C, 4 hrs. | SEM tribometry |
| Sample B Side 1 | MW-CVD Dia. on α-SiC unpolished, ~1.5 μm thick 10% $F_2$ in He, UV, 1 hr. | --- | XPS |
| Sample B Side 2 | MW-CVD Dia. on α-SiC **polished**, ~10 μm thick 10% $F_2$ in He, UV, 1 hr. | DC-CVD Dia. on α-SiC unpolished, ~1.5 μm thick 10% $F_2$ in He, UV, 2 hrs. | XPS, SEM tribometry |

Table 1. Fluorination parameters and test combinations of CVD diamond film coated specimens.

| Sample B | Element (at. %) | C(1s) | N(1s) | O(1s) | F(1s) | Al(2p) | Si(2p) | Na(1s) | Fe($2p^3$) | Ca (2p) |
|---|---|---|---|---|---|---|---|---|---|---|
| Side 1 unpolished | No etch | 82.63 | 0.22 | 6.94 | 8.90 | 0.23 | 0.40 | 0.68 | - | - |
| | 15 sec | 92.19 | - | 1.86 | 3.82 | 0.30 | 0.56 | 1.28 | - | - |
| Side 2 polished | no etch | 62.44 | 0.48 | 20.01 | 11.87 | - | 2.15 | 0.61 | 2.45 | - |
| | 15 sec | 69.59 | 0.26 | 9.29 | 10.69 | - | 3.26 | 1.48 | 5.43 | - |
| | 30 sec | 71.80 | 0.28 | 8.01 | 9.19 | 1.14 | 2.95 | 1.40 | 4.60 | 0.63 |

Table 2. Atomic concentration table for polished and unpolished fluorinated CVD diamond, listed as a function of argon etch time.

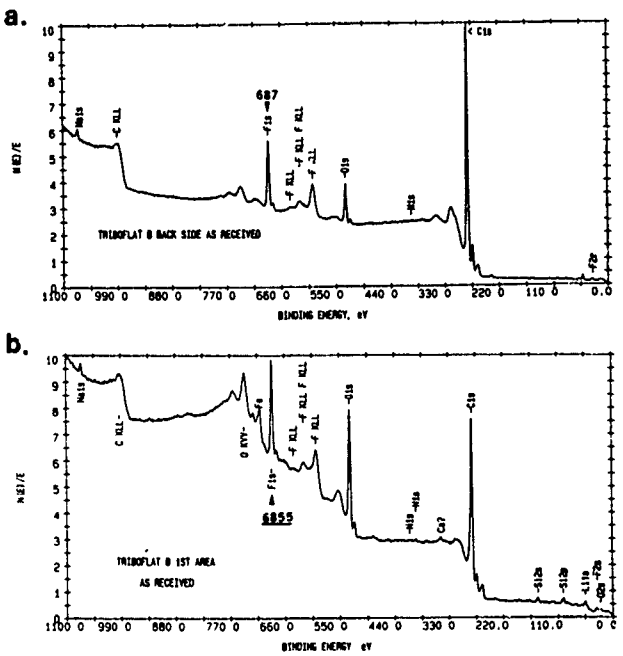



Figure 2. XPS spectra of fluorinated CVD diamond films: a) Sample B, Side 1 (unpolished) b) Sample B, Side 2 (polished).

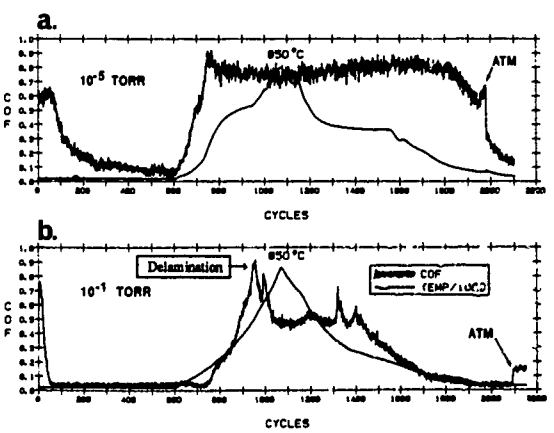



Figure 3. Coefficients of friction (COF) of unpolished-fluorinated diamond on an α-SiC pin vs. polished-fluorinated diamond on an α-SiC flat in vacuum and $P_{air}$.

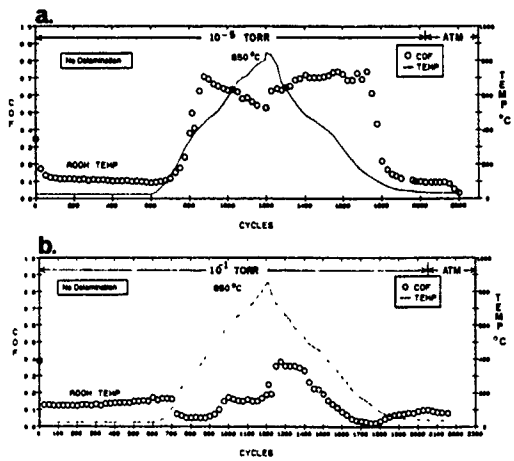



Figure 4. Coefficients of friction (COF) of as-deposited diamond on an α-SiC pin vs. as-deposited diamond on an α-SiC flat in vacuum and $P_{air}$.(3).

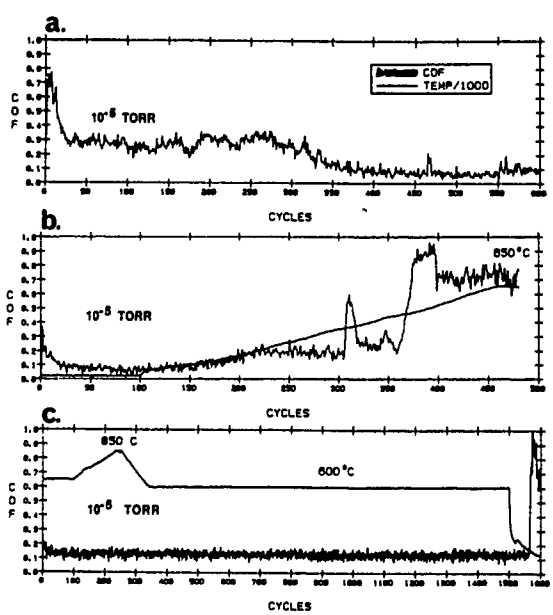



Figure 5. Coefficients of friction (COF) of unpolished-fluorinated diamond on an α-SiC pin vs. unpolished-fluorinated diamond on a Si(100) flat in vacuum: a) test run 1, b) test run 2, and c) test run 3 at elevated temperatures.

# TEMPERATURE AND BIAS EFFECTS ON THE PHYSICAL AND TRIBOLOGICAL PROPERTIES OF DIAMOND-LIKE CARBON.

**A.Grill, V.Patel and B.S.Meyerson**

IBM Research Division, T.J.Watson Research Center, Yorktown Heights, N.Y. 10598.

## ABSTRACT.

Diamond-like carbon films deposited by rf PACVD from acetylene at temperatures of 100 to 250 °C and -80 to -200 V DC have been annealed in vacuum at temperatures up to 590 °C for 3-4 hours. The hydrogen content of the films was found to decrease after annealing above 390 °C, yet approximately 20% hydrogen was retained in all the films after annealing at 590 °C. The index of refraction of as-deposited films or post-annealed at up to 390 °C was found to be independent of the deposition temperature for a given substrate bias, but increasing with increasing deposition power and decreasing bias. The $sp^2$:$sp^3$ carbon ratio increases with increasing annealing temperature, and only $sp^2$ bound carbon is identified in the FTIR spectra after annealing at 590 °C. The wear resistance in nitrogen of the as-deposited DLC is not affected by the deposition parameters in the investigated range. However, better stability to higher annealing temperatures was observed for DLC deposited at higher temperature or higher bias. DLC films deposited at 250 °C and -150 V, remain wear resistant in nitrogen even after annealing at 590 °C.

## INTRODUCTION

Diamond-like carbon, or DLC films, are metastable amorphous materials, composed primarily of $sp^2$ and $sp^3$ coordinated carbon atoms in a disordered network. DLC films have been prepared by a variety of methods including DC and rf plasma assisted CVD, sputtering, or ion beam deposition, from a variety of carbon bearing, solid or gaseous source materials (1-3). These films are characterized by extreme hardness, measured to be in the range 2000-9000 kg/mm$^2$, a generally low friction coefficient, between 0.01 and 0.28, as well as very high internal stresses (1). The films typically have high optical transparency over a wide spectral range, high electrical resistivity, and chemical inertness to both acids and alkalis.

Depending upon the precursor materials and preparation technique used for deposition, DLC films contain a significant amount of hydrogen, whose concentration has been shown to vary between less than 10% up to 50% (4). The hydrogen content critically determines film structure, e.g. the $sp^2$:$sp^3$ ratio and thus the properties of the films. Hydrogen content is also key to obtaining a wide optical gap ($E_{opt}$) and high electrical resistivity, as it passivates the dangling bonds in the amorphous structure (2).

The properties of DLC films are known to depend strongly upon both the deposition method and the specific deposition conditions. Deposition is generally done at relatively low

substrate temperatures, $T_d < 300$ °C, in that for substrate temperatures above 325 °C the bandgap goes to zero, ($E_{opt} \rightarrow 0$ eV) electrical resistivity declines rapidly ($\sigma \rightarrow 10^2\ \Omega^{-1}cm^{-1}$), and the films soften significantly (e.g.Meyerson and Smith [1]).

The unique properties of DLC films make them useful as protective coatings on metals, optical or electronic components, and in particular for applications where layers of order of 100 nm thickness or less are required. In present applications DLC films are employed at about room temperature, but one may envision applications requiring higher usage or post-deposition processing temperatures, where the thermal stability of DLC films becomes important.

Thermal stability has been previously examined for some DLC films (6-9), with emphasize on changes of the hydrogen content or infrared absorption. The general trend observed was a reduction in the hydrogen content in the films and changes in IR absorption with annealing temperature. However, the behavior of the films after thermal annealing appears to be dependent upon the preparation methods used by the different authors, similar to the properties of the as-deposited DLC films.

Given the dependence of the properties of DLC films on the specifics of the deposition system and chemistry, it is important to characterize the films deposited by a specific methodology (apparatus and precursor). This paper presents the characterization of DLC films deposited by rf PECVD from acetylene as a function of deposition parameters, their tribological properties, and the effect of thermal annealing on the properties of the films.

## EXPERIMENTAL

The presently discussed DLC films were deposited, as described in detail elsewhere (10).. by the rf plasma decomposition of acetylene, on Si(100) substrates at a bias between -80 and -200 V, rf power densities of 0.1 to 0.2 $mW.cm^{-2}$, and temperatures of 100 to 250 °C. The Si substrates were cleaned with electronic grade acetone and ethanol, and rinsed with 18MΩ DI water. Prior to deposition, the substrates were additionally in-situ sputter cleaned in an argon plasma. Following deposition, the DLC layers were annealed under vacuum for up to four hours at temperatures up to 590 °C.

The index of refraction of the DLC films was measured by ellipsometry at $\lambda$ = 6238 Å. Infrared absorption was measured between 1000 and 4000 $cm^{-1}$ using a Fourier transform infrared spectrometer (FTIR) at a resolution of 4 $cm^{-1}$ as described in detail elsewhere (11). The hydrogen content of the DLC films was determined by the forward recoil elastic scattering method (FRES) using a 2.3 MeV $^4He$ beam and fitting the calculated energy distribution of the recoiled atoms to the experimental data (12), by adjusting the hydrogen concentration in the calculations.

The wear resistance and friction coefficients of thin DLC films were investigated using a specially designed pin-on-disk type tribotester (13). The tribotester was contained in a box where the humidity was controlled by continuous purging with dry nitrogen. The wear of Si wafers coated with DLC films was measured against stainless steel riders (440C ball bearings). A load of 0.088N (9g) was applied to the riders of a diameter of 0.794cm, corresponding to an initial Hertzian stress (14) of 215 MPa. The wear test was performed by running the apparatus for a preset number of rotations and measuring the resulting wear tracks with a profilometer.

## RESULTS and DISCUSSION

Consecutive FRES measurements at the same spot on DLC films deposited at 100 °C showed a decrease of the hydrogen content as a result of the bombardment with the energetic ion beam, as shown in Figure 1. This behavior indicates the existence of a polymeric component, which decomposes under the bombardment with the energetic ions. A similar behavior was observed previously for DLC films deposited at 30 °C and to some extent for films deposited at 150 °C (15). however it is not observed for the films deposited at temperatures in excess of 180 °C, for which the FRES data remains constant during consecutive measurements at same position on the films.

Figure 2 shows the hydrogen concentration in DLC films deposited at a substrate bias of -80 V and three different substrate temperatures, as a function of annealing temperature. The concentration values are accurate to ± 2 %. Identical behavior to that presented in Figure 2 was observed for films deposited at -150 V DC bias, indicating that the change of the substrate bias from -80 to -150 V does not affect the amount of hydrogen incorporated in the film. As can be seen, the hydrogen concentration in the films is not affected by annealing at 390 °C and starts to decrease only after annealing the film above 440 °C, reaching essentially identical values of hydrogen content in all films, independent of their deposition conditions. After annealing at 590 °C for 3 hours, the DLC films deposited in the present work still retain approximately 22% hydrogen. Couderc and Catherine (8) also found retention of hydrogen in DLC films deposited at certain conditions after annealing at 800 °C, while for films deposited at other conditions complete removal of hydrogen was observed after annealing at 600 °C (8,9). However, due to the different deposition parameters used by the various authors, it is not possible to perform a one to one comparison of their work in an effort to isolate what aspect of film growth determines the hydrogen stability in the annealed films.

The infrared absorption peaks of DLC (at 2100-3100 $cm^{-1}$ and at 1400-1500 $cm^{-1}$) should provide an indication of the hydrogen content in the films and has been used to determine its bonding to $sp^2$ or $sp^3$ carbon atoms (16). Figure 3 presents the relevant regions of the IR absorbance spectra of DLC films deposited under three different combinations of temperatures and bias, as a function of the annealing temperature. Additional FTIR data for DLC films deposited at other temperatures can be found elsewhere (11). The identification of the absorption peaks, according to (16,17) is presented in Table I. As can be seen in Figure 3, the spectra of the as-deposited films are similar for all deposition conditions. The peak at 2800-3000 $cm^{-1}$, corresponds to a superposition of stretching vibrations of C-H with hydrogen bonded to $sp^3$ carbon, while the peaks at 1450 $cm^{-1}$ and 1370 $cm^{-1}$ correspond, respectively, to the asymmetrical and symmetrical deformation frequencies of $C-CH_3$. A small absorption peak is observed in some cases at 1700 $cm^{-1}$. This peak is identified as corresponding to C=O vibrations in the -COOH group (17). As AES measurements showed that the bulk of the DLC films does not contain oxygen, both before and after annealing, the peak at 1700 $cm^{-1}$ is probably caused by oxygen adsorbed on the surface of the films or at the film-substrate interface.

Previous high resolution NMR spectroscopy showed that DLC films deposited at 250 °C and -80 V contain carbon in the two bonding states $sp^2$ and $sp^3$, at a ratio $sp^2:sp^3 \approx 3:2$ and that hydrogen was bound in that film in almost equal parts to the two differing coordinations of carbon atoms (15). However the FTIR spectra of the as-deposited films do not show an absorption peak corresponding to the $sp^2$ CH stretching mode at 3045 $cm^{-1}$. The high resolution

NMR spectroscopy provides well separated peaks for the two carbon coordinations, $sp^2$ and $sp^3$ and has the ability to determine accurately both the ratio of carbon atoms in the two configurations and the relative distribution of hydrogen on carbon atoms in each coordination. The FTIR spectra could therefore not be used for the determination of the $sp^2/sp^3$ ratio in the present DLC films. Nevertheless they provide information on the relative behavior of the films as a function of deposition conditions or annealing temperatures.

As can be seen in Figure 3, the major change occurring in the IR spectra of the DLC films after annealing them at 390 °C is the appearance of the stretch peak of conjugated aromatic C=C $sp^2$ carbon at 1600 $cm^{-1}$, without a significant change in the intensity of the peak at 2800-3100 $cm^{-1}$. This result is consistent with the FRES results (Figure 2) and indicates that the major change resulting from annealing at 390 °C is the reorganization of carbon atoms in local graphitic coordination, without a significant loss of hydrogen from the films. Only after annealing above 450 °C does the hydrogen peak corresponding to hydrogen bound to $sp^3$ C decrease, while the peak of the $sp^2$ CH stretch mode appears at 3045 $cm^{-1}$. This is accompanied by a further increase of the C=C peak at 1600 $cm^{-1}$ and a decrease in the peaks of C-$CH_3$ at 1450 $cm^{-1}$ and 1370 $cm^{-1}$. The similarity of the spectra of DLC films deposited at 250C for biases either -80 and -150 V (Figure 3 (b) and (c)) indicates identical hydrogen bonding in the films deposited at different biases.

After annealing at 590 °C, only a small peak at 3045 $cm^{-1}$, corresponding to $sp^2$ CH, and the peak at 1600 $cm^{-1}$, corresponding to $sp^2$ C=C are observed in the IR spectra. The FRES results indicated that about 22% hydrogen remains in the films after annealing at 590 °C. The FTIR peak at 3045 $cm^{-1}$ indicates that a significant fraction of it is hydrogen bound to $sp^2$ coordinated carbon. It should be emphasized that the changes occurring during annealing take place at lower annealing temperatures for films deposited at the lower temperature (see Figure 3 (a) and reference (11)). This may be correlated to the break-up of the polymeric fraction existent in DLC deposited at lower temperatures.

The index of refraction of the films deposited at a substrate bias of -80 V and rf power density of 0.1 $W.cm^{-2}$ was found to be insensitive to deposition temperature, and was measured as $n = 1.9 \pm 0.2$ (11). It was found, however, to increase with deposition power, at constant bias, but to decrease with increasing bias, at constant power (18). The decrease of the index of refraction with increasing bias, at constant power, does not contradict other reports of increasing index of refraction with increasing bias because in those cases the self-bias has been increased by increasing the applied rf power (e.g. references (19-21)). It appears therefore that the effect related to the bias in previous works was in fact an effect of the power (and eventually pressure).

Figure 4 presents the index of refraction of three DLC films, deposited at different conditions, as a function of annealing temperature. As can be seen, the index of refraction remains nearly constant with annealing temperatures up to 390 °C, independent of deposition temperature and substrate bias. Annealing at temperatures above 390 °C results in an increase of the index of refraction for films deposited at 100 °C, while the index of refraction starts changing only at temperatures above 440 °C, for the films deposited at 250 °C. However, after annealing above 440 °C, the indexes of refraction of the film deposited at 100 °C and -80 V and of the film deposited at the larger negative bias of -150 V and 250 °C increase much faster than the index of refraction of the film deposited at 250 °C and -80 V.

The correlation between the index of refraction and hydrogen content is presented in Figure 5 for the same films as in Figure 4. For a given set of deposition conditions, the index of refraction increases with decreasing hydrogen content, as was also reported by other authors (20,21). However, in our case, for identical hydrogen content, the index of refraction of the as-deposited or annealed DLC is dependent on the deposition conditions and different values of index of refraction are obtained at same hydrogen content.

These results indicate that DLC films deposited under different conditions of the present study, yet containing the same amount of hydrogen, have different distributions of the hydrogen among the $sp^2$ and $sp^3$ carbon, and different ratios of $sp^2/sp^3$ C in the films. This, however, was is not reflected in the IR spectra, and has to be further investigated by high resolution NMR. The behavior of the refractive index (Figure 4) together with the FTIR results (Figure 3) demonstrate that DLC films deposited at high substrate temperatures are stable to higher annealing temperatures.

The value of the static friction coefficients of the as-deposited DLC films is 0.20±0.05. The changes observed in the friction coefficients after annealing the films were essentially within the experimental error. Nevertheless, it appears that the smallest changes in the friction coefficients after annealing occurred in the films deposited at -150 V and 250 °C, indicating again, that deposition under this conditions results in a DLC film that is stable to higher temperatures. Figure 6 shows the initial record of the friction coefficient between a steel ball (440C) and a bare silicon wafer, and the steel ball and a silicon wafer coated with DLC. As can be seen, the friction coefficient with DLC is less than half that with silicon and the friction between the steel and DLC is characterized by a strongly reduced stick-slip behavior (indicated by the spread between the maxima and minima of the friction coefficient).

The effect of coating the silicon wafer with DLC on the wear of the wafer is illustrated in Figure 7 which shows the profiles of wear tracks obtained in the pin-on-disk tribotester on silicon, after 30,000 passes, and on DLC, after 250,000 passes. The depth scale in Figure 7 (a) is 100 times larger than in (b). The results show that by coating the Si wafer with DLC, wear is greatly reduced. In addition, considerable wear was observed on the steel rider after the wear test on silicon, while no wear could be seen on the steel rider after the wear test on DLC. By preventing the wear and formation of fracture particles from the worn surface of the disk, the DLC film protects also the uncoated (softer) steel rider from wear.

The wear of DLC films is presented in Figure 8 as a function of the annealing temperature. The wear is expressed, on a logarithmic scale, in track depth per $10^4$ rotations in the tribotester. The wear tracks were obtained after 260,000 rotations. The bars extending over the whole height of the box indicate that the respective DLC films were completely worn-through after only a few thousand rotations. As can be seen, the as-deposited films showed very little wear, independent of the deposition temperature, with the film deposited at a bias of -150 V DC having only a negligible amount of wear. After annealing at 390 °C, the films deposited at -80 V DC, at 100 and 180 °C had little wear resistance, and were completely worn through after a few thousand rotations. The film deposited at -80 V DC and 250 °C and annealed to 440 °C, did wear at a higher rate than the as-deposited film and was worn-through after annealing at 490 °C. On the other hand, the wear of the DLC film deposited at 250 °C and -150 V was negligible after annealing at 390 °C, increased after annealing at higher temperatures, but remained low even after annealing at 590 °C for three hours (see Figure 8). Thus, while the other characterization

methods revealed only small changes in the DLC films after annealing at 390 °C, with almost no differences between the films deposited at the various temperatures and same bias, wear testing showed that only the film deposited at the higher temperature or higher bias is still wear resistant after annealing for four hours at 390 or 440 °C.

Few papers report the effect of the deposition temperature on the properties of DLC films. It was for example reported (1,5) that the optical gap decreases with increasing substrate temperature, with a rapid decrease above 250 °C. The deposition is most probably controlled by the interaction between the radicals produced in the plasma and the surface. This interaction may in turn be affected by the coverage of the surface with atomic hydrogen, as in the case of a-Si:H deposition (22). According to Catherine (23), the growth rate is indeed intermediated by a layer adsorbed at the surface. Higher deposition temperatures apparently reduce the hydrogen coverage of the surface which then affects the growth rate and the properties and structure of the deposited film.

The results show that an increase of the negative surface bias from 80 to 150 V causes significant improvement in the wear resistance and thermal stability of the films, making them less sensitive to annealing. Though the hydrogen content (Figure 2), the index of refraction (Figure 4), and the IR spectra (Figure 3 (c)) of the film deposited at the higher bias all change with increasing annealing temperature, indicating modifications in the structure of the film, these modifications have little effect on the friction coefficients and the wear behavior of the as-deposited films. The comparison of the mentioned physical properties of the films deposited at the higher bias with those of the films deposited at the lower bias does not indicate that one has to expect a different wear behavior of the DLC films. However, the observed behavior of the friction coefficient and of the wear rates indicates that the films deposited at higher bias have significantly different local structures, in the as-deposited and annealed state, than the films deposited at the lower bias. I that films deposited at one temperature but different biases contain the same amount of hydrogen, it is again clear that what is changing is the local atomic coordination, and the films may have significantly different ratios of $sp^2$ and $sp^3$ carbon.

The effect of bias on DLC properties has been investigated before by different authors (8,19,24-27), and the bias has been found to affect the structure or hardness of the films. However, there appears to be no systematic study of the effect of the bias on the structure and bonding (e.g. $sp^2/sp^3$) in the films. To what extent this happens has to be determined by a method more sensitive to structure than FTIR, or even Raman spectroscopy. High resolution NMR, with the proton decoupling option, may eventually be able to elucidate the difference in the structure and its relation to wear behavior between DLC films deposited under different conditions.

## CONCLUSIONS

Annealing in vacuum up to 390 °C of DLC films deposited by rf decomposition of acetylene has only slight effects on their optical properties or hydrogen content. Annealing at higher temperatures results in a reduction in the hydrogen content and an increase in the index of refraction, with larger changes found for films deposited at lower temperatures or lower biases. About 22% hydrogen is retained in the films after annealing at 590 °C for three hours. The index of refraction increases with decreasing hydrogen content in the films but is also dependent on the deposition conditions, at a fixed hydrogen content.

After annealing at 390 °C, films deposited at 15 W and -80 V, and at temperatures of 100 °C and 180 °C provide no wear resistance. Films deposited at 250 °C are still wear resistant after annealing at 440 °C, and films deposited at 23 W, -150 V and 250 °C remain wear resistant even after annealing at 590 °C. The results indicate that the DLC films deposited at higher temperature or bias are more stable to higher annealing temperature.

Although IR absorption indicates similar structures for the films deposited under different conditions, the wear behavior of the as deposited and annealed films is strongly dependent on the deposition conditions, reflecting differences local atomic structure of the films.

**Table I.** IR absorption frequencies in Diamond-Like Carbon.

| Line | Wavenumber | Assignment | Type |
|---|---|---|---|
| | ($cm^{-1}$) | | |
| a | 3045 | $sp^2$ CH | stretching |
| b | 2960 | $sp^3$ $CH_3$ asymm. | stretching |
| c | 2920 | $sp^3$ $CH_2$ | stretching |
| d | 2875 | $sp^3$ $CH_3$ symm. | stretching |
| e | 1600 | $sp^2$ C=C conjugated | stretching |
| f | 1450 | C-$CH_3$ asymm. | deformation |
| g | 1370 | C-$CH_3$ symm. | deformation |

## REFERENCES


[1] J. C. Angus, P. Koidl, and S. Domitz, in *Plasma Deposited Thin Films*, edited by J.Mort and F.Jansen (CRC Press Inc., Boca Raton, FL. U.S.A., 1986), p. 89.

[2] H. Tsai and D. B. Bogy, J.Vac.Sci.Technol. **A5**, 3287 (1987).

[3] A. Grill, B. S. Meyerson, and V. Patel, in *Diamond Optics, Proc.SPIE*, edited by Albert Feldman and Sandor Holly (SPIE, Bellingham, WA, 1989), Vol. 969, p. 52.

[4] M. J. Mirtich, D. M. Swec, and J. C. Angus, Thin Solid Films **131**, 245 (1985).

[5] B. Meyerson and F. Smith, J.Non Cryst.Solids **35/36**, 435 (1980).

[6] B. Dischler, A. Bubenzer, and P. Koidl, Solid State Commun. **48**, 105 (1983).

[7] S. Kanazawa and K. Ebihara, in *Proc. 9th Int.Symp. on Plasma Chemistry*, edited by R.d'Agostino (IUPAC, Sept.,1989), p. 1473.

[8] P. Couderc and Y. Catherine, Thin Solid Films **146**, 93 (1987).

[9] J. Gonzalez-Hernandez, B. S. Chao, and D. A. Pawlik, J.Vac.Sci.Technol. **A7**, 2332 (1989).

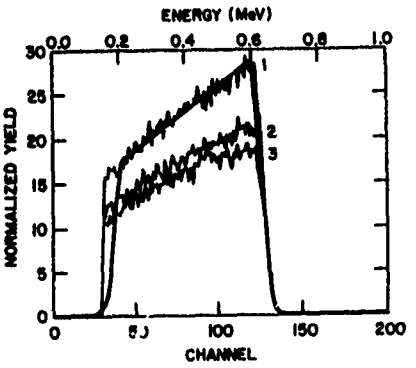
[10] A. Grill, B. Meyerson, and V. Patel, J.Mater.Res. **3**, 214 (1988).

[11] A. Grill, V. Patel, and B. S. Meyerson, J.Mater.Res. **5**, 2531 (1990).

[12] A. Turos and O. Meyer, Nucl.Instr.and Metods in Phys.Res. **B4**, 92 (1984).

[13] A. Grill, B. S. Meyerson, and V. V. Patel, *IBM Report RC 13117*, IBM Research Division, Yorktown, NY, 1987.

[14]J. Hamrock and D. Brewe, J.Lubrication Tech. **105**, 171 (1983).
[15]A. Grill, B. Meyerson, V. Patel, J. A. Reimer, and M. A. Petrich, J.Appl.Phys. **61(8)**, 2874 (1987).
[16]B. Dischler, R. E. Sah, P. Koidl, W. Fluhr, and A. Wokaun, in *Proc.7th Int.Symp. on Plasma Chemistry*, edited by C. J. Timmermans (IUPAC, Eindhoven, July,1985), p. 45.
[17]L. J. Bellamy, *The Infra-red Spectra of Complex Molecules* (Chapman and Hall, London, 1975), pp. 14, 38, 74, 184.
[18]A. Grill, V. Patel, and B. S. Meyerson, in *Diamond and Diamond-like Films and Coatings, NATO-ASI Series*, edited by John C. Angus, Robert E. Clausing, Linda L. Horton, and Peter Koidl (Plenum Publishing Corp., New York).
[19]A. Bubenzer, B. Dischler, G. Brandt, and P. Koidl, J.Appl.Phys. **54**, 4590 (1983).
[20]T. J. Moravec and J. C. Lee, J.Vac.Sci.Technol. **20**, 338 (1982).
[21]P. Koidl, C. Wild, R. Locher, and R. E.Sah, in *Diamond and Diamond-like Films and Coatings, NATO-ASI Series*, edited by John C. Angus, Robert E.Clausing, Linda L.Horton, and Peter Koidl (Plenum Publishing Corp., New York).
[22]C. C. Tsai, J. C. Knights, G. G.Chang, and B. B.Wacker, J.Appl.Phys. **59**, 2998 (1986).
[23]Y. Catherine, in *Diamond and Diamond-like Films and Coatings*, edited by John C. Angus, Robert E. Clausing, Linda L. Horton, and Peter Koidl (Plenum Publishing Corp., 1991).
[24]K. Enke, Thin Solid Films **80**, 227 (1981).
[25]S. Kaplan, F. Jansen, and M. Machonkin, Appl.Phys.Lett. **47**, 750 (1985).
[26]R. Kato, K. Hiraoka, and K. Masuhara, in *Proc. 9th Int.Symp. on Plasma Chemistry*, edited by R.d'Agostino (IUPAC, Sept.,1989), p. 1456.
[27]P. Wood, T. Wydeven, and O. Tsuji, in *Proc. 9th Int.Symp. on Plasma Chemistry*, edited by R.d'Agostino (IUPAC, Sept.,1989), p. 1485.



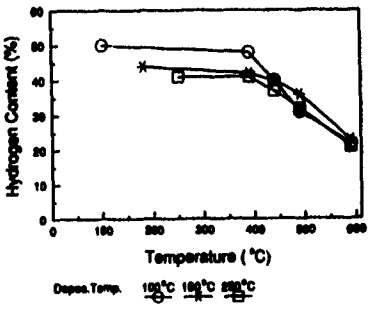




**Figure 1.** **(left) FRES results for a DLC film deposited at 100 °C:** The ragged lines show the experimental data; the smooth line is the calculated fit to the data group 1. The numbers indicate consecutive measurements on same spot.

**Figure 2.** **(right) Variation of hydrogen content with annealing temperature.**

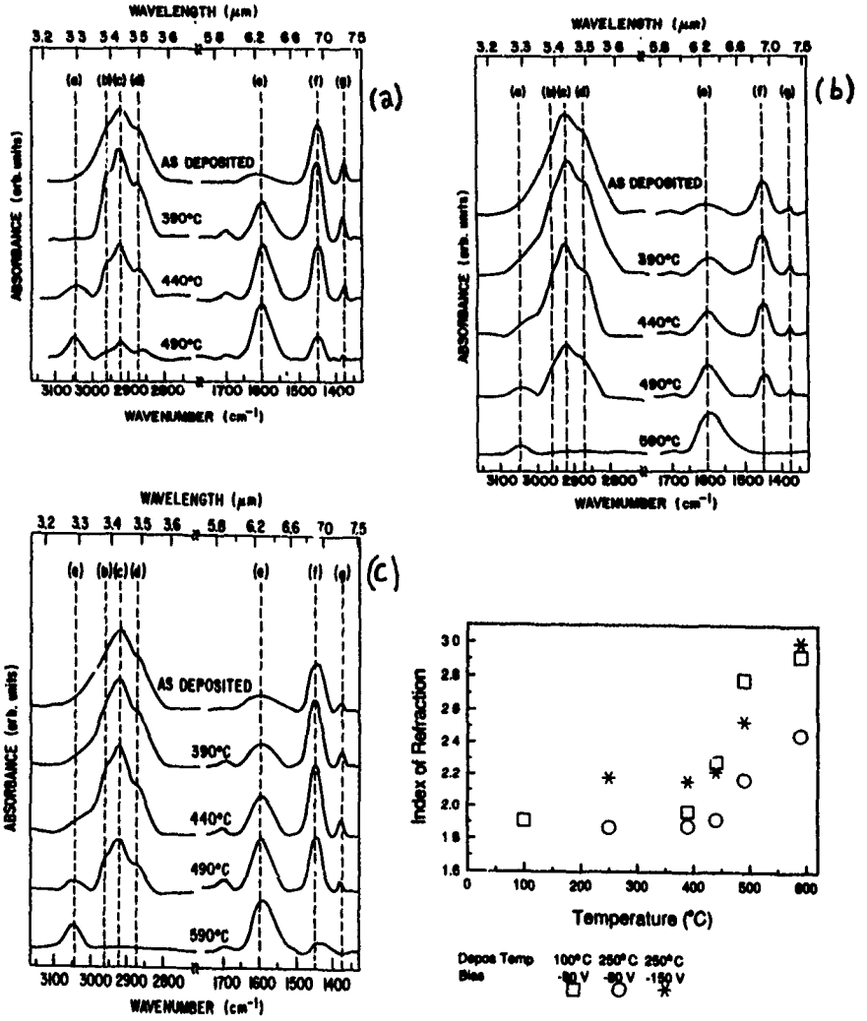



**Figure 3. IR absorbance spectra of DLC vs annealing temperature.:** (a)-DLC deposited at 100 °C and -80 V; (b)-DLC deposited at 250 °C and -80 V; (c)-DLC deposited at 250 °C and -150 V;

**Figure 4. (bot.right) Variation of index of refraction with annealing temperature.**

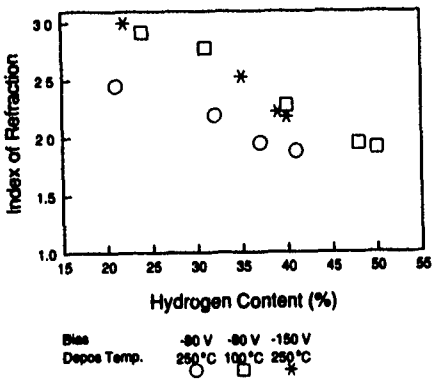



Figure 5. Index of refraction vs hydrogen content.

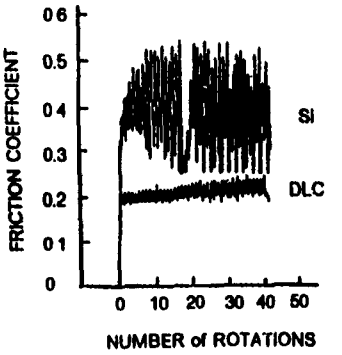
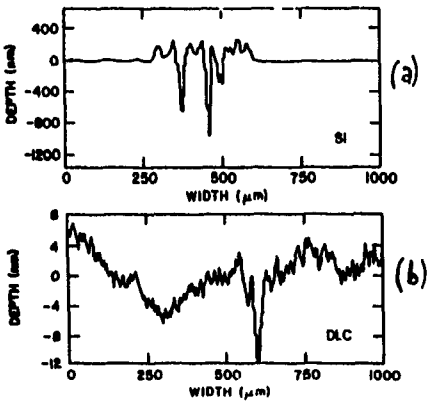



Figure 6. Friction coefficients vs number of rotations



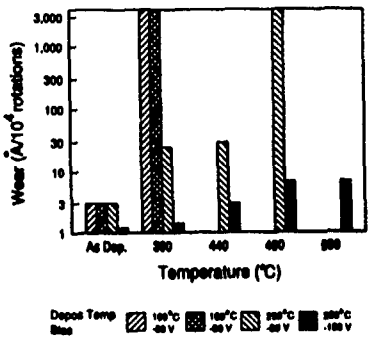




Figure 7. (left) Profiles of wear tracks produced by a steel rider on Si and DLC: (a) on Si after 30,000 passes; (b) on DLC, after 250,000 passes

Figure 8. (right) Wear of DLC films vs annealing temperature

# ATOMIC COORDINATION AND MACROSCOPIC PROPERTIES OF HYDROGENATED DIAMONDLIKE CARBON

M. A. Tamor and K. R. Carduner

Research Staff, Ford Motor Company, SRL MD-3028
Dearborn, MI 48121-2053

## ABSTRACT

Carbon bonding environments in plasma-deposited hydrogenated amorphous carbon (a-C:H) have been examined by nuclear magnetic resonance (NMR) spectroscopy. These local measurements of carbon bonding are connected to the elastic properties of a-C:H through the random covalent network concept of Phillips and Thorpe. It is shown that a-C:H consists of a slightly overconstrained random network in which small graphitic clusters, which determine the optical properties, are embedded.

## INTRODUCTION

Thin films of hard carbon materials are rapidly gaining in technological importance.[1] While true diamond can be produced by chemical vapor deposition, the required growth environment is destructive to many substrates of interest. Amorphous carbon, although not as hard as diamond, can be produced at or below room temperature. Hydrogenated amorphous carbon (a-C:H) can be deposited from hydrocarbon vapor by plasma or ion-beam, while hydrogen-free material (a-C) can be formed by a variety of ion-beam, arc-plasma and laser-plasma techniques. Despite popular use of the term "diamondlike" in reference to hard, insulating amorphous carbon films, the degree to which the observed properties of "diamondlike" carbon (DLC) reflect an "amorphous diamond" structure (analogous to amorphous silicon) is unclear and highly controversial. To date, the degree of "diamondlike" character has been inferred from measurements of dielectric response (optical gap, electron-energy loss) and film hardness and density. However, Tamor and Wu have demonstrated how a structure composed of very little quaternary carbon might exhibit the same properties that are cited as evidence for an "amorphous diamond" structure.[2] Thus, more direct probes of local atomic structure are required. Here we describe results of a systematic study of atomic coordination in a-C:H by nuclear magnetic resonance spectroscopy.

## EXPERIMENT

### NMR

Hydrogenated amorphous carbon films were deposited from an RF-biased methane plasma (50 mT) at several bias voltages ranging from 0 to 1000 V. Solid-state $^{13}C$ magic angle spinning (MAS) NMR spectra were acquired at 75.5 MHz in a Bruker MSL 300 spectrometer equipped with a Bruker MAS probe with a spinning speed of 4.5 kHz. It was found that with sufficient sample mass (100 mg) and long averaging times (48 h) the natural abundance of $^{13}C$ was sufficient to obtain quantitative spectra. A series of pulse sequences were tested in the search for conditions which ensured quantitative spectra of different carbon bonding environments. Following this investigation, spectra were obtained using two sequences: (1) acquisition following a single $90^{o}$ pulse under high-power proton decoupling (HPPD) and (2) the same using 60 $\mu$s of interrupted decoupling. Four classes of carbon bonding environments can be resolved: three-fold with protonation (aromatic or olefinic), three-fold without protonation (graphitic), four-fold with protonation (aliphatic or methine) and four-fold without protonation (quaternary, as in diamond). The fractions of each are labelled $f_3^H$, $f_3^C$, $f_4^H$, $f_4^C$ respectively, and normalized such that $f_3^H + f_3^C + f_4^H + {}_4^C = 1$. The inferred hydrogen content, $X_H$ and four bonding fractions are shown as a function of $V_b$ in Figs. 1a and 1b.

### Hydrogen Content

The hydrogen content (atomic fraction, $X_H$) was determined from the NMR data as:

$$X_H = (Af_3^H + Bf_4^H)/(1 + Af_3^H + Bf_4^H), \qquad (1)$$

where A varies from 1 to 2 to reflect the relative abundance of $CH_1$ and $CH_2^*$ structures and B varies from 1 to 3 to reflect the relative abundances of $CH_1$, $CH_2$, and $CH_3$ structures. Three of these seven bonding configurations can be eliminated. First, $CH_2^*$ is a highly unstable pendant radical and is unlikely to persist in significant amounts: A = 1. The characteristic methyl rotor NMR signature was evident only in the soft low-voltage films and was normalized out of the coordination average for that film: $B \leq 2$. Assuming B = 1 (all $\equiv$C-H) yields $X_H = 0.3$ independent of $V_b$, grossly at variance with published values.[3] Assuming B = 2 yields $X_H = 0.6$ at low bias, decreasing to less than 0.3 at high bias, in good agreement with published measurements. [The assumption of all aliphatic carbon probably leads to a slight systematic overestimate of $X_H$. See appendix.] The established trend from a polymeric material rich in aliphatic carbon at low bias to graphitic material rich in unprotonated three-fold coordinated carbon at high bias is reproduced in the NMR data. However, an unexpected feature of the

data is that quaternary carbon is maximized in an intermediate range of $V_b$ (200 to 400 V).

### Hardness

Figure 2 shows the nano-indentation hardness of several films grown in our laboratory (solid circles) compared with those of films grown under identical conditions elsewhere[4] (solid squares). These data show that hardness increases rapidly at low bias voltage (assuming that polymeric, low density films are very soft) peaks near $V_b$ = 250 V, and then decreases gradually with further increase in $V_b$. The correlation between quaternary carbon and hardness is clear.

## RANDOM COVALENT NETWORKS

### RCN Basics

Several authors have attempted to make a connection between the statistics of local carbon coordination and macroscopic film properties, through random covalent network (RCN) theory.[5] The RCN concept as described by Phillips and Thorpe[6] is based on the fundamental statement that a network cannot be rigid unless the number of translational oscillators of non-zero frequency is equal to 3N, the number of translational degrees of freedom in the network (where N is the number of nodes in the network). A simple derivation shows that this condition is met when the mean atomic coordination, $N_{av}$ (the average number of bonds to other nodes party to the network; i.e. not dangling atoms or clusters) is exactly 2.4. $N_{av}$ greater than 2.4 is termed "overconstraint" and is quite reasonably taken to imply increased rigidity and therefore hardness. However, because it implies more than 3N constraints (or 3N oscillators), which is physically impossible, it really means that constraints have not been counted correctly. This failure of the RCN treatment occurs because method for counting constraints is local and does not apply to an overconstrained network (by this definition) in which some or all oscillators are not local. Thus there is no strong connection between optimally constrained networks and macroscopically hard materials. Fortunately, He and Thorpe[7] have treated overconstrained random fourfold coordinated networks by a simulation in which atoms were removed at random from a diamond lattice and the elastic properties of the resulting network calculated. They found an entirely empirical relationship between hardness, H, and $N_{av}$:

$$H = H_0[(N_{av} - 2.4)/(N_0 - 2.4)]^{1.5} \qquad (2)$$

where $N_0$ = 4 for the diamond lattice and $H_0$= 105 GPa for diamond. The open circles in Figure 2 show the hardness for a-C:H as calculated by Eq. 2 using

$$N_{av} = 4f_4^C + (4\text{-}B)f_4^H + 3f_3^C + (3\text{-}A)f_3^H \qquad (3)$$

with A = 1 and B = 2. Given the simplicity of the simulation method and the complexity of a-C:H, the calculated "hardness" is in surprisingly good quantitative and qualitative agreement with the measured values. [See appendix.]

**Clustering**

The role of clustering in determining film hardness can be explored by simple manipulations of the RCN formalism and the NMR data. The extreme case of clustering is to assume that all atoms of a single type are grouped in a single highly internally overconstrained node for which the ratio of external bonds to the number of internal atoms is infinitesimal (i.e. a "super-atom" with many bonds to the network). This is simulated by removing one bonding class and renormalizing the sum of the remaining classes. Setting $f_3^C = 0$ is equivalent to creating one large graphite cluster which presumably does not effect the elastic properties of the remaining "tissue" in which it is embedded. The effect of large graphitic clusters is shown in Fig. 2 as the open squares. The general behavior is the same, but the decrease in hardness at high $V_b$ is more pronounced. Along with many published Raman measurements,[8] this is strong evidence for the presence of graphitic clusters. In contrast, the open triangles in Fig. 3 show that clustering of quaternary carbon removes all network rigidity except at high $V_b$ where there is sufficient graphitic carbon (now presumed to be dispersed) to achieve rigidity. This shows that there are no diamond or "amorphous diamond" clusters in a-C:H and that its hardness relies on a random dispersion of unclustered quaternary carbon.

**The RCN "Phase Diagram"**

Although it cannot describe truly rigid solids, the RCN concept can be used to generate the "phase diagram" for a-C:H first proposed by Angus and Jansen.[5] They applied the RCN formalism to an optimally constrained ($N_{av} = 2.4$) network consisting of carbon and hydrogen. They showed that without reference to the details of carbon coordination, the overall degree of fourfold coordination must vary with hydrogen content as:

$$f_4 = f_4^{C^*} + f_4^H = (8X_H - 3)/5(1 - X_H). \qquad (4)$$

This defines the curve on the plane of $f_4$ vs. $X_H$ shown in Fig. 3. [See appendix.] Materials lying on the curve are covalent networks without clustering. Polymers lie in a narrow band to the right of the RCN curve. [Note that this diagram refers only to the polymer "backbone" and the degree to which it is crosslinked through shared carbon sites, and ignores pendant groups with which the backbone is decorated.] Liquids and finally gasses lie to the right of the polymer band.

The effect of graphitic clusters can be simulated in the RCN formalism by placing all three-fold coordinated carbon in large clusters and renormalizing the number of nodes accordingly (without clustering each node is one atom). The new curve representing optimally constrained networks with large graphitic clusters given by

$$f_4 = 5X_H/8(1 - X_H) \qquad (5)$$

is shown as the dashed curve in Fig. 3 (labelled C-RCN) and coincides neatly with the measured values. This result is consistent with the proposal by Angus and Wang[9] that a-C:H consists of a random covalent network in which small graphitic clusters (which determine the optical properties) are locked. However, with or without multi-atom nodes, an optimally constrained RCN cannot have significant macroscopic hardness. Thus not all overconstraint is relieved by clustering. Furthermore, the finite clusters which must exist in the real material can contribute to network rigidity. Nevertheless, the close correspondence with the C-RCN prediction is quite striking and emphasizes how little overconstraint is required to achieve "diamondlike" hardness.

## CONCLUSIONS

We have used NMR spectroscopy to obtain a detailed description of hydrogenated amorphous carbon films formed under a wide range of conditions. A qualitative and semiquantitative connection between local atomic coordination and macroscopic elastic properties can be made through random covalent network concepts. We conclude that the elastic properties of DLC are characteristic of a random network with only a small degree of overconstraint and that the hardness of DLC relative to non-carbon materials (e.g. ceramics) is a consequence of the extreme stiffness and shortness of the C-C bond. This implies that very much harder networks are possible. Given the observed trend toward graphitic clustering to maintain near-optimal constraint, the ability to form highly constrained all-fourfold networks ("amorphous diamond") from hydrocarbon vapor is questionable. However, there is evidence that hydrogen free networks with high degree of fourfold coordination can be deposited from a ion beams of roughly 100 eV energy. This is the same energy range at which the content of quaternary carbon is maximized in a-C:H. [This effect is explained by Lifshitz, Kasi and Rabalais[10] in terms of the larger atomic displacement energy of quaternary relative to graphitic carbon (80 vs. 25 eV).] This implies that in the absence of hydrogen, a largely four-fold coordinated carbon network may indeed be realizable. Given the difficulties of inferring atomic structure from optical spectra, direct measurements such as those described here will be essential in determining the true degree of four-fold coordination in these new materials.

## APPENDIX

Figure 3 also shows the overall $sp^3$ fraction derived from our NMR results (solid symbols) and measurements of several other investigators (open symbols). These are in excellent agreement except for the point corresponding to the $V_b$ = 1000 V film, where it appears that $X_H$ has been slightly overestimated (i.e. B < 2). This omission of ≡C-H sites results in an underestimate of $X_H$ in Fig. 2 and hardness in Fig. 3. Also, large graphitic clusters are not really the points by which they are described in RCN theory, but are equivalent to pancake-shaped voids in the connectivity of the network. Given the complexity of this material and the simplifications of the simulations by He and Thorpe, interpretations of the quantitative agreement between experiment and theory, or elaborate corrections to improve that agreement, are unlikely to be meaningful.


## ACKNOWLEDGEMENTS

The authors with to thank M. Rokosz for acquiring the NMR spectra, Professor Michael Thorpe for his patient explanations of covalent network theory, Dr. Kenneth Hass for many helpful discussions of this work, and Dr. Carl McHargue for arranging for the nano-indentation measurements at Oak Ridge National Laboratory.


## REFERENCES


1. J. C. Angus and C. C. Hayman, Science 241, 913 (1989).

2. M. A. Tamor and C. H. Wu, J. Appl. Phys. 67, 1007 (1990).

3. S. Kaplan, F. Jansen and M. Machonkin, Appl. Phys. Lett. 47, 750 (1985).

4. X. Jiang, K. Reichelt and B. Stritzker, J. Appl. Phys. 66, 5805 (1989).

5. J. C. Angus and F. Jansen, J. Vac. Sci. Tech. A 6, 1778 (1988).

6. J. C. Phillips and M. F. Thorpe, Solid State Commun. 53, 699 (1985); M. F. Thorpe, J. Non-Crystalline Solids 57, 355 (1983).

7. H. He and M. F. Thorpe, Phys. Rev. Lett. 54, 2107 (1985).

8. M. A. Tamor, J. A. Haire, C. H. Wu and K. C. Hass, Appl. Phys. Lett. 54, 123 (1989) and references therein.

9. J. C. Angus and Y. Wang, NATO Advanced Study Institute on Diamond and Diamondlike Materials, Castelvecchio Pascoli, Italy, 1990.

10. Y. Lifshitz, S. R. Kasi and J. W. Rabalais, Phys. Rev. Lett. 62, 1290 (1989).

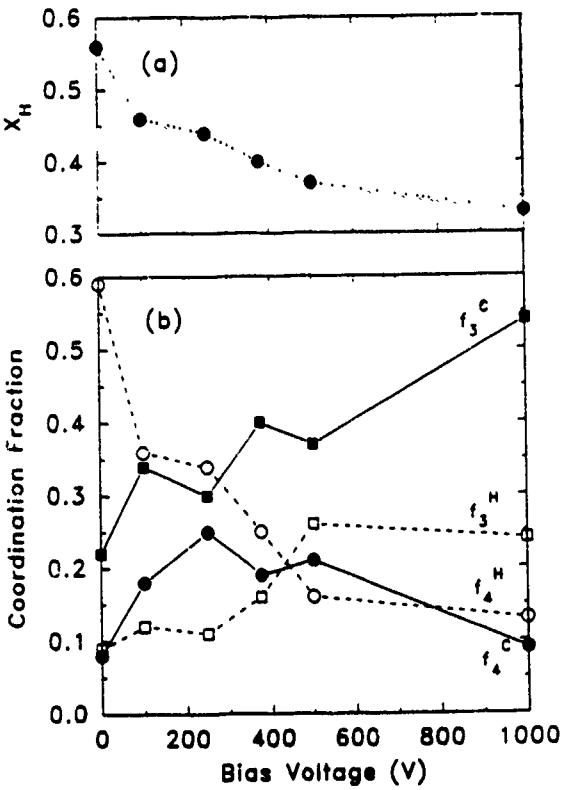



**Figure 1. a) Atomic fraction of hydrogen, $X_H$, as a function of substrate bias voltage, $V_b$. b) Bias voltage dependance of the four carbon coordination fractions. The estimated error on each fraction is ±0.05.**

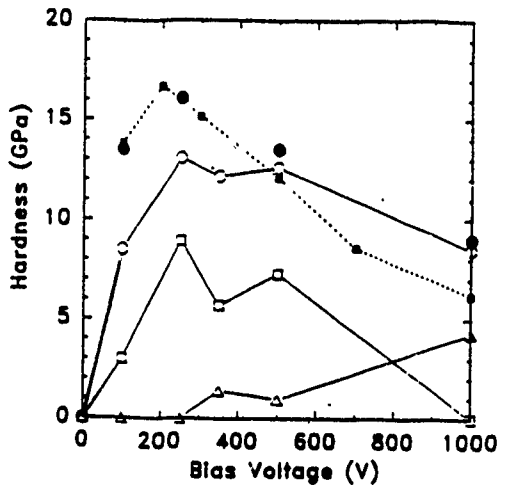



Figure 2. Bias voltage dependance of the nano-indentation hardness of DLC films deposited in our laboratory (solid circles) and elsewhere (solid squares).[4] The open symbols are hardness calculated from the Eq. 2 for all atoms(o), with graphitic clusters (open squares) and quaternary clusters(Δ).

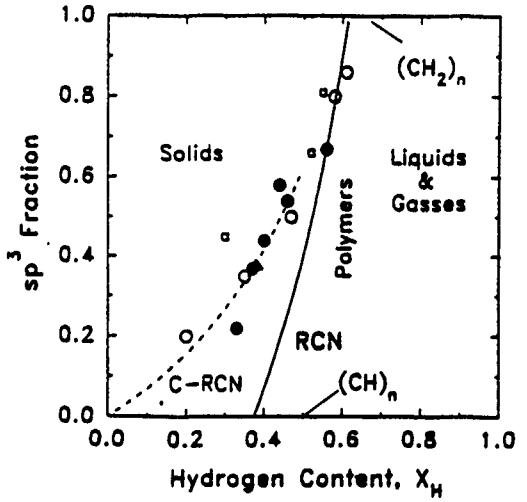



Figure 3. Hydrocarbon phase diagram, modified from that proposed by Angus and Jansen. The solid line is the existence curve for optimally constrained random tworks without clustering. The dashed curve is for random networks wi .i graphitic clusters. Solid symbols are our NMR measurements, open symbols are NMR results from other laboratories.

# DIAMOND-LIKE NANOCOMPOSITES
# A NEW CLASS OF ELECTRONIC MATERIALS

V. F. Dorfmann, T.A. Skotheim, B. N. Pypkin[1],
Moltech Corporation, Stony Brook, NY 11794-2275
[1] Moscow Institute of Controlling Machines, Moscow-117812, USSR.

## ABSTRACT

A new class of diamond-like materials have been synthesized, consisting of nano-composite structures of Si-O and transition metal networks imbedded in a diamond-like carbon matrix. The two-network (a-C:H, a-Si:O) and three-network (a-C:H, a-Si:O, a-Me) structures provide mutual stabilization, which prevents the growth of graphitic structures at high temperatures. The composite structures have reduced internal stress, resulting in enhanced adhesion to a wide variety of substrates. The materials are amorphous and do not contain clusters, and the random networks are bonded to each other mainly by weak chemical forces.

In metal containing nano-composites, the conductivity can be varied continuously over 18 orders of magnitude by varying the concentration of metal atoms. Conductivities as high as $10^4$ S/cm have been achieved with W-containing films.

## INTRODUCTION

Recently, there has been a great deal of work devoted to synthesis of carbon-base microcomposites[1-3]. The term "composite" is typically used to stress that the main microstructural feature of this class of materials, distinguishable, e.g. by electron microscopy, is the existence of regions of one of the constituents dispersed randomly in the matrix of another. In the dielectric regime such microstructural inhomogeneities (small metallic inclusions) are dispersed in an organic matrix. As the metal concentration is increased, the metal inclusions grow and form a maze network (transition regime). At this percolation threshold most of the characteristics of the material change abruptly. As the relative concentration of the metallic component is further increased, a metallic regime is finally reached, and the material can be characterized as a metallic continuum with dielectric inclusions. In this respect, plasma polymer/metal films differ from those of plasma polymerized organometallics, where the metals are usually dispersed as chemically bonded atoms[4].

Considerable amount of work has also been devoted to investigate a-C:H/metal composites, including the amorphous carbon-metal composites with W and other heavy transition metals[5-7]. Typically, metals form carbides in such films. Weissmantel et al.[8] produced amorphous carbon films with extremely small metal clusters. However, upon annealing above 1000 °K, a segregation of small carbide or small metal crystallites was observed. The presence of only a small amount of the metal (~3at%) appeared to influence the microstructure of the metastable carbon matrix, which exhibited a sharp drop in microhardness and resistivity. Unintentional clusters destroy the local symmetry of the medium, and are able to

serve as active centers of degradation. A key problem, therefore, is to maintain uniformity and stability of the matrix.

Plasma deposition processes take place at exceptionally high rates of relaxation of the initial particle energy. An estimate of this rate can made by taking into account the upper limit of the particle energy which can be elastically dissipated by the crystal lattice (about 25 eV), and the typical time of this dissipation ($10^{-11}$ - $10^{-12}$ sec). In principle virtually any compositions of the amorphous nano-composites can be produced by plasma-ion deposition techniques. If the formation of clusters can be excluded during films growth, the resulting structure has high stability. Minimizing the formation of clusters in the sources, in the primary plasma and in the chamber during film growth is essential to achieve the stable, amorphous structure.

## SYNTHESIS OF DIAMOND-LIKE NANOCOMPOSITES

We have synthesized a new class of amorphous diamond-like materials which consists of nano-composite structures of Si-O and transition metal networks imbedded in a diamond-like carbon matrix. The two-network (a-C:H, a-Si:O) and three-network (a-C:H, a-Si:O, a-Me) structures provide mutual stabilization, which prevents the growth of graphitic structures at high temperatures.

The synthesis of the diamond-like nanocomposites (DLN) can be achieved by codeposition of clusterless beams of ions, atoms and/or radicals, if the mean free path of each particle species exceeds the distance between its source and growing film surface. This excludes interparticle collisions in the deposition chamber, and every beam contains the particles in a well defined energy range.

We have developed several methods of two-network DLN depositions. The most effective are based on plasma polymerization of organo-silicon precursors, such as siloxanes, by ion bombardment (Ar+, Kr+, 30-150 keV) of siloxane vapor (about $3 \times 10^{-4}$ torr), and by plasma enhanced deposition with quasi closed plasmatron (0.3 - 5.0 keV)[10-12]. In first case the self-stabilized DLN growth is controlled by the tunneling relaxation of the charge of the adsorbed radicals through the growing dielectric diamond-like carbon (DLC). The films growth, therefore, stops at 6-8 nm. DLN films are extremely uniform and non-porous even at thicknesses as low as 3-5 nm.

With plasma enhanced deposition, the DLN growth is stable to thicknesses of at least 10 μm. A specially constructed plasmatron allows direct injection of high boiling point liquid agents into the active plasma region[10-12]. The formation of the third network of DLN is achieved by co-evaporation and/or sputtering of metals during the deposition process.

Substrates are placed in an adjacent chamber on a multiposition drum which ensures double rotary motion. A negative RF or DC potential is applied to the substrate during the deposition process. No external heating is required. Substrates are cleaned *in situ* by plasma etching prior to deposition. The typical values of some process parameters are: discharge power of 750 W, chamber pressure of $2 \times 10^{-2}$ Pa and growth rates between 1 and 3 microns/hour.

A special method has been developed for protection of biomaterials and electronic devices. The flow of the neutral radicals with optimum kinetic energy is reflected from a high voltage target and is directed to the devices to be coated. This process avoids damage to the devices by charged or/and fast particles during the film growth.

## COMPOSITION AND STRUCTURE OF DLN FILMS.

Investigations of the structure and chemical bonding of DLN films have been carried out by glancing X-ray and electron diffraction, electron paramagnetic resonance, Auger and IR spectroscopy, differential thermal analysis, transmission electron microscopy, atomic force microscopy, electron projection and Rutherford backscattering. The films do not contain areas of ordering greater than that defined by one third of the radius of the coordination sphere. The metals are distributed as separate atoms or as a separate disordered network and all three interpenetrating networks are bonded to each other primarily by weak chemical forces.

Analysis of comparative chemical activity of DLN deposited under different conditions, yields important additional information. Annealing of DLN in air at 700 °C removes the carbon diamond-like matrix while preserving the silicon glass-like network. Etching of DLN in HF acid, on the other hand, removes the Si-network, while preserving the diamond-like carbon matrix.

## ELECTRICAL CONDUCTIVITY OF DLN FILMS

Many of the main electron transport mechanisms [13] can be observed in dielectric and intermediate state of DLN. The electrical conductivity of three-network DLN can be varied over a wide range by controlling the metal concentration[14]. A variation of 18 orders of magnitude, from $10^{14}$ ohm-cm to $10^{-4}$ ohm-cm, have been observed with W-containing films, as shown in figure 1. At low concentrations, the metallic atoms enter the unconnected nanopores in the DLC matrix. The diameter of the nanopores varies from about 2.8 to 3.5 Å. Upon filling of the nanopores (estimated pore volume about 10 %), the W enters the matrix of the film, resulting in a homogenous distribution of metallic and dielectric phases.

Higher concentrations of W lead to the formation of connected networks and metallic conductivity of the film. Similar behavior has been observed with other metals as well. It should be pointed out that carbide formation was not observed even at concentrations of transition metals as high as 50%.

## STABILITY

Extreme stability to high temperatures, and to thermal and mechanical cycling has been observed with dln films[14]. Two hour exposure to flowing HCl at temperatures over 1250 °C, and immersion in various inorganic and organic liquid agents have shown these films to be impermeable to highly aggressive media.

Experiments on the determination of Schottky diode characteristics of W-alloyed DLN/GaAs contacts were carried out after annealing at 850 °C. Barrier heights in the range 0.82-0.86 eV were observed, and the amorphous state of the DLN was preserved. Short-time tests (with 100 μs pulses) have shown that DLN thermal resistors were stable after $2 \times 10^8$ pulses maximum temperatures above 750 °C, and $10^6$ pulses with maximum temperatures above 1250 °C.

## APPLICATIONS

The DLN films have many applications as both protective coatings and as electroactive materials. DLN protective coatings have the properties of the diamond-like state, while at the same time provide elasticity and virtually stress-free interfaces to a wide variety of substrates. DLN films have strong adhesion to any magnetic disk material, while traditional DLC coatings require special adhesive sublayers and induce the internal stress in the active layer of the magnetic disk. DLN also provide the possibility of self-lubricating effects by control of the polymer component in the surface layer of the protective coating. The process of DLN deposition does not influence the functional parameters of hard disk magnetic layers. In addition, the electronic conductivity of DLN eliminates undesirable electrostatic effects during the deposition and running of coatings. More than 30 000 start-stop cycles without any observable change has been demonstrated with films of 25-40 nm thickness[15]. DLN films are, therefore, particularly interesting for developing high density hard disk technology with a distance between the head and the magnetic medium in the 250 nm range.

Three-network films containing heavy transition metals, such as W, can be used as Schottky barrier contacts. Extremely stable, low leakage current, Schottky barrier contacts have been formed between three-network W-containing nano-composite films and Si and GaAs. Barrier heights and ideality factors of 0.82-0.86 eV and 1.2-1.5 respectively for GaAs, and reverse breakdown voltages in excess of 25 V with GaAs and 100 V with Si have been measured. These values are comparable with those quoted for the best refractory metals, nitrides and silicides. The DLN films have additional potential applications as insulating, passivating and protecting films in Si and GaAs MIS structures, as optically transparent protective windows for GaAs opto-electronic circuits, and in self-aligned FET technology[16].

W-containing DLN have also shown to have the highest stability reported as thermal resistors for ink-jet printers. DLN thermal resistors were stable to $2 \times 10^8$ shock pulses with maximum temperature above 700 °C, and $10^6$ pulses with maximum temperatures above 1250 °C.

Microbiological and clinical tests have demonstrated a high degree of biocompatibility of two-network DLN, with applications as protective coatings for improved orthopedic devices and biomaterials, surgical tools, artificial implants and implantable electronic devices. Microbiological tests have shown exceptional inertness to different cultures and tissues. Both plastic, metallic, and combined stomatological implants have been protected by DLN. In all cases, undesirable side effects associated with the implantation were dramatically reduced, particularly during the period of adaptation.

## CONCLUSIONS

Atomic scale self-stabilized amorphous composites a-(C:H, Si:O) and a-(C:H, Si:O, Me) define a new class of materials with a unique combination of electrical, chemical and mechanical properties. The combination of dielectric and metallic states in the same DLN structure preserves the main properties of the diamond-like state, while providing enhanced stability and adherence to a wide variety of substrates.

The combination of diamond-like and electroactive properties opens entirely new possibilities for applications, such as Schottky barrier contacts, protective coatings for integrated circuits, anti-static protective coatings for hard disks, thermal resistors for ink-jet printers, anti-corrosion coatings and protective coatings for biomechanical implants.

Atomic scale composites can be considered as complimentary materials to classical crystalline, amorphous and composite materials. This opens the possibility of creating organized structures and devices in continuous amorphous media.

ACKNOWLEDGEMENT

The authors would like to acknowledge technical assistance and useful discussions with I.D. Khan, G. Kirpilenko, A. Bozhko, D. Rodichev, V.I. Panov, S.V. Savinov, V.N. Schrednik, O.L. Golubev, A.R. Srivatsa, J. Gluck, T. Hong and R. Borra.

REFERENCES


1. E. Kay, *Z.Phys.*, D3 (1986) 251.
2. H.Biederman, *Vacuum* 37 (1987) 367.
3. H.Biederman, L.Martinu, D.Slavinska, I.Chudacek, *Pure and Appl.Chem.*, 60 (1987) 607.
4. R. d'Agostino (eds), Plasma Deposition, Treatment, and Etching of Polymers, Ac. Press, San Diego, 1990.
5. H.Dimigen, H.Hubsh, and V.Schaal (1985) Proc. IPAT'85, Munich, p.267.
6. H.Koberle, and R.Memming (1987) Proc. E-MRS Conf. Strasbourg, Vol. XYII, p.485.
7. W.D.Munz, V.Kopacz, H.Schussler (1987) Proc. IPAT'87, Brighton, p.265.
8. Ch.Weissmantel, E.Ackerman, K.Bewilogua, G.Hecht, H.Kupfer, and B.Rau, *J. Vac. Sci. Technol.* A.4, 2892.
9. Richard Zallen, The Physics of amorphous solids, John Wiley & Sons, N.Y., 1983.
10. V.F.Dorfman, B.V.Kozeikin, V.V.Sevastyanov, Mikroelektronica (in Rus.), 1982, v.11, n.4, 349-355.
11. V.F.Dorfman, S.A.Petruschinina, B.N.Pypkin, U.P.Smirnov, Sov. Acad. Science Reports, 1983, No.1, p.69-72.
12. V.Dorfman. Synthesis of Solid State Structure, Metallurgia, Moscow, 1986.
13. N.F.Mott and E.A.Davis, Electron Processes in non-crystalline materials, Clarendon Press, Oxford, 1979.
14. V.F.Dorfman and B.N.Pypkin, Proc. First European Conference on Diamond and Diamond-like Carbon Coatings, Crans-Montana, Switzerland, 1990 (to appear in Thin Solid Films).
15. D. Latev, V.F.Dorfman and B.N.Pypkin, Proc. First European Conference on Diamond and Diamond-like Carbon Coatings, Crans-Montana, Switzerland,1990.
16. V. F. Dorfman, B. N. Pypkin, V. P. Ageev, T. N. Glushko, A. V. Kuzmichev, B. N. Dunaev, G. G. Kirpilenko, A. Emelyanov and G. Kirpilenko, Proc. First European Conference on Diamond and Diamond-like Carbon Coatings, Crans-Montana, Switzerland, 1990.

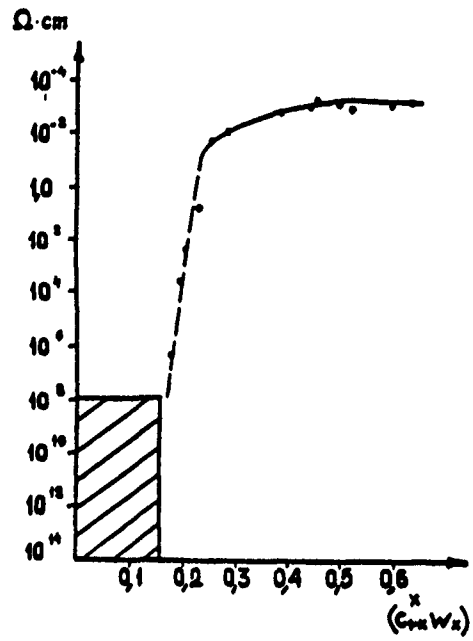



Figure 1. Conductivity of a W-containing DLN film as a function of the W concentration.

# PHYSICAL DEPOSITION OF DIAMOND - TECHNOLOGY, PROPERTIES, AND APPLICATIONS

S. Aisenberg[+], A. Altshuler[+*], and J. L. Sprague[*]
+ International Diamond Development Institute,
Box 2970, Natick, MA 01760
* John L. Sprague Assoc., Inc.,
One Cranberry Hill, Lexington, MA 02173

## Abstract

The objective is to demonstrate that Physical Deposition (PD) has significant advantages over Chemical Vapor Deposition (CVD) and Plasma Enhanced Chemical Vapor Deposition (PECVD). Evolution of the technology and nomenclature will be described. We know of techniques that are able to produce artificial diamond material in pound quantities, and at a very low cost per pound. Growth rates are 20,000 microns/second. Low cost artificial diamond material can then be used to fabricate larger diamond structures and to grow large area diamond films. Basic advantages, advances, and applications of the various Physical Deposition processes will be discussed.

## Technology

A brief analysis of the evolution of artificial diamond material and hard carbon technology can provide understanding to aid in developing future improvements and important applications. Even more important, it is desirable to be aware of future developments and potential developments in order to try to avoid surprises that could have a large effect on the usefulness and commercialization of current artificial diamond technology.

There are two major types of diamond deposition. One is produced by physical deposition and the other is produced by chemical vapor deposition. Many different names are used for the various processes and forms of artificial diamond material, and this can be confusing and counterproductive.

As was shown in 1971, physical deposition has the advantage of permitting deposition of artificial diamond on co or cold substrates, about 10 °C to 40 °C above ambient, and even on surfaces at liquid nitroge temperatures (1,2). This permits deposition on a wider range of substrates, including plastics. Physical deposition can involve combinations of various factors: high vacuum, inert gas, ion beam deposition, ion assisted deposition, sputtering sources, thermal evaporation sources, e-beam evaporation sources, laser evaporation sources, plasma deposition. Plasma processes can use dc, rf, and microwave plasma sources and diode, triode, or similar electrode configurations.

Chemical vapor deposition involves hot substrates and therefore limits the types of substrates that can be used. The substrates must be able to survive deposition temperatures of hundreds of degrees up to about 1,000 °C. Chemical vapor deposition involves combinations of various factors: hydrocarbon gas plus extra hydrogen (to be partially converted into atomic hydrogen), surface decomposition, plasma decomposition, microwave plasma, electron cyclotron resonance (ECR), and hot substrates to drive out excess hydrogen. The atomic hydrogen and hot substrates result in artificial diamond with very little hydrogen impurities. Other gases such as fluorine, oxygen, or chlorine in the atomic form can be used to assist or substitute for atomic hydrogen.

For cold substrates, another form of carbon results from plasma activated deposition where the gas pressure is not low. Because of low mean free path, the ions and carbon atoms arrive at the cool substrate with lower kinetic energy. Examples of plasma sources are magnetron sputtering

sources, as well as dc and rf plasma sources using diode, triode, or similar electrode configurations. The plasma or sputtering gases can include added hydrocarbon gases such as methane or acetylene. Because of the higher gas pressures and relatively low substrate temperatures, much of the background gas, particularly the higher pressure hydrogen, may be incorporated into the resulting film. Resulting hard carbon films are sometimes called hydrogenated carbon or amorphous carbon.

Physical Deposition

Physical deposition of diamond films using low pressure physical deposition was developed, demonstrated, and described by Aisenberg, et al. in 1971 (3). This ion beam process and the properties of the resulting artificial diamond carbon films were independently confirmed by Spencer and Schmidt in 1976 (4). These films were shown, by x-ray diffraction and other measurements, to be that of diamond with nanometer crystal order, and had many other properties similar to that of diamond. Therefore this material was initially named diamond-like carbon (DLC) (3,4). The diamond-like carbon material was a result of the initial work of Aisenberg, et al. as part of a NASA contract to develop and demonstrate the use of ion beams to fabricate thin film field effect transistors and was described in more detail in a 1968 contract report (5).

These early carbon films were named diamond-like carbon (DLC) because although they did not produce large crystals, it was shown by x-ray studies that they consisted of nano-crystals with sizes of about 50 Angstroms to 100 Angstroms (3,4). They are now sometimes also called amorphous carbon even though they had a nano-crystal structure and properties similar to diamond.

The pioneering papers, published in 1971 (3) and in 1976 (4) described the use of physical deposition of hard carbon films using ion beam deposition, and without the need for hydrogen components or for hot substrates. In ion beam deposition, carbon atoms were released into an argon plasma by carbon sputtered from graphite electrodes. Some of the carbon was ionized and was extracted along with argon ions into a low pressure (1E-5 Torr) deposition chamber where the deposition substrate (at essentially room temperature) was biased negatively with a bias ranging from -40 eV to -100 eV. The average energy of the deposited carbon material is very high and this permits non-equilibrium processes.

The initial ion beam deposition was subsequently shown to involve ion assisted deposition (6,7). It was able to grow artificial diamond material films at a rate of about 1 A/second or 0.36 microns per hour (2).

Apparently the name of diamond-like carbon is now used for other forms of hard carbon with significant amounts of hydrogen (from about 30% to 50% hydrogen.) As a result it is suggested, based upon current terminology, that a more descriptive and appropriate name for the results of the initial work on physical deposition described in 1971 and 1976 shall now be termed Artificial Diamond Material (ADM) or alternately, nano-diamond material, or nano-crystalline diamond.

The properties of the resulting carbon films were very similar to that of diamond, including high electrical resistivity, optical clarity, and crystal structure. Other properties of the initial artificial diamond material (including composition, dielectric constant, mechanical properties, density, low friction, and wear resistance) were measured and reported (6) to be very similar to that of natural diamond. At that time, Raman spectroscopy was not considered or used.

A key feature of the ion beam process, (responsible for the diamond like properties) is the associated ion assisted deposition process which was described and explained in 1973 (6) and also in a patent issued in 1976 (7). Additional details are provided in several recent papers (8,9). Details about related deposition technologies are also provided in "Plasma Deposited Thin Films" (10). The ability to deposit at low pressures is also important since the long mean free path of the

carbon atoms, as well as of the carbon and argon ions, means that the carbon atoms on the surface are very energetic and are better able to form $sp^3$ bonds. Also the energetic surface atoms and ions (carbon and argon) are able to remove surface impurities such as $sp^2$ (graphitic) carbon and surface gas atoms, preferentially leaving $sp^3$ carbon. The film adhesion is also improved.

It is also possible to deposit impurity free artificial diamond material by sputtering provided that the gas pressure is low enough so that the sputtered atoms and associated ions have a large mean free path and can retain much of their energy on the way to the substrate. A low deposition pressure also permits the energetic carbon atoms on the surface to retain much of their energy because there are less gas atoms arriving at the surface to collide with and drain energy from the energetic carbon surface atoms.

High temperature substrates are not always needed for artificial diamond material, and in fact artificial diamond material can be deposited on cryogenic temperature substrates. The ability to deposit artificial diamond films by low pressure sputtering and on cold substrates, at liquid nitrogen temperatures, was demonstrated by Golyanov and Demidov and described in a 1977 U.S. patent (11).

A paper by Golyanov and Grigoryev in 1974, (2) also described ion sputtering deposition of diamond on NaCl substrates at liquid nitrogen temperature. Deposition rates of 2 A per minute were quoted and coatings of 10 A were obtained. The objective apparently was to produce diamond substrates suitable for use in electron microscopy. This paper can be considered as demonstrating the physical feasibility of physical deposition on cold substrates. It remains to find ways to increase the deposition rates and areas for other applications. It may be difficult to find applications where deposition on cryogenically cooled substrates is uniquely beneficial and practical.

In a 1977 U.S. patent, Golyanov and Demidov described a device to produce artificial diamond coatings or films by sputtering of graphite cathodes (1). In a chamber with a base pressure of 1E-10 Torr or less, they sputtered carbon using krypton at a deposition pressure of 1E-6 Torr to 1E-5 Torr. This low deposition pressure resulted in a long mean free path and a low rate of background gas arrival on the substrate along with the depositing carbon. This aided in the surface formation of carbon with the desired $sp^3$ diamond bonds and with less of the graphitic $sp^2$ bonds, and without the need for a hot substrate.

In early work to investigate various ways to increase the deposition rate by physical deposition, Aisenberg showed in 1971 that deposition rates of over 600 A/minute (10 A/second or 3.6 microns per hour) could be obtained by the addition of 20% $CH_4$ to the argon gas in the plasma of the ion beam source (12). This method added another and larger source of carbon atoms and increased the deposition rate on cool substrates. Because of the addition of hydrocarbon gas to the plasma source, there was probably some hydrogen included in the resulting films. These faster deposited films showed many of the interesting and useful properties of the earlier hard carbon films, including transparency, high resistivity, hardness, and good substrate adhesion.

This work can be considered as an early use of ion assisted chemical vapor deposition (using a plasma decomposition of a hydrocarbon gas) and on substrates close to room temperature. This early work was not published (except in a company brochure) (12) and was not continued at that time because the objective then was for high purity, smooth, artificial diamond films for semiconductors and low friction, wear resistant applications.

Apparently an important factor in successfully producing artificial diamond material is surface carbon atoms with average energy of many electron volts. If the carbon is deposited at a rate faster than the corresponding surface energy can be provided by ion bombardment, then the ability to form a preponderance of $sp^3$ bonds is reduced and the film quality suffers. The ability of energetic ion bombardment or atomic hydrogen or atomic fluorine to preferentially remove $sp^2$ graphitic

carbon is important in leaving behind the $sp^3$ diamond bonded carbon. More efficient producers of ions, atomic hydrogen, atomic chlorine, or atomic fluorine will improve the process of making artificial diamond materials.

Continued work in Russia using physical deposition and ion assisted deposition has resulted in processes that are faster and more practical than CVD. For example, 30 micron films have been produced commercially at practical rates and on cool substrates (13,14). Room temperature deposition rates of 10 micron/hour, over hundreds (about 200 to 700) of square inches have been obtained (13,14). For deposition rates of 10 microns/hour over about 170 square inches, the calculated costs for 1 micron thick diamond films are about $0.18/square inch. This includes equipment depreciation, labor, overhead, and materials.

Chemical Vapor Deposition

Many practical applications will require faster production of artificial diamond material and over larger surfaces. The deposition rate and area can be increased by raising the pressure and concentration of carbon atoms available for deposition. This led to chemical vapor deposition which takes place at higher pressures and with very hot substrates.

A method for producing micron size crystals of carbon, without hydrogen residue, involves very high thermal or plasma decomposition of hydrocarbon gas, together with deposition on very hot substrates (about 1,000 °C). Atomic hydrogen is apparently responsible for the removal of graphitic $sp^2$ carbon and the predominance of $sp^3$ bonded carbon, while the very hot substrate removes the hydrogen from the resulting carbon films. The need for hot substrates may limit the potential applications of this method.

Homoepitaxial growth of diamond on diamond, and heteroepitaxial growth of diamond single crystal on Silicon, Molybdenum, and other substrates has been reported, including large 50 micron crystals (16).

Subsequent extension of the technology by Russian and Japanese researchers increased the deposition rate significantly by the introduction of substantial amounts of hydrocarbon gases and through the chemical vapor deposition (CVD) process. This provided an increased source of carbon atoms and hydrogen. The addition of large portions of hydrogen permits the formation of atomic hydrogen which is responsible for the preferential removal of graphitic $sp^2$ carbon from the deposited carbon films.

One adverse consequence of the CVD process is that the resulting films (now commonly called diamond-like carbon) can have large amounts of hydrogen (up to 30% to 40%), which is not a property of true diamond. A second unfortunate consequence was that the name of diamond-like carbon (DLC) was corrupted by being also applied to the hydrogenated hard carbon material produced by the low temperature CVD process. A more appropriate and accurate name should have been Diamond-Like HydroCarbon (DLHC) or even Hydrogenated Diamond-Like Carbon (HDLC). This hydrogenated carbon material could also be considered as a hard polymer rather than pure diamond material. A more serious consequence of CVD was the reduced development and application of physical vapor deposition since CVD appeared to have some advantages over physical deposition.

Other gases that are reactive in the atomic form can be used in place of hydrogen. One example is fluorine where atomic fluorine is expected to be more readily produced and more reactive and effective in removing graphitic $sp^2$ carbon, and thus can permit lower deposition temperatures to be used.

Atomic hydrogen is produced as part of the CVD process and uses the fact that atomic hydrogen is very reactive, particularly for graphite, and less reactive for diamond. This means that

the graphitic components in the deposited film are removed by the atomic hydrogen (under proper conditions) while leaving behind carbon in the desired diamond form.

In the filament assisted process for deposition of CVD diamond, a hotter filament surface (at about 2,000 °C) produces free carbon and atomic H, which then deposit on a substrate that is also hot (about 1,000 °C) but is not as hot as the first filament surface. Atomic hydrogen can also be produced by a plasma. Of particular interest are high density, intense plasmas produced by microwave energy and a magnetic field, with the plasma intensity increased by operating in the cyclotron resonance (ECR) mode.

By operating at higher density, and at close to atmospheric pressure, the rate of deposition can be increased by orders of magnitude. One example is the attainment of fast deposition by using an acetylene torch or a plasma torch. Hirose et al. have described the growth of diamond at rates of 30 microns/hour or greater using a combustion flame, and Acetylene, ($C_2H_2$), and very hot substrates (15).

Properties

The following are some of the important basic properties and advantages for artificial (and, in some cases, natural) diamond. Combinations of these properties are related to various unique applications.

| | |
|---|---|
| Mechanical: | hard, rigid, smooth, low friction, good substrate adhesion |
| Thermal: | high thermal conductivity, (5 x copper) |
| Electrical: | high resistivity, high dielectric constant, high breakdown voltage, semiconducting with high energy gap (5.1 eV), capability of high power density, high packing density permitting short signal propagation distances and higher speed. |
| Optical: | transparent from uv to ir, high index of refraction |
| Chemical: | resistant to acids, bases, and solvents |

Physical vapor deposited materials have better properties of adhesion, smoothness, and uniformity, and particularly pinhole free films.

Applications

There are a number of factors to be considered when determining the suitability for commercial applications of production processes and the resulting artificial diamond material: do the processes work?, are they practical?, do they need major investment for development?, do they need expensive equipment for production?, are there better processes?, are the resulting products needed?, and finally, is there a large enough market? One should also consider the patent situation and ownership of the technology.

Strong adhesion to substrates, hardness, strength, thermal stability, and other properties of physically deposited artificial diamond coatings suggest novel uses. Potential applications and products benefiting from the special properties of artificial diamond material and diamond-like carbon include: cutting tools, grinding tools, low friction bearing surfaces, sliding parts, wear resistant surfaces, diamond heat sinks, diamond semiconductors, light emitting diodes, laser diodes, high power transistors, integrated circuits, radome coatings, window coatings, bulk diamond radomes, bulk diamond windows, thin x-ray windows, thin supports for x-ray lithography, coatings on magnetic disks, coatings on optical and magnetic heads, protective coatings on gems, tarnish resistant coatings on silver and jewelry, high power laser mirrors and windows, and durable mold release coatings.

The various types of diamond films have different crystal sizes: Nano-diamonds (10A-100A and sub-micron), Micro-diamonds (microns), or Macro-diamonds (millimeter sizes). Each type has different surface roughness and this has an effect on suitable applications. For example, micro-diamond and macro-diamond films are not suitable for bearing or sliding surfaces unless expensive polishing steps are used to produce smooth surfaces after the deposition. Physical deposition producing nano-diamonds has an advantage for mechanical applications because of better adhesion, better smoothness, and low temperature deposition. Physical deposition of nano-diamond films can provide important protection of optical components.

The most important opportunities for diamond film materials will be potentially in electronics, particularly if one realizes that when properly used, single crystals are not a requirement. This is a controversial statement, but should be seriously considered. For example, poly-crystalline or amorphous silicon is successfully used for electronic devices.

Electronic applications will include diamond ceramic substrates for heat sinks, for thermal control, and for diamond semiconductors and diamond integrated circuits. Special semiconductor capabilities include high power dissipation, high temperature, high device density, short propagation distances, and radiation resistance.

Practical Requirements

The following factors involved in the fabrication of artificial diamond material will have an important effect on the practicality of various applications: diamond properties, fast deposition rates, large deposition areas, good substrate adhesion, acceptable substrate temperature, suitable substrate texture, diamond deposition texture, low or no graphitic impurities, doping with desired additives, and low hydrogen content. Diamond with 30% to 50% hydrogen content is really a hard hydrocarbon.

Physical deposition with proper equipment can provide fast deposition, large area coverage, good adhesion, smooth surfaces, and can wok on low temperature substrates. CVD will provide fast deposition, limited area coverage, rough surfaces, poorer adhesion, and requires substrates that can take high temperatures.

The costs should be acceptable for the application. Costs are determined by the following factors: electricity, gases, capital equipment depreciation, maintenance, labor, overhead, and finally yield of suitable material. Based upon personal experience, commercial costs for ECR (Electron Cyclotron Resonance) deposition is $63.00/square inch and 1 micron thickness. Our analysis of cost suitability for commercial applications indicates a current cost of about $5.00 per device, while the commercial market will need a cost of about 5 cents per device.

Future Technology

While CVD of synthetic diamond material is the technology most often used today, especially in the U.S., other approaches such as PD and explosive techniques have definite advantages, depending upon the end applications. There are apparently technical advances by U.S.A. and international workers that open up new opportunities not known to many others.

Pinhole free, artificial diamond films ranging in thickness from 200 A to 10 microns thickness have been deposited at room temperature on almost any vacuum suitable material and with good film adhesion. Samples can be provided and also in high volume production. (14) For commercial applications, areas of square meters can now be coated by physical deposition (14).

Based upon insight and experience involving the physics and technology of artificial diamond materials, the technology can be extended into many new and surprising practical applications. Practical applications require the ability to grow diamond rapidly, and over large areas. In

addition, the ability to grow the diamond material on relatively cool substrates will permit applications involving substrates that can not survive very high temperatures.

We know of techniques that are able to produce artificial diamond material in pound quantities, and at a very low cost per pound (14). Growth rates are 20,000 microns/second. (14,17) This low cost diamond material can then be used to fabricate low cost, larger diamond structures (such as radomes and windows) and large area diamond films.

Recent analysis of the past and current technology of artificial diamond has resulted in improvements that could go far beyond the present state of the art. The emphasis should include practical applications of artificial diamond material. Growth from the liquid phase may be technically feasible and advantageous. Various approaches can lead to important applications and production efficiency that will advance and possibly obsolete much of the current development and application work.

Consideration of the fundamental physical processes involved in successful production of artificial diamond shows that non-equilibrium process are important. Ion beam, ion assisted deposition is one example. Removal of graphitic carbon by atomic hydrogen involves non-equilibrium atoms. Another non-equilibrium process can be used to make pounds of diamond powder, quickly and at a remarkably low cost (17). Additional processes will permit these low cost powders to then be fabricated into relatively large bulk diamond structures at costs much lower than for other processes we are aware of. Conversion into single crystal diamonds using simple techniques are being considered. Non-equilibrium process permits the attainment of high pressures and temperatures (20 gigapascals and 4000 K) and protects diamond from conversion to graphite.

By extensions of these technologies it is possible to explosively and inexpensively apply diamond coating to a wide range of substrates.

Some of the priority applications for the low cost diamond powder and low cost explosive physical deposition include artificial diamond radomes, windows, commercial low cost heat sink substrates and low cost cutting tools. Further away are new advances producing very low cost diamond semiconductors, diamond integrated circuits, diamond electron emitters, and diamond optical sources.

Unconventional impurity-free electron and hole doping techniques as well as "soft" annealing of diamond films are being investigated.

Summary

Some of the newer Physical Deposition techniques have advantages and capabilities that can lead to improvements over the Chemical Vapor Deposition processes that are currently being extensively employed. These new and lower cost techniques can lead more quickly to important and practical applications.

# # #

## References


1. V. M. Golyanov, O. P. Demidov, US Patent Number 3,840,451, Oct. 8, 1974.
2. V. M. Golyanov, V. B. Grigoryev, "Diamond Substrates for use in Electron Microscopy Examinations", Doklady of the USSR Academy of Sciences, 215, 6, 1974, pp. 1485-87.
3. S. Aisenberg and R. Chabot: Ion Beam Deposition of Thin Films of Diamond-like Carbon. J. Appl. Phys., 42, 2953 (1971).
4. E. G. Spencer, P. H. Schmidt, D. C. Joy, and F. J. Sansalone: "Ion-Beam-Deposited Polycrystalline Diamond-like Films," Appl. Phys. Lett., 29, 118, 1976.
5. S. Aisenberg and R. Chabot, "Study of the Deposition of Single Crystal Silicon, Silicon Dioxide, and Silicon Nitride on Cold-Substrate Silicon," Final Report prepared for NASA Electronics Research Center under Contract #NAS 12-541 (October, 1969). (Describes the technology and early use of ion beam deposition for producing the special thin films, including artificial diamond, particularly for semiconductor applications.)
6. S. Aisenberg and R. W. Chabot: Physics of Ion Plating and Ion Beam Deposition. Journal of Vacuum Science and Technology 10(1):104 (1973).
7. S. Aisenberg, Film Deposition, U.S. Patent No. 3,961,103, June 1, 1976.
8. S. Aisenberg and F. M. Kimock, "Ion Beam and Ion-Assisted Deposition of Diamond-like Carbon Films," in Preparation and Characterization of Amorphous Carbon Films, Material Sciences Forum, Volumes 52 & 53 (1990), edited by John J. Pouch and Samuel A. Alterovitz (NASA Cleveland, Ohio) (Trans Tech Publications LTD, Aedermannsdorf, Switzerland, 1990).
9. Sol Aisenberg, "The Role of Ion Assisted Deposition in the Formation of Diamond-Like Films," J. Vac. Sci. Technol., A 8(3), 2150-2154 (1990).
10. J. Mort and F. Jansen, eds., Plasma Deposited Thin films, CRC Press, (Boca Raton, FL), 1986.
11. V. M. Golyanov, and O. P. Demidov, Device for producing coatings by means of ion sputtering, U.S. Patent number 4,049,533, Sept. 20, 1977.
12. Brochure IBD-101 dated 12/17/71, from the Space Sciences Division of Whittaker Corporation. Product Description Brochure describing an Ion Beam Deposition system (IBD-101) and typical performance, based upon the initial work by Aisenberg and Chabot of the Space Sciences Division). (Describes increased deposition rates using hydrocarbon additives to the ion beam argon plasma, and the measured strong film adhesion.)
13. A. Altshuler, Diamond Technology in the USSR (From Synthesis to Application), Delphic Associates, (Falls Church, VA), 1989.
14. (Private communication)
15. Y. Hirose, S. Amanuma, N. Okada, and K. Komani, Proc. 1st Int. Symp. on Diamond and Diamond-like Films, (The Electrochemical Society, Inc. Pennington, NJ 1989), p.80. (growth of diamond at rates of 30 microns/hour using a combustion flame, and Acetylene $C_2H_2$)
16. B. V. Spitsyn, L. C. Boulov and B. V. Deriagun, Vapor Growth of Diamond on Diamond and Other Surfaces, J. of Crystal Growth, 52, 1981, pp. 219-226.
17. V. M. Titov, V.F. Anisichkin, and I. Yu Mal'kov, "Study of Synthesis of Ultra Fine Diamond", in Detonation Waves, Combustion, and Explosion Physics, 25, 3, 1989, pp 117-126.

# VISIBLE LIGHT EMISSION FROM DIAMOND

Alan T Collins

Wheatstone Physics Laboratory, King's College London,
Strand, London WC2R 2LS, United Kingdom.

Luminescence is a valuable tool in the purely scientific study of the properties of diamonds. It is also important in characterising the defects present in a given sample, and in the selecting of specimens for specific applications. In this paper the major processes for producing visible light emission - photoluminescence, cathodoluminescence, X-ray excited luminescence and electroluminescence - are reviewed. The natures of the vibronic centres responsible for the blue, green, yellow and red photoluminescence are examined, and the excitation of diamond by an electron beam (to produce cathodoluminescence) is discussed. Problems with the donor-acceptor pair model, conventionally used to interpret the broad blue and green emission bands in cathodoluminescence, are outlined and the fundamental differences between photoluminescence and cathodoluminescence are presented. Various applications are considered and the view is re-stated that diamond light-emitting diodes are unlikely to be successful.

## 1 Introduction

The luminescence from diamond has been studied extensively for more than forty years. Much of the early work was carried out using ultraviolet radiation (1), X-rays (2), etc. to excite the luminescence. The use of a focused electron beam (of typical energy 50 keV) to stimulate luminescence in diamond was pioneered at King's College London in the late 1950's using first a converted electron microscope (3) and later custom-built cathodoluminescence equipment. Today scanning electron microscopes with a cathodoluminescence facility are routinely available, and lasers are frequently used to generate photoluminescence (sometimes as an unwanted effect in Raman measurements; see, for example, reference (4)). More than 100 luminescence centres have been documented for diamond, spanning the spectral range from 230 nm (5.3 eV) for the "edge emission" (5) in the ultraviolet to around 1000 nm (1.2 eV) for the "H2" vibronic band (6) in the near infrared. Most of the known optical centres are listed either by Davies (7) or in the forthcoming review by Clark et al (8). Many of the emission bands lie in the visible spectral region 400 to 700 nm (3.10 to 1.78 eV), and will be considered later in this article.

## 2. Defects in diamond

Before discussing the luminescence bands, we need to consider briefly the defects which are present in diamond. The perfect diamond crystal absorbs strongly at energies above 5.5 eV (< 225 nm) corresponding to the indirect energy gap, and has weak vibrational absorption in the two- and three-phonon combination bands between about 4000 and 1500 $cm^{-1}$ (2.5 to 6.7 μm), but there are no absorption or luminescence bands in the visible spectral region. No crystal, of course, is perfect and the deviation from perfection results in the optical systems so common in diamond. The defects may be chemical or structural, or a combination of both, and are briefly considered below.

### 2.1 Nitrogen

Nitrogen is by far the most common impurity in diamond, occurring in concentrations up to about 0.25% in some natural stones. A recent description of nitrogen in diamond has been given by Woods (9), and some of the essential points are briefly reiterated here. In type Ia diamond the majority of the nitrogen is present in either the A form (a nearest-neighbour pair of substitutional nitrogen atoms) or the B form (four nitrogen atoms on substitutional sites symmetrically surrounding a vacancy). In type Ib diamond the nitrogen is present on isolated substitutional sites. Very few natural diamonds are of this type, but all commercial synthetic diamonds (produced by high-pressure synthesis) are type Ib, containing around 200 ppm of nitrogen. The different forms, and concentrations, of nitrogen may be determined from the impurity-activated one-phonon absorption, most of which lies between 1350 and 800 $cm^{-1}$ (7.5 to 12.5 μm). Nitrogen is also the dominant impurity in type IIa diamonds, although it is present in too low a concentration to be detected by infrared absorption. It is also difficult to measure the one-phonon absorption for thin films of diamond grown by chemical vapour deposition (CVD), but the evidence discussed below shows that when this material contains nitrogen most of it is on isolated substitutional sites.

The isolated nitrogen and the A nitrogen both have donor-like properties with ionisation energies around 1.7 and 4.0 eV respectively (10), but there is no evidence that the B nitrogen behaves as a donor.

### 2.2 Boron

When boron is the major impurity in diamond the material is slightly semiconducting. The properties of semiconducting (type IIb) diamond have been reviewed by Collins and Lightowlers (10), and discussed again more recently in the context of electronic and opto-electronic devices (11). Natural semiconducting diamond is rare, and typically has an uncompensated boron concentration of $5 \times 10^{16}$ $cm^{-3}$. Semiconducting synthetic or CVD diamond may readily be made by doping with boron (and excluding nitrogen), and much higher acceptor concentrations can be obtained than in natural diamond. The acceptor ionisation energy is 0.37 eV and only around 0.2% of the acceptors in a typical natural specimen are ionised at room temperature.

## 2.3 Radiation damage products

When diamond is subjected to radiation damage by, for example, high-energy electrons or fast neutrons, some of the carbon atoms are displaced into interstitial positions, leaving a vacancy. For annealing temperatures above about 550°C the vacancy becomes mobile, and can be trapped at other defects in the crystal. This gives rise to a number of optical centres having absorption and luminescence bands in the visible region. Centres which are formed at lower annealing temperatures are presumed to involve the interstitial.

## 2.4 Ion implantation

Most of the luminescence centres produced by irradiation with high-energy electrons or fast neutrons are also generated by ion implantation. However, some ions (e.g. Ni, Zn, Ag, Tl, Si) produce, in addition, unique luminescence bands (12).

## 2.5 Dislocations

Optical centres may form in the vicinity of slip lines, stacking faults and growth planes. In some cases the optical centres are the same as those produced by radiation damage and annealing (13), and can be understood simply in terms of the trapping of vacancies and interstitials. In other cases the slip lines, or extended defects such as platelets (discussed in reference 9) appear to be "decorated" and give rise to characteristic emission bands (14).

# 3 Excitation of luminescence

With the exception of the "band A" luminescence to be discussed below in section 4.1, all of the different luminescence bands are associated with vibronic centres. These centres have their ground and excited energy levels situated somewhere in the forbidden energy gap between the valence band and the conduction band (figure 1a). The absorption process produces a sharp zero-phonon line and a band at higher energy (shorter wavelength) as shown in figure 1b; in luminescence a sharp zero-phonon line and a band at lower energy are observed (figure 1c).

## 3.1 Photoluminescence

The photoluminescence process is the simplest to visualise. (We shall assume here that the photons used for excitation have an energy less than the bandgap of diamond, so that no electron-hole pairs are produced.) The optical centre is excited using a wavelength lying in the absorption band (see figure 1b); after a short time the centre relaxes to the ground state, emitting light in the luminescence sideband. Many of the absorption bands in natural diamond extend into the ultraviolet spectral region, and excitation with a mercury "black lamp" (365 nm) produces blue, green, yellow or red luminescence in suitable specimens.

If the diamond contains a large number of centres that emit visible light they will all be excited to some extent using ultraviolet illumination. However, within certain limitations, the longer wavelength bands can be excited selectively. Suppose we have two optical centres 1 and 2 with absorption spectra as shown in figure 2. Excitation at wavelength A will excite both centres and luminescence will be observed from each; excitation at wavelength B, however, will only excite system 2. If in a diamond the concentration of centre 2 is very much less than that of centre 1, then if both systems are excited the luminescence from centre 2 will be completely obscured by that from centre 1. By adjusting the exciting wavelength the luminescence from centre 2 can be preferentially excited, and its spectrum may be studied.

It is clear that, in order to produce strong luminescence, an appreciable fraction of the exciting radiation must be absorbed; therefore a sufficient concentration of the relevant optical centre must be present to produce that absorption. However, weak luminescence does not necessarily mean that the concentration of corresponding defects is low. As the A nitrogen concentration in a diamond is increased the luminescence from the H3 and N3 centres (see below) is quenched because of a non-radiative transfer of energy to the A nitrogen (15). As we shall see, most of the optical centres in diamond involve nitrogen, and so the photoluminescence may be weak both at very low and at very high nitrogen concentrations.

When a laser is used to excite photoluminescence the Raman scattered line is also present in the spectrum. Since the photoluminescence and Raman scattering intensities depend upon the volume of the crystal excited, as well as the intensity of the exciting light, the ratio of the photoluminescence intensity to the first-order Raman scattering intensity measured in the same spectrum provides a useful semi-quantitative technique for comparing the emission spectra from different samples and after various treatments (16).

### 3.2 Cathodoluminescence

Electron-beam excitation is simply a very convenient method of producing a high concentration of electron-hole pairs. The generation rate of a typical 50 kV beam, at a current density of 0.01 $A/cm^2$, is about $2 \times 10^{23}$ electron-hole pairs per $cm^3$ per second in a region of the diamond about 9 to 18 μm below the surface. Cathodoluminescence is a "near-surface" technique; the emitting region at V kilovolts is located $(0.007 \text{ to } 0.014) \times V^{1.825}$ μm below the surface (17). Electrons and holes may recombine in a variety of different ways. In very pure diamond the electron and hole recombine directly to give the free-exciton "edge emission" (5); in diamonds containing both nitrogen and boron the broad "band A" emission (see below) has been identified as donor-acceptor pair recombination (18), and problems with this model are discussed later. In addition many (but not all) vibronic centres may capture an exciton and subsequently de-excite producing luminescence. The luminescence decay time of many optical centres in

diamond is very short (typically 10 to 50 ns) and so even very small concentrations of such defects can produce bright cathodoluminescence. By way of illustration, if we assume that 10% of the electron-hole pairs at the above generation rate recombine by capture at a luminescence centre with a decay time of 20 ns, the concentration of centres required is only $3 \times 10^{14}$ $cm^{-3}$. This is quite different to the situation with photoluminescence where, if the defect concentration is small, the amount of exciting light absorbed is small and the luminescence is weak.

In many diamonds non-radiative traps are present, and, in addition, the same comments about quenching of the luminescence by A nitrogen apply as for photoluminescence. In general, therefore, the brightest cathodoluminescence is obtained from relatively pure diamonds.

### 3.3 Hard ultraviolet and X-ray excited luminescence

Electron-hole pairs may also be produced in diamond by the absorption of electromagnetic radiation with energy greater than the band-gap of 5.5 eV (wavelengths less than 225 nm) (1). Laboratory sources of continuous radiation in this wavelength region (a deuterium arc, for example) are rather feeble, and lasers such as the ArF excimer laser at 193 nm can only be operated in the pulsed mode at a low repetition frequency. Very little spectroscopic work has therefore been carried out using these methods of excitation. At X-ray wavelengths diamond is relatively transparent, and, with a sufficiently intense source, luminescence (associated with the recombination of electron-hole pairs) is produced throughout the bulk of the diamond (2). Some diamonds emit an intense luminescence when placed in a synchrotron beam at wavelengths chosen for X-ray topography (19), and measurements with interference filters (20) have shown that the emission spectrum with the diamond at room-temperature is similar to that seen in cathodoluminescence. Once again, very few detailed spectroscopic measurements have been made for diamonds excited by X-rays.

### 3.4 Electroluminescence

At sufficiently high electric fields the carbon-carbon bond in diamond may be ruptured, producing electron-hole pairs. In semiconducting diamond this field may be produced at a Schottky barrier, and blue electroluminescence was first observed in such diamonds more than 30 years ago (21). High voltages applied to contacts deposited on insulating diamonds may also generate blue or green light, and Prior and Champion (22) showed that the bandshape of the spectral emission is the same as that observed in cathodoluminescence. More recently blue or green emission has been observed from forward and reverse biased Schottky diodes on boron-doped CVD layers (23, 24) and again the electroluminescence and cathodoluminescence spectra have been shown to very similar (23). The intensity of the light produced by electroluminescence is relatively low, and very few detailed spectroscopic investigations have been carried out.

## 4. Luminescence spectra

After dealing with band A emission (§4.1) the major luminescence spectra are discussed below in order of increasing wavelength. Because of space limitations in this review very few spectra will be shown, and the original references will need to be consulted. Note that most authors do not correct their spectra for the wavelength-dependent response of their system, so detailed comparisons of spectral shapes are not always possible. The zero-phonon lines of all the optical centres in diamond are much sharper at 77K than at room temperature (7), and in only a few cases is any further sharpening observed on cooling to 4.2K. It is important to realise that the energy of the zero-phonon line also changes with temperature, and the standard values are tabulated at 77K (7, 8); some spectra in the literature, however, have been recorded at room-temperature.

### 4.1 Band A

Band A is the most commonly observed cathodoluminescence emission from diamond. Figure 3 shows typical spectra observed from natural type Ia and IIb diamonds, and from a synthetic type IIb diamond. The emission from the latter is green, whilst that from the natural diamonds is two different shades of blue. Dean (18) suggested that the spectra could be interpreted in terms of donor-acceptor pair recombination. If a donor centre and acceptor centre are in close proximity, the extra electron on the donor occupies the hole on the acceptor. When electron-hole pairs are generated in the sample the donor captures an electron, the acceptor captures a hole and then this electron and hole recombine releasing energy E (in eV) given by

$$E = E_g - (E_A + E_D) + e/(4\pi\epsilon r) - A/r^6 \qquad (1)$$

where $E_g$ is the energy gap, $E_A$ and $E_D$ are the acceptor and donor ionisation energies, $\epsilon$ is the permittivity, r is the separation of the donor and acceptor and A is a constant. Dean argued that random strain in the diamond would broaden the discrete lines expected from equation 1 into a band and that in natural diamond close-separation pairs predominate, resulting in blue luminescence, whilst in synthetic diamonds the pairs are more diffuse and the emission occurs in the green.

When Dean proposed this model it was believed that there was only one possible donor with an ionisation energy of 4 eV, and indeed the low energy limit (as $r \rightarrow \infty$ in equation 1) of the band A emission in synthetic diamond seemed consistent with this. However, we now believe that the donor ionisation in synthetic diamond is about 1.7 eV which should result in a donor-acceptor pair band in the ultraviolet region (10). Furthermore the model does not account for the differences between natural type Ia and type IIa diamonds evident in figure 3.

Data on CVD diamond cast further doubt on the above model; it was proposed (18) that the much longer growth time of natural diamond (compared with synthetic diamond) favoured close separation pairs. However both green and blue luminescence are observed from CVD diamond

films grown under identical conditions, apart from accidental boron contamination in the case of green luminescence (25). What is more, blue cathodoluminescence is observed from the small {110} growth sectors of synthetic diamond in which the nitrogen content is low (26).

In natural type IIb diamond (27), and in undoped CVD diamond films (23), the blue luminescence clearly originates from dislocations, and it has been assumed, on the basis of Dean's model, that these dislocations are decorated with donor-acceptor pairs (27). This conclusion may not be valid, however. Finally we note in this section that for facetted CVD particles both the blue and the green luminescence are much stronger from the {100} faces than from the {111} faces (25).

At present there is no theory which accounts adequately for all of the phenomena described, and it is probably better to use the description "band A", rather than "donor-acceptor pair recombination".

## 4.2 The 3.188 eV system

The 3.188 eV (388.8 nm) system is observed in the cathodoluminescence spectra of most diamonds following radiation damage and annealing (28), and the vibronic band extends into the visible region. Many as-grown films of CVD diamond exhibit some 3.188 eV luminescence, and in the study by Collins et al (29) it was much stronger in the relatively poor quality specimens grown at high methane concentrations. Isotope substitution studies (28) have shown that the optical centre involves a carbon interstitial and a single nitrogen atom. Observation of this system in the spectra from CVD diamond provides unmistakeable evidence that the material contains some nitrogen.

## 4.3 The N3 system

The N3 system, with a zero-phonon line at 415.2 nm (2.985 eV) is one of the most studied vibronic bands in diamond and is responsible for the blue emission observed in samples excited by a mercury "black lamp". The N3 centre is believed to be three nearest-neighbour nitrogen atoms on a {111} plane "bonded" to a common vacancy (30). The intensity of the N3 absorption band is correlated with the intensity of the "platelet" peak at 1365 $cm^{-1}$ (7.3 μm), but there is no correlation with the concentration of A or B nitrogen (9, 31). High concentrations of A nitrogen quench the luminescence, so that many diamonds that have a substantial N3 absorption may nevertheless exhibit no blue luminescence. In cathodoluminescence some type IIa diamonds and many type IaB diamonds (those type Ia diamonds containing mostly B nitrogen) show an N3 luminescence band superimposed on the blue band A emission.

## 4.4 The H3 and H4 systems

The H3 and H4 systems with zero-phonon lines at 503.2 and 496.0 nm (2.463 and 2.499 eV) are produced in type Ia diamond by radiation

damage followed by annealing at temperatures above about 550°C (32). Davies and Summersgill (33) have shown that the H3 and H4 centres are due to a vacancy trapped at the A form and the B form of nitrogen, respectively. In diamonds with relatively low concentrations of A nitrogen (so that there is no quenching of the luminescence) these centres produce bright green luminescence when the diamonds are illuminated with long wave ultraviolet (365 nm). The H3 centre (and, very rarely the H4 centre) occurs naturally in some diamonds (34).

Both centres exhibit strong cathodoluminescence which can be much brighter than the blue band A in the same diamond. There is a sharp line at 537.8 nm (2.305 eV) superimposed on the H3 band, and correlated in intensity with it, which is absent from the photoluminescence spectrum; the reason for this is not known.

Many synthetic diamonds exhibit intense H3 cathodoluminescence from the {100} faces only, and Dodge (35) has put forward a model to explain how small concentrations of H3 centres can be grown-in during synthesis. The concentration of H3 centres is, however, far too small to detect any photoluminescence with 365 nm excitation (36).

## 4.5 The 484 nm system

When cooled to 77K synthetic diamonds grown using a nickel-based solvent-catalyst emit an intense green cathodoluminescence from the {111} faces, particularly in specimens with a low nitrogen concentration (37). The emission band has a complex zero-phonon multiplet at 484 nm (2.56 eV). The system can also be observed using photoluminescence, but only if the exciting wavelength is shorter than 400 nm; unlike most vibronic bands, there does not appear to be any absorption immediately to the short-wavelength side of the zero-phonon line (38). For both photoluminescence and cathodoluminescence the emission is quenched as the temperature is increased above about 200K (38).

## 4.6 The 2.721 eV system

Some as-mined gem-quality diamonds, colour-graded as "brown" exhibit a bright yellow luminescence when excited with 365 nm ultraviolet radiation (39). This is produced by a vibronic band with a zero-phonon line at 2.721 eV (455.5 nm) and a maximum near 2.3 eV (540 nm). Such diamonds invariably have a featureless absorption band with a maximum near 2.6 eV (477 nm) and excitation of the diamond with light lying in this band (using, for example the 488 nm line from an Ar ion laser) produces red luminescence (39) in a broad band with a maximum near 1.8 eV (690 nm). The nature of the defects giving rise to these luminescence bands is not known.

In cathodoluminescence both the yellow and the red bands are excited, together with blue band A and a multitude of zero-phonon lines (40). Under certain excitation conditions the emission therefore appears almost white.

## 4.7 The 575 nm system

Following radiation damage and annealing most diamonds exhibit some cathodoluminescence in a system with a zero-phonon line at 574.9 nm (2.156 eV). The emission is strongest in type Ib diamonds which generate an intense pink or orange luminescence. Plastic deformation of type Ib diamond also produces this emission system (41), and it is frequently observed in CVD diamond (29). In nitrogen-doped thermal-CVD diamond, and some material produced by the oxy-acetylene flame technique, the 575 nm system is the most intense in cathodoluminescence spectra. Collins and Lawson (42) have reviewed the information available on the 575 nm optical centre, and conclude that it is comprised of a single nitrogen atom and a vacancy.

The 575 nm centre is readily excited using photoluminescence, and is responsible for the pink emission observed from some natural diamonds with long-wave ultraviolet illumination. The zero-phonon line responds relatively rapidly to stress, and the width of the line can be used to estimate the random stress present in a given sample. Collins and Robertson (43) proposed that the the stress S in GPa can be estimated from the linewidth W in meV using the expression $S = W/10$ (this is equivalent to $S = w/2.7$ where w is the linewidth in nm).

## 4.8 The 1.945 eV system

The major absorption band produced by radiation damage of type Ib diamond, followed by annealing at 800°C, has a zero-phonon line at 1.945 eV (637.2 nm). The 1.945 eV centre has been shown to be a vacancy trapped at a single substitutional nitrogen atom (44). This is one of the major centres in diamond which does not exhibit cathodoluminescence (another is the H2 centre (6)); the reasons for this are not understood.

The 1.945 eV system has been observed in photoluminescence spectra from as-grown CVD diamond produced by the oxy-acetylene flame technique (45), again indicating that this material contains significant concentrations of nitrogen. The width of the zero-phonon line may also be used to estimate the random stress in a given sample (16) using (with the notation from §4.7) $S = W/10$ or $S = w/3.3$.

# 5 Applications

In this paper we have reviewed the major optical centres in diamond that give rise to visible light emission. Currently accepted models for these centres have been discussed, where they have been established. Many other luminescence systems in the visible region have been documented (7, 8) but either occur very rarely, or make only a minor contribution to the total light emitted.

Visible luminescence generated by X-rays is, and in the forseeable future will remain, a major technique for sorting diamonds at the mines (see reference 46, for example). We have discussed in this paper that

photoluminescence and cathodoluminescence techniques are proving extremely valuable in characterising defects in natural, synthetic and CVD diamond; in particular, the the widths of zero-phonon lines can be used to estimate the random stresses present in CVD films grown by various processes. As an example, figure 4 shows the cathodoluminescence spectrum from the centre of a specimen grown by the oxy-acetylene flame technique; the luminescence is an intense blue and is predominantly due to band A. There are, however, a number of sharp lines for which there is no explanation at present. Near the outside of the sample the luminescence is pink, and is dominated by the 575 nm system showing that significant concentrations of nitrogen are present; in this region the linewidths are much larger, and other "unknown" emission bands appear. Clearly there is still much to learn about flame-grown diamond, and luminescence spectroscopy has a vital role to play. [This sample was grown by Kathy Doverspike and kindly made available by Jim Butler, both of the Naval Research Laboratory, Washington DC.]

The growth bands in natural diamond are often clearly revealed by cathodoluminescence, and Nishimura (47) has shown that the performance of single-point turning tools is greatly increased if these regions are avoided near the cutting tip of the tool.

We have drawn attention to the fact that blue and green light have been produced at Schottky barriers on semiconducting samples of natural, synthetic and CVD diamond. However, diamond is an indirect-gap semiconductor, so that the conversion of electrical power to visible light is inefficient; furthermore it is difficult to generate a high concentration of electron-hole pairs at a Schottky barrier (11). Light-emitting devices based on diamond therefore seem unlikely at the present time.

## REFERENCES


1. P J Dean and J C Male, J. Phys. Chem. Solids **25** 1369 (1964).
2. I G Matthews, Proc. Phys. Soc. **72** 1074 (1958).
3. J E Ralph, Proc. Phys. Soc. (London) **76** 688 (1960).
4. S A Grot, C W Hatfield, G Sh Gildenblat, A R Badzian and T Badzian, Proc. Second Int. Conf. on Electron. Materials, 633 (1990).
5. P J Dean, E C Lightowlers and D R Wight, Phys. Rev. **140** A352 (1965).
6. S C Lawson, A T Collins, S Satoh and H Kanda, Proc. Int. Conf. on New Diam. Sci. and Technol., Washington DC., September 1990 (to be published).
7. G Davies, Chem. Phys. Carbon **13** ! (1979).
8. C D Clark, A T Collins and G S Woods in "The Properties of Diamond" (ed. J E Field; Academic Press 1992) to be published.
9. G S Woods, Proc. R. Soc. A **470** 219 (1986).
10. A T Collins and E C Lightowlers in "The Properties of Diamond" (ed. J E Field; Academic Press 1979) chapter 3.
11. A T Collins, Mat. Res. Symp. Proc. **162** 3 - 14 (1989).

12. V S Vavilov, A A Gippius, A M Zaitsev, B V Deryaguin, B V Spitsyn and A E Aleksenko, Sov. Phys. Semicond. **14** 1078 (1980).
13. P L Hanley, I Kiflawi and A R Lang, Phil. Trans. R. Soc. A **284** 329 (1977).
14. A T Collins and G S Woods, Phil. Mag. B **45** 385 (1982).
15. G Davies and M D Crossfield, J. Phys. C **7** L104 (1973).
16. T Evans, S T Davey and S H Robertson, J. Mat. Sci. **19** 2405 (1984).
17. G Davies in "The Properties of Diamond" (ed. J E Field; Academic Press 1979) chapter 5.
18. P J Dean, Phys. Rev. **139** A588 (1965).
19. A M Moore, Daresbury News, No. 129, 1 (1982).
20. A Yacoot, PhD Thesis, University of London (1990).
21. R Woods and J Woods, Phys. Rev. **105** 921 (1957).
22. J R Prior and F C Champion, Proc. Phys. Soc. (London) **80** 849 (1962).
23. H Kawarada, Y Yokota, Y Mori, K Nishimura and A Hiraki, J. Appl. Phys. **67** 983 (1990).
24. N Fujimori and T Imai, Proc. Second Int. Conf. on Electron. Materials, 601 (1990).
25. H Kawarada, K Nishimura, T Ito, J Suzuki, K-S Mar, Y Yokota and A Hiraki, Japan. J. Appl. Phys. **27** L683 (1988).
26. G S Woods and A R Lang, J. Cryst. Growth **28** 215 (1975).
27. N Yamamato, J C H·Spence and D Fathy, Phil. Mag. B **49** 609 (1984).
28. A T Collins and G S Woods, J. Phys. C **20** L797 (1987).
29. A T Collins, M Kamo and Y Sato, J. Phys. D **22** 1402 (1989).
30. J A van Wyk, J. Phys. C **15** L981 (1982).
31. A T Collins, P Haynes and G S Woods, Diamond Conference, Oxford (1991).
32. C D Clark, R W Ditchburn and H B Dyer, Proc. R. Soc. A **237** 75 (1956).
33. G Davies and I Summersgill, Diamond Research 1973 (Suppl. to Indust. Diam. Rev. **33**) pp. 6 - 15.
34. A T Collins, J. Phys. D **15** 1431 (1982).
35. C N Dodge, PhD Thesis, University of Reading (1986).
36. J E Shigley, E Fritsch, C M Stockton, J I Koivula, C W Fryer, R E Kane, D R Hargett and C W Welch, Gems Gemology **23** 187 (1987).
37. A T Collins, H Kanda and R C Burns, Phil. Mag. B **61** 797 (1990).
38. P M S ..ar, Diamond Conference, Reading (1990).
39. A T Collins and K Mohammed, J. Phys. C **15** 147 (1982).
40. K Mohammed, G Davies and A T Collins, J. Phys. C **15** 2789 (1982).
41. E J Brookes, A T Collins and G S Woods, Diamond Conference, Reading (1990).
42. A T Collins and S C Lawson, J. Phys.: Condens. Matter **1** 6929 (1989).
43. A T Collins and S H Robertson, J. Mater. Sci. Letters **4** 681 (1985).
44. G Davies and M F Hamer, Proc. R. Soc. A **348** 285 (1976).
45. G Janssen, W J P van Enckevort, J J D Schaminee, W Vollenberg, L J Giling and M Seal, J. Crystal Growth **104** 752 (1990).
46. E Bruton, in "Diamonds", N.A.G. Press, London (1978).
47. K Nishimura, Proc. First Int. Conf. on New Diam. Sci. and Technol., Tokyo 1988 (to be published).

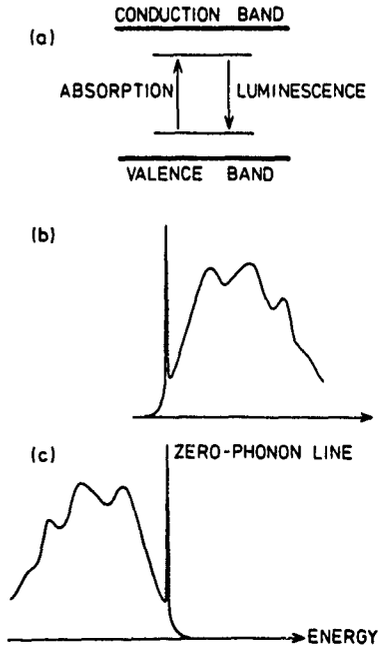



Fig. 1 (a) Simplified energy level scheme for a vibronic centre, and representative spectra: (b) absorption and (c) luminescence.

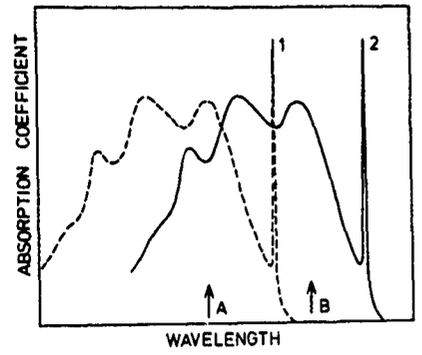



Fig. 2 Representative absorption spectra of two optical centres 1 and 2. Photoexcitation at wavelength A excites both centres, but at B excites only centre 2.

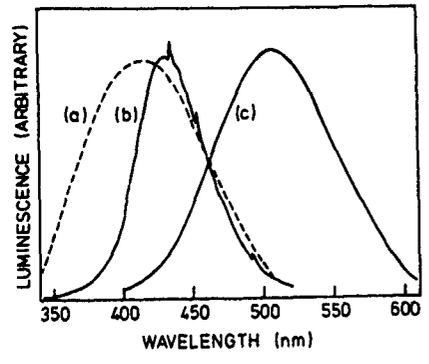



Fig. 3 (above). Band A cathodoluminescence at 77K; (a) type Ia diamond (b) natural type IIb diamond and (c) synthetic type IIb diamond.

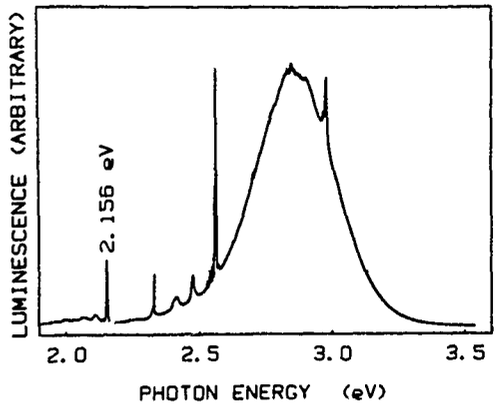



Fig. 4 (left). Cathodoluminescence spectrum at 77K from the central region of a CVD film grown by the oxy-acetylene flame technique.

# FREE EXCITON AND BOUND EXCITION RECOMBINATION RADIATION IN UNDOPED AND BORON-DOPED CVD DIAMONDS

H. Kawarada, Y. Yokota*, H. Matsuyama**, T. Sugi*, and A. Hiraki*

School of Science and Engineering, Waseda University,
Shinjuku, Tokyo 169, Japan.
*Faculty of Engineering, Osaka University, Suita, Osaka 565, Japan.
**Fuji Electric Corporate Research and Development Ltd., Yokosuka,
Kanagawa 240-01, Japan.

## ABSTRACT

In undoped CVD diamonds formed by plasma CVD using $CO/H_2$, the free exciton recombination radiation equivalent to that of natural type IIb diamond has been observed by cathodoluminescence. It indicates extremely high crystallinity and purity of the CVD diamonds. The luminescence intensity correlates with the amount of boron doped in the crystals. The bound exciton is a measure for the acceptor concentration in semiconducting diamonds.

## INTRODUCTION

Excitonic recombination radiation has considerable information concerning crystallinity, impurities, defects, etc. in semiconducting materials. However, in diamonds, a few reports on the edge emissions due to free excitons and bound excitons have been reported (1-4). Studies based on impurity controlled CVD samples have been limited (3,4). In this study, we have intensively studied the relation between free exciton and bound exciton recombinations in undoped and boron-doped CVD diamonds using cathodoluminescence (CL) at liquid nitrogen temperature. The locations of emission regions have been also studied in different emission energies using a monochromatic CL imaging technique.

## EXPERIMENTAL

Diamond particles and polycrystalline films were formed by microwave plasma CVD using $CO(5\%)/H_2$ or $CO(15\%)/H_2$ on Si. The substrate temperatures were between 850-900°C. Boron was doped into the diamonds during the depositions using $B_2H_6$ diluted with $H_2$. The boron/carbon (B/C) ratios during the depositions were 50-$10^4$ ppm. The electrical conductivities of the films were measured by the 4 point probe method. The boron concentration was measured by secondary ion mass spectroscopy (SIMS). CL was obtained using a scanning electron microscope with an accelerating voltage of 20 kV and a probe current of $5 \times 10^{-7}$ A. The sample temperature during the observations varied from 80 K to 200 K.

## INDIRECT EXCITON RECOMBINATIONS IN DIAMOND

Diamond is a wide band-gap semiconductor having the band-gap of 5.5 eV at room temperature. The band structure is very similar to that of Si in the sense that the optical transition dominantly occurs through the indirect transitions from the $\Delta$ line near the X point of the conduction band to the $\Gamma$ point of the valence band. In natural type IIb (semiconducting) diamonds, the same type of recombination radiation of free excitons and bound excitons as that of Si has been observed (1). A free exciton (Fig. 1(a)) is an electron and hole which forms due to coulombic attraction. An ionized or neutral acceptor attracts a

free exciton to form a bound exciton (Fig. 1(b) or (c)). In the case of indirect transitions, the absorption or emission of phonons is inevitable to preserve momentum conservation. To illustrate indirect recombination radiation of excitons with the emission of multiple phonons, schematic band structures of diamond superimposed with the dispersion curves of phonons are shown in Fig. 2(a) and (b). In the one phonon process, the energy of emitted photon is

$$h\nu = Eg - Ex - Ep$$

where EP is the energy of phonon emitted to satisfy the momentum conservation, Ex is the binding energy of exciton, and Eg is the band gap. A transition also occurs with the emission of one or more optical phonons at k=0 ($\Gamma$ point) in addition to the momentum conserving phonon, although the transition probability becomes lower. The photon emission energy is

$$h\nu = Eg - Ex - Ep - nEop$$

where Eop is the energy of the k=0 optical phonon and n is the number of optical phonons emitted per transition. The peak obtained in the one phonon process is replicated at several low photon energies (5).

## NATURAL TYPE IIb AND UNDOPED CVD DIAMOND PARTICLES

The photon emission spectrum of a natural type IIb diamond is shown in Fig. 3 (a). The emission energies of peaks A1 and B1 are 5.30 eV and 5.27 eV respectively. According to Eq. 1, they are interpreted to be due to free exciton recombination radiation with the emissions of transverse acoustic (TA) and transverse optical (TO) phonons to conserve the crystal momentum. The free exciton binding energy is 0.08 eV (1). Peaks B2 and B3 are phonon replicas of peak B1 based on the emission process shown in Eq. 2. Peak D1 (5.21 eV) is explained by the bound exciton recombination radiation with the emission of one momentum conserving phonon (TO phonon in this case). The emission process is the same as that of the free exciton. It is also accompanied by phonon replicas such as peak D2. The difference of the emission energies between B1 and D1 (0.06 eV) is the binding energy of a free exciton and an acceptor.

In the undoped CVD diamond particle, the intrinsic components due to the free exciton have been observed. The peak positions and half widths of the spectrum shown in Fig. 3(b) are the same as those of natural type IIb in Fig. 3 (a). The spectrum is from an isolated 5 μm diameter particle. This type of spectrum is reproducibly observed in isolated particles formed by $CO/H_2$, which is effective in suppressing non-diamond phase formation (6). The extrinsic components due to bound excitons have not been found, because the samples are not intentionally doped.

The area of the free exciton recombination radiation has been visualized by a monochromatic CL image. The difference in luminescent sectors is distinct in large particles from by $CO(15\%)/H_2$. Fig. 4 (a) and (b) show an SEM image of a 40 μm particle and the corresponding monochromatic CL image of the 5.27 eV ± 0.01 eV signal. The emissions are primarily from the three {100} sectors and with a minor contribution from the four {111} sectors. In general, free exciton recombination radiation is very sensitive to impurities or defects introduced during the growth stage. The nonradiative centers decrease the recombination radiation and are concentrated in the {111} sectors formed with $CO(15\%)/H_2$.

## BORON-DOPED POLYCRYSTALLINE CVD DIAMOND FILMS

SIMS measurements reveal that the amount of boron in the polycrystalline films has a linear relationship with the B/C doping ratios during the depositions. For example, boron concentrations of $3x10^{17}$ $cm^{-3}$ and $3x10^{19}$ $cm^{-3}$ have been obtained from the doping ratios of B/C = $10^2$ ppm and $10^4$ ppm, respectively. The effects of doping from B/C = 50 ppm to $10^3$ ppm shown in the CL spectra of Fig. 5. In addition to the intrinsic components, extrinsic components due to bound excitons are prominently observed. The intensity of the main peak D1, increases as the doping ratio increases. On the other hand, the intensity of B1 is almost constant to $10^3$ ppm. The B1 and D1 peaks represent the characteristics of the intrinsic and extrinsic components, i.e., the behavior of free excitons and bound excitons. Thus we shall designate B1 and D1 as $FE_{TO}$ and $BE_{TO}$, respectively.

In Fig. 6, $BE_{TO}/FE_{TO}$ ratios in boron doped diamonds are correlated with the B/C ratios during the depositions. The $BE_{TO}FE_{TO}$ ratio increases linearly with the B/C ratio to $10^3$ ppm and almost saturates above that. The electrical conductivities at room temperature have a linear relationship with the B/C ratios, as shown in Fig. 7. It indicates that the acceptor concentrations have a linear relationship with the doping ratios. Thus, the $BE_{TO}/FE_{TO}$ ratios obtained from low temperature photoluminescence (7).

The saturation of $BE_{TO}/FE_{TO}$ above B/C = $10^3$ ppm indicates that there is a change in the environment of excitons bound to acceptors. The CL spectra of boron-doped CVD diamonds with the B/C ratios of $10^3$ - $10^4$ ppm are shown in Fig. 8. As the dopant increases, a shoulder emerges at the low energy side of the $BE_{TO}$ (peak D1). In B/C = $10^4$ ppm, an apparent peak at 5.15 eV is observed. The same tendency has been reported in phosphorous-doped or boron-doped silicon where $BE_{TO}$ moves to lower energies as the amount of the impurities increases. The phenomenon has been explained by the presence of the excitons bound to two donors or two acceptors located nearby (8). Another interpretation for the 5.15 eV peak is that a direct transition from the bottom of the conduction band ($k \approx 0.8 \cdot 2\pi a^{-1}(100)$ to the acceptor ($k \approx 0$) (1). The probability of the process is negligible when the acceptor level is very shallow such as boron in silicon, because an indirect process is inevitable to preserve momentum conservation. However it becomes dominant in deep acceptors like indium in silicon. Although the origin of the peak at 5.15 eV is not identified at present, it is certain that it is strongly correlated with dense acceptors in CVD diamonds.

In order to study the situation of excitons bound to acceptors, the temperature dependence of $BE_{TO}/FE_{TO}$ has been in Fig. 9. Since the intensity of $FE_{TO}$ is almost constant from 80 K to 140 K in the boron doped samples, $BE_{TO}/FE_{TO}$ simply reflects the variation of $BE_{TO}$. The degree of the temperature dependence in the B/C = 50 ppm is estimated by an activation energy of 25 meV. This value is about three times higher than that in the B/C = 5 x $10^3$ ppm. The steep slope implies that bound excitons are dissociated to be free excitons as temperature increases. The high concentration of acceptors prevents these excitons from being free, since free excitons are easily attracted to other acceptors before they recombine. Thus, the $BE_{TO}/FE_{TO}$ ratio in heavily-doped samples is not temperature-dependent.

## REFERENCES

(1) P.J. Dean, E.C. Lightowlers, and D.R. Wight, Phys. Rev. A **140**, 352 (1965).
(2) A.T. Collins, M. Kamo, and Y. Sato, J. Phys. Condensed Matter **1**, 4029 (1989).

(3) H. Kawarada, Y. Yokota, and A. Hiraki, Appl. Phys. Lett. **57**, 1889 (1990).
(4) H. Kawarada, Y. Yokota, S. Sogi, H. Matsuyama, and A. Hiraki, Proc. SPIE, *Diamond Optics* III, Vol. **1325**, 152 (1990).
(5) For example: J.I. Pankove, *Optical Processes in Semiconductors*, Dover, 115 (New York, 1971).
(6) K. Ito, T. Ito, and I. Hosoya, Chem. Lett. **4**, 588 (1988).
(7) M. Tajima, Appl. Phys. Lett. **32**, 719 (1978).
(8) Y. Shiraki and H. Nakashima, Solid State Commun. **29**, 295 (1979).

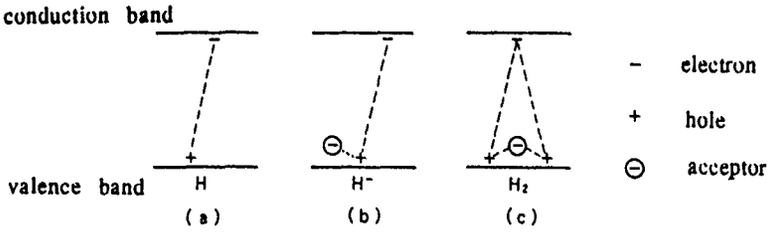



Fig. 1. Schematic diagram of excitons. (a) a free exciton. (b) a bound exciton composed of a free exciton bound to an ionized acceptor. (c) a bound exciton composed of a free exciton bound to a neutral acceptor.

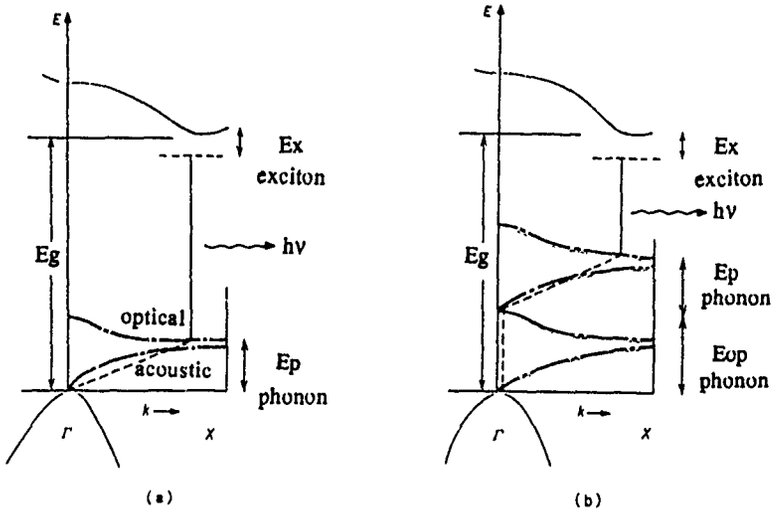



Fig. 2. Illustration of the indirect exciton recombination with (a) one momentum conserving phonon emission, (b) one momentum conserving phonon and one optical phonon emissions.

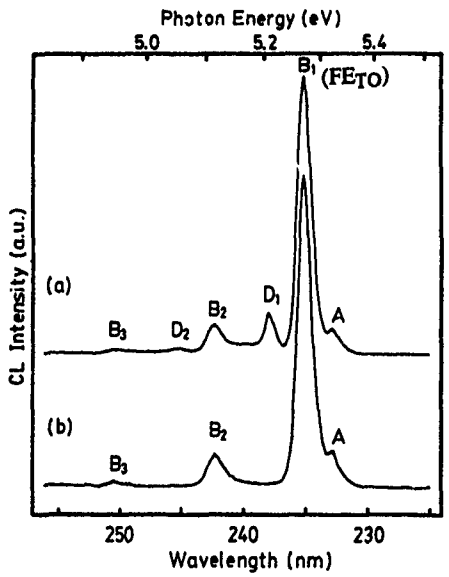



Fig. 3. CL spectra of edge emissions from diamonds obtained at 80 K.
(a) a natural type IIb diamond.
(b) an undoped CVD particle formed with $CO(5\%)/H_2$.

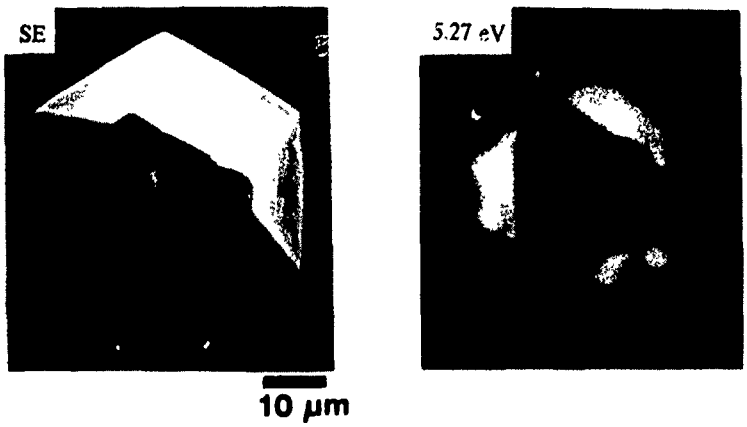



Fig. 4. (a) SE image of an undoped CVD diamond particle formed with $CO(15\%)/H_2$.
(b) Corresponding monochromatic CL image taken with 5.27 eV ± 0.01 eV signal at 90 K.

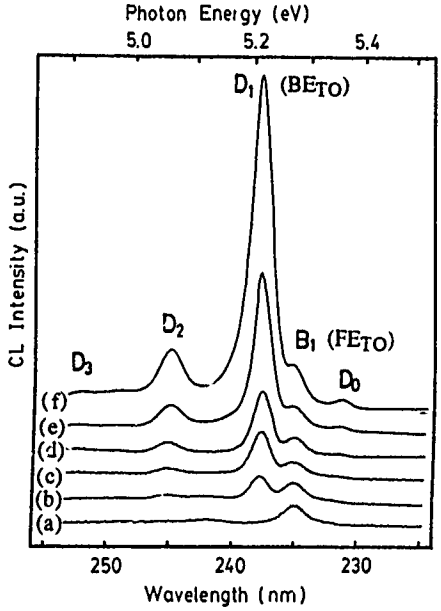



Fig. 5. CL spectra of edge emissions from boron-doped CVD polycrystalline diamond films observed at 80 K. The films were formed with CO(5%)/$H_2$ and 4 μm in thickness. The B/C ratios during the depositions were (a) 0 ppm, (b) 50 ppm, (c) 100 ppm, (d) 250 ppm, (e) 500 ppm, and (f) $10^3$ ppm.

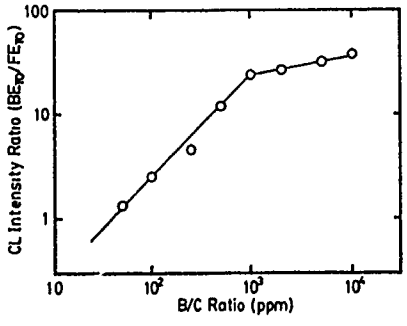



Fig. 6. Emission intensity ratio $BE_{TO}/FE_{TO}$ in boron-doped polycrystalline diamond films as a fucntion of doping ratio B/C.

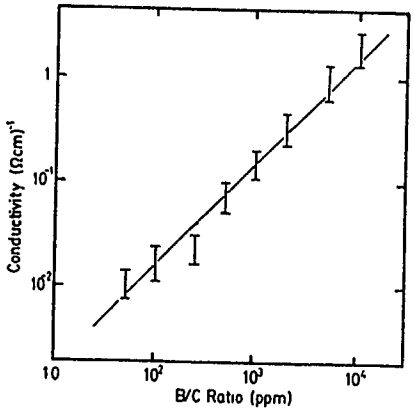



Fig. 7. Electrical conductivities in boron-doped filmes shown in Fig.6 as a function of doping ratio B/C.

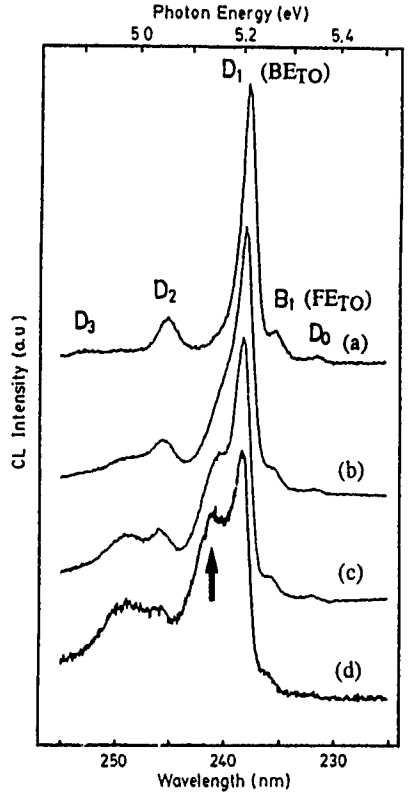



Fig. 8. CL spectra of edge emissions from boron-doped CVD polycrystalline diamond films observed at 80 K. The films were formed with CO(5%)/$H_2$ and 4 μm in thickness. The B/C ratios during the depositions were (a) $10^3$ ppm, (b) 2 x $10^3$ ppm, (c) 5 x $10^3$ ppm, and (d) $10^4$ ppm.

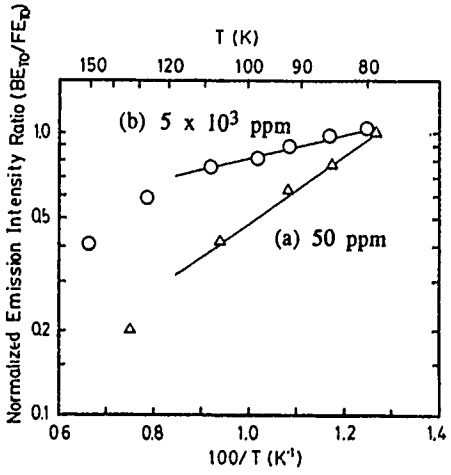



Fig. 9. Normalized emission intensity ratio of $BE_{TO}/FE_{TO}$ as a function of temperature. The ratios $BE_{TO}/FE_{TO}$ are normalized at 80 K to clarify the temperature dependence. The B/C ratios during the depositions were (a) 50 ppm and (b) 5 x $10^3$ ppm.

# SPATIALLY AND SPECTRALLY RESOLVED CATHODOLUMINESCENCE MEASUREMENTS OF CVD-GROWN DIAMOND PARTICLES AND FILMS

Lawrence H. Robins, Edward N. Farabaugh, and Albert Feldman
National Institute of Standards and Technology, Gaithersburg, MD 20899

## ABSTRACT

Spatially and spectrally resolved cathodoluminescence (CL) was used to investigate the spatial distribution of luminescence centers in CVD-grown diamond particles and polycrystalline films. For single particles grown at a low substrate temperature (nominally 650° C), one of the two most intense CL bands, the 2.156 eV band, was found to be associated with {111} facets. The CL image of the other intense band, the 2.85 eV band, showed considerable particle-to-particle variation among the same particles. The images of the 2.156 eV and 2.85 eV CL bands were found to have a complementary relationship for some particles. A model of competing recombination centers is proposed to help explain these results. Cross-sectional measurements of the CL spectra of polycrystalline films on silicon showed that the intensity of a silicon-impurity-related CL band decreases with increasing distance from the film-substrate interface. This depth variation is interpreted as due to a silicon impurity concentration gradient.

## 1. INTRODUCTION

Luminescence spectroscopy is a useful method for defect characterization in diamond (1). Point defects (e.g., single-atom vacancy) and impurity atoms (e.g., nitrogen) are believed to be the primary constituents of the luminescence centers in diamond. Cathodoluminescence (CL) can be excited with high efficiency in diamond by a keV-range electron beam (2). Utilization of a scanning electron microscope (SEM) as the excitation source for CL allows the spatial distribution of the emission to be mapped with high resolution (3).

Results are presented here of a spatially and spectrally resolved CL study of diamond particles and polycrystalline films grown by hot-filament CVD. The CL from these specimens was found to consist of at least four distinct bands. Spectrally resolved images of the two most intense bands, at 2.156 eV and 2.85 eV, were obtained from diamond single particles grown at a nominal deposition temperature of 600° C. For these particles, the 2.156 eV band is associated with {111} facets, while the 2.85 eV band is associated in some cases with {100} facets and in other cases with {111} facets. In particles grown at a higher temperature, both bands are associated with {100} facets. These results are discussed in the context of a model of competing recombination

centers. Spatially resolved CL of diamond films on silicon substrates, viewed in cross-section, showed that the intensity of a silicon-impurity-related CL band decreases with increasing distance from the substrate. This behavior is attributed to a silicon impurity concentration gradient.

We previously presented CL imaging and spectroscopy results for CVD-grown diamond films and particles (4). In the previous work, only particles grown at a deposition temperature of 750° C were examined; in these particles, the CL arose primarily from {100} facets at all wavelengths. Other researchers have obtained similar CL imaging results for films grown by microwave-plasma CVD (5).

## 2. EXPERIMENTAL PROCEDURE

The diamond particles were grown in a tube-furnace hot-filament CVD reactor which has been described previously (6); the polycrystalline films were grown in a bell-jar hot filament CVD reactor. The following conditions were used for all depositions: gas mixture, 0.5% methane and 99.5% hydrogen; gas flow rate, 52 standard $cm^3/min$; pressure, $5x10^3$ Pa; filament temperature, 1800° C; substrate, (100) oriented silicon. The particles were grown on as-received substrates which had a low density of diamond nucleation sites; the films were grown on diamond-polished substrates which had a higher diamond nucleation density. Particle depositions were carried out at nominal substrate temperatures of 600° C and 750° C; the films were deposited at 750° C. Because of filament heating, the true growth temperature is probably higher than the nominal temperature measured by a thermocouple placed beneath the substrate.

The experimental apparatus for CL imaging and spectroscopy in the SEM has been described previously (4). The electron-beam voltage for the CL measurements was 20 kV, and the electron-beam current was $\sim 10^{-8}$ A. CL images with a spatial resolution of ~0.5 μm were recorded by a photomultiplier tube (PMT) with a wavelength range of 200 to 850 nm. Optical bandpass filters, with center wavelengths from 400 nm to 850 nm and full widths at half maximum of 40 nm, were used to obtain spectrally resolved CL images. CL spectra were measured by a 0.34 meter grating spectrograph that utilizes an intensified-photodiode-array multichannel detector and covers a wavelength range of 200 to 900 nm.

## 3. EXPERIMENTAL RESULTS

A typical CL spectrum from a particle deposited at 600° C, shown in Fig. 1, contains four distinguishable components, which are indicated in Fig. 1 by arrows. Three components give rise to sharp zero-phonon lines, at 1.68 eV, 2.156 eV, and 2.325 eV, as well as lower-energy phonon sidebands. The intense phonon sidebands of the 2.156 eV line are due to coupling to 0.045 eV and 0.085 eV acoustic phonons and to the 0.165 eV longitudinal optical phonon (7). The fourth component is a

broad, structureless band with maximum intensity at ~2.85 eV.

The structures of the luminescence centers that give rise to these components have been tentatively identified by comparison to spectra reported in the literature (4). The 1.68 eV band is attributed to a center that contains a silicon impurity atom (8). The 2.156 eV and 2.325 eV bands are attributed to nitrogen-vacancy centers (centers that contain both a nitrogen atom and an atomic vacancy) with distinct structures (7),(9). The broad 2.85 eV band is attributed to a dislocation-related center, which may be either a donor-acceptor pair or an intrinsic state associated with dislocations (10).

The two most intense CL components, the 2.156 eV and 2.85 eV bands, can be selected by bandpass filters with center wavelengths of 600 nm and 450 nm respectively. The photon energy ranges of these filters are indicated by dashed lines in Fig. 1. For conciseness, spectrally resolved CL images obtained with the 600 nm and 450 nm filters will be referred to respectively as 600 nm and 450 nm images.

Spectrally resolved CL images and secondary-electron (SE) images of two particles grown at 600° C are shown in Fig. 2. One particle, shown in Fig. 2(a), has a cubo-octahedral form, and the other, shown in Fig. 2(b) has a pseudo-five-fold twinned form. The CL images appear blurred, compared to the SE images, because of electron beam spreading. According to semi-empirical models of electron scattering in solids, the penetration range of 20 keV electrons in diamond is ~2.8 $\mu$m, and the depth of greatest energy dissipation is ~1.4 $\mu$m (3),(11). The particles shown in Fig. 2 are ~20 $\mu$m in diameter; the CL is thus excited in the near-surface regions of these particles.

In the 600 nm image of the particle shown in Fig. 2(a), bright regions are associated with the centers or edges of triangular {111} facets, and dark regions are associated with the centers of square or octagonal {100} facets. In the 450 nm image, bright regions are associated with the centers of {100} facets. The two CL images shown in Fig. 2(a) are thus approximately complementary; bright regions in one image are correlated with dark regions in the other.

The 600 nm images of the two particles shown in Fig. 2 are similar; in both particles, bright regions are associated with {111} facets and dark regions are associated with {100} facets. Bright regions in the 450 nm image of the particle shown in Fig. 2(b) are, however, associated with {111} facets, in contrast to Fig. 2(a). The two spectrally resolved CL images in Fig. 2(b) are neither complementary nor identical to each other.

We have examined spectrally resolved CL images of other particles from the 600° C deposition, with results similar to those shown in Fig. 2; bright regions in the 600 nm images are always associated with {111} facets, while the location of bright regions in the 450 nm images varies from particle to particle. The variation of the 450 nm images does not

appear to be correlated in a consistent manner with the variation of the crystal growth habit (cubo-octahedral or five-fold twinned).

For particles deposited at 750° C, bright regions in both the 600 nm and 450 nm images are associated with {100} facets, and the two spectrally resolved images are very similar to each other. These results are in agreement with the results of previous studies by the present authors and by other researchers (4), (5).

The depth dependence of the CL in a continuous polycrystalline diamond film on a silicon substrate was investigated by breaking the specimen after deposition and examining it in cross-section. Two spatially resolved CL spectra, taken from near the top surface and the film-substrate interface of such a specimen, are shown in Fig. 3. These spectra are seen to contain the same features as the particle spectrum shown in Fig. 1. The primary difference between the two spectra is the relative intensity of the 1.68 eV band, which is several times greater in the spectrum taken near the film-substrate interface.

A number of spectra were taken from the cross-sectioned specimen to examine the depth dependence of the 1.68 eV band in more detail. In Fig. 4, two quantities are plotted as a function of distance from the film-substrate interface: the intensity ratio of the 1.68 band to the CL background in the same spectral region (which may arise from the low-energy tail of the 2.156 eV band), and the intensity of the CL background. The relative intensity of the 1.68 eV band decreases rapidly with increasing distance from the film-substrate interface, and is greatest when the electron beam is focussed on the substrate side of the interface. Because of its large penetration depth and lateral spreading, the electron beam can excite the diamond film when it is focussed on the silicon substrate near the interface (11).

## 4. DISCUSSION

We have developed a simple recombination model that can be used to relate the image contrast in the spectrally resolved CL images (Fig. 2) to the spatial distributions of the CL centers (12). The key assumptions are as follows: the initial step in the excitation of CL is electron-hole pair creation by the primary electron beam; several types of CL centers and non-radiative recombination centers compete for excitation by the free electron-hole pairs; the numbers of excited centers of each type are directly proportional to the number of free electron-hole pairs. The following equation may then be written for the CL intensity from centers of a particular type, labelled type (a).

$$I_{CL}(a) = [\eta_a B_a N_a \; / \; (\Sigma(B_i N_i) + \Sigma(b_j n_j))] \; G_{eh} \qquad (1)$$

where N represents the concentration of CL centers of a particular type; B represents the rate for excitation of CL centers by electron-hole pairs; the subscript i represents a summation over all CL centers; n,b,

and j are the analogous quantities to N, B, and i for non-radiative centers; $\eta_a$ is the luminescence efficiency of centers of type (a); and $G_{eh}$ is the electron-hole pair generation rate. It is assumed that the concentrations N and n may vary from location to location within the specimen, but the other quantities in Eq. (1) are constant.

If there are only two dominant types of CL centers, labelled (a) and (b), and no non-radiative centers, then Eq. (1) simplifies to:

$$I_{CL}(a) = [\eta_a B_a N_a \; / \; (B_a N_a + B_b N_b)] \; G_{eh} \qquad (2)$$

and a similar equation can be written for the type (b) centers. The sum of $I_{CL}(a)$ and $I_{CL}(b)$, weighted by the inverse quantum efficiencies, is then equal to $G_{eh}$. In a region where $I_{CL}(a)$ is higher than average, $I_{CL}(b)$ is correspondingly lower. This argument implies that the images of the two dominant CL bands will be complementary to each other. The complementary relationship of the 2.156 eV and 2.85 eV CL bands observed for some particles [e.g, Fig. 2(a)] is explained by this case.

Suppose next that there are two dominant types of CL centers, but non-radiative centers are also present. Eq. (1) then has the form:

$$I_{CL}(a) = [\eta_a B_a N_a \; / \; (B_a N_a + B_b N_b + \Sigma(b_j n_j))] \; G_{eh} \qquad (5)$$

In this case, the sum of $I_{CL}(a)$ and $I_{CL}(b)$ is not constant, and the two images do not necessarily have a complementary relationship. According to the model, in specimens where the images of the two dominant CL bands are not complementary, non-radiative recombination must have a significant influence on the CL images. This appears to be the case for some of the particles grown at 600° C [e.g., Fig. 2(b)], and for all of the particles grown at 750° C. (Recall that the images of the two dominant CL bands are very similar for the latter).

According to Eq. (1), the ratio of the CL intensities from two types of centers, $I_{CL}(a)/I_{CL}(b)$, is proportional to the ratio of concentrations, $N_a/N_b$. The intensity ratio of the 1.68 eV band to the tail of the 2.156 eV band, plotted in Fig. 4, should thus represent the concentration ratio of 1.68 eV centers to 2.156 eV centers. Because the 1.68 eV centers are believed to contain silicon impurity atoms, the depth dependence shown in Fig. 4 may be due to a decrease in the concentration of silicon atoms with increasing distance from the silicon substrate. Such a silicon impurity concentration gradient might be due to diffusive transport of silicon atoms from the substrate into the film during the deposition process.

## 5. CONCLUSION

Spatially and spectrally resolved cathodoluminescence (CL) was used to investigate the spatial distribution of luminescence centers in CVD-grown diamond particles and polycrystalline films. For single

particles grown at a low substrate temperature (nominally 650° C), one of the two most intense CL bands, the 2.156 eV band, was found to be associated with (111) facets. The CL image of the other intense band, the 2.85 eV band, showed considerable particle-to-particle variation among the same particles. The images of the 2.156 eV and 2.85 eV CL bands were found to have a complementary relationship for some particles. A model of competing recombination centers is proposed to help explain these results. Cross-sectional measurements of the CL spectra of polycrystalline films on silicon showed that the intensity of a silicon-impurity-related CL band decreases with increasing distance from the film-substrate interface. This depth variation is interpreted as due to a silicon impurity concentration gradient.

## ACKNOWLEDGEMENTS

This work was supported in part by the Office of Naval Research.

## REFERENCES

1. J. Walker, Rep. Prog. Phys. 42, 1605 (1979)
2. G. Davies, in The Properties of Diamond, ed. by J. E. Field (Academic Press, 1979), p. 165
3. B. G. Yacobi and D. B. Holt, J. Appl. Phys. 59, R1 (1986)
4. L. H. Robins, L. P. Cook, E. N. Farabaugh and A. Feldman, Phys. Rev. B 39, 13367 (1989)
5. H. Kawarada, K. Nishimura, T. Ito, J. Suzuki, K. Mar, Y. Yokota and A. Hiraki, Jpn. J. Appl. Phys. 27, L683 (1988)
6. E. N. Farabaugh, A. Feldman, L. H. Robins and E. S. Etz, in Diamond Optics, ed. by A. Feldman and S. Holly, Proc. SPIE 969, 24 (SPIE, Bellingham, WA, 1989)
7. A. T. Collins and S. C. Lawson, J. Phys. Condens. Matter 1, 6929 (1989)
8. J. Ruan, W. J. Choyke, and W. D. Partlow, Appl. Phys. Lett. 58, 295 (1991)
9. V. S. Vavilov, A. A. Gippius, A. M. Zaitsev, B. V. Deryagin, B. V. Spitsyn and A. E. Aleksenko, Fiz. Tekh. Poluprovodn. 14, 1811 (1980) [Sov. Phys. Semicond. 14, 1078 (1980)]
10. N. Yamamoto, J. C. H. Spence and D. Fathy, Phil. Mag. B 49, 609 (1984)
11. K. Kanaya and S. Okayama, J. Phys. D: Appl. Phys. 5, 43 (1972)
12. L. H. Robins, E. N. Farabaugh, A. Feldman and L. P. Cook, Phys. Rev. B 43, 9102 (1991)

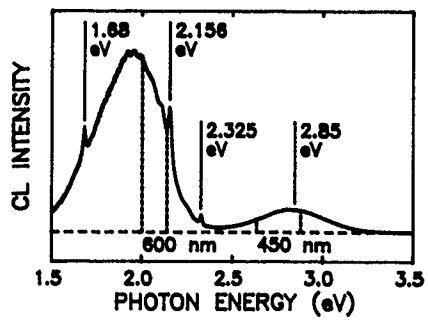



Fig. 1. CL spectrum of a diamond single particle grown at 600° C. The four indicated spectral features are attributed to a silicon impurity center (1.68 eV zero-phonon line) two types of nitrogen-vacancy centers (2.156 eV and 2.325 eV zero-phonon lines), and a dislocation-related defect (2.85 eV band). Dashed lines indicate the ranges for the 600 nm and 450 nm CL images.

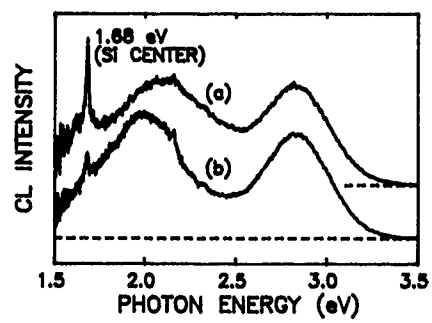



Fig. 3. Spatially resolved CL spectra of polycrystalline diamond film on silicon viewed in cross-section, taken from (a) near film-substrate interface, (b) near top surface.

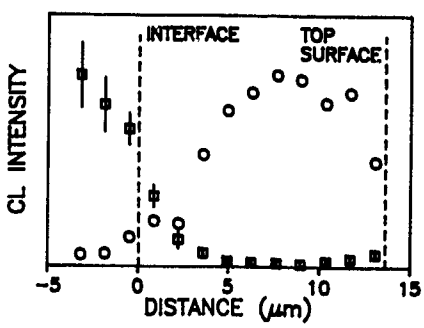



Fig. 4. Intensity ratio of 1.68 eV CL band to spectral background (squares), and intensity of background (circles), as function of distance from film-substrate interface. Locations of interface and top surface of film are indicated by dashed lines.

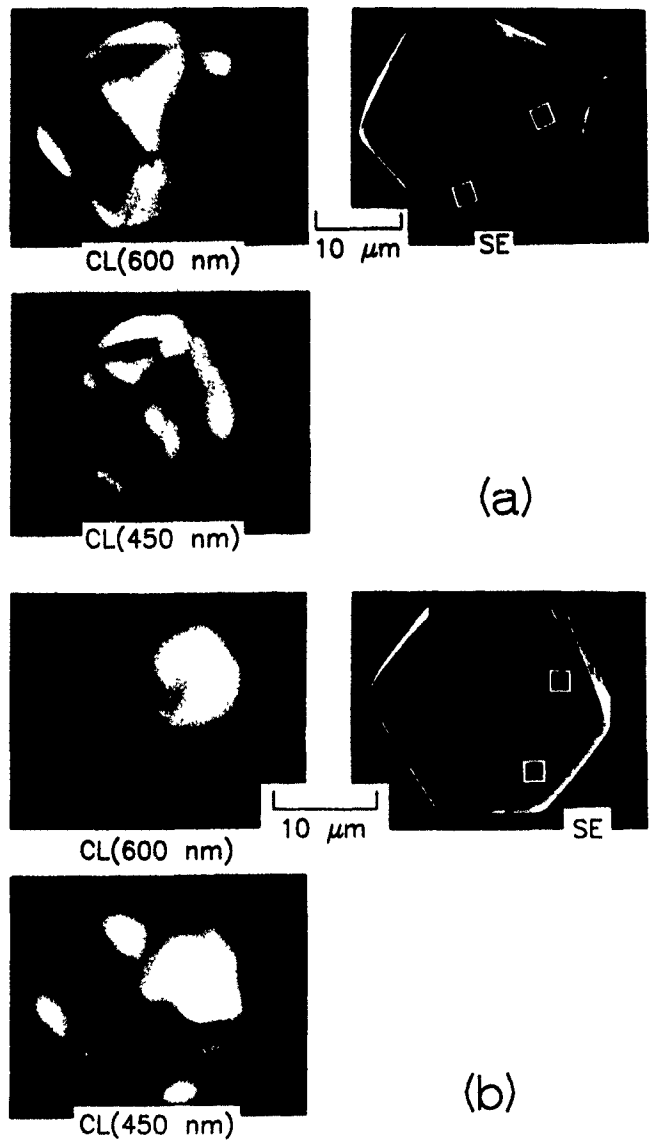



Fig. 2. Secondary-electron (SE) and spectrally resolved CL images of two diamond particles grown at 600° C. Two spectrally resolved CL images, taken with 600 nm and 450 nm bandpass filters, are shown for each particle. (a) Particle with cubo-octahedral habit. (b) Particle with pseudo-five-fold twinned habit.

# LATTICE VIBRATIONAL MODES AND DEFECT-ACTIVATED IR ABSORPTIONS IN CVD DIAMOND

C. Klein, T. Hartnett, R. Miller, and C. Robinson
*Raytheon Research Division, Lexington, MA 02173*

Chemically vapor-deposited (CVD) diamonds are polycrystalline and defect-rich, which destroys the translational symmetry of the lattice and activates first-order infrared absorptions. The work described in this paper takes advantage of this situation for the purpose of (a) detecting and locating the critical-point phonons of diamond, (b) obtaining meaningful information on residual impurities, and (c) searching for evidence regarding postulated diamond-polytype structures. This effort has been quite successful and should provide valuable data for assessing the performance of CVD diamond as an optical material for the 8- to 12- μm spectral region.

Diamond crystals have thermal, mechanical, and optical properties that are highly attractive for infrared (IR) applications involving severe environmental conditions. The selection rules for 3C cubic material imply that single-phonon processes are IR inactive and, therefore, that perfect diamond should be transparent at wavelengths beyond 7.5 μm. Chemically vapor-deposited (CVD) diamond artifacts, however, are polycrystalline and defect-rich, which destroys the translational symmetry of the lattice and may activate first-order IR absorptions, as initially reported by Smith and Hardy(1). The purpose of the work described in this paper was to take advantage of this situation in the sense that the breakdown of selection rules in CVD diamond may allow us to detect and identify the critical-point phonons in a straightforward manner; this task relies on the availability of a set of dispersion curves deduced from inelastic neutron scattering experiments(2) and benefits from the superior accuracy of optical measurements. By using Fourier-transform infrared (FTIR) techniques, we have obtained detailed and reproducible absorption spectra that also provide meaningful indications on residual impurities in our deposits. Since relatively little has been published on IR properties of CVD diamond(3), the present paper may throw some light on the ultimate optical performance of this material and assist the reader in assessing its merit for operation in the 8- to 12- μm spectral band.

Our diamonds were grown on polished molybdenum and polished silicon substrates by means of microwave-plasma as well as hot-filament assisted methane-hydrogen chemical vapor depositions at 900°C. The free-standing 200- to 400- μm thick specimens examined in this study are of outstanding crystalline quality as demonstrated by Raman spectroscopy. First-order Raman spectra display a sharp intense line at approximately 1332.5 $cm^{-1}$ with no evidence of additional features: the full width at half maximum varies with the morphology but tends towards a 3-$cm^{-1}$ "limit" and, thus, to approach widths that are comparable to those of natural diamonds(4). Infrared absorption spectra as recorded in this paper reflect the results of evaluating "absorbances" defined as $A \equiv \ln(T_0/T)$, where $T$ is the measured transmittance and $T_0$ refers to an *ad hoc* baseline "fit". The measured transmittances are as obtained on an FTIR Bomen Inc. spectrometer operating at a resolution of 4 $cm^{-1}$, the instrument control computer collecting and co-adding up to one hundred scans per run. An appropriate polynomial approximation provides the baseline fit, which serves the purpose of eliminating low-spatial-frequency contributions originating from processes such as scatter and, therefore, enhances the absorption features of interest here.

Figure 1 displays the IR absorption spectrum of an in-house produced microwave-plasma CVD diamond specimen grown on a molybdenum substrate. The frequency range extends from 500 to 4000 wavenumbers thus covering the one-, the two-, and the three-phonon regimes of diamond. It is immediately seen that (a) the two-phonon processes dominate and generate the same pattern as described by Hardy and Smith(5); (b) the three-phonon region shows evidence of molecular absorption bands near 2900 $cm^{-1}$, which can be attributed to C-H stretch vibrations(6), and (c) there are weak absorption features at frequencies below that of the Raman phonon, in accord with some recent observations by Thomas and Joseph on type-IIa diamond(7). These single-phonon absorptions are the features we wish to discuss in this paper. In effect, the traces recorded in Figs. 2, 3, and 4 clearly demonstrate that the base-line fitting procedure yields a surprisingly rich structure, which can be interpreted in the light of existing information about the lattice dynamics of diamond(2) and about IR features associated with impurities, defects, and disorder(8).

At this point, it should be emphasized that, below 1000 wavenumbers, the signal-to-noise ratio deteriorates (see Fig. 2) owing to the degraded instrumental response as well as the reduced density of states; at low frequencies, our best results are as illustrated in Fig. 4, which refers to hot-filament material deposited on silicon and, therefore(3), may show features originating from a non-diamond phase that consists of polytypic SiC with axial acoustic, planar optical, and axial optical modes as listed in Ref. 9.

If one uses the neutron-scattering phonon-dispersion data(2) for guidance, a careful examination of our CVD-diamond absorbance traces yields the positions of the critical-point phonons with much improved accuracy (see Table 1). This applies not only to the high-symmetry points X, L, and W, but also to point K, which is remarkable considering that only three of the six $\Sigma$-direction branches have density-of-state "singularities" typical of critical points. With regard to first- and second-order Raman-scatter experiments as interpreted in Ref. 4, we note the excellent agreement in terms of center-of-the-zone phonons; at the zone boundary, however, there are some discrepancies (see Table 1) that will require further attention and, in particular, a reevaluation of assignments in the two-phonon region(10). But first, it should be of interest to evaluate Brout's sum at all the Brillouin-zone points for which we now have what appears to be accurate phonon energies (see Table 2). Evidently, the sums are not independent of the wavevector, which confirms that, indeed, Brout's sum rule does not apply to diamond thus suggesting the presence of non-electromagnetic forces in this material(11). Still, we find that Brout's equation as modified by Mitra and Marshall(12),

$$\sum_{i=1}^{6} \omega_i^2(q) = 16\sqrt{3}r_o/(\chi\mu),$$

yields $1.9\times10^{29}$ $Hz^2$ upon inserting proper numbers for the internuclear distance $r_o$, the bulk compressibility $\chi$, and the residual mass $\mu$, which agrees quite well with the experimental result at point $\Gamma$.

With regard to impurity-activated IR absorptions, it has been recognized (see Table 3) that at least four major species of nitrogen-related imperfections (substitutional, A center, B center, and platelets) can generate lattice as well as localized modes in type-I diamond(13). In Figs 2 and 3, we demonstrate that CVD

material exhibits a similar but weaker impurity-band pattern, which has interesting implications from the point of view of the "defect genealogy" in diamond(8) and correlates well with cathodoluminescence-based observations(14). We have also seen traces of substitutional boron in all our specimens; there are, however, no indications of C-H bending modes(6), judging from the absence of a sharp absorption line at 1405 $cm^{-1}$ (see Fig. 1).

For the sake of completeness, we are also including here relevant segments of the absorption spectrum of a CVD-diamond specimen prepared at The Pennsylvania State University (Fig. 5) and the transmission spectrum of a purchased Drukker type-IIa diamond (Fig. 6). At wavelengths below 10 μm, the single-phonon features identified in Tables 1 and 3 are clearly apparent, which strongly suggests that the breakdown of selection rules occurs even in high-quality natural diamond. We note, however, that while the O(Γ) line appears to be very weak in Fig. 6, a strong absorption emerges at 1310 $cm^{-1}$, which points to an IR-active vibrational mode of the 2IR diamond polytype(15); similarly, the doublet we observe at 662/669 $cm^{-1}$ in CVD diamond (see Fig. 4) may well signal an IR-active mode ($2A_{2u}$) of the postulated 8H diamond structure, thus providing positive evidence to support the recent predictions of Spear, Phelps, and White(15).

## REFERENCES


1. S. Smith and J. Hardy, Phil. Mag. 5, 1311 (1960).
2. J. Warren, *et al.*, Phys. Rev. 158, 805 (1967).
3. X. Wang, *et al.*, J. Mater. Res. 5, 2345 (1990).
4. S. Solin and A. Ramdas, Phys. Rev. B 1, 1687 (1970).
5. J. Hardy and S. Smith, Phil. Mag. 6, 1163 (1961).
6. C. Wild, *et al.*, ECS Proc. 89-12, 283 (1989).
7. M. Thomas and R. Joseph, SPIE Proc. 1326, 120 (1990).
8. G. Davies, Chem. Phys. Carbon 13, 1 (1977).
9. D. Feldman, *et al.*, Phys. Rev. 173, 787 (1968).
10. C. Klein, T. Hartnett, & C. Robinson, SPIE Proc. 1534, to be published.
11. H. Rosenstock and G. Blanken, Phys. Rev. 145, 546 (1966).
12. S. Mitra and R. Marshall, J. Chem. Phys. 41, 3158 (1964).
13. J. Walker, Rep. Prog. Phys. 42, 1605 (1979)
14. L. Robins, *et al.*, Phys Rev. B 39, 13367 (1989).
15. K. Spear, A. Phelps, and W. White, J. Mater. Res 5, 2277 (1990).

Table 1. Critical-Point Phonon Frequencies (in $cm^{-1}$) of Diamond

| Symmetry Point | Phonon Branch[a] | "Neutron" Ref. (2) | "Raman" Ref. (4) | This Work |
|---|---|---|---|---|
| Γ | $\Delta'_2(O)/\Delta_5(O)$ | N/A | 1332.5±.5 | 1332.5±1 |
| X | $\Delta'_2(O)/\Delta_1(A)$ | 1184±21 | 1185±5 | 1191±3 |
| | $\Delta_5(O)$ | 1072±26 | 1069±5 | 1072±2 |
| | $\Delta_5(A)$ | 807±32 | 807±5 | 829±2 |
| L | $\Lambda_1(O)$ | 1242±37 | 1252±5 | 1256±4 |
| | $\Lambda_3(O)$ | 1210±37 | 1206±5 | 1220±2 |
| | $\Lambda_1(A)$ | 1035±32 | 1006±5 | 1042±2 |
| | $\Lambda_3(A)$ | 552±16 | 563±5 | 553±2 |
| K | $\Sigma_1(O)$ | 1232±27[b] | 1230±5 | 1239±2 |
| | $\Sigma_2(O)$ | 1110±21[b] | 1109±5 | 1111±1 |
| | $\Sigma_3(O)$ | 1046±21 | 1045±5 | 1033±2 |
| | $\Sigma_1(A)$ | 1020±11[b] | 988±5 | 1019±3 |
| | $\Sigma_3(A)$ | 972±16 | 980±5 | 978±1 |
| | $\Sigma_4(A)$ | 765±21[b] | N/A | 764±4 |
| W | Z(U) | N/A | 1179±5 | 1146±1 |
| | Z(M) | 993±53 | 999±5 | 992±3 |
| | Z(L) | 919±11 | 908±5 | 918±12[c] |

(a) The notations are as in Ref. 2.

(b) Interpolated using Newton's method.

(c) Very weak feature and not always discernible.

Table 2. Experimentally Derived Brout Sums at High-Symmetry Points of the Brillouin Zone

| Symmetry Point | Brout Sum ($10^{29}$ $Hz^2$) |
|---|---|
| Γ | 1.89 |
| X | 2.31 |
| L | 2.22 |
| K | 2.28 |
| W | 2.23 |

Table 3. Impurity/Defect Related Absorption Features in the 1000 to 1400 $cm^{-1}$ Wavenumber Range

| Impurity/Defect[a] | Recorded Positions[b] | This Work |
|---|---|---|
| substitutional N | ~1130 | 1124±1 |
| | ~1350 | 1358±2 |
| A center | ~1215 | 1204±3 |
| | ~1282 | 1282±2 |
| B center | ~1010 | 1010±2 |
| | ~1175 | 1175±4 |
| A and B centers | ~1100 | 1099±3 |
| platelets | ~1370 | 1373±4 |
| substitutional B | ~1298[c] | 1300±2 |

(a) See Refs. 8 and 13.
(b) Prominent features are underlined.
(c) At room temperature (see Fig. 13 of Ref. 8).

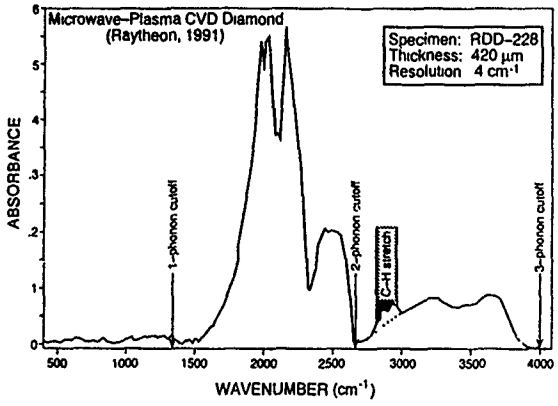



Fig. 1. Absorption spectrum of a microwave-plasma assisted CVD-diamond specimen in the one-, two-, and three-phonon summation regions; note the C-H stretch vibrational modes at *ca.* 2900 $cm^{-1}$.

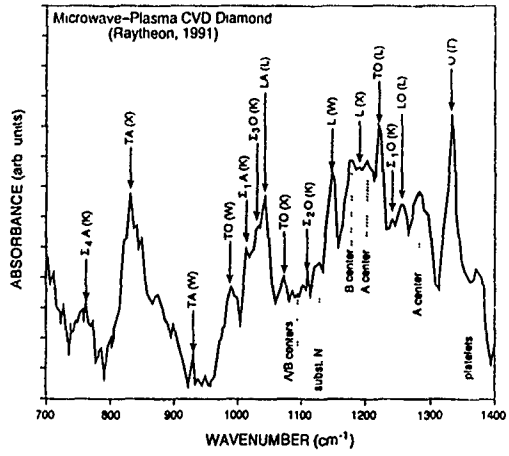



Fig. 2. Absorption spectrum of a microwave-plasma assisted CVD-diamond specimen in the one-phonon region; for the sake of clarity, some of the features are not identified in this plot.

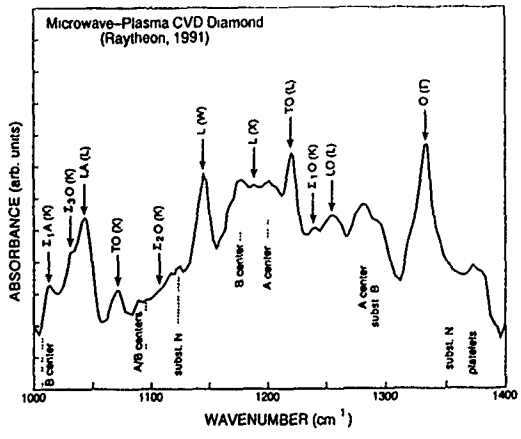



Fig. 3. Absorption spectrum of a microwave-plasma assisted CVD-diamond specimen in the 1000 to 1400 $cm^{-1}$ wavenumber range; this trace identifies all relevant features as assigned in Tables 1 and 3.

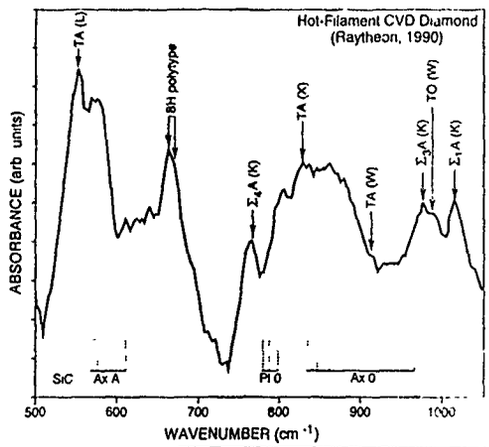



Fig. 4. Absorption spectrum of a hot-filament assisted CVD-diamond specimen in the 500 to 1000 $cm^{-1}$ wavenumber range; some of the features appear to be caused by polytytic SiC (see Ref. 9).

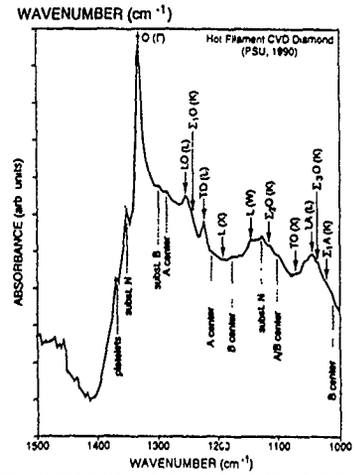



Fig. 5. Absorption spectrum of a CVD-diamond specimen prepared at The Pennsylvania State University; critical-point phonons and impurity-induced features are as previously assigned in Tables 1 and 3.

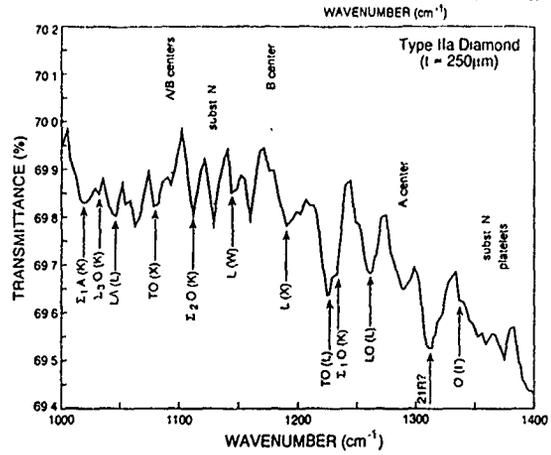



Fig. 6. *Transmission* spectrum of a 250-μm thick type-IIa natural diamond specimen; note the "strong" absorption at 1306/1310 $cm^{-1}$ tentatively assigned to a 2IR rhombohedral diamond polytype.

# THERMAL CONDUCTIVITY OF NATURAL TYPE IIA DIAMOND BETWEEN 500K AND 1250K

J.W. Vandersande, C.B. Vining and A. Zoltan
Jet Propulsion Laboratory/California Institute of Technology
Pasadena, CA 91109

## ABSTRACT

The thermal conductivity of a natural type IIa diamond was measured between 500K and 1250K using the flash diffusivity method. This is the first time that the thermal conductivity of natural diamond has been measured above 450K. The results provide a baseline for comparison to the recently obtained results on isotopically pure diamond. Also, it provides a goal for the thermal conductivity of diamond films which are now routinely being fabricated and have numerous possible high temperature applications.

## INTRODUCTION

The thermal conductivity of diamond has taken on increased significance with the high value very recently obtained on isotopically pure diamond (1). Also, the discovery of the synthesis of diamond films by means of chemical vapor deposition (CVD) at low pressures (2) has made numerous high temperature applications for diamond films now possible. A good baseline is thus needed to determine the improvement in conductivity of the isotopically pure diamond compared to the best natural diamonds (type IIa) and to be able to compare the thermal conductivity of the films with that of the best natural diamonds to assess their quality. However, the thermal conductivity of diamond has been measured only up to 450K and then on different samples, over a variety of temperature ranges, using different measurement techniques. There is scatter in these data and some disagreement between different measurement techniques. The accurate measurement of the thermal conductivity of a natural type IIa diamond (the best heat conducting type natural diamond) over a wide temperature range is thus badly needed to provide the needed baseline. Data above 450K would then provide, at least initially, an upper limit or goal for the thermal conductivity of diamond films at high temperatures. The values could be used to calculate the potential benefit of the use of diamond films at high temperatures for numerous applications.

The thermal conductivity of isotopically pure diamond at room temperature (the only sample measured to date) was found to be 33 W/cm-K(1) compared to 22-25W/cm-K found for three single crystal type IIa diamonds (3, 4). This increase in thermal conductivity appears to be around 50 percent, which would indeed be a significant improvement. There appears to be uncertainty as to the exact cause of this improvement. Whereas Anthony et al. (1) suggested it was the removal of the one percent $^{13}C$ from their sample, standard thermal conductivity theory predicts less than a 5 percent improvement as a result of eliminating the one percent $^{13}C$

isotope (5). The cause of the improvement could be due to different mechanisms. Natural type IIa diamonds, although generally whitish, do have numerous impurities and defects (especially dislocations). A reduction in the concentration of these impurities and defects could easily result in a natural diamond with a considerably higher thermal conductivity. The Anthony et. al. (1) result was compared to the Berman et al. (3, 4) results. The latter, very likely, were samples that came from brownish rather than white type IIa stones (6) since the diamond supplier (DeBeers Corp.) usually kept, and still keeps, the large pure whites for jewelry purposes.

The thermal conductivity of several diamond films have been measured up to 300K (7, 8). At that temperature, the thermal conductivities of three films were found to be between 5 and 10 W/cm-K which compares to between 22 and 25 W/cm-K for natural type IIa diamond. These lower values are most likely due to the polycrystalline nature (very small grains) of the films.

The thermal conductivity of diamond has up until now not been measured above 450K due to the lack of a proper measuring technique and lack of sufficiently large samples. Both these obstacles were overcome by obtaining a large type IIa stone and by using the flash diffusivity method on diamond for the first time. The results are presented here.

## EXPERIMENTAL

The natural diamond measured was determined to be a type IIa based on the UV absorption spectrum. The color was white but according to the supplier (DeBeers Corp.) it came from a slightly brownish stone (not quite good enough for gem stone purposes). The dimensions of the sample were 8.04mm by 8.84mm by 2.35mm thick.

The thermal diffusivity was determined by the flash method in an apparatus described elsewhere (9, 10). Briefly, a xenon flash lamp applies a heat pulse to one side of the sample, by means of a sapphire light pipe, while an InSb infrared detector measures the temperature rise of the rear surface of the sample. The output of the detector is fed through a Textronic differential amplifier into a Nicolet digital storage scope which displays the rear-face sample temperature rise (in mV) versus time (in ms). A flash lamp has several advantages over a laser. The main ones are that it is inexpensive, is capable of higher power levels, and has a very reproducible flash intensity. The main disadvantage is a larger finite pulse time but corrections to that have been developed (11).

The sample was coated (sputtered) all over with a few micrometer thick layer of tantalum on top of which was sputtered a few micrometer thick layer of graphite, to ensure that no light from the flashlamp would pass directly through the sample. The double layer was needed to prevent light being transmitted through the sample. The tantalum layer by itself reflected too much light while the graphite by itself allowed some transmission. The diffusivity was measured both through the short

direction (2.35mm) and the long direction (8.04 cm) of the sample. The latter required minor redesign of the sample holder and fixtures to minimize the amount of flash lamp light entering the detector.

The high thermal diffusivity of diamond means that the heat pulse can propagate through the sample in only a few milliseconds around room temperature. Since the flash lamp pulse itself lasts about 4.61 msec, proper account must be taken for this effect. Both the exact solution to the heat pulse problem as well as an approximate solution have been given previously (11). The approximate solution is quite accurate for usual purposes, but the very short pulse times of this sample raised a question about the reliability of the approximate method in this case.

This concern was addressed in two ways. First, the full solution of the equations for the temperature of the backface was performed numerically to calculate the thermal diffusivity and heat loss from the time to half maximum ($t_{1/2}$) and the time to maximum ($t_{max}$). Results calculated in this way were lower than calculated using the approximate expressions given previously. The difference between the two calculations is negligible (less then 1%) for the 'long' data, as expected since the half-times are long enough in this case to make the approximate solution quite reliable.

For the 'short' data, the approximate solution was about 3% high at 1000 C, 12% high at 500 C, 23% high at 400 C and rapidly getting worse as the temperature decreases further. Because of this the exact solution was used in the 'short' data case. Data below 400 C were rejected because the corrections were too large to be reliable.

The second check on the heat pulse corrections was done by recording the full temperature vs. time history of the backface for several data points, rather than simply $t_{1/2}$ and $t_{max}$. There are still only two adjustable parameters, the diffusivity and the heat loss, so it is a good test of the theory to see how well the full time dependence of the backface temperature can be accounted for by the theory. The diffusivity calculated using the fit of the full curve agrees with the diffusivity calculated using only $t_{1/2}$ and $t_{max}$ to better than 1%. This indicates that the theory works.

The analysis used assumes the heat pulse travels down the sample in one direction only and also assumes that heat is lost only from the front and back faces. In the usual case, and for the diamond in the short direction, this appears to be an excellent assumption. Unfortunately, for the diamond in the long orientation, heat losses from the edges are no longer small compared to heat loss from the front and back faces, simply because most of the sample surface is now edge. From the analysis of the $t_{1/2}$ and $t_{max}$ data for the long direction it is estimated that the total heat loss correction is very small up to about 1000 C. Above this temperature, heat loss corrections are no longer negligible. Unfortunately, the analysis neglects edge heat loss from the edges. In this case, the problem becomes a strongly two-dimensional heat flow problem with a non-trivial geometry. Thus, the long results

above about 1000 K are probably somewhat higher than the actual diffusivity of diamond.

The thermal conductivity was calculated from the measured diffusivity, measured density (3.5 gm/cm$^3$) and the published specific heat (12).

## RESULTS AND DISCUSSION

The experimental results (both "short" and "long" direction data) are shown in figure 1. The Berman et al. (3, 4) data on three type IIa diamonds and the Burgermeister data (13) on one type IIa diamond are also shown. Several aspects are worth noting. First, the data reported here is a reasonable extension to high temperatures of the previously published data. However, upon closer examination there is an interesting difference. Figure 2 shows both the "short" direction and "long" direction data expanded. The best fit lines through each one is drawn and extended down to 300K. There clearly is a difference in slope ($T^{1.13}$ for the "long" direction and $T^{1.54}$ for the "short" direction). Also, the slope through the "long" data extends back up to Berman et. al. data at 300K while the slope through the "short" data extends back to around where the Anthony et. al. data point is for the isotopically pure diamond. As was discussed in the experimental section, the "long" data above 1000 K is probably slightly high due to the heat losses associated with the more complex geometry. At lower temperatures(below 600 K), "long" data was noisy due to the lower sensitivity of the detector at these lower temperatures. There is thus a larger error bar on that data but it is definitely systematically lower (possibly due to the operator systematically reading the noisier data). Based on these two considerations it would be tempting to consider the "short" data to be more accurate and, hence, the correct thermal conductivity. If it is, then it would appear that the Anthony et. al. data on isotopically pure diamond is about the same as the thermal conductivity of a purer (white or less brownish) type IIa diamond.

The thermal conductivity should vary as $T^{-1}$ at the highest temperatures (above the Debye Temperature of around 2000K) since phonon-phonon interactions dominate the phonon scattering at these temperatures. The "long" data with a slope of -1.13 is closer to this -1 value than the "short" data with a slope of -1.54. No compelling case can thus be made for either the "short" or the "long" data. To resolve this impasse, the sample has been sent to Cornell University where the thermal conductivity will be measured between 200K and 400K. Those results will be reported shortly.

Figure 3 shows the results reported here, the Berman et. al. data on the best type IIa diamond as well as published data on two diamond films (7, 8). This high temperature data will be an upper limit for diamond films until high purity single crystal films can be synthesized. The data also indicates that thermal conductivity of the films shown in figure 3 probably peaks at around 300K and then would probably drop sharply with increasing temperature in order to stay below the high temperature data reported here. The data reported here can be used to calculate the

best current performance of the numerous possible high temperature applications of diamond films.

## SUMMARY

The thermal conductivity of a natural type IIa diamond was measured between 500 and 1250K. This is the first time that the thermal conductivity of natural diamond has been measured above 450K. The measurement was performed through both the "short" and "long" direction of the sample. Although the data from these two measurements agree well between 700 and 1000K, there were two distinct slopes through the two sets of data points. An extension of the lower slope ($T^{1.13}$) data down to 300K agreed with the Berman et. al. data while an extension of the higher slope ($T^{1.54}$) data agreed well with the Anthony et. al. data on isotopically pure diamond. The thermal conductivity of the diamond will be measured at Cornell University using the 3Ω method between 200 and 400K in order to resolve the difference. That data will be published shortly. The reported thermal conductivity can be used as a goal value for the thermal conductivity of diamond films and hence be used to calculate performance of devices using diamond films at high temperatures.

## ACKNOWLEDGEMENTS

The authors would like to thank Dr. R. Caveney from the DeBeers Research Laboratory for supplying the diamond. The work described in this paper was carried out at the Jet Propulsion Laboratory/California Institute of Technology, under contract with the National Aeronautics and Space Administration. The work was partially funded by the Wright Research and Development Center.

## REFERENCES

1) T.R. Anthony, W.F. Banholzer, J.F. Fleischer, L. Wei, P.K. Kuo, R.L. Thomas, and R.W. Pryor, Phys. Rev. 42, 1104 (1990)

2) B.V. Spitsyn, L.L. Bouilov and B.V. Deraguin, J. Crys. Growth 52, 219 (1981)

3) R. Berman, E.L. Foster and J.M. Ziman, Proc. Roy. Soc. (London), A237, 344-54 (1956)

4) R. Berman, P.R.W. Hudson and M. Martinez, J. Phys. C: Solid State Phys. 8, L430-434 (1975)

5) J.M. Ziman, Electrons and Phonons, Oxford University Press, London, p. 310 (1960)

6) Private Communication, DeBeers Research Laboratory, Johannesburg

7) D.T. Morelli, C.P. Beetz and T.A. Perry, J. Appl. Phys. 64 (6), 3063 (1988)

8) T.R. Anthony, J.L. Fleischer, J.R. Olson and D.G. Cahill, to be published

9) J.W. Vandersande, C. Wood, A. Zoltan and D. Whittenberger, Thermal Conductivity, Vol. 19, D.W. Yarborough ed. (Plenum, New York, 1998), pp. 445-452

10) J.W. Vandersande, A. Zoltan and C. Wood, Int. Jour. of Thermophysics, Vol. 10, 251 (1989)

11) C.B. Vining, A. Zoltan and J.W. Vandersande, Int. Jour. of Thermophysics, Vol 10, 259 (1989)

12) A.C. Victor, J. Am. Chem. Soc. 36, 1903-11 (1962)

13) E.A. Burgemeister, Physica 93B, 165-79 (1978)

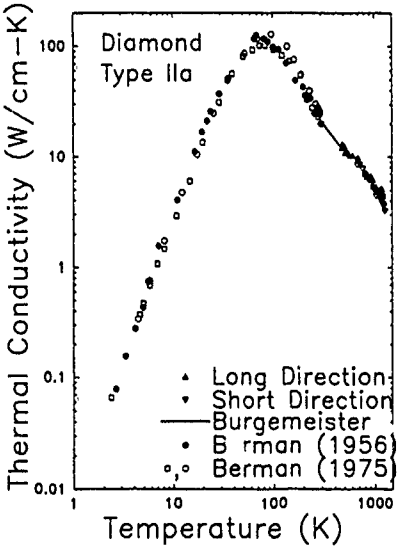



Figure 1: Thermal conductivity of a natural type IIa diamond between 500 and 1250K measured in two directions. The Berman and Burgemeister data is shown for comparison.

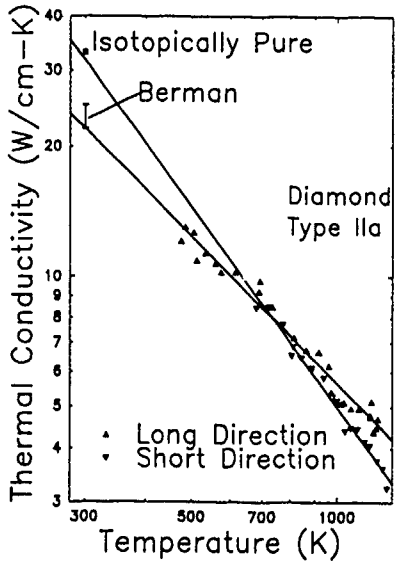



Figure 2: The "long" and "short" direction thermal conductivity data shown expanded. The two slopes are 1.13 and 1.54 respectively. The Berman 300K data range and the isotopically pure 300K data point are shown for comparison.

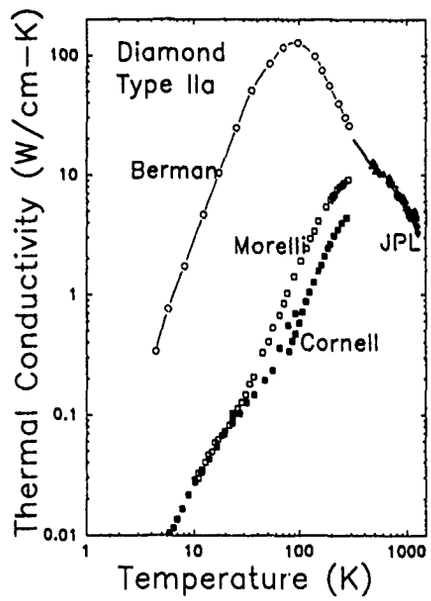



Figure 3: The thermal conductivity of a natural type IIa diamond between 500 and 1250K. The Morelli and Cornell data on diamond films is shown for comparison.

# THE ROLE OF ELASTIC INTERACTION OF PHONONS IN DIAMOND

V.I.Nepsha, V.R.Grinberg, Yu.A.Klyuev, N.A.Kolchemanov, A.M.Naletov

State Institute of Diamond Research (VNIIALMAZ)
129110 Moscow, Gilyarovsky st. 65 (USSR)

It is shown, that the dependence of synthetic diamonds thermal conductivity from isotope $^{13}C$ contents can be explained if one takes into account elastic phonon-phonon interactions at which the total quasi-impulse is preserved (N-processes). In diamonds with reduced $^{13}C$ contents the effects of Poiseuille phonon flow and the second sound can be revealed.

In case, when one cannot neglect the processes of three-phonons interactions with the conservation of the total quasi-impulse (N-processes) the dielectric thermal conductivity $\varkappa$ in Debye approximation can be expressed as follows (1):

$$\varkappa = \varkappa_1 + \varkappa_2 \qquad 1.$$

where $$\varkappa_1 = \frac{k}{2\pi^2 v}\left(\frac{k}{\hbar}\right)^3 T^3 \int_0^{\theta/T} \frac{\tau_c x^4 e^x}{(e^x-1)^2}\,dx$$

and $$\varkappa_2 = \frac{k}{2\pi^2 v}\left(\frac{k}{\hbar}\right)^3 T^3 \frac{\left[\int_0^{\theta/T} (\tau_c/\tau_N) x^4 e^x (e^x-1)^{-2}\,dx\right]^2}{\int_0^{\theta/T} (\tau_c/\tau_N\tau_R) x^4 e^x (e^x-1)^{-2}\,dx}$$

Here k and $\hbar$ are Boltzman and Plank constants, $\theta$ - Debye temperature, v is the mean velocity of phonons, $x=\hbar\omega/kT$ ($\omega$ is phonon frequency), $\tau_N$ is the relaxation rate for N-processes, $\tau_R$ is the relaxation rate with the quasi-impulse alteration including the three-phonon interactions (U-processes) and $\tau_c$ is the combined relaxation rate ($\tau_c^{-1} = \tau_N^{-1} + \tau_R^{-1}$).

Using expression 1. and selecting the values of parametres in the expression for relaxation rates for N-processes $\tau_N^{-1} = A_N T^4 x$ (4), and U-processes $\tau_U^{-1} = A_U T^4 x^2 \exp(-\alpha/T)$ (4,5), one can describe the experimental thermal conductivity depэndence in perfect synthetic diamonds from the concentration of $^{13}C$ isotopes at 300 K, which was obtained in paper (2) (Fig.1), and also the results of measurement $\varkappa$ in defectless natural diamonds at 320 and 450 K from paper (3). In the last case c=1.1%, which corresponds to the natural spread of $^{13}C$ isotope.

This testifies, that N-processes are of great importance. Moreover, Ziman's limit is well practicable when one supposes $\tau_N \ll \tau_R$. Consequently, the consideration of related hydrodynamic effects in the phonons system is correct.

It is known, that if the phonon free length in N-processes $\ell_N = v\tau_N$ is much less, than in processes with quasi-impulse alteration $\ell_R = v\tau_R$, and $\ell_N \ll D$ (where $D$ is the characteristic sample size), then the effective scattering at boundaries $\ell_b^{eff} \simeq D^2/\ell_N$ and Poiseuille phonon flow occurs. It leads to the thermal conductivity growth in $D/\ell_N$ times in comparison with the widespread situation when the phonon free length is limited by the sample size $D$ and $\ell_b^{eff} = \ell_b$. AS a matter of fact for Poiseuille flow the condition $l \ll l$ is insufficient and the more strict relation $l\, l \gg D$ is necessary to be fulfilled (3-5).

For taking into account Poiseuille flow in $\tau_R$ ($\tau_R^{-1} = \sum \tau_i^{-1}$) we used in the expression 1. instead of $\tau_b$ the following expression:

$$\tau_b^{eff} = \frac{D^2 + v^2 \tau_b \tau_N}{v^2 \tau_N} \qquad 2.$$

which in the required limit cases $\tau_N \gg D/v$ and $\tau_N \ll D/v$ gives for $\tau_b^{eff}$ the values $\ell_b$ and $D^2/\ell_N$ correspondingly. Besides that at $\tau_N \ll \tau_R$ from 1. it follows the above mentionso criterion $\ell_N \ell_R \gg D^2$ for Poiseuille flow. In the narrow region at $\tau_N \sim D$ the expression 2. gives the overestimated $\ell_b^{eff}$, but not more than two times greater.

On Fig.2 the results of calculation for diamonds with c=0 and 0.07% are presented. One can see, that for isotopically pure diamonds Poiseuille flow can be displayed in the temperature range from 15 to 120 K. At T>15K the thermal conductivity increases with temperature steeper than $T^3$ and at $T \approx 70$ K exceeds the thermal conductivity of purest natural diamonds by two orders of magnitude. This effect must be also displayed in diamonds with c=0.07% which is described in paper (2). But in this case the maximum thermal conductivity reduces by one order of magnitude.

If the role of N-processes is so great then it will be correct to consider the possibility of oscillations spread in the phonon gas that is the second sound having the velocity $v/\sqrt{3}$.

The conditions for the existance and observation of the second sound in solids were discussed in papers (6-8) and they reduce to the demands $\ell_N \ll \ell_R$ and $\lambda/\ell_N \gg 1$ ($\lambda$ is the wavelength of sound). At these conditions the sound dissipation is proportional to the value $\delta = (\ell_N/\lambda) + (\lambda/\ell_R)$. From this we can find the value $\lambda = \lambda_m$, at which the value $\delta$ is minimum. It is easy to show that $\lambda_m = \sqrt{\ell_N \ell_R}$ and $\delta_m = 2\sqrt{(\ell_N/\ell_R)}$.

By averaging the expression for $\tau_N$ and $\tau_R$ for phonons frequencies we can get $\langle \ell_N \rangle$ and $\langle \ell_R \rangle$ and consequently and $\delta_m$ .

On Fig.3 the calculated values $\langle \ell_N \rangle$, $\langle \ell_R \rangle$, $\lambda_m/\langle \ell_N \rangle$ and $\delta_m / \lambda_m$ are indicated for isotopically pure diamond with the sample cross section D=10mm. The optimum conditions for the second sound existance correspond to temperature range 30-70 K at frequency $f_m \approx (1-7)10^6$ Hz.

The examined experimental results can be also satisfactorily described using the expression for the relaxation rates in the form $\tau_N^{-1} = A_N T^5 x^2$ and $\tau_U^{-1} = A_U T^5 x^2 \exp(-\alpha/T)$. In this case the hydrodynamic effects are not so strong as was obtained above. Nevertheless it follows from our calculations that at such a consideration Poiseuille phonon flow and second sound can be displayed rather clearly in isotopically pure diamonds at D=10mm.

In conclusion we must note that the results of this paper have the character of estimations, which in more degree admit, than prove the possibility of observation in diamonds such rare effects as Poiseuille phonon flow and second sound.

## REFERENCES


1. J. Callaway, Phys. Rev. 113, 1046 (1959).
2. T.R. Anthony, W.F. Banholzer, J.F.Fleischer, Lanhua Wei, P.K. Kuo, R.L. Thomas, R.W. Pryor, Phys. Rev.B 42, 1104 (1990).
3. E.A. Burgemeister, Physica 93 B, 165 (1978).
4. R. Berman, Thermal conduction in solids, Clarendon Press, Oxford (1976).
5. R. Berman, M. Martinez, Diamond Research, Suppl. Industr. Diam. Rev., p.7 (1976).
6. R.N. Gurzhi, Uspehi Fisicheskih Nauk 94, 689 (1968) (in Russian).
7. E.W. Prohofsky, J.A. Krumhansl, Phys. Rev. 133, 1403 (1964).
8. R.A. Guyer, J.A. Krumhansl, Phys. Rev. 133, 1411 (1964).

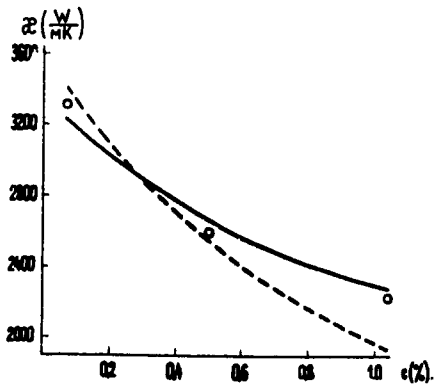



Fig.1. The dependence of diamond thermal conductivity from the content of carbon isotope C at T=300 K. O experimental results (2); – – – calculated results in Ziman's limit; —— results, calculated according to the expression 1.

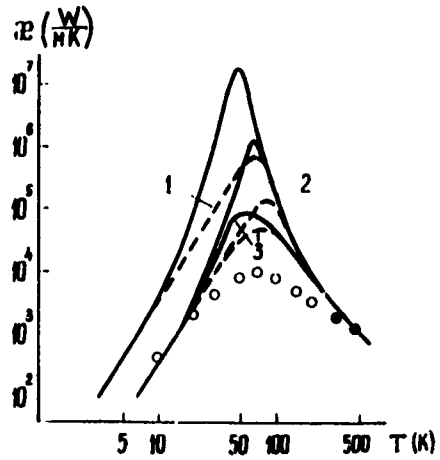



Fig.2. The calculated results for diamond thermal conductivity dependence on temperature ( —— with taking into account Poiseuille phonon flow and – – – without it).
1 - c=0, D=10mm; 2 - c=0, D=1mm; 3 - c=0.07%, D=1mm. The experimental results are for natural diamond with D≈1mm ( O from paper (5), ● from paper (3)).

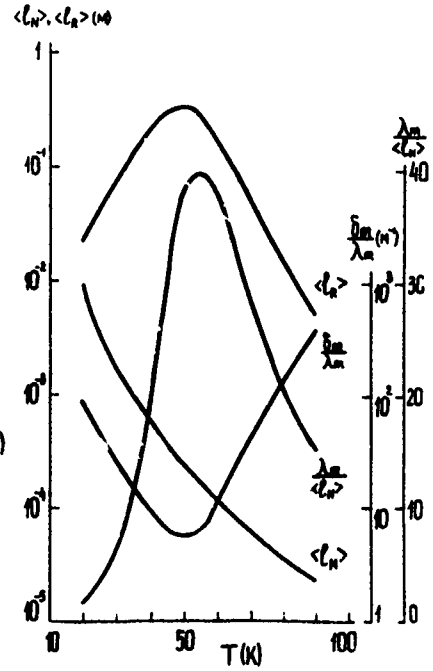



Fig.3. The calculated results $\langle \ell_N \rangle$, $\langle \ell_R \rangle$, $\delta_m / \lambda_m$, $\lambda_m / \langle \ell_N \rangle$ for a diamond with c=0 at D=10mm.

# HIGH TEMPERATURE GRAPHITIZATION OF DIAMOND

J. K. Lewis, H. Chen, S. Nafis, M. Nielsen,
S. Bonafede*, R. O. Dillon
Department of Electrical Engineering and
Department of Chemistry*
University of Nebraska, Lincoln, NE 68588

T. Furtak
Department of Physics
Colorado School of Mines, Golden, CO 80401

## ABSTRACT

Synthetic Type Ib diamonds have been heated from 1700°C to 2000°C in atmospheres of helium and nitrogen. CVD films have been heated at 1800°C for comparison to the bulk diamonds. The percent of graphitization for the (111), (100), and (110) orientations of natural type IIa diamond have been studied. It was found that the (110) orientation had the highest graphitization while the (100) was slightly graphitized and the (111) was least graphitized. Surface to volume ratios confirmed that graphitization is controlled by surface rather than bulk nucleation up to 1900°C. IR and UV-Visible spectra were found to be a sensitive indication of graphitization.

## INTRODUCTION

The work of Friedel and Ribaud (1) has shown that there are two regimes of diamond graphitization when heated in an inert atmosphere. For lower temperatures graphitization is confined to the surface and the bulk of the diamond remains undamaged. However, for temperatures above 1700°C, graphitization occurs in the bulk of the diamond causing cracks, and usually disintegration. The transition temperature between the two distinct regimes, called Tg, has also been quantified by Seal (2) to be around 1700°C for diamonds heated 30 minutes. He suggests that in the lower temperature regime the direct diamond to graphite change either is very slow or does not occur. Above Tg, the change is primarily a bulk reaction because the nuclei of graphite formed on the surface are insufficient to account for the observed rate of graphitization.

The purpose of our work was to determine the effects of graphitization for periods of two to four minutes, study how nitrogen content of type Ib diamonds affects graphitization, and compare our CVD films to the bulk diamonds.

## EXPERIMENTAL

Initial experiments were performed with faceted diamonds in a helium atmosphere to determine an approximate graphitization temperature. Quantitative experiments were then achieved in this temperature range with synthetic and natural diamonds.

Synthetic type Ib diamonds were supplied by Sumitomo Electric Carbide Inc. and natural type IIa diamonds were from Dubbeldee Harris Diamond Corporation.

The furnace was an Astro Model 1000, which had a minimum warm-up time of an hour. Therefore, modifications were made to dispense the diamond from a room temperature environment into the center of the furnace, and, after a few minutes, extract the diamond out of the "hot zone." The temperature was monitored with an optical pyrometer and corrected for passage through the quartz viewport. Inert atmospheres of nitrogen and helium were controlled by flow meters supplied with the Astro furnace. Pressure was maintained at approximately 1 atm.

The Raman spectra were used to analyze changes in bonding structure. The surface morphology was characterized by optical micrographs both before and after graphitization. The rate of graphitization was examined by UV-Visible and IR spectroscopy.

In addition, the percent of graphite was calculated from Archimedes' principle using the volume change of the heated diamonds. The volume was determined by weighing in air and in a liquid with a density of 2.10 $\pm$ 0.05 gm/cc at 23°C. Due to the precision of the balance when weighing small masses, large uncertainties were introduced with the Archimedes' measurement. The densities of graphite and diamond are 2.26 and 3.515 gm/cc respectively, so complete conversion to graphite would be associated with more than a 50% change of volume. The percentage of increased volume was defined and calculated from the following equation:

$$\Delta V \equiv \frac{\text{experimental volume change}}{\text{volume change from 100\% diamond to 100\% graphite}}$$

$$= \frac{(W_a - W_l)/D_l - W_a/D_d}{W_a * (1/D_g - 1/D_d)} * 100\% \qquad (1)$$

where, $W_a$ and $W_l$ are weights in air and liquid, $D_l$, $D_g$, and $D_d$ are the densities of the liquid, graphite and diamond, respectively. If volume changes due to cracking are neglected, then this equation calculates the percent of graphite with reference to a totally graphitized specimen.

## RESULTS AND DISCUSSION

### 1. Crystal plane dependence

The graphitization was determined for the (100), (110), and (111) planes by subjecting Type IIa natural diamond, samples 1, 2 and 3, to a 1800°C helium atmosphere for two minutes, as shown in Table 1. All planes were specified by the vendor to within $\pm 3°$. Both the UV-Visible and IR spectra decrease in magnitude with increasing temperature, but the shape of the IR spectra is not significantly modified by heating. Therefore, changes in the IR spectra are characterized in Table

1 by the IR transmission ratio, the ratio of transmittance before heating to after heating. Since graphite is opaque to this radiation, large ratios correspond to more graphitization. Table 1 shows that the IR transmission ratio at the arbitrarily chosen wave number 4000 $cm^{-1}$ increases slightly from 1.2 to 1.4 in changing from (111) to (100) orientations and then rises substantially to 69 with the (110) orientation. The percent graphite calculated from Archimedes' principles also remains consistent with this ordering.

The plane with the lowest graphitization rate does not agree with Seal's (2) result which had a lowest rate on (100). A possible reason is due to the different grades of diamond. However, the results indicate that the (111) and (100) surfaces have very similar surface activation energies which are significantly larger than the energy of (110) surface.

Optical micrographs of these three samples after the two-minute heating show discretely distributed graphitization sites. This observation confirmed that the initial stage of graphitization does not cover all the surface (3).

2. Temperature dependence

The synthetic diamonds were subjected to temperatures from 1700°C to 2000°C, and the Archimedes' measurement, UV-Visible and IR spectra indicated the amount of graphitization. Figure 1(a) gives the IR spectrum for an unheated CD2016 diamond while Figure 2(a) gives the UV-Visible spectrum. Figures 1 and 2 also give the spectra of CD2016 diamonds at 1700, 1800, and 1900°C in the same fashion. The IR transmission ratios show a large increase occurring between 1800 and 1900°C, wnich agree with the calculated percent of graphite.

The UV-Visible spectra for the same diamonds illustrate an impurity to conduction gap of 2.7 eV (465 nm). The absorption feature at 660 nm was due to a poor diode in the detector array and should be neglected in all the UV-Visible spectra. In addition, the discontinuity at 400 nm was due to a lamp change, and thus should also be neglected. The 2.7 eV gap is not significantly changed at 1700 or 1800°C, but when subjected to 1900°C, an abrupt change occurs in the UV-Visible spectrum. In particular, the gap disappears, and the sample is almost totally opaque to this radiation. Optical micrographs of the synthetic diamonds show that cracks in the diamond surface act as nucleation sites for graphitization as illustrated in Figure 3. This type of nucleation was not apparent in the natural diamond.

In addition to IR and UV-Visible spectra, Raman spectra were taken on CD2016, sample 1, as illustrated in Figure 4(a), after being subjected to 1800°C for two minutes in a helium atmosphere. The only feature of the spectrum is the diamond line at 1333 $cm^{-1}$. Figure 4(b) shows the appearance of graphite peaks in addition to the diamond line when sample 3 was exposed to 1900°C in the same environment. Peaks were at 1333, 1347, and 1589 $cm^{-1}$ with half-widths of 6, 71, and 66 $cm^{-1}$ respectively. The peak at 1347 $cm^{-1}$ appears when long range order is lost and momentum is no longer conserved in the solid. This can happen when the structure is amorphous or when the grapnite particles are microcrystalline (less than 10 nm) (4). The half-widths of the 1347 and 1589 $cm^{-1}$ peaks are consistent with either microcrystalline graphite or amorphous carbon, so Raman spectroscopy alone cannot distinguish between these two alternatives. However, the appearance of an amorphous

structure at such a high temperature is very unlikely, so the microcrystalline explanation is probably correct.

3. Time dependence

An indication of the effect of time on graphitization was studied by extending the furnace time from two to four minutes at 1800°C in a helium atmosphere for both natural and synthetic diamonds. Table 1 shows the expected increase in graphitization with time, although it should be noted that some diamond remains intact after four minutes at 1800°C. In addition, Figure 5(a),(b), and (c) illustrate the UV-Visible spectra as a function of time. In Figure 5(b), after heating for two minutes, the transmittance is reduced throughout the entire spectral range, the absorption edge is still well defined at 225 nm, and a broad absorption feature appears at 260 nm. When time is extended to four minutes, Figure 5(c), the transmittance is further reduced, a broad absorption feature occurs at 285 nm, and the band edge is no longer defined.

4. Nitrogen atmosphere

The effect of a nitrogen atmosphere on Type Ib synthetic diamonds was studied because graphitization occurs predominantly along cracks in synthetic diamonds, but not in natural diamonds. A comparison of helium and nitrogen atmospheres is made in Table 1, synthetic diamonds (CD1210) samples 1, 5, 6, and 7. The percent graphite calculated with the Archimedes' technique does not change significantly as nitrogen is introduced, but the weight loss incurred rises. In addition, Figures 6(a) and 6(b) are micrographs of synthetic diamonds subjected to 1900°C in helium and nitrogen, respectively. They indicate that cracking is accelerated in the nitrogen atmosphere, accompanied by a dendritic-like growth. The increased weight loss is probably due to the formation of carbon-nitrogen gaseous compounds.

5. CVD diamond

Another set of temperature-dependent studies was done using our films deposited by rf plasma enhanced chemical vapor deposition (5). The substrates were poor quality natural faceted and flat diamond containing some graphite inclusions. In run 156, 3.19 mg of film was deposited on a substrate of 42.11 mg, resulting in a composite specimen containing about 7.0% by mass of film. This was put in a helium atmosphere for two minutes at 1800°C, and a weight loss of 0.02 mg was recorded. The Archimedes' results were interpreted with a slight modification to equation (1) to yield the volume percent graphite for the composite specimen. This measurement determined that the heated material contained $(2\pm1)$ % by volume of graphite, or $(1.3\pm0.7)$ % by mass of graphite; thus, establishing that a large portion of the film survived this temperature in the diamond phase. Typical optical micrographs of these films are illustrated in Figure 7(a), before heating, and 7(b), after two minutes in a 1800°C environment. The morphology in Figure 7(a) consists of an interesting pattern of pyramids and under higher magnification the micrographs clearly exhibit an orthogonal set of crack patterns. Figure 7(b) shows that the most extensive black regions are at the intersection of cracks. Thus, cracks appear to be the dominant nucleation centers for graphitization in films as well as synthetic diamonds.

## SUMMARY

We have determined that the relative change in IR transmission is a very good diagnostic for graphitization. An abrupt change in the rate of graphitization of natural

and synthetic diamonds occurred between 1800 and 1900°C for the two minute heating time. Therefore, the onset of the second temperature regime, Tg, for bulk reaction is between 1800 and 1900°C. IR transmission ratios for the (100) and (111) orientations indicate that natural diamonds are slightly less graphitized than synthetic diamonds. We also have determined that our CVD films are as resistant to graphitization at 1800°C as the bulk diamonds.


## ACKNOWLEDGEMENT

The authors wish to thank Wright-Patterson Air Force Base for funding this research through Contract #: F33615-86-D-2720.


## REFERENCES


1. G. Friedel and G. Ribaud, Bull. Soc. Franc. Min., **47**, 94 (1924)
2. M. Seal, Phy. and Chem. of Solids, **3**, 658 (1963)
3. G. Davies and T. Evans, Proc. R. Soc. Lond., **A328**, 413 (1972)
4. R.O. Dillon, J.A. Woollam, and V. Katkanant, Phys. Rev. B., **29**, No. 6, 3482 (1984)
5. D.E. Meyer, R.O. Dillon, and J.A. Woollam, J. Vac. Sci. Technol, **A7** (3), 2325 (1989)


Table 1. Summary of experimental conditions and results

| Samples | | # | T (°C) | Gas | Time (min) | IR Ratio | ΔV % | Comment |
|---|---|---|---|---|---|---|---|---|
| Natural Type IIa Diamond | | | | | | | | |
| | (100) | 1 | 1800 | He | 2 | 1.4 | 5±2 | darker & transparent |
| | (110) | 2 | 1800 | He | 2 | 69 | 13±2 | darkest & opaque |
| | (111) | 3 | 1800 | He | 2 | 1.2 | 1±4 | light dark & transparent |
| | (100) | 5 | 1800 | He | 4 | 3.7 | >25 | partly disintegrated |
| Synthetic Type Ib Diamond | | | | | | | | |
| UP303015 | (100) | 1 | 1800 | He | 2 | 1.6 | 3±1 | light dark |
| | (100) | 2 | 1800 | He | 4 | 12 | >6 | partly disintegrated |
| CD2016 | (111) | 1 | 1800 | He | 2 | 1.5 | 5±2 | light dark |
| | (111) | 2 | 2000 | He | 2 | | | black & disintegrated |
| | (111) | 3 | 1900 | He | 2 | 34 | 14±2 | dark |
| | (111) | 4 | 1700 | He | 2 | 1.4 | 2±2 | light dark |
| CD1210 | (111) | 1 | 1900 | He | 2 | | 30±7 | dark & opaque |
| | (111) | 5 | 1800 | He | 2 | 0* | 6±6 | light dark |
| | (111) | 6 | 1900 | $N_2$ | 2 | 0.80* | 30±7 | dark & opaque |
| | (111) | 7 | 1800 | $N_2$ | 2 | 0.03* | 7±6 | light dark |

* Weight loss (mg)

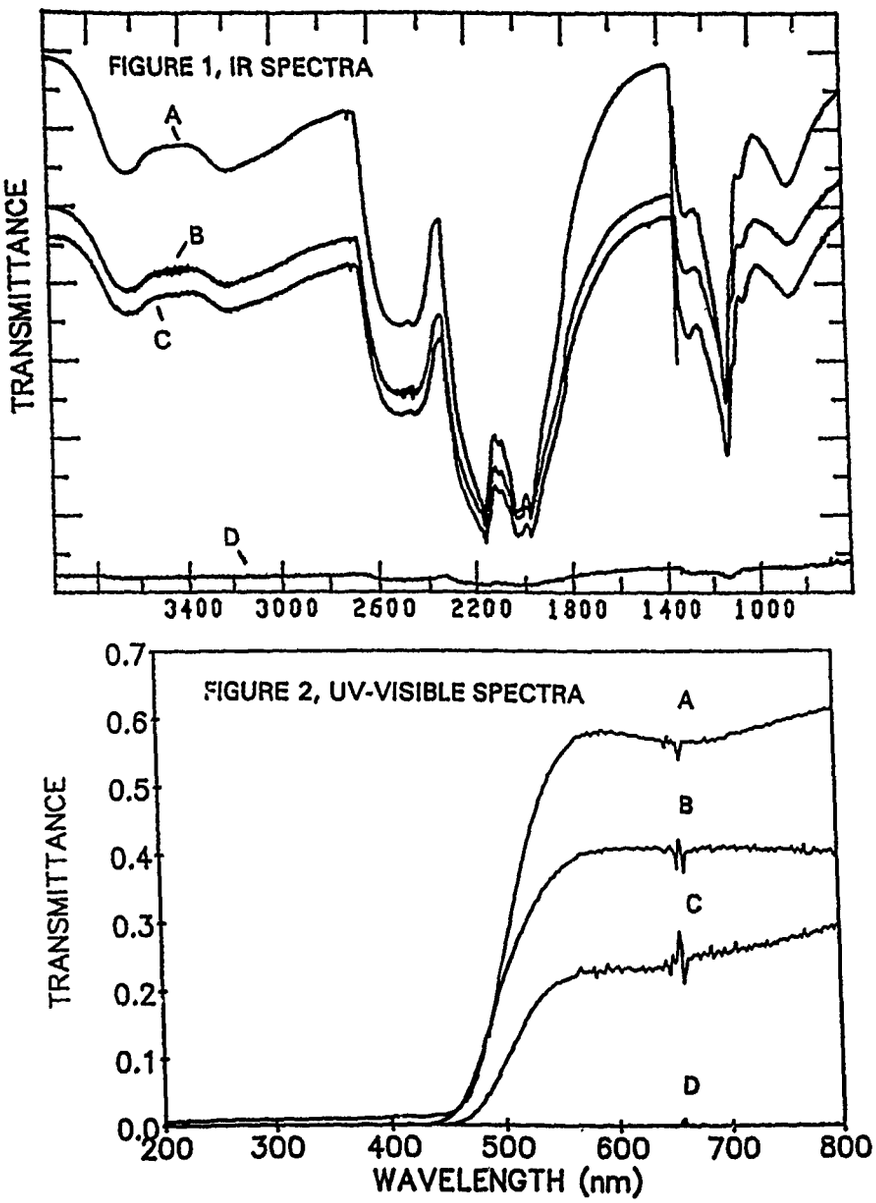



**FIGURE 1 & 2, SYNTHETIC DIAMOND, HELIUM, 2 MIN.**
**(A) UNHEATED, (B) 1700°C, (C) 1800°C, (D) 1900°C**

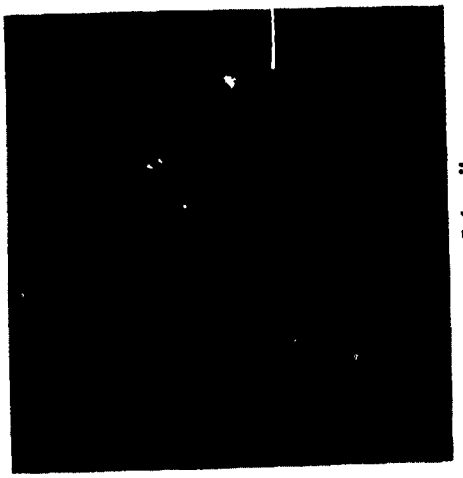


FIGURE 3, SYNTHETIC DIAMOND
1800°C, 400X

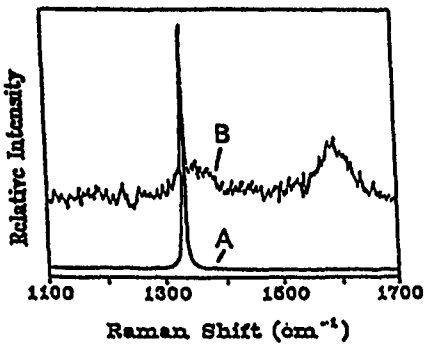



FIGURE 4, SYNTHETIC DIAMOND
(A) 1800°C, (B) 1900°C

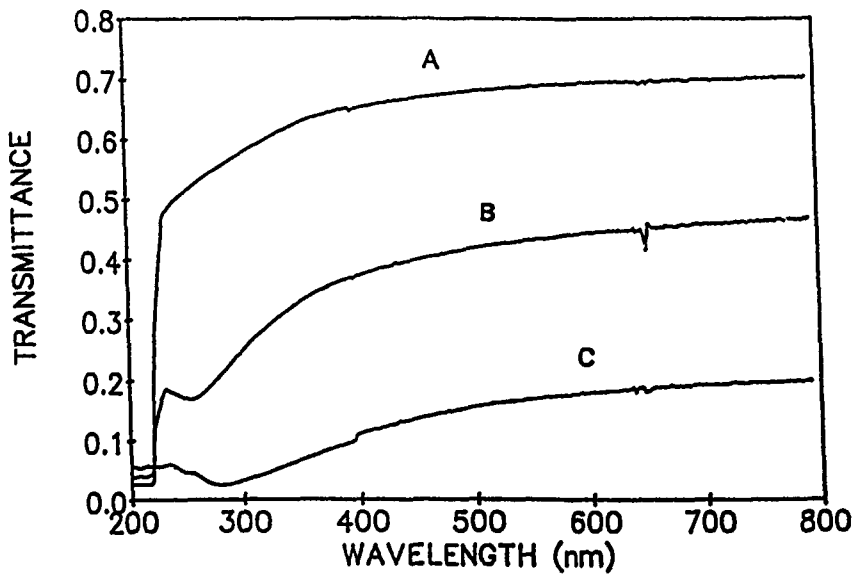
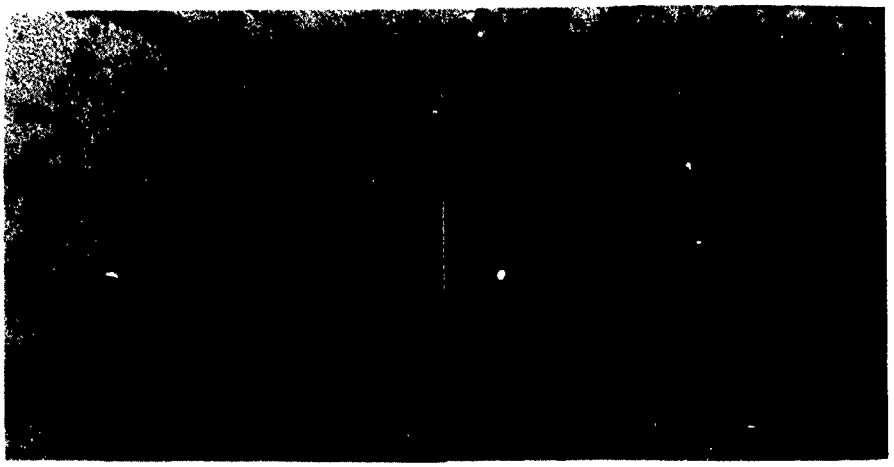
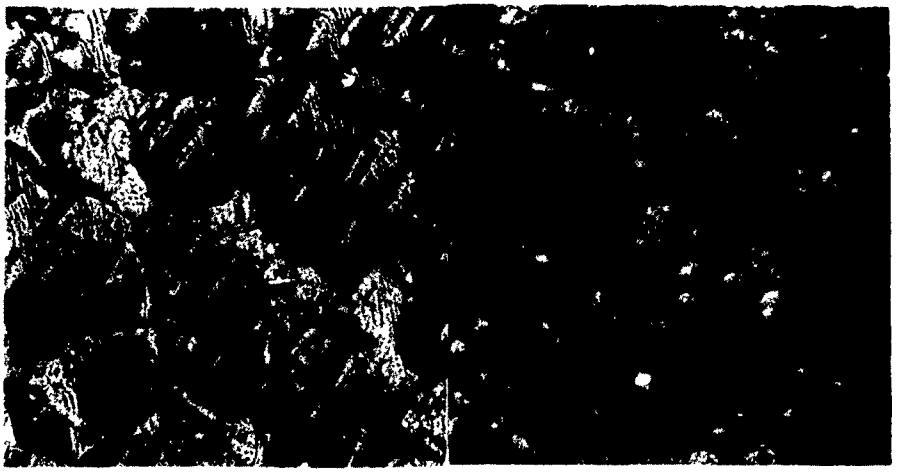



FIGURE 5, NATURAL DIAMOND, HELIUM, 1800°C
(A) UNHEATED, (B) 2 MIN., (C) 4 MIN.



A B

FIGURE 6, SYNTHETIC DIAMOND, 1900°C, 400X, 2 MIN.
HELIUM ON LEFT, NITROGEN ON RIGHT



A B

FIGURE 7, CVD DIAMOND FILM, 100X, 2 MIN.
UNHEATED ON LEFT, AFTER 1800°C ON RIGHT

# OXIDATION OF CVD DIAMOND FILMS

Q. Sun and M. Alam
Department of Materials and Metallurgical Engineering
New Mexico Institute of Mining and Technology
Socorro. New Mexico 87801

## ABSTRACT

Thermal oxidation of CVD diamond films on 111 oriented silicon wafers in oxygen at atmospheric pressure and up to 1273 K was investigated by thermogravimetry. The data is compared with that of 100 and 111 oriented type IIa natural diamond wafers, natural diamond and graphite powders. As deposited diamond films on one side of a silicon wafer appear gray in color and turn black on oxidation. A free standing diamond film has a pale yellow color which is unaffected by oxidation. Extensive oxidation occurs by etching pits on the surfaces and edges of diamond grains. X-ray diffraction do not indicate transformation to non-diamond carbon forms. Raman spectroscopy indicates a decrease in the amount of non-diamond carbon on oxidation. Diamond films start to oxidize at a much lower temperature as compared to natural diamond and graphite powders. The rate of oxidation of diamond films is lower than the rates of oxidation of 111 and 100 oriented diamond wafers. The oxidation behavior is consistent with at least two reaction paths.

## INTRODUCTION

The potential applications of CVD diamond films in advanced materials technology are numerous (1). It is anticipated that in the very near future, products coated with diamond by the CVD method would be commercially available (2). In many of the applications, diamond coated components would be exposed or could get exposed to oxygen in air at elevated temperatures. Such an exposure may lead to graphitization and/or oxidation of the diamond film with associated degradation in properties followed by premature failure of the component. A study of the thermal oxidation of CVD diamond films is vital for seeking information regarding environmental limitations in terms of temperature and oxygen potential for safe use of such films in potential applications. There is considerable amount of interest among the researchers in this area. This is evident from several papers that have appeared recently (3-

9). The purpose of this documentation is to further understand the mechanism and kinetics of thermal oxidation of CVD diamond films.

## EXPERIMENTAL

Diamond films were synthesized from $CH_4$-$H_2$ gas mixtures on 111 oriented silicon wafers by the hot filament assisted CVD technique. All films were prepared under identical conditions. (Filament temperature = 2275 K, Substrate temperature = 1225 K, System pressure = 30 torr, Total gas flow rate = 100 sccm, Methane content of input gas = 0.5 v%, Distance between filament and substrate = 0.5 cm). The films grew at a rate of 0.35 μm/hr and were grown for 20 hrs. The average film thickness was about 7 μm.

Oxidation measurements were carried out in a thermogravimetric system. Initially silicon wafer coated with diamond on one side is placed in a quartz sample hanger which is then suspended from one arm of the Cahn balance with a fine platinum wire into the hot zone of the furnace (0.05 m long in the middle). UHP grade oxygen is allowed to flow at $8.3 \times 10^{-6}$ $m^3/s$ at STP and the furnace is turned on. Weight loss sustained by the sample and furnace temperature is monitored continuously as a function of time as the furnace is heated up to 1273 K. In case of isothermal experiments, the system is first purged with UHP grade argon flowing at $8.3 \times 10^{-6}$ $m^3/s$ at STP for at least 3600 s before the furnace is turned on. Preheating is carried out under flowing argon till the furnace reaches the desired temperature. At this stage argon flow is terminated and oxygen is allowed to flow at $8.3 \times 10^{-6}$ $m^3/s$. All oxidation measurements were conducted at atmospheric pressure.

## RESULTS AND DISCUSSION

### Macroscopic Observations

The films attached to one side of a silicon wafer appear gray in color. On the other hand a free standing diamond film obtained by etching the silicon wafer in a HF-$HNO_3$ solution (in the ratio of 1:3) is pale yellow in color. When a diamond film attached to the silicon wafer, a free standing diamond film, a 100 and a 111 oriented natural diamond wafer are heated in flowing argon gas, no weight change is observed and samples do not undergo any color change. When heating is carried out in flowing oxygen, all samples lose weight. Diamond film attached to the silicon wafer changes its color from gray to black, where

as a free standing diamond film and natural diamond wafers do not experience color change. This suggest that the color change is not a result of a simple physical transformation of diamond to nondiamond carbon forms. The presence of substrate and oxygen is essential for color change.

Electron Microscopy

Typical SEM micrographs of the growth side and the substrate side of the diamond films before and after oxidation are presented in Fig. 1a-1d. Oxidation was carried out at 973 K till films lost 25% of their initial weight. In case of unoxidized films the growth side is dominated by octahedral, {111} morphology. The individual grains are 0.5 - 3 $\mu$m in size. The substrate side is extremely smooth. Grain boundaries are clearly visible along with voids. After oxidation the growth side shows pits of various sizes. Well faceted crystals cannot be seen. The degree of attack appears to be the same all over. The oxidation behavior of the substrate side of the film is quite different. Etching appears to be more severe at the boundaries between the grains rather than the interior of the grains.

SEM micrographs of {100} and {111} surfaces of natural diamond wafers before and after oxidation are presented in Fig. 2a-2d. The figures show that {100} surface is more resistant to oxidation as compared to {111} surface. Such a behavior has been reported previously (9). Such surfaces in the CVD diamond films before and after oxidation are presented in Fig. 3a and 3b respectively. After oxidation {100} surfaces (square shaped) remain smooth, while {111} surfaces (triangle shaped) show pits on the surface due to etching with oxygen. Such differences have been attributed to defect sites on {111} surface (10). These defects are believed to be dislocations running normal to the {111} faces (10).

X-ray Diffraction

X-ray diffraction patterns of diamond films on silicon wafer, before and after partial oxidation are presented in Fig. 4a and 4b respectively. In the 2$\theta$ range scanned unoxidized diamond film show all peaks of diamond. After partial oxidation diamond peaks are still visible, despite the loss of well faceted crystals as evidenced by SEM. Peaks pertaining to other carbon phases were not detected after oxidation. Therefore, either no phase transformation occurred or the transformed phases are amorphous.

Raman Spectroscopy

Raman spectra of diamond films before and after partial

oxidation are presented in Fig. 5a and 5b respectively. The sharp peak at 1331.7 $cm^{-1}$ is characteristic of diamond. The broad peak centered at about 1500 $cm^{-1}$ arises from a highly disordered phase consisting both $sp^2$ and $sp^3$ hybridised carbon that need not be graphitic in nature. The lowering of the intensity of the broad maximum relative to the diamond peak after oxidation indicates that the non-diamond carbon in the film is oxidised at a higher rate as compared to diamond. Raman spectroscopy did not reveal the formation of graphite. Either no phase transformation occurred or if diamond transformed to a form represented by the peak centered at around 1500 $cm^{-1}$, the rate of oxidation of the transformed phase is higher than the rate of its transformation.

Thermogravimetry

The thermogravimetric curves for the oxidation of a typical diamond film on one side of a silicon wafer, {100} and {111} oriented type IIa natural diamond wafers are presented in Fig. 6. The film was 22 mm in diameter, 3.5 μm thick and weighed 4.8 mg. The natural diamond wafers were 2.5 x 2.5 x 0.25 mm in size and weighed 5.5 mg each. The geometric surface area available for oxidation was 380 $mm^2$ for the film and 15 $mm^2$ for the wafers. The figure indicates that the diamond film begins to oxidize at the lowest temperature followed by {111} natural diamond wafer and finally {100} oriented natural diamond wafer. The lower inception temperature of {111} surface as compared to {100} surface is due to the higher oxidation resistance of {100} surface as compared to {111} surface. The lower inception temperature for the oxidation of CVD diamond film can be attributed to the presence of small amounts of non-diamond carbon, hydrogen, high concentrations of crystal defects such as vacancies, twins, dislocations, etc. and residual stress. The slopes of the curves indicate that CVD film oxidizes at the highest rate, followed by {111} and {100} surfaces of natural diamond. Thermogravimetric curves for the oxidation of natural graphite powder (1 μm) and natural diamond powder (43 μm) are also presented in Fig. 6. The specific surface areas of the two powders were not measured. However, the geometric surface area available for oxidation was 80 $mm^2$ in each case. The samples weighed 8 mg each. Again diamond film begins to oxidize at a lower temperature as compared to graphite and diamond powder.

## CONCLUSIONS

In flowing oxygen and at atmospheric pressure, CVD diamond films begin to oxidize at temperature close to 950 K.

This temperature is lower than that of {111} and {100} surface of natural diamond. Similarly natural graphite and diamond powders begin to oxidize at higher temperatures as compared to CVD films. On oxidation, diamond films deposited on one side of silicon wafer turn black. This dark appearance is not a result of phase transformation of diamond as evidenced by X-ray diffraction and Raman spectroscopy. At 973 K extensive oxidation occurs by etching pits on the surface and edges of diamond grains. {100} surfaces appear to be more resistant to oxidation as compared to {111} surfaces. The oxidation proceeds either by direct formation of CO and $CO_2$, or if an intermediate carbon phase in involved, the oxidation rate of the intermediary is higher than its rate of formation.

## ACKNOWLEDGEMENT

Financial support for this research was provided by the National Association of Corrosion Engineers under the seed grant program.

## REFERENCES

1. K.E. Spear: J. Am. Ceram. Soc., v.72, p.171, 1989.
2. Editorial Staff: Mat and Proc. Rep., v.5, 1990.
3. L.S. Plano: Proc. of the SDIO/IST-ONR Diamond Technology Initiative Symposium, July 11-13, 1989, Crystal City, VA.
4. D.M. Tung, W.L. Hsu and K.F. McCarty: Proc. 1st Int. Symp. on Diamond and Diamond Like Films, 175th Electrochemical Soc. Meeting, p. 500, 1989.
5. A. Joshi, R. Nimmagadda and J. Herrington: J. Vac. Sci. Tech., v.A8, p.2137, 1990.
6. K. Tankala, T. DebRoy and M. Alam: J. Mater. Res., v.5(11), p. 2483, 1990.
7. C.E. Johnson, M.A.S. Hasting and W.A. Weimer: ibid, p. 2320.
8. R. Nimmagadda, A. Joshi and W.L. Hsu: ibid, p. 2445.
9. W. Zhu, X.H. Wang, D Pickrell, A. R. Dabzian and R. Messier: Proc. of the ICNDST-2, Sep. 23-27, 1990, Crystal City, VA.
10. F.C. Frank and A.R. Lang: In Physical Properties of Diamond, R. Berman, ed., Clarendon Press, Oxford, 1965, p.69.

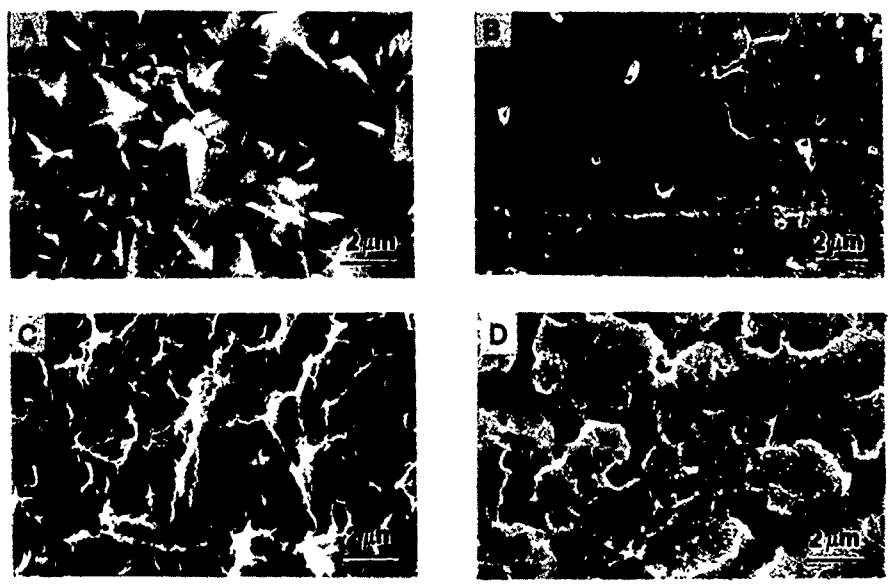



Fig. 1 SEM micrographs of diamond films (a) growth side before oxidation (b) substrate side before oxidation (c) growth side after oxidation and (d) substrate side after oxidation.

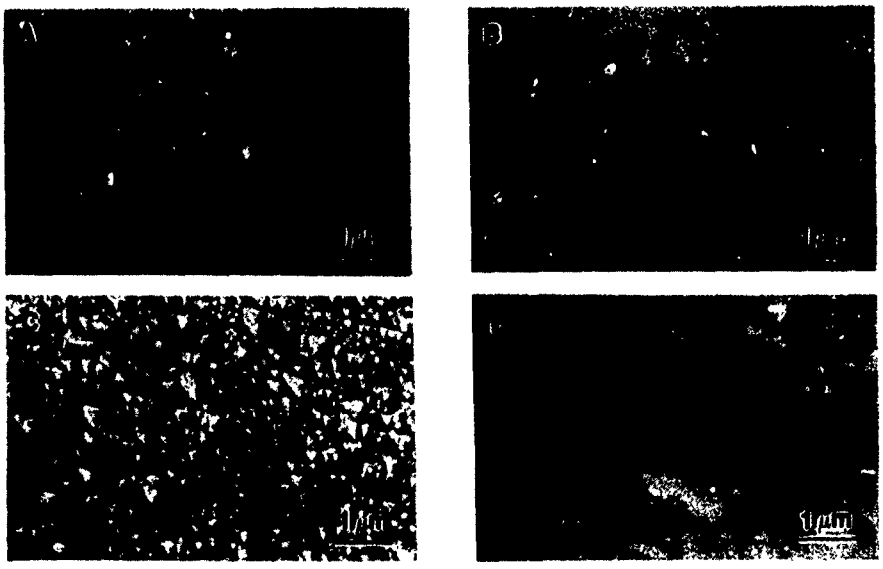


Fig. 2 SEM micrographs of (a) {111} natural diamond before oxidation (b) {100} natural diamond before oxidation (c) {111} natural diamond after oxidation and (d) {100} natural diamond after oxidation.

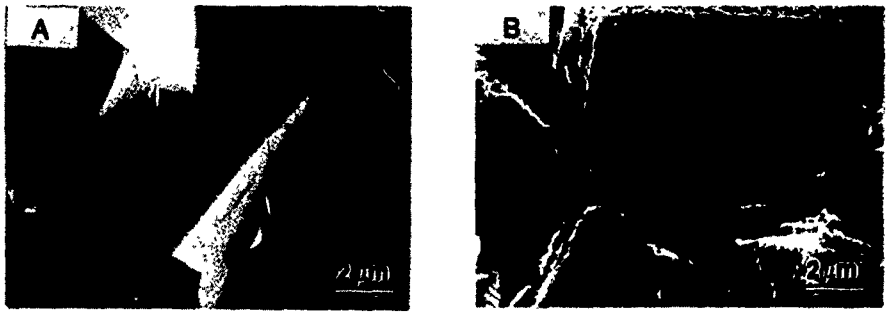



Fig. 3 SEM micrographs of diamond films showing {100} and {111} surfaces (a) before oxidation (b) after oxidation.

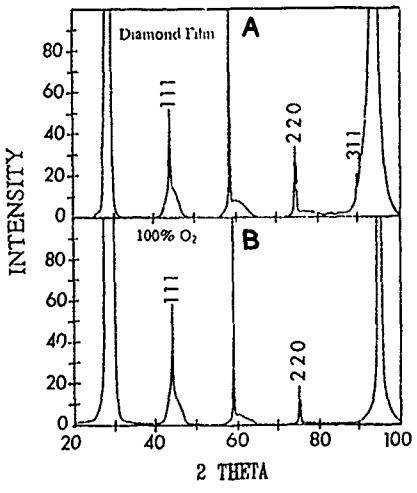



Fig. 4 X-ray diffraction patterns of (a) unoxidized and (b) oxidized diamond film.

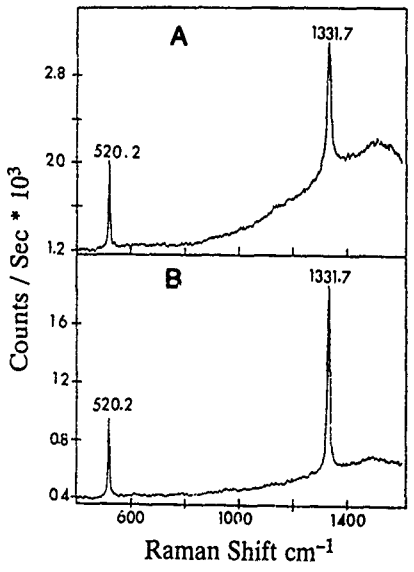



Fig. 5 Raman spectra of (a) unoxidized and (b) oxidized diamond film.

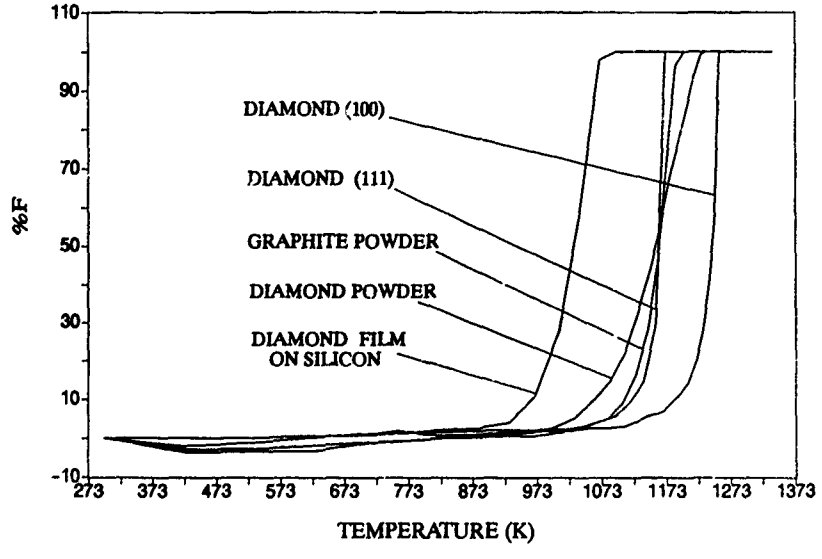



Fig. 6 Thermogravimetric curves.

# ELECTRICAL CONDUCTIVITY OF DIAMOND FILMS FROM ROOM TEMPERATURE TO 1200C

S.F. Adams[a], J.W. Vandersande[b], D. Zolton[b],
B.R. Stoner[c], and J.A. von Windheim[c]

[a]Wright Laboratory/POOC
Wright Patterson AFB, OH 45433

[b]Jet Propulsion Laboratory
California Institute of Technology
Pasadena, CA 91109

[c]Materials Research Center
North Carolina State University
Raleigh, NC 27695

## ABSTRACT

Diamond films have the potential of being used as the high temperature insulator in space nuclear power components such as thermionic and thermoelectric energy conversion devices. The bulk electrical resistivity of the films should be sufficiently high and the films should be stable at the highest operating temperatures of these components. There appears to be a large difference (several orders of magnitude) in room temperature resistivity between films fabricated using various techniques, conditions, and substrates. A variation in resistivity between films at high temperatures has also been observed but is not as pronounced as at room temperature. The resistivities of several films have been measured from room temperature to 1200C and will be reported. The films were characterized by Raman and scanning electron microscopy. The resistivities have also been compared to that for natural type IIa diamond.

## INTRODUCTION

The energy conversion components of high temperature space nuclear power sources (thermionic and thermoelectric) have the need for a high temperature electrical insulator that is structurally and electrically stable under the continuous exposure to the harsh environment of a space nuclear reactor. The insulator would need to maintain exposure to at least a temperature of 800C, a 1 MeV neutron fluence of $10^{22}$n/cm$^2$, and possibly direct contact with a liquid alkali metal coolant. The ideal material for this application would maintain a high bulk electrical resistivity to prevent leakage current losses while providing a high thermal

conductivity to enhance the cooling of certain components. A diamond film is an excellent candidate to be this insulator if it can fulfill these requirements.

The diamond films that appear to have the most promise of meeting these requirements are those synthesized by plasma-enhanced chemical vapor deposition (PECVD) techniques. These films display typical Raman spectra of diamond with a strong, sharp diamond bonded carbon signal at 1332 wave numbers and, for some films, a lesser and more broad non-diamond bonding signal at 1550 wave numbers representing a graphitic or amorphous carbon component. A comparison of the electrical properties of these films with those of natural diamond over a wide range of temperature is a good indicator of the high temperature insulating performance of state-of-the-art diamond films.

The thermal conductivity of PECVD diamond films at room temperature has been measured to be around 18 W/cm-K [1] indicating that these diamond films are superior in this property to all known materials at room temperature except for natural diamond (20 W/cm-K for type IIa). The electrical resistivities of many diamond and diamond-like films have been measured at room temperature. Resistivity values at this temperature have ranged anywhere from $10^6$ - $10^{14}$ ohm-cm compared to $10^{16}$ ohm-cm for natural type IIa (low nitrogen content) diamond. From this prior data, it appears that diamond films deposited to date have not equaled the electrical insulating properties of natural diamond at room temperature. There is a lack of data, though, for diamond films and natural diamond resistivity at high temperatures (above 700C).

We recently presented results which were the first electrical conductivity/resistivity measurements of diamond and diamond film at temperatures up to 1200C [2]. Two natural IIa diamonds, two diamond films, and three diamond-like films were evaluated in this study. The diamond films displayed high temperature resistivities that, in one case, approached that of the natural diamond and, in the other, actually exceeded the resistivity of the natural diamond. An activation energy of 1.4 eV was found for both of the natural diamonds from the slope between 300 and 1200C. The diamond films appeared to have different conduction mechanisms between the temperature ranges of 200 to 600C and 600 to 1200C with activation energies of 0.9 eV and 1.8 eV respectively.

It is clear from a review of previous studies that the processing techniques of the diamond films has a substantial effect on the electrical quality of the sample. As the deposition of diamond films is becoming popular among many researchers, the importance of utilizing well established sources of test samples is emphasized.

Measuring the electrical resistivity of diamond films to higher temperatures and then back down to room temperature will also provide information regarding the stability of the films and the bonding of the film to the substrate. There is also evidence that post-growth heat treatment of diamond films stabilizes the electrical activity of the hydrogen within the film which increases the bulk electrical resistivity [3]. This behavior can be verified by the resistivity measurements during thermal cycling.

## EXPERIMENTAL

An apparatus was specifically designed and built with the ability to measure very high resistivity insulators up to a temperature of 1200C. The sample holder and oven are shown in Figure 1. The holder was made of 998 pure alumina and all of the wiring feedthroughs and connections were made in such a way to ensure that leakage currents bypassing the sample were as low as possible. A DC two probe method with a guard ring and volume guard were used to measure the bulk electrical resistivity of the samples perpendicular through the plane of the samples. A long niobium center probe rested, with some pressure, on a small iridium disk on top of the sample. A cylindrical niobium volume guard fit around the center probe and also rested on the top of the sample. A large area iridium electrode was placed underneath the sample as the second probe.

The conductivity measurement limits of the apparatus have been characterized and the results presented [2]. Below 900C, a slight conductivities of $10^{-16}$ to $10^{-17}$ $ohm^{-1}cm^{-1}$ were measured using a highly resistive sapphire sample. It is believed that lower conductivities cannot be measured with this apparatus (i.e. a maximum resistivity of $10^{16}$ to $10^{17}$ ohm-cm).

The diamond films used in this study were two samples from Crystallume, two samples from North Carolina State University, and one sample from a joint research effort by Wright Laboratory and Universal Energy Systems (UES). A natural type IIa diamond was also evaluated. One diamond film from Crystallume, sample CSW-M-6-NS, was deposited on a silicon substrate by a microwave assisted PECVD method. The film thickness was calculated by Crystallume, based on nominal growth rates, to be 6 microns. The other film from Crystallume, sample 7-B-171 was a 3 micron diamond film deposited on a molybdenum substrate using DC plasma-enhanced CVD techniques. The molybdenum substrate is a refractory metal material that will likely be used in thermionic or thermoelectric energy conversion components. The DC deposition technique would also likely be used in fabricating a thermionic diamond sheath insulator. Both of these samples were heat treated after growth at Crystallume's facility.

Both samples from North Carolina State University were grown in an Astex cylindrically coupled stainless steel microwave plasma CVD reactor. The first film, sample BS13-B2, was grown immersed and the second sample, BS3-A, was grown down stream from the plasma. Both films were grown on undoped silicon (100) substrates with a methane-to-hydrogen ratio of 1%. Neither film received any post deposition treatment. Samples BS13-B2 and BS3-A were approximately 9 microns and 5.5 microns thick respectively, as determined from cross-sectional SEM.

The UES/ Wright Laboratory sample was a 5 micron thick film deposited on a silicon substrate using a microwave assisted PECVD technique. The deposition process was still being optimized for high resistivity films at the time that this sample was submitted. This sample was, therefore, considered to represent a slightly less than state-of-the-art quality insulating diamond film.

## EXPERIMENTAL RESULTS AND DISCUSSION

The electrical conductivity measurements of the two diamond film samples from Crystallume compared with a type IIa natural diamond are shown in Figure 2. The room temperature resistivities of both samples were extremely high, with the diamond film on molybdenum, sample 7-B-171, approaching natural diamond at the maximum measurement limit (just below $10^{16}$ ohm-cm). At a temperature of 1000K, the resistivities of both films were approximately equal at 5 x $10^5$ ohm-cm, while the natural diamond remained slightly higher at $10^6$ ohm-cm. The activation energies, determined from the slope between 40°C and 300°C, of CSW-M-6-NC and 7-B-171 were 0.6 eV and 0.9 eV respectively. A different conduction mechanism between 300°C and 800°C was most likely responsible for higher activation energies of 0.9 eV and 1.1 eV for the respective films. These higher values can be compared to the natural diamond activation energy of 1.4 eV in that temperature range [2].

The electrical conductivity measurements of the UES/ Wright Laboratory diamond film are shown in Figure 3. The sample had a room temperature resistivity of approximately $10^{13}$ ohm-cm but the resistivity at 1000K was slightly higher than that of natural diamond. The conduction mechanisms of this film can be characterized by activation energies of 0.1 eV between 40°C and 300°C and 0.8 eV between 300°C and 900°C.

The electrical conductivity measurements of the North Carolina State University diamond films are shown in Figure 4 and 5. The most outstanding features of these two plots are the initial room temperature resistivity measurements. The resistivity values are several orders of magnitude less than the eventual room temperature resistivity after the films had undergone at least one temperature cycle. Since these films were not heat treated after growth, this observation agrees with earlier results [3], where it was theorized that electrical activity of hydrogen in the film is responsible for the excess electrical conduction at room temperature. The resistivities at 1000K for both films were between $10^5$ and $10^6$ ohm-cm. Both films displayed activation energies of 0.8 eV at temperatures above 300°C.

## SUMMARY

The electrical conductivity of five diamond films from three different sources were measured from room temperature to 1200°C. The room temperature electrical resistivities of the different films varied by several orders of magnitude depending on the processing techniques used during deposition. One of the Crystallume samples had a room temperature resistivity which is the highest measured to date, but still below the "actual" value for natural diamond. The initial room temperature resistivities of both of the North Carolina State University diamond films were very low due to the absence of post-growth heat treatment in the processing of these samples.

The electrical conductivity values converged at higher temperatures and there was much less variation between films at a temperature of 1000K. The natural diamond and all

of the diamond films had measured resistivities between $10^5$ and 2 x $10^6$ ohm-cm at 1000K. This is of much interest since a diamond film would most likely be maintained near this temperature in a space nuclear power component application. Systems studies must be completed to realize if these electrical properties at 1000K are adequate for each thermionic or thermoelectric application.

The activation energies of the five diamond films ranged from 0.1 eV to 1.1 eV compared to 1.4 eV for the natural diamond. This range of activation energies shows how different processing techniques can lead to a variation in impurity characteristics and conduction properties. It is suggested that vacancy loops or acceptor/donor impurities at the grain boundaries of the diamond films are responsible for the various conduction mechanisms and resulting activation energies. Considerably more work needs to be done to get a better understanding of the fundamentals of the conduction mechanisms.

*Research supported by SDIO/IST & managed by Wright Laboratory*

## REFERENCES

1. J.A. Herb, C. Bailey, K.V. Ravi, and P.A. Dennig, "The Impact of Deposition Parameters on the Thermal Conductivity of CVD Diamond Films," Proceedings of The First International Symposium on Diamond and Diamond-Like Films, Proc. Vol. 89-12, The Electrochemical Society, Los Angeles (1989), p366.

2. J.W. Vandersande and L.D. Zolton, "High Temperature Electrical Conductivity Measurements of Natural Diamond and Diamond Films," To be published in "Surface and Coatings Technology", Proceedings of the First European Conference on Diamond and Diamond-Like Carbon Coatings, Sept 17-19, 1990.

3. M.I. Landstrass and K.V. Ravi, "The Resistivity of CVD Diamond Films," Appl. Phys. Lett. 55, 1391 (1989).

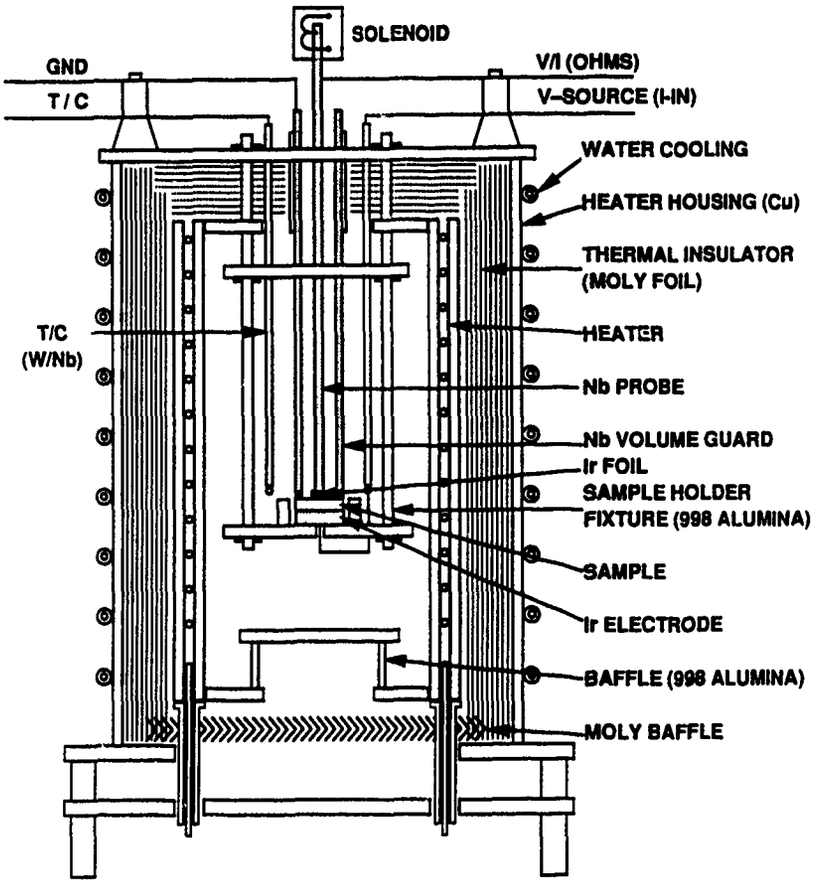



Figure 1. High Temperature Insulator
Electrical Resistivity Station

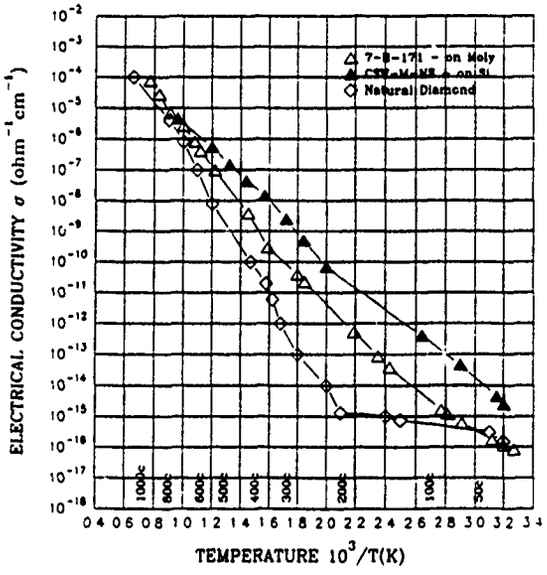



Figure 2. Electrical Conductivity of Crystallume Films

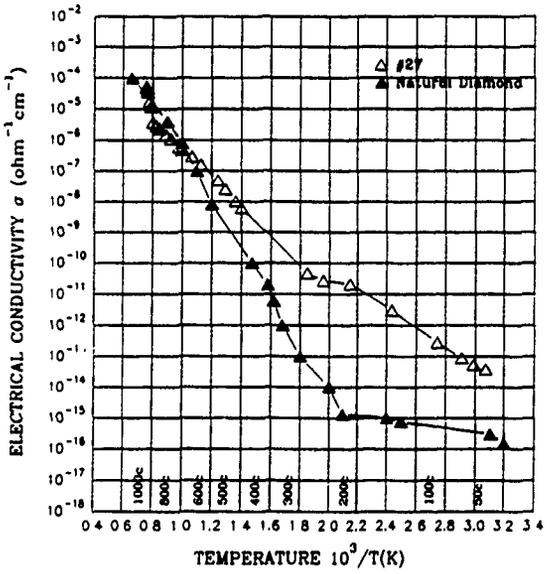



Figure 3. Electrical Conductivity of UES/ Wright Laboratory Film

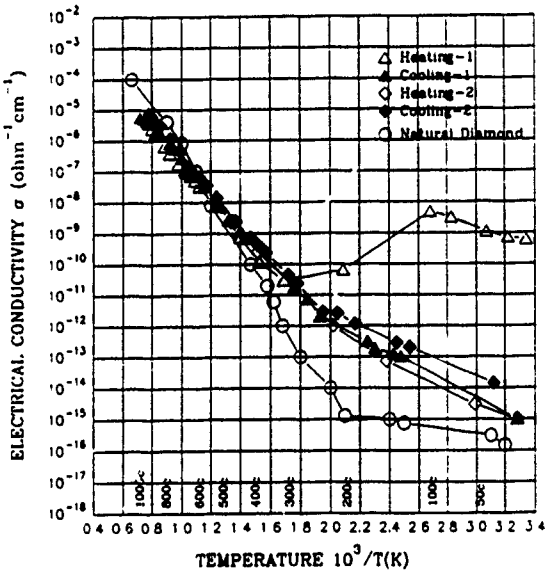



Figure 4. Electrical Conductivity of NCSU Films #BS13-B2

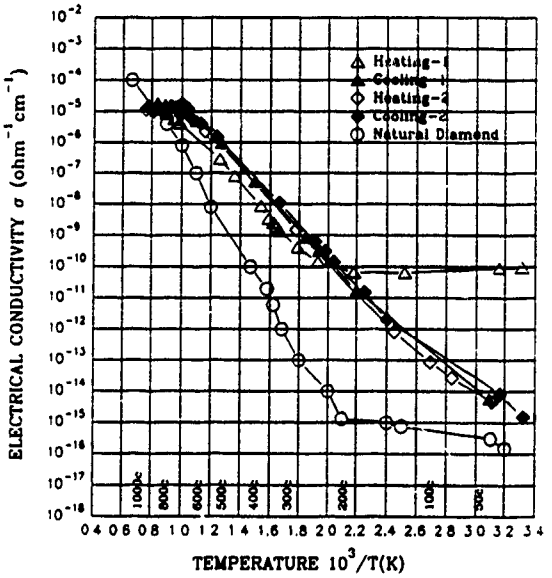



Figure 5. Electrical Conductivity of NCSU Film #BS3-A

# THE EFFECT OF HYDROGEN ON THE ELECTRICAL RESISTIVITY OF POLYCRYSTALLINE DIAMOND FILMS.

M.L. LAKE
Applied Sciences, Inc.
Yellow Springs OH 45387

D.C. INGRAM
Department of Physics and Astronomy
Ohio University
Athens OH 45701

J. W. VANDERSANDE and D. ZOLTAN
Jet Propulsion Laboratory
California Institute of Technology
Pasadena CA 91109

**ABSTRACT.**

The electrical resistivity of diamond films can vary from sample to sample by as much as six to seven orders of magnitude at room temperature. Sources for these variations include differences in impurities and structural defects, and the amount of graphitic component in the films. Proton recoil measurements have shown hydrogen to be the greatest impurity present in quantities of 0.5% to 1.0% throughout the diamond film thickness. These measurements are complemented by electrical resistivity measurements from room temperature to 1200 C, Raman spectroscopy, Auger analysis and SEM. It was determined that hydrogen can be removed from the surface of the CVD diamond film through heat-treatment, but that bulk hydrogen concentrations and the bulk electrical resistivity are essentially not affected.

**INTRODUCTION.**

While the electrical resistivity of naturally occurring diamond has been measured to be on the order of $10^{16}$ ohm centimeters at room temperature[1], and undoped, defect-free diamond would have a room-temperature electrical resistivity many, many orders of magnitude higher, the electrical resistivity of diamond thin films produced by chemical vapor deposition (CVD) is typically lower than that of naturally-occurring diamond[2]. The impurities in diamond films grown from the plasma-enhanced chemical vapor deposition technique vary from sample to sample as a function of the deposition parameters, but hydrogen is commonly a major impurity in films grown by this method. It is speculated that deep traps within the diamond may be passivated by hydrogen, both in CVD diamond films, and in natural diamond crystals. It has previously been reported that heat treatment of CVD diamond films can result in removal of hydrogen from the film, with consequent improvement in the electrical resistivity to values comparable to natural diamond.[3] In the current study, the hydrogen concentration has

been measured in CVD diamond films both before and after cyclic measurement of the temperature dependent electrical resistivity of the diamond film to a temperature of 1200 C, to seek correlation between the electrical resistivity and the hydrogen content of the film. Relatively little change was observed in both the electrical resistivity of the films from first to second cycle, as well as little difference in the bulk hydrogen content of the film, even after heat treatment to 1200 C.

**EXPERIMENTAL.**

Diamond films were produced on molybdenum and silicon substrates using plasma enhanced chemical vapor deposition in an Astex tube reactor. Methane concentrations ranged between 0.5% and 2.0%, with the remaining gas being hydrogen. The pressure was maintained at 28 torr, with a flow rate of 100 sccm. The substrate was heated by microwave induction and plasma heating, with microwave power set at approximately 250 watts. The temperature of the substrate was approximately 925 C as determined by optical pyrometry, with no corrections applied for the quartz window or for emissivity changes. Diamond films were analyzed using Raman and Auger spectroscopy, Rutherford Backscattering (RBS), Proton Recoil Detection (PRD), and SEM both before and after electrical resistivity measurements were made over the temperature range from room temperature to 1200 C.

The electrical resistivity of the films was measured through the plane of the diamond films using a DC two probe method with a guard ring and volume guard[4]. To verify the accuracy of the measurement apparatus, the resistivity of a single crystal sapphire sample was made and was found to compare well to accepted values. The heating of the films during the resistivity measurement was expected to alter the hydrogen content, and possibly other properties of the diamond films.

Concentrations of hydrogen and other impurities were measured by proton recoil detection (PRD) and Rutherford Backscattering (RBS). In both techniques a mono-energetic helium ion beam of between typically 2 to 3 MeV is incident on the target to be examined. In RBS, the beam is backscattered through an angle greater than 90°. In this work the angle was 168°. With this scattering angle and using a 3.05 MeV helium beam it is possible to enhance the scattering of oxygen through an enhanced resonant scattering process[5]. Using conventional RBS it is possible to easily detect the presence of impurities heavier than the substrate atoms. The detection limits for impurities heavier than carbon varies from 0.1 at% to 0.001 at%, in proportion to the square of their atomic number[5].

In PRD, the number of *forward* scattered protons is measured as a function of their energy. For this measurement, either the target must be thin (<25$\mu$m) or placed at a glancing angle to the beam[6]. In this work the target was placed with the incident helium beam at 75° to the target's surface normal and the detector was placed at an angle of 30° to the incident beam to detect the forward recoiled protons from the target. To aid normalization of the

data, an RBS spectrum was taken simultaneously during the acquisition of the PRD data. The cross-section for proton recoils by MeV ions has been measured by Ingram et al[6] and is sufficiently high for the hydrogen content of polymers to be measured without significant radiation damage, unlike the heavy ion techniques for measuring hydrogen. Also, with PRD a complete profile can be measured simultaneously, whereas, with the heavy ion techniques (which are very strongly resonant nuclear reactions) each data point in the concentration profile requires a different energy for the incident ion beam and therefore the time required to acquire data is much longer and the radiation damage produced in the sample is much larger. A disadvantage of PRD is the relatively poor depth resolution of about 100 nm.

**RESULTS.**

Electrical resistivity measurements of the diamond films, as shown in figure 1, showed a resistivity of approximately $10^{14}$ ohm-cm at room temperature., compared to the resistivity of natural diamond of typically $10^{16}$ ohm-cm. At elevated temperatures (800-1200 C), the resistivity of the diamond films was found to exceed the resistivity of natural diamond by approximately one order of magnitude. This difference, and the difference in slope of the resistivities of the films compared to natural diamond is indicative of a difference in type and number of defects and impurities which can account for conductivity in diamond. Thermal cycling of the films to 1475 K showed no permanent changes in the resistivity of the diamond films.

In figure 2, Raman spectra for pre- and post-resistivity measurements (thus pre- and post-heat-treated) show a prominent line in proximity to the 1332 $cm^{-1}$ diamond line, in comparison to the spectral features in the vicinity of 1500 $cm^{-1}$ in both spectra. This spectral line is a reliable indicator of large crystals with predominantly $sp^3$ bonding within the film both before and after the resistivity measurement. The shift in the position of the diamond line around 1332 $cm^{-1}$ is attributed to the degree of residual stress in the diamond film for pre- and post heat-treatment. The spectral feature in the vicinity of 1500 $cm^{-1}$ is attributed to a disordered carbon band. The ratio of this peak to the diamond peak is reduced following heat-treatment. The interpretation of this phenomenon is incomplete, but taken as evidence that the bulk diamond properties are not degraded by heat-treatment.

In contrast, figure 3 indicates essentially the opposite effect in the surface of the diamond films following heat treatment. The differences in shape of the Auger spectra for unheated and heated diamond films observed may result from the pre-heat-treated diamond films being hydrogen terminated, while the post-heat-treated films are graphite terminated. Williams and Glass[7] report a similar change in the shape of the Auger spectrum following argon sputtering, which may also remove hydrogen from the film surface. In the Auger spectrum of natural diamond[8], the intensity of the fine structure peak closest to the primary C KLL peak is larger than the peak appearing at slightly lower energy, while for the case of graphite, the relative intensities of these

two features is reversed. These features correspond well to the Auger spectra of as-grown and heat-treated diamond films studied here, supporting the assumption that hydrogen is removed from the film surface through the heating of the film.

Figure 4 shows the RBS spectra taken from a sample of diamond film on a molybdenum surface. The spectra were taken before and after heat-treatment to 1200 C. In the as-deposited sample there appears to be about 0.1 at% oxygen in the bulk of the material. This is not present in the annealed spectrum. The PRD spectra in figure 5 were taken simultaneously with the spectra in figure 4. These spectra demonstrate how stable hydrogen is in the bulk of the diamond film. A constant level of 0.5 at% extending into the bulk of the material was detected before and after the 1200 C heat-treatment. Although the depth resolution of PRD is about 100 nm for the system used, hydrogen near the surface was clearly removed by heat-treatment.

**CONCLUSIONS.**

Elemental analysis of diamond films was obtained using RBS and PRD. The elemental compositions were predominantly carbon (greater than 98 at%), with oxygen detected by RBS to be 0.1 %, extending uniformly through the bulk for unheat-treated samples. One sample was determined to have 0.5 at% within 100 nm of the surface of the film. Oxygen may be present as $H_2O$ or OH groups at the surface of the film.

From PRD analysis it was determined that hydrogen is the principal impurity in the films, with up to 1.8 at% hydrogen near the surface of some films (first 100 nm), but falling to approximately half of that value in the bulk of the films.

Following the electrical resistivity measurements, RBS and PRD indicated that the elemental composition of the samples was still predominantly carbon (greater than 98 at%). A small amount of oxygen (less than $3 \times 10^{15}$ O/cm$^2$) was detected near the surface, and no oxygen was detectable in the bulk of the film. PRD analysis indicated a drop in the hydrogen content at or near the surface of the film (100 nm), but no change in the hydrogen concentration was observed deeper into the diamond film.

Previous published results indicate that hydrogen may be removed by heat-treatment to 780 C[3]. The current effort, to correlate the change in resistivity as hydrogen concentration is altered, has not succeeded in documenting this relationship owing to the stability of the bulk hydrogen concentration. Hydrogen at or near the surface of the film can be removed through heat-treatment, but bulk concentrations are unaffected by heating to 1200 C.

Removal of hydrogen from the surface of the film was determined from Proton Recoil Detection. This result was also supported by Auger analysis and Raman analysis, which indicate a graphitic termination of the carbon on the film surface following heat-treatment, concurrent with no substantive change in the

diamond peak at 1332 $cm^{-1}$. The presence of oxygen at the surface of the film may also indicate absorption of water or OH groups on the surface of the diamond. The stability of the bulk hydrogen concentration was an unexpected result based on results reported previously for both natural diamond and for CVD diamond films. This finding and the unusual shape of the resistivity of these diamond films, particularly the higher values of resistivity at elevated temperatures when compared to the resistivity of natural diamond, indicate possible fundamental differences in the quality of the diamond films produced in this study with respect to diamond films studied previously, and shows that CVD diamond films can be produced with resistivities which exceed the resistivity of natural diamond at elevated temperature.

**ACKNOWLEDGEMENT.**

This work supported in part by SDIO/IST under Contract Number F33615-89-C-2960.

1. Collins, A. T. and Lightowlers, "Electrical Properties of Diamond" in The Properties of Diamond, J. E. Field, editor, Academic Press: New York, 1979.

2. Vandersande, J. W. and Zoltan, L. D., "High Temperature Electrical Conductivity Measurements of Natural Diamond and Diamond Films" Switzerland, Sept. 1990.

3. Landstrass, M. I. and Ravi K. V., "Hydrogen Passivation of Electrically Active Defects in Diamond" Appl. Phys. Lett. 55 (14) October, 1989.

4. J. W. Vandersande, D. Zoltan, and S. Adams, "Electrical Conductivity of Diamond Films from Room Temperature to 1200 C" presented at the Second International Symposium on Diamond Materials, Washington, D.C., May, 1991.

5. W.-K. Chu, J. W. Mayer, M.-A. Nicolet, Bacscattering Spectrometry Academic Press: New York, 1974.

6. D.C. Ingram, A.W. McCormick, P.P. Pronko, J.D. Carlson, and J.A. Woollam, Nucl. Instr. and Meths. B6 (1985) 430.

7. Williams, B. E. and Glass, J. T., "Characterization of Diamond Thin Films: Diamond Phase Identification, Surface Morphology, and Defect Structures" J. Mater. Res. 4 (2) Mar/Apr 1989.

8. Lurie, P. G. and Wilson, J. M., Surface Science 65 476, (1977).

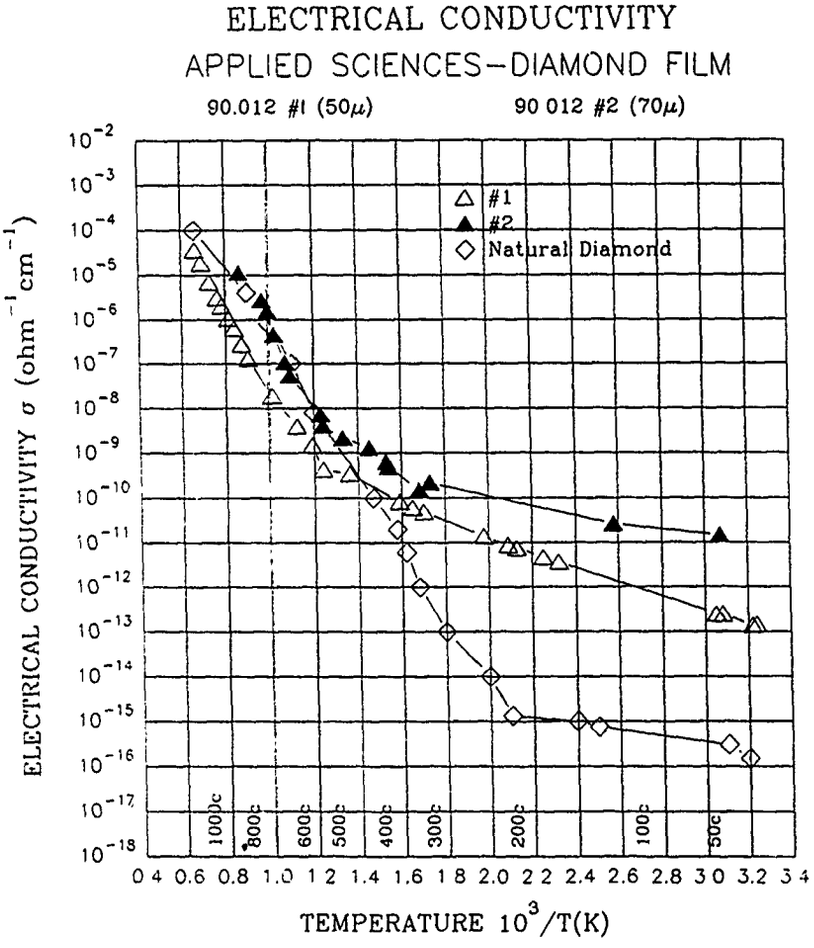



**Figure 1. Electrical conductivity of CVD diamond films compared to natural diamond.**

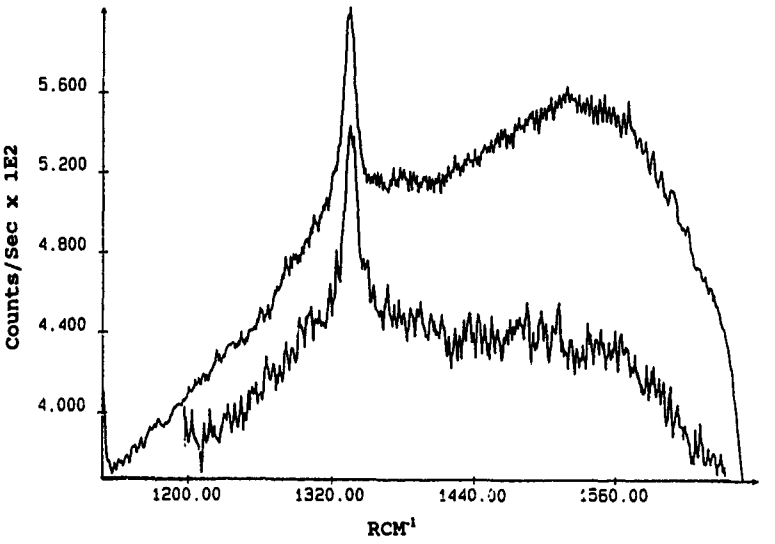
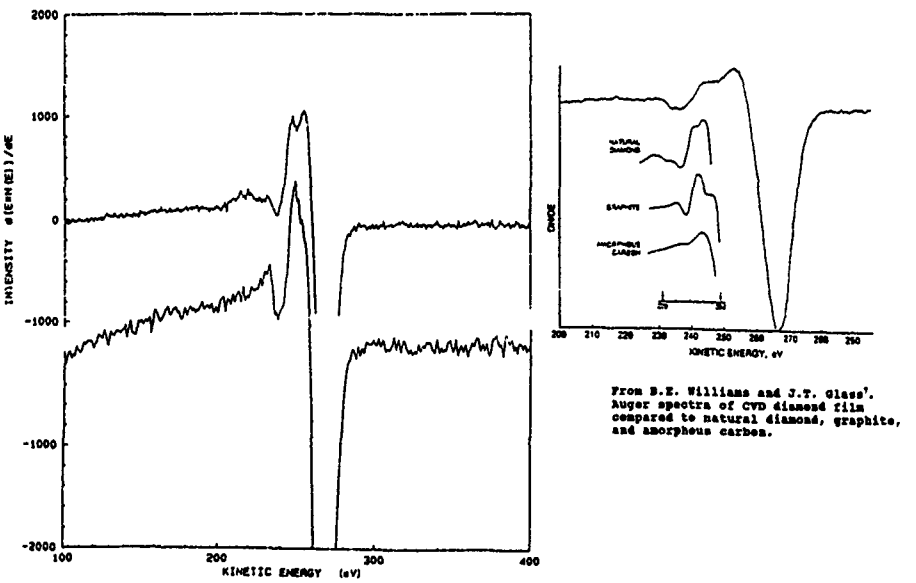



**Figure 2. Raman spectra of CVD diamond film before and after heat treatment.**




From B.E. Williams and J.T. Glass[7]. Auger spectra of CVD diamond film compared to natural diamond, graphite, and amorphous carbon.

**Figure 3. Auger spectra of CVD diamond film before and after heat treatment.**

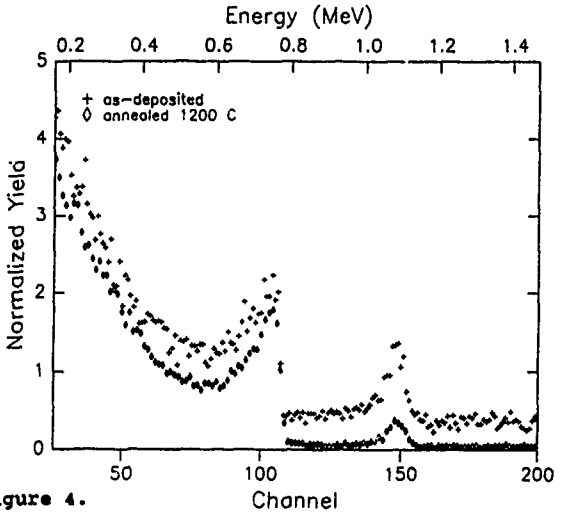



**Figure 4.**
**RBS spectra from a sample of CVD diamond in the as-deposited state and following heat treatment to 1200°C.**

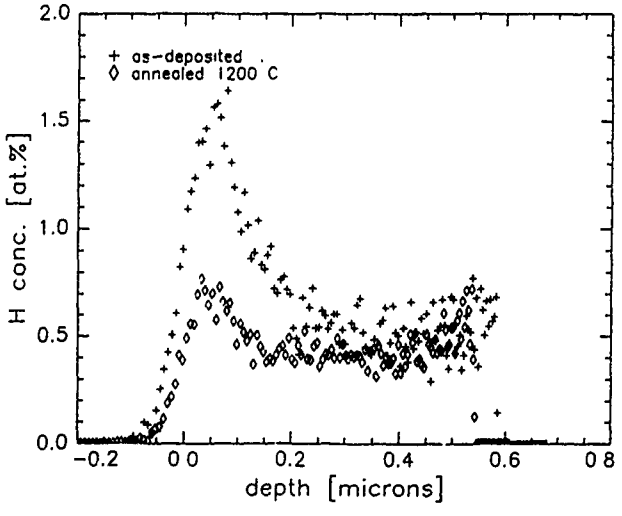



**Figure 5.**
**Hydrogen concentration profiles obtained by PRD for the same sample as figure 4.**

# CHANGE OF RESISTANCE OF DIAMOND SURFACE BY REACTION WITH HYDROGEN AND OXYGEN

Hiroaki Nakahata, Takahiro Imai, and Naoji Fujimori

Sumitomo Electric Industries, Ltd., Itami Research Lab., 1-1, 1-chome Koyakita Itami-city, Hyogo, 664, Japan

## ABSTRACT

It was found that a conductive layer exists on the surface of a CVD diamond film as deposited. This is related to hydrogen which was absorbed on the diamond surface. By reaction with oxygen this conductivity is canceled and the resistance of the film increases to its original value.

## INTRODUCTION

Diamond has a wide band gap of 5.5 eV and is an insulator. But recently, it was found that the resistance of diamond films prepared by the microwave plasma CVD method was much lower than expected and could be increased by some treatments.[1)2)3)] It was reported by Ravi that treatment of polycrystalline diamond film in hydrogen plasma made its resistance decrease and this decreased resistance could be increased by heating. He referred to some electrically active level made by hydrogen in the diamond film that seemed to affect the resistivity. Gildenblat reported that resistance of an as-deposited epitaxial diamond film increased by treatment with $CrO_3+H_2SO_4$, and referred to the presence of a non-diamond structure on the surface of the diamond film that was responsible for the conductivity. However, a clear explanation of the mechanism of these phenomena has not yet been made. To better understand the phenomena, studies of an epitaxial film are required. In this study, various polycrystalline diamond films, and the role of oxygen and hydrogen was investigated.

## EXPERIMENTAL

Epitaxial diamond films were prepared by the microwave plasma CVD method. The substrates used were single-crystal diamonds of high-pressure synthesized Ib and IIa, 1.5x2.0x0.3 mm in size, and natural Ia crystal about 2 mm in size. All the substrates were insulating, with resistivity of more than $10^{14}$ Ω·cm. $CH_4$ and $H_2$ were used as reactant gases. The ratio of $CH_4/H_2$ was 1/200. The power of the microwave at 2.45 GHz was 400 W and the reaction pressure was 40 Torr. The thickness of the films deposited was from 0.4 to 5.0 μm.

A pair of electrodes of (Au/Mo/Ti) was formed by e-beam evaporation on the films, as shown in Fig. 1. Six different treatments were carried out as follows upon the diamond films; their resistance was measured, as shown in Fig. 2, before and after the treatments.

(1) Heated in air at temperatures from 200°C to 500°C.
(2) Heated in oxygen gas under a pressure of 1 Torr at 500°C for 1 hour.
(3) Heated in argon gas under a pressure of 0.07 Torr at 500°C for 1 hour.
(4) Treated in RF plasma of oxygen under a pressure of 0.05 Torr with RF power of 30 W at room temperature for 2 minutes. In this treatment, an epitaxial diamond film deposited on boron-doped single-crystal Ib diamond substrate was also included and its resistance was measured as shown in Fig. 3. The substrate had enough conductivity for the measurement.
(5) Treated in microwave hydrogen plasma under a pressure of 40 Torr with microwave power of 400 W for 2 minutes.
(6) Heated in hydrogen gas at 500°C for 1 hour.

Polycrystalline diamond films from 3 to 7 mm in thickness were also deposited on silicon substrate of 14x14x1.5 mm under the same condition and on which an (Au/Mo/Ti) electrode was evaporated. Resistance of the films was measured as shown in Fig. 4 before and after some of the above treatments.

## RESULTS AND DISCUSSION

All of the as-deposited epitaxial diamond films exhibited resistances from $10^4$ to $10^6$ Ω. However, by heat treatment in air, the resistance of the films increased by several orders. Fig. 5 is the I-V characteristics of the sample as-deposited and after heating in air at 500°C. Table 1 shows the changes in resistance by heating in air at various temperatures for six hours. The higher the heating temperature, the larger the increase in resistance, and above 400°C saturation of the increase was observed at the value of $10^{13}$ Ω by only a few minutes treatment. It was confirmed that this increase in resistance had no relation to electrode changing, for the increase was also observed by forming electrodes after the heat treatment. In all the experiments in this study, no change of the electrode was observed after any treatment.

Table 2 shows the results for epitaxial diamond films of different film thicknesses deposited on various kinds of single-crystal diamond substrates and their different planes. After heating in air at 500°C, all the samples showed much the same change, with their resistances increased to $10^{13}$ from the $10^5$ W as-deposited value. No difference was observed between samples of different substrates and different film thicknesses. As for polycrystalline diamond films, the same change of resistance was observed. It was $10^4$ Ω as-deposited, and $10^{10}$ Ω after heating in air at 500°C.

By heat treatment in oxygen gas, the resistance of an epitaxial diamond film 2 μm in thickness on a Ib(110) substrate was also increased from $10^6$ to $10^{13}$ Ω even under an oxygen pressure of 1 Torr. On the other hand, no change was observed from heat treatment in argon gas at 500°C. From these data, it is concluded that reaction with oxygen is responsible for the increase in resistance, and treating at high temperatures is not an essential factor of the increase in resistance.

To confirm the effect of oxygen, treatment with RF plasma of oxygen was carried out. By this treatment the resistance of an epitaxial diamond film 1 μm in thickness on a Ib(100) substrate was also increased from $10^5$ Ω to $10^{13}$ in only 3 minutes. Surface temperature of the samples is thought to have remained below 100°C. Fig. 6 is the relation between the time of the treatment with oxygen plasma and the resistance after the treatment. It was found that the increase of the resistance saturates in a few minutes.

After this oxygen treatment the electrodes were removed by $HCl+HN0_3$ aq and HF aq, and the resistance of the diamond surface was measured by a pair of probes. It was found that the resistance of the area of the surface where an electrode had been evaporated and which had been isolated from the oxygen plasma was still as low as $10^6$ Ω, while the area which had not been covered and was subjected to oxygen plasma was more than $10^{13}$ Ω. These results are schematically shown in Fig. 7. These results suggest that the increase of the resistance is caused by a reaction of oxygen with the surface of as-deposited diamond.

From the following experiments we determined whether only the surface of the as-deposited diamond film or the entire as-deposited film is conductive. The resistance of an as-deposited epitaxial diamond film 1.5 μm in thickness on a Ib(100) substrate measured as shown in Fig. 3 was $10^4$ Ω, and after treatment by oxygen plasma for 2 minutes the resistance increased by 3 orders and showed non-ohmic characteristics (Fig. 8). From these data it can be concluded that the conductivity of the as-deposited film had existed only on the surface of the film, and not in the entire film. If the entire film were conductive the resistance measured through the film as shown in Fig. 3 would be the same as that of the as-deposited film. The characteristics of Fig. 8(a) are considered to be due to surface conductivity not presenting the characteristic of the entire film; Fig. 8(b) shows the mean I-V characteristics of the epitaxial diamond film measured throug the film. Similar results were obtained from a polycrystalline diamond film.

The treatments in hydrogen plasma and hydrogen gas were carried out on the epitaxial diamond films whose resistance had increased by heating in air or treating with oxygen plasma. When treated in hydrogen plasma the resistance decreased to $10^6$ Ω which was the same value as the as-deposited film. This result was the same as that which Ravi et.al. reported. On the other hand, no

change was observed from treatment in hydrogen gas at 500°C. We can clearly recognize that active hydrogen such as atomic hydrogen makes the resistance decrease. And as mentioned previously, this conductivity caused by hydrogen is considered to exist only on the surface or near the surface layer of the diamond film.

By surface analysis of epitaxial diamond films by RHEED and STM it was confirmed that the surface consists of crystalline diamond. No report of the existence of amorphous or graphite phases on the surface has been made. The authors consider that hydrogen is absorbed on the surface of diamond films just after the deposition. STM observation indicates that the surface structure of the diamond film is quite similar to that of silicon which is considered to be determined with hydrogen.[4] After the reaction with oxygen, there will be oxygen on the surface. Nishibayashi et. al. reported on the existence of oxygen analyzed by XPS on the surface of epitaxial diamond films heated in air.

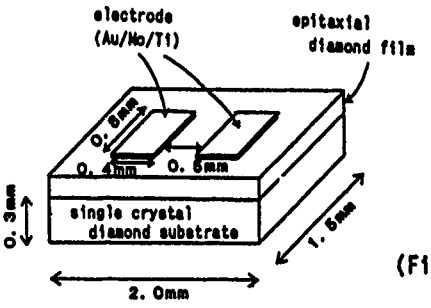
As for the mechanism of conductivity, the authors consider that some electrically active state is produced by hydrogen that may exist on or near the surface whose contribution is still not clear but at least does not affect the entire film, and is the cause of the conductivity. This hydrogen can be easily removed by reaction with oxygen on the surface, reducing the conductivity. A clearer explanation cannot be made now, and more surface analysis will be required for further study.

## CONCLUSION

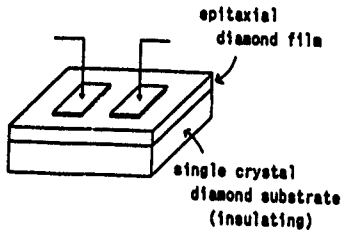
The change of resistance of CVD diamond films by various treatments was studied. Both epitaxial and polycrystalline diamond films as deposited had quite low resistance. This low resistance is considered to be due to a surface conductive layer which was caused by hydrogen that had reacted with the diamond surface. And it was made clear that this effect of the conductivity is canceled by reaction with oxygen, by which the resistance increases to its original value.

## REFERENCES

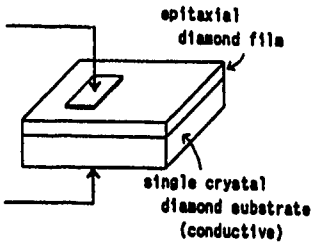

1. K.V. Ravi et. al., Appl. Phys. Lett. 55(10), 975(1989)
2. Gildenblat et.al., IEEE ED Lett.11(2) 100(1990)
3. S. Albin, L. Watkins, IEEE ED Lett. 11(4) 159(1990)
4. T. Tsuno et.al., to be published in Jap. J. Appl. Phys. Vol. 30 (1991)



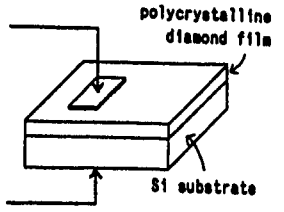

(Fig.1) Schematic of Sample



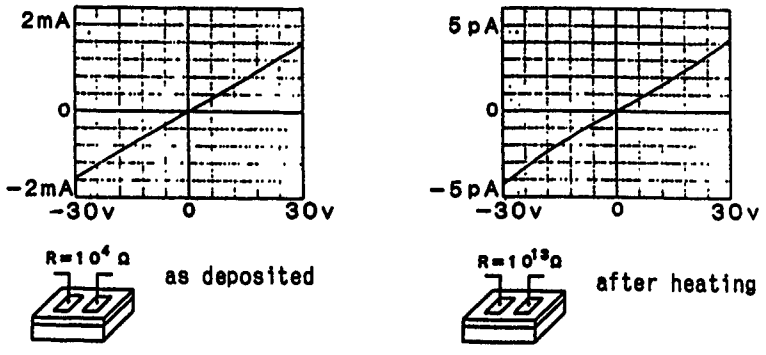

(Fig.2) Schematic of Measurement of Resistance of Epitaxial Diamond Film on Insulating Substrate




(Fig.3) Schematic of Measurement of Resistance of Epitaxial Diamond Film on Conductive Substrate




(Fig.4) Schematic of Measurement of Resistance of Polycrystalline Diamond Film on Si Substrate



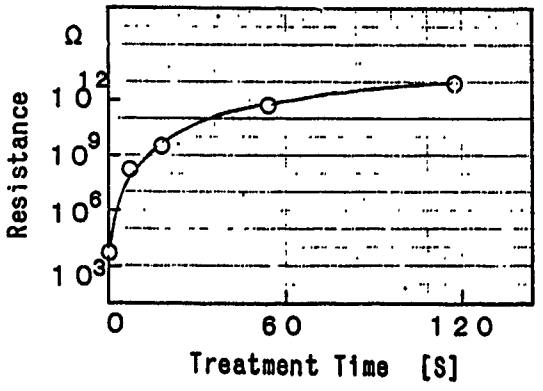

(Fig.5) Measurement of Resistance before and after heating

| heating temp. | heating time | resistance as deposited | resistance after heating |
|---|---|---|---|
| 230℃ | 6hours | $10^4\ \Omega$ | $10^6\ \Omega$ |
| 310℃ | 6hours | $10^6\ \Omega$ | $10^9\ \Omega$ |
| 430℃ | 6hours | $10^8\ \Omega$ | $10^{13}\Omega$ |
| 500℃ | 6hours | $10^4\ \Omega$ | $10^{13}\Omega$ |
| 430℃ | 5min. | $10^8\ \Omega$ | $10^{13}\Omega$ |
| 500℃ | 5min. | $10^6\ \Omega$ | $10^{13}\Omega$ |

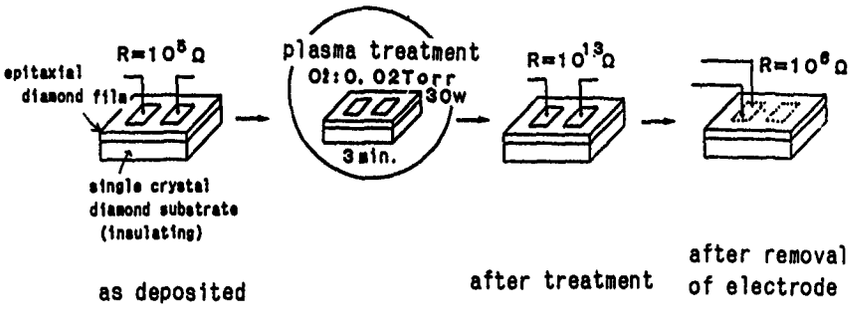
(Table.1)
Resistance of Epitaxial Diamond Film before and after Heating in the Air at Different Temperatures

| substrate | | | film thickness | resistance as deposited | resistance after heating |
|---|---|---|---|---|---|
| high-pressure synthesized | Ib | 110 plane | 0.4μm | $10^6\ \Omega$ | $10^{13}\Omega$ |
| | | | 1.5μm | $10^6\ \Omega$ | $10^{13}\Omega$ |
| | | | 5.0μm | $10^4\ \Omega$ | $10^{13}\Omega$ |
| | | 100 plane | 0.4μm | $10^6\ \Omega$ | $10^{13}\Omega$ |
| | | | 1.0μm | $10^6\ \Omega$ | $10^{13}\Omega$ |
| | IIa | 111 plane | 0.4μm | $10^6\ \Omega$ | $10^{13}\Omega$ |
| | | | 5.0μm | $10^5\ \Omega$ | $10^{13}\Omega$ |
| natural | Ia | 111 plane | 0.4μm | $10^6\ \Omega$ | $10^{13}\Omega$ |

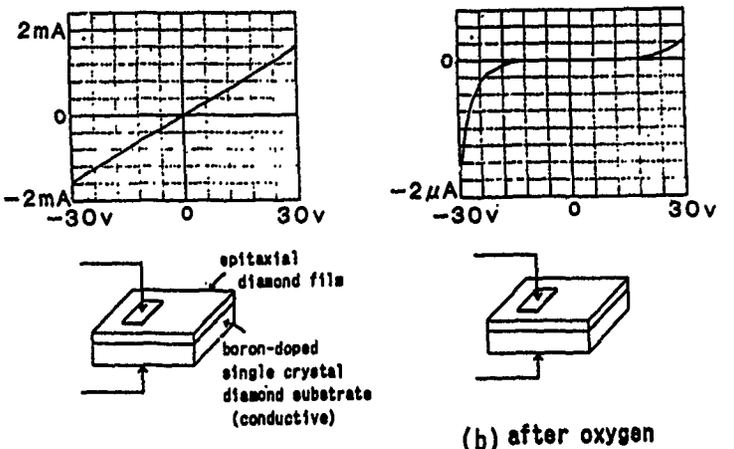
(Table.2)
Resistance of Epitaxial Diamond Film on Different Substrate and of Different Film Thickness before and after Heating in the Air at 500 C




(Fig.6)
Resistance after Oxygen Plasma Treatment by Different Treatment Time




(Fig.7) Schematic of Measurement of Resistance of Epitaxial Diamond Film on Insulating Substrate before and after Oxygen Plasma Treatment




(Fig.8) Schematic of Measurement of Resistance of Epitaxial Diamond Film on Conductive Substrate before and after Oxygen Plasma Treatment

# HALOGENATION OF DIAMOND (100) USING ATOMIC BEAMS

Andrew Freedman and Charter D. Stinespring†
Aerodyne Research, Inc.,
45 Manning Road
Billerica, Massachusetts 01821

## ABSTRACT

Both diamond (100) and graphite (basal plane) surfaces have been halogenated using atomic beams of fluorine and chlorine. XPS analyses of the resulting adlayers indicate that fluorine atoms chemically bond to both diamond and graphite; saturation coverages at room temperature are ~3/4 and 1/4 of a monolayer for diamond and graphite respectively. The diamond-fluoride adlayer is stable up to ~700 K; the graphite-fluorine adlayer, ionic in nature, becomes unstable at ~550 K. Chlorine atoms weakly adsorb on both surfaces; saturation coverage rapidly decreases as temperature increases above an initial 200 K. Molecular halogen species are virtually unreactive under these low flux conditions.

## INTRODUCTION

The study of halogen atom interactions with diamond surfaces have become increasingly relevant as new thin film deposition schemes have been developed (1). The impetus for using halogen-based systems for diamond growth involves their thermodynamic and kinetic instability compared to that of simple hydrogen-hydrocarbon based systems. The first report of a halogen-based system came from a group at Research Triangle Institute which used a thermal process involving $CF_4$ and $F_2$ (with some hydrogen impurity)(2); this group has recently extended this work by developing a plasma-based system involving $CF_4$ and $H_2$ (3). Another group, at Rice University, has reported growing diamond films by a thermal process using a variety of halocarbon species including methyl iodide and bromoform (4). The efficacy of these systems (especially the plasma-based system) lies in the presence of free halogen atoms and the nature and stability of their chemical bonding to diamond surfaces.

We have studied the interaction of both chlorine and fluorine atoms with the diamond (100) surface in an ultrahigh vacuum environment using atomic beams. X-ray photoelectron spectroscopy (XPS) and low energy electron diffraction (LEED) have been used to determine the nature of the chemical bonding between these atoms and the diamond surface. The studies will, when complete, provide information as to the stability of halogenatoms on diamond surfaces,

† Permanent Address: Department of Chemical Engineering, West Virginia University

whether they etch diamond at high temperatures, and whether they can play a role in an atomic layer epitaxy scheme.

In addition, we also present preliminary data on halogen atom interactions with the basal plane of graphite. There is already a rich literature on the properties of both covalent and ionic forms of graphite fluoride, the only known stable halogen-graphite compound (5). Sato has noted that the covalent form of graphite fluoride involves the conversion of planar $sp^2$-bonded graphite to a 2-dimensional zigzag structure with $sp^3$ bonding (6). He states that this suggests that graphite structures may be transformed to diamond structures through bond formation with other elements.

## EXPERIMENTAL

The experimental apparatus used in these studies comprises a turbomolecular pumped, liquid nitrogen trapped ultrahigh vacuum cell (ultimate vacuum ~ $3 \times 10^{-10}$ Torr) interfaced to an ion/sublimation pumped analysis chamber. The diagnostics available in the analysis chamber are x-ray photoelectron spectroscopy and low energy electron diffraction. The sample is transferred between chambers using a linear motion feedthrough with sample heating (1225 K) and cooling (120 K) capabilities.

The 5 x 5 $mm^2$ (0.50 mm thick) type 2A diamond substrate, provided by Dubbeldee Harris, is highly polished with diamond grit and has a specified surface roughness of less than 400 Å; x-ray diffraction results confirmed the orientation of the (100) crystal. Annealing the diamond at 1225 K in vacuo removed all traces of oxygen and contaminants within the 0.5% of a monolayer sensitivity of the XPS diagnostic. Ion etching was not used as this produced graphitization of the diamond surface. Simple (1x1) LEED patterns were observed at beam energies as low as 45 eV; sample charging precluded observations at lower beam energies.

The graphite sample was a piece of highly oriented pyrolytic graphite (HOPG) (7) that was cleaved in air using the "scotch tape" technique. The sample was cleaned by heating it in vacuo to 700 K. A basically hexagonal LEED pattern was observed, although the presence of multiple domains complicated any interpretation of patterns. It should be noted that HOPG is not single crystal graphite and the data obtained in this study may be complicated by the lack of long range order.

The fluorine atom source has been described in detail elsewhere (8) Briefly, it consists of a miniature fast flow tube whose output is sampled by a small aperture (40 μm), which produces an atomic or molecular beam. A 5% fluorine in argon gas mixture (2 Torr) flows (500 sccm) through an alumina tube which is surrounded by an Evenson-type microwave discharge cavity, past the aperture, and exhausts through a co-annular passage. Operating the discharge at

70 W power produces nearly 100% dissociation of the fluorine. The alumina flow tube is readily passivated and no recombination of F atoms in the gas or on the walls is seen when the beam is sampled by a mass spectrometer. Production of atomic chlorine requires replacement of the alumina tube with a halocarbon wax coated quartz tube. In addition, a skimmer with a 90 μm aperture is used to sample the flowstream. Dissociation efficiencies of 60-70% are reached.

The XPS analyses were performed using a PHI 15 keV, Mg $K_\alpha$ x-ray source and a PHI 15-255 GAR double pass cylindrical mirror electron energy analyzer operated at a pass energy of 25 eV. The analyzer was calibrated using the Au $4f_{7/2}$ peak at 83.8 eV and is accurate to ±0.2 eV. Due to the insulating properties of the diamond sample, significant charging effects were observed. For this reason, diamond spectra presented here are referenced to the C 1s peak (285.0 eV) of bulk diamond. This peak has a full width at half maximum (FWHM) of 1.4 eV and its assignment is never ambiguous. All spectra involving the graphite studies are referenced to the C 1s peak at 284.6 eV; no charging effects were observed.

## RESULTS

Figure 1 presents a C 1s spectrum of an an annealed diamond sample, and samples which have been exposed to saturation doses of atomic fluorine and chlorine. The annealed spectrum consists of a bulk peak at 285.0 eV and a shoulder at lower binding energy (283.9 ±0.2 eV) associated with a diamond surface state (9,10). The spectrum of the fluorinated sample reveals a new peak at 286.8 ±0.2 eV associated with a carbon monofluoride species (10,11). The saturation coverage for fluorine can simply be estimated by comparing the relative integrated intensities of the surface diamond peak and carbon fluoride peak. Assuming one binding site per carbon atom, a coverage of approximately three quarters of a monolayer is obtained (12).

On the other hand, the XPS spectrum of the chlorinated diamond sample is virtually indistinguishable from that of the annealed sample. Thus, in order to obtain a value for saturation coverage, it is necessary to measure the chlorine atom uptake using the Cl 2p peaks. The quality of the data is limited by poor signal levels and fluctuations in beam intensity. By comparing normalized signal levels for chlorine and fluorine and correcting for differences in photo-ionization cross sections and spectrometer detection efficiencies, the chlorine atom saturation coverage at room temperature can be estimated at no more than half a monolayer.

The fact that the spectra of the annealed and chlorinated samples are quite similar would seem to indicate that the chlorine atom-diamond surface interaction is fairly weak. This hypothesis is confirmed by the data in Figure 2 which show the effect of heating a substrate which had been saturated with chlorine atoms at 223 K and measuring the residual chlorine concentration at each temperature. It

is clear that the chlorine coverage is not stable at room temperature and is completely desorbed at temperatures used in processing diamond films. Similar data for fluorine, shown in Figure 3, show a carbon fluoride adlayer stable to 700 K. This is consistent with the picture of a fairly strong surface-atom interaction for fluorine indicated by the formation of a distinct C-F XPS peak. This evidence raises the questio as to whether F atoms etch diamond at high temperatures. It should be noted that hydrogen atoms desorb as $H_2$ even though etching is energetically allowed (13).

Carbon 1s XPS spectra of halogenated HOPG graphite show strong similarities to those of halogenated diamond surfaces. As seen in Figure 4, the spectrum of the HOPG basal plane exposed to chlorine atoms is identical to that of the annealed sample. The measured chlorine atom concentration is a small fraction of a monolayer. Fluorine atoms, on the other hand, interact strongly with the graphite surface, forming a C-F bond as shown by the observation of a new XPS peak, ~2.5 eV to higher binding than bulk graphite. This C-F peak is virtually identical to that observed in bulk graphite fluoride intercalation compounds (14) (also known as the ionic form of graphite fluoride). But by integrating the F 1s spectra and comparing the observed intensity to that obtained on diamond, it is clear that no penetration of the surface has occurred; the fluorine atom coverage saturates at approximately 1/4 of a monolayer at room temperature. Figure 5 presents the amount of fluorine left on the surface at various temperatures; the adlayer is quite stable until the substrate is heated to approximately 550 K. Given that Rosner and Strakey (15) found a sharp fall-off in fluorine-induced graphite etching below 1050 K, it is likely that the fluorine simply desorbs as opposed to etching.

Molecular halogens do not seem to form stable halide adlayers with either diamond or graphite. Molecular fluorine does leave behind some residual adlayer on diamond, but this may simply be due to surface defect induced reaction. Otherwise, virtually no traces of halogen atoms could be observed at room temperature or at 473 K.

## DISCUSSION

The data presented in this paper indicate that chlorine and fluorine atoms will play quite different roles in any potential diamond deposition scheme. Chlorine atoms are not strongly bound to diamond surfaces at any useful temperatures and thus will not affect the deposition process to any great extent. Fluorine atoms, on the other hand, form a stable adlayer at potential deposition temperatures. Thus, they are probably suitable for an atomic layer epitaxy (ALE) scheme, where they can be used to cap the surface. We will soon perform experiments in this laboratory to determine if atomic hydrogen can be used to abstract fluorine atoms as a way of controlling diamond growth. We will also determine if fluorine atoms simply desorb in atomic or molecular form or if they etch diamond by forming volatile

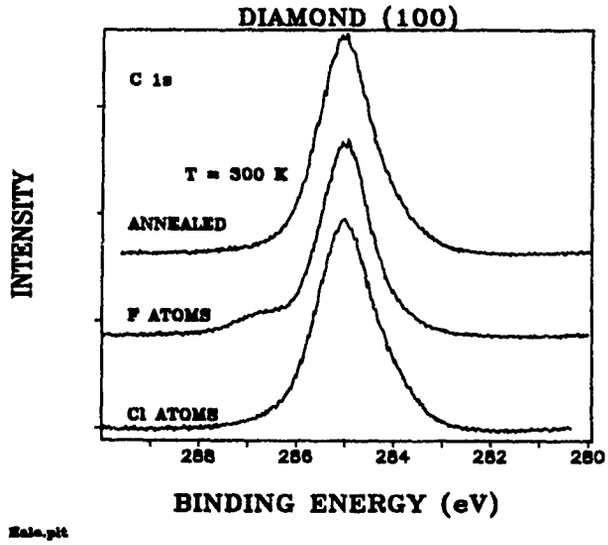
$CF_x$ species. From the preliminary data on graphite fluorination, it would seem that halogen atoms will not convert graphite to diamond, at least at the low temperatures and fluxes involved in this experiment. Further experiments will continue to study graphite etching at high temperatures. We will also attempt to form the covalent form of graphite fluoride.

## ACKNOWLEDGEMENTS

This research was sponsored by the Strategic Defense Initiative Organization/Office of Innovative Science and Technology (managed by the Office of Naval Research).

## REFERENCES

1. M. Yoder, Private Communication.
2. R.A. Rudder, J.B. Posthill, and R.J. Markunas, Electronics Letters 25, 1220 (1989).
3. R.A. Rudder, G.C. Hudson, J.B. Posthill, R.E. Thomas, and R.J. Markunas, Appl. Phys. Lett., in press.
4. D.E. Patterson, B.J. Bai, J. Chu, R.H. Hauge, and J.L. Margrave, "Halogen Assisted CVD of Diamond", presented at 2nd International Conference on New Diamond Science and Technology, September 1990, Washington, DC.
5. T. Nakajima and N. Watnabe, "Graphite Fluorides and Carbon Fluorine Compounds," CRC Press, Boca Raton (1990).
6. Y. Sato, "An Approach to the Mechanism of Diamond Growth from Vapor Phase," in Japan Reviews in New Diamond, p4 (1990).
7. Union Carbide.
8. C.D. Stinespring, A. Freedman, and C.E. Kolb, J. Vac. Sci. Technol. A4, 1946 (1986).
9. B.B. Pate, M. Oshima, J.A. Silberman, G. Rossi, I. Lindau, and W.E. Spicer, J. Vac. Sci. Technol. A2, 957 (1984).
10. J.F. Morar, F.J. Himpsel, G. Hollinger, J.L. Jordan, G. Hughes, and F.R. McFeely, Phys. Rev. B33, 1340 (1986).
11. D.S.Y. Hsu and N.H. Turner, "Fluorination of Diamond (111) Single Crystal Surfaces by $XeF_2$," 4th SDIO/IST Diamond Technology Initiative Symposium, Crystal City, VA, July 1989, Unpublished.
12. A. Freedman and C.D. Stinespring, Appl. Phys. Lett. 57, 1194 (1990).
13. A. Hamza, G.D. Kubiak, and R.H. Stulen, Surf. Sci. 237. 35 (1990).
14. I. Palchan, M. Crespin, H. Estrade-Szwarcopf, and B. Rousseau, Chem. Phys. Lett. 157, 321 (1989).
15. D.E. Rosner and J.P. Strakey, J. Phys. Chem. 22, 690 (1973).




Hale.plt

Figure 1. XPS Spectra of Diamond (100) Substrates which have been (from Top to Bottom): a) annealed at 1200 K; b) exposed to a saturation coverage of fluorine atoms and c) chlorine atoms at 300 K.

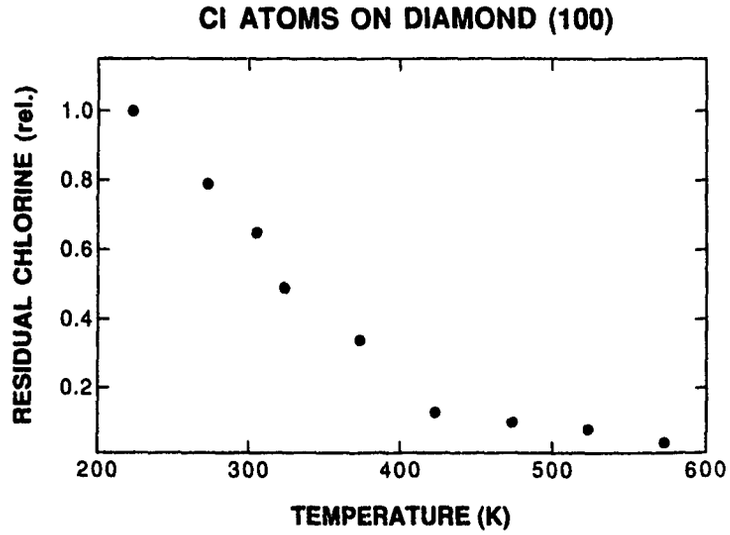



Figure 2. Thermal Stability of Chlorinated Diamond Layer. The substrate was chlorinated to saturation at 223 K before heating. Relative chlorine concentrations are measured by integrating the Cl 2p XPS peak.

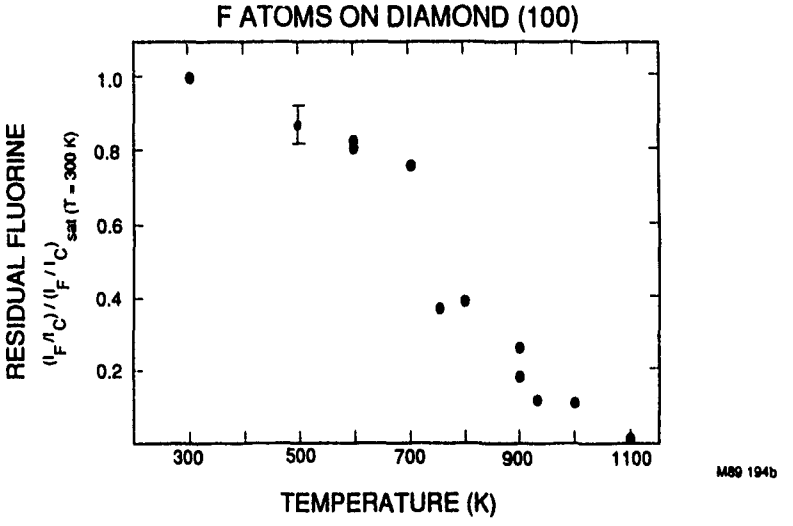



Figure 3. Thermal Stability of Fluorinated Diamond Layer. The substrate was fluorinated to saturation at room temperature before heating. Relative fluorine concentrations are measured by integrating the F 1s XPS peak.

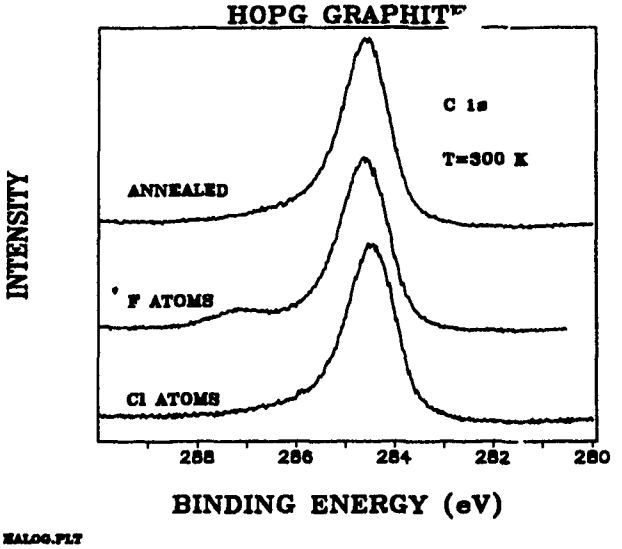



Figure 4. XPS Spectra of Graphite (Basal Plane) Substrates Which Have Been a) Annealed at 500 K; b) Exposed to 40 ML of Atomic Fluorine; and c) Exposed to 40 ML of Atomic Chlorine) at 300 K.

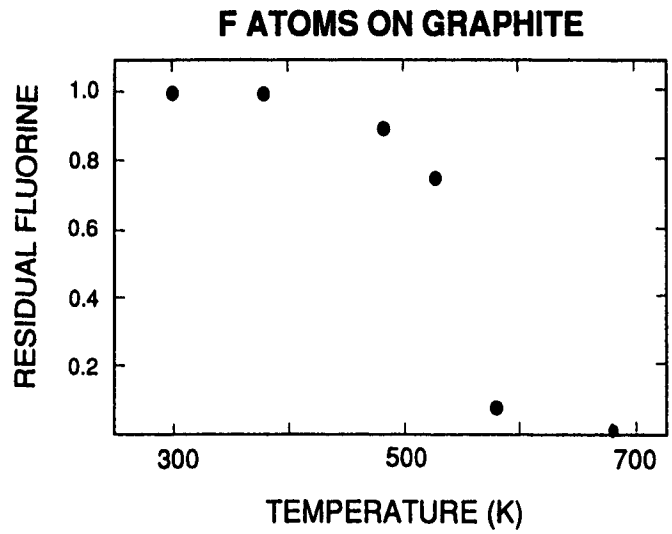



**Figure 5. Thermal Stability of Fluorinated Graphite Adlayer; the Substrate Was Fluorinated to Saturation at Room Temperature Before Heating.**

# CHARACTERIZATION OF CVD DIAMOND FILMS WITH ATOMIC FORCE AND SCANNING TUNNELING MICROSCOPY

A. W. Phelps and T. W. Owens
University of Dayton Research Institute
c/o: Phillips Laboratory
Edwards AFB, CA 93523-5000

## ABSTRACT

Images of CVD boron doped diamond films have been obtained by using atomic force and scanning tunneling microscopes (AFM and STM). The images comfirm earlier studies on the effects of boron additions to diamond films during growth.

## INTRODUCTION

It is our goal to use established diamond deposition processes to solve specific engineering problems. Our current research involves analysis and application of diamond films for bearing applications. Therefore, there is an interest in the control of microstructure and roughness of as-grown CVD diamond surfaces. A unique means of investigating these two features of diamond films is with the recently developed scanning probe microscopies. Atomic force (AFM) and scanning tunneling microscopy (STM) have been shown to be capable of atomic resolution on a wide variety of conducting and insulating materials. These techniques appear to hold promise for the study of the structure of CVD diamond films. This paper reports the results obtained by AFM and STM examination of a series of boron doped CVD diamond films.

### Scanning Microscopies

The development of the scanning microscopies has provided new methods of investigating surface chemistry and physics on an atomic scale of materials. Other analytical techniques are incapable of examining the diamond surface from the macroscopic to near atomic scale. There has been a large amount of work published on the construction and use of these microscopes in the last five years. The reader is directed to some general references on the application and use of scanning tunnelling and atomic force microscopes. The operation and use of the STM [1] and the uses and operation of the AFM [2] have been recently examined.

Typically, secondary electron microscopes begin to lose their lateral resolution between 60 and 100 KX magnification or on features smaller than 500 nm in diameter. Transmission electron microscopy is possible in this magnification range, but extensive samples preparation is usually necessary for this technique and the average TEM is incapable of atomic resolution. There is a significant problem with the use of electron beam based microscopies for the examination of diamond. Diamond is usually an

insulator and typically requires a conductive coating of gold or carbon to be applied to the sample surface in order to avoid charging effects on the image. Modifying the diamond surface in this way makes it unsuitable for other characterization techniques. The AFM does not require any sample preparation.

Boron in CVD Diamond

A series of CVD diamond films were examined by AFM and STM to observe the effects of boron doping on their morphology. Boron doped CVD diamond films have been made by several different techniques and have been found to simulate natural type IIb semiconducting diamond. Boron doped diamond growth on diamond and other substrates has been described in a number of recent works [3, 4, 5].

Sato et al. (1987) [3] grew their boron doped diamond films by microwave plasma enhanced CVD with diborane as the dopant source. They noted several changes in film properties with variations in amount of diborane added to the gas phase. The electrical conductivity of their films were found to increase with increased diborane flow similar to that observed others [4]. Significant reductions in the background of the Raman spectra of boron doped diamond films have also been observed [4, 5]. The changes observed in the Raman spectra scaled with the amount of boron added to the system. Features observed in the Raman spectra of diamond films have been suggested to be the result of defects in the diamond structure and boron doping of the material appears to substantially affect its Raman spectra [7].

Additions of noncarbon atoms to the growth environment of CVD diamond have been predicted to result in the formation of a smaller number of structural defects during growth [8, 9]. Bernholc et al. (1988) [8] predicted that with boron as a dopant "...the reduced self-diffusion activation energy should lead to better quality material." The presence of the boron atoms would also result in a lowering of the surface diffusion energy during CVD crystal growth needed for the carbon atoms to align themselves in their preferred crystal structure. This doping model suggests that the crystalline quality of a standard undoped diamond film will be improved by an addition of boron during growth.

## EXPERIMENTAL

The atomic force and scanning tunneling microscopes and electronics used in this study were made by Digital Instruments, Santa Barbara, California. The microscopes were operated and image acquisition was performed using the Nanoscope II operating system and software. Atomic force images were obtained with the Nanoscope II system from a very simple sample arrangement. This microscope operates in air or can be used in a controlled atmosphere glovebox or under a drop of oil etc. This study was performed in air. Sample preparation consisted of mounting a piece of CVD diamond onto a sample stub. The diamond was deposited onto a silicon wafer and was cut down to approximately 1 $cm^2$ so that it could fit in the microscope. The wafer was mounted to the top of a cylindrical piezoelectric translation element. This tube provides a stable, low drift,

three dimensional scan that varies in size depending on the overall length of the tube. This study was performed using two different scan heads. Each head contained a piezoelectric element of different length. The maximum lateral scan length of one head was approximately 1 μm and that of the other was approximately 13 μm. Both heads are capable of being used to observe atomic structure although the head with the shorter scan length has a much greater degree of lateral resolution and a smaller amount of hysteresis during raster. The tip of a mirrored, triangular, cantilever is placed in near contact with the sample surface as the sample is rastored beneath the tip. Variations in surface topography are detected via a laser beam reflected into a photo diode from the tip of the cantilever.

The microscope hardware and software provided the capability to image the sample surface in either a height or applied force mode for the AFM and in either a height or current mode for the STM. Height mode imaging with the AFM is performed by controling the voltage applied to the z axis of piezoelectric element in order to hold the sample and the cantilever at set contact force (distance) and then using the changes in the voltage applied to the piezoelectric to produce an image in conjunction with the x-y raster on the CRT. Force mode imaging is performed by keeping the z voltage constant and imaging the changes in voltage produced by the deflection of the cantilever tip. The height mode was used in this study in order to have enhanced vertical resolution and to avoid damage to the cantilever tip and the sample. Similar means are used in the STM for height and current imaging but with the current being the observed parameter.

The samples of boron doped CVD diamond films examined in this study were prepared by microwave plasma deposition with various amounts of diborane added to the feedstock gas during deposition. The various levels of diborane in the feedstock gas provided different doping levels of boron in the films. A detailed description of the deposition parameters for these films is provided in [6]. The effects of boron on the diamond films were observed by four point electrical probe measurments and Raman spectra [4, 6]. The surfaces of the films had a matte appearance and were blue-grey in color.

The growth parameters used for the diamond deposition were not optimized to produce diamond films with the sharpest Raman spectra. These films were grown at a reasonably rapid rate in the microwave device. Fast in this context means uniform diamond films four to five microns thick were deposited in the space of about five hours. The Raman spectrum of the undoped film shows the presence of a significant amount of graphitic bonding which would not have been present under slower film growth conditions.

## RESULTS

A limited number of AFM and STM images are presented here. These techniques have shown themselves to be singularly capable of imaging unprepared diamond surfaces. Figures 1 through 4 show the surface features of the series of diamond films whose growth environment had an incrementally increased diborane content. Figure 1 shows the undoped diamond film. Figure 2 is an image of the diamond film grown in the

presence of 100 ppm diborane. The image was obtained at a similar magnification as Figure 1 and shows that the morphology of the film has undergone a marked change when some diborane was added to the growth environment. Figure 3 is an AFM image of a diamond film grown in the presence of 180 ppm of diborane and Figure 4 is of the film grown in the presence of 300 ppm diborane. The crystallites in Figures 3 and 4 are much larger than those in Figures 1 and 2 and much more euhedral showing the effects of further boron additions. Figure 5 shows an STM image of the diamond film grown with 300 ppm diborane. This film was continuous and fairly pinhole free. Tunnelling had to occur through the bulk of the diamond film. The film grown in the presence of 180 ppm diborane did not tunnel and attempts to image it with the STM resulted in numerous tip crashes. One aspect of this study provided a large amount of frustration.

Numerous attempts have been made to image the atomic structure of the surface of diamond with the AFM. Figures 1 through 4 show features on the diamond film surface that are observable down to tens of nanometers but resolution is usually lost below approximately 30 nm scan width images. Atomic scale images have yet to be obtained with the AFM. It has been suggested that a force between 100 and 1000 times greater than that typically used to obtain atomic images on graphite may be needed to produce an atomic image of the diamond surface [10]. This has yet to be confirmed, but it was found during the course of this study that it was possible to maximize the force on the cantilever tip on this instrument and still be unable to image atoms. Atomic imaging of graphite and muscovite surfaces is a fairly routine process. However, the operational parameters typically used for those materials do not apply to diamond.

Obtaining images of diamond on an atomic scale will be very useful for understanding the surface crystal structure and nature of defects and doping in the diamond. At present, most atomic imaging is being done on bulk samples in high resolution transmission electron microscopes (HRTEM) and surface structure studies are being performed with low energy electron diffraction (LEED) [11, 12]. The AFM and STM could serve to answer many questions about the material that these techniques are as yet unable determine.

## SUMMARY

It is clear from Figures 1 through 4 that the addition of diborane to the growth environment has a very large effect on the crystallite morphology and size in addition to the previously examined conductivity and Raman spectra. The atomic force microscope is uniquely suited to the study of the the surface morphology of diamond films. This technique has shown its usefulness in the study of the effects of a changing deposition environment on the microstructure of CVD diamond films. Results obtained from a series of boron doped diamond films confirms earlier work on the effects of boron additions to the diamond film growth environment.

## ACKNOWLEDGEMENTS

Thanks are due to W. P. Hoffman, C. Selph and D. Silver. This work was supported in part by AFSC Contract No. F04611-88-C-0020.

## REFERENCES


[1] Hamers. R. J. 1991. Atomic-scale imaging with the scanning tunneling microscope. MRS Bull. 16: 22.

[2] Burnham, N. A., Colton, R. J. 1991. Force microscopy. *in* Scanning tunneling microscopy: Theory and application. ed. D. Bonnell. VCH Pub.to be published.

[3] Sato, Y., M. Kamo and N. Setaka. 1987. Growth of semiconducting diamond films by plasma-assisted vapor deposition. Mater. Sci. Monogr. 38B: 1719.

[4] Phelps, A. W. and R. Koba. 1989. P-type diamond stripper foils for tandem ion accelerators. Electrochem. Soc. Proc. 89: 38.

[5] Mort, J., D. Kuhman, M. Machonkin, M. Morgan, F. Jansen, K. Okumura, Y. M. LeGrice and R. J. Nemanich. 1989. Boron doping of diamond thin films. Appl. Phys. Lett. 55: 1121.

[6] Phelps, A. W. 1990. The vibrational spectra of diamond polytypes and defects in diamond and cubic boron nitride. Ph. D. Thesis, The Pennsylvania State University.

[7] Phelps, A. W. 1991. The breakdown of vibrational selection rules in CVD diamond. *in preparation.*

[8] Bernholc, J., Del Sole T. M. Antonelli, Y. Bar-Yam and S. T. Pantelides. 1988. Mechanism of self-diffusion in diamond. Phys. Rev. Lett. 61: 2689.

[9] Kajihara, S. A., A. Antonelli and J. Bernholc. 1990. N-type doping and diffusion of impurities in diamond. Accepted for Mat. Res. Soc. Symp. Proc. 162.

[10] Girard, C., Maghezzi, S., Van Labeke, D. 1990. Interaction between a spherical probe and an atomic lattice: Implication for atomic force microscopy on graphite and diamond. Surf. Sci. 234: 181.

[11] Williams, B. E., H. S. Kong and J. T. Glass. 1990. Electron microscopy of vapor phase deposited diamond. J. Mater. Res. 5: 801.

[12] Pate, B. B. 1986. The diamond surface: atomic and electronic structure. Surf. Sci. 165. 83.

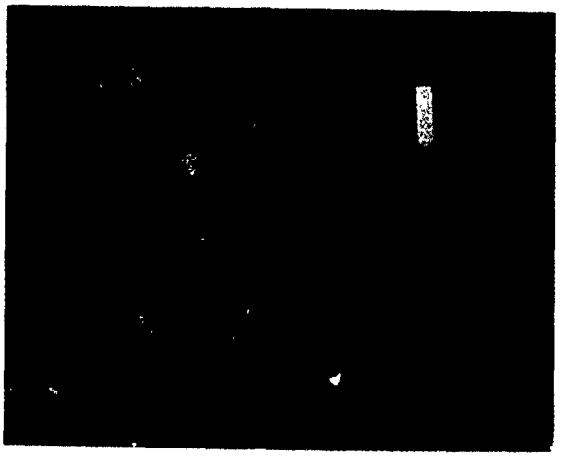


Figure 1. AFM image of CVD diamond film - undoped.



Figure 2. AFM image of CVD diamond film - 100 ppm Diborane.

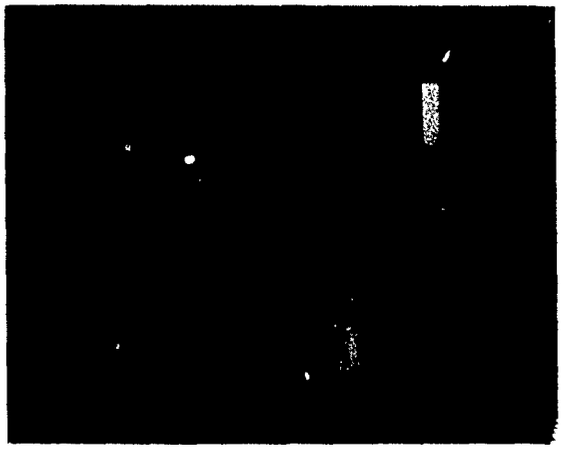


Figure 3. AFM image of CVD diamond film - 180 ppm Diborane.



Figure 4. AFM image of CVD diamond film - 300 ppm Diborane.

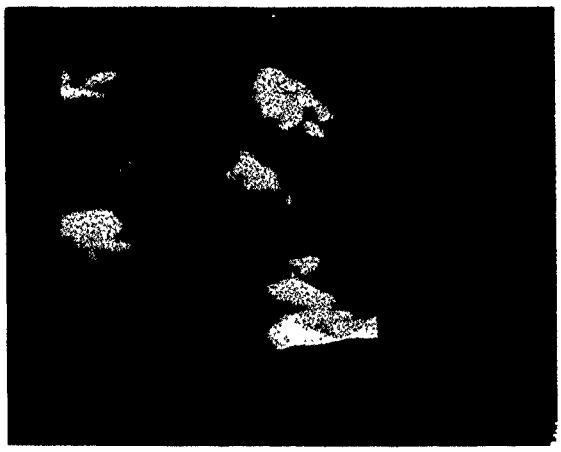


Figure 5. STM image of CVD diamond film - 300 ppm Diborane.

# PART IV: APPLICATIONS

# DIAMOND: WHAT, WHEN, AND WHERE

Max N. Yoder
Electronics Division
Office of Naval Research
Arlington, Virginia 22217

ABSTRACT

A brief history of artifact diamond films is presented. Several basic approaches to growth are heuristically presented within the successful boundary conditions for such growth followed by qualitative results. New approaches to growth are presented with an emphasis on their basic differences with past approaches. Applications are presented as a function of their market size, introduction date and dependence on research advances.

**WHAT** is all the recent activity in diamond all about? The answer is films, films, and more films. Although artifact diamond films could be grown as early as the 1960s, their growth rates were abysmal and their quality uncertain. The advances of the mid and late 1950s in high pressure, high temperature artifact diamond were so striking and industrial production so certain and profitable that research in films waned -- except in the U.S.S.R. There it was found that the combination of **atomic** hydrogen and hydrocarbons was efficacious in the deposition of diamond films. This work was further developed by the Japanese at the National Institute for Research in Inorganic Materials (NIRIM). Their major contribution was the introduction of the microwave plasma whereby the atomic hydrogen concentration (deemed so necessary in diamond film growth) could be significantly increased. The successes in Japan soon stimulated research in the USA, and more recently in Western Europe, Canada, Australia, India, China, Union of South Africa, and Taiwan. Diamond research programs are now underway in most industrialized nations.

The vast majority of the diamond films being deposited use the basic process whereby a hydrocarbon gas is diluted in hydrogen. Nucleation on non-diamond substrates is usually preceded by scratching the substrate with a diamond paste and using a feed stock mixture of up to 4% hydrocarbon in hydrogen. While such a mixture stimulates diamond nucleation, it does not lead to high quality diamond films. The highest quality films grown by this basic procedure use but 0.5% hydrocarbon dilution in hydrogen.

There are four commonly employed procedures for the creation of the essential atomic hydrogen from the mixture. The first is the aforementioned **microwave plasma**. Its basic advantage is the relative ease with which a very dense and high temperature plasma may be created in a comparatively small volume. The **direct current plasma** is also widely used in various configurations. Its basic advantage is the extremely high plasma temperatures it provides. It can be statistically shown that higher growth rates ensue from high plasma temperatures. Although not yet proven, the higher plasma temperatures engender a greater number of very simple hydrocarbon radicals and it is probably that these short-lived radicals contain more of the immediate precursors most suited to diamond growth. The radio frequency (**RF**) **plasma** sources provide advantages of uniformity over large areas. The **hot filament** approach to diamond film growth offers a conceptually unlimited large area uniformity advantage, but suffers from filament aging, a comparatively low "plasma" temperature, and the increased probability of film contamination by filament material. Argon or other noble gases are frequently used as carrier gases in the plasma systems as a means of stabilizing the plasma and increasing the lifetime of the atomic hydrogen.

The introduction of oxygen into the feed stock mixture was recently shown to be efficacious from a number of perspectives. The reason for this can be derived from Table I. To do this, one must first recall why atomic hydrogen was believed to be so essential for diamond film growth. When the surface of diamond is **unterminated**, the carbon bonds dangling from its surface will reconstruct as unwanted $sp^2$ pi bonds.

**Table I.**

APPROXIMATE BINDING ENERGIES TO DIAMOND

| Terminating Species | Binding Energy (kCal/mol) |
|---|---|
| Oxygen | 127 |
| Fluorine | 107 |
| Hydrogen | 101 |
| Carbon | 88 |
| Hydroxyl (OH) | 85 |
| Chlorine | 80 |
| NO | 42 |
| Nickel | low |
| Copper | very low |

This reconstruction predisposes to the graphitic allotrope of carbon thereby preventing subsequent diamond growth. Hydrogen, however, is both a blessing and a curse. As seen in Table I, it binds to the diamond surface with an energy greater than that of carbon! Its tenacious hold can be broken by kinetic bombardment with another proton during molecular ($H_2$) reformation at an energy of 104 kCal/mol. Statistically it is known that for every $10^4$ such atomic hydrogen abstractions, only one is replaced by carbon. The process is thus very inefficient. Moreover, approximately 0.1% of the hydrogen atoms remain in the diamond film. At substrate temperatures above 850 °C, hydrogen is also energetically driven from the diamond surface but again is predominately replaced by other hydrogen rather than by carbon. For this reason, diamond film growth using the method of hydrocarbons diluted in hydrogen is best accomplished at temperatures above 850 °C. The introduction of oxygen significantly relaxes the acceptable conditions under which diamond films will grow. An examination of Table I indicates that oxygen binds to the diamond surface with an even greater tenacity than does hydrogen. It is thus very improbable that the presence of oxygen results in an oxygen-terminated diamond surface. Although the means by which this happens has not been fully ascertained, two possible reasons are postulated. The first is that since atomic oxygen bonds to hydrogen with an energy of 118 kCal/mol, this may be (depending on barrier height) sufficient for its presence to abstract a carbon-terminating hydrogen atom from the diamond surface and thus provide a greater "frequency" of carbon dangling bonds to be reterminated with carbon. A more probable postulate, however, is that hydroxyl radicals are formed and that it is these radicals that terminate the surface. From Table I it can be seen that they will bind to the diamond surface with slightly less energy than does carbon. Thus they will desorb at much lower temperatures (e.g., 450 °C). In the presence of energetic protons, it is energetically favorable (117 kCal/mol vs 85 kCal/mol) to form $H_2O$ and detach from the surface with an even greater frequency. Oxygen addition to the feed stock has been accomplished in many forms. While the most common are the addition of CO and $O_2$ to the feedstock, various alcohols have also been used to replace hydrocarbon feedstocks. CO diluted in $H_2$ has also proven successful as has the addition of $CO_2$ to hydrocarbons diluted in hydrogen. Diamond does not usually grow when the atomic oxygen concentration exceeds the atomic carbon concentration since the formation of CO and $CO_2$ is energetically favorable to that of diamond formation. Peter Bachman has statistically compiled the results of published experiments using oxygen in the feedstock (1). Successful diamond growth accrues within a narrow range of mixtures. An abbreviated description of the

Bachman findings is shown in figure 1 and denoted as the magic Bachman wedge. It is only within the shaded narrow wedge of the triangle that diamond has successfully been grown. Recently diamond films have been shown to grow without any dilution in molecular hydrogen gas (2) (3). The only hydrogen present during growth derives from the hydrocarbon feed stock.

The seemingly necessary requirement to maintain the diamond surface with a terminator capable of inhibiting the unwanted carbon pi bonding requires considerably more investigation. How low can the binding energy be and still prevent the unwanted reconstruction? Since it appears that the lower this terminating energy is (at least in the case of the hydroxol), the easier it is to grow diamond, other species should be investigated. From Table I it would seem that NO may be the next appropriate choice of terminating radicals. Its binding energy is less than half that of the carbon-carbon bond in diamond. One possible disadvantage of this approach is that residual nitrogen left in the films would be inappropriate for semiconducting diamond. Thermal conductivity would also be decreased. Since the C-N bond is actually stronger than the C-C bond, residual nitrogen could further strengthen and harden the diamond films.

The use of halocarbons provides an alternative to hydrocarbon feedstocks. A prima facie case for the use of halocarbons cannot be made from casual observation of Table I. Indeed, it would appear to be counterproductive to use halogens for terminating the diamond surface and the most common one exhibits binding energies stronger than that of hydrogen. The efficacy of the halogens lies not in their binding energy to carbon, but in their binding energy to hydrogen. The H-F bond is 134 kCal/mol. The halogen atom on any halocarbon radical absorbing on a hydrogen-terminated surface has a 100% probability of abstracting the hydrogen from the diamond surface and forming an HF molecule. This abstraction leaves a nascent carbon dangling bond on the surface and in nearest proximity to it a halocarbon radical. The probability of this halocarbon radical terminating the dangling surface bond is extremely high. Using such extraction/exchange mechanisms, it should be possible to grow diamond at room temperature.

When will diamond film growth be emancipated from the growth rate inhibiting restrictions of surface terminators? Soon. Diamond is known to grow at substrate temperatures approaching 1500 °C (4) (5) (6). At these temperatures the lifetime of any surface terminators is extremely short-lived. Although the selectivity ratio governing the replacement of surface-terminating bonds with hydrogen or carbon is most probably not

significantly changed, the frequency of occurrence is appreciably increased.

Total emancipation from the hydrogen curse has also been demonstrated. The first such hydrogen-free growth was by the implantation of a large (i.e., $10^{18}/cm^2$) fluence of carbon ions into single crystalline copper (for which there is no measurable solubility for carbon) and by virtue of the 900 °C temperature, effusing the carbon to the surface whereupon it formed a 50 nanometer thick single crystalline diamond film heteroepitaxially oriented to the underlying copper (7). This experiment by Johan Prins and Horace Gaigher is thought to be best reproduced under conditions wherein any non-diamond carbon allotropes are actively and completely removed from the surface during the nucleation. In this situation the diamond film appears to grow from its underside and that (presumably by virtue of the heteroepitaxial relationship between the diamond and the underlying single crystalline copper) unwanted pi bonding does not accrue. While the carbon-copper bond energy is not accurately known, it is apparently sufficient (at least when heteroepitaxial orientation occurs) to prevent the unwanted diamond reconstruction.

A most interesting and efficacious variation of the Prins technique was subsequently published (8). Here the carbon implanted copper was subjected to a 45 nanosecond duration laser pulse of up to 5 Joules/$cm^2$ -- an energy level sufficient to melt the copper. A 50 nm thick single crystalline diamond film resulted. The growth rate translates to about 4000 meters/hour! Although the exact temperature was not given, copper melts around 1380 °C. Presumably, the temperature did not exceed 1477 °C above where it is improbable that diamond can grow (4).

Further analysis of the liquid-copper-induced diamond nucleation and subsequent growth is in order. The volume expansion of copper upon melting is small. Therefore the copper bonds (although flexible) are still of substantially the same length as in the solid (and hence within about one percent of those of diamond). As such, they could influence the nucleation of effusing carbon into the diamond allotrope. If the diamond was, in fact, nucleated and partially grown while the copper was still in the molten state, this procedure is not that different from the formation of common ice, from the formation of silicon boules, or from the formation of gallium arsenide boules pulled through liquid boric oxide from an underlying molten GaAs melt. More recently, 1-2-3 high temperature superconductors have been spontaneously nucleated and grown on the surface of oxide melts. If such nucleation on the surface of a molten copper surface can be ascertained,

then even greater possibilities arise. Individual islands of diamond nucleation on such a surface are free to rotate. As such islands coalesce, they are free to rotate in such a manner so as to configure at their lowest energy state if the time constants are appropriate. Conceptually, this means the elimination of grain boundaries and large area single crystals. Figure 2 illustrates a means of accomplishing this over a larger area than possible with a laser pulse. For such nucleation to happen, it is mandatory to maintain the copper surface absolutely free of carbon **until** the copper is actually melted so as to prevent a non-diamond carbon seed from forming. An iridium crucible may be necessary for cleanliness and the carbon "feedstock" introduction delayed until growth temperature is reached.

A hundred years ago aluminum was more costly than gold. Today it litters our highways! Hydrogen-free growth techniques are seen as the most-plausible approach to reducing the cost of diamond film growth.

**What** is the material whose properties are most likely to represent the extremus of all values in any matrix table of materials and their physical, optical, acoustical, and electronic properties? Diamond, of course. Even when the value for diamond does not represent an extremus (e.g., electron mobility), its other extremus properties (e.g., charge carrier velocity at high electric field) permit the use of clever applications that circumvent it less-than-superlative properties. It is because of these superlative properties that diamond films will become ubiquitous.

**Where** will diamond be applied? Diamond is noted for its corrosion resistance. At temperatures under 1000 °C only oxygen containing materials will attack diamond. The U. S. Navy spends $200,000,000 each year in reduced fuel efficiency and drydocking because of barnacles and corrosion. The world-wide merchant marine spends even more. Not only do barnacles not attach to diamond, but diamond coatings would protect underlying steel from salt water corrosion. For this promising application and solution to be consummated, a lower cost method of applying diamond films must accrue. A more realistic possibility is that of diamond coating for artificial heart valves so as to eliminate the need for patients to require blood thinners for the remainder of their lives. Still other anti-corrosive biological applications include virtually all prosthetic device implants or their coatings.

Several properties of diamond combine to render it the material of choice for optical coatings. Being the hardest and strongest of all applicable materials, it does not easily shatter when impacted by a raindrop at mach 4. Having a low loss tangent and very broad optical spectrum of transparency, diamond is ideally suited for use in radomes used in dual or multispectral electromagnetic systems. By far the largest use of diamond optical coatings will be in military systems. As lower temperature (i.e., halogen-based) growth techniques become better understood, the coating of plastic optics (e.g., eyeglasses) will also see widespread application. Still other applications of diamond optical coatings include those of coating solar cells and IR detectors with diamond anti-reflection films. Such coatings reduce deterioration resulting from microparticle abrasion.

Natural diamond is unexcelled in thermal conductivity. Homoepitaxial diamond films appear to be equally superlative. Polycrystalline diamond films exhibit thermal conductivities of up to 14 W/°C-cm in the direction of growth. Isotopically pure diamond may exhibit thermal conductivity 50% higher than that of natural diamond. The combination of its thermal attributes with its erosion and corrosion resistance render it ideal for fluid flow heat exchangers. By combining microwave loss tangent with dielectric constant and thermal conductivity a figure of merit for diamond as a substrate for electronic integrated circuits is derived. A comparison is shown in Table II where loss tangents are taken in the millimeter wave spectrum. The coefficient of thermal expansion for diamond is much less than that of most semiconductors. This aspect is mitigated by the ability of diamond to keep the semiconductor temperature rise to a minimum and by the ability to bond extremely thin (e.g., < 1 micron) semiconductor integrated circuits to diamond by Van der Vaals bonding wherein small lateral translation is tolerated, but vertical adhesion remains strong as does thermal conductivity.

TABLE II.

| Material | Dielectric Constant (relative) | Loss Tangent ($\times 10^{-4}$) | Thermal Conductivity (W/cm-°C) | FOM |
|---|---|---|---|---|
| Diamond | 5.5 | 6 | 20 | 0.6 |
| BeO | 6.5 | 5 | 2.5 | 0.07 |
| cBN | 5.8 | 6* | 13# | 0.37 |
| Sapphire | 9.0 | 10 | 3.5 | 0.04 |
| AlN | 8.0 | 5* | 3.2 | 0.08 |

* value uncertain # theoretical

It is as a semiconductor that diamond may find its ultimate application. The first such application is most likely to be that of a solid state cold cathode. Whereas thermionic cathodes operating at 1100 °C tend to be rather inefficient, exhibit a built-in wear-out mechanism ( amperes times hours is a constant), and are subject to "poisoning" of the surface by oxygen at pressures as low as $10^{-11}$ Torr, diamond appears to be immune from all of these. If fact, the efficiency of diamond cathodes is actually improved by exposure to oxygen (10). While thermionic cathodes used in cathode ray tubes typically exhibit emission density of 10 $A/cm^2$, semiconductors typically exhibit current densities of several x $10^5 A/cm^2$. Although diamond cold cathodes have not yet exhibited such emission current density, they are within striking distance of replacing thermionic devices. Even polycrystalline diamond has been shown to emit electrons. In separate demonstrations, polycrystalline diamond has been grown with predominately {111} faces; it is the {111} face of diamond that has the negative electron affinity property.

Diamond has a higher dielectric strength than any other semiconductor ($10^7$ volts/cm) and higher charge carrier velocities at high electric fields than do other semiconductors. By virtue of these properties, the figure of merit for diamond as a microwave power amplifier exceeds that of silicon by a factor of 8200. Its high bandgap (5.5 eV) renders it most useful for high temperature operations in that leakage current is negligible at temperatures of 300 Celsius. While its high frequency performance potential obviously degrades at high temperatures, it still exhibits the highest performance at the highest temperature of any known semiconductor. The high bandgap also renders possible an ideal configuration for a photodetector of ultra violet, x-ray, and other radiation. Since it has negligible leakage current at room temperature and above, the conventional need for a P_N junction is eliminated. The ability to construct such a detector in such a simple manner as a parallel plate capacitor not only reduces fabrication cost, but improves the electric field distribution across the diode thereby reducing signal dispersion caused by unequal fields presented the electrons and the holes in conventional devices. Insulated gate Field Effect Transistors (FETs) made of diamond can also be simplified -- they need no channel backdoping to reduce leakage. This also eliminates ionized impurity scattering.

**Where** are the markets? **When** will they materialize? The cutting tool and hard surfacing markets will be well developed by the end of the decade. In that time span these markets for diamond films will easily exceed $1.5 B/yr. All other diamond

film products are expected to reach $0.5B/yr by 2010 if the diamond semiconductor device market does not materialize. If it does, that market alone could reach $1B/yr.

## REFERENCES


1. P. Bachman, "CVD Diamond Technology: Status and Options", Plenary Paper, International Conference on Metallurgical Coatings and Thin Films (ICMCTF), San Diego, 22-26 April 1991

2. M. Yuasa, H. Kawarada, J. Wei, J. Sheng-Ma, J. Suzuki, S. Okada, and A. Hiraki, "Fabrication of Diamond Films under High Density Helium Plasma Formed by ECR", ICMCTF, San Diego, 22-26 April 1991

3. C. Chen, T. Hon, & C. Lin, " Growth of Diamond Film from $C_2H_2$ + $CO_2$ System by Microwave PCVD", ICMCTF, San Diego, 22-26 April 1991

4. S. Chauhan, N. Gardner, and J. Angus, J. Appl. Phys. 47, (1976) p 4746-54

5. Y. Matsui, H. Yabe, and Y. Hirose, Jap. J. Appl. Phys, 29, (1990) p 1552-60

6. K. Snail, E. Skelton, L. Hanssen, J. Butler, & J. Freitas, "High Rate Homoepitaxial Synthesis of Diamond in a Flame" Paper 133, The 179th Meeting of The Electrochemical Society, Washington, D.C., 5-10 May 1991

7. J. Prins and H. Gaigher, "A TEM Study of Layers Grown on Copper using Carbon Ion Implantation", New Diamond Science and Technology: (edited by R. Messier & J. Glass), Proc. of the 2nd Intl. Conf. on New Diamond Sci. and Tech., MRS Intl. Conf. Proc., Pittsburgh, PA (in press)

9. J. Narayan, V. Godbole, and C. White, Science, Vol 252, (1991) p 416

10. M. Geis, N. Efemow, J. Woodhouse, and N. McAleese, "Diamond Cold Cathodes", Paper 85, The 179th Meeting of the Electrochemical Society, Washington, D.C., 5-10 May 1991

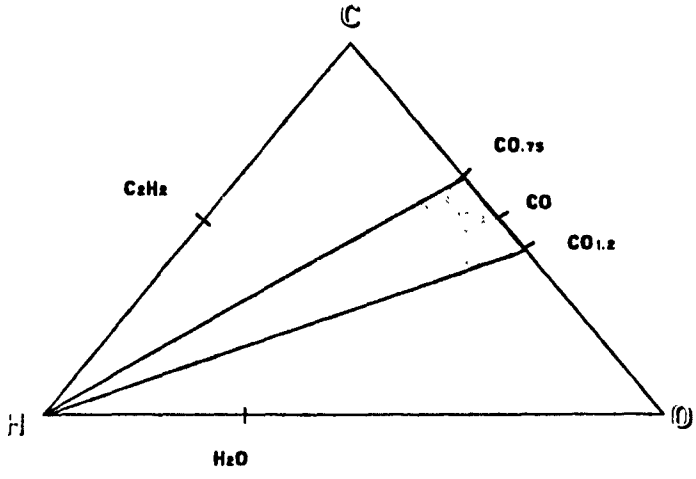



Figure 1. The Bachman Magic Wedge

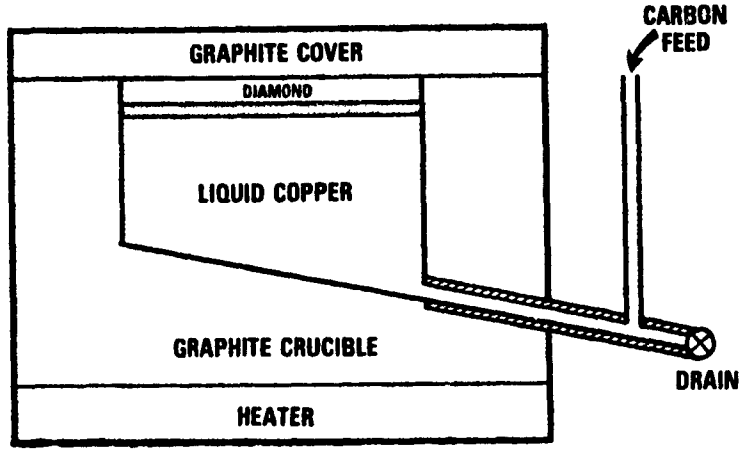



Figure 2. Diamond on Liquid Copper

# IGFET FABRICATION ON HOMOEPITAXIAL DIAMOND USING IN SITU BORON AND LITHIUM DOPING

G.G. Fountain, R.A. Rudder, D.P. Malta, S.V. Hattangady,
R.G. Alley, G.C. Hudson, J.B. Posthill, and R.J. Markunas
Research Triangle Institute, Research Triangle Park, NC 27709

T.P. Humphreys and R.J. Nemanich
North Carolina State University
Raleigh, NC 27695-8202

V. Venkatesan and K. Das
Kobe Steel Research Laboratories
Electronic Materials Center
Research Triangle Park, NC 27709

## ABSTRACT

The use of boron and lithium as dopant impurities in diamond has been investigated using diborane and lithium fluoride as in situ dopant sources. The lithium was investigated as a possible n-type dopant. The diamond material, grown by rf plasma discharge at low pressure, was characterized electrically and microstructurally. The boron was found to be p-type, as expected, with an activation energy of 0.24 eV. The lithium doped material was also found to be p-type with a similar activation energy. SIMS data indicates that the lithium doped samples also contain significant concentrations of boron, enough to account for the electrically active species. However the mobility of the carriers in the Li/B doped material seem to be somewhat higher. Schottky barrier diodes were formed on the Li/B doped material which showed good rectifying behavior. The minority carrier diffusion length in the material was estimated from EBIC measurements to be $\sim$ 0.5 $\mu$m. The lithium appears to be electrically inactive in this material, although it may improve the electrical characteristics of the material. IGFET devices were fabricated in the B doped and Li/B doped materials using a selective deposition fabrication scheme. The boron doped device exhibited a transconductance of 38 $\mu$S/mm.

## Introduction

The extremely selective nature of the plasma activated diamond deposition process provides a very useful and flexible vehicle for device fabrication sequences. Other workers have already reported diamond insulated gate field effect transistor (IGFET) fabrication using selective diamond deposition with a sputtered quartz insulator [1]. The doping of active layers for diamond devices is a crucial topic and is currently under study by several groups [2,3,4]. Boron has been established as a p-type

The B doped samples were determined to be p-type as expected with a carrier density in the $10^{17}cm^{-3}$ range. Two levels were seen in the plot of carrier density vs. temperature as shown in Figure 1. One had a low activation energy of 0.0062 eV, and the other had an activation energy of 0.24 eV. The origin of the low activation energy level is unknown at this point. The 0.24 eV level is more characteristic of B activation in diamond [3]. Hall mobilities measured were on the order of 45 $cm^2/Vsec$. It is likely that the B is compensated by some other level in the diamond, possibly a damage or crystalline defect related level.

Lithium samples were also characterized by Hall measurements. Data from a heavily Li doped sample is shown in Figure 2. Data from a more lightly doped sample is shown in Figure 3. Both samples exhibit p-type behavior, which was unexpected. The activation energies of the acceptor levels in the samples seemed surprisingly close to the level measured for the boron doping. The lightly doped sample did however exhibit the higher mobility than the B doped sample.

SIMS analysis of the heavily Li-doped sample showed both Li and B in the film. The amount of Li was $\sim 10^{21}$ $cm^{-3}$; the amount of B was $\sim 10^{18}$ $cm^{-3}$. The source of the B is at this point undetermined; however, it is likely to be a deposition system component. It is very probable that the p-type behavior is from the boron in the film and not the Li. The Li does, however, seem to have a beneficial effect on the electrical properties of the film.

Gold Schottky diode structures were fabricated on a heavily lithium-doped sample that had received a 30 minute hydrogen plasma treatment (1500 watts of RF power into the plasma), at 5 Torr, at approximately 700 ° C. These diodes showed good rectification behavior with a turn-on voltage of 2.5 V and a breakdown voltage of 6 to 8 V. The reverse leakage current at 6 volts is on the order of 12.5 $\mu A/cm^2$. Gold contacts which had been deposited on material doped with boron alone (which had received a similar hydrogen plasma treatment) exhibited ohmic behavior.

The Au Schottky contact was used to perform electron-beam induced current (EBIC) measurements. EBIC was used to estimate the minority-carrier diffusion lengths. A thin Au Schottky contact was used for charge collection, and the induced current was measured as a function of distance, in plan-view, from the contact. For primary beam energies from 10keV - 20 keV, the minority-carrier diffusion length was measured to be 0.5$\mu$m. This compares with measured minority-carrier diffusion lengths of $\sim 3\mu$m in natural type IIb diamond (B-doped) [7].

### Diamond IGFET Fabrication and Testing

Transistor structures were fabricated on a Type IA natural diamond (100) substrate from Drucker-Harris. The diamond substrate was cleaned using a conventional RCA wet chemical clean [8]. Polysilicon layers as well as $SiO_2$-polysilicon composite

layers were used as masking materials. During diamond deposition the top layer of the silicon is carbonized making it impervious to the hydrogen etching environment. It was found that $SiO_2$ masks were removed by the hydrogen environment if no oxygen was used in the process. The composite structure assures that the carbonized silicon layer can be removed from the wafer. The mask was patterned using standard lithographic techniques and wet etching to open holes for deposition of the conducting p-type diamond areas. Following diamond deposition, the silicon mask was etch removed. The sample was then coated with a 250 Å RPECVD $SiO_2$ gate dielectric. This process has been used to deposit low temperature, gate-quality dielectrics on Si and other semiconductors [9,10]. Titanium gate electrodes were formed using liftoff. Source-drain contact openings were patterned and openings etched in the oxide using buffer HF solution. Titanium contacts were formed using liftoff. The contacts were ohmic as deposited. The gate length and width of the transistors was 8$\mu$m and 50$\mu$m, respectively.

Two types of working IGFET structures were fabricated, one using boron doping alone and one using the lithium doping. In both cases a major limitation on the device fabrication process was control of the dopant concentration.

The boron doped diamond IGFET source drain I-V characteristics are shown in Figure 4. The device showed transistor action characteristic of a p-channel, depletion mode device. The device cannot be pinched off with the available gate voltage. The leakage current is most likely due to defects in the material or surface leakage. The maximum transconductance of the device is 38 $\mu$S/mm at 8 V drain to source. The transconductance of the device is slightly larger for the 1 to 2 V gate step than for the 0 to 1 V gate step. This increase in transconductance with increasing depletion is indicative of a relatively high density of surface states at or near the diamond/$SiO_2$ interface. The geometry of the FET is such that the source to gate resistance is on the order of $2 \times 10^5\ \Omega$. This resistance would decrease the transconductance of the device by a factor of about 2.

The diamond material used for the transistor channel had a resistivity of 12 $\Omega$-cm. The specific contact resistance of the titanium contacts on this material were measured using a transmission line model test structure. The specific contact resistance is 0.09 $\Omega$-cm$^2$. Titanium contacts were also fabricated on heavily boron doped material with a resistivity of 0.08 $\Omega$-cm. These contacts exhibited a specific contact resistance of $1.4 \times 10^{-4}\ \Omega$–cm$^2$. Such layers could be used for contact layers to reduce parasitic resistances in the source and drain using an additional selective diamond deposition step.

The Li/B doped diamond IGFET source drain I-V characteristics are shown in Figure 5. This device exhibited much better saturation behavior than the boron doped device. This device has a more lightly doped channel than the boron doped device as evidenced by the lower saturation current. This device showed both depletion and enhancement behavior. However it is not clear whether this enhanced current is due to accumulation of a conducting layer at the surface or just un-depleting of the channel. It

is likely that, since the doping level is approximately 2 orders of magnitude lower in this device than the first device, the channel is nearly fully depleted at 0.0 V gate bias. The device has a substantial leakage current. Comparison of this leakage current level with the leakage between isolated devices indicated that the current is principally substrate current.

## Conclusions

In situ B and Li doping of diamond has been carried out using a $B_2H_6$ gas source and a LiF solid source in a low pressure rf diamond deposition process. The B was found to be p-type with an activation energy of 0.24 eV. The Li was judged to be electrically inactive in the material evaluated here. The activation energy of the conductivity along with SIMS data on impurity levels indicated that the conduction is probably due to unintentionally incorporated B in the film. The Li appeared to have some beneficial effects on the electrical properties of the the doped diamond films. This effect requires further study. Working IGFET devices were fabricated using the B doped material and the Li/unintentional B doped material. A maximum transconductance of 38 $\mu$S/mm was measured for the B doped device. Improvements in device performance could be achieved through reducing the source drain parasitic resistances and by improving the diamond/$SiO_2$ interfacial characteristics.

*Acknowledgements* The authors wish to thank the Strategic Defense Initative Organization/Innovative Science and Technology Office through the Office of Naval Research (N-00014-86-C-0460) for the financial support of this work. TPH and RJN gratefully acknowledge the support of this work by the ONR, Contract No. N00014-90-J-1707.

## REFERENCES

1. S.A. Grot, C.W. Hatfield, G. Sh. Gildenblat, A.R. Badzian, and T. Badzian, presented at the Second International Conference on the New Diamond SCience and Technology (ICNDST-2), Washington, DC(USA), September 23-27, 1990.

2. Naoji Fujimori, Kideaki Nakahata, and Takahiro Imai, Jap. J. Appl. Phys. 29, 824 (1990).

3. B.V. Derjaguin, B.V. Spitsyn, A.E. Goridetsky, A.P. Fakharov, L.L. Bouilov, and A.E. Sleksenko, J. Cryst. Growth, 31, 44 (1975).

4. G.Sh. Gildenblat, S.A. Grot, C.W. Hatfield, C.R. Wronski, A.R. Budzian, T. Badzian, and R. Messien, Mat. Res. Soc. Symp. Proc. 162, 297 (1990).

5. Ken Okano, Hideo Kiyota, Tatsuya Iwasaki, Tateki Kurosu, Masamori Iida and Terutaro Nakamura, presented at ICNDST-2, Washington, DC(USA), September 23-27, 1990.

6. J. Bernholc, S. Kajihara, and A. Antonelli, presented at ICNDST-2, Washington, DC(USA), September 23-27, 1990.

7. D.P. Malta, S.A. Willard, J.B. Posthill, and R.J. Markunas, unpublished results, Research Triangle Institute, 1989.

8. R.A. Rudder, G.C. Hudson, Y.M. LeGrice, M.J. Mantini, J.B. Posthill, R.J. Nemanich, and R.J. Markunas, Mat. Res. Soc. EA-19, 89 (1989).

9. G.G. Fountain, R.A. Rudder, S.V. Hattangady, R.J. Markunas, P.S. Lindorm, J. Appl. Phys., 63, 4744 (1988).

10. D.J. Vitkavage, G.G. Fountain, R.A. Rudder, S.V. Hattangady, R.J. Markunas, Appl. Phys. Lett., 53, 692 (1988).

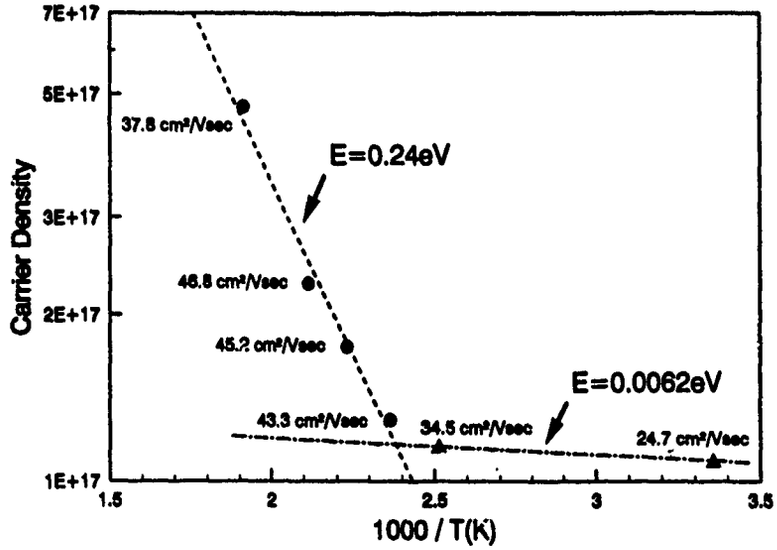



Figure 1 Carrier concentration vs. reciprocal temperature for a boron-doped homoepitaxial film. The material is p-type. Hall mobilities are listed.

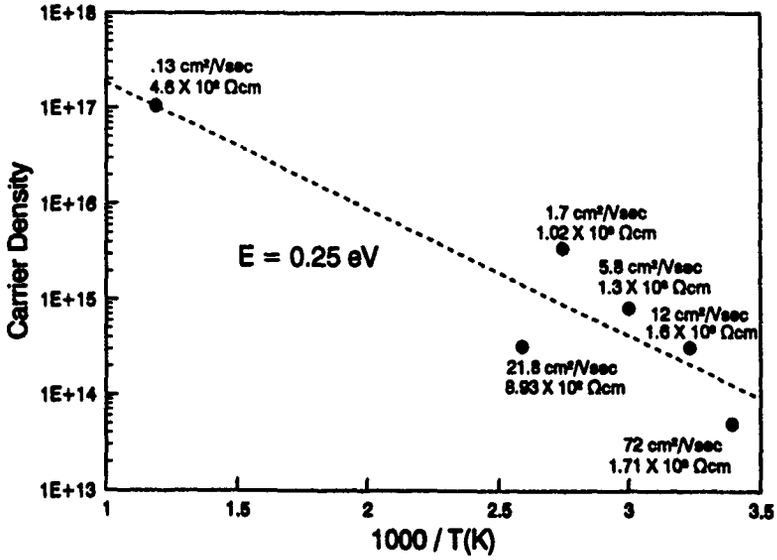



Figure 2 Carrier concentration vs. reciprocal temperature for a heavily Li doped homoepitaxial film. The material is p-type, probably due to boron contamination. Hall mobilities are listed.

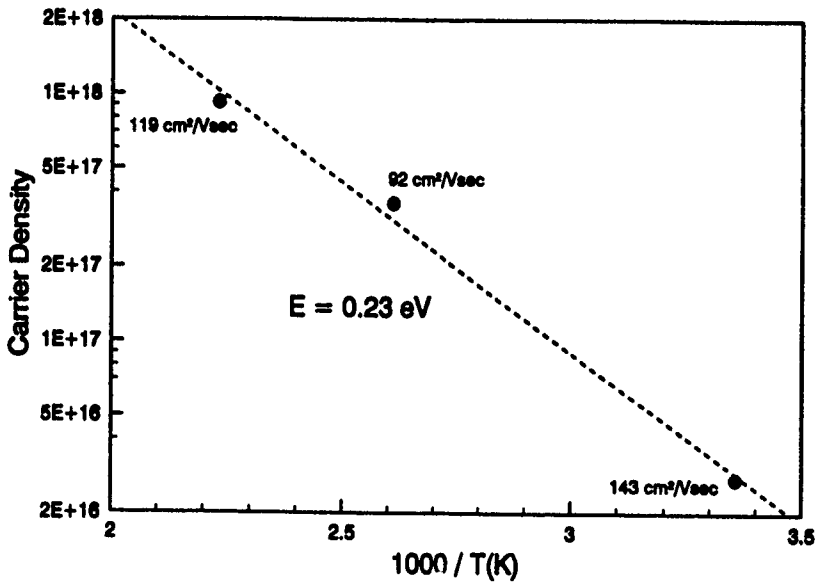



Figure 3 Carrier concentration vs. reciprocal temperature for a lightly Li doped homoepitaxial film. Note the improved Hall mobilities.

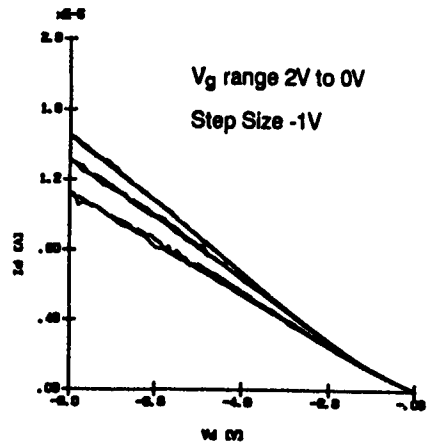



Figure 4 Drain Source I–V characteristic from Boron doped IGFET.

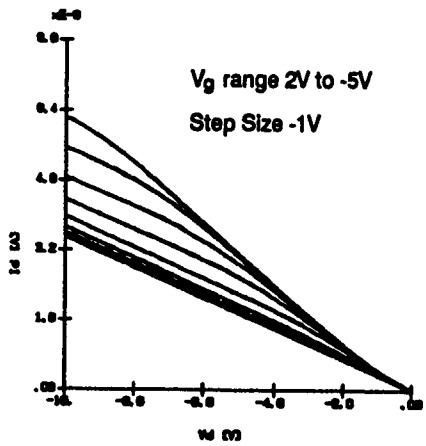



Figure 5 Drain Source I–V characteristic from Lithium/Boron doped IGFET

# SIMULATION OF DIAMOND POWER DIODES

K. Grahn, S. Eränen and P. Kuivalainen
Semiconductor Laboratory
Technical Research Centre of Finland
Olarinluoma 9, SF-02200 Espoo
Finland

Abstract: The performance of the diamond power pin diodes is studied by using the 2D device simulator SCORPIO. A comparison is made between the electrical properties of Si and diamond diodes in a wide temperature range. The results show, that the diamond devices may be operational even at 900 K. Further, the breakdown voltages in excess of 10 kV and high current density operations are possible in diamond. However, due to the large energy gap the on state losses are in the diamond diodes larger than in the silicon diodes.

## INTRODUCTION

Today practically all the power semiconductor devices are made of silicon. The rapid development of the silicon technology has also affected the semiconductor power devices in such a way, that some of the device structures are now approaching their ideal performance, which is achievable in silicon (1). This does not necessarily hold true for all the device structures in all the voltage classes, but in any case the research of the semiconductor materials, which could replace silicon, has by now been active for several years (2). The semiconductors with the wide forbidden energy bandgap such as silicon carbide and diamond have been anticipated to be excellent candidates for the replacement material of silicon because of their high speed, high temperature and high power properties. Several articles have recently emphasized the superiority of the material figures of merit calculated for SiC and diamond as compared to those of silicon (3,4,5). However, in the calculations of the figures of merit typically a few of the numerous material parameters are needed, only. In the real devices practically all the material parameters affect the performance, and, in addition, the depences of the parameters on the dopant concentrations, electrical

fields and temperature have to be taken into account. Consequently, it is not in advance self-evident, that all the device structures made of SiC or diamond will be superior to equivalent silicon devices in all of the various operating conditions.

In this article we report simulated results on the electrical performance of the diamond power pin diodes in a wide temperature range. These results are compared with results obtained for the equivalent silicon structures. The simulations are made for both the forward and reverse bias in the dc terminal conditions. This work is a part of the larger research project, which is aimed to study the performance of the semiconductor power devices made of SiC and diamond. In addition to the pin diode the device structures of interest include at least Schottky diodes and vertical JFET devices (SIT). In the first phase of the research we rely on the methods of the numerical simulations of the device physics, which are well established with the silicon structures. Since the material parameters of diamond and SiC greatly differ from those of silicon, this work is at the same time a direct test of the applicability of the familiar device simulation codes, which work satisfactorily with the silicon devices, to the wide bandgap materials.

## SIMULATION AND PHYSICAL MODELS

In addition to the figures of merit the electrical performance of the devices made of the wide bandgap materials has been theoretically estimated so far in one publication, only (3). In Ref. (3) the temperature dependence of the electrical response of the Schottky and abrupt junction diodes has been calculated by using the well known analytical expressions. In our case the calculations of the electrical properties of devices were made with the 2D device simulator SCORPIO (6).

SCORPIO solves the Poisson equation and the drift diffusion current continuity equations for the electrons and holes (7). In these equations the difference between the materials are contained in the physical model functions, which describe the mobility, diffusivity and generation and recombination properties of the charge carriers. The model functions in turn depend on the charge carrier concentrations and electric field, thus making the set of the differential equations to be solved highly non linear. The dielectric constant is contained

in the Poisson equation and is generally taken to be constant.

Our model functions for the mobility of the electrons and holes include the influence of the temperature, doping and carrier densities and electric field with the saturation of the carrier velocity at high fields (7,8). Consequently, we write

$$\mu = \mu_o(T/T_o)^m(1+(\mu_o E/v_s)^\beta)^{-1/\beta}, \quad (1)$$

where

$$\mu_o = \mu_{min}+(\mu_{max}+\mu_{min})(1+(N_T/N_{ref})^k)^{-1} \quad (2)$$

$$N_T = 0.34(N_A+N_D)+0.66(p+n). \quad (3)$$

Here T is the absolute temperature, E the absolute value of the electric field and $v_s$ the saturation velocity and $T_o$=300K. Further, $N_A$, $N_D$, p and n are the acceptor, donor, hole and electron concentrations. The other parameters in Eqs. (1)...(3) depend on the material and are given in Table I. In our case the diffusion constants are related to the mobilities with the Einstein relation.

In the generation and recombination model we include the Shockley Read Hall, Auger and impact ionization mechanisms. Thus

$$R = R_{SHR} + R_{AU} + R_{II}, \quad (4)$$

where

$$R_{SHR} = (pn-n_i^2)/(\tau_p(n+n_i)+\tau_n(p+n_i)) \quad (5)$$

$$R_{AU} = (pC_p+nC_n)(pn-n_i^2) \quad (6)$$

$$R_{II} = (\alpha_p J_p+\alpha_n J_n)/e. \quad (7)$$

e is the elementary charge and $J_n$ ($J_p$) is the absolute value the electron (hole) current. Moreover

$$\alpha_{n,p} = A_{n,p}\exp(-E_{n,p}/E). \quad (8)$$

Finally, the temperature dependence of the intrinsic carrier density is modeled with the expression

$$n_i(T) = n_i(T_o)(T/T_o)^{3/2}\exp(-E_g/2k_BT+E_g/2k_BT_o), \quad (9)$$

where $k_B$ is the Boltzmann constant and $E_g$ the forbidden energy gap. The analytical form of the model functions and the values of the model parameters depend on the reference used. Of course, here the user has to make a trade off between the simplicity and the limits of the validity of the model.

| TABLE I | | silicon | diamond |
|---|---|---|---|
| $\mu_{max,n}$ | ($cm^2/Vs$) | 1360 | 2000 |
| $\mu_{max,p}$ | ($cm^2/Vs$) | 495 | 1800 |
| $\mu_{min,n}$ | ($cm^2/Vs$) | 92 | 250 |
| $\mu_{min,p}$ | ($cm^2/Vs$) | 48 | 200 |
| $N_{ref,n}$ | ($cm^{-3}$) | $1.3*10^{17}$ | like Si |
| $N_{ref,p}$ | ($cm^{-3}$) | $1.7*10^{17}$ | like Si |
| $v_{s,n}$ | (cm/s) | $10^7$ | $2.7*10^7$ |
| $v_{s,p}$ | (cm/s) | $8*10^6$ | $2.5*10^7$ |
| $\beta_n$ | | 1.18 | like Si |
| $\beta_p$ | | 1.21 | like Si |
| m | | 2.42 | 2.5 |
| $k_n$ | | 0.91 | like Si |
| $k_p$ | | 0.76 | like Si |
| $\varepsilon_r$ | | 11.8 | 5.5 |
| $\tau_n$ | (s) | $4*10^{-5}$ | $10^{-9}$ |
| $\tau_p$ | (s) | $2*10^{-5}$ | $10^{-9}$ |
| $C_p$ | ($cm^6/s$) | $10^{-31}$ | like Si |
| $C_n$ | ($cm^6/s$) | $7*10^{-32}$ | like Si |
| $A_n$ | (1/cm) | $10^6$ | $10^6$ |
| $A_p$ | (1/cm) | $1.5*10^6$ | $10^6$ |
| $E_n$ | (V/cm) | $1.4*10^6$ | $5.7*10^7$ |
| $E_p$ | (V/cm) | $1.8*10^6$ | $5*10^7$ |
| $n_i(T_o)$ | ($cm^{-3}$) | $1.4*10^{10}$ | $10^{-22}$ |
| $E_g$ | (eV) | 1.12 | 5.45 |

In our case the models are relatively general and can express most of the usual physical depences. One missing

thing is the doping dependence of SHR-recombination parameters, which is usually taken into account.

Table I lists the parameters of Eqs. (1)...(9) for silicon and diamond. As is clear from Table I, all the parameters for diamond are not available from the literature, and in these cases we have to rely on the structural similarity of silicon and diamond. As to the SHR parameters the values of $\tau_n$ and $\tau_p$ are exceptionally small for diamond. In diamond the forbidden energy gap between the conduction and valence bands is indirect (9), and, thus it should be possible to achieve values, which are closer to those of silicon. In principle the model functions describe very complicated physical phenomena, and it is no wonder, that commonly accepted parameter values exist only for the very extensively studied materials such as silicon.

## RESULTS AND DISCUSSION

The simulations were carried out on the silicon and diamond pin structures at the temperatures from 300 K up to 900 K. For simplicity the structures were taken to be strictly one dimensional. The length of the structure was chosen to be 45 μm, but a few results were also calculated for a diamond diode with the length of 4.5 μm. Further, the donor concentration in the lightly doped central region is $10^{14}$ $cm^{-3}$. So, in our case the lightly doped region is n-type also in diamond, although in practise the diamond films tend to be p-type. With these dimensions and dopings the breakdown voltage of the silicon diode should in the ideal case be around 800 V...900 V, and, thus, with the long SHR recombination time (20 μs) it would represent e.g. a power rectifier diode. The doping profiles of the heavily doped n- and p-type contact regions were first calculated using the Monte Carlo simulator TRIM, which can estimate the ion implantation profiles of the dopant atoms in several substrates. We have boron and phosphorus as the dopants. These profiles were then fitted to the gaussian functions and put in SCORPIO. Since the diffusion of the impurity atoms were not considered, the depths of the two contact regions remain approximately at 350 nm and the maximum concentration is roughly $10^{19}$ $cm^{-3}$ in both contacts.

The calculated breakdown voltage in the 45 μm silicon diode is 800 V, and this value is in good agreement with

the text book rules of thumb for the breakdown calculations. The corresponding value in the 45 μm diamond diode is 14100 V, and thus the value for diamond is 17.6 times higher than the value in silicon. In our case the breakdown voltages remain independent of the temperature, because no temperature effects were included in Eq. (8), and most of the breakdown calculations were for simplicity made using the avalanche integral (8,10). At 300 K the agreement of the avalanche integral with the sudden increase of the reverse current at the breakdown voltage was confirmed, only. In fact the breakdown voltage should increase with increasing temperature (10), and thus the room temperature value is the worst case estimate in the power applications.

In the planar silicon technology the breakdown voltages of the devices is often controlled with the diffused field rings (8). Typically, the deeper the diffusion the easier is the field ring design, whereas the blocking of high voltages with shallow diffusions may propose a very demanding design problem. Thus it may partly depend on the diffusion properties of the electrically active impurity atoms, whether the material advantage in the electric breakdown offered by diamond can be fully utilized in the real devices.

Fig.1 shows the reverse current densities as a functions of the reverse voltage in the 45 μm silicon and diamond diodes at several temperatures. At 700 K and 900 K the leakege currents in the Si diodes are very high. Further, the minor dependence on the applied voltage at high temperatures indicates the dominant role of the diffusion current over the generation current in Si (11). Usually in the silicon power devices the leakage currents are considered to be at the acceptably low level at 150 C (423 K). From Fig.1 it is seen, that the leakage current in the diamond diode at 900 K is the same as the leakage current in the Si diode at 400 K. This gives a hint, that as far as the leakage is considered the diamond devices may be a working solution even at 900 K. One should note, that in Fig.1 the recombination lifetime for diamond (1 ns) is much shorter than that in Si (20 μs). Were we comparing the devices with the equal lifetimes, the advantage of diamond would be even clearer.

In Fig.2 we have the forward current densities for the same structures and temperatures as in Fig.1. The curves for silicon show the normal temperature dependence of the leakage current and the saturation of the forward current, when the applied forward voltage becomes

comparable with the energy gap (10). This is quite similar to the situation in the signal diodes, although the temperature dependence in the pin structres is a bit more complicated. In the diamond diode the curves show qualitatively similar behaviour as in silicon, but the forward current capability remains much smaller than in Si. This is due to the large band gap and short recombination time or diffusion length of diamond. These facts are further illustrated in Fig.3, where we have the electron concentrations in the silicon and diamond diodes at 300 K and at equal current densities. In both cases the electron concentration is high in the n-type contact region near the origin and vanishes in the p-type anode on the right. The Si device is in the high injection mode and the excess carrier density is practically flat throughout the structure. On the other hand in the diamond diode slight modulation over the background density is seen near the $pn^-$ juntion, only. However, if the recombination lifetime is increased from 1 ns to 100 ns, the diamond diode operates in the high injection, too. This is shown in the uppermost curve in Fig.3. Fig.4 indicates, that the increase in the recombination time significantly increases the forward current density and the comparison with Fig.2 gives a preliminary result, that the diamond diode is capable of operating at higher current densities than the Si diode. However, the large bandgap of diamond still leads to the higher on state voltage. In Fig.5 the diamond diode is also capable of the higher current operation, when we are comparing the devices, which are almost in the same voltage class.

## REFERENCES


(1) K. Shenai et al, IEEE EDL-10,101(1989)
(2) R.F. Davies et al, Mat. Sci. & Eng.,B1,77(1988)
(3) K. Shenai et al, IEEE ED-36,1811(1989)
(4) K. Shenai, IEEE EDL-11,520(1990)
(5) B.J. Baliga, IEEE EDL-10,455(1989)
(6) K. Grahn, to be published
(7) S. Selberher: Analysis and Simulation of Semiconductor Devices. Springer-Verlag,1984
(8) B.J. Baliga: Modern Power Devices. John Wiley & Sons,1987
(9) V.K. Bazhenov et al, Sov. Phys. Semic. 19,829(1985)
(10) S.M. Sze: Physics of Semiconductor Devices. John Wiley & Sons,1981
(11) A.S. Grove: Physics and Technology of Semiconductor Devices. John Wiley & Sons,1967

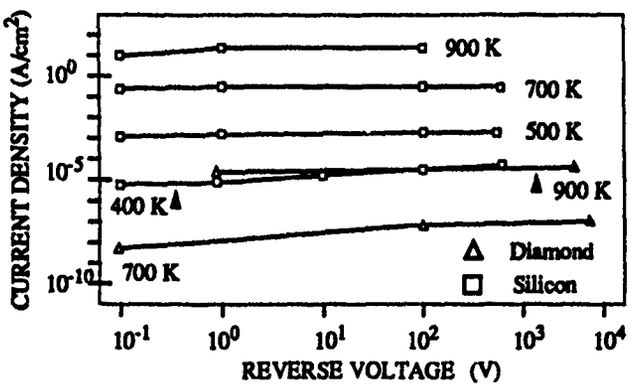



Fig.1. Reverse current densities in diamond and silicon $p^+n^-n^+$-diodes at various temperatures. The lifetimes of holes in the n-region are 1 ns and 20 μs in diamond and silicon, respectively.

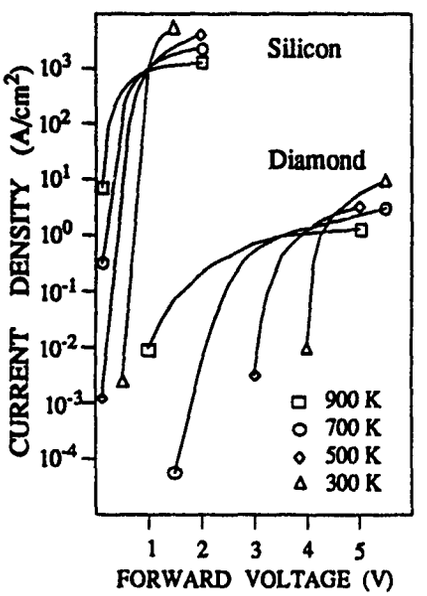



Fig.2. Forward current densities in the diamond and silicon $p^+n^-n^+$-diodes at various temperatures.

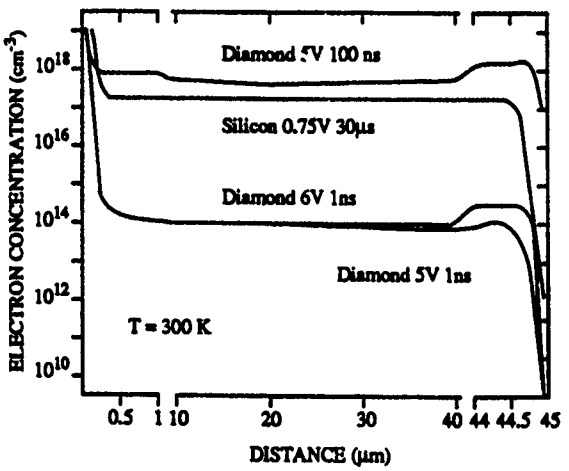



Fig.3.
Electron concentrations in diamond and silicon $p^+n^-n^+$-diodes at T=300 K and at equal current densities. In the calculation of the uppermost curve for diamond the minority carrier lifetime was increased from 1 ns to 100 ns.

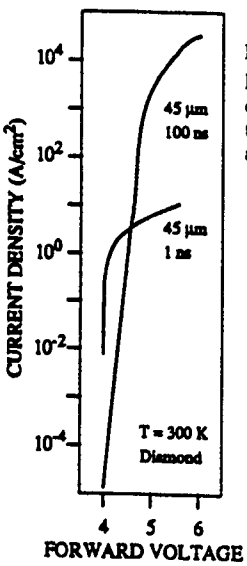
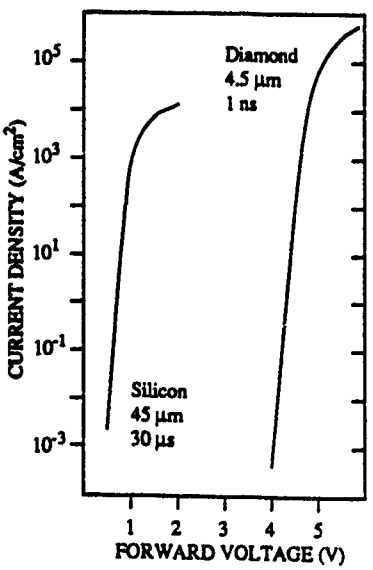



Fig.4.
Forward current densities in the diamond diode at T = 300 K for the recombination lifetimes 1 ns and 100 ns.

Fig.5.
Forward current densities in diamond and silicon diodes having breakdown voltages of 1900 V and 800 V, respectively. Notice that the active region of the diamond diode has been reduced to 4.5 μm.



# DIAMOND COLD CATHODES

M. W. Geis, N. N. Efremow, J. D. Woodhouse, and M. D. McAleese

Lincoln Laboratory, Massachusetts Institute of Technology

Lexington, Massachusetts 02173-9108

Robust, high-current-density (> 1000 A $cm^{-2}$) cathodes would have wide applications if such devices could be made. Most cathodes are composed of very reactive materials that cannot withstand exposure to air or water. However, there is a class of wide-bandgap (> 5 eV) materials, including NaCl, MgO, $SiO_2$, and diamond, that have their conduction band within 1 eV of the vacuum energy level, even in the presence of $O_2$ and $H_2O$. Most of these materials are insulators because of low charge-carrier concentrations, low mobilities, and high trap densities, and they are therefore unacceptable for high current density cathodes. However, diamond can be doped either n- or p-type and grown with sufficient quality to have low trap densities and high carrier mobilities, making it a semiconductor instead of an insulator. Here, we report on diamond cold cathodes, which we believe are the result of diamond's negative electron affinity.[1]

The diamond cold cathodes are produced by forming diodes in p-type, semiconducting diamond using carbon ion implantation into heated (320°C) substrates, as described by Prins.[2] After implantation, the substrates are coated with 1 μm of electron-beam-evaporated Al, which is patterned into 60 × 60-μm squares on 100-μm centers using standard photolithography. The substrates are then etched to a depth of 1.1 μm with ion-beam-assisted etching. The Al squares are used as a mask to form mesa structures consisting of Al, carbon-implanted diamond, and substrate, as shown in Fig. 1.

Emitted current densities as high as 10 A $cm^{-2}$ with emission efficiencies (emitted current divided by diode current) of > $10^{-5}$ were easily obtained when passing current

through these diodes. Figures 2 and 3 show the anode current as a function of anode voltage and as a function of diode current, respectively. The cathodes are not affected by cleaning in an oxygen plasma, water, or acetone. The presence of oxygen in the vacuum chamber at a pressure of ~ $10^{-2}$ Torr was found to increase the emission efficiency during cathode operation, as shown in Fig. 4, but hydrogen had little effect at the same pressure.

These are the most robust cold cathodes reported to date. Although the emission efficiencies are low, they are the highest for any non-cesium-coated cathode,[3] and with different geometries both current density and emission efficiency are expected to increase.

Acknowledgment

This work was supported by SDIO/OST through the Office of Naval Research.

References

1. M.W. Geis, N.W. Efremow, J.D. Woodhouse, M.D. McAleese, M. Marchywka, D.G. Socker, and J.F. Hochedez, to be published in *IEEE Electron Device Lett.*
2. J. F. Prins, *Appl. Phys. Lett.* **15**, 950 (1982).
3. J. Y. Ea, B. Lalevic, D. Zhu, Y. Lu, and R. J. Zeto, *IEEE Electron Device Lett.* **11**, 403 (1990).

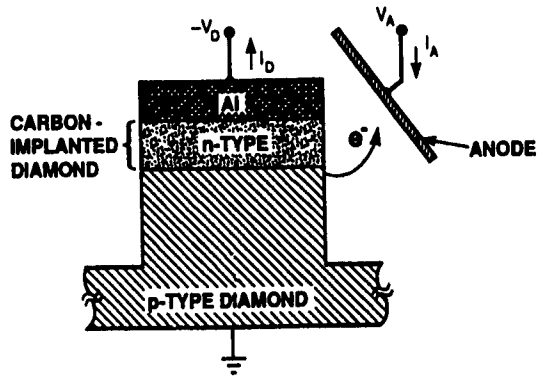



Fig. 1 Schematic drawing of a diamond cold cathode. The diode current ($I_D$) was varied from 0.1 to 10 mA with a bias voltage ($V_D$) of -60 to -150 V. The anode voltage ($V_A$) was usually 100 V, and the anode current ($I_A$) varied from $1 \times 10^{-13}$ to $5 \times 10^{-7}$ A.

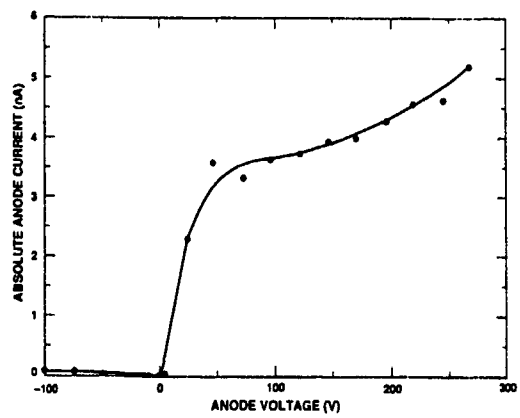



Fig. 2 Anode current ($I_A$) as a function of anode voltage ($V_A$) for a diode current ($I_D$) of 1 mA.

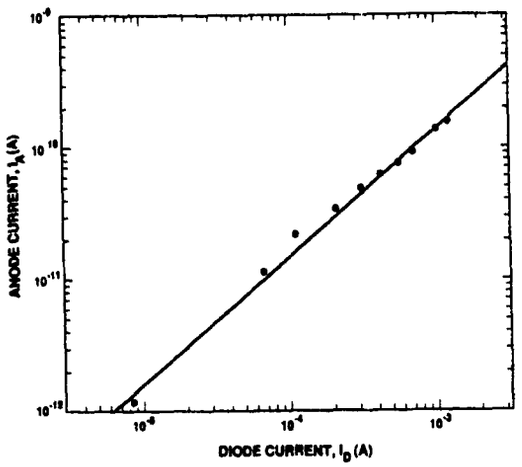



Fig. 3 Anode current ($I_A$) as a function of diode current ($I_D$) for an anode voltage ($V_A$) of 100 V.

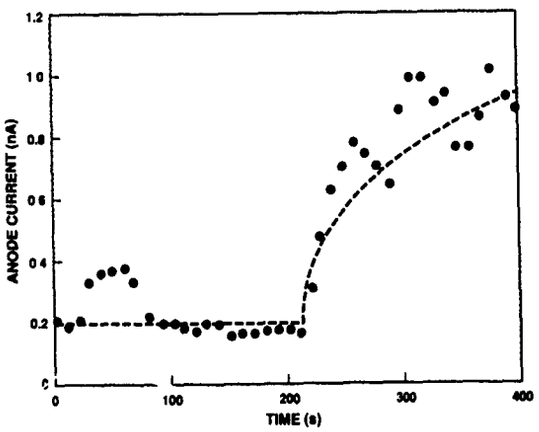



Fig. 4 Anode current ($I_A$) as a function of time for diode current $I_D$ = 10 mA. At 200 s the pressure in the vacuum probing system was changed from $10^{-5}$ to $10^{-2}$ Torr of $O_2$.

# METAL-INSULATOR-SEMICONDUCTOR DIODES USING POLYCRYSTALLINE DIAMOND THIN FILMS

K. Miyata[a,b], D.L. Dreifus[a], K. Das[a], J.T. Glass[b], and K. Kobashi[c]

[a]Electronic Materials Center, Kobe Steel Research Laboratories, USA, 79 TW Alexander Drive, Research Triangle Park, NC 27709
[b]Materials Science and Engineering Department, North Carolina State University, Raleigh, NC 27695
[c]Electronics Research Laboratory, Kobe Steel, Ltd., 1-5-5, Takatsuka-dai, Nishi-ku, Kobe, 673-02, Japan.

## ABSTRACT

The electrical characteristics of an Al/undoped/B-doped polycrystalline diamond structure have been investigated. B-doped diamond films containing various B to C ratios were deposited on (111) oriented B-doped Si substrates by a microwave plasma chemical vapor deposition. For gas phase B to C ratios of 40 ppm and below, the resistance of the B-doped diamond films increased from 2 to 7 orders of magnitude after an annealing treatment at 525 °C. Such a large change in a resistance after an annealing treatment has been attributed to the dissociation of hydrogen from diamond films. Undoped diamond layers were deposited for 60 min in a second growth chamber. The existence of a bilayer structure was confirmed by secondary ion mass spectroscopy. For the film with a gas phase B to C ratio of 400 ppm, significant improvements in the rectifying characteristics could be obtained with the insertion of an undoped diamond layer.

## INTRODUCTION

Diamond has a number of attractive characteristics including mechanical strength, high thermal conductivity, optical transparency, and various electrical properties(1). With regard to electronic applications, diamond is expected to be suitable for electronic devices to be operated under hostile conditions such as high temperature and high radiation, or at high frequencies. This is due to its wide bandgap(5.5 eV), high breakdown voltage($10^6$-$10^7$ V/cm), and low dielectric constant($\varepsilon_s$=5.68). There has been an increased interest in using diamond for electronic devices since the success in producing diamond thin films by a Chemical Vapor Deposition (CVD) technique(2). Recently, several groups have reported active devices such as a Field Effect Transistors(FET) fabricated from homoepitaxial diamond films(3,4). However, in the case of homoepitaxial diamond films, a single crystal diamond substrate is required, and the active device area is limited to less than a square centimeter due to its cost and size. Despite recent successes in heteroepitaxial growth of diamond films on c-BN and single crystal Ni substrates, more efforts will still be required to use these systems for the fabrication of electronic devices(5,6). On the other hand, it is possible to deposit polycrystalline diamond films on large areas, such as a 4" Si substrate, by using a microwave plasma CVD method(7). The

possibility of using polycrystalline diamond films for electronic devices should be investigated along with improving the overall crystal quality and examining critical issues such as carrier scattering at grain boundaries and surface roughness. Here, the improvement of rectifying characteristics using an Al/undoped/B-doped polycrystalline diamond metal-insulator-semiconductor (MIS) structure is reported and the thermal instability of the polycrystalline B-doped diamond films is also discussed.

## EXPERIMENTAL

A schematic diagram of the Al/undoped diamond/B-doped diamond structure is shown in Fig. 1. P-type (111)-oriented B-doped Si substrates with a resistivity of less than 1 Ω·cm were used. Prior to deposition, 20mm x 10mm substrates were polished with 0.25 μm diamond paste for 1 hour in order to increase the diamond nucleation density. A microwave plasma CVD system, similar to that described in Ref. (8), was used for the preparation of B-doped and undoped diamond films. The arrangement of the reactor used in this work differs in that a vertical configuration was employed rather than the horizontal chamber described in Ref (8). At first, several B-doped diamond films with different B to C(B/C) ratios in gas phase were deposited on the Si substrates using $CH_4$, diluted in $H_2$ to 0.5% as a source gas, and $B_2H_6$ as the dopant gas. During deposition, the total gas pressure and substrate temperature were maintained at 35 Torr and 800 °C, respectively. B-doped diamond films were deposited for 7 hr and the film thickness obtained was approximately 1.0 -1.1 μm. The B/C ratios in the reaction gas were 4, 20, 40, 200, and 400 ppm. After preparation, the samples were diced into 5mm x 5mm sections, and then cleaned in $H_2SO_4$ at 80 °C for 10 min, followed by a standard RCA cleaning technique(9). After the RCA cleaning, samples were dehydrated on a hot plate at 120 °C for 5 min. The atomic B concentrations of these films were determined by Secondary Ion Mass Spectroscopy(SIMS). Oxygen ions(15 keV) were used as primary ions and $B^+$ ions were detected. A B-implanted(150 keV, $1x10^{15}$ $cm^{-2}$) type Ia single crystal diamond standard was used to calibrate the atomic B concentration. Also, resistance as a function of temperature(25 °C-525 °C) was investigated using a point probe method. Undoped diamond layers were deposited for 60 min on B-doped diamond films in a second growth chamber in the absence of $B_2H_6$. Other than the preparation time and the addition of 0.1% oxygen to the reaction gas, the growth conditions of undoped diamond layers were the same as those of B-doped diamond layers. As will be reported elsewhere, the introduction of oxygen in the gas phase dramatically reduces the B incorporation in the grown film. The undoped layer was grown in the presence of $O_2$ to minimize auto-doping effects. Aluminium, 2000 Å-thick, was deposited on the diamond films using an electron beam evaporation technique. During evaporation, the chamber pressure was maintained below $5x10^{-7}$ Torr. Circular dots with 100 μm diameters were patterned photolithographically on the Al and this mask was then used to etch the unwanted metal by using an Al etchant solution. Ohmic contacts were formed on the back side of the Si substrate using silver paste.

## RESULTS & DISCUSSIONS

The depth profile of the atomic B concentration for the films with various B/C ratios is shown in Fig. 2. Note that the atomic B concentration is quite uniform with

respect to depth, and increases with increasing B/C ratio. The variations in the atomic B concentration at a depth of 1 μm are due to the interface between the diamond film and Si substrate. The resistance vs. temperature characteristics of B-doped diamond films were measured by using tungsten point probes and a hot stage in air. A series of temperature cycling was investigated, and the resistance vs. reciprocal temperature characteristics of a B-doped diamond film with a B/C ratio of 4 ppm is plotted in Fig. 3. In general, the samples were maintained at the measured temperature for 5 min prior to the resistance measurements. At first, the resistance of this film was measured during heating to a maximum temperature, 250 °C, and subsequently cooling to room temperature. The resistance of the film increased by an order of magnitude due to this heat treatment at 250 °C. Subsequently, the sample was heated to 350 °C, and then cooled down to room temperature. At this time, the resistance of this film increased by 5 orders of magnitude as compared to that of the as-grown film. However, the resistance of this film decreased by more than 3 orders of magnitude after this film was kept at room temperature for 12 hours. It is not clear what mechanism caused this decrease in resistivity, but this phenomenon has been reported previously by Totterdell et al(10). Finally the same measurements were performed with heating to a maximum temperature of 525 °C. As a result, the resistance increased by at least 6 orders of magnitude as compared to that of the as-grown film, and remained constant over time. This indicates that the resistance of B-doped diamond films can be stabilized by a heat treatment at 525 °C. It should be noted that the downturn of the plotted resistance in Fig. 3 for the cool down cycle is an artifact and is due to an instrument limitation of $5x10^{13}$ Ω. The calculated activation energy, $E_A$, of the heat-treated film was in excess of 1.0 eV. This indicates that the conductivity of the diamond film is due to defects or other impurities, since the activation energy that has been reported for lightly B-doped diamond is approximately 0.37 eV(1). The atomic B concentration of the same film was determined to be $5x10^{17}$ $cm^{-3}$ by SIMS. In comparison to a 525 °C-annealed undoped diamond film, however, this film was equally as resistive and exhibited a similar activation energy. The resistance before and after heat treatment at 525 °C vs. B/C ratio is summarized in Fig. 4. For B/C ratios of 200 ppm and above, a heat treatment does not change the resistance of the B-doped diamond films. On the other hand, for B/C ratios of 40 ppm and below, the resistance increased by 2 to 6 orders of magnitude after a heat treatment at 525 °C. In summary, the resistance of B-doped diamond films, as deposited, were thermally stable for B/C ratios of 200 ppm and above, corresponding to an atomic B concentration of $3\text{-}4x10^{18}$ $cm^{-3}$ as determined by SIMS.

Several researchers have already reported the drastic increase in resistivity after a heat treatment in the case of CVD undoped diamond films and lightly B-doped diamond films(11-15). According to their explanations(12), an anneal treatment causes the evolution of hydrogen from diamond films, and as a result, defects, which had been passivated by hydrogen, are reactivated and carriers are trapped by these defects. If it is possible to apply these explanations to the results, the following speculation is possible. Since the defect density after a heat treatment at 525 °C is larger than or equal to the carrier concentration due to B for B/C ratios of 40 ppm and below, the carrier concentration, and thus the conductivity, dramatically decreases due to compensating defects. For B/C ratios of 200 ppm and above, the compensating trap density is below the carrier density resulting from the B impurities. Thus, the resistance remains constant irrespective of a heat treatment. According to the SIMS results, the atomic B concentration of the films with a B/C ratio of 200 ppm is less than twice that of the film

with a B/C ratio of 40 ppm. Although the activation of B impurities may change in this regime, this variation cannot account for over two orders of magnitude increase in the resistance of the annealed sample. After heat treatment, the ionized carriers must exceed the trap density in order to contribute to the contribute to conductivity.

Thin, undoped diamond layers were deposited for 60 min on B-doped diamond films with a B/C ratio of 400 ppm in a second growth chamber. In order to confirm a bilayer structure in terms of atomic B concentration, SIMS measurements were performed. The atomic B concentration depth profile of this bilayer structure is shown in Fig. 5. Note that there is an approximately 2500 Å-thick undoped diamond surface layer with an atomic B concentration less than $10^{17}$ $cm^{-3}$. As a result, the atomic B concentration of the undoped diamond layer is more than 2 orders of magnitude less than that of the underlying B-doped diamond film.

To obtain current-voltage (I-V) characteristics of the MIS structure, a Hewlett Packard Co. 4145B Semiconductor Parameter Analyser was used. Typical I-V characteristics of an Al Metal/Semiconductor (MS) contact and a MIS contact are shown in Fig. 6. Both measurements were performed prior to any anneal treatment. Poor rectification was observed for the MS structure without an undoped diamond layer. The rectification ratio ($I_f/I_r$) at 5 V was around 3. However, the rectifying characteristic was dramatically improved with the addition of the undoped diamond layer between the metal electrode and B-doped diamond films. The reverse leakage current at 5 V was several micro-amperes, and the rectification ratio at 5 V was more than $10^3$. This result obtained here is similar to that observed for the case of homoepitaxial diamond films(3).

Reverse leakage current decreased and the breakdown voltage increased with the addition of an undoped diamond layer between the Al metal electrode and the B-doped diamond films. The barrier height of a Schottky diode, $\phi_{BP}$, is generally determined by the metal work function, $\phi_m$, the semiconductor electron affinity, $\chi_s$, and the semiconductor bandgap, $E_g$, in the case of p-type semiconductor(assuming an unpinned Fermi level at the surface). Thus, theoretically the same barrier height, $\phi_{BP}$, exists irrespective of doping concentration. However, the depletion layer is very thin in the case of heavily B-doped films, since the thickness of the depletion layer is proportional to the inverse square root of the carrier concentration. As a result, in the case of an MS structure, carriers can easily tunnel through the thin depletion layer. Alternatively, the current transport mechanism is dominated by field emission theory, so that a clear rectification could not be observed. However, the tunneling current through the thin depletion layer could be reduced by including the undoped diamond layer between the metal contact and the B-doped diamond. As a result, rectifying characteristics could be obtained. It is important to note that rectifying characteristics could be obtained by adopting this MIS structure, despite an atomic B concentration of $10^{19}$ $cm^{-3}$ in the B-doped diamond film.

## CONCLUSIONS

The increase in resistance of B-doped diamond films due to a heat treatment was systematically investigated. For B/C ratios of 200 ppm and above, there was little change in the resistance regardless of the heat treatment. However, for B/C ratios of 40 ppm and below, the resistance of the B-doped diamond films drastically increased after the heat

treatment at 525 °C. The lower the atomic B concentration, the larger the increase in the resistance after the heat treatment. It is speculated that these phenomena have an intimate relation with the dissociation of hydrogen from the film and the compensation of carriers by electrically activated defects. The electrical characteristics of an Al/undoped diamond/B-doped diamond (MIS) structure using polycrystalline diamond films have also been investigated for the film with a B/C ratio of 400 ppm. The existence of a bilayer structure was confirmed by SIMS. Poor rectification was observed for the MS structure sample, while rectifying characteristics could be dramatically improved in the presence of the undoped diamond layer.

## ACKNOWLEDGEMENTS

The authors would like to thank Dr. D. Griffis for SIMS measurements and analyses, and Mr. J. Bade, Ms. M. Hartsell, Mr. J. Tassitino, and Mr. S. Sahaida for their technical support. This research was partially supported by the NEDO International Joint Research Program.

## REFERENCES

(1) J.E. Field, *Properties of Diamond* (Academic, London, 1979).
(2) S. Matsumoto, Y. Sato, M. Kamo, and N. Setaka, Jpn. J. Appl. Phys. **21**, L183 (1982).
(3) H. Shiomi, Y. Nishibayashi, and N. Fujimori, presented at the 2nd Intl. Conf. on the New Diamond Sci. & Tech., Washington D.C., Sept 23-27, 1990.
(4) G.Sh. Gildenblat, S.A. Grot, C.H. Hatfield, A.R. Badzian, IEEE Electron Dev. Lett., 12, 37 (1991).
(5) S. Koizumi, T. Murakami, and T. Inuzuka, Appl. Phys. Lett. **57** (6) 563 (1990).
(6) M. Kamo, and Y. Sato, Extended abstract of Japan New Diamond Symposium, January (1991)(in Japanese).
(7) M. Kamo, F. Takamura, and Y. Sato, Extended abstract of The 1st Intl.Conf. on the New Diamond Sci. & Tech. Tokyo, Oct. 24-26, 1988.
(8) K. Kobashi, K. Nishimura, Y. Kawate, and T. Horiuchi, Phys. Rev. **B**, Vol.38, No.6, 4067 (1988).
(9) W. Kern, and D.A. Puotinen, RCA Rev. **31**, 187 (1970).
(10) D.H.J. Totterdell, R.E. Harper, and N.G. Blamires, Report on the 2nd Meeting of the NEDO International Research Project on Diamond Films(not published).
(11) M.I. Landstrass, and K.V Ravi, Appl. Phys. Lett. 55(10), 975 (1989).
(12) M.I. Landstrass, and K.V. Ravi, Appl. Phys. Lett. 55(14), 1391 (1989).
(13) R.E. Harper, C. Johnston, N.G. Blamires, P.R. Chalker, and I.M. Buckley-Golder, The 1st European Conf. on Diamond and Diamond-like Carbon Coatings, Crans-Montana, Switzerland, September 17-19 (1990) (to be published).
(14) S. Albin, and L. Watkins, IEEE Electron Dev. Lett., Vol. 11, No. 4, 159 (1990).
(15) Y. Muto, T. Sugino, J. Shirafuji, and K. Kobashi, submitted for publication: Appl. Phys. Lett.

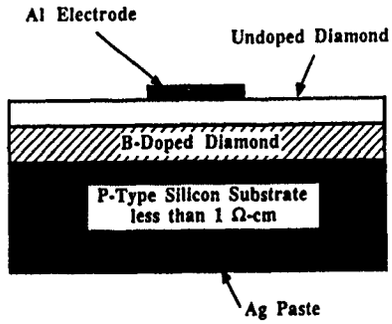



Figure 1. Cross-sectional schematic diagram of an Al/undoped diamond/B-doped diamond Metal-Insulator-Semiconductor structure.

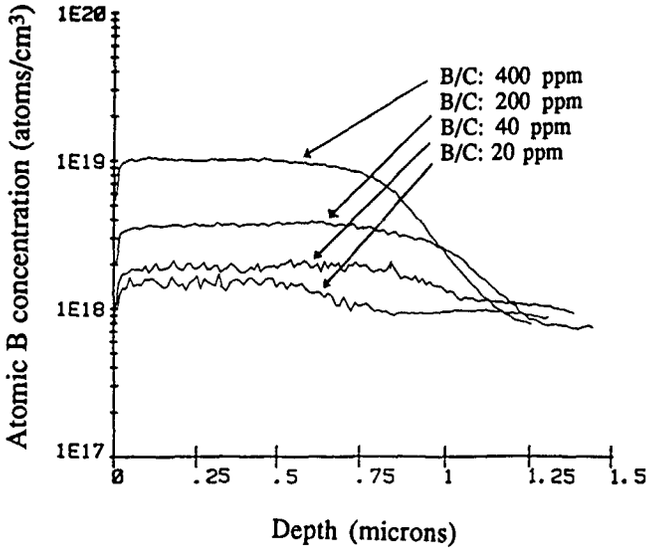



Figure 2. Atomic B concentration vs. Depth as determined by Secondary Ion Mass Spectroscopy. Note the increasing B-concetration with respect to the B to C ratio in the reaction gas.

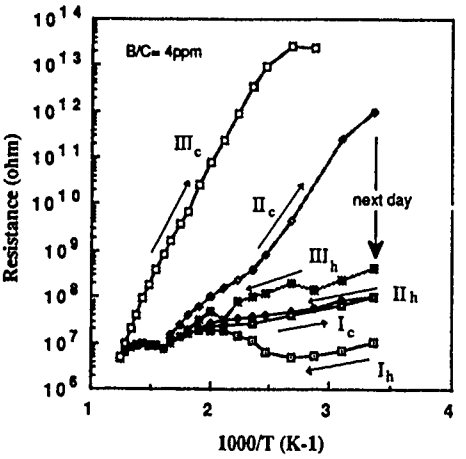



Figure 3. Resistance vs. Temperature of B-doped diamond films with a gas phase B to C ratio of 4 ppm for three temperature cycles.
I) 25 °C → 250 °C → 25 °C,
II) 25 °C → 350 °C → 25 °C, and
III) 25 °C → 525 °C → 25 °C.

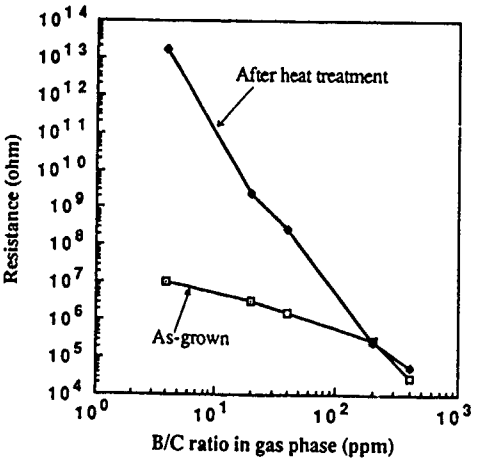



Figure 4. Resistance vs. B to C ratio in the reaction gas for B-doped diamond films. Note that the pre- and postanneal measured resistances for B to C of 200 ppm and above are the same, indicating a thermally stable film.

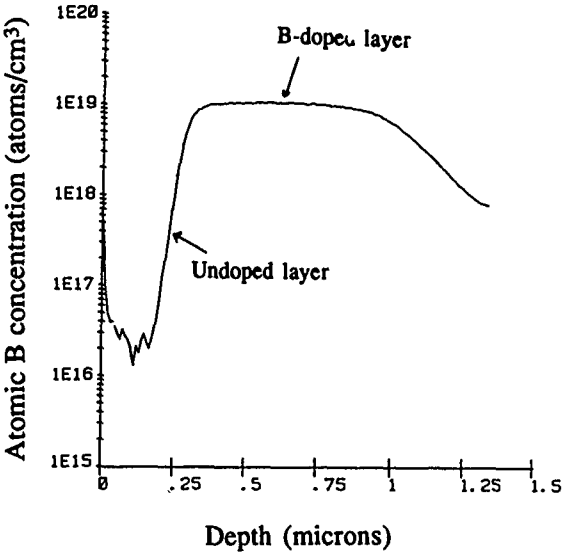



Figure 5. Secondary Ion Mass Spectroscopy depth profile of the atomic B concentration for an undoped diamond/B-doped diamond bilayer structure film.

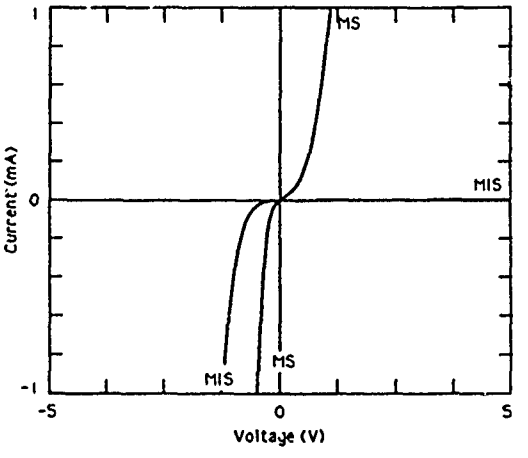



Figure 6. Current-voltage characteristics of a) Metal-Semiconductor (MS), and b) Metal-Insulator-Semiconductor (MIS) structure. In both cases, the B-doped diamond film had an atomic B concentration of $1 \times 10^{19}$ cm$^{-3}$.

# RELIABILITY OF OHMIC CONTACTS TO DIAMOND

M. Roser*, C.A. Hewett*, K.L. Moazed*** and J.R. Zeidler**
** Code 555 and * Code 7601,
Naval Ocean Systems Center, San Diego, CA 92152-5000
***Department of Materials Science and Engineering,
North Carolina State University, Raleigh, NC 27695-7916

## ABSTRACT

Several metallizations have been demonstrated to produce ohmic contacts to semiconducting diamond through a solid state reaction process. This process is compatible with existing micro-electronic techniques and produces adherent contacts exhibiting low contact resistance. Investigated here is the long-term reliability of these refractory metal-diamond contacts at the elevated temperatures for which diamond devices are intended. Measurements of resistance as a function of time with Mo/Au contacts on a Type IIb diamond crystal are presented for temperatures in the range 450 to 625 °C with isothermal annealing times of greater than 130 hours in a purified inert ambient.

## INTRODUCTION

There is an established need for electronic devices that operate reliably at temperatures ranging from 400 to 600 °C. Sensors and control devices mounted on or in aircraft engines at temperatures from 500 to 600 °C for periods of up to 100 hours are needed for increased design feedback, and diminished testing and maintenance costs.(1) Electronics to be used in planetary-surface space probes must be able to operate at surface temperatures above 500 °C for extended periods of time.(2) The use of geothermal wells as an alternative energy source will require devices operating at extended time periods at temperatures in excess of 600 °C. These are temperatures far above those temperatures at which silicon and gallium arsenide cease to function as semiconductors, their intrinsic limits are 350 and 450 °C respectively. Devices based on these ubiquitous electronic materials are able to meet some high temperature needs only with the added presence of a cumbersome cooling apparatus. The added weight due to such cooling equipment accounts for over one half of the payload in current space-based vehicles, constituting a major expense at a launch rate of $6000/pound. The existence of devices intended for application in high temperature environments would not only meet existing needs, but also allow sensor or control access to areas not previously considered. Due primarily to the wide band gap (5.5 eV) and the unequaled thermal conductivity (20 $W/cm^2K$), diamond, with an intrinsic limit of 1100 °C, appears to be a device material well suited to meet these special device needs.(3) Included in proposed devices, many of which have been realized in the laboratory,(4-6) are rectifying diodes, Gunn diodes, LEDs, transistors, photodetectors and nuclear radiation sensors, and thermistors.(7) All aspects of the diamond device must meet the demands of the operating environment, but many of the critical device characteristics have not yet been demonstrated at high temperature.

A process utilizing conventional photolithographic techniques for forming low-resistance, strongly adherent ohmic contacts by metallization of diamond has previously

been developed(8-10) and successfully employed with natural bulk diamond(11) and synthetic diamond films.(12) This process includes the deposition of a carbide-forming metal on diamond followed by the deposition of a thin film of gold to protect the metal from corrosion. The refractory and quasi-refractory metals that have been demonstrated to form these ohmic contacts include molybdenum, titanium, and tantalum. The final and most critical step of the process is subjecting the metallized sample to a high temperature anneal in a purified-hydrogen ambient.

Extensive characterization of the ohmic contacts resulting from this solid-state reaction process was performed using Auger electron spectroscopy, secondary ion mass spectrometry, Rutherford backscattering spectrometry, scanning electron microscopy, X-ray diffraction, and optical metallography. It was determined that, during the annealing process, the refractory metal reacted with the diamond to produce a carbide precipitate by means of a nucleation-and-growth mechanism at the metal-diamond interface. The strong adherence and low resistance of these contacts are attributed directly to the carbide precipitates formed.(8)

This metallization process has produced ohmic contacts to diamond that fulfill four essential requirements for high temperature devices. The process is compatible with present micro-electronic processing techniques; the contacts are strongly adherent; they exhibit low specific contact resistance($10^{-5}$ $\Omega$-cm$^2$), and they operate at high temperatures.(12,13) Here we investigate the long-term reliability of these ohmic contacts in the high temperature interval, 450 to 625 °C.

## EXPERIMENTAL

The sample used was a <100> bulk, p-type semiconducting (Type-IIb) diamond in the shape of a square plate, 5 x 5 x 0.25 mm$^3$. The natural boron concentration is considered to be on the order of $10^{15}$/cm$^3$ and the room temperature carrier concentration on the order of $10^{13}$/cm$^3$ (14)

The polished sample was cleaned in a saturated solution of $Cr_2O_3$ in $H_2SO_4$ for 10 minutes at 160 °C followed by a de-ionized water rinse. This removes any graphitic layers that may be present.(11) This was followed by an acetone rinse and then a soak in boiling methanol for 4 minutes to remove any surface contaminants. Using plasma-assisted CVD, a 200 nm layer of silicon nitride was grown on the sample surface. Standard photolithographic techniques and a Shockley transmission-line-model (TLM) mask were used to pattern openings in the silicon nitride. A 10 nm layer of molybdenum followed by a 150 nm layer of gold was deposited on the sample in an ion-pumped, UHV evaporating chamber. Electron-beam heating was employed for the refractory metals and resistive heating was used for the gold. The pressure during the evaporation was $10^{-8}$ Torr, and the rates of deposition for Au and Mo as measured with a crystal monitor were 0.4 nm/s and 0.05 nm/s, respectively. The remaining photoresist and that part of the Mo/Au layer above it were subsequently etched away with acetone. A TLM pattern of rectangular 120 x 300 $\mu$m$^2$ Mo/Au mesas separated by $Si_3N_4$ remained on the diamond surface. The sample was then annealed in a purified hydrogen ambient at 950 °C for 6 minutes in order to form the carbide contact. The $Si_3N_4$ was left in place to prevent spreading of the Au during the anneal. The details of the entire process and a discussion of optimum annealing time can be found elsewhere.(8,9)

The sample was mounted in an organically cleaned alumina chip carrier and was held in place with a tungsten clip. Gold wires were wire bonded to Mo/Au contacts that were separated by distances of 10, 20 and 30 μm. The other ends of the leads were attached to gold-plated pad contacts on the chip carrier. The carrier was then mounted in the apparatus shown in Figure 1.

This apparatus was designed for variable-temperature, electrical-transport measurements of diamond samples. Strict control of the ambient in the measurement space is essential, not only to prevent oxidation of the metal in the apparatus, but also to prevent a transformation from diamond to graphite which happens in the presence of oxygen or water vapor at elevated temperatures. There is also mounting evidence that adsorbed gases have a significant effect on the measured electrical properties of diamond.(11,15-19) It is for these reasons that the sample was placed in a quartz chamber sealed at the cold end with a viton o-ring, and that the ambient inside the chamber was limited to purified argon gas. This gas was obtained by passing technical grade argon through a purifier system that employs hot titanium chips. This getter system removed non-inert contaminants before the argon entered the measuring space. The purity was monitored continously by a hygrometer situated in the outgoing gas line. Backflow into the system is prevented by a check valve in the outgoing gas line and a continual positive pressure as monitored by a mineral oil bubbler at the end of the line. These precautionary steps allowed the entire investigation to be performed with the ambient at a dew point of less than -115 °C (less than 0.3 PPB water weight in air).

The sealed quartz chamber provided an air-tight space and stability for high temperatures, and allowed for the radiative heating of the sample from the furnace coils. The heat was controlled by a Variac attached to the furnace coils, and the temperature inside the chamber was measured with a K-type thermocouple in a stainless steel sheath attached to the stainless steel support as shown in Figure 1. The long annealing times inherent in the experiment provide for adequate thermal equilibrium within the measurement apparatus. Without a feedback mechanism for the furnace coils, the temperature tended to slowly and randomly drift as much as 3% about a mean temperature during the extended measuring periods. The copper electrical leads were fed into the measuring space through an insulating ceramic rod which was sealed at the cold end. These leads were attached to the chip carrier leads using BeCu clips. The resistance between contacts was measured with a Keithley 617 electrometer and was continuously monitored with a chart recorder. The measuring chamber was shielded from light to eliminate photoconductive effects.

## RESULTS AND DISCUSSION

The resistance of the sample was continuously monitored for a period of nearly 36 days. The first data were recorded immediately after the sample was placed in the measurement apparatus and before the quartz chamber was purged. The chamber was then purged with the purified argon gas at room temperature for a period of 15 hours. This resulted in a vast increase in resistance, from 17.2 kΩ before the purge to 790 kΩ after.

The effects of exposure to hydrogen plasma on the electrical characteristics of natural Type IIa (17) and Type Ia and Type IIb (18) diamond crystals and on synthetic diamond films(16-19) have been the subject of many recent investigations. In those studies, it was demonstrated that this exposure severely decreases the measured resistance

of the diamond sample by as much as five to ten orders of magnitude. It has been suggested that this effect is due to hydrogen passivation of deep level traps, and that high temperature annealing effectively removes the hydrogen, causing activation of the traps and an accompanying rise in resistivity.(17,18) Using nuclear resonance reaction analysis to determine hydrogen depth profiles in diamond CVD films, Celii *et al*(19) have concluded that in diamond films, the majority of the hydrogen is not eliminated but is simply displaced to grain boundaries.

Hydrogenation occurs in CVD diamond films due to the hydrogen plasma utilized in the growth process,(16) but bulk diamond crystals are not routinely exposed to plasmas. The types of plasma used to hydrogenate the diamond samples in the above studies include rf, microwave, and dc plasmas at various temperatures and pressures, and for various exposure times. It has been suggested that hydrogenation is independent of plasma power and the hydrogen pressure, and it is limited only by the diffusion rate of hydrogen into diamond.(18) Where it was studied, the de-hydrogenation, or re-activation of the traps was accomplished with a high temperature anneal, resulting in the restoration of the high measured resistivity.

The IIb sample in this study was exposed to an rf plasma during the growth of the silicon nitride layer prior to metallization. The sample was positioned directly in an rf plasma created from $SiH_4$ (silane), and $NH_3$ for 25 min at 325 °C. This is consistent with the above hydrogenation methods, but the 950 °C anneal of the contacts in molecular hydrogen may have been another potential source of hydrogen.

The sample was heated over the course of 15 days to 500 °C where stability in the resistance was eventually observed. The electrical resistance at thermal annealing times in excess of 130 hours were measured at three temperatures, 500, 600 and 450 °C consecutively. The resistance between all lead pairs were measured, and all pairs exhibited qualitatively identical behavior. The electrical resistance at these three different temperatures as a function of time for the contacts separated by 50 μm is shown in Figure 2. Each solid line represents the mean resistance at a given temperature. The variation of the resistance about each mean temperature is due to the slow variation of the ambient temperature in the quartz chamber as described in the previous section. The resistance simply tracked with that temperature variation. It should also be noted that the maximum temperature investigated was a constraint imposed by the measurement apparatus and not by the sample or the contacts.

The sustained sensitivity of the contacts to electrical changes in the material can be seen in Figure 3 where both the resistance and temperature are plotted as a function of time for one temperature region, 600 °C. The resistance consistently maintains an inverse relationship with respect to temperature, as would be expected for semiconducting diamond, and it does so reproducibly. Focusing on one fixed temperature over the course of time, reveals differences in resistances of no more than 1% . It is clear from the resistance data that the contacts are stable against drift or degredation in the times and for the temperatures investigated.

## CONCLUSION

A previously developed metallization technique was used to form ohmic contacts to a Type IIb bulk diamond sample. The resistance between the contacts was measured during long thermal annealing times in excess of 130 hours at temperatures of 450, 500 and 600 °C. The Mo/Au contacts appeared to be stable and reliable at these high temperatures with no indication of deterioration or degradation of performance. Indications of hydrogen passivation were observed and a long thermal anneal was used before reported measurements were taken.

## ACKNOWLEDGEMENTS

We would like to acknowledge the assistance and support of our colleagues at NOSC, Dr. Carl Zeisse, Richard Nguyen, Dr. Don Mullin, and Dr. Howard Rast, and especially Marylin Taylor and Dr. Paul de la Houssaye. The authors gratefully acknowledge the support of SDIO/IST through Mr. Max Yoder of the Office of Naval Research.

## REFERENCES

1. W.C. Nieberding and J.A. Powell, Trans. on Ind. Electronics **IE-29**(2), 103(1982).
2. R.F. Jurgens, Trans. on Ind. Electronics **IE-29**(2), 107(1989).
3. K. Shenai, R.S. Scott, and B.J. Baliga, IEEE Trans. on Electron Dev. **36**(9), 1811(1989).
4. H. Shiomi, Y. Nishibayashi, and N. Fujimori, Jpn. J. Appl. Phys. **28**(12), 2153(1989).
5. M.W. Geis, D.D. Rathman, D.J. Ehrlich, E.A. Murphy and W.T. Lindley, IEEE Electron Dev. Lett. **8**(8), 341(1987).
6. G.SH. Gildenblat, S.A. Grot, C.R. Wronski, A.R. Badzian, T. Badzian, and R. Messier, Appl. Phys. Lett **53**(7), 586(1988).
7. V.K. Bazhenov, I.M. Vikulin, and A.G. Gontar, Sov. Phys. Semicond. **19**(8), 829(1985).
8. K.L. Moazed, J.R. Zeidler, and M.J. Taylor, J. Appl. Phys. **68**(5), 2246(1990).
9. K.L. Moazed, R. Nguyen, and J.R. Zeidler, IEEE Electron Dev. Lett. **9**(7), 350(1988).
10. K.L. Moazed, J.R. Zeidler, M.J. Taylor, and C.A. Hewett, to be published in Diamond and Diamond-Like Films and Coatings,(Plenum, New York, 1991).
11. P.R. de la Houssaye, C.M. Penchina, C.H. Hewett, R.G. Wilson, and J.R. Zeidler, to be published in Proc. Second International Conf. on New Diamond Science and Technology, (1990).
12. G.Sh. Gildenblat, S.A. Grot, C.W. Hatfield, A.R. Badzian, and T. Badzian, IEEE Electron Dev. Lett., 11(9), 371-372(1990).
13. C.A. Hewett, J.R. Zeidler, M.J. Taylor, C.R. Zeisse, and K.L. Moazed, to be published in Proc. Second International Conf. on New Diamond Science and Technology, (1990).
14. P.T. Wedepohl, Proc. Phys. Soc. **B70**, 177(1957).
15. S.A. Grot, G.SH. Gildenblat, C.W. Hatfield, C.R. Wronski, A.R. Badzian, T. Badzian, and R. Messier, IEEE Electron Dev. Lett. **11**(2), 100(1990).
16. M.I. Landstrass and K.V. Ravi, Appl. Phys. Lett **55**(10), 975(1990).

17. S. Albin and L. Watkins, IEEE Electron Dev. Lett. 11(4), 159(1990).
18. S. Albin and L. Watkins, Appl. Phys. Lett. 56, 1454(1990).
19. F.G. Celii, A.J. Purdes, B.E. Gnade, and D.L. Weathers, to be published in Proc. Second Intl. Conf. on New Diamond Science and Technology, (1990).

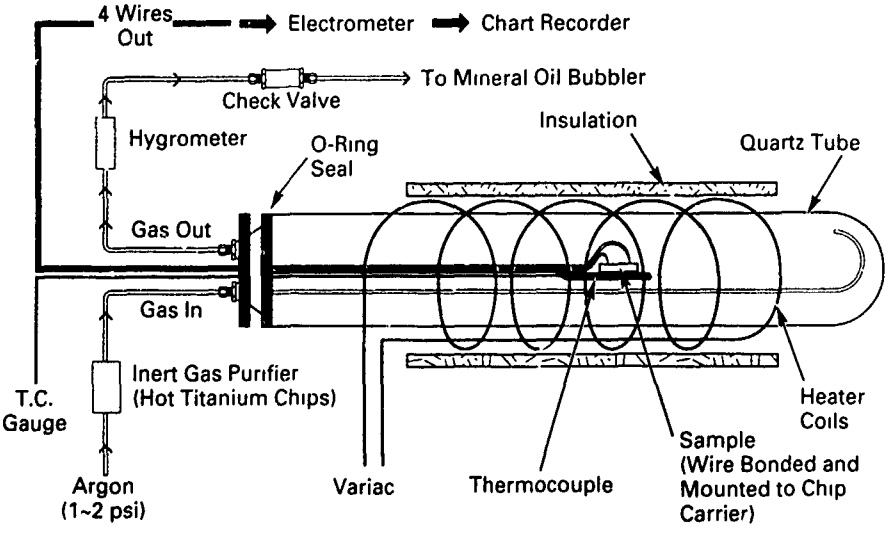



Figure 1. Apparatus used for electrical resistance measurements of the diamond sample.

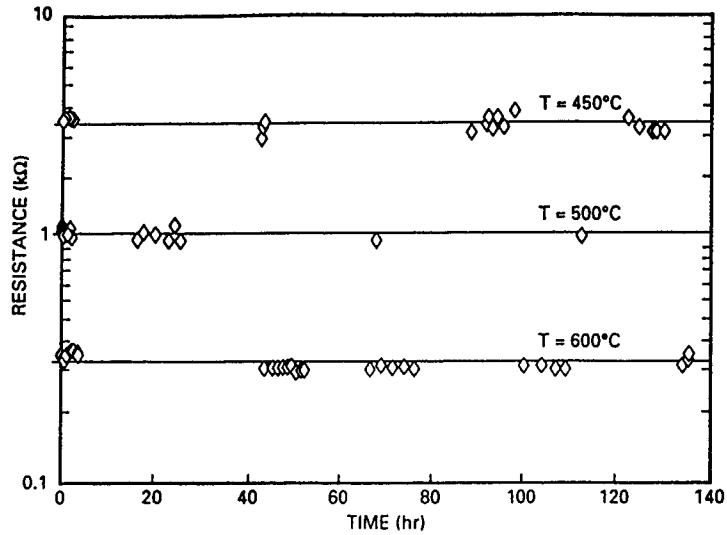



Figure 2. Resistance vs time for three temperatures. Solid lines represent mean temperatures.

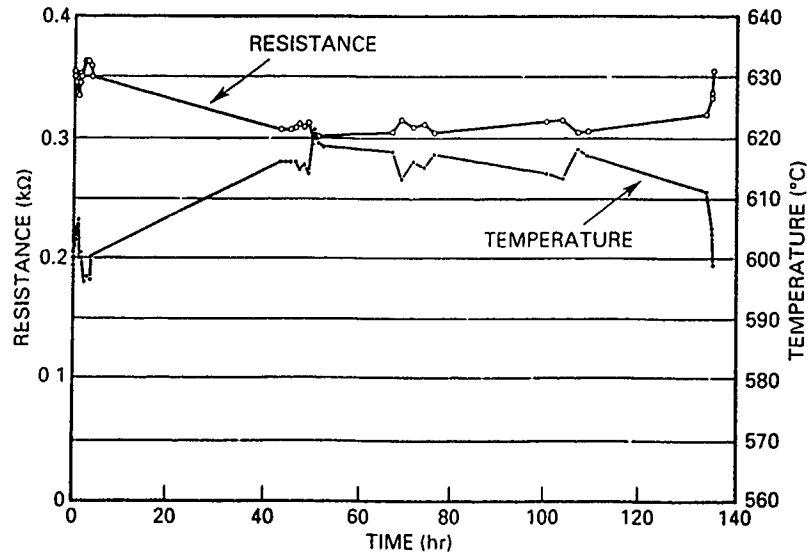



Figure 3. Resistance and temperature as a function of time near 600 °C.

# EFFECT OF THIN INTERFACIAL $SiO_2$ FILMS ON METAL CONTACTS TO BORON DOPED DIAMOND FILMS

V. Venkatesan[1], K. Das , D. L. Dreifus[1], G. G. Fountain[2], R. A. Rudder[2], J. B. Posthill[2], and R. J. Markunas[2]

[1]Kobe Steel Research Laboratories, USA, Electronic Materials Center, P. O. Box 13608, Research Triangle Park, NC 27709

[2]Research Triangle Institute, Research Triangle Park, NC 27709-2194

## ABSTRACT

The effect of thin interfacial films of $SiO_2$ (~20 Å) on the electrical characteristics of metal contacts fabricated on polycrystalline and homoepitaxial diamond films has been studied. These films were grown using plasma-enhanced chemical vapor deposition techniques. In order to minimize the effect of defects and / or hydrogen on the metal contact characteristics, these films were annealed at 950°C for 30 min. Metal-semiconductor contacts were formed by electron-beam evaporation of aluminum on both as-received and annealed polycrystalline films, whereas, gold metallization was used for the homoepitaxial film. Active diode dots were defined by a standard photolithographic process. It has been demonstrated that the introduction of a thin $SiO_2$ film at the interface between the metal and the diamond semiconductor film allows the fabrication of a rectifying contact, that is not otherwise possible for the films studied here.

## INTRODUCTION

Semiconducting diamond, as a potential material for high temperature, high speed and high power device applications, has been the subject of some excellent reviews (1, 2). A number of these devices will rely on a rectifying metal / semiconductor contact for their operation. A metal / semiconductor contact also provides a suitable vehicle for electrical characterization of the device material. However, it has been observed that the formation of good rectifying contacts is not always easily accomplished on diamond films grown by chemical vapor deposition (CVD) (3). Contacts established with Al or Au on CVD films exhibit highly resistive ohmic or nominally asymmetric behavior, whereas these metals can be used almost routinely to form rectifying contacts on synthetic (4) and natural semiconducting diamond crystals (5). In the case of CVD grown homoepitaxial films, a chemical treatment in a hot $CrO_3 + H_2SO_4$ solution has enabled the fabrication of Au rectifying contacts (6). Characteristics of rectifying contacts on CVD grown films of both homoepitaxial (7) and polycrystalline diamond (8) have been improved by growing an insulating undoped diamond film on a previously deposited B doped semiconducting film.

In the present investigation, the effect of thin interfacial $SiO_2$ films on the electrical characteristics of metal contacts fabricated on B doped polycrystalline and homoepitaxial films has been studied. It has been demonstrated that the introduction of a thin $SiO_2$ film at the interface between the metal and the diamond semiconductor film allows the fabrication of a rectifying contact, that is not otherwise possible for the films studied here.

## EXPERIMENTAL DETAILS

Both the polycrystalline and homoepitaxial B doped diamond films used for the study were grown using plasma-enhanced chemical vapor deposition (PECVD) techniques. The diamond films were materially characterized by scanning electron microscopy (SEM) and by Raman Spectroscopy. In addition, secondary ion mass spectroscopy (SIMS) analysis of selected samples were performed in order to determine the atomic concentration of B in the films.

### As-deposited diamond films

A microwave plasma CVD reactor described in reference (9), was employed in this study for the deposition of the polycrystalline diamond films. These films were grown on low resistivity (<1 Ω cm) boron doped Si ((111) oriented) substrates using $H_2$ (99.5 %) and $CH_4$ (0.5 %) at a pressure of 35 torr. The substrates were maintained at 800°C during deposition. Moreover, these films were doped with B using $B_2H_6$. The ratio of $B_2H_6$ to the total gas flow was adjusted to obtain (B/C) ratios of 0.8, 2.0, 3.2, 4.0, 20.0, 200.0, and 400.0 ppm in the gas phase. In some cases $O_2$ (0.1 %) was also included in the gas mixture (for (B/C) ratios of 0.8, 2.0, 3.2, 4.0 ppm). These films were grown for 14 hr. For the higher (B/C) ratios ( 4.0, 20.0, 200.0 ppm) $O_2$ was not used and films were grown for 7 hr. Details of the rf plasma CVD reactor utilized for the homoepitaxial film growth are given in reference (10). The homoepitaxial film was grown on a type I A insulating natural diamond crystal using 0.4 % $CH_4$ and 1 % CO in $H_2$ rf plasma. The film was also doped with $B_2H_6$ during growth. Metal contacts on control samples without an $SiO_2$ interfacial layer were fabricated in the following way. After deposition, the diamond films were cleaned using the RCA cleaning procedure (11). Approximately 2000 Å of aluminum was then electron-beam evaporated directly onto the 0.8 ppm (B/C) polycrystalline diamond sample to form a metal-semiconductor contact. For the homoepitaxial diamond sample a chemical treatment in a hot $CrO_3 + H_2SO_4$ solution (to remove any non-$sp^3$ component in the diamond film) was also included and a gold metallization employed. An important point to note in the gold metallization procedure is that the electron-beam evaporation was a two step process. The deposition rate was 1Å/s for the first 100 Å of gold and then 5 Å/s for the rest of the ~ 2000Å film. This procedure markedly improved the adhesion of gold. Active diode areas were delineated by standard photolithography followed by Au or Al etching as the case may be. A mask pattern proposed by Ioannou et al.(12) was used for this process. The fabricated diodes, 100 μm in diameter were separated from the field region by a 100 μm annular ring. The 'infinitely' large area of the field-region ensured an adequate quasi-ohmic contact with the required current handling capability, particularly in the case of the homoepitaxial film that was deposited on an insulating natural diamond crystal. Similar metal contact diodes were also fabricated on a representative 0.8 ppm (B/C) sample on

which a ~ 20 Å thick film of $SiO_2$ had been deposited by a remote plasma-enhanced CVD technique (13) prior to Al metallization. For the homoepitaxial film, following electrical measurements on the Au contacts fabricated on the control sample (i.e. without the $SiO_2$ interfacial film), the metal was etched in aqua regia (3HCl and 1$HNO_3$). This test sample was then cleaned employing the RCA cleaning procedure and a ~ 20 Å thick film of $SiO_2$ was deposited. Approximately 2000 Å Au was subsequently electron-beam evaporated onto the test sample. Active diode areas were defined by photolithography and Au etching. Cross-sectional diagrams of the contact structure on the diamond films, (a) without, and (b) with the the $SiO_2$ film are shown in Fig. 1. The control and test samples were then electrically characterized using a HP 4145 B semiconductor parameter analyzer equipped with a probe station for high temperature measurements.

### Heat treated diamond films

The polycrystalline films were annealed at a temperature of 950°C for 30 min, in order to minimize the effect of defects and / or hydrogen on the electrical characteristics of metal contacts on these films. Aluminum metal contacts were then fabricated on the annealed films both with and without an $SiO_2$ interfacial layer, following the procedure described in the previous section. Current-voltage (I-V) measurements were then performed on these metal-semiconductor contacts. For the contacts fabricated on annealed 20.0 ppm ((B/C) ratio) samples with an $SiO_2$ interfacial layer, I-V measurements were conducted from room-temperature up to ~ 250 °C, at increments of ~ 50 °C.

## RESULTS AND DISCUSSION

### As-deposited diamond films

Scanning electron microscopy of the B-doped diamond films investigated here showed clear (111) facets and five-fold multiply twinned particles. Scanning electron microscopy also indicated that the polycrystalline diamond films grown with $O_2$ (lower (B/C) ratio) had a quality superior to those grown without $O_2$ (higher (B/C) ratio). The crystal quality was investigated using laser Raman spectroscopy. The Raman peak position characteristic of diamond was located near 1333 $cm^{-1}$. A relatively small $sp^2$ peak at 1500 $cm^{-1}$ was also observed in the Raman spectrum of the diamond films. A SIMS analysis of the as-deposited 20.0 ppm ((B/C) ratio) diamond film showed an atomic B concentration of ~ $1.0 \times 10^{18}$ $cm^{-3}$.

Current-voltage characteristics of Al contacts to as-deposited polycrystalline sample (0.8 ppm (B/C) ) are shown in Figs. 2 (a) and (b). Directly deposited Al contacts (Fig. 2 (a)) on this sample without the interfacial $SiO_2$ film showed near-ohmic I-V characteristics. The subsequent introduction of the $SiO_2$ film provided rectifying characteristics as shown in Fig. 2 (b). Directly deposited Au contacts on the as-deposited homoepitaxial film also exhibited near-ohmic I-V characteristics as shown in Fig. 3 (a). With the introduction of the thin $SiO_2$ film good rectification was obtained as shown in Fig. 3 (b). In the presence of the $SiO_2$ film, low leakage currents (< 1 nA at 5 V) in the reverse direction were observed in both the polycrystalline and the homoepitaxial film. A breakdown voltage of ~7 V was observed for both as-deposited polycrystalline and the homoepitaxial films.

## Heat treated diamond films

Current-voltage characteristics on Al contacts fabricated on annealed films with the lower (B/C) ratios, showed a drastic reduction in current in both the forward and reverse directions. Since the magnitude of the current was approximately the same in all the films (for (B/C) ratios of 0.8, 2.0, 3.2, 4.0 ppm), a representative plot from the 4.0 ppm sample is shown in Fig. 4. This reduction in current conduction on annealing is in conformity with observations reported by Landstrass et al. (14, 15), Albin et al. (16) and Muto et al. (17). Hydrogen dissociation and / or defect annihilation could account for the increased resistivity in these annealed diamond films.

Current-voltage characteristics of Al contacts deposited directly on annealed, 20.0 ppm ((B/C) ratio) polycrystalline sample without the interfacial $SiO_2$ film are shown in Fig. 5 (a). The subsequent introduction of the $SiO_2$ film provided rectifying characteristics as shown in Fig. 5 (b). A breakdown voltage of ~ 6 V was observed for this film. A background doping concentration of ~ $5.3 \times 10^{18}$ $cm^{-3}$ in this film was obtained using an approximate 'universal' expression for the breakdown voltage given by (18):

$$V_B = 60(E_g/1.1)^{3/2}(N_B/10^{16})^{-3/4}$$

where, $V_B$ is the breakdown voltage for a plane-parallel junction, $E_g$, the band-gap of the material, and $N_B$, the doping concentration. A band gap of 5.45 eV for diamond and the experimentally observed breakdown voltage of 6 V was used in the above calculation. Assuming that the active B concentration in this high B concentration film is not very different from the atomic concentration (~$1.0 \times 10^{18}$ $cm^{-3}$) as determined from SIMS analysis, the calculated value of the background doping concentration seems to agree within an order of magnitude with the SIMS results. It should be noted that for high concentrations of B of the order of $10^{19}$ - $10^{20}$ $cm^{-3}$ in diamond, a complete activation of the impurity has been reported (19). However, it has not been established whether a similar effect can be expected at a B concentration of $1.0 \times 10^{18}$ $cm^{-3}$. It should also be pointed out that a plane-parallel junction approximation will provide an underestimation of the breakdown voltage as edge effects are expected to produce a significant lowering of the breakdown voltage for a given doping concentration (18). An estimation of doping concentration from the observed breakdown voltage of the structure used here, therefore, will provide an overestimation of the doping concentration. Moreover, since the dielectric strength of $SiO_2$ is $10^7$ V/cm (Appendix I of reference (18)) the breakdown voltage of ~ 20 Å $SiO_2$ film is ~ 2 V. This indicates that the experimentally observed breakdown voltage of this film (~ 6 V) is likely to be the breakdown voltage of the diamond film and not that of the dielectric. The I-V characteristics of this annealed diamond film (20.0 ppm (B/C) ratio) with interfacial $SiO_2$ measured at temperatures ranging from room temperature (RT) to 248 °C in ~ 50 °C increments, are shown in Fig. 6. It is seen that as the temperature is increased the reverse leakage current increases and the reverse breakdown voltage decreases. Nevertheless, a fairly good rectification behavior can be observed up to ~ 100 °C.

## Conclusions

It has been demonstrated that the introduction of a thin $SiO_2$ film at the interface between the metal and the diamond semiconductor film allows the fabrication of a rectifying

contact, that is not otherwise possible for the films studied here. This improvement in characteristics is probably due to a modification in the barrier height and field distribution and / or to passivation of the surface. Further work in this area, in order to fully understand the mechanisms involved in determining the observed characteristics, is in progress .

## Acknowledgements

The authors are grateful to Dr. K. Kobashi, ERL, Kobe Steel, Ltd. Kobe, Japan, for providing the polycrystalline diamond films used in this study and to C. P. Tully, Kobe EMC for his assistance in preparation of the manuscript. GGF, RAR, JBP, and RJM gratefully acknowledge support from SDIO/IST through ONR (Contract No. N00014-86-C-0460).

## References

1. A.T. Collins, Semicond. Sci. Technol. 4, 605 (1989).
2. G.Sh. Gildenblat, S.A. Grot, A. Badzian, to be published, Proc. IEEE.
3. V. Venkatesan, and K. Das, unpublished work, (1990).
4. G.H. Glover, Solid St. Elect. 16, 973 (1973).
5. E.C. Lightowlers and A.T. Collins, J. Phys. D : Appl. Phys. 9, 73 (1976).
6. S.A. Grot, G.Sh. Gildenblat, C.W. Hatfield, C.R. Wronski, A.R. Badzian, T. Badzian, R. Messier, IEEE Electron Dev. Lett. 11, 100 (1990).
7. H. Shiomi, Y. Nishibayashi and N. Fujimuro, presented at the 2nd Intl. Conf. New Diamond Sc. Tech., Washington, D.C., Sept 23-27 (1990).
8. K. Miyata, D.L. Dreifus, K. Das, J.T. Glass and K. Kobashi, to be presented at the Electrochem. Soc. Meeting, Washington, D.C., May 6-10 (1991).
9. 14. K. Kobashi, K. Nishimura, Y. Kawate, and T. Horiuchi, Phys. Rev. B 38, 4067 (1988).
10. R.A. Rudder, G.C. Hudson, Y.M. LeGrice, M.J. Mantini, J.B. Posthill, R.J. Nemanich, and R.J. Markunas, Mat Res. Soc. EA-19, 89 (1989).
11. W. Kern, and D. A. Puotinen, RCA Rev. 31, 187 (1970).
12. D. E. Ioannou, N. A. Papanicolaou, and P. E. Nordquist, Jr., IEEE Trans Electron Devices, ED-34, 1694(1987).
13. G.G. Fountain, R.A. Rudder, S.V. Hattangady, R.J. Markunas, and P.S. Lindorme, J. Appl. Phys. 63 (9), 4744 (1988).
14. M.I. Landstrass and K.V. Ravi, Appl. Phys. Lett. 55, 975 (1989).
15. M.I. Landstrass and K.V. Ravi, Appl. Phys. Lett. 55, 1391 (1989).
16. S. Albin and L. Watkins. IEEE Electron Dev. Lett. 11, 159 (1990).
17. Y. Muto, T.Sugino, J. Shirafuji and K. Kobashi, submitted for publication: Appl. Phys. Lett. (1990).
18. S.M. Sze, 'Physics of Semiconduction Devices', Wiley-Interescience publication, New York, 1981.
19. K. Nishimura, K. Das and J.T. Glass, J. Appl. Phys. 69, 3142 (1991).

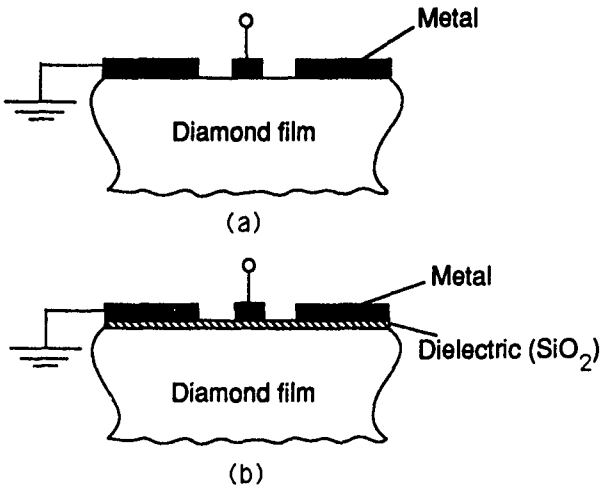



Figure 1: Cross-sectional diagram of contact structure on diamond film, (a) without dielectric layer and (b) with dielectric layer.

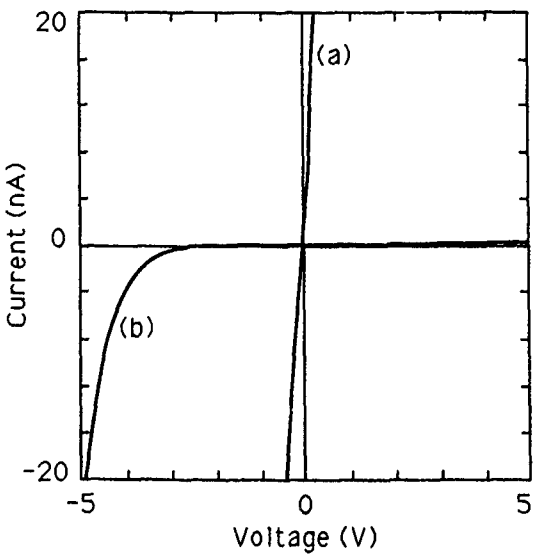



Figure 2: Current-voltage characteristics of Al contacts on polycrystalline diamond film (0.8 ppm), (a) direct metalization and (b) with interfacial $SiO_2$

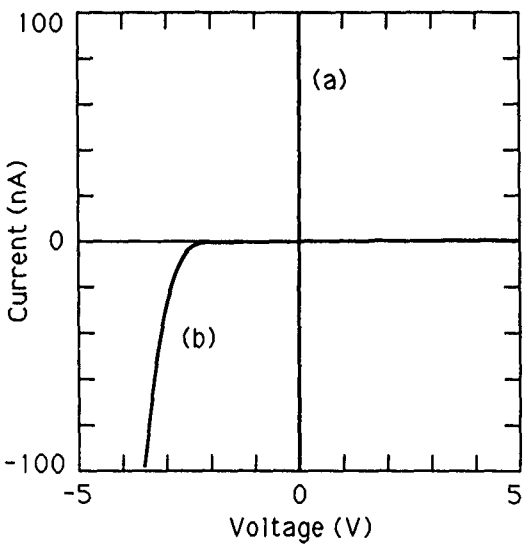



Figure 3: Current-voltage characteristics of Au contacts on homoepitaxial diamond film, (a) direct metalization and (b) with interfacial $SiO_2$.

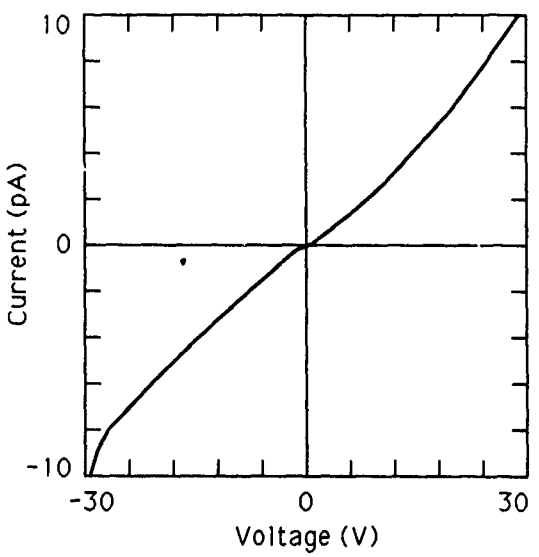



Figure 4: Current-voltage characteristic of Al contacts on annealed diamond film (4.0 ppm).

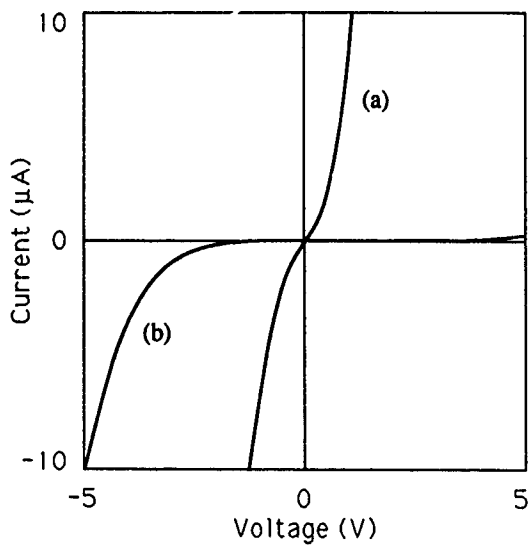



Figure 5: Current-voltage characteristic of Al contacts on annealed diamond film (20.0 ppm), (a) direct metalization and (b) with interfacial $SiO_2$.

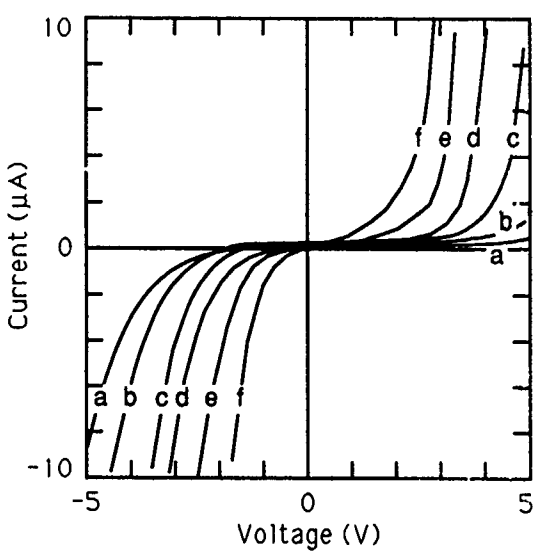



Figure 6: Current-voltage characteristic of Al contacts on annealed diamond film (20.0 ppm) with interfacial $SiO_2$ at (a) RT, (b) 50°C, (c) 99°C, (d) 149°C, (e) 198°C, and (f) 248°C.

# FORMATION OF SINGLE-CRYSTAL SEMICONDUCTOR - a-C:H FILM HETEROJUNCTIONS.

V.M. ELINSON,V.V. SLEPTSOV,S.S. GERASIMOVICH,G.F. IVANOVSKY
NPO "Vacuummaspribor",USSR,113105 Moscow,Nagorny pr. 7.

V.I. POLYAKOV,O.N. ERMAKOVA, M.G.ERMAKOV, P.I.PEROV
Institute of Radiotechnic and Electronic Academy of Sciences USSR,103907 Moscow, K.Marx pr., 18.

Considerable interest has been aroused in formation of single-crysal semiconductor - diamond-like film heterostructures that can be used for various applications,such as multilayer quantum-dimensional structures, sensitive photodetectors,varicaps, dynamic memory elements with electrical and optical recording and information reading.Heterojunctions were formed by ion-assisted methods on Si and GaAs wafers with different type of conductivity and resistivity.The film thickness was 5.0 - 100.0 nm.MIS structures with a 5.0 nm thick a-C:H film were obtained.The possibility of a-C:H films formation which are resistant to temperature range no less than 450 C and films in which diamond phase content is increased up to 450 C during heating has been demonstrated.The effect of preliminary treatment conditions of wafers, particle energy and thermal treatment of films and heterostructures upon density of surface states at the semiconductor - a-C:H film interface was shown.

## 1.Introduction.

Single-crystal semiconductor - diamond-like film heterostructures are exiting challenge to the development of active elements of micro- and optoelectronics (photodetectors, dynamic memory elements, transistors) due to high hardness,chemical inertness,ecological cleanliness of starting materials and possibility of changing electrical and optical properties of a-C:H films in a wide range (1,2).

In the paper the dependence of formation process and wafer preliminary treatment conditions upon the properties of single-crystal semiconductor - a-C:H film interface has been investigated in order to create heterostructures with

reliable properties and thermal stability.

For this purpose complex research of deep level parameters, zone bending in the single-crystal - a-C:H interface, electronic structure, chemical composition has been carried out.

The effect of temperature upon the properties of interface and a-C:H films was studied.

## 2.Experimental details.

Heterojunctions were formed on monocrystalline GaAs and Si substrates of different conductance type and resistivity.The thickness of a-C:H films prepared by ion-assisted methods in different conditions was 5.0 - 100.0 nm.

The electronic structure of films was studied by Auger electron spectroscopy (3).Percentage of bonds on the basis of $sp^2$ - and $sp^3$ -hybridization of carbon atom,the size of graphite-like clusters and change in electronic structure of films at annealing up to 400 C were determined.The presence of carbon and hydrogen in chemical composition of films was detected by the technique of secondary-ion mass spectroscopy (4).

The value of optical bandgap ($E_{\alpha\text{-}C:H}$) was determined by method discribed in (5).The values of optical bandgap of a-C:H films used for examining properties of heterostructures in this paper were 1.5-1.7 eV (E a-C:$H_I$) and 2.0-2.2 eV (E a-C:$H_{II}$).It has been found that $E_{\alpha\text{-}C:H_{II}}$ is practically constant in the thickness range from 5 nm up to 300 nm under specified production conditions (Fig.1).

The monocrystalline semiconductor-a-C:H film interface was studied by charge-relaxation spectroscopy method (6); the value of zone bending at the interface was determined by photoelectromotive force and photoresponse kinetics (6).

## 3.Results and Discussion.

Just after annealing of heterostructures based on a-C:H films the change in electronic structure corresponds only to decrease of "dangling" bonds density (Fig.2a,peak at E = 4-5 eV) due to their thermal stability.Just after annealing of heterostructures based on a-C:$H_I$ films, the peaks were observed at energy of 14.5; 19 and 20-25 eV corresponding to C-H and C-$H_2$ bonds in density spectrum of

states (Fig.2b).An increase in output of bonds based on $sp^3$ -hybridization of carbon atom of diamond-like phase and decrease of number of dangling bonds was detected at the same time.

Q-DLTS spectra of a-C:H -Si heterostructures obtained at some temperature value are shown in Fig.3.The deep level parameters of heterostructures based on a-C:H films are given in Table 1.

The monocrystalline semiconductor - a-C:H film heterojunction is characterized by the presence of 2 deep levels (A and B).The ionization energy level A (E=0.36 eV) is practically independent of thickness in the thickness range from 50 nm to 300 nm.It can be supposed that heterojunction location is due to the presence of traps in a-C:H layer at the distance of 50 nm from the heteroboundaries.The ionization energy of level B is varied depending on substrate type (Table 1) and conditions of preliminary treatment of substrates (2).

The decrease in dangling bonds density then annealing heterostructures based on a-C:H films may lead to a reduction in density of traps up to (2-7)*$10^{11}$ $cm^{-2}$ for A level.May be the changes in phase composition also have been influenced on state density in this case.

When we decrease the mean energy of particles while forming the Si - a-C:H heterojunction from 0.6 keV to 0.1 keV we can observe peak A at another value of energy (Table 1, E = 0.54-0.59 eV).The density of these states is independent of thickness up to 5 nm.That is why we suppose that this traps are concentrated at the distance from interface no more then 5 nm.

In case of a-C:H film just after annealing we can observe only the reduction of dangling bonds density (Fig.2a).Then we conclude that dangling bonds density may be connected with density of level A states.

The photoelectromotive force kinetics $V_{ph}$ of a-C:H - GaAs heterostructures is shown in Fig.4.The values of zone bending at the Si-aC:H interface are given in Table 2.It has been found that increase in a-C:H layer thickness results in a negligible change in value ($V_{ph}$ ).An increase in Si-aC:H layer thickness leads to the decrease in $V_{ph}$ and increase in energy from 0.12 eV to 0.22 eV where $C_6H_{12}$ is used.For $C_3H_8$ as starting hydrocarbon another thickness dependence may be observed.

The dependence of heteroboundary properties on

preliminary treatment conditions of monocrystalline semiconductors substrates is shown in Table 3.It has been found that the density of traps decreases at level connected with the substrate type when increasing treatment duration.

## 5.Conclusions.

The investigations presented here demonstrate the possibility of controllable formation of interfaces, especialy surface state control connected with a-C:H film whi'e changing in deposition conditions,preliminary treatment of substrates.The thermal stability of a-C:H films and heterostructures in temperature range from 293 K to 673 K was shown.The usage of a-C:H films of 5 nm in thickness for MIS-structures production is possible due to the low defectness of a-C:H layers,prepared by ion-assisted methods in different environments.It has been found that variations in values of zone bending at the interface as a function of a-C:H layer thickness,starting gaseous medium and formation conditions.

The dependence of zone bending in Si - a-C:H interface on the a-C:H film thickness has shown the volume distribution of traps,while for a-C:H films zone bending does not depend upon the film thickness in the thickness range to 5 nm.

This research has shown the possibility of HS forming as with high as well as with little surface states density which is reliable for different applications, for example for memory systems or MIS-structures formation.

Controllable operating on zone bending permits to create planar electronic devices with optimal characteristics.

## R E F E R E N C E S


[1] V.M.Elinson, V.V.Sleptsov, V.I.Polyakov, P.I.Perov, Abstracts First European Conference "Diamond-Like Films" Crans-Montana, Switzerland, 1990, 13.6.

[2] V.V.Sleptsov,V.M.Elinson,G.F.Ivanovsky,V.I.Polakov Abstracts First European Conference "Diamond-Like Films" Crans-Montana, Switzerland, 1990, 7.8.

[3] M.B.Gooseva, V.G.Babaev, V.V.Hvostov, O.Yi.Rylova, G.F.Ivanovsky, V.V.Sleptsov and V.M.Elinson, Poverkh.

Fiz. Khim. Mekh. N.11 (1987) 101.
[4] G.F.Ivanovsky, V.V.Sleptsov, V.M.Elinson, P.E.Kondrashov, Elektron. Promyshl. N2 (1989) 26.
[5] A.M. Baranov, S.S.Gerasimovich, V.M.Elinson, A.A.Kuzin, V.V.Sleptsov and P.E.Kondrashov, Phys. Stat. Sol. (A) V.122 (1990) K139.
[6] V.I.Polyakov, P.I.Perov, A.I.Rukovishnikov, O.N.Ermakova A.L.Alexandrov,B.G.Ignatov Mikroelektronika,v.16,N4,(1987) 326.

Table 1.Electrical features of heterostructures based on layers of a-C:H.

| Type of hetero-structures | Thickness of a-C:H layer,A | EA, eV | EV, eV | NT1,cm T=293 K | NT1,cm T=450 K | NT2,cm T=293 K |
|---|---|---|---|---|---|---|
| a-C:H -Si | 100 | 0.36 | 0.5 | $1.2*10^{12}$ | $2*10^{11}$ | $1.3*10^{11}$ |
| a-C:H -Si | 50 | 0.36 | 0.5 | $10^{12}$ | $7*10^{11}$ | $1.5*10^{11}$ |
| a-C:H-GaAs | 100 | 0.36 | 0.77 | $10^{12}$ | — | $1.5*10^{11}$ |
| a-C:H-GaAs | 100 | 0.36 | 0.31 | $3*10^{11}$ | — | $3*10^{10}$ |
| a-C:H -Si | 100 | 0.54 | — | $5*10^{11}$ | $1.6*10^{10}$ | — |
| a-C:H -Si | 30 | 0.54 | — | $1.6*10^{12}$ | — | $0.5*10^{12}$ |
| a-C:H -Si | 20 | 0.54 | — | $10^{12}$ | — | $0.4*10^{12}$ |
| a-C:H -Si | 5 | 0.59 | — | $2.4*10^{12}$ | $5*10^{11}$ | — |

Table 2.The dependence of heterostructure photoelectromotive force on layer thickness of a-C:H.

| Type of heterostructure | Thickness of layer | Environment | V ,V |
|---|---|---|---|
| a-C:H - Si | 5 | $C_6H_{12}$:Ar | 0.32 |
| a-C:H - Si | 10 | $C_6H_{12}$:Ar | 0.38 |
| a-C:H - Si | 100 | $C_6H_{12}$:Ar | 0.28 |
| a-C:H - Si | 50 | $C_3H_8$ | 0.27 |
| a-C:H - Si | 200 | $C_3H_8$ | 0.15 |
| a-C:H - Si | 50 | $C_6H_{12}$ | 0.12 |
| a-C:H - Si | 100 | $C_6H_{12}$ | 0.22 |

Table 3.The dependence of density traps NT on operating time by Ar ions.

| Type of heterostructures | ,min | NT1,om | NT2,om |
|---|---|---|---|
| a-C:H - Si | 10 | $1.2*10^{12}$ | $1.3*10^{11}$ |
| a-C:H - Si | 30 | $3*10^{11}$ | $< 10^{9}$ |

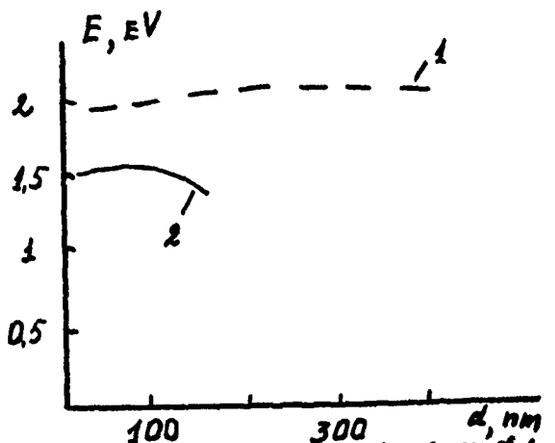



Fig.1. The dependence of optical band gap of $\alpha$-C:H films on thinckness: 1-$\alpha$-C:$H_1$, 2- $\alpha$-C:$H_{II}$.

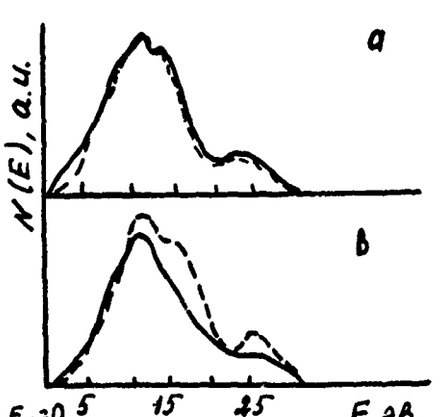



Fig. 2. Electronic structure of $\alpha$-C:$H_I$ (a) and $\alpha$-C:$H_{II}$ (b) films: ——— T=673 K, ——— T= 293 K.

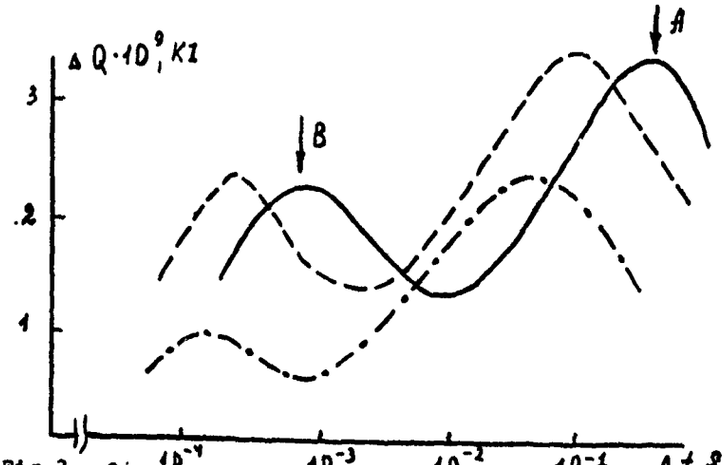



Fig.3. Q -DLTS spektra of $\alpha$-C:H - Si heterostructures at temperature, K: 1-T= 380,2-T= 400,3-T=420.

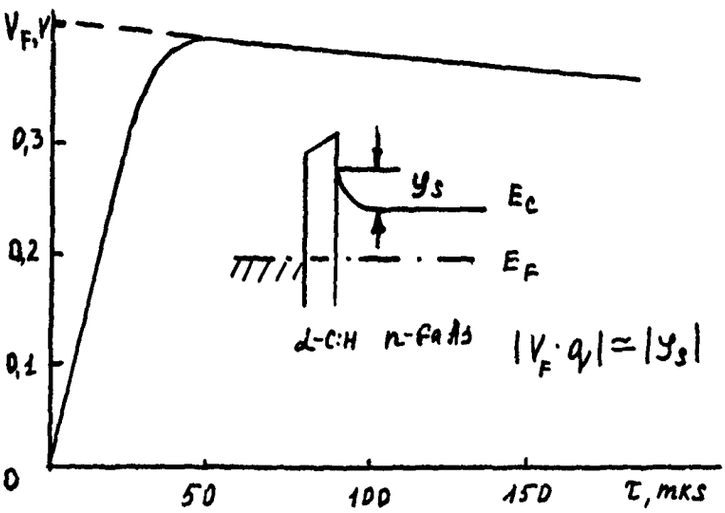



Fig.4. Photoelectromotive force kinetics of $\alpha$-C:H - GaAs heterostructures. Insertion-zone energy diagram of heterostructure.

# Implantation and Diffusion of Electrically Active Dopants in Polycrystalline Diamond

M. I. Landstrass[1], M. A. Plano[1], D. Moyer[1], S. P. Smith[2], and R. G. Wilson[3]

[1]Crystallume, 125 Constitution Drive, Menlo Park, CA 94025

[2]Charles Evans and Associates, Redwood City, CA 94063

[3]Hughes Research Laboratories, Malibu, CA 90265

## ABSTRACT

Polycrystalline diamond films have been doped by ion implantation with nitrogen, boron, lithium, and hydrogen. Secondary ion mass spectroscopy (SIMS) was used to determine the chemical content of these films and to follow their diffusion during thermal processing. We have determined that grain boundary diffusion of lithium occurs at 1000°C suggesting that it is unsuitable for use as an n-type dopant in polycrystalline diamond. We have compared the hydrogen concentration measurements to electrical data. A qualitative comparison of the SIMS data with device electronic behavior is consistent although quantitatively most of the incorporated hydrogen is electrically inactive. The electrical behavior of all measured ion implants was dominated by conductive defects that appeared to be lattice damage related.

## INTRODUCTION

Diamond films have a broad range of electronic applications which depend critically on the ability to control the impurity content of the deposited layers. While most of the potential applications of diamond require a versatile range of both n-type and p-type dopants, most documented dopant behavior is restricted to nitrogen and boron found in naturally occurring diamond(1). Ion implantation is a technique that allows for the precise metered introduction of a wide variety of dopants into both single crystal and polycrystalline diamond(2). The electrical behavior of potential n-type dopants such as lithium and residual hydrogen have been shown to be complex(3-5). Through the

application of known ion implants we were able to use secondary ion mass spectrometry (SIMS) to measure diffusion, in situ incorporation and implant behavior of nitrogen, boron, lithium and hydrogen.

## EXPERIMENTAL

The unintentional dopant, hydrogen, has been shown to be extremely electrically active(3,4). Figure 1 plots the current voltage characteristics of two diamond capacitors. The films used in these devices were grown with oxygen containing precursors of differing concentration. The curves in Fig. 1 show characteristics obtained on the as-grown films, after a 600°C inert anneal and a 400°C hydrogen plasma anneal. From the figure it can be seen that the major affect of the different growth conditions is on the as-grown resistivity and that after a 600°C anneal very little difference remains. Figure 2 plots the leakage current of an annealed capacitor as a function of temperature up to 400°C. After annealing these films are very stable and have been measured up to temperatures as high as 1200°C(6).

Figure 3 is a plot of the SIMS depth profiles of two different films, grown with and without oxygen precursors and annealed at different temperatures. From these plots no hydrogen movement can be seen except at 1350°C. None of the low temperature anneals produced measurable movement. Figure 4 shows a depth profile of a 2H implant into a fine grain diamond film that shows much faster hydrogen diffusion at 1350°C. Figure 4 also shows diffusion of a boron implant at 1350°C. The kinetics of the electrical behavior of hydrogen also are faster on fine grain diamond(4,5). The lack of any diffusion tail suggests that the electrical instabilities related to hydrogen are unrelated to grain boundary diffusion and are likely a bulk effect. This also suggests hydrogen is only electrically active in the bulk and not at grain boundaries. Quantitative measured chemical hydrogen concentrations of $5x10^{19}cm^{-3}$ are much higher than the electrically active hydrogen levels of $1x10^{10}cm^{-3}$. The absence of grain boundary diffusion of hydrogen, and also boron, was not expected.

From the SIMS data shown in Fig. 3 the small reduction in hydrogen concentration can be attributed to oxygen containing growth precursors. This difference is also many orders of magnitude different than the electrical activity differences shown in Fig. 1. The deuterium implant is used to increase the dynamic range of the measurement due to the background hydrogen concentration of $6.0x10^{19}cm^{-3}$ (340ppm).

Figure 5 shows SIMS depth profiles of lithium and sodium annealed at temperatures up to 1350°C. Lithium diffuses readily at 1000°C and sodium can be seen to move at 1350°C. The shape of the profile is indicative of grain boundary diffusion only, as the main dopant peak is unaffected. These dopants would not be desirable for polycrystalline material, due to this affect, but should be usable for single crystal devices. This is clearly different from the behavior of hydrogen in diamond but typical of other materials such as boron in polycrystalline silicon.

Lithium is of interest as an interstitial n-type dopant. Lithium activation is low and its use has been problematic due to erratic electrical behavior(3). We believe that the electrical anomalies in lithium doped polycrystalline diamond are due to a large segregation

of lithium to the grain boundaries as evidenced by the large diffusion "tail" after anneal shown in Fig. 4.

Table 1 lists the measured resistivity of the implants used in this study when implanted into an in situ boron doped polycrystalline diamond layer. All the implants were annealed in nitrogen at 1180°C before electrical and Raman measurements were performed. In all cases the implanted layers were conductive. Figure 5 shows the Raman spectra measured on the implanted annealed samples. Only the phosphorus implant produced any change in the Raman spectra. As the diamond layers are much thicker than the implant this effect was due to the implanted layer being highly opaque. This was verified by removing the implanted layer and remeasuring. All the implanted layers were visibly discolored by the implant.

Table 1. Implanted layer resistivities for various species

| Implanted Species | Implant Energy | Implant Dose | Resistivity (Ω-cm) |
|---|---|---|---|
| N | 160 keV | $3x10^{15}$ $cm^{-2}$ | 0.0454 |
| H | 50 keV | $2x10^{15}$ $cm^{-2}$ | 0.0908 |
| Li | 100 keV | $3x10^{14}$ $cm^{-2}$ | 0.0681 |
| P | 200 keV | $1x10^{14}$ $cm^{-2}$ | 0.00681 |

Table 2 lists data on phosphorus implantation showing the dependence on boron doping and implant dose. It was found that the implant conductivity was higher as the substrate conductivity increased. It was also found that for the phosphorus implants at the higher doses the layer conductivity decreased. Diodes were made from all the boron doped diamond layers implanted with the above tabulated species. No simple diode behavior was observed for any of the implants.

From the electrical data it appears that all the implanted film properties are dominated by a conductive damage related diamond defect similar to that induced by laser damage(7). This is thought to be a diamond defect due to its diminishing effect as the diamond lattice is destroyed as evidenced by the dose dependence of the phosphorus implants with simultaneous reduction in the lattice Raman signal.

Table 2. Phosphorus implanted layer resistivities ( 200keV energy)

| B-layer Resistivity | Implant Dose | Resistivity (Ω-cm) |
|---|---|---|
| 0.225 | $1x10^{14}$ $cm^{-2}$ | 0.00681 |
| 0.225 | $1x10^{15}$ $cm^{-2}$ | 0.00908 |
| 1.96 | $1x10^{14}$ $cm^{-2}$ | 0.0114 |
| 1.96 | $1x10^{15}$ $cm^{-2}$ | 0.136 |

## CONCLUSIONS

Ion implantation, SIMS and electrical resistivity measurements have been used to investigate hydrogen in polycrystalline diamond films as a function of annealing. It has been shown that hydrogen diffusion at high temperatures occurs in the bulk grains unaffected by grain boundaries similar to the hydrogen electrical activity at low temperatures. It was not possible to see chemical diffusion at low temperatures but due to the hydrogen chemical concentration of $5x10^{19}cm^{-3}$ exceeding the electrical concentration of $1x10^{10}cm^{-3}$ (from the hydrogen treated resistivity) it was not possible to directly measure this effect. The electrical properties of H,Li,P and N ion implanted diamond films was dominated by conductive, damage related defects and does not appear to result in simple dopant behavior.

## ACKNOWLEDGEMENTS

This work received partial support from the Air Force at Eglin AFB and SDIO/IST through ONR.

## REFERENCES

1. A.T. Collins, Semi. Sci. and Tech. **4**, 605 (1989).
2. R. G. Wilson, Proceedings of Diamond Films '90, Sept. 1990, Crans-Montana Switzerland(to be published)
3. K. Okumura, J. Mort and M. Machonkin, Appl. Phys. Lett., **57**, 1907, (1990).
4. M. I. Landstrass and K. V. Ravi, Appl. Phys. Lett., **55**, 975 (1989).
5. M. I. Landstrass and K. V. Ravi, Appl. Phys. Lett. **55**, 1391, (1989).
6 J. W. Vandersande and L. D. Zoltan, , Proceedings of Diamond Films '90, Sept. 1990, Crans-Montana Switzerland (to be published).
7. M. W. Geis, M. Rothschild, R. R. Kunz, R. L. Aggarwal, K. F. Wall, C. D. Parker, K. A. McIntosh, N. N. Eremow, J. J. Zayhowski, D. J. Ehrlich,and J. E. Butler, Appl. Phys. Lett., **55**, 2295 (1989)

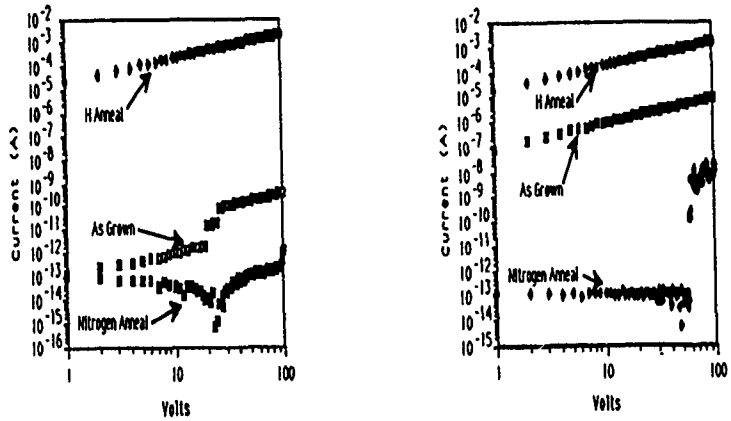



Figure 1. Current voltage characteristics of two diamond capacitors. Both films are grown with oxygen containing precursors of different concentrations. Oxygen strongly controls the as-grown resisitivity but only has little affect on the hydrogen plasma treated value or the thermally stable annealed resistivity.

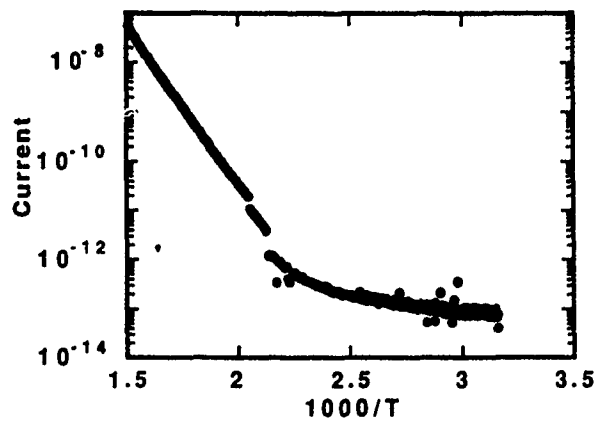



Figure 2. Leakage current versus inverse temperature for a diamond insulator. After an initial low temperature anneal, the insulating properties of the diamond films are very stable at elevated temperatures as shown in this figure up to 400°C and in Ref. 5 to 1200°C.

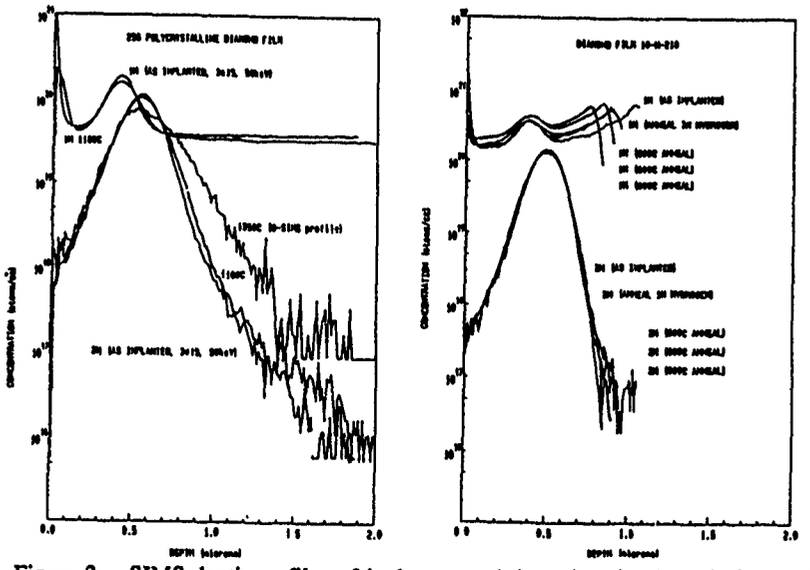


Figure 3. SIMS depth profiles of hydrogen and deuterium implants before and after annealing. The anneals were either performed in an inert atmosphere or a hydrogen plasma. The sample on the left was grown with oxygen containing precursors while the sample on the right contained no oxygen.

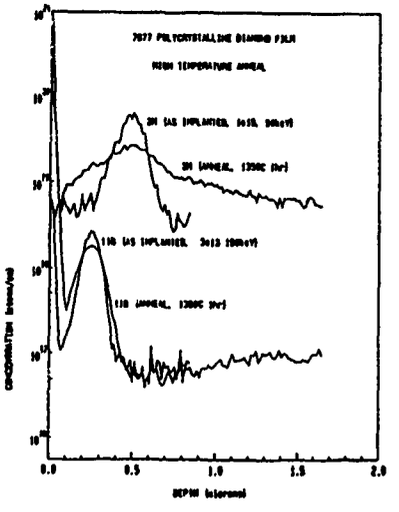


Figure 4. SIMS depth profiles of boron and deuterium implants before and after a 1350°C anneal. This sample had a much smaller grain size than the samples in Fig.3.

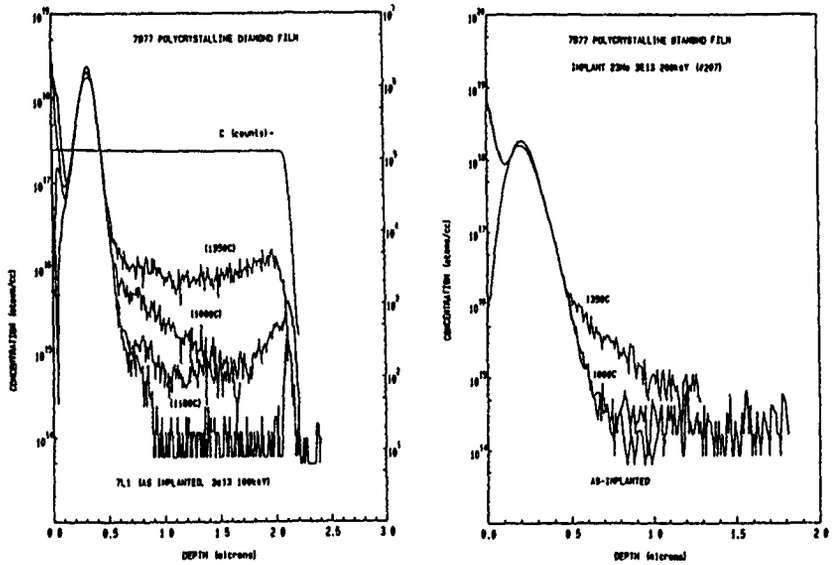


Figure 5. SIMS depth profile of a lithium implant into polycrystalline chemical vapor deposited diamond both before and after anneals compared with similar profiles for sodium implanted diamond.

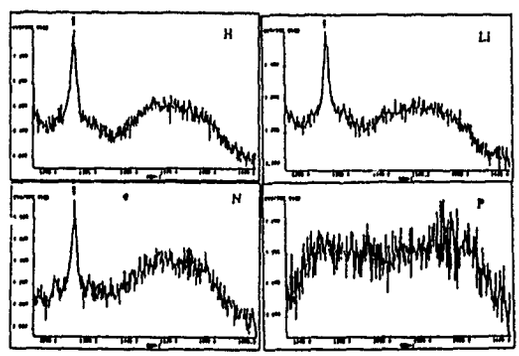



Figure 6. Four Raman spectra of diamond films singly implanted with hydrogen, lithium, nitrogen and phosphorus respectively. The 1332 $cm^{-1}$ peak indicative of diamond is observed in the hydrogen, lithium and nitrogen implanted films, but not in the phosphorus implanted film.

# ELECTRICAL CHARACTERIZATION OF BORON-IMPLANTED DIAMOND

C. A. Hewett[a], P. R. de la Houssaye[b], M. Roser[a], R. G. Wilson[c], and J. R. Zeidler[d]

[a]Naval Ocean Systems Center, Code 555, 271 Catalina Blvd., San Diego, CA 92152-5000
[b]Naval Ocean Systems Center, Code 553, 271 Catalina Blvd., San Diego, CA 92152-5000
[c]Hughes Research Laboratories, 3011 Malibu Canyon Road, Malibu, CA 90265
[d]Naval Ocean Systems Center, Code 7601, 271 Catalina Blvd., San Diego, CA 92152-5000

## ABSTRACT

Natural type IIa (insulating) diamonds were implanted at liquid nitrogen temperature with either boron or carbon plus boron. Van der Pauw resistivity and Hall effect measurements as a function of temperature were used to determine the effect of the implantation, in comparison with the unimplanted side of the sample. Implantation with carbon plus boron resulted in a carrier concentration more than an order of magnitude greater than that resulting from implantation with boron alone, but with a much lower hole mobility.

## INTRODUCTION

Previous attempts to utilize ion implantation to introduce electrically active dopants into semiconducting diamond have yielded inconsistent results [1-3], primarily because the implantation produces a variety of damage mechanisms in the diamond lattice. In addition to the vacancy and interstitial defect centers common to other materials, diamond has an additional damage mechanism due to the transformation of the tetrahedrally bonded diamond lattice to a carbon lattice consisting of graphitic-type bonds. These graphitic layers may show electronic conduction similar to that of an n-type layer. Removal of the damaged layer is a non-trivial task, but was accomplished in [3]. Analysis of the effects of implantation is also greatly complicated by the wide variations in electrical properties observed in natural diamond. An arbitrary designation of resistivity is used to separate natural diamond into insulating type IIa diamond and semiconducting type IIb diamond, but the resistivity values range continuously over several orders in magnitude. Several other complications may arise in the electrical characterization of diamonds, including the role of hydrogen [4], adsorbed gases [5,6], and

possible photoconductivity contributions [7]. In spite of these difficulties, many authors have attempted to draw conclusions based on a comparison of the relative temperature dependencies of the resistance of two different diamond samples, one implanted, one not.

Prins [1] proposed a technique which allows controllable doping of diamond via ion implantation. This technique requires that implantation be carried out with the diamond held at a temperature low enough to reduce the diffusional motion of both vacancies and interstitials produced in the collision cascade. The result is a high density of vacancies and interstitials in close proximity. Dopant atoms are then implanted into this layer of "frozen" vacancies and interstitials. Subsequent annealing at a temperature high enough to allow diffusion of the interstitials and/or the vacancies results in recombination of the vacancies with both the self-interstitials and the dopant interstitials. The implanted layer then contains substitutional dopants with a low level of residual radiation damage. Prins [1], and Sandhu *et al.* [8] have verified this technique using resistance measurements as a function of temperature to determine activation energies.

In this paper, we describe a system to allow resistivity and Hall effect measurements to be made as a function of temperature in an inert ambient. This allows a direct measurement of both the net carrier concentration and the temperature dependence of the mobility. As noted in a previous work [9], a comparison of results between the front and back sides of the same thin (0.25 mm) diamond slice, with only one side having been implanted, can essentially eliminate sample to sample variation. By also carrying out the measurements in a purified argon ambient, with a pre-measurement heat treatment, we believe extraneous conductivity due to adsorbed gases or other effects are minimized. Thus, we are better able to observe the net change in the electrical transport due to the implant.

## EXPERIMENTAL PROCEDURE

The starting material consisted of two natural semi-insulating (type IIa) diamonds, 5 mm x 5 mm x 0.25 mm in size. One sample was implanted with boron ions at 77 K using a multiple implant scheme (25 keV, 1.5 x $10^{14}$ $B^+/cm^2$; 50 keV, 2.1 x $10^{14}$ $B^+/cm^2$; and 100 keV, 3.0 x $10^{14}$ $B^+/cm^2$) intended to provide an approximately uniformly doped p-type layer of about 210 nm (as verified by SIMS on a similarly implanted sample) in thickness. The second sample was first implanted with carbon ions at 77 K using a similar multiple implant scheme (30 keV, 1.5 x $10^{14}$ $C^+/cm^2$; 60 keV, 2.1 x $10^{14}$ $C^+/cm^2$; and 120 keV, 3.0 x $10^{14}$ $C^+/cm^2$), immediately followed by a boron implantation identical to that of the first sample.

After implantation, the diamonds were removed from the cold stage and annealed at 990°C for 10 minutes in dry nitrogen to remove implantation damage and activate the implanted boron.

The diamonds were then cleaned by etching in a boiling saturated solution of chromic oxide ($Cr_2O_3$) in sulfuric acid. The purpose of the etch was to remove any graphitized layer which might have formed. The diamonds were then rinsed in deionized water, boiled in acetone, and then rinsed with methanol. After the methanol rinse, the diamonds were blown dry using dry nitrogen and loaded into an ultra-high vacuum chamber for ohmic contact metallization. The base pressure of chamber was approximately $1 \times 10^{-8}$ Torr. Contacts were deposited on the sample corners, and were defined using a stainless steel shadow mask. The contact metallization consisted of 100 Å of molybdenum deposited by electron beam evaporation, followed by 1500 Å of gold deposited from a resistively heated boat. After removal from the vacuum chamber the samples were baked at 120°C for 20 minutes, then loaded into a furnace and annealed in a dry hydrogen ambient (dew point < -60°C) for 6 minutes at 960°C.

A schematic outline of the high temperature van der Pauw resistivity and Hall effect measurement apparatus is shown in Figure 1. A great deal of care was taken to control the ambient to which the diamonds were exposed at high temperature. High purity argon was generated and fed into the system to maintain a dew point of less than -115°C. The system as originally described [8] utilized a ceramic chip carrier, with a stainless steel support structure, and was used to measure the sample implanted with boron only up to a temperature of 600°C. At high temperatures this combination was found to leave a film of contamination on the surface of the diamond. As a result, we have rebuilt part of the system to leave only quartz, the diamond, and copper and gold electrical connections in the annealing ambient, with the copper wires sheathed in quartz capillary tubing. The temperature was monitored via a thermocouple inserted in a socket below the sample platform. This system was used to measure the sample implanted with carbon plus boron up to a maximum temperature of 700°C.

## RESULTS AND DISCUSSION

Shown in Fig. 2 is the net carrier concentration plotted as a function of inverse temperature for the sample implanted with carbon plus boron. We measured the carrier concentration both as temperature was increased and as temperature was reduced. The results presented here were obtained only after annealing at a temperature of 375°C in the argon ambient of the measurement system to stabilize measured data. This was found to be necessary

to obtain data which did not drift upwards with time for the sample implanted with boron only. An additional, similar effect seemed to occur at a second, higher temperature with the carbon plus boron implanted sample. Note that the curve generated as the temperature was decreased does not match the curve generated as the temperature was increased. Upon increasing temperature a second time, however, the carrier concentration data retraced the "temperature falling" curve. The carrier mobility for this layer, shown in Fig. 3, exhibits a similar effect. The reason for this behavior is not clear at the present time, but might be due to the desorption of a gaseous impurity at high temperature. Because the "temperature falling" curves appear to be reproducible, we use them for comparison with the layer implanted with boron alone.

Plotted in Figs. 4 and 5 respectively are the sheet carrier concentrations and the mobilities as a function of inverse temperature for the implanted sides of the samples implanted with boron and carbon plus boron. Measurement of these properties on the unimplanted side of each sample (not shown here) allows us to directly compare the two different samples. Clearly, there is a much greater activation efficiency for the sample implanted with carbon plus boron (approximately 1% versus 0.1% for the layer implanted with boron only). Note, however, that the sample implanted with carbon plus boron has a lower mobility and a lower temperature dependence than that implanted with boron only. Since the boron dose is equivalent in the two samples, this may be an indication of greater residual damage due to the additional carbon dose. This can be checked by comparing samples with the same total implantation dosage, i.e. the total dose of carbon plus boron ions implanted in one sample should be equal to the boron dose implanted in the other sample. According to Prins [10] activation of boron is more efficient in samples implanted with carbon plus boron, implying that it might be possible to have a higher carrier concentration than that in the sample implanted with boron alone, but without a reduction in carrier mobility.

We have also fabricated an insulated gate field effect transistor (IGFET) on the sample implanted with boron only [11]. Assuming that the implantation is roughly uniform over a layer thickness of approximately 2100 Å, we obtain a volume carrier concentration of about $2 \times 10^{16}/cm^3$. The device geometry was chosen to provide data without requiring a mesa etch. It consisted of a central drain contact 400 μm in diameter, with concentric 200 μm gate and source contacts 1000 μm and 1600 μm in outer diameter, respectively. The source and drain contacts consisted of a 10 nm molybdenum/160 nm gold bilayer structure described elsewhere [12]. The gate insulator was an $SiO_2$ film approximately 100 nm thick deposited by indirect plasma enhanced chemical vapor deposition at 300°C, and the gate metal consisted of a 10

nm titanium/160 nm gold bilayer structure. Current saturation was observed with gate bias ranging from zero volts up to pinch-off at a gate bias of approximately 12 volts. The trans-conductance was measured to be 6.9 μS/mm.

## CONCLUSIONS

We have verified the technique proposed by Prins [10] for increasing the activation of boron in diamond by direct measurement of carrier concentration and mobility as a function of temperature. The use of a carbon pre-implant resulted in a carrier concentration more than an order of magnitude greater than that without the carbon implant, for equal doses of boron. There was, however, a degradation observed in the mobility for the sample implanted with the carbon. The layer implanted with boron only was be used to fabricate an IGFET with excellent characteristics.


### Acknowledgments

The authors would like to acknowledge Dr. Michael Seal of Sigillum, B.V. And Drukker International, B.V. for the loan of the samples used in this work. The assistance of Marylin Taylor is greatly appreciated. This work was funded by the Naval Ocean Systems Center Independent Research Program, administered by Dr. Alan Gordon.


## REFERENCES


1. J. F. Prins, Phys. Rev. B 38(8), 5576-5584 (1988).
2. B. Liu, G. S. Sandhu, N. R. Parikh, M. L. Swanson, and W.-K. Chu, Nucl. Instr. and Meth. B45, 420-423 (1990).
3. G. Braunstein and R. Kalish, J. Appl. Phys. 54(4), 2106-2108 (1983).
4. S. Albin and L. Watkins, Appl. Phys. Lett. 56(15), 1454-1456 (1990).
5. J. M. Thomas, in The Properties of Diamond, edited by J. E. Field, Academic Press, New York, 1979. pgs. 211-244
6. B. B. Pate, Surf. Sci. 165, 83-1 .2 (1986).

7. C. D. Clark, E. W. J. Mitchell, and B. J. Parsons, in The Properties of Diamond, edited by J. E. Field, Academic Press, New York, 1979. pgs. 23-78.

8. G. S. Sandhu, M. L. Swanson, and W.-K. Chu, Appl. Phys. Lett., 55(14), 1397-1399 (1989).

9. P. R. de la Houssaye, C. Penchina, C. A. Hewett, R. G. Wilson, and J. R. Zeidler, presented at the Second International Conference on the New Diamond Science and Technology, Washington D. C., September 1990. To be published in the conference procedings.

10. J. F. Prins, Nucl. Instrum. And Meth., B35, 484-487 (1988).

11. C. A. Hewett, R. Nguyen, C. R. Zeisse, and J. R. Zeidler, To be presented at the Hi-Temperature Electronics Conference, Albuquerque, New Mexico, June 1991. To be published in the conference procedings.

12. K. L. Moazed, J. R. Zeidler, and M. J. Taylor, J. Appl. Phys., 68(5), 2246-2255 (1990).

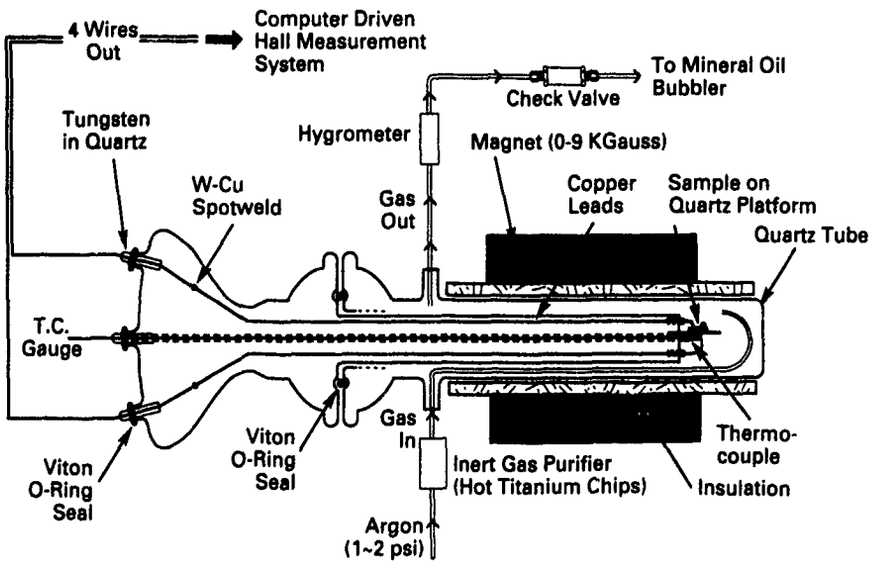



Figure 1. Schematic outline of the high temperature Hall effect measurement system.

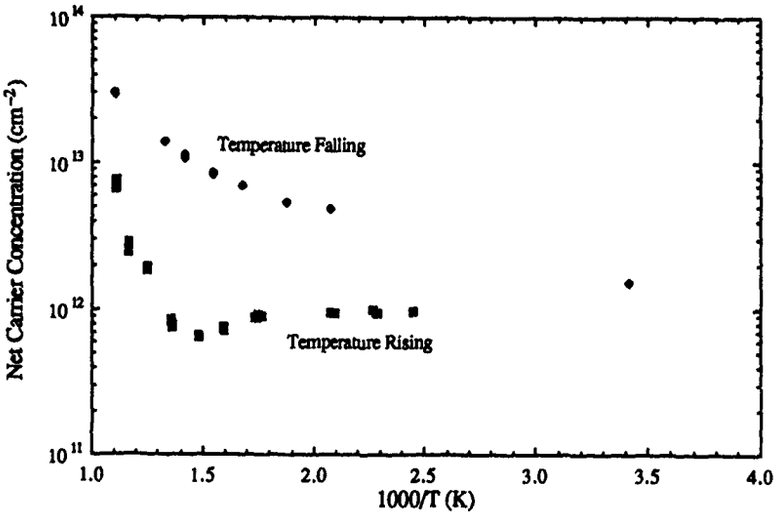



Figure 2. Log of the free carrier concentration versus inverse temperature for the layer implanted with carbon plus boron as the temperature was increased, and as the temperature was decreased.

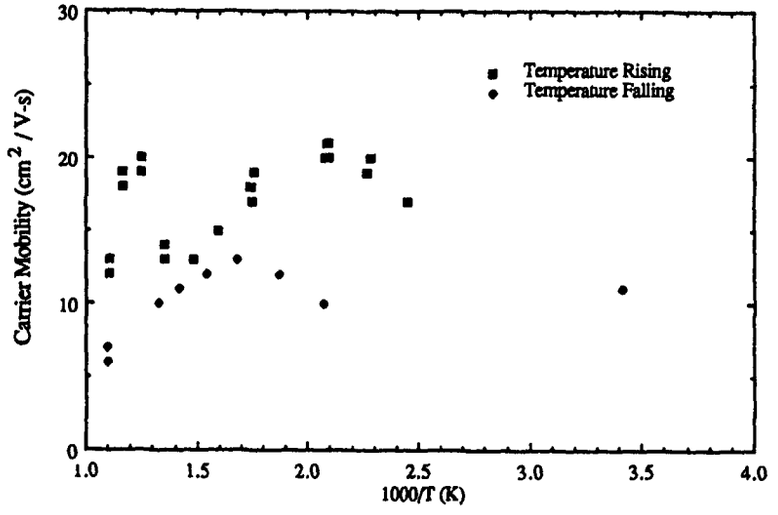



Figure 3. Carrier mobility versus inverse temperature for the layer implanted with carbon plus boron as the temperature was increased, and as the temperature was decreased.

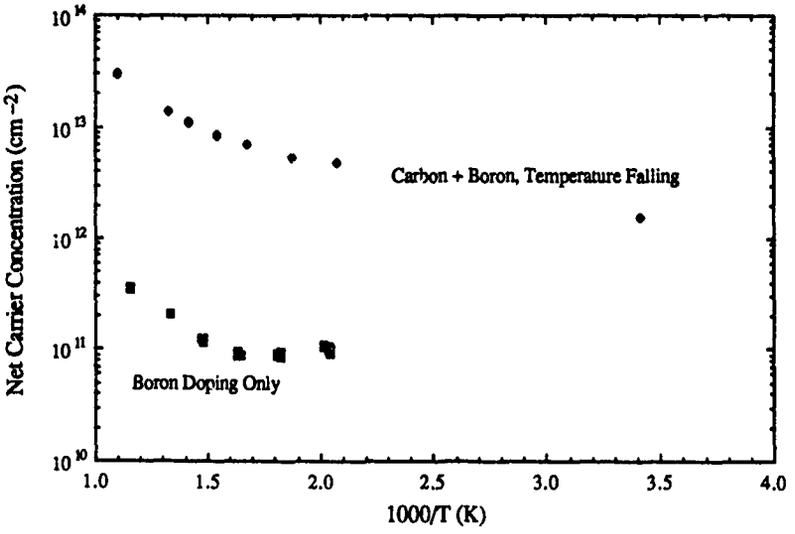



Figure 4. Log of the free carrier concentration versus inverse temperature for the layer implanted with carbon plus boron as the temperature was decreased and for the layer implanted with boron alone.

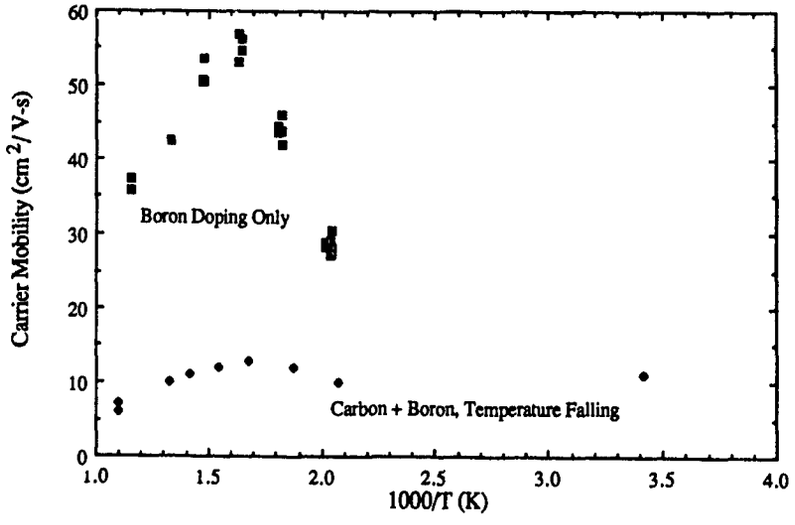



Figure 5. Carrier mobility versus inverse temperature for the layer implanted with carbon plus boron as the temperature was decreased and for the layer implanted with boron alone.

# THIN, BORON DOPED DIAMOND FILMS

**M. I. Landstrass, M. A. Plano, and D. Moyer**

**Crystallume**
**125 Constitution Drive**
**Menlo Park, CA 94025**

## ABSTRACT

The ability to fabricate thin, doped diamond films is essential to the development of diamond semiconducting devices. Boron doped polycrystalline diamond films as thin as 3.3nm have been grown by plasma assisted CVD and characterized. Electrical measurements indicate that the thin doped films behave similarly to bulk layers as far as resistivity and temperature dependence. By controlling the surface roughness and nucleation it is possible to grow thin diamond layers with uniform properties.

## INTRODUCTION

Successful utilization of diamond as a semiconductor despite the lack of shallow p-type dopants requires the innovative use of boron acceptors. The acceptor level of boron is 0.38eV above the valence band(1) which is quite deep compared to other semiconductors. However, when a diamond layer is heavily boron doped the observed activation energy is smaller and more acceptable for device design considerations.(2) One problem with the heavily doped layers is the large number of charges present which would limit device performance. Thin, heavily doped layers would have both a lower activation energy and a small number of charges making them ideal for use in semiconducting diamond devices.

## EXPERIMENTAL RESULTS

Thin film growth of CVD diamond is problematic due to the difficulties involved in controlled nucleation of both single crystal and polycrystalline layers. The diamond films studied in this work were polycrystalline in nature with grain sizes ranging from 200nm to 1 μm. Control of the nucleation mechanisms during growth allows for continuous films to be grown which are much thinner than the grain size. Figure 1 is an SEM cross-sectional micrograph of a boron doped diamond layer 120 nm thick sandwiched between two insulating diamond layers. The interface between the insulating and boron doped diamond is abrupt and planar illustrating the possibility of thin layer growth. SEM cross-sectional micrographs of two other boron doped diamond films are shown in Figs. 2 and 3. These layers are 60nm and 38.5nm respectively and are shown at 50k magnification. Films as thin as 3.3nm were grown and their presence confirmed through electrical measurements but good SEM micrographs of these thinnest layers could not be obtained.

A comprehensive study of the electrical properties of thin and bulk boron doped polycrystalline diamond films was performed to test the thickness scalability of diamond layers. The films studied were grown by plasma assisted CVD and were doped in-situ using diborane gas. Both bulk layers with thicknesses of 1 to 2 μm and thin films of 3.3-120nm were grown with doping concentrations ranging from $5x10^{19}/cm^3$ - $2x10^{21}/cm^3$. Several of the films were analyzed using SIMS to determine the chemical concentration of boron present and to calibrate the gas flow parameters. The SIMS measurements were successful only for those boron doped films grown on very smooth polycrystalline diamond. Otherwise the boron signal was smeared due to the wavy nature of the polycrystalline films.

For all samples resistivity was measured as a function of temperature over the range 300K to 650K. Figure 4 is a graph of resistivity vs. 1000/Temperature for several samples with different doping concentrations but similar thicknesses. The resistivity vs. temperature data was fit with a full Fermi analysis which allows for degenerate conditions, so as to determine the acceptor energy. The acceptor energy was found to be inversely related to the acceptor concentration i.e., with higher doping the boron level is at a lower energy. The thin films exhibited similar electrical behavior and variation with doping as the bulk layers. Figure 5 is a graph of sheet resistance vs. 1000/Temperature for three samples of similar doping but different thicknesses. The sheet resistance of the films with the same doping scales with thickness as one would expect and confirms the uniformity of the films as thin as 10nm.

Several diamond films of thicknesses ranging from 3.3nm to 1μm were grown using a 1000ppm B2H6/CH4 ratio and a 100ppm B2H6/CH4 ratio. The sheet resistance of these films was measured and is plotted as a function of layer thickness in Figs. 6 and 7. The variation of sheet resistance with layer thickness is linear with some noise and indicates that the thin films are behaving as expected. Also, several diamond films were grown with the same thickness of 10nm using various B2H6/CH4 ratios. This data is plotted in Figure 8. There is a linear relationship between the sheet resistance of the thin layers and the boron doping. This result shows that even at thicknesses of 10nm it is possible to control the electrical properties of the layer by controlling the diborane to methane ratio. Figure 9 is a plot of the resistivity of both thick and thin samples as a function of boron doping and shows that the electrical properties of the layer can be controlled by controlling the diborane to methane ratio.

## CONCLUSIONS

We have successfully grown boron doped diamond layers as thin as 3.3nm. The electrical behavior of these thin diamond layers is readily controlled and scales with thickness. Heavily boron doped, thin diamond layers are advantageous since they have a lower activation energy than lightly doped layers and have a small total charge. The ability to fabricate thin, doped diamond films is essential to the development of diamond semiconducting devices.

## ACKNOWLEDGEMENTS

This work received partial support from the Air Force through Eglin AFB and SDIO/IST through ONR.

## REFERENCES

1. J. E. Field: Properties of Diamond (Academic Press, London 1979) Chapter 3 p.79.

2. K. Okano, H. Naruki, Y. Akiba, T. Kurosu, M. Iida, Y. Hirose and T. Nakamura, Jpn. J. Appl. Phys. **28**, 1066 (1989).



Figure 1. SEM cross-sectional micrograph of a boron-doped diamond layer sandwiched between insulating diamond layers grown on Si. A Si cap has been added to enhance contrast and an oxidation process delineates the interface between the doped and undoped diamond. The boron doped layer in this sample is 120nm thick.



Figure 2. SEM cross-sectional micrograph of a boron-doped diamond layer between two insulating diamond layers. A Si cap has been added to enhance contrast and an oxidation process was used to delineate the interface between the doped and undoped diamond. The boron doped layer is 60nm in this sample.



Figure 3 SEM cross-sectional micrograph of a boron-doped diamond layer between two insulating diamond layers grown on Si. A Si cap has been added to enhance contrast and an oxidation process was used to delineate the interface between the doped and undoped diamond. The boron doped layer is 38.5nm in this sample.

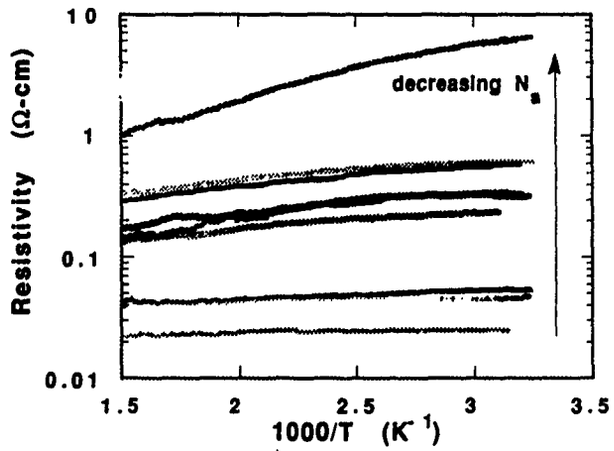



Figure 4. Graph of resistivity vs. 1000/T for several diamond layers with different boron concentrations but similar thicknesses. As the concentration of acceptors decreases the activation energy of the boron acceptor increases.

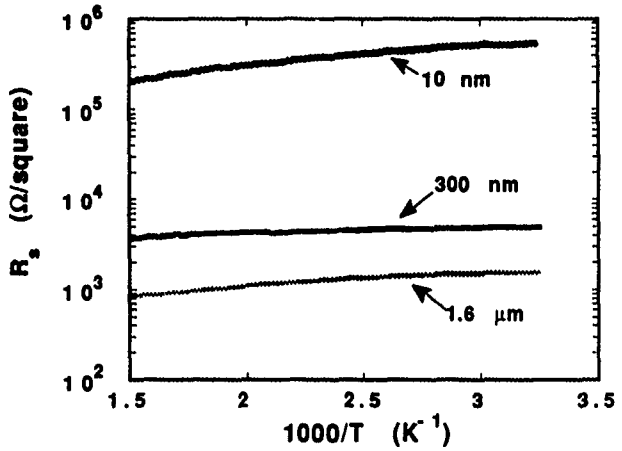



Figure 5. Graph of sheet resistance vs. 1000/T for three samples of similar doping but different thickness. The slope for these three thicknesses is similar, indicating the activation energy is the same, but the resistance scales with the thickness, as expected.

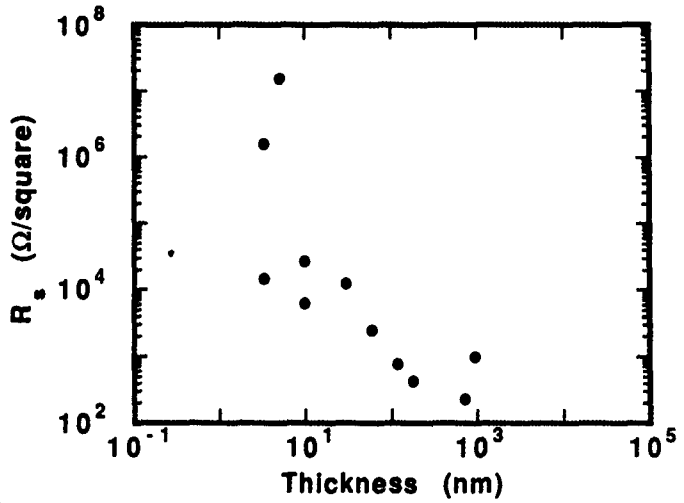



Figure 6. Log-log graph of sheet resistance vs. thickness for several samples grown with a 1000ppm B2H6/CH4 ratio. For similar doping the sheet resistance should increase as the thickness decreases.

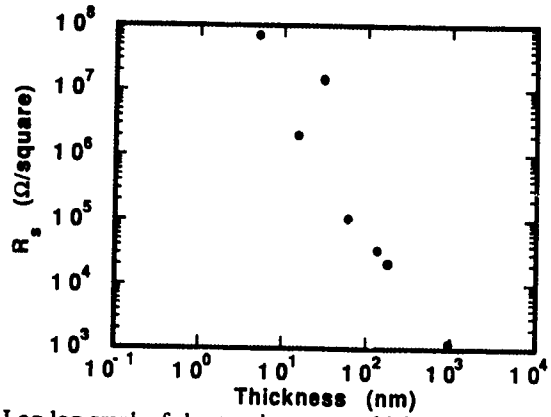



Figure 7. Log-log graph of sheet resistance vs. thickness for several samples grown with a 100ppm B2H6/CH4 ratio. The sheet resistance is linear with thickness, as expected and the values are larger than for the heavier doped samples shown in Fig.4 .

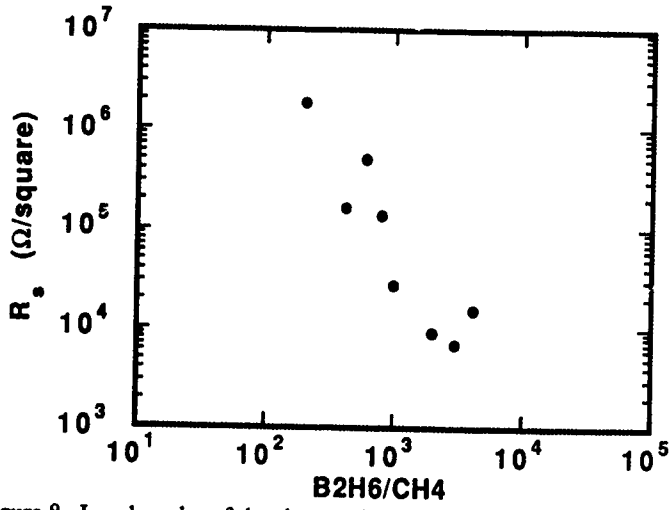



Figure 8. Log-log plot of the sheet resistance of several samples of similar thickness as a function of boron doping. The data shows a linear dependence, with the most heavily doped samples having the lowest sheet resistance.

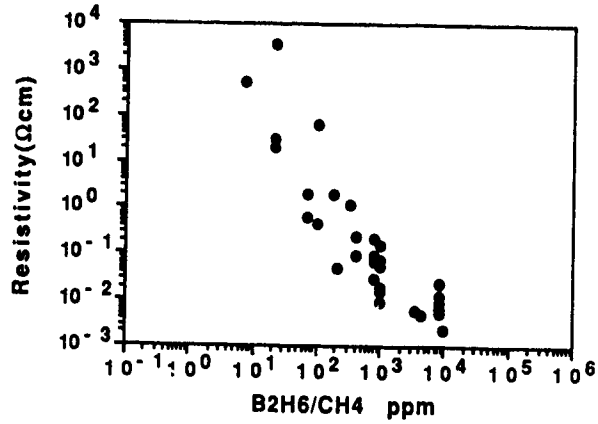



Figure 9. Log-log graph of the resistivity of several boron doped diamond layers as a function of boron doping. The data is fairly linear with an upturn in resistivity at the lower B2H6 to CH4 ratios. This trend at the lower doping ratios is consistent with grain boundary effects.

# THE GROWTH AND SOME PROPERTIES OF DIAMOND FILMS OF P- AND N-TYPE CONDUCTIVITY OBTAINED BY CRYSTALLIZATION FROM THE GAS PHASE

B.V.Spitsyn and A.E.Alexenko, Institute of Physical Chemistry of the USSR Academy of Sciences, Leninsky Prospekt, 31, Moscow 117915, USSR

Geometrical and energy factors determining the entering of substitution impurities into diamond lattice are analysed. Doping with boron, phosphorus, sulphur and lithium are realized during the growth of epitaxial diamond films (DF) on (111) face of natural diamond by high-gradient chemical gas-transport reaction. Semiconducting p-type DF were grown during doping with boron and n-type DF - during the doping with phosphorus and sulphur. Doping with lithium does not decrease the resistance of D . Ways of controlling the concentration and mobility of carriers in DF are discussed.

## 1. Introduction.

The discovery and development of the methods for the diamond synthesis from the vapour phase at low pressure opened new opportunities for preparation of dielectric DF and single microcrystals. At the same time the range of possibilities for control of structure and properties of different diamond materials in the course of their synthesis became much wider.

Since impurity-free and low-defective diamond is known to be a perfect dielectric, the problem of desirable and controllable changing of electrical resistance of diamond is becoming more and more important. Only after the appropriate solution of this problem diamond-based electronic devices of a more sophisticated design may be

developed.

Obviously, there are two ways for tuning electrical properties of diamond. The first way is producing self-defects (not connected with impurites) having different dimensionality, e.g.:-zero (vacancies, interstitials), unity (dislocations), - unity (dislocations), - two (tetrahedral stacking faults), - three (microinclusions of polytype modifications of cubic and hexagonal diamond and/or non-crystalline carbon with tetrahedral configuration of carbon atoms).

The above defects may be generated both in the course of DF and crystal diamond synthesis and by some kind of postsynthesis treatment: physical, mechanical and, possibly, chemical.

Introducing impurities into diamond lattice is the other way for producing electrically controllable diamond. Ion implantation is a well-known technique of diamond doping. However, the cocrystallization of atomically dispersed impurities in the course of diamond crystallization is, obviously, more efficient. We have used this method /1/ under the conditions of the chemical gas-transport reaction /2/.

The epitaxial growth of diamond films, first discovered and studied using the high-temperature high-gradient chemical transport reaction, is being investigated now using a number of other methods of activated chemical crystallization of diamond. Along with the processes of growing pure (non-doped) DF the processes of producing semiconducting diamond films acquire special importance. Their development may contribute largely to the use of DF in solid-state electronic devices of further generations.

Our works on the synthesis of non-doped single and polycrystalline DF were followed by an experimental study of their doping in the process of crystallization. The

use of the chemical transport reaction made it possible to introduce ready-made gaseous dopants, as well as to produce them directly in the crystallization zone.

2. Geometric and energy factors governing diamond doping.

Despite the low value of the covalent radius of the carbon atom (0.77 Å) in the crystal lattice and its high rigidity the number of chemical elements, that are able to give true (equilibrial) solid solutions in diamond, is rather restricted. Much smaller is the number of atom-dispersed impurities, that may produce the levels of permitted energy in the energy gap equal to 5.5 eV.

A general consideration of the resulting equilibrium solid solutions should be accomplished with the analysis of both geometrical and energy factors. The data necessary for estimation of the possibility of different atoms to enter into substitution positions are presented in the table below.

TABLE

Geometric and energy parameters of some single bonds element-carbon

| Element | Covalent radius r, Å | Relative difference of covalent radii $\frac{r_E - r_c}{r_c} \times 100,\%$ | Bond energy E-C, kcal/mol |
|---|---|---|---|
| C | 0.77 | 0 | 82.6 |
| B | 0.85 | +19 | 89 |
| N | 0.70 | -9 | 72.8 |
| S | 1.04 | +31 | 62 |
| P | 1.10 | +43 | 63 |

From the data presented in the table it follows that atoms of impurity elements may have a valency n not equal to four, which is typical of carbon atoms. It is just the case, so the impurity atom in the substitution position may act as a donor (n 4) or an acceptor (n 4), and its bonding with the surrounding carbon atoms will be electron- exessive or electron-deficient, respectively. Thus, the energy values listed in the table may be considered to be a rough estimation. However, according to the data of the table it is possible to suggest, that the introduction of such impurities as nitrogen and boron into the diamond lattice be energetically favourable. This actually takes place.

3. Doping by boron. It was carried out under the conditions of the high-temperature transport reaction in the sandwich system graphite-hydrogen-diamond /3/. The temperature of the graphite source of carbon ranged from 2000 to 2200°C, and the temperature of the substrate- a diamond seed crystal - ranged from 750 to 900°C. The flat parallel gap between the surface of the source and that of the substrate was 0.2-1.5 mm, the total pressure in the gas phase was 12 Torr. The doping of the epitaxial DF by boron occurred with the participation of simple carboranes ($HBC_2$ and $H_2B\text{-}CH_3$) forming on the surface of boron doped graphite placed outside the thermally homogeneous part of the source /3/. The resulting 0.2-2 $\mu$m thick epitaxial DF of p-type conductivity were light-blue and blue, which was due to the absorption band in the visible region related to the presence of impurity boron atoms in the diamond lattice sites. The growth rate of highly doped DF could be 1.5-2 times as much as that observed under the same conditions of crystallization for non-doped DF. One of the reasons for the increase in the growth rate is an additional carbon

flow delivered to the DF by the carboranes. The maximum conductivity of the films and concentration of boron in them were $5.10^2$ $Ohm^{-1}cm^{-1}$ and 2.6 at.%, respectively, exceed greatly the respective values for diamond doped by boron obtained by other methods. The mobility of the current carriers calculated according to the measured values of boron concentration in the DF ($7.6x10^{19}cm^{-3}$) and its conductivity at 300 K could be equal to 50 $cm^2/V.s$.

The doping of both single crystal and polycrystal DF was also carried out under the conditions of electrical activation of the gas phase. Vapors of the ready-made solid compound - neocarborane $C_2B_{10}H_{12}$ were introduced in the crystallization zone. The average concentration of boron in the polycrystalline DF according to the XPS data was 0.1 at.%.

4. Doping by phosphorus, if only the geometric (the covalent radius of the phosphorus atom) and energy ( the bond energy of the C-P) factors were taken into account, seemed hardly possible. Nevertheless, like the case of doping by boron, we managed to obtain positive results using the chemical transport reaction (fig.1). Since volatility of phosphorus is very high, we used a separate evaporator to introduce its vapor in the crystallizing DF. The evaporator was placed in the vicinity of the crystallization zone. Before the experiment a portion of 99.999% red phosphorus was introduced into the evaporator (fig.1). Changing the position of the evaporator with respect to the most heated part of the graphite source, we fixed the required temperature of the evaporator measured using a thermocouple (fig.2). The resulting colourless epitaxial DF had the specific conductivity from $10^{-4}$ to $10^{-1}$ $Ohm^{-1}cm^{-1}$ and the activation energy of conductivity $E_a$ equal to 0.11 and 0.04 at the phosphorus concentrations in DF equal to 0.01 and 1 wt.%,

respectively. It is noteworthy, that at high levels of doping by phosphorus the linear rate of the DF decreased by 3 and more times (fig.3). This, undoubtedly, is related at least partly to the "dilution" of the crystallization medium by phosphorus vapors, whose partial pressure may amount to an appreciable share of the total pressure. The Seebeck coefficient measured on the DF doped by phosphorus was equal to 120 V/K. Its sign points to formation of semiconducting diamond with n-type conductivity.

According to RBS-data most of the boron and phosphorus atoms in p- and n-type DF (at a doping level of 0.1 at.%) occupied substitution positions in the diamond lattice. As regards the general peculiarities, it is necessary to note, that the distribution coefficient for impurity in vapour and diamond phase normally is $\sim 1$ for boron and $\sim$ 1 for phorphorus. The DF obtained recently by M.Kamo et al.[4], who used phosphine $PH_3$ as a source of phosphorus, have much lower conductivity of about $10^{-6}$ $Ohm^{-1}cm^{-1}$. Possibly, the higher conductivity of our DF is due to a relatively low concentration of bonded hydrogen and/or other impurity or intrinsic defects. It is rather probable, that the control of electrically inactive impurities, especially, of bonded hydrogen in DF disclosed the route to more efficient doping by electrically active impurities.

5. The doping of DF by other impurities was studied using lithium and sulphur as an example. High concentrations of lithium (and its compounds) introduced into the growth medium by the evaporation of LiH, did not lead to an apreciable increase in conductivity of the DF. However, the introduction of sulphur vapors in the gas phase allowed films with a conductivity of $10^{-4}$ - $10^{-3}$ $Ohm^{-1}cm^{-1}$ and $E_a$=0.17 eV to be obtained. The difficulty in producing

ohmic contacts to the DF doped by sulphur, probably, points to n-type conductivity of the DF doped by sulphur.

6. Aknowledgement.

The authors thank Dr.G.A.Ramendik and Dr.V.I.Derjiev for measurements of boron and phosphorus contents in DF by the spark-spectroscopy technique. We are endebted to Dr.A.I.Kozlyonkov for X-ray microprobe investigations of the boron concentration in the DF and to Dr.V.S. Kulikauskas for determining the position of boron and phosphorus atoms in vapour-grown DF by the RBS method.

REFERENCES

1. B.V.Spitsyn and A.E.Alexenko. Archivum Nauki o Materialakh, v.7, p.201 (1986).
2. B.V.Spitsyn and A.V.Smolyaninov. USSR authors certificate N 987912. A method of growing diamond layers. File N 1533329/23-26. Filed 21 April 1971.
3. B.V.Spitsyn, G.A.Sokolina, A.E.Alexenko, V.A.Laptev Proc. 2-nd Int.Conf. on New Diamond Science and Technology, Washington, September 1990 (in press).
4. M. Kamo et al., Appl. Surf. Sci. 33/34, 553 (1988)

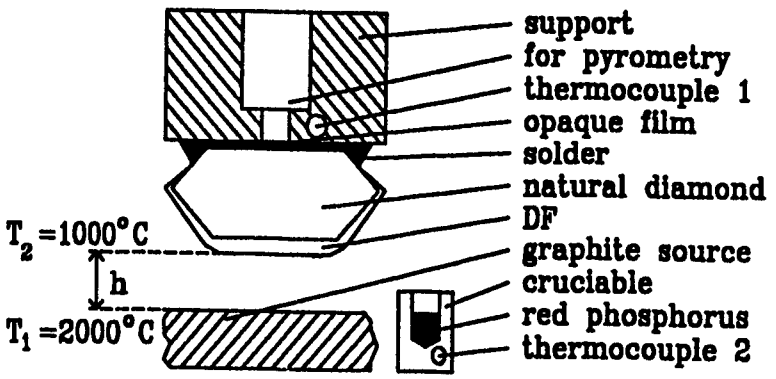



Fig. 1 High-gradient chemical gas transport diamond reactor.

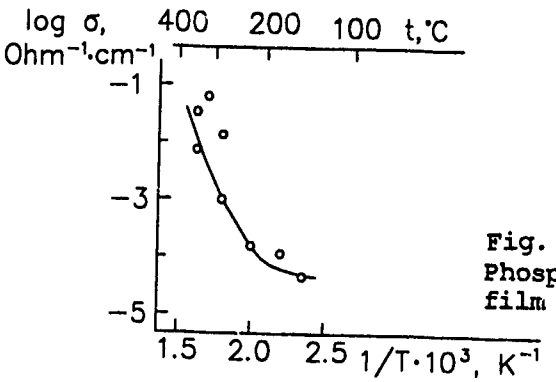



Fig. 2
Phosphorus-doped diamond film conductivity.

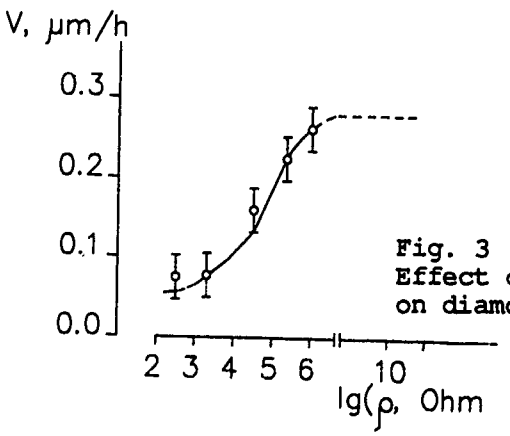



Fig. 3
Effect of phosphorus doping on diamond growth rate.

# PRODUCTION OF LARGE-AREA MOSAIC DIAMOND FILMS APPROACHING SINGLE-CRYSTAL QUALITY

M. W. Geis
Lincoln Laboratory, Massachusetts Institute of Technology
Lexington, Massachusetts 02173-9108

H. I. Smith
Department of Electrical Engineering and Computer Science
Massachusetts Institute of Technology
Cambridge, Massachusetts 02139

A process has been developed to obtain large-area mosaic diamond films approaching single-crystal quality.[1] The technique includes patterned etching of structures in Si substrates, deposition and orientation of diamond seeds in the structures, and chemical vapor deposition overgrowth of the diamond seeds to form a continuous film. Patterned etching of (100)-oriented Si substrates is performed using standard photolithography to obtain 90-$\mu$m-square etch pits, faceted on (111) planes, on 100-$\mu$m centers. Commercially available (111)-faceted diamond seeds, 75 to 100 $\mu$m in diameter, are deposited on the patterned substrates and become fixed and oriented in the etch pits. From optical and x-ray characterization, up to 95% of the pits over an area of several square centimeters contained diamond seeds oriented to within a few degrees of the substrate crystallographic axes. An example distribution of the <100> crystal axes of the seeds about the <100> axis of the Si substrate is shown in Fig. 1. After deposition, homoepitaxial diamond is grown on the seeds to obtain a continuous diamond film.

Figure 2 is an optical micrograph of a diamond-seeded Si substrate before diamond homoepitaxy, and Fig. 3 shows a seeded sample with ~ 240 $\mu$m of homoepitaxial diamond. The stepped surface of the continuous film is the result of variation in the size of the diamond seeds. The film consists of single-crystal diamonds joined by low-angle grain boundaries of a few degrees or less. We believe that such grain boundaries will not affect the electrical properties of majority carrier devices, since similar grain boundaries in Si

films do not affect majority carrier transistors. The crystalline quality of these diamond films is expected to improve with more uniformly shaped, smoother-faceted diamond seeds and with growth techniques better suited for coalescent growth.

Acknowledgment

This work was supported by SDIO/OST through the Office of Naval Research.

Reference

1. M. W. Geis, H. I. Smith, A. Argoit, J. Angus, G.-H. M. Ma, J. T. Glass, J. Butler, C. J. Robinson, R. Pryor, *Appl. Phys. Lett.* **58**, 2485 (1991).

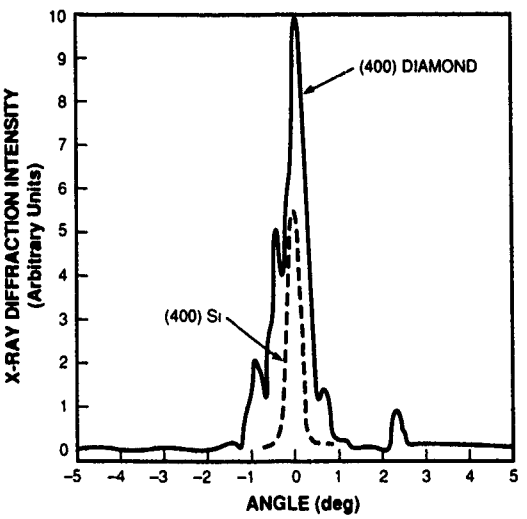



Fig. 1. X-ray diffraction from the (400) planes of diamond seeds on a patterned substrate as a function of the angle between the <400> axis of the Si substrate and the axis bisecting the primary and diffracted x-ray beams. The tip angle, half width at half the maximum x-ray intensity, is ~ 0.35°. The x-ray diffraction from the Si substrate is intended to show the resolution of the system and is not to scale.

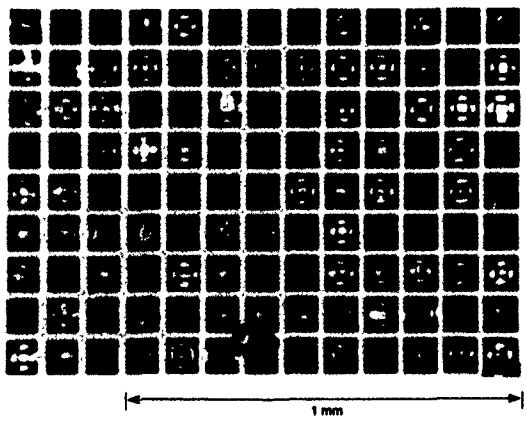



Fig. 2. Optical micrograph of diamond seeds fixed and oriented in square etch pits on a Si substrate. Over 95% of the etch pits are filled with oriented diamond seeds.

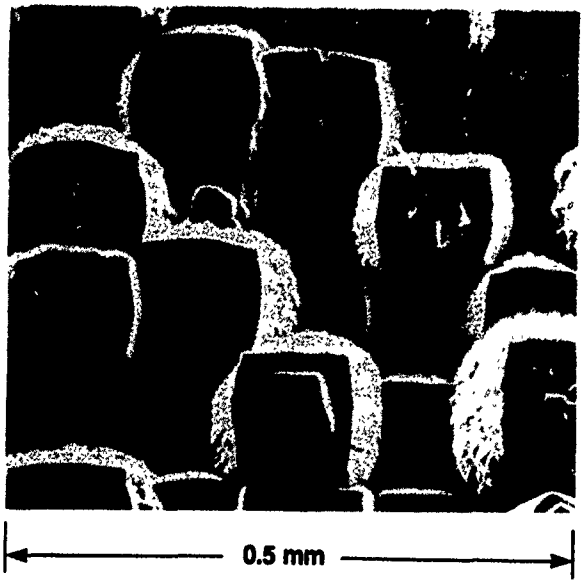



Fig. 3. Scanning electron micrograph after homoepitaxial diamond growth on a substrate similar to that shown in Fig. 2.

# CONSTRUCTION AND CHARACTERIZATION OF A DIAMOND THIN FILM ANEMOMETER

D. A. Jaworske*, C. D. Ellis**, R. Ramesham**, and T. Roppel**
*Lewis Research Center
National Aeronautics and Space Administration
Cleveland, Ohio, 44138-3127
**Electrical Engineering Department
Alabama Microelectronics Science and Technology Center
Auburn University, Alabama, 36849-5201

## ABSTRACT

Diamond films prepared by chemical vapor deposition are finding applications in a number of areas, based on diamond's unique combination of properties such as high thermal conductivity and hardness. This paper describes the use of a diamond film in a gas flow sensor that operates much like a hot-wire anemometer.

## INTRODUCTION

New applications for high quality polycrystalline diamond thin films are now possible owing to recent developments in the selective deposition of diamond on silicon (1-2). One application under consideration is a diamond thin film sensor suitable for measuring gas flow in corrosive and abrasive environments (3). The proposed gas flow sensor utilizes several properties of diamond. The high thermal conductivity of diamond serves to carry heat from a heat source to a heat sink. Gas flow across the surface of the diamond changes the heat balance established in the diamond and these changes are detected by resistors embedded in the silicon below the diamond. The high electrical resistance of the diamond prevents any leakage current across the embedded resistors. Diamond's hardness adds lifetime to the sensor in corrosive or abrasive environments.

This paper summarizes the synthesis and characterization of a first generation diamond film gas flow sensor. The diamond for the sensor was deposited by a microwave plasma chemical vapor deposition technique. Patterning of the diamond was accomplished by selectively oxidizing the silicon surface prior ot diamond deposition. The performance of the sensor conformed to hot-wire anemometry theory, and the thermal responce of the sensor compared favorably to results from a thermal analysis model. The model was used to predict changes in sensor performance with geometry. Improvements in the design of the sensor will also be discussed.

## MATERIALS AND METHODS

The gas flow sensor was similar in design to a constant temperature hot-wire anemometer, with the polycrystalline diamond thin film serving as the active element, as shown in figure 1. The diamond film was deposited between two resistor regions which consisted of boron diffused in silicon. Dual four-point probes were chosen as the configuration for the heat source and heat sink resistors, and they were placed symmetrically about the diamond window so they could be interchanged if necessary. Electrical current passing through one resistor created heat and this heat was conducted along the diamond element to the other resistor. Gas flowing across the surface of the diamond removed heat from the system and altered the temperature of the sensing resistor. Current was added to the heater

resistor to compensate for the decrease in temperature at the sensing resistor, and the added current determined gas flow.

In order to build the gas flow sensor, it was necessary to merge two technologies, the selective deposition process for diamond, and the batch fabrication processes for silicon. For example, the diffused resistors had to be formed before diamond film deposition and the resistor contact pads had to be opened and metallized after diamond film deposition.

Briefly, the heat source and the heat sensor resistors were derived from doping the n-type silicon substrate with boron. Boron-doping was carried out in a two step process, with diffusion of the boron occurring at 1050°C and drive-in of the boron occurring at 1100°C.

Next, the silicon substrate was prepared for the selective deposition of diamond according to the method of Davidson et al. (1). The surface of the silicon was first scratched with 0.25 μm diamond paste. A mixture of dichlorosilane and ammonia gas at 800°C was used to deposit a layer of $Si_3N_4$ over the entire wafer to protect the scratches in the desired areas from the subsequent oxidation. After the $Si_3N_4$ was removed from all areas except those desired for diamond growth, a layer of $SiO_2$ approximately 1 μm thick was grown on the wafer using pyrogenic steam at 1000°C. Removing the remaining nitride opened a window exposing the original scratched area.

The diamond was grown in 4x10 mm exposed regions by microwave plasma chemical vapor deposition using a mixture of hydrogen and methane gas, at a substrate temperature of 900°C. The growth occurred only in the nonoxidized regions. The 1332 $cm^{-1}$ line in the Raman spectrum confirmed the presence of diamond, as shown in figure 2, and an SEM photograph showing the selectivity of this process is shown in figure 3. The as-grown diamond was a continuous film 10 to 20 μm thick.

After diamond growth, contact windows were opened in the oxide region remaining over the resistor contact pads. Next, an array of aluminum pads was defined in order to wire bond to the diffused resistors. The completed device was mounted on a ceramic substrate, and attached to an electrical circuit capable of energizing the heater resistor and measuring the resistance change in the sensing resistor. A completed device is shown in figure 4.

The thermal performance of the device was modeled using TAK2, a thermal analysis program, using the node configuration shown in figure 5a. The thermal response of the model at the node corresponding to the heat sink resistor was matched to the experimental results by varying the input power at the node corresponding to the heat source resistor and by varying the loss of heat due to convection. After matching the response of the model to the experimental results, the response of the flow sensor was evaluated for the ideal case of a free-standing diamond bridge (figure 5b), as a free-standing diamond bridge was unable to be made experimentally.

## RESULTS AND DISCUSSION

The diamond film flow sensor described above is similar, in kind, to a hot-wire anemometer. The relationship between the heater power and the gas flow rate is given by equation 1[4]:

$$I^2R = (t_s - t_g)\,(S)\,[C_1 + C_2\,(\sigma\,V)^{1/2}] \qquad (1)$$

where $t_s$ is the operating temperature of the sensor, $t_g$ is the temperature of the gas, S is the surface area of the hot-wire, $C_1$ and $C_2$ are constants, $\sigma$ is the density of the gas, and V is the velocity of the

gas. The flow sensor works by forcing sufficient current through the heater resistor to maintain a constant temperature at the sensing resistor. According to equation 1, a linear relationship should exist between $I^2$ and $V^{1/2}$.

Heater current and gas flow data for one of the diamond sensors are presented in figure 6. The data are linear up to 5 *l*/min, the highest velocity tested. Although the sensor worked according to theory, several problems surfaced during testing.

In a typical experiment, the current used in the heater resistor was approximately 8 mA. With this current, the resistance of the sensing resistor increased by only 1.5 ohms, and this change occurred after an elapsed time of nearly 60 seconds. Using the temperature coefficient of resistance of the boron-doped resistors, this 1.5 ohm change in resistance corresponded to a change in temperature of about 2°C.

The response time observed for the diamond flow sensor is compared to the response time obtained from the thermal analysis model in figures 7a and 7b. To make the model fit the experimental data, an input power of 15.63 mW was applied to the heat source node and a convective constant of 0.007 $W/cm^2C$, typical of forced air convection, was applied across the top of the entire anemometer. These constants were used for all subsequent modeling calculations. The input power used at the model heat source node was about 28% of the actual input power sent to the resistance heater, suggesting that nearly three quarters of the power was dissipated along the boron-doped regions away from the diamond coating.

The model was changed to reflect a free standing diamond bridge structure, as shown in figure 5b, and the results are summarized in figure 7c. Using this geometry, the response time of the free standing diamond bridge structure was found to be similar to the non-free standing case. Hence, one can conclude that the rate of temperature increase detected by the heat sink resistor must be dominated not by the thermal conductivity of the diamond, but by the thermal capacitance of the silicon being heated by the heat source resistor.

Conventional hot-wire anemometers typically operate at several hundred degrees Celsius, and have a response time on the order of 10 milliseconds (4). Hence, the diamond anemometer described here is considerably less efficient than conventional hot wire anemometers. Part of the problem may be traced to the bulky nature of the chosen geometry, where the large thermal capacitance yields a sluggish response. Decreasing the size of both the diamond and the silicon components would most certainly improve the response time. Further improvements may be derived by using metal components for the heat source and heat sink resistors so that higher temperature operation may be achieved.

## CONCLUSIONS

A first generation diamond gas flow sensor was built by merging two technologies, selective deposition of polycrystalline diamond, and batch fabrication of silicon semiconductors. The performance of the sensor followed conventional hot-wire anemometry theory, but was found to have a slow response time, and was limited by low temperature operation. Future generations of these diamond gas flow sensors will require smaller dimensions and higher temperature operation. Such diamond sensors may prove to be useful and durable in measuring gas flow in corrosive and abrasive environments.

## REFERENCES


1. J. L. Davidson, C. Ellis, and R. Ramesham, J. Electron. Mater., 18, 711 (1989).
2. J. S. Ma, H. Kawarada, T. Yonehara, J. I. Suzuki, J. Wei, Y. Yokota, and A. Hiraki, Appl. Phys. Lett. 55, 1071 (1989).
3. C. Ellis, D. A. Jaworske, R. Ramesham, and T. Roppel, Technical Digest of the IEEE Solid-State Sensor and Actuator Workshop, Hilton Head Island, SC, pp 132-134, 1990.
4. T. Sasayama, T. Hirayama, M. Amano, S. Sakamoto, M. Miki, Y. Nishimura, and S. Ueno, Sensors and Actuators, SP-511, pp 87-94, 1982.

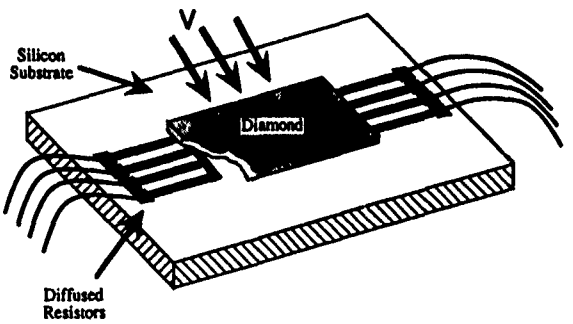



Figure 1. Schematic diagram of the diamond gas flow sensor.

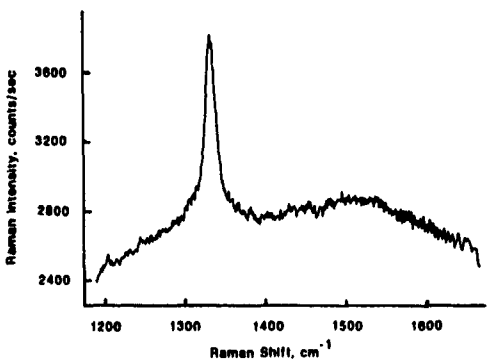



Figure 2. Raman spectrum of the diamond film showing the characteristic peak at 1332 $cm^{-1}$.



Figure 3. Scanning electron micrograph showing the selective deposition of diamond films.

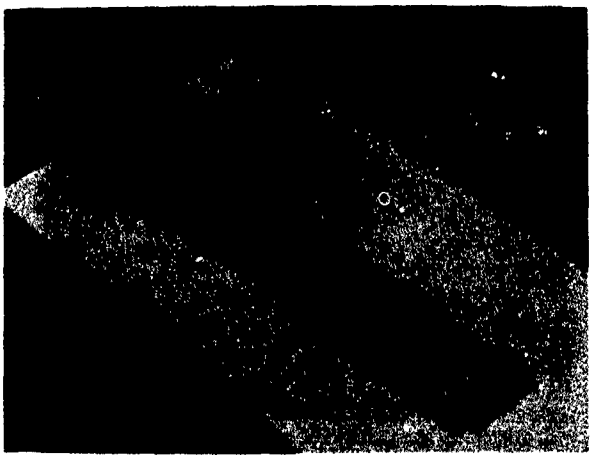


Figure 4. Complete diamond heat flow sensor, attached to a ceramic substrate.

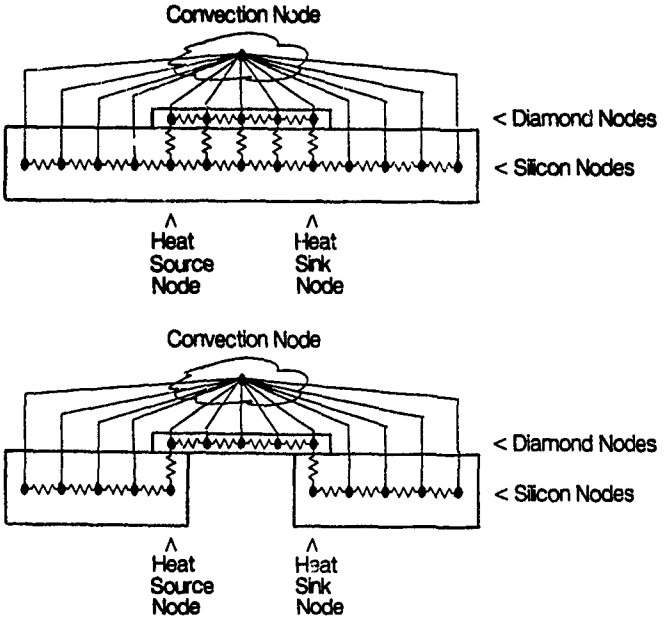



Figure 5. Node configuration used for modeling the heat transfer in the diamond anemometer, (a) node assignment for experimental prototype, (b) node assignment for free-standing design.

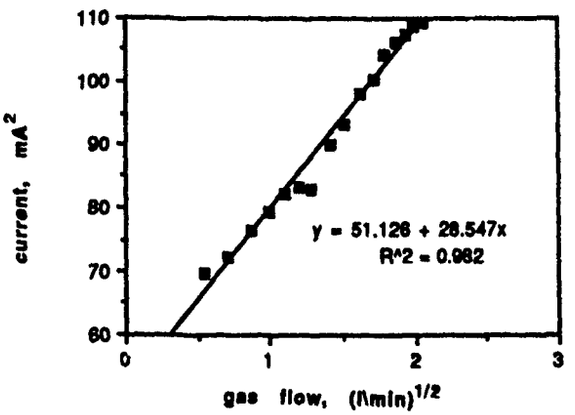



Figure 6. Gas flow velocity versus current, according to hot-wire anemometer theory.

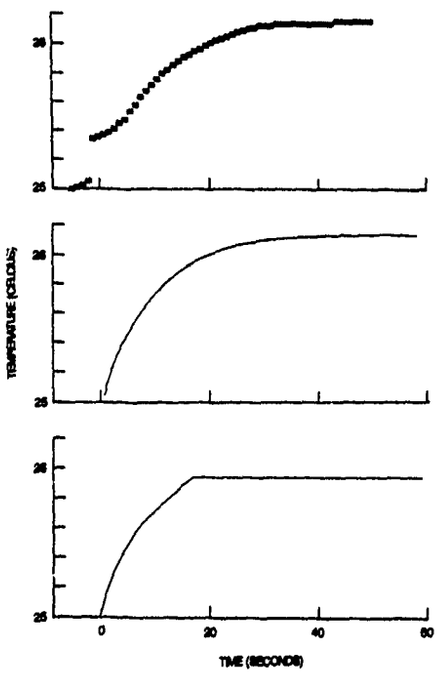



Figure 7. Response time of the diamond anemometer, as measured by the change in resistance of the heat sink resistor, (a) experimental data, (b) experimental prototype model, and (c) free-standing design model.

# FABRICATION OF MICROCHANNELS IN SYNTHETIC POLYCRYSTALLINE DIAMOND THIN FILMS FOR HEAT SINKING APPLICATIONS

R. Ramesham, T. Roppel, C. Ellis, and M.F. Rose#

Electrical Engineering Department
Alabama Microelectronics Science and Technology Center
Auburn University, AL 36849-5201

#Space Power Institute
Auburn University, AL 36849-5320

## ABSTRACT

A novel process for the formation of microchannels in synthetic polycrystalline diamond thin film on a single crystal silicon substrate is developed using anisotropic chemical etching of silicon and selective growth of diamond. The polycrystalline diamond thin films were grown by high pressure microwave plasma assisted chemical vapor deposition using a gas mixture of methane and hydrogen gases. Fabrication procedure, scanning electron microscopy views of surface morphology, cross-sectional features of microchannels in polycrystalline diamond thin films, and potential applications of microchannels are described.

## INTRODUCTION

The thermal conductivity of natural diamond, 20 W/cm-°K, is 4.65 times that of copper. Copper has been widely used as a heat sink material for electronics packaging technology. However, the prospect of an insulating heat sink offers significant advantages for hybrid microelectronics packaging and other applications. Thus the high thermal conductivity of diamond makes this material very attractive for a wide range of heat sink applications.

The highest thermal conductivity of chemical vapor deposited (CVD) diamond thin films obtained so far was about 10 W/cm-°K, which is ~2.3 times that of copper (1,2). If the films used in heat sinking applications are of the same or better quality, then a significant improvement in heat dissipation is possible if diligent steps are taken to reduce interfacial thermal resistance (device/diamond). This could lead to an effective and compact technique for heat removal from high power electronic devices.

Recently, there has been considerable interest in convective heat-transfer microstructures for cooling of silicon chips wherein liquid (water etc.) or gas flows through microchannels etched in the backside of silicon wafers (3-6). Heat dissipation from chips of various sizes is effective, with little rise in temperature for the device during service. Similarly, microchannels in polycrystalline diamond thin films may be used for forced gas or liquid cooling of planar integrated circuits to dissipate the heat in the device to achieve compact, high-performance characteristics (better than copper, silicon, etc.).

Figure 1 shows schematically the microchannels fabricated in polycrystalline synthetic diamond thin films on a silicon substrate with the attached high power density electronic device on the diamond. A prerequisite for building such a structure to use the high thermal conductivity is to develop a process to fabricate microchannels in synthetic diamond thin films.

## EXPERIMENTAL PROCEDURE

Starting substrates were n-type silicon wafers, 5 cm in diameter, (100) orientation, polished on both sides, and with a resistivity of 2-6 ohm-cm. They were manually scratched only on the top side using diamond paste, 0.25 μm mean particle size. The wafers were then washed in running DI water for 10 minutes, rinsed with methanol, ultrasonically agitated in DI water for 10 minutes, and dried with nitrogen. Silicon nitride was then deposited, thickness = ~0.2 μm, using a low pressure chemical vapor deposition (LPCVD) technique with dichlorosilane and ammonia at a substrate temperature of 800°C. The silicon nitride was then photolithographically patterned, plasma etched in $CF_4/O_2$ (10:1), and then the photoresist was removed with acetone. With the nitride patterned, the exposed silicon area was etched in KOH solution to form 30-50 μm deep microchannels in the silicon. The silicon wafers were then thermally oxidized using pyrogenic steam at 1000°C for 45 hours to form a silicon dioxide thickness of 1.5 - 2.0 μm. The oxidized wafers were immersed in a buffered oxide etch ($NH_4F$ + HF) for 30 seconds to remove a thin layer of oxide on the silicon nitride, then rinsed in running DI water for 15 minutes. The silicon nitride was completely etched in hot phosphoric acid (~180°C), washed with running DI water for 10 minutes, rinsed with acetone, and methanol, and dried in nitrogen.

To supplement this process description for selective

diamond deposition (7,8) and microchannel formation in polycrystalline diamond, a schematic process flow is shown in Figure 2. An enlargement of step VIII in Figure 2a is shown in Figure 2b. The lateral growth of diamond was anticipated as shown in Figure 2b with dashed profile lines. The width and thickness of the diamond "stripe" inside the dashed line is proportional to the diamond deposition time. Over a period of time during diamond deposition, neighboring diamond stripes merge together, resulting in a continuous diamond surface on the silicon substrate.

A commercially available high pressure microwave plasma-assisted CVD system (Applied Science and Technology, Inc., Cambridge, MA) was used in our experiments to grow the polycrystalline diamond thin films. Typical deposition parameters are: base pressure: $10^{-6}$ Torr; deposition pressure: 60 Torr; substrate temperature: 930-950°C; hydrogen flow rate: 500 SCCM; methane flow rate: 3.6 SCCM; forward power: 1200-1250 watts; reflected power: <100 watts; deposition time: 139 hours. The deposition rate was typically 1 μm/hour at the temperature mentioned.

## RESULTS AND DISCUSSION

Figure 3a is a scanning electron micrograph of a selectively deposited diamond (deposition time: 24 hours) on a silicon substrate and (b) the magnified view in the microchannel area. Well faceted diamond and the lateral growth from the desired pattern are quite clearly seen in Figure 3b. Figure 3c is the morphology of the top side of the diamond film after all the selectively deposited polycrystalline diamond areas have impinged. The thickness of polycrystalline diamond film is about 80 - 100 μm. Total deposition time to obtain a continuous diamond surface depends on the channel separation distance. In Figure 3 the channel width is 75 μm and the separation is 225 μm. The diamond deposition time was 139 hrs.

As predicted by Figure 2, the distance between diamond stripes decreases as a function of the time of diamond deposition. Eventually they impinge on the top portion of the diamond thin film but leave open space underneath, forming microchannels with the aid of intentionally etched silicon areas between selectively deposited diamond areas.

An experiment was started with a reduced microchannel width (17 ± 1 μm). Figure 4 shows the measured microchannel width as a function of time of deposition of polycrystalline

diamond. This plot clearly shows that lateral growth is very high initially but reduces asymptotically to nearly zero.

Figure 5 is a scanning electron micrograph of a cross-section of a microchannel in diamond on a silicon substrate. The channel is an open space underneath the diamond between two selective diamond deposition areas. The contour of the diamond growth within the channel is clearly similar to that anticipated. The dashed lines in Figure 2b may now be visualized to understand the growth of diamond.

The diamond film was removed from the silicon surface and the morphology of the microchannels on the backside of the polycrystalline diamond thin film was observed. Figure 6 is a magnified view of a single microchannel in the polycrystalline diamond. The edge of the microchannels in the diamond film has the opposite slope of the silicon etch area.

Figure 7 shows an optical micrograph of the top view of the complete device of fabricated microchannels in synthetic polycrystalline diamond on silicon substrate. Size of the device is 1.9 cm x 1.9 cm. The two transparent rectangular regions in the micrograph are free-standing polycrystalline diamond where silicon is etched from the backside to provide inlet and exhaust plenums for the coolant fluid.

Figure 8 shows an optical micrograph of polycrystalline diamond thin film cantilever beams (one side supported) on a single crystal silicon substrate. This structure has been designed for thermal diffusivity studies of the polycrystalline diamond, in which a high wattage laser is focused on a beam end, while the transient thermal response is measured using spatially resolved IR spectroscopy.

Efforts are underway to reduce internal stress in the polycrystalline diamond thin films, thereby improving adhesion strength, by growing diamond at lowered substrate temperatures (9). Additional efforts include optimizing deposition parameters to obtain the highest possible thermal conductivity (and high electrical resistivity) in the as-grown thin films by reducing nitrogen and other impurities such as graphite, amorphous carbon, etc., identifying suitable bonding materials to interface active devices to the diamond microchannel heat sink., investigating potential coolant gases to flow through the microchannels to maximize heat transfer, optimization of the microchannel cross-section dimensions as well as the channel depth to channel spacing ratio for maximum cooling efficiency (10).

In summary, a novel process has been developed and demonstrated to fabricate microchannels in polycrystalline diamond thin films on a silicon substrate using selective growth of diamond for heat sink applications. Free standing polycrystalline diamond cantilever beams have been fabricated to characterize thermal conductivity properties.

## ACKNOWLEDGEMENTS

This work was supported in part by the Strategic Defense Initiative Organization's Office of Innovative Science and Technology (SDIO/TNI) through Navy Contract #N60921-86-C-A226 with the Naval Surface Warfare Center and in part by the Alabama Microelectronics Science and Technology Center.

## REFERENCES

1. A. Ono, T. Baba, H. Funamoto, and A. Nishikawa, **Jpn. J. Appl. Phys.**, 25, L808 (1986).

2. D.T. Morelli, C.P. Beetz, and T.A. Perry, **J. Appl. Phys.**, 64, 3063 (1988).

3. D.B. Tuckerman and R.F.W. Pease, **IEEE Electron Dev. Lett.**, EDL-2, 126 (1981).

4. R.J. Phillips, **The Lincoln Laboratory J.**, 1, 31 (1988).

5. M. Mahalingam, **Proc. IEEE.**, 73, 1396 (1985).

6. N. Goldberg, **IEEE. Trans. Components, Hybrids, Manufacturing Technol.**, CHMT-7, 154 (1984).

7. J.L. Davidson, R. Ramesham, and C. Ellis, **Fourth Annual SDIO/IST-ONR Diamond Technology Initiative Symposium**, Crystal City, VA, Paper #TP3 (1989).

8. J.L. Davidson, C. Ellis, and R. Ramesham, **J. Electron. Mater.**, 18, 711 (1989).

9. R. Ramesham, C. Ellis, T. Roppel, D.A. Jaworske, and W. Baugh, **J. Mater. Res.**, **June 1991 (In Press)**.

10. W. Anacker, **IBM Tech. Disclosure Bulletin**, 20, 3742 (1978).

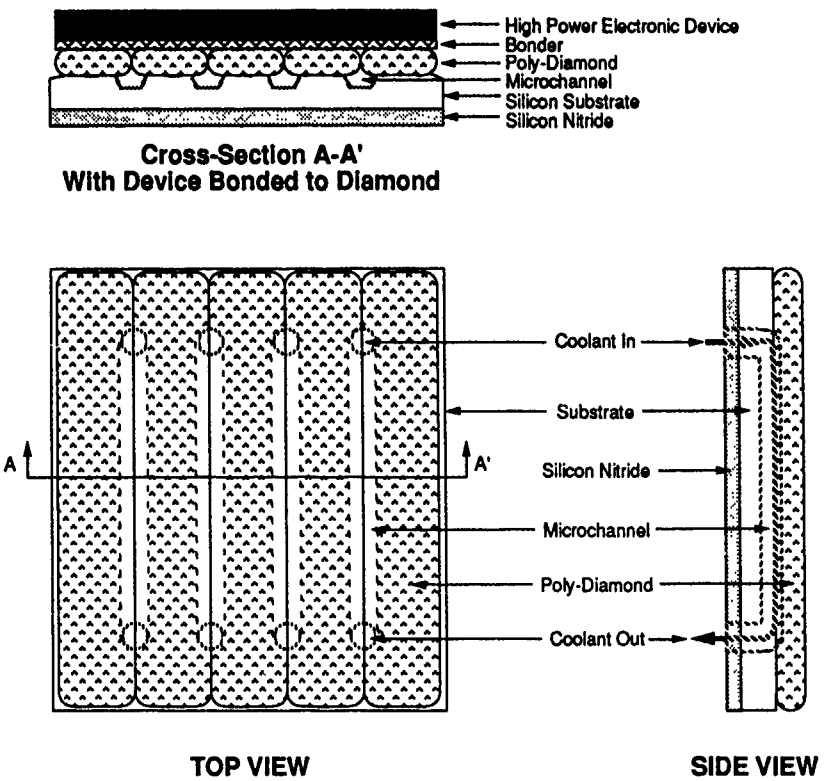



**Figure 1.** Schematic diagram showing several views of microchannels fabricated in polycrystalline synthetic diamond film on a silicon substrate.

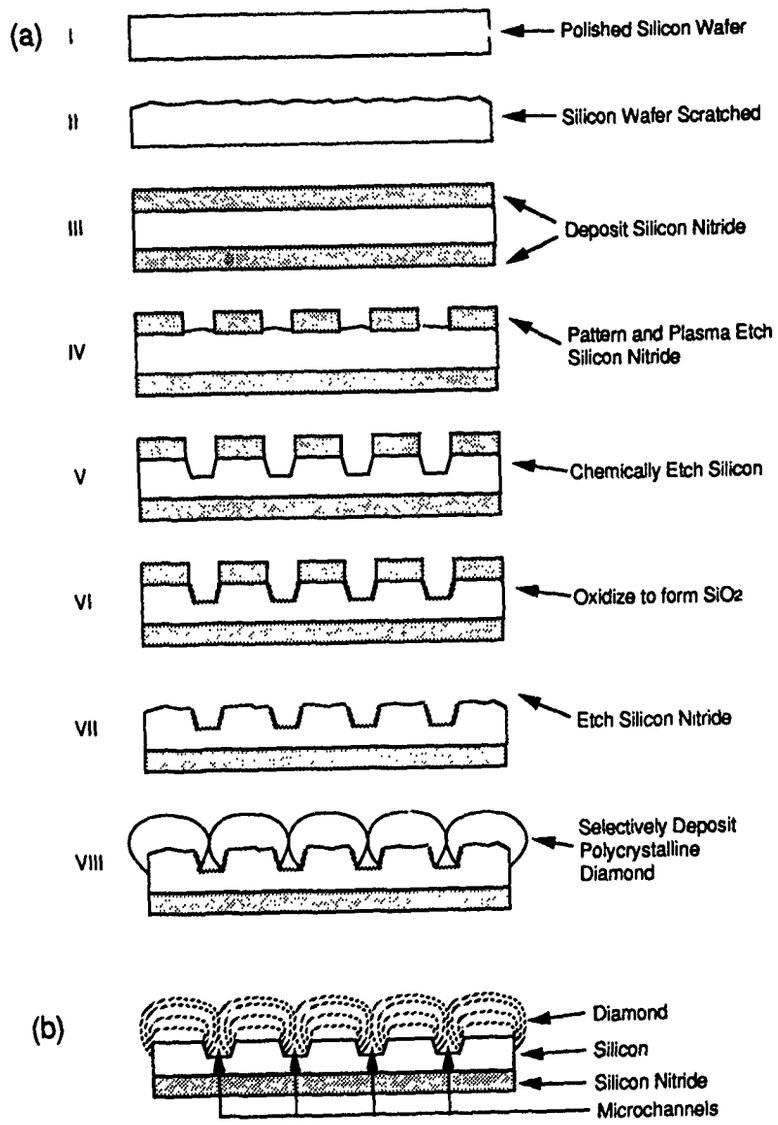



**Figure 2. (a) Schematic diagram of the process flow steps to form microchannels in polycrystalline diamond thin films on a silicon substrate and (b) Detail of step VII in Figure 2a.**

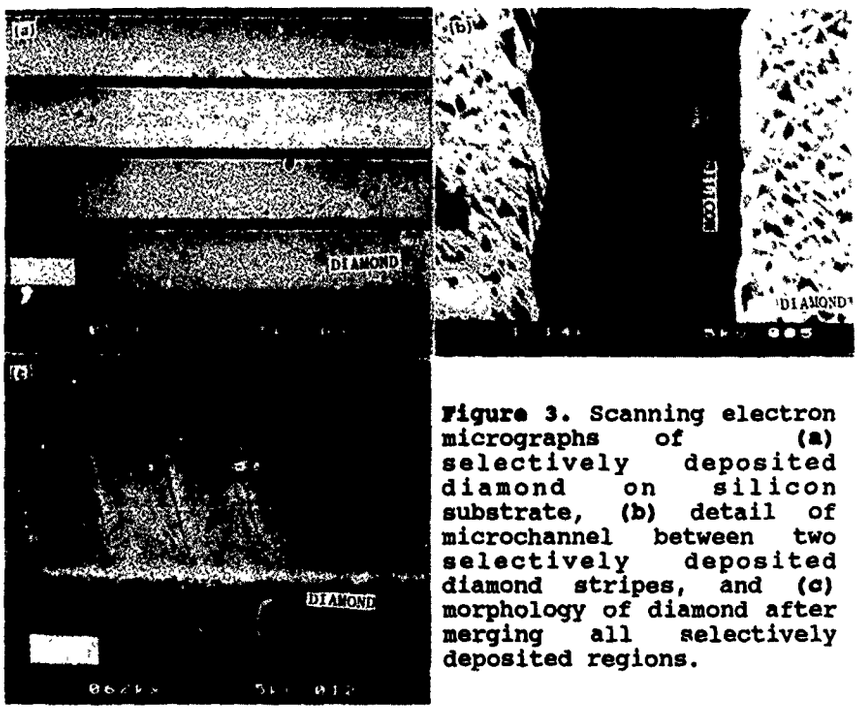



**Figure 3.** Scanning electron micrographs of (a) selectively deposited diamond on silicon substrate, (b) detail of microchannel between two selectively deposited diamond stripes, and (c) morphology of diamond after merging all selectively deposited regions.

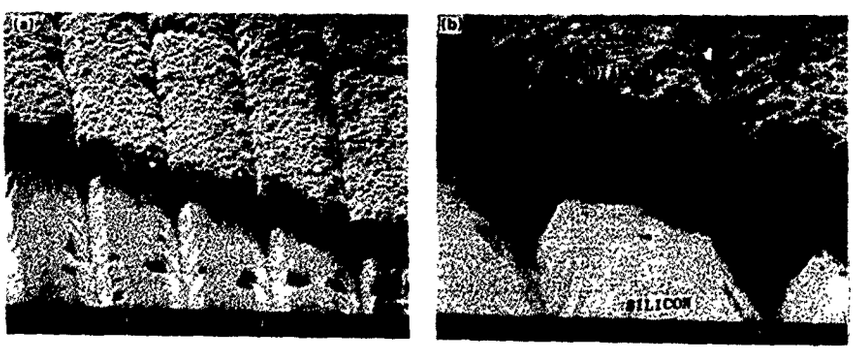



**Figure 4.** Scanning electron micrograph of cross-section of as-grown polycrystalline diamond microchannels on a silicon substrate.

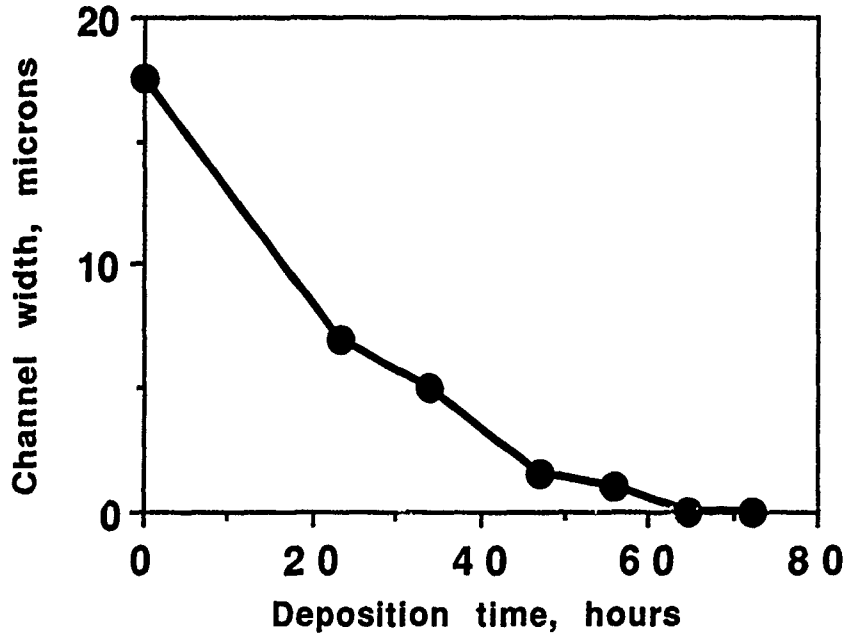



**Figure 5.** Measured microchannel width (distance between two diamond lines) as a function of time of deposition of polycrystalline diamond.

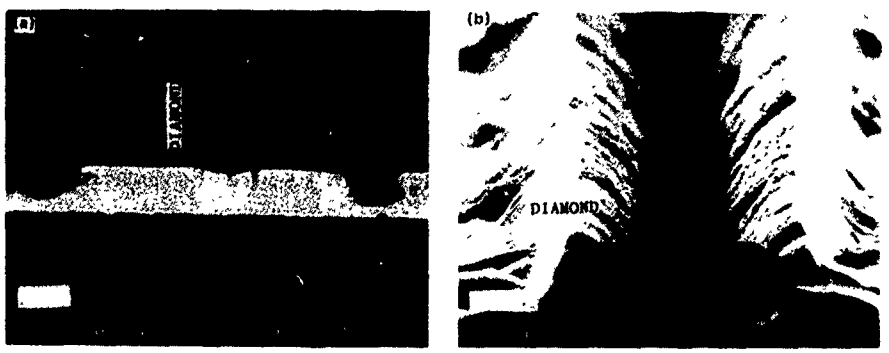



**Figure 6.** Scanning electron micrograph of the backside of the polycrystalline diamond microchannel after the silicon substrate is chemically etched.

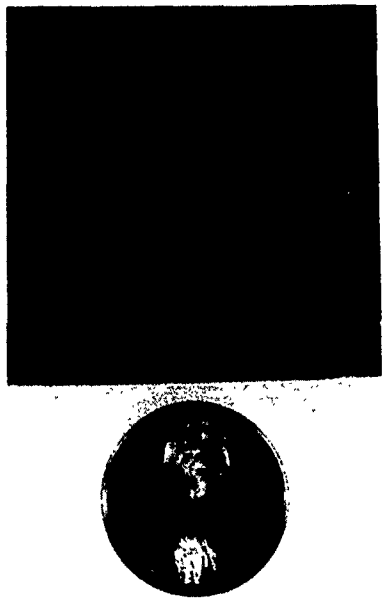


**Figure 7.** Optical micrograph of the complete device of the fabricated microchannels in polycrystalline diamond on silicon substrate (Top view, size: 1.9 cm x 1.9 cm). Transparent two rectangular free-standing diamond areas.



**Figure 8.** Optical micrograph of polycrystalline diamond cantilever beams (one side supported).

# NEW MATERIAL FOR ELECTRONIC PACKAGING: DIAMOND THIN FILMS BY CHEMICAL VAPOR DEPOSITION

M. Buck, T.J. Chuang, H. Seki and M. Anschel*
*IBM Corporation, East Fishkill Facility,
Hopewell Junction, New York 12533-0999
IBM Research Division, Almaden Research Center
650 Harry Road, San Jose, California 95120-6099

One of the important considerations in electronic packaging is the dissipation of heat generated by the electronic devices and their interconnections. Diamond has a unique combination of highly desirable properties, i.e., high thermal conductivity combined with high electrical insulation, chemical inertness, hardness and optical transparency. In our program seeking new materials for electronic packaging, diamond films have been deposited on silicon and quartz using chemical vapor deposition (CVD). Two CVD techniques were studied. Following established practice, uniform diamond films were grown from low methane concentrations in hydrogen gas using hot filament CVD. In another method of microwave plasma assisted CVD, it was found that diamonds of relatively high purity are obtained using methanol without additional hydrogen, in contrast to the general notion that excess hydrogen is necessary.

## INTRODUCTION

Most power intensive semiconductors require enhanced thermal dissipation to lower their junction temperature to acceptable levels. This involves the heat from a source, usually a semiconductor chip, to be transferred to a sink, usually an air cooled, finned heatsink. Generally, electrically insulating adhesives with thermal conductivity of approx. 1.1 W/m°C are used as the internal thermal enhancement. This conductivity could be improved upon by a factor of seven (silver-epoxy) to eighty (silver-solder). However, most or all of these higher conductivity adhesives are electrically conductive. Therefore, if the inactive side of the chip is held to some electrical potential or the chip requires isolation from electrostatic discharge, the metal doped adhesives fail to meet a basic criteria for selection. Polycrystalline diamond thin films can provide a thermal enhancement path that has high thermal conductivity and excellent electrical insulation/isolation between the source and sink (1).

In addition, worldwide interest in diamond films arises because of its very low coefficient of friction and wear rate which is well known in tribology, as well as, the unique optical (uv-vis-ir transparency) properties with chemical inertness.

Polycrystalline diamond films can be deposited on various substrates by plasma-assisted chemical vapor deposition (PACVD) or by hot filament chemical vapor deposition (HFCVD) (2). Both methods were applied in this work using different feed gases. The quality of the diamond deposits was determined by Raman spectroscopy i.e., the sharpness of the 1332 $cm^{-1}$ diamond band and the background level as an indication of the amount of non-diamond carbon.

## EXPERIMENTAL

The hot filament chamber consisting of UHV components was pumped by a mechanical pump to a base pressure of 1Pa. A tungsten coil about 12mm in length and 3mm in diameter was used and kept at a distance of 4mm from the substrate during deposition. If the hot filament is exposed to the mixture of hydrogen and methane, it changes chemically and becomes very brittle. Therefore, care was taken to isolate the reaction chamber vibrationally from the mechanical pump. During deposition the temperature of the filament was 2000-2200°C measured with a pyrometer. At a pressure between 5.3kPa and 6kPa this was sufficient to heat the substrate up to that temperature required for the diamond deposition. The temperature on the substrate was not measured directly on the substrate but with a thermocouple attached close to the edge of the substrate. Therefore, the measured temperatures were systematically lower than the true substrate temperatures. Nevertheless, this arrangement was sufficient to enable reproducible depositions.

The microwave deposition chamber was designed similar to that described by Meiners, et.al. (3). The cavity was made of brass with an inner diameter of 203mm and an adjustable length of 63mm to 130mm. A 22.5mm o.d. quartz tube was set at the center of the cavity passing the two end plates. The magnetron was mounted in the wall of the cavity. To prevent leakage of microwave radiation lead foil was put between the cavity wall and the magnetron housing. The components to generate the microwave radiation were taken from a portable 600W microwave oven operating at 2.45GHz. An additional variable transformer was used for adjusting the power input to the magnetron.

The substrate holder consisted basically of an alumina ceramic rod 12.7mm in diameter and was placed inside the cavity to enable the plasma to reach the substrate. With two molybdenum clamps the substrate was attached to the holder. A chromel-alumel thermocouple was attached on top of the substrate. Those parts of the thermocouple exposed to the microwave radiation were shielded by thin alumina tubes to prevent the thin wires from burning through. The reaction cell was pumped by a mechanical pump and therefore, the base pressure was about 1Pa. The leak rate of the system was smaller than 0.01sccm compared to a gas flow of 50-100sccm during deposition. The flow was controlled by Vacuum General mass flow sensors. Typical deposition pressure was 6.6-8kPa.

A common observation in diamond deposition is that the substrate has to be roughened. The quartz and silicon substrates were scratched with a diamond tip or mechanically polished with 3um diamond powder. The feed gases used were high purity hydrogen (Liquid Carbonics, 99.9%), methane (Matheson, 99.9%) and methanol (Baxter, water content less than .009%). The deposition procedure was as follows. First, the substrate was heated up to the required temperature in a pure hydrogen atmosphere and in the case of pure methanol in a pure helium atmosphere. Then the methane was added or the helium was replaced by methanol.

## RESULTS AND DISCUSSION

Fig. 1a shows a SEM micrograph of a diamond film deposited by HFCVD at a measured temperature of 750°C. Silicon was used as a substrate. The gas mixture was 1% methane in hydrogen. The facets of the diamond crystals, together with twinning and dislocations, can clearly be seen. The cross section of the same film is depicted in Fig. 1b. The film with a thickness of 7um is dense containing many grain boundaries. Fig. 2 shows the corresponding Raman spectrum. No other peak than the typical diamond peak appears indicating a very pure diamond film. The peak position of the band is at 1333cm$^{-1}$ with a line width of 8cm$^{-1}$. The wave-like structure of the background is an artifact caused by the Raman spectrometer. In our present experimental arrangement, which is focused primarily on the investigation of the basic mechanisms of diamond deposition, only an area of 1cm in diameter was covered. For technical applications it should be no problem to cover larger areas by simply changing the filament arrangement and/or translating the substrate.

Fig. 3 shows a Raman spectrum of a diamond film deposited on quartz. The experiment was carried out with pure methanol in the microwave deposition chamber. The microscope reveals well faceted crystals with a size of 8-10um. The deposition time was about 1 hr. at a temperature of 850°C. The sharp peak at $1332cm^{-1}$, which is characteristic for diamond, clearly dominates this spectrum. The halfwidth of the peak is about $9cm^{-1}$. This is considerably larger than the value of about $2cm^{-1}$ found for natural or high pressure diamonds. No graphitic peak can be seen in this spectrum which should appear at about $1580cm^{-1}$. The background and the broad band around $1520cm^{-1}$ can be caused by amorphous structures, graphitic carbon and microcrystallinic effects. This background structure is basically the same as in the so called diamond-like carbon films which do not show the characteristic diamond peak, but have some properties similar to diamond i.e., hardness or electrical resistivity. For a detailed discussion of the characterization of diamond films with Raman spectroscopy the reader is referred to (4). The spectrum shown here is representative for most of the substrate area. Due to inhomogeneities in the plasma and temperature gradients on the substrate the deposition was not uniform over the whole substrate area. Depending on the areas, the background level of the spectra differed, and generally, the linewidth of the diamond band decreased with the background level down as low as $5cm^{-1}$.

The spectrum of Fig. 2 is interesting because it represents a deposition using pure methanol. Use of organic compounds other than methane has been reported in the literature. In those cases the gases were always mixed with an excess amount of hydrogen (5,6). This excess of hydrogen is generally considered to be essential for the deposition of diamond films because of its selective etching of graphite (7). Another role ascribed to hydrogen is to maintain the $sp^3$ hybridization of the unreconstructed diamond surface by reacting with the surface dangling bonds (8). On the other hand, it has been observed that the addition of oxygen can improve the deposition of diamond (9-11). Our result is consistent with the work of Tanabe et al.(12), who also found that diamond films could be deposited from a mixture of $O_2$-$CH_4$ without additional hydrogen.

## CONCLUSION

This work presents results of diamond deposition carried out with both a microwave plasma deposition chamber and a hot filament reactors both of which can be scaled up to deposit larger areas. It is also shown that high quality diamond films can be grown using only an oxygen containing hydrocarbon. Lateral thermal conductivity measurements of diamond films reported so far (13,14) indicate that high quality diamond films, inspite of their polycrystalline structures, can have conductivity level higher than that of copper at room temperature Thus, indications are that diamond films can play a significant role in electronic packaging.

Despite the fact that very pure diamond films can be grown, the SEM micrographs show a problem which is presently limiting some of the technical applications of diamond films. In order to obtain smooth films the nucleation sites on the substrate have to be very dense. Up to now, it is not clear what factors influence the nucleation. Roughening the substrate has been found to promote nucleation but it leads to a microscopically rough diamond surface. Successful attempts to grow diamond epitaxially have been reported only on diamond substrates (7). Reports of heteroepitaxy of diamond films (15) have started to appear but the area is still quite limited. Another problem which must be overcome is the adhesion of the films to the substrate. In the case of diamond on silicon, the films showed good adhesion and no cracks, but uniform deposition directly on quartz turns out to be difficult. The films show cracks and above a thickness of a few micrometers the film can peel off. Future experiments have to be focused on the early stage of nucleation in order to get an understanding of the important initial steps of diamond deposition which determine the properties of the film.

## ACKNOWLEDGEMENT

The authors wish to thank Hal Rosen for taking the Raman spectrum shown in Fig. 2.

## REFERENCES


1. Anschel, M. and Sammakia, B.G., U.S. Patent No.4, 914, 551, April 3, 1990.
2. Angus, J.C., and Hayman, C.C., Low-Pressure, Metastable Growth of Diamond and "Diamondlike" Phases, Science, 241, 913, (1988).
3. Meiners, L.G., and Alford, D.B., Simple Low-cost Microwave Plasma Source, Rev. Sci. Instr., 57, 164, (1986).
4. Knight, D.S., and White, W.B., Characterization of Diamond Films by Raman Spectroscopy, J. Mater. Res., 4, 385, (1989).
5. Hirose, Y., and Teresawa, Y., Synthesis of Diamond Thin Films by Thermal CVD Using Organic Compounds, Jap. J. Appl. Phys., 25, L519, (1986).
6. Watanabe, I., and Sugata, K., Diamond Films Synthesized by Microwave Plasma CVD of Ethyl Alcohol, etc., Jap. J. Appl. Phys., 27, 1997, (1988).
7. Spitsyn, B.V., Bouilov, L.L., and Derjaguin, B.V., Vapor Growth of Diamond on Diamond and Other Surfaces, J. Cryst. Growth, 52, 219, (1981).
8. Waclawski, B.J., Pierce, D T., Swanson, N., and Celotta, R.J., Direct Verification of Hydrogen Termination of the Semiconducting Diamond (111) Surface, J. Vac. Sci. Technolo., 21, 368, (1982).
9. Chang, C.P., Flamm, D.L., Ibbotson, D.E., and Mucha, J.A., Diamond Crystal Growth by Plasma Chemical Vapor Deposition, J. Appl. Phys. 63, 1744 (1988).
10. Kawata, T., and Kondo, K., Effects of Oxygen on CVD Diamond Synthesis, Jap. J. Appl. Phys., 26, 1429, (1987).
11. Watanabe, I., and Sugata, K., Diamond Films Synthesized by Microwave Plasma CVD, Jap. J. Appl. Phys., 27, 1397, (1988).
12. Tanabe, T., Nishibayashi, Y., Imai, T., Ikegaya, A., and Fujimori, N., Deposition of Diamond Thin Film From the $O_2$-$CH_4$ System, Int. Conf. New Diamond Sci. Technolo., paper 1-13, (1988).
13. Ono, A., Baba, T., Funamoto, H., and Nishikawa, A., Thermal Conductivity of Diamond Films Synthesized by Microwave Plasma CVD, Jap. J. Appl. Phys., 25, L808, (1986).
14. Morelli, D.T., Beetz, C.P., and Perry, T.A., Thermal Conductivity of Synthetic Diamond Films, J. Appl. Phys., 64, 3063, (1988).
15. Narayan, J., Srivatsa, A.R., Peters, M., Yokota, S., and Ravi, K.V., On Epitaxial Growth of Diamond Films on (100) Silicon Substrates, Appl. Phys. Lett., 53, 1823, (1988).

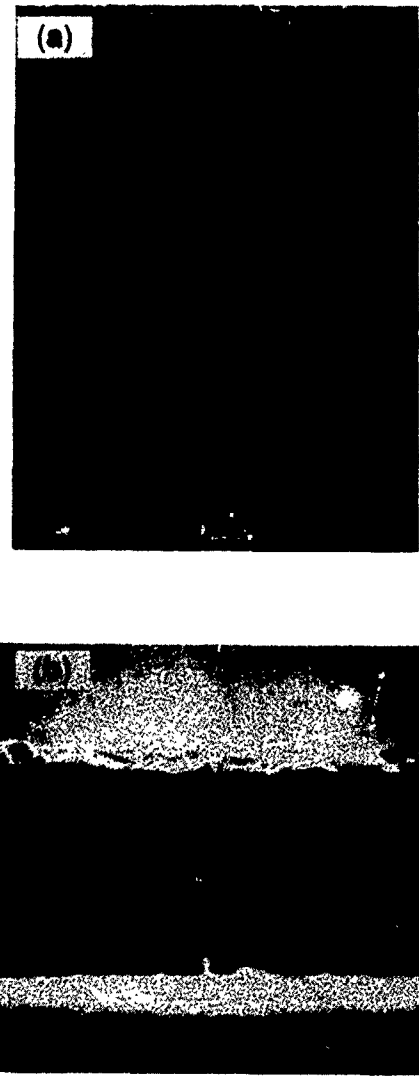



Fig. 1 a) SEM micrograph of a diamond film on silicon obtained by HFCVD with a mixture of 1% methane in hydrogen. b) The cross section of the film. The film thickness is 7 μm.

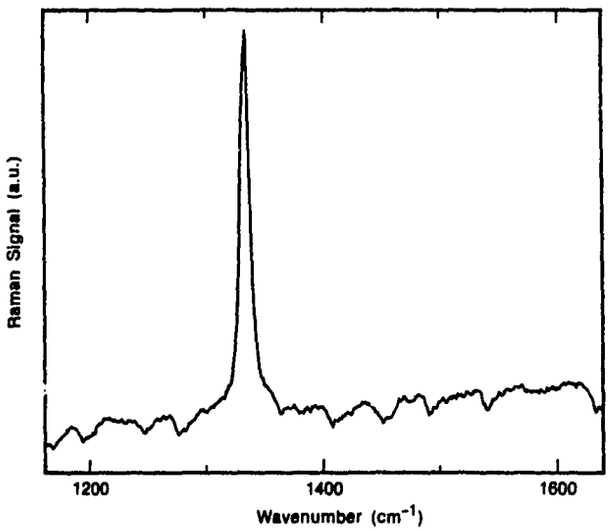



Fig. 2 Raman spectrum of the diamond film shown in Fig. 1.

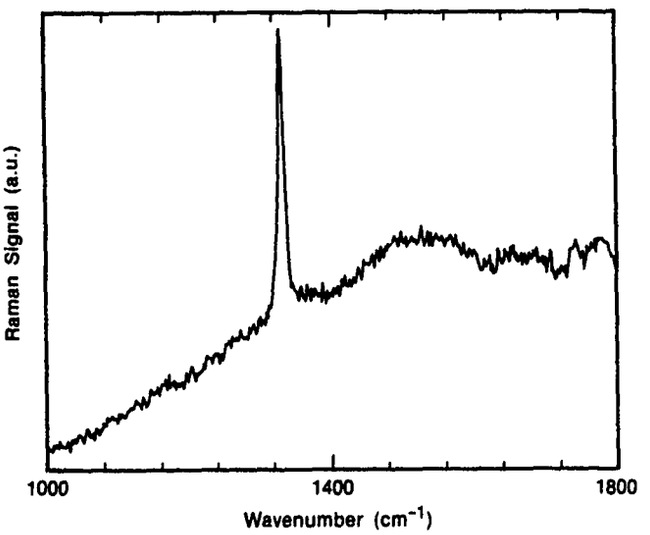



Fig. 3 Raman spectrum of diamond crystallites deposited from methanol in a microwave plasma CVD.

# PROGRESS IN THE DIAMOND FILM RESEARCH AT UT DALLAS

F. Davanloo, D. R. Jander, T. J. Lee,
H. Park, J. H. You, and C. B. Collins

University of Texas at Dallas
Center for Quantum Electronics
P.O. Box 830688
Richardson, Texas 75083-0688

## ABSTRACT

Amorphic diamond films can be grown in a UHV environment free from hydrogen with a laser plasma discharge source. In this technique the output from Nd-YAG laser is focused on a graphite target. The gross effect of the laser beam is to eject a plume of carbon vapor and then to ionize it. At laser intensities used to produce nominal quality films, the plasma is fully ionized. It is composed of multiply charged carbon ions with kinetic energies in order of 1 keV. Quenching of such energetic ions yields diamond films that adhere more readily to materials for which there are important applications as protective coatings. Analyses of the interfaces of these films on different substrates show interfacial layers with significant thicknesses. The adhesion and mechanical properties of these amorphic diamond films on different substrates will be reported.

## INTRODUCTION

Recently, we remarked (1) upon the return of interest to the class of diamond-like carbon films which contain minimal amounts of hydrogen, if any. The first extensive survey of the properties of hydrogen-free diamond films condensed from laser plasma discharges was reported subsequently (2). There were documented the optical and mechanical properties that are so essential to the practical applications of the new material termed amorphic diamond. Scanning tunneling microscopic (STM) examinations revealed a conglomerate structure containing dense particles. At the high electric fields used in those examinations the particles were found to be more resistant to erosion than the binding component, and so were concluded to represent the most diamondlike phase. The combination of structural size together with the large band gap obtained by simple optical absorption techniques placed the material produced with our laser plasma source far outside the range accommodated by the model of graphitic islands.

In a continuation of research (3), optical properties and mass densities of deposited films were studied in detail. It was determined that the net film transparency arose from a physical mixture of clear and opaque materials and the apparent band gap served as a lower limit to the actual value characteristic of the more transparent component. The residual absorption of the films was a result of the physical mixing into the material of undigested graphite collected during the laser deposition.

Very recently microstructural studies of amorphic diamond were performed and a clear prevalence of dense nodules was observed. Grain sizes were in order of 1000 Å and the diamond character was attested by the agreement of morphology, high density, optical properties, soft x-ray spectroscopy, and lack of appreciable hydrogen. The principal conclusion was that material prepared with a laser plasma source had the structure which agreed closely with the theoretical predictions (5).

Amorphic diamond films have the unique properties of being hard but resilient, extremely resistant to chemical attacks and transparent in the infrared region of the spectrum. These properties together with the room temperature growth environment make this material suitable for abrasion and corrosion protection and for antireflective coating of sensitive and fragile optical materials used in various applications

Reported here are details of the adhesion and mechanical properties of amorphic diamond films prepared by a laser plasma discharge source. Internal compressive stress was measured using a beam bending method and a low value of 0.86 GPa was obtained. Analyses of the interfaces of these films on different substrates showed interfacial layers with significant thicknesses. The adhesion properties on ZnS and other substrates were also studied under harsh environmental conditions. It was shown that the coating of laser plasma diamond can protect substrates and increases the lifetime against abrasive wear from particulate impacts.

## PREPARATION AND CHARACTERIZATION

Figure 1 shows a schematic representation of the system reported earlier (1-3) for growing diamond films from laser plasma discharges. Basically, the mechanism for producing the laser ablation was straightforward, as seen in Fig. 1. Passing through a window into the UHV chamber with a diameter of about 8 mm, the pulsed laser beam was turned and focused with high quality optics fixed in the evacuated space. The laser delivered 250-1400 mJ to a graphite feedstock in a UHV system at a repetition rate of 10 Hz. For the production of films with nominal qualities, the beam was focused to a diameter chosen to keep the intensity on the target near $5 \times 10^{11}$ W cm$^{-2}$ and the graphite was moved so that each ablation occurred from a new surface. A high current discharge confined to the path of the laser-ignited plasma was used to heat and process the ion flux further. Discharge current densities typically reached $10^5$-$10^6$ A cm$^{-2}$ through the area of the laser focus (1). A planetary drive

system for rotating substrates within the core of the plasma where they were exposed to the ions insured the simultaneous deposition of uniform layers of amorphic diamond over several substrates disks 30 mm in diameter.

Modeling studies have recently shown that the laser input alone is sufficient to insure that the resulting plasma is fully ionized (6). At laser intensities around $5x10^{11}$ W/cm$^2$, the plasma is composed of multiply charged carbon ions with kinetic energies on the order of 1 keV (6). The impact of the laser plasma upon a substrate is equivalent to an irradiation with a very high fluence ion beam. Quenching of such energetic ions yields diamond while the condensation of neutral carbon produces only graphite (3,4).

In general, films deposited onto substrates in vacuum show internal mechanical stress which causes the substrates to bend by very small amounts. From measurements of the bending of a well-defined substrate the internal stress of the film can be calculated (7,8). Such a beam-bending method was utilized in this work to measure the internal compressive stresses of our films. As seen in Fig. 1, a thin Corning cover-glass strip was used as a film substrate. Both ends of the glass were clamped and on it a uniform diamond film with a thickness of 0.3 μm was deposited. Central deformation under the influence of the film was obtained by profiling the middle of the glass strip with a surface profilometer. A well-known equation (7) was used to calculate the stress and the value of 0.86 GPa was obtained. This value is among the low values of compressive stresses reported for diamondlike films. We believe that this stress is due to the graphitic contents introduced by the arrival of spurious particles of undigested feedstock and that the stress could be reduced further by improving the $sp^3$ content of our films.

To date, over 1500 different amorphic diamond films of thicknesses varying from 0.1 to 5.5 μm have been deposited on a variety of substrates. The fact that the films do not wrinkle, buckle, crack, or unbond, and that they exhibit good adherences is indicative of low stress values and of the deep penetration of the coating into the substrate materials.

Analyses of the interfaces of amorphic diamond films on different substrates by Rutherford Back Scattering (RBS) confirmed the formation of interlayers. Data points in Fig. 2 show a RBS spectrum of a nominal quality, 1 μm thick amorphic diamond film on a Si substrate. The composition of the interfacial layer was determined by a numerical simulation as shown in Fig. 2 by the solid line. The fit to the RBS data was obtained by assuming a composition of $10500x10^{15}$ C/cm$^2$ and $200x10^{15}$ SiC/cm$^2$. Attempts to fit the RBS data without considering SiC interlayer failed as shown in Fig.2. The dashed line plotted the simulation curve assuming $10500x10^{15}$ C/cm$^2$ while the dotted line was obtained by considering $10600x10^{15}$ C/cm$^2$. Similar RBS examinations and simulations were conducted on films deposited on ZnS, $TiAl_6V_4$, and $SiO_2$ and interfacial layers with composition of $C_{2.5}ZnS$, $C_{0.62}Ti_{0.35}Al_{0.05}V_{0.02}$, and $C_{0.5}SiO_2$ were found, respectively.

Interfacial layer formation was also observed with Transmission Electron Microscopy (TEM) examinations of interfaces between films and substrates. Fig.3 shows a transmission electron micrograph of the amorphic diamond interface with the $TiAl_6V_4$ substrate. The interface was underlined by a discontinous crystalline precipitation of TiC compounds. The electron diffraction pattern in this region was found to be characteristic of an usual epitaxial relationship with the substrate. These results indicated that amorphic diamond films had been chemically bonded to a wide variety of substrates by the condensation of crystalline or amorphic interface layers of compounds or alloys between the substrate and the film. The intermixing of the substrate and coating were expected to be the cause of good adherence between amorphic diamond films and a variety of substrate materials.

## PROTECTIVE COATINGS OF AMORPHIC DIAMOND

Amorphic diamond films have the potential to protect optical windows such as Ge and ZnS when it is important to maintain the integrity of the IR transmittance of the window. In such applications films must be adherent and durable so that they can protect the windows from rain and particulate erosions. In order to establish a general magnitude of improvements in the resiliency of films to the dust erosions, a quick look test apparatus has been constructed at our laboratory. A sand blaster has been modified and incorporated into a test fixture for measuring both the surface erosion effect on diamond film coating and the substrate material. Although natural diamond is not thought to be resistant to the chipping caused by impacts of high velocity particles, our amorphic diamond films were found to be resistant. Using the sand abrader with glass beads 20-40 μm in diameter it was found that only 1.0 μm of diamond significantly improved the resistance of a Si substrate to chipping.

Figure 4 plots Log $[(I-I_0)/I_S]$ as a scale of damage versus the times for which bare and coated Si substrates were sand blasted. The scattered He-Ne laser intensity at 20° from the damaged film is given by I, while $I_0$ is the same quantity measured before damage and $I_S$ is the intensity from a standard scattering object for calibration. Differences in the details of the damage mechanisms between single crystal Si and amorphic diamond give different slopes and forms to the curves making it difficult to extract a single number for improvement. However, considering that a half order of magnitude increase in light scattering from the damage pits is clearly significant the levels of damage can be drawn in Fig.4. It can be seen that a 1 μm thick coating of amorphic diamond extends the lifetime against chipping of a Si wafer by a factor of 30 to 50.

## ACKNOWLEDGMENT

The authors acknowledge the contributions of J.C. Pivin of the CNRS Laboratory at Orsay, France, for measurements of the RBS spectra and TEM examinations. We express our appreciation to R.K. Krause for arranging and maintaining the deposition system. This work was supported by Wright Patterson Air Force Base through Research applications, Inc.

## REFERENCES

1. C. B. Collins, F. Davanloo, E. M. Juengerman, W. R. Osborn, and D. R. Jander, Appl. Phys. Lett. 54, 216 (1989).

2. F. Davanloo, E. M. Juengerman, D. R. Jander, T. J. Lee, and C. B. Collins, J. Appl. Phys. 67, 2081 (1990).

3. F. Davanloo, E. M. Juengerman, D. R. Jander, T. J. Lee, and C. B. Collins, J. Mater. Res. 5, 2398 (1990).

4. C. B. Collins, F. Davanloo, D. R. Jander, T. J. Lee, H. Park, and J. H. You, J. Appl. Phys. (June 1991).

5. J. C. Angus, Y. Wang, and R. W. Hoffman, Proceedings of the ICNDST-2 Conference, (Washington, D.C., Sept. 1990) pending.

6. J. Stevefelt and C. B. Collins, Paper 5-16 presented at ESCAMPIG Conference, Orleans, France, Aug. 28-31, 1990.

7. H. K. Pulker, Proc. 8th Int. Conf. on Vacuum Metallurgy, Linz, Sept. 30 - Oct. 4, 1985, Session C4.2, 115.

8. B. Goranchev, K. Schmidt, and K. Reichelt, Thin Solid Films, 149 (1987) L77.

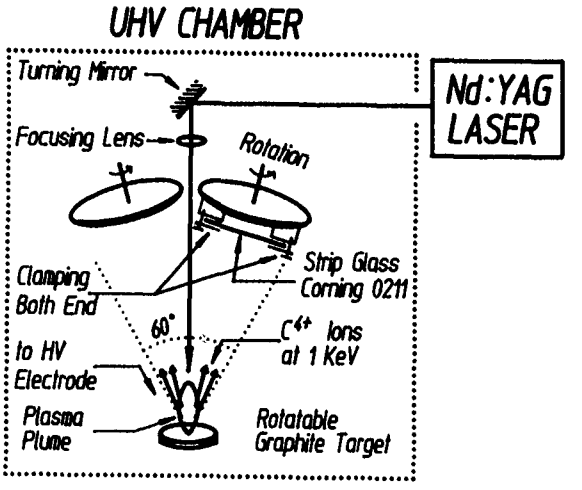



Figure 1: Schematic representation of the laser source used to deposit thin film amorphic diamond. The strips of glass were used as substrates in order to measure the stress.

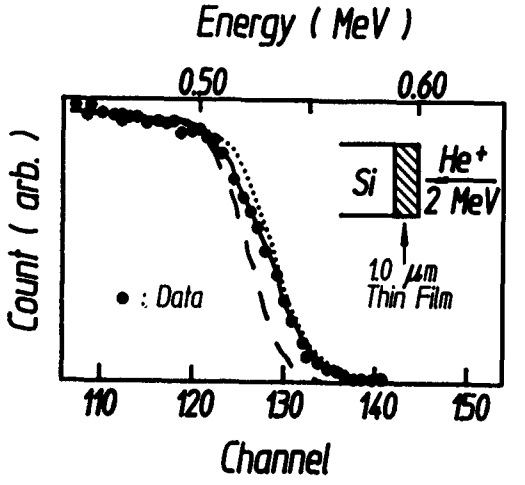



Figure 2: A $He^+$ backscattering spectra of amorphic diamond film on a Si substrate. The solid line shows the best fit obtained with the simulation considering an interfacial SiC layer. Dashed and dotted lines are simulation attempts to fit the data assuming pure carbon interlayers. (Courtesy of J. C. Pivin, Orsay, France)




Figure 3: Transmission electron micrograph of the amorphic diamond film on a $TiAl_6V_4$ substrate. An interfacial layer of TiC with precipitation feature is clearly seen. (Courtesy of J. C. Pivin, Orsay, France)

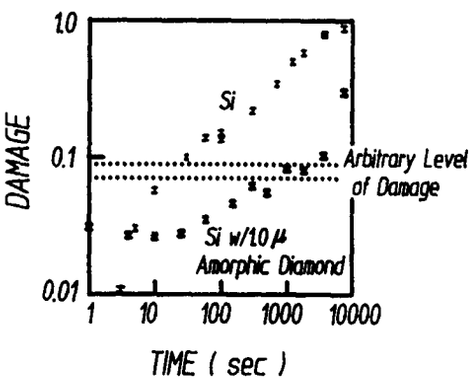



Figure 4: Plot of the damage observed on test samples as functions of the times for which they were exposed to the high velocity impact of a flux of glass beads. Damage is plotted in units of the ratio of the relative scattering of laser radiation incident at a 20° angle from the surface. Data describe measurements on a sample of amorphic diamond film chemically bonded to a Si substrated in comparison to a similar uncoated substrate.

# WIDE-BANDGAP DIAMOND-LIKE CARBON FILMS FORMED BY RF-DEPOSITION USIMG MAGNETRON DISCHARGE.

V.V. Sleptsov,V.M. Elinson,N.V. Simakina,A.M. Baranov
NPO "Vacuummashpribor",USSR, Moscow 113105, Nagorny pr.7

ABSTRACT.

RF-deposition method using magnetron discharge has the properties which are summarized below:the ion energy is not in excess of 350 eV,specific output power of substrate is 1.5 $W/cm^2$.

The a-C:H films with following optical properties n=1.8-1.9; k=0-0.1; $E_g$=2-2.5 eV have been obtained.Growth rate was 0.18 $\mu m/min$.

With introduction of fluorinated components into medium of hydrocarbons a-C:H films with optical band gap in range $E_g$ =2.5-3.2 eV and specific resistance up 10 Oh*cm were produced.

Diamond-like carbon films permit to use them as protective,passivating and tearless coatings as well as active elements for micro- and optoelectronics due to their high hardness,chemical inertness,transparency in IR region and possibility to change optical and electrical properties in wide range.

Among the formation methods of films on the basis of carbon, differing in energy range of particles and power supply process[1-4], the low-energy, low-temperature methods based on heterogeneous ion- assisted reaction of hydrocarbons on the substrate surface attracts a great deal of interest, Reduction in particle energy taking part in formation of films permits the film production with increased content of diamond phase and corresponding film properties.

Besides, low-energy particles permited the semiconductor-diamond-like film heterojunctions with negligible quantity of surface states on the interface to be formed.

The purpose of this work is to investigate formation features and properties of wide bandgap diamond-like films obtained by RF-deposition using RF magnetron discharge.

The deposition process was carried out by equipment which provided individual operation of 100 mm diameter plates with irregularity +3 %.There are water-cold cathod-substrateholder and magnetic system in the center of the camera.The magnetic system creates field (B =180 W) near electrode.RF bias with frequency of 13.56 MHz was applied to the cathod.The applied to the operated surface power could reach 1.5 $W/cm^2$.Carbon films were formed by partially-ionized hydrocarbon flow ($C_6 H_{12}$ ).Operating presure was in the range 0.2-4.0 Pa.Ion current density reached to 4.5 $mA/cm^2$.Growth rate was 0.18 μm/min.Films thicknesses were more than 1.5 μm.

The dependences of growth rate,optical constants (n,k) and optical bandgap ($E_g$) on ion energy and operating pressure were studied.

The growth rate increase proportionally to applied RF power (Fig.1).The dependence of growth rate on operating pressure is the similar and is presented in Fig.2.

Calculation of n,k and d values based on the measurement of transmission (T) as well as the film (R) and substrate (R') reflectivity in the visible and IR-region.Measurement of T,R and R' were performed by SPECORD M-40.Measurements accuracy of transmission and reflection was 0.3 % and 0.5 %,respectively.The effects of light interference in the film and multiple reflection of light in the quartz wafers were taken into account.

The optical bandgap of these films were determined.The dependence of $E_g$ on RF power are presented in Fig.1.The E reachs the maximum value when power was 80 W.The ion energy in this case was 80 eV.

In the wavewlenght range 5-10 μm all the films are transparent.In the range 0.6-0.8 nm the transmission strongly depends on formation conditions.

The resistivity value of a-C:H films changes from $8*10^9$ up to $8*10^{10}$ Ohm*cm and depends on formation conditions.

The composition of a-C:H films was studied by SIMS.Regular spectrum of a-C:H film contained $^{12}C^+$, $^{13}CH^+$ and $^1H^+$ secondary ions is shown in Fig.3.It was found that spectra with maximum value of $E_g$=2.0 eV had minimum peaks values of $^1H^+$ and$^{13}CH^+$ and maximum values of $^{12}C^+$ peak.

With introduction of fluorinated components into medium of hydrocarbons,the a-C:H films with optical band

gap in the range Eg=2,5-3,2 eV and specific resistance (up $10^{15}$ Ohm*cm) are produced.

So, RF-deposition was employed for generation of wide-bandgap a-C:H and a-C:H:F films with high specific resistance and producability.

## R E F E R E N C E S.


[1]. J.W. Zuo,K. Reichelt, K.Schmiot, J. Appl. Phys. 65, N10, 1989.

[2]. V.M.Elinson, V.V.sleptsov, V.I.Polyakov, P.I.Perov, Abstract of Fist European Conference "Diamond and Diamond-like Carbon Coatings", Switzerland, Crans-Montana, Sept.17-19,1990,p. 18.

[3]. G.F.Ivanovsky, V.M.Elinson, V.V.Sleptsov, V.I.Polyakov, Abstract of Fist Conference "Physical basis of solid state Electronic", USSR, Leningrad, 1987, v.A, p.67.

[4]. G.F.Ivanovsky,V.M.Elinson,V.V.Sleptsov,P.E.Kondrashov, Electronic Industry, 1989, N12, p.26 (in Russian).

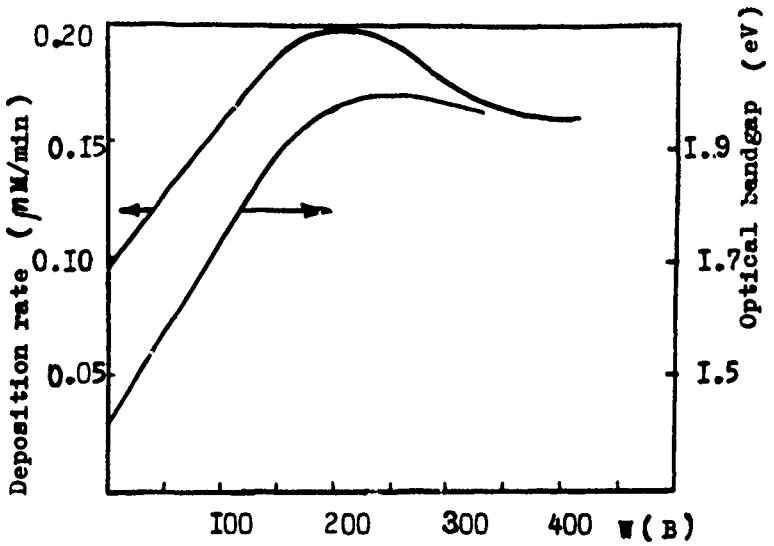



Fig. 1, Deposition rate and optical bandgap depending on power to substrate

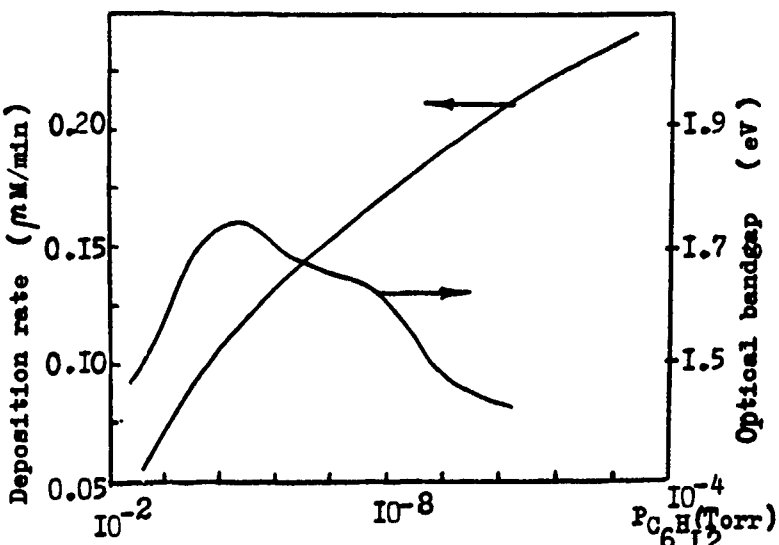



Fig. 2, Deposition rate and optical bandgap depending on pressure $C_6 H_{12}$

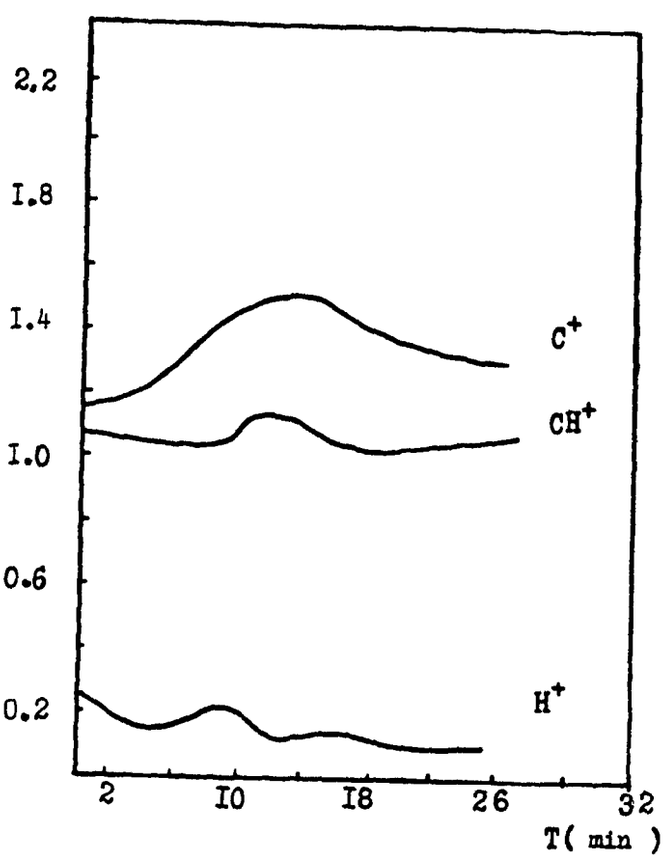



Fig. 3 Mass - spectrum of carbon surface.

# DIAMOND-LIKE CARBON FILMS: DEPOSITION PROCESSES, PROPERTIES AND APPLICATIONS.

G.F. IVANOVSKY, V.V. SLEPTSOV, V.M. ELINSON, A.M.BARANOV, A.A. KUZIN, S.S. GERASIMOVICH
NPO "VACUUMMASHPRIBOR", USSR, Moscow, 113105,Nagorny pr.,7.

P.E. KONDRASHOV
Institute of Electronic Mashinbuilding USSR, Moscow, 109028, Bol.Vuzovsky per.,3/12

ABSTRACT

The comperative analysis of properties of diamond-like carbon films formed by plasma-enhanced CVD-method and magnetron sputtering of graphite target is carried out.

The influence of process parameters and film thickness on the phase composition, electrical and optical properties as well as mechanism of a-C:H film conductivity are investigated.

By means of effective medium approximation it is shown that a film's properties depend on phase composition.

It is shown that carbon films may be used as protective coatings for optical elements of power laser and traditional optics.

Heterostructures, Si-,GaAs- a-C:H films were obtained. The correlation between deposition condition and density of surface states at the semiconductor - a-C:H film interface is determined.

Multilayer quantum well structures also have been obtained on the base of a-C:H films of different phase composition.

## 1. Introduction.

Having a great number of stable and metastable modifications, and high activated barriers between them,

carbon is a basis of class of compounds, as distinct from some ones with concrete properties(1).

So carbon films, exhibiting many unique physical properties, such as high microhardness, high transparancy, high resistivity, chemical inertness, ecological cleanliness of starting materials may be considered as new perspective material for optics and as reflective and steering mirrors in X-ray optics as well as elements of electronics (2,3).

Amorphous carbon films(a-C:H) may be produced by means of different ion-plasma methods (4-6).In this paper the properties of carbon films obtained by two methods (plasma-enhanced CVD-method and magnetron sputtering of graphite target) are presented and possible application fields are defind

2.Experimental details.

Amorphous carbon films were prepared by plasma-enhanced CVD-method formed by cyclohexen vapour and by the sputtering of graphite target in Ar,$C_6H_{12}$ and their mixtures.The deposition was carried out on fused quartz,Si,GaAs wafers and others.The preliminary oxygen and argon cleaning of wafers took place.

In the first case particle energy range was 0.5-5.0 keV,ion current density was in interval 0.5-1.5 $mA/cm^2$ ,power applied to the substrate was in the range 100-800 W.In the second case particle energy was in the range 0.1-0,5 keV,ion current density was in the range 0.1-10.0 $mA/cm^2$;power applied to the substrate was 1-100 W.

Calculations of refractive index (n),extinction index (k) on the wavelength ($\lambda$) and film thickness (d) are based on the measurement of light transmission (T) and reflection from the side of the film(R) and substrate(R').The effects of the light interference in the film and multiple reflection of light in wafer were taken into account.Measurement of T,R and R' were performed by SPECORD M-40.

The aluminium contacts and other metals produced by thermal deposition were deposited in order to study the electrical properties of the films and structure.The additional potential drop on the metallic contacts was considered during resistivity measurement.

3.Results and Discussion.

It was found that the variation of film formation condition using first method resulted in the changes in resistivity ($\rho$) from $10^5$ upto $10^8$ Ohm*cm and optical band gap ($E_g$) 1.0-1.5 eV obtained from Tauc's coordinates (7).When the graphite target is sputtered in various medium, change from 1.0 to $10^{10}$Ohm*cm,and $E_g$ changes in the range 0.6-2.0 eV at considerably smaller power which releazed on the substrate.

On the basis of optical constants of films the phase composition was calculated.The calculation of phase composition was made by means of effective medium theory (8).The investigated films are assumed to consist of diamond-, graphite- and polymer-like component and free volume(microvoids) (9).

Films deposited by plasma enhanced CVD-method according their optical constants (Fig.1,curve 1) and phase composition (upto 40 % sp -hybridization bonds) were came nearer to diamond-like films.

Films grown by sputtering in argon consist of graphite phase (70-95 %) and have corresponding optical properties(Fig.1,curve2).

Films obtaned by magnetron sputtering in Ar and $C_6H_{12}$ contain mainly polymer phase (70-80 %) and dispersive dependence of n on k brings in evidence(Fig.1,curve 3).

The influence of thickness on the film properties is observed only during magnetron sputtering in Ar.The change in dispersive dependence of n and k at $E_g$ =0.55 eV takes place (10).

The dependence of resistivity of carbon films produced by magnetron sputtering in Ar on thickness is presented in Fig.2.It is seen that the experimental curve may be divided into 2 ranges. So far as films with thickness more 50 nm is concerned the resistivity is not practically depended on d.Reduction in thickness upto 30 nm leads to sharp increase in resistivity.

In order to elucidate the dependence of resistivity on the thickness the temperature conductance $\sigma$=f(T) have been analyzed for films with different thickness in the temperature interval 77-300 K (11).

It was found that the logarithm of conductance (In $\sigma$) is directly propertional $T^{-1/4}$ and the slopes of line are

not dependent on thickness of films when d > 100 nm (Fig.3).Such variation of corresponds to jumped mechanism of conductance along the localized states at Fermi level with variable length of jump.

Observed relations are violated when thickness of films is reduced (less then 30-35 nm); It starts to change with temperature proportional by $T^{-1/3}$ .The slopes of curve are dependent on thickness of films (a -C).Such behaviour (T) corresponds to jumped mechanism of conductance with vari le length of jump in two-dimensional case.

For films with thickness more than 100 nm the values of density of states at Fermi level $N(E_F)$,radius of localisation of wave function( $\alpha^{-1}$ ) and mean length of jump(R) were calculated at T=77 K.The density of states at Fermi level is $10^{18}$ $cm^{-3}$ $eV^{-1}$,the radius of localization of wave function is 2.4 nm and mean length of jump is 19 nm.

In higher temperature range mechanism of conductivity has been transformed from jumped to activational one.

Investigations of electrical and optical properties,high values of microhardness (>3000 $kg/mm^2$ ), density(1.2-2.8 $g/cm^3$),small value of friction coefficient permit to realize protective coatings for optical elements of power laser and traditional optics.

Coatings for laser optical elements were formed by means of magnetron sputtering of graphite target using gas phase containing different hydrocarbons.The thickness of a-C:H films depositing on the surface of element is 25.0-50.0 nm.Coating transparency ranging from 4.6 up to 5.6 $\mu m$,hardness,porosity,corrosion- and beam resistance were studied (12).

The reflection coefficients of mirrors protected by a-C:H films and without them are coincided.The reflection coefficients were 98.0$\pm$ 0.5.The results of investigation of copper mirrors with diamond-like coating have been shown that there were no changes in scattering coefficient after mirror exposure in fluorine atmosphere during 15 hours at p ssure 35 tor.

The structure of protective coatings on the basis of a-C:H films as well as short-range order,size and type of clusters are studied by Auger-electron spectroscopy (13).Microhardness of films depending on formation conditions was 3000-4000 $kg/mm^2$.

Optimal thickness of protective coating having maximum

beam resistance was determined.Service life of laser mirrors with protective coating based on a-C:H films was increased by 3-4 times.

Multilayer coatings on the basis of a-C:H films increase beam resistance of mirrors compared with monolayer ones.In addition the multilayer coatings may be considered as protective coatings for laser optical elements of nearest IR region.

Besides these traditional applications areas selective multilayer reflective mirrors based on Cr-C and W-C systems(reflective coefficient 20-25 %) and stirring mirrors (reflective coefficient 60 %) for soft X-ray region have been prepared (14).

The properties of single-crystal semiconductors - carbon films heterostructures formed on Si and GaAs substrates have been studied.The thickness of carbon films was 30.0-100.0 nm.Si and GaAs substrates have a different type of conductivity and various resistivity.

Voltage-current and voltage-capacitance and charge transient characteristics of these structures have been studied by Q-DLTS method (15).

The alternation of "ultra thin" diamond-like films with different phase composition permits multilayer quantum well structures with minimum diffusion processes to be formed.Quantum effects have been demonstrated in voltage-current characteristics behavior.

It also found out that films formed by mentioned methods could be utilized as protective coatings for photomasks and protective and passivating coatings for electronic scheme and devices.

4.Conclusions.

It was found that the change of properties under changing deposition conditions might be related to phase composition variation.

The phase composition of a-C:H films and their optical and electrical properties may be also changed during growth process.The observed change was found in the films obtained in Ar.

The results of using a-C:H films as protective coatings for optics were presented.Such coatings increase

the service life of power laser optical element in 3-4 times.

It has been shown that essential possibility of heterostructures production with density of surface states about $5*10^{10}$ cm$^{-2}$ at the semiconductor-a-C:H film interface being acceptable for production of MOS-device.

## REFERENCES.


[1] J.Robertson, Phil. Mag. Let. V.57 (1988) N2 143.
[2] Jae E. Oh., Joel D. Lamb, Paul G. Snyder, John A. Woollam, David C. Lin, Sol. St. Elect. V.29 (1986) N6 933.
[3] Z.M.Chen, J.N.Wag, X.Y.Mei, G.L.Kong, Solid St. Commun. V.58 (1986) N6 379.
[4] S.Aisenberg and R.Chabot, J. Appl. Phys. V.42 (1971) 2953.
[5] A.Bubenzer, B.Dishler, G.Brandt and P.Koidl, J. Appl. Phys. V.54 (1983) 4590.
[6] T.Mori and Y.Namba, J. Appl. Phys. V.55 (1984) 3276.
[7] J.Tauc, R.Grigorovici, A.Wancu, Phys. Stat. Sol. V.15 (1966) 627.
[8] I.Webman, J.Jortner and M.H.Cohen, Phys. Rev. B15 (1977) 5712.
[9] M.B.Gooseva, V.G.Babaev, V.V.Hvostov, O.Yi.Rylova, G.F.Ivanovsky, V.V.Sleptsov and V.M.Elinson, Poverkh. Fiz. Khim. Mekh. N.11 (1987) 101.
[10] A.M. Baranov, S.S.Gerasimovich, V.M.Elinson, A.A.Kuzin, V.V.Sleptsov and P.E.Kondrashov, Phys. Stat. Sol. (A) V.122 (1990) K139.
[11] A.M.Baranov, V.M.Elinson, P.E.Kondrashov and V.V.Sleptsov, Zh. tekh. Fiz., Pisma N3, 36 (1990).
[12] G.F.Ivanovsky, V.V.Sleptsov, V.M.Elinson, P.E.Kondrashov, Elektron. Promyshl. N2 (1989) 26.
[13] O.Yi.Sokol, G.F.Ivanovsky, V.V.Sleptsov, V.M.Elinson and S.S.Gerasimovich, Mikroelekronika,19,103 (1990).
[14] A.V.Vinogradov, V.M.Elinson, V.I.Zhilina, N.N.Zorev, G.f.Ivanovsky, I.V.Kozhevnikov, M.E.Plotkin, S.I.Sagitov, Nuclear Instruments and Methods in Physics Research A(261) (1987) 101.
[15] V.M.Elinson, V.V.Sleptsov, V.I.Polyakov, P.I.Perov, Abstracts First European Conference "Diamond-Like Films" Crans-Montana, Switzerland, 1990, 13.6.

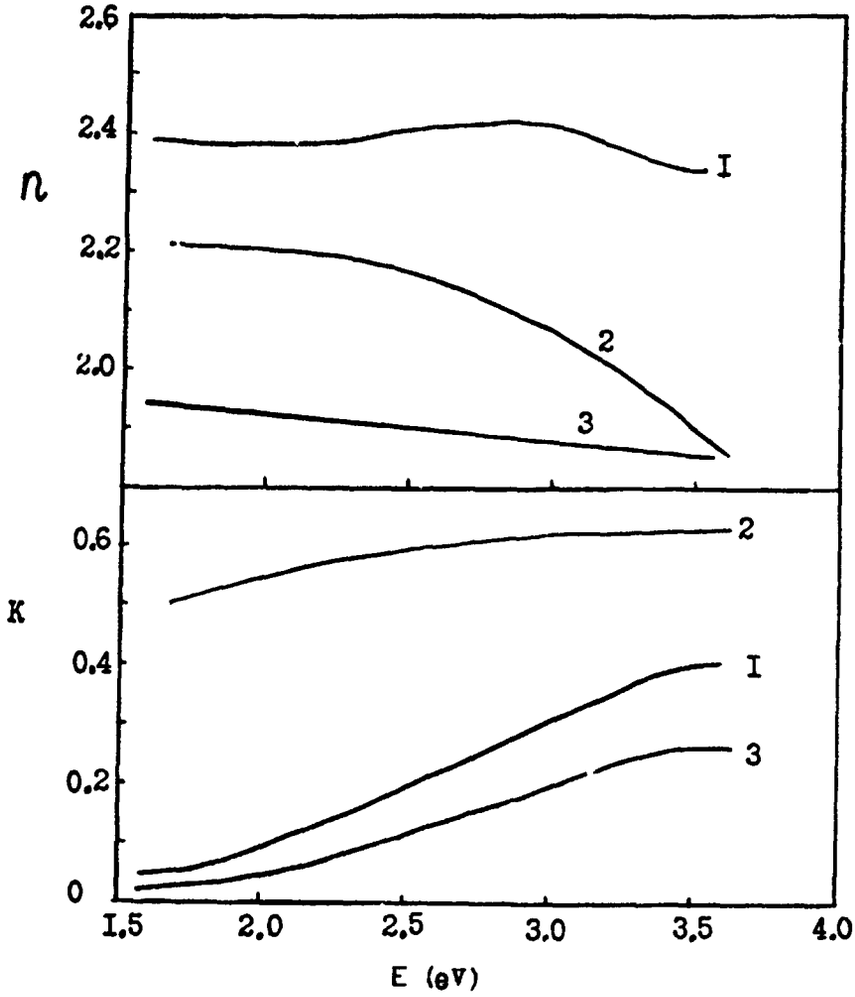



Fig.I. Refraction (n) and extinction (k) coefficiens for films obtained by:
I- plasma-enhanced CVD method;
2- magnetron sputtering of graphite target in Ar environment;
3- magnetron sputtering of graphite target in $Ar/C_6H_{12}$ = I/I environment.

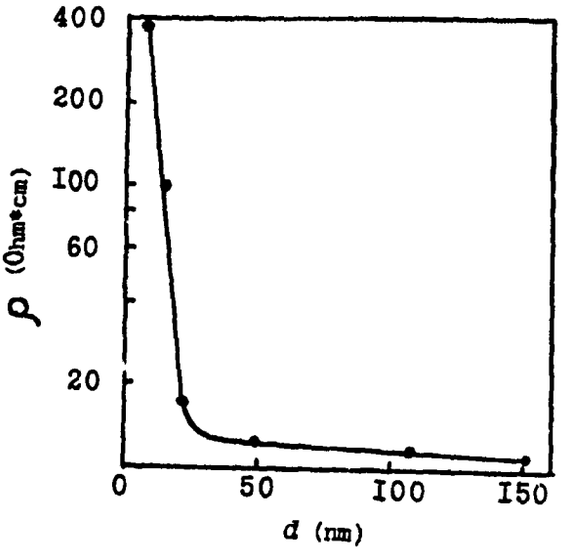



Fig.2. Dependence of a-C:H films resistivity on the films thickness.

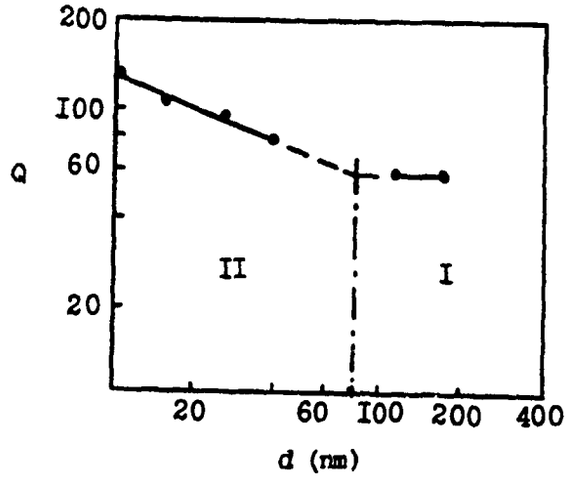



Fig.3. Influence of a-C:H films thickness on dependences slope for $\ln(\sigma)=f(T^{-1/4})$ (region I) and $\ln(\sigma)=f(T^{-1/2})$ (region 2).

## AUTHOR INDEX


| Author | Page |
|---|---|
| Adams, S.F. | 471 |
| Aisenberg, S. | 400 |
| Aklufi, M. | 39 |
| Alam, M. | 348, 463 |
| Alexenko, A.E. | 597 |
| Alley, R.G. | 523 |
| Altshuler, A. | 400 |
| Anderson, A.B. | 125 |
| Angus, J.C. | 125 |
| Anschel, M. | 625 |
| Ascarelli, P. | 266 |
| Bai, B.J. | 3 |
| Baragiola, R.A. | 181 |
| Baranov, A.M. | 640, 645 |
| Belton, D.N. | 170 |
| Black, D.R. | 274 |
| Blatter, A. | 357 |
| Bogli, U. | 357 |
| Bonafede, S. | 455 |
| Bonnot, A.M. | 282 |
| Boring, J.W. | 181 |
| Bouilov, L.L. | 357 |
| Brock, D. | 39 |
| Buck, M. | 625 |
| Cao, X. | 333 |
| Cappelli, E. | 266 |
| Carduner, K.R. | 385 |
| Carruthers, J.R. | 290 |
| Celii, F.G. | 249 |
| Chapliev, N.I. | 357 |
| Chen, H. | 455 |
| Chen, X.K. | 73 |
| Chu, C.J. | 3 |
| Chuang, T.J. | 625 |
| Collins, A.T. | 408, 633 |
| Craigie, C.J. | 91 |
| Crosley, D.R. | 202 |
| Das, K. | 523, 543, 558 |
| Davanloo, F. | 633 |
| Davidson, J.L. | 333 |
| Dillion, R.O. | 455 |
| Dorfmann, V.F. | 393 |
| Doty, F.P. | 181 |
| Dreifus, D.L. | 543, 558 |
| Drory, M.D. | 326, 340 |
| Eckermann, T. | 224 |
| Efremow, N.N. | 539 |

| Author | Page |
|---|---|
| Elinson, V.M. | 566, 640, 645 |
| Ellis, C.D. | 608, 615 |
| Eranen, S. | 530 |
| Ermakova, M.G.. | 566 |
| Ermakova, O.N. | 566 |
| Farabaugh, E.N. | 427 |
| Feldman, A. | 427 |
| Fontana, S. | 266 |
| Fountain, G.G. | 274, 523, 558 |
| Freedman, A. | 494 |
| Freitas, J.A. | 81, 91 |
| Frenklach, M. | 142 |
| Fujimori, N. | 487 |
| Furtak, T. | 455 |
| Furukawa, S. | 154 |
| Gardinier, C.F. | 326 |
| Gardos, M.N. | 365 |
| Gat, R. | 125 |
| Geis, M.W. | 125, 539, 605 |
| Gerasimovich, S.S. | 566, 645 |
| Girshick, S.L. | 57 |
| Glass, J.T. | 543 |
| Grahn, K. | 530 |
| Grill, A. | 374 |
| Grinberg, V.R. | 451 |
| Han, Q.Y. | 115 |
| Hanssen, L.M. | 81 |
| Hattangady, S.V. | 523 |
| Hartnett, T. | 435 |
| Harris, S.J. | 170 |
| Haubner, R. | 314 |
| Hauge, R.H. | 3, 365 |
| Heberlein, J. | 99, 107, 115 |
| Herres, N. | 224 |
| Hewett, C.A. | 551, 581 |
| Hiraki, A. | 258, 420 |
| de la Houssay, P.R. | 581 |
| Hsu, W.L. | 217 |
| Hudson, G.C. | 12, 209, 274, 523 |
| Humphreys, T.P. | 209, 274, 523 |
| Hunn, J. | 65 |
| Hunziker, L.E. | 202 |
| Imai, T. | 487 |
| Ingram, D.C. | 479 |
| Ivanovsky, G.F. | 566, 645 |
| Jander, D.R. | 633 |
| Jaworske, D.A. | 608 |
| Jeffries, J.B. | 194, 202 |
| Jesser, W.A. | 181 |

| Author | Page |
|---|---|
| Kamo, M. | 12 |
| Kawarade, H. | 258, 420 |
| Klein, C. | 435 |
| Klyuev, Yu. A. | 451 |
| Kobashi, K. | 543 |
| Koidl, P. | 224 |
| Kolchemanov, N.A. | 451 |
| Komplin, N.J. | 3 |
| Konov, V.I. | 357 |
| Kulvalainen, P. | 530 |
| Kuzin, A.A. | 645 |
| Lake, M.L. | 479 |
| Landstrass, M.I. | 574, 589 |
| Lau, Y.C. | 57 |
| Lee, T.J. | 633 |
| LeGrice, Y.M. | 209 |
| Leroy, J. | 282 |
| Lewis, J.K. | 455 |
| Li, C. | 57 |
| Li, Z. | 125 |
| Lopez-Rios, T. | 282 |
| Lu, Z.P. | 99, 107, 115 |
| Lux, B. | 314 |
| Ma, J.S. | 258 |
| Mantani, M.J. | 12 |
| Mathis, B. | 282 |
| Markunas, R.J. | 12, 186, 209, 274, 523, 558 |
| Margrave, J.L. | 3, 365 |
| Malta, D.P. | 274, 523 |
| Marks, C.M. | 91, 99 |
| Matera, G. | 73 |
| Matsuyama, H. | 420 |
| McAleese, N.D. | 539 |
| Mehandru, S.P. | 125 |
| Meier, U.E. | 202 |
| Meyerson, B.S. | 374 |
| Miller, A.K. | 240 |
| Miller, R. | 435 |
| Miyata, K. | 543 |
| Moazed, K.L. | 551 |
| Molinari, E. | 266 |
| Moyer, D. | 574, 598 |
| Muller-Sebert, W. | 224 |
| Nafis, S. | 455 |
| Nakahata, H. | 487 |
| Naletov, A.M. | 451 |
| Narayan, J. | 65, 73 |
| Nemanich, R.J. | 209, 274, 523 |

| Author | Page |
|---|---|
| Nepsha, V.I. | 451 |
| Nielsen, M. | 455 |
| Oikawa, S. | 154 |
| Or, T.W. | 115 |
| Owens, T. | 502 |
| Park, H. | 633 |
| Park, J.L. | 65 |
| Patel, V. | 374 |
| Patterson, D. | 3, 365 |
| Peebles, D.E. | 348 |
| Peters, M.G. | 340 |
| Perov, P.I. | 566 |
| Pfender, E. | 99, 107, 115 |
| Phelps, A.W. | 502 |
| Phillips, R. | 49 |
| Pimenov, S.M. | 357 |
| Pinneo, J.M. | 326 |
| Plano, L.S. | 290 |
| Plano, M.A. | 574, 589 |
| Polini, R. | 266 |
| Polyakov, V.I. | 566 |
| Posthill, J.B. | 209, 274, 523, 558 |
| Pramanick, S. | 73 |
| Purdes, A.J. | 24? |
| Pypkin, B.N. | 393 |
| Ramesham, R. | 608, 615 |
| Ravi, K.V. | 12, 240, 301 |
| Rengan, A. | 65 |
| Robins, L.H. | 427 |
| Robinson, C. | 435 |
| Roppel, T. | 608, 615 |
| Rose, M.F. | 615 |
| Roser, M. | 551, 581 |
| Rudder, R.A. | 12, 186, 209, 274, 523, 558 |
| Sato, Y. | 12 |
| Seki, H. | 625 |
| Sekine, C. | 154 |
| Simakina, N.V. | 640 |
| Skotheim, T.A. | 393 |
| Sleptsov, V.V. | 566, 640, 645 |
| Smith, G.P. | 194 |
| Smith, H.I. | 605 |
| Smith, S.P. | 574 |
| Smolin, A.A. | 357 |
| Snail, K.A. | 81, 91, 99 |
| Sogi, T. | 420 |
| Soriano, B.L. | 365 |
| Speck, J.S. | 326 |

| Author | Page |
|---|---|
| Spitsyn, I.V. | 357, 597 |
| Sprague, J.L. | 400 |
| Stachowicz, L. | 107 |
| Stevenson, D.A. | 290 |
| Stinespring, C.D. | 494 |
| Stoner, B.R. | 471 |
| Sullivan, P.A. | 181 |
| Sun, Q. | 463 |
| Sunkara, M. | 125 |
| Tallant, D.R. | 348 |
| Tamor, M.A. | 385 |
| Terranova, M.L. | 266 |
| Thomas, R.E. | 12, 186, 209, 274 |
| Tsuda, M. | 154 |
| Tzeng, Y. | 49 |
| Vandersande, J.W. | 443, 471, 479 |
| Vardiman, R.G. | 91 |
| Venkatesan, V. | 523, 558 |
| Vining, C.B. | 443 |
| Vold, C.L. | 81 |
| von Windheim, J.A. | 471 |
| White,Jr., D. | 249 |
| Wild, C. | 224 |
| Wilson, R.G. | 574, 581 |
| Woodhouse, J.D. | 539 |
| Xiao, Z.L. | 3 |
| Yagyu, H. | 258 |
| Yoder, M. | 513 |
| Yokota, Y. | 420 |
| Yonehara, T. | 258 |
| You, J.H. | 633 |
| Zeidler, J.R. | 551, 581 |
| Zoltan, A. | 443 |
| Zoltan, D. | 471, 479 |

## KEYWORD INDEX


| Keyword | Page(s) |
|---|---|
| (100) electron channeling pattern | 312 |
| (100) faces | 34, 38, 83, 227 |
| (110) faces | 83 |
| (111) faces | 34, 38, 40, 70 |
| (110) phosphorus profile | 29 |
| (110) surface | 170 |
| (100) surface oxidation | 467 |
| (111) surface oxidation | 467 |
| (100) texture | 228, 353 |
| (110) texture | 229, 251 |
| (111) texture | 251 |
| (1x1) pattern | 187 |
| (2x1) pattern | 187 |
| $^{13}C$ content | 451 |
| abrasive powders | 316 |
| absorption spectra - hot filament | 442 |
| absorption spectra - infrared | 419, 440, 441, 442 |
| absorption spectra - microwave deposition | 441 |
| absorption spectra - UV-visible | 22, 419 |
| acceptor energy | 590 |
| acetone | 117 |
| acetylene ($C_2H_2$) | 82, 91, 170, 209 |
| activation energy - conduction | 475 |
| active electronics applications | 306 |
| adhesion | 348, 351, 369 |
| adhesion values | 352 |
| alcohol | 6 |
| alternate deposition | 311 |
| alternating chemistry | 31, 36 |
| amorphous carbon | 633 |
| anemometer | 608 |
| applications | 513, 645 |
| argon ion etching | 259 |
| aromatic condensation | 143 |
| atmospheric plasma jet | 115 |
| atomic coordination | 385 |
| atomic force microscope | 502 |
| atomic force microscope image | 507, 508, 509 |
| atomic hydrogen | 85, 391, 513 |
| atomic steps | 34, 38 |
| Auger spectrum - heat treatment | 485 |
| band A emission | 413 |
| bandgap | 567 |
| binding energies to diamond | 514 |
| boat configuration | 134 |

boat-boat conformers 138
bond lengths 135
boron concentration 29
boron depth profile 548
boron doped conductivity 425
boron doping 422, 523, 546, 559, 589, 597
boron impurity 409
bound exciton recombination 420
boundary layer 61, 94, 195
brale indentation 345
breakdown field 560
breakdown voltage 534, 561
Brout sums 440
C atom addition 197
C implantation into Cu 517
$C(^1D)$ addition 155
$C_2H_2$ production 215
$C_2H_2$ vs. $CH_3$ 148
$C_2H_2^-$ 182
$C_{60}$ 128
cantilever beams 624
carbide formation 317
carbon atom inventory 223
carbon bridge formation 162
carrier concentration - B doping 528
carrier concentration - Li doping 528
carrier concentration vs. temperature 587, 588
cathodoluminescence (CL) 22, 26, 411, 427
cathodoluminescence centers 431
cathodoluminescence image 424, 434
cathodoluminescence intensity ratio 433
cathodoluminescence spectra 419, 424, 433
$CCl_4$ 121
cemented carbide substrates 318, 340
$CF_3$, $C_2F_2$, HF 17
$CF_4$ 14
CH 196
$CH_3$ 196
$CH_4$ concentration dependence 21, 32
$CH_4$ to $C_2H_2$ conversion 211
$CH_4/C_2H_2$ ratio 219
$CH_4/H_2$ ratio 113
chair configuration 134
chemical gas transport 597
chemical gas transport reactor 604
CHEMKIN 195
chlorine 494
chlorine - surface coverage 499
cholorofluorocarbon 7

clustering 388
coefficient of friction 372, 373
cold cathodes 539
columnar growth 238
competative shadowing 247
concentration vs. reaction time 201
conductivity 399
conductivity - P doping 604
contact resistance - ambient effects 553
contact resistance vs. time/temperature 557
contacts - Al 544, 559
contacts - heat treated Al 561
contacts - refractory metal 552
contacts - $SiO_2$ interfacial layer effect 558
contamination 20
copper substrate 9, 73
corrosion resistance 518
counter-flow liquid injection reactor 119
covalent radii of dopants 599
crack length 329
critical-point phonon frequencies 439
cross-section 281, 311, 631
cross-section - B doped 592
crystal perfection 76
cycle time 52
cyclic growth 49
D and G bands 68
dc plasma 290, 358, 366
dc-arc-jet 194
Debye temperature 446
defect characterization 427
density 456
density simulation 248
deposition rate 216, 403, 643
diamond properties 403
diamond to graphite conversion 360
diamond/substrate adhesion 321
diamondlike carbon (DLC) 65, 374, 385, 393, 401, 640, 645
dielectric strength 520
diffusion - grain boundary 575
diffusion - Li 574
dimer row growth 169
diode - MIS 543
diode - polycrystalline diamond 543
diodes - power simulation 530
disequilibrium ratios 149
dissociation time 43
DLC deposition 66
DLC renucleation 244

DLTS spectra - Si/α-C:H 573
edge emission 28
elastic light scattering 282
electrical conductivity -- 1200 C 471
electrical conductivity vs. temperature 477, 478, 484
electrical testing - high temperature 583, 586
electroactive 397
electrode spacing 294
electroluminescence 412
electron affinity 539
electron-hole pairs 413
emission efficiency 540
emission intensity ratio 426
energy transfer 100
enthalpy changes 174
epitaxy 600
etch rate 364
ethanol 117
excimer laser 357
F abstraction 147
faceted octagonal growth 88
field emitter array 313
film decohesion 346
five-fold twinning 139
flame deposition 81
flame front 92, 96
flame shape 96
flame synthesis 240
flash diffusion 444
flashback limit 97
floating potential profile 296
flow modeling 252
flow pattern 257
flow profiles 118
fluorinated diamond 365
fluorination parameters 371
fluorine 4, 494
fluorine - surface coverage 500
forward recoil elastic scattering 382
fracture mechanics 342
fracture surface 339
fracture toughness 326, 331
free energy 5, 10
free energy change 171
free exciton 420
free-jet expansion 217
freestanding films 50, 315, 436
friction 365
friction coefficients 384
gas activation 145
gas flow measurement 608

gas flow sensor 612
gas mixing 91
gas phase chemistry 194
gas temperature 204
gaseous composition 217
gasification products 212
grain boundaries 605
grain size 110
grain structure 79
graphite edges 135
graphite flakes 128
graphite growth 76
graphite hydrogenation 141
graphite-producing plasma 294
graphitization - high temperature 455
growth kinetics 143, 324
growth mechanisms 151
growth methods 513
growth modeling 130
growth parameters - dc jet 116
growth parameters - dc plasma 291
growth parameters - plasma torch 108
growth parameters - rf plasma 59
growth parameters - torch 100
growth processes 125
growth rate 30, 37, 41, 75, 80, 176, 223, 272, 354
growth rate - P doping 604
growth rate model 246
growth rate requirements 310
growth rate simulations 132
growth sectors 89
growth velocity 225
H abstraction 144, 175, 515
H addition to benzene 140
H atom addition 133
H atom concentration 218, 222
H binding energies 134
H dosing 189
H superequilibrium 145
$H^-$ 182
H2 emission profile 296
H3 and H4 centers 414
halogen chemistry 3, 12
halogenation of (100) diamond 494
hardness 392
hardness tester 341
heat transfer modeling 613
heterojunction - Si/α-C:H 566

| | |
|---|---|
| hexagonal crystals | 138 |
| high growth rate | 58, 107 |
| high temperature deposition | 82 |
| HOMO | 159 |
| homoepitaxial surface | 280 |
| homoepitaxy | 81, 99, 274 |
| homoepitaxy morphology | 105 |
| hot filament | 73, 126, 181, 202, 217, 266, 282, 349, 428, 464, 626 |
| hydrocarbon concentration | 146 |
| hydrocarbon mole fractions | 222 |
| hydrogen anneal | 488 |
| hydrogen content | 376, 382, 386 |
| hydrogen desorption spectra | 188 |
| hydrogen evolution | 545 |
| hydrogen plasma | 293 |
| hydrogen profiles | 486 |
| hydrogenated (100) surface | 186 |
| I-V characteristics - Al contact | 563 |
| I-V characteristics - Au contact | 564 |
| I-V characteristics - cold cathode | 541, 542 |
| I-V characteristics - diamond capacitors | 578 |
| I-V characteristics - IGFET | 529 |
| I-V characteristics - interfacial SiO2 | 565 |
| I-V characteristics - MIS | 550 |
| I-V characteristics - silicon and diamond diodes | 537, 538 |
| IGFET | 523, 584 |
| impact damage | 639 |
| implant activation efficiency | 584 |
| implantation - B/C | 581 |
| implantation - N/B/Li/H | 574 |
| implantation damage | 581 |
| implantation profiles | 579 |
| impurity-activated IR absorption | 437 |
| indentation behavior | 340 |
| index of refraction | 377, 383, 651 |
| indirect exciton recombination | 423 |
| induction time | 175 |
| infrared absorption (see also IR) | 49, 56, 376 |
| insitu coatings | 315 |
| interface toughness | 341, 347 |
| internal stress | 618 |
| ion beam deposition | 401 |
| ion implantation | 69 |
| IR absorbance spectra, DLC | 380, 383 |
| IR absorption | 435 |
| IR transmission spectra | 442, 460 |
| IR transmission stability | 459 |
| isotope-labeled hydrocarbons | 148 |

| | |
|---|---|
| kinetic growth model | 142 |
| KrF excimer laser | 358 |
| laminer flow | 93 |
| Langmuir probe | 292 |
| laser deposition | 633 |
| laser etching | 357 |
| laser induced fluorescence | 203 |
| laser plasma deposition | 65 |
| laser polishing | 357 |
| lateral growth | 307 |
| lattice vibration modes | 435 |
| Laue x-ray pattern | 90 |
| leakage current | 535, 546 |
| leakage current vs. temperature | 578 |
| LEED | 187 |
| liquid copper nucleation | 522 |
| liquid precursors | 117 |
| lithium doping | 523 |
| low temperature growth | 5, 23, 516 |
| luminescence | 408 |
| luminescence centers | 429 |
| LUMO | 159 |
| mass spectrometer | 184 |
| mass spectrometry | 12, 181, 209 |
| mass spectrum | 185 |
| mechanical properties | 326, 334 |
| membranes | 304 |
| methanol | 628 |
| microchannels | 615, 620, 621 |
| microstructure - oxidized | 468, 469 |
| microwave discharge ion beam | 495 |
| microwave plasma | 20, 39, 249, 333, 480, 504, 544, 559, 617, 626 |
| Mie resonances | 285 |
| mobility vs. temperature | 587, 588 |
| model parameters for silicon and diamond | 533 |
| mole fractions | 201 |
| molecular beam epitaxy | 154 |
| molecular orbitals | 132, 155 |
| molecular orbital distributions | 161, 167 |
| molybdenum substrate | 337 |
| monel | 7 |
| monel substrate | 9 |
| morphological instability | 241, 305 |
| morphology - boron doped | 503 |
| morphology of mosaic film | 607 |
| mosaic films | 605 |
| multichip modules | 305 |
| N-processes | 452 |
| N3 centers | 414 |

nanocomposites 393
natural gas 6
negative ion 181
nitrogen impurity 409
NMR spectroscopy 376, 386
nuclear power sources 471
nucleation 314
nucleation control 589
nucleation density 74, 80, 127, 129, 273
nucleation enhancement manipulations 319
nucleation kinetics 324
nucleation on different substrates 317
nucleation precursors 126
nucleation processes 125
nucleation time 267, 324
nuclei distance 225
nuclei distribution 271
Obreimoff analysis 346
octahedral morphology 68
OH concentration dependance 208
OH radical 202
ohmic contacts - reliability 551
optical applications 303
optical bandgap 572, 641
optical centers 416
optical coatings 519
optical emission 290, 297
optical properties 24
optical reflection 236
optimally constrained network 388
organic precursors 115
organo-silicon precursors 394
oxidation 33, 463
oxy-acetylene torch 50, 54
oxygen 4, 8, 31
oxygen - surface 482
oxygen addition 515
oxygen anneal 489
packaging 615, 625
particle evolution 264
particle morphology 270
particle shape 237
particle size distribution 268
passive electronics applications 304
patterned substrates 259
perylene 127, 141
phase purity 302
phonon elastic interaction 451
phosphorus doping 23, 597
photoelectromotive force 568

photoluminescence 84, 90, 98, 410
physical deposition 400
physical properties 519
pin-on-disk tester 375
pin-on-flat testing 366
pink luminescence 416
plasma cell 15
Poiseuille phonon flow 453
polishing 276, 327
polycrystalline microchannels 622
polycrystalline morphology 18, 35, 47, 64, 122, 120, 255, 287, 325, 330, 336, 354
potential energy stabilization 162, 168
potential profile 298
preferential etching 142
preferential growth 260
preferred orientation 251
prenucleation steps 316
pressure effects 109, 114
process requirements 308
protective coatings 375, 396, 636
proton recoil detection 480
pull-test results 356
pulsed plasma 39
quantum chemistry 154
quantum yield 203
quenching distance 93
radiation damage 410
Raman half width 27
Raman peak ratios 351
Raman spectra - combustion flame 55, 89, 97
Raman spectra - dc torch 106
Raman spectra - DLC laser plasma 67, 71, 72
Raman spectra - deposition/etching cycles 55
Raman spectra - excimer laser polishing 363
Raman spectra - halogen growth 10, 11
Raman spectra - heat treatment 461, 485
Raman spectra - hot filament 78, 355, 632
Raman spectra - implanted 580
Raman spectra - microwave 21, 26, 30, 257, 331, 337, 632
Raman spectra - oxidized 470
Raman spectra - pulsed plasma 48
Raman spectra - rf plasma 63, 214, 281
random covalent networks 387
rate constants 174
Rayleigh scattering 284
RCA cleaning 275
reaction mechanisms 199

reaction pathways 177
recombination model 532
reflectivity 287
relative growth rate 232
relative reflectivity 288
renucleation 240, 247
requirements 405
residence time 249
residual stress 350
resistance - heating effect 491, 492, 545
resistance - oxygen plasma treatment 493
resistance change - with hydrogen and oxygen 487
resistance vs. temperature - boron doped 549
resistivity 250
resistivity - hydrogen effects 479
resistivity - implanted 576
resistivity vs. P implantation dose 577
resistivity vs. temperature 593, 594, 595, 596
responce time - flow sensor 610, 614
Reynolds number 92
rf deposition 640
rf plasma 13, 209, 274, 374, 377, 386, 458
rf-thermal plasma 57
ring compounds 136
rotational distribution 204
rotational excitation spectrum 207
Rutherford backscattering 480
scanning tunneling microscope 502
Schottky diode - gold 524
SCORPIO device sumulator 531
seeding 126
selection rules 438
selective deposition 609, 612, 616
selective diamond array 263
selective nucleation 258, 307
semiconductor devices 520
shadowing 240
silicon substrate 266
SIMS 23
SIMS profile 28
single crystal absorption 27
single-phonon absorption 436
smoothness of films 250
$sp^2$ 66
$sp^2/sp^3$ ratio 309, 378
$sp^3$ 66
$sp^3$ fraction 392

spectrally-resolved CL 429
sputtering 402, 647
stability 395
stacking sequence 131
state functions of C 158
statistical nucleation 241
statistical orientation 242
step growth 157, 163
step morphology 101
steric repulsion 172
strain energy 172, 342
strain vs. temperature 355
stress 635
structural changes 160, 164
structural requirements 308
structure-property relations 301
substrate bias 377
substrate impurities 320
substrate pretreatment 109
substrate temperature 114
substrate/gas interactions 316
sulphur doping 597
surface activation energy 457
surface conductivity 490
surface diffusion 306
surface morphology 235
surface morphology change 462
surface planarization 277
surface radicals 144
surface reconstruction 188
surface roughness 361
surface termination 514
surface topography 276
TEM 71, 98, 265
temperature gradient 146
tensile load 339
tensile strength 333
tensile stress 359
terraced atomic morphology 139
texture development 238
textured growth 224, 226
thermal activation 3
thermal cell 14
thermal conductivity 310, 360, 443, 625
thermal conductivity vs. $^{13}C$ content 454
thermal conductivity vs. temperature 449
thermal desorption 186
thermal desorption spectra 191, 192, 193
thermal plasma 99, 107

thermal stability 375
thermochemical quantities 173
thermogravimetric analysis 464
thermogravimetric data 470
three-network films 396
tool substrate materials 315
transconductance 585
transconductance - IGFET 526
transistor action - IGFET 525
transmission spectra, UV-visible 460
transmittance 94
tribological properties 374
tribometry 365
triple torch 104, 111
tungsten substrate 348, 358
turbulent flame 91
twin formation 231
twinning 224
Type Ia diamond 278, 279
Type IIa diamond 101, 275, 443, 457
Type IIa surfaces 279
Type IIb diamond 421
unreconstructed diamond 156
uplift displacement 343
UV excited luminescence 412
Vickers indentation 332
vinyl groups 176
visible light emission 408
wear tracks 378, 384
wear-resistant coatings 314
windows 303
x-ray diffraction 41, 48, 112, 138, 239, 363, 470
x-ray diffraction - mosiac film 606
x-ray pole figures 234
x-ray rocking curve 236
x-ray texture 256
x-ray topograph 279
x-ray transmission 309
XPS 19, 366, 372
XPS spectrum - halogenated diamond 496
XPS spectrum - halogenated graphite 497
yellow luminescence 415
zero-phonon lines 428